Advanced 1,2,3-Triazolate-Based Coordination Compounds:

From Carbonic Anhydrase Mimics, Molecular Building Blocks, and Catalyst Supports to Electrically Conducting Spin-Crossover MOFs

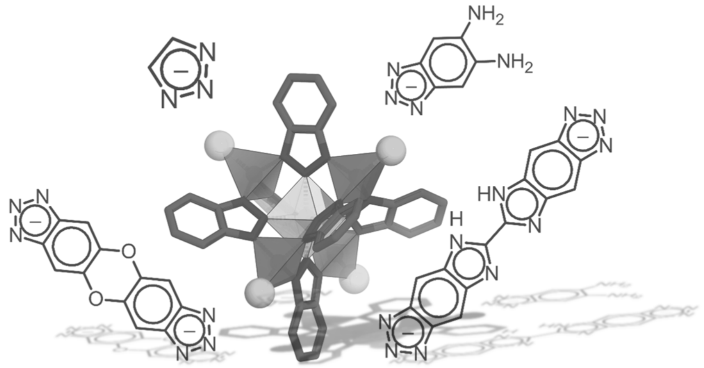

Kumulative Dissertation

zur Erlangung des akademischen Grades
Dr. rer. nat.

eingereicht an der
Mathematisch-Naturwissenschaftlich-Technischen Fakultät
der Universität Augsburg

von

M. Sc. Richard Röß-Ohlenroth

Augsburg, Dezember 2022

Erstgutachter:	**Prof. Dr. Dirk Volkmer**
Zweitgutachter:	**Prof. Dr. Achim Wixforth**

Tag der mündlichen Prüfung: **15.03.2023**

Table of contents

List of abbreviations

bta	*benzotriazolate*
CP	*coordination polymer*
DEF	*N,N-diethylformamide*
DMF	*N,N-dimethylformamide*
DMSO	*dimethyl sulfoxide*
DRIFTS	*diffuse reflectance infrared fourier transform spectroscopy*
DSC	*differential scanning calorimetry*
EDX	*energy dispersive X-ray*
FT-IR	*Fourier transform infrared*
GC-MS	*gas chromatography-mass spectrometry*
H$_2$-bbta	*1H,5H-benzo(1,2-d:4,5-d’)bistriazole*
H$_2$-bibta	*1H,1’H-5,5’-bibenzo[d][1,2,3]triazole*
H$_2$-btdd	*bis(1H-1,2,3-triazolo[4,5-b],[4’,5’-i])dibenzo[1,4]dioxin))*
H$_2$-spirta	*7,7,7’,7’-tetramethyl-6,6’,7,7’-tetrahydro-3H,3’H-5,5’-spirobi[indeno[5,6-d]-[1,2,3]triazole]*
H$_2$-tqpt	*6,6,14,14-tetramethyl-6,14-dihydroquinoxalino[2,3-b]phenazinebistriazole*
H$_4$-bibt	*1,1',5,5'-tetrahydro-6,6'-biimidazo[4,5-f]benzotriazole*
H-bta	*1H-1,2,3-benzotriazole*
H-btda	*1H-benzotriazole-5,6-diamine*
H-cybta	*5,6,7,8-tetrahydro-1H-naphtho[2,3-d][1,2,3]triazole*
H-dibanta	*2,5-di-tert-butylacenaphtho[1,2-d][1,2,3]triazole*
H-Me$_2$bta	*5,6-dimethyl-1H-1,2,3-benzotriazole*
HOF	*hydrogen-bonded organic framework*
H-OMe$_2$bta	*5,6-dimethoxy-1H-1,2,3-benzotriazole*
H-ta	*1H-1,2,3-triazole*
H-TTFN$_3$	*6-(4,5-bis(propylthio)-1,3-dithiol-2-ylidene)-1H-[1,3]dithiolo[4’,5’:4,5]benzo[1,2-d][1–3]triazole*
MAF	*metal azolate framework*
MAO	*methylaluminoxane*
MBB	*molecular building blocks*
M-HOF	*metal hydrogen-bonded organic framework*
MMAO-12	*modified methylaluminoxane – type 12*
MOF	*metal-organic framework*
MOP	*metal organic polyhedra*
MPM	*molecular porous materials*
MS	*mass spectrometry*
NMF	*N-methylformamide*
NMR	*nuclear magnetic resonance*
OMS	*open metal site*
PXRD	*powder X-ray diffraction*
RT	*room temperature*
SAW	*surface acoustic wave*
SBU	*secondary building unit*
SCO	*spin crossover*
TCNQ	*tetracyanoquinodimethane*

TEM	*transmission electron microscopy*
TGA	*thermogravimetric analysis*
THF	*tetrahydrofuan*
TOF	*turnover frequency*
Tp	*hydrotris(pyrazolyl)borate*
Tp*	*hydrotris(3,5-dimethyl-1-pyrazolyl)borate*

Abstract

Kuratowski complexes and related metal-organic frameworks (MOF), especially of the MFU-4-type, built from 1,2,3-triazolate-based ligands gained increasing interest in the last years due to their variable side ligands and metal sites. Such materials and their post-synthetic modifications have shown an outstanding potential for applications such as adsorption, capture, separation and kinetic trapping of gases, drug delivery, atmospheric water harvesting, sensing, H_2/D_2 quantum sieving, investigation of fundamental magnetic phenomena, and in particular catalysis. In this respect, MFU-4-type MOF catalysts were shown to outperform other heterogeneous catalysts for the dimerization and polymerization of olefins with some applications already advancing toward commercial applicability.

This thesis mainly aims to extend the functionality of 1,2,3-triazolate-based coordination materials via advanced linker designs, novel framework assembly strategies, and post-synthetic modifications, as well as through a better understanding of the underlying material properties. During this project, several new organic and complex building blocks, as well as advanced framework structures were prepared and characterized. Furthermore, additional emphasis was directed to the investigation and interpretation of resulting physical phenomena like phase transitions, magnetism, and electrical conductivity.

The **Zn-MFU-4*l*** ($[\mathrm{Zn_5^{II}Cl_4(BTDD)_3}]$; $\mathrm{H_2}$-BTDD = bis(1*H*-1,2,3-triazolo[4,5-*b*][4′,5′-*i*])dibenzo[1,4]dioxin) and **Co-MFU-4*l*** ($[\mathrm{Zn_{1.3}^{II}Co_{3.7}^{II}Cl_4(BTDD)_3}]$) metal-organic frameworks were prepared according to the literature procedures and modified by a post-synthetic side ligand exchange of the chloride anions, which led to MFU-4-type structures featuring organometallic metal-carbon bonds. Overall, five new **Zn-MFU-4*l*** structures of the general formula $[\mathrm{Zn_5^{II}L_{\mathit{x}}Cl_{4-\mathit{x}}(BTDD)_3}]$ ($4 \geq x > 3$; L = methanido, ethanido, *n*-butanido, *tert*-butanido, 3,3-dimethyl-1-butyn-1-ido; **Zn-MFU-4*l*-Me*, *-Et**, **-*n*-Bu**, **-*t*-Bu**, **-Butyne**) and two new **Co-MFU-4*l*** structures, **Co-MFU-4*l*-Me** ($[\mathrm{Zn_{1.5}^{II}Co_{3.5}^{II}Me_{3.1}Cl_{0.9}(BTDD)_3}]$) and **Co-MFU-4*l*-OH** ($[\mathrm{Zn_{1.4}^{II}Co_{3.6}^{II}(OH)_{3.1}Cl_{0.9}(BTDD)_3}]$), were obtained. Such side ligands were not characterized for MFU-4-type MOFs before, although they are presumed responsible for the metal site activation during olefin catalysis reactions, which require organometallic co-catalysts. For this purpose, a combination of simulated and measured IR spectra was developed as well-suited characterization technique for such insoluble materials, which preclude analytical methods like liquid state NMR and mass spectroscopy. A high stability of the organometallic **Zn-MFU-4*l*** derivatives was observed, whereas the **Co-MFU-4*l*-Me** was of a pyrophoric nature and reacted upon water contact to **Co-MFU-4*l*-OH**, which exhibited a CO_2 binding mechanism comparable to that of carbonic anhydrase.

Synthesis of Kuratowski complexes built from 1*H*-benzotriazole-5,6-diamine (**H-btda**) ligands and post-synthetic exchange of the chloride side ligands with Tp/Tp* (Tp= hydrotris(pyrazolyl)borate; Tp* = hydrotris(3,5-dimethyl-1-pyrazolyl)borate) provided us with a variety of six-fold diamine-functionalized molecular building blocks intended for the development of novel MOF construction pathways. Crystallization of those compounds have already led to the assembly of porous metal hydrogen-bonded frameworks (M-HOF), some of which have even exhibited permanent porosity. This is a rare property of this material class, which is still in its infancy with only a few structures reported so far. Overall, five new metal hydrogen-bonded framework assemblies (**CFA-20-X** ((2,6-lutidinium)$^+$[Zn$_5$X$_4$(btda)$_6$X]$^-\cdot$ *n*(DMF); X= Cl$^-$, Br$^-$), **CFA-20-Tp**, **CFA-20-Tp***, **CFA-20-Tp*-DMSO** ([Zn$_5$Y$_4$(btda)$_6$]; Y = Tp, Tp*) could be characterized, thus representing a significant contribution to this field of study. Although no MOFs could be crystallized from reactions of these complexes with metal salts, preliminary results have shown that direct incorporation of metal sites is a suitable pathway to convert M-HOFs into more stable MOFs.

Taking the functionality of MFU-4-type frameworks to the next level, the novel 1,1',5,5'-tetrahydro-6,6'-biimidazo[4,5-*f*]benzotriazole (**H$_4$-bibt**) ligand was developed to potentiate the post-synthetic modification possibilities compared to other MFU-4-type frameworks via introduction of additional and easily accessible biimidazole coordination sites at the linker backbone. This gave rise to the five most sophisticated MFU-4-type structures prepared so far. Post-synthetic Tp ligand exchange in the resulting MFU-4-type **CFA-19** ([Co$_5^{II}$Cl$_4$(H$_2$-bibt)$_3$]) provided the stable **CFA-19-Tp** ([Co$_5^{II}$Cl$_{0.4}$Tp$_{3.6}$(H$_2$-bibt)$_3$]) framework, in which the additional coordination sites were saturated in a third modification step with M^{I}Br(CO)$_3$ (M= Re, Mn) moieties or deprotonated via introduction of ZnEt moieties. The resulting materials exhibit high metal site density single-crystal X-ray structures with over 1700 atoms per unit cell for the **ReBr(CO)$_3$@CFA-19-Tp** ([Co$_5^{II}$Cl$_{0.4}$Tp$_{3.6}$(H$_2$-bibt)$_3\cdot$(Re^{I}Br(CO)$_3$)$_{2.8}$]) and a thermally induced release of all CO ligands for the **MnBr(CO)$_3$@CFA-19-Tp** ([Co$_5^{II}$Cl$_{0.4}$Tp$_{3.6}$(H$_2$-bibt)$_3$(Mn^{I}Br(CO)$_3$)$_3$]$\cdot$3.1(Mn^{I}Br(CO)$_x$)). Preliminary results also indicate a facile incorporation of other coordination moieties such as M^{II}Cl$_2$ (M= Pd^{II}, Pt^{II}). These proof-of-principle incorporations of coordination moieties and open metal sites render such CFA-19-type scaffolds promising supports for an even larger variety of active species intended for the binding and activation of small molecules in future investigations.

Coincidental synthesis of the novel **CFA-23** ((((propan-2-yl)oxidanium)$^+$[Mn$_6^{II}$Cl$_5$(ta)$_8$]$^-$; H-ta= 1*H*-1,2,3-triazole) coordination framework provided the opportunity to investigate changes of the resulting magnetic properties in comparison to a similar structure built from 1*H*-1,2,3-benzotriazole, as well as the ultra-narrow character of the pore channels in **CFA-23**.

High purity samples of the literature-known Fe(ta)$_2$ (H-ta= 1*H*-1,2,3-triazole) framework were prepared and investigated in detail to unveil its record hysteresis spin-crossover phase transition. Aiming at the use of Fe(ta)$_2$ in surface acoustic wave-based sensor applications, experimental and theoretical insights into the material's electrical conductivity changes upon adsorption of inert gases were assisted with the measurement of adsorption isotherms and the determination of the resulting isosteric enthalpies of adsorption.

1. Introduction

1.1. Porous Materials and Coordination Chemistry

Porous materials with their high internal surface areas are used in a wide range of applications, especially in the chemical and petroleum industry. The use for capture, separation and storage of gases, heterogeneous catalysis, the catalytic cracking of hydrocarbons, ion exchange, electrode materials, and water purification are among the most important ones.[1,2] In contrast to porous metal-oxides and active carbon materials, zeolites have been proven advantageous in heterogeneous catalysis due to size- and shape-selectivity induced by their well-defined and small pores, but they suffer from a lack of structural diversity.[2] Near infinite possibilities to control the size, shape and chemical properties of pores are enabled by new classes of porous materials originating from the field of coordination chemistry.

The study of coordination compounds and complexes, constitutes a combination of organic and inorganic chemistry. Coordination complexes are defined as a composition of central atoms or ions, usually metals, and surrounding ligands. The ligands can consist of charged or uncharged atoms and molecules usually bound via coordination bonds, also called dative bonds, to the central atom. Such ligand molecules can be of organic or inorganic nature. In contrast to covalent bonding, the ligands donor atom usually contributes both electrons to the bond, acting as a Lewis base, whereas the metal ions act as Lewis acids. Such compounds are of significant relevance for biological processes like photosynthesis and oxygen transport in blood, as well as drugs, and catalysts for example used in acetic acid synthesis or olefine metathesis.[3] Through interconnection and repetition of coordination entities via multi-functional ligands, coordination polymers (CPs) are formed, which can extend in 1, 2, or 3 dimensions.

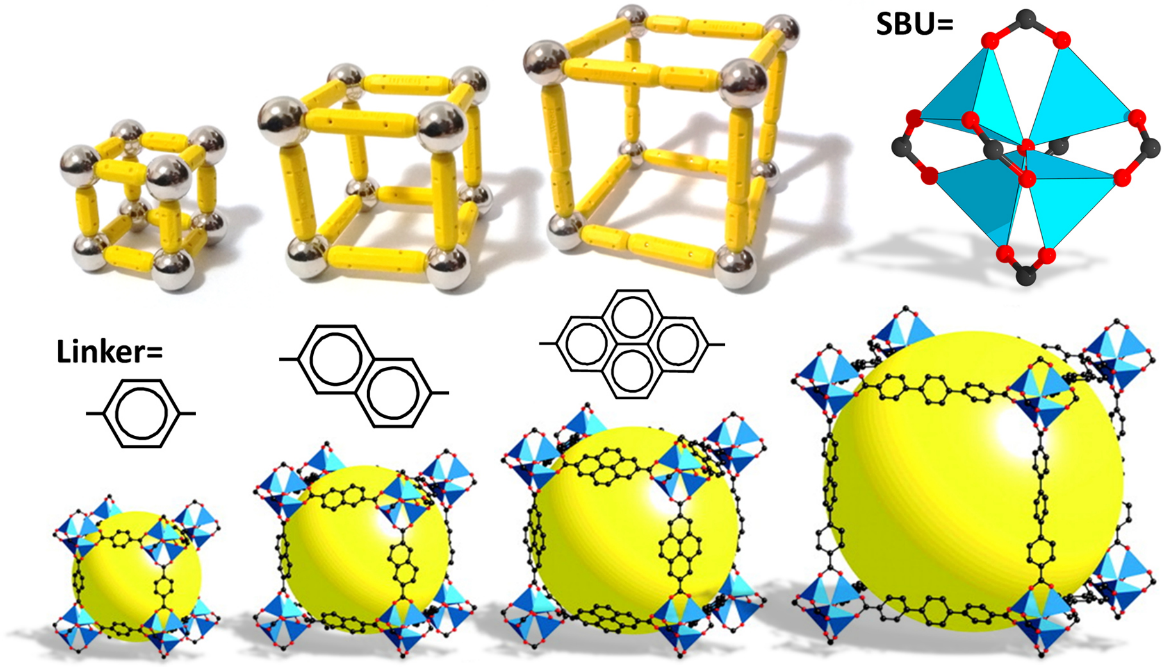

Figure 1. Visualization of the modular building-block construction principle of MOFs from SBU vertices and linker bridges leading to a variety of different isoreticular MOF-5 structures (From reference [4]. Reprinted with permission from AAAS) with increasing size of the pores (yellow).[4]

Coordination polymers are divided further into the subgroups of coordination networks, if they are interconnected in more than one dimension, and as metal-organic frameworks (MOFs), if the structure exhibits potential voids in addition.[5] This allows for a modular design principle similar to toy bricks resulting in the so-called isoreticular (same topology) construction of frameworks from the same complex units, the secondary building units (SBUs), and the linker, which is the varying backbone of the interconnecting ligand molecules (Figure 1).[4,6]

Even younger classes of potentially porous materials related to MOFs are the hydrogen-bonded organic frameworks (HOFs) and metal hydrogen-bonded organic frameworks (M-HOFs), which are constructed via intermolecular hydrogen-bonding interactions from organic molecules or metal complexes, respectively.[7] In contrast, covalent organic frameworks are porous materials constructed only from organic building blocks via covalent bonds, which are crystalline in comparison to porous polymers.[8] Intriguingly, porosity does not exclusively occur in solids but also a variety of molecular porous materials (MPMs) like metal organic polyhedra (MOP) or even porous liquids are known in literature.[9]

Starting from fundamental science with the first permanently porous MOFs reported in 1999,[10] the possibility for their rational design has led to an exponential increase in structures and anticipated applications.[11,12] A wide range of MOFs is already commercially available on the market as raw materials or even applied in the first commercial products.[12] Furthermore, these materials are expected to play a key role in the future battles against e.g. climate change, diseases, and water scarcity. In those efforts, MOFs have recently been implemented successfully in devices for energy-effective atmospheric water harvesting even in very arid desert environments.[13] Significant progress was also achieved in medicinal applications ranging from contrast agents to multifunctional drug delivery vehicles[14] and some materials even entering the first clinical trials for anticancer treatments.[15] Furthermore, they are not only envisaged for the capture of CO_2 from flue gases,[16] but also investigated especially for direct capture from the atmosphere and further catalytic conversion into valuable resources.[17] For such catalytic applications, the high surface areas and accessible active metal sites render MOFs the perfect heterogenous advancements of complexes usually only applicable in a homogeneous fashion.[18] Especially the petroleum and chemical industry is constantly looking for novel and better catalysts allowing them to save energy and money in their processes, as well as to adapt to sustainable raw materials instead of fossil ones.[19] Another aspect resulting from the tunability of interactions between MOF matrix and guest molecules is the application in sensor devices for various gases and substances.[20]

Moreover, MOFs and related framework structures are not only popular for their industrial applications but also for the fundamental understanding of physical phenomena in research fields like magnetism,[21] where they allow for the design of geometrically frustrated systems leading to spin-ice, -glass, or -liquid behavior.[22]

Although an enormous number of such framework compounds is now already known in literature (114.373 structures in the CSD MOF subset accessed with ConQuest Version 2022.1.0 software),[23] the aforementioned applications still thirst for novel materials with advanced and adapted designs. A promising series of coordination compounds in this regard, which are based on 1,2,3-triazolate-type ligands and feature pentanuclear Kuratowski-type coordination moieties have gained increasing interest in the last decade.

1.2. Kuratowski Complexes

The Kuratowski-type coordination motif, which exhibits T_d symmetry and is named after the mathematician Casimir Kuratowski,[24,25] was first reported in 1978 with the $[Cu_5(acac)_4(bta)_6]$ complex.[26] It consists of six μ_3-triazolate ligands, which are coordinated to a cluster of five metal ions. The central metal ion is octahedrally coordinated by the central triazolate N atoms and surrounded by the four peripheral metal ions in a tetrahedral arrangement. The peripheral metal ions are each coordinated by three lateral triazolate N atoms and one additional and variable side ligand (Figure 2), thus, each resembles the coordination in mononuclear hydrotris(pyrazolyl)borate (Tp) complexes.[27] In the last century and at the beginning of 21st century a few more Cu-Kuratowski complexes with varying side ligands or valences were investigated,[28] as well as similar Ni^{II} complexes, in which one bta ligand is replaced by a hydroxide anion.[29]

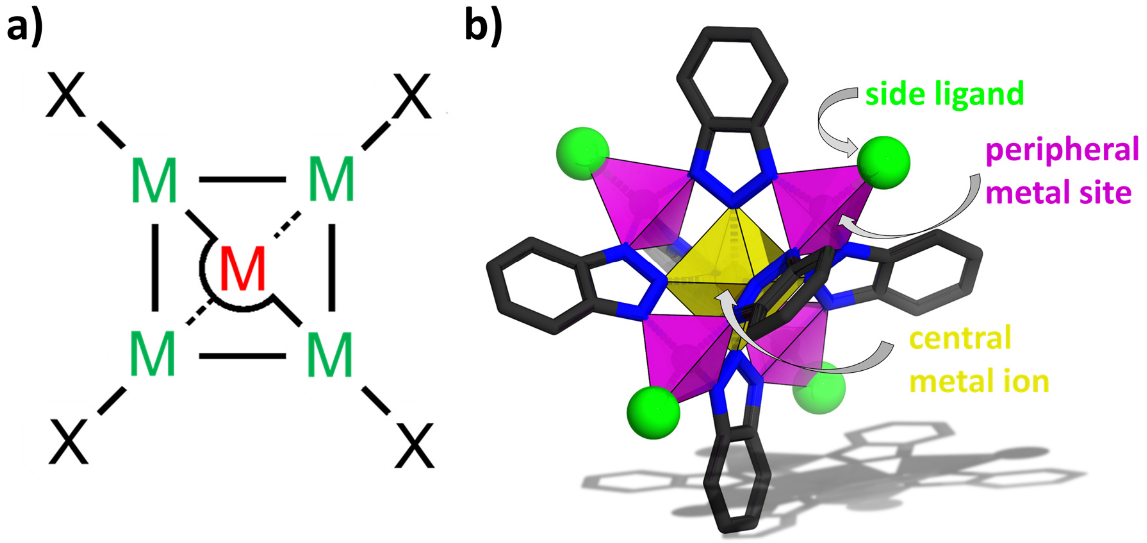

Figure 2. a) 2D-representation of a Kuratowski complex depicting the central (red) and peripheral (green) metal centers (M), which are coordinated by the triazolate ligands (lines connecting Ms) and side ligands (X). b) Example $[M_5Cl_4(bta)_6]$-Kuratowski complex (**bta**= benzotriazolate) showing the central (yellow octahedron) and peripheral (purple tetrahedra) metal ions in addition to the chloride side ligands (green).

More recent investigations resulted in a larger variety of Kuratowski complexes with different triazolate ligands, metal ions and side ligands (**Figure 3**). A series of heterometallic Kuratowski complexes of the general formula $[MZn_4(L)_4(L')_6]$ (M= Fe^{II}, Co^{II}, Ni^{II}, Cu^{II}, Zn^{II}, Ru^{II}; L= Cl$^-$, acac$^-$; L′= **H-bta** (1*H*-1,2,3-benzotriazole), **H-Me$_2$bta** (5,6-dimethyl-1*H*-1,2,3-benzotriazole)) have been described.[25,30,31] Out of these, the Ru-Kuratowski complex was investigated in detail regarding its photophysical properties, revealing a long-lived photoexcited state (6.05 ns), which results from an internal singlet to triplet conversion.[31] Last year, the Kuratwoski complexes of the composition $[MZn_4Cl_4(L)_6]$ (L= **H-cybta** (5,6,7,8-tetrahydro-1*H*-naphtho[2,3-*d*][1,2,3]triazole), **H-dibanta** (2,5-di-*tert*-butylacenaphtho[1,2-*d*][1,2,3]triazole)) were described and also characterized regarding their photophysical properties.[32] The π-extension of the **H-dibanta** ligand (λ_{max}^{em} = 440 nm (ligand), 470 nm (complex)) leads to a red shift of the fluorescence emission in $CHCl_3$ solutions in comparison to **H-cybta** (λ_{max}^{em} = 357 nm (ligand), 357 nm (complex)), which is shifted even stronger for the complex. In addition, as consequence of the sterically demanding **H-dibanta** ligand, the crystal structure exhibits voids with a BET surface area of 333 m^2g^{-1} determined by argon adsorption at 77 K. The only other examples of functionalized triazolate ligands in Kuratowski complexes are the **H-OMe$_2$bta** (5,6-dimethoxy-1*H*-1,2,3-benzotriazole) used for its shift in ligand field strength[33] and the π–extended redox-active **H-TTFN$_3$** (6-(4,5-bis(propylthio)-1,3-dithiol-2-ylidene)-1*H*-[1,3]dithiolo[4′,5′:4,5]benzo[1,2-*d*][1–3]triazole) ligand in the [$Cu_5(tta)_4(TTFN_3)_6$] (tta^- = 4,4,4-trifluoro-1-(thiophen-2-yl)butane-1,3-dione) complex.[34] Variation of the side ligands in Kuratowski complexes has led to highly stable organometallic complexes featuring methanido and ethanido ligands,[35] as well as to the [$Co_5Tp^*_4(Me_2bta)_6$] complex obtained from a postsynthetic exchange procedure, achieving an improved solubility and manipulation of the magnetic properties due to changes of the coordination environment of the peripheral Co^{II} ions.[36]

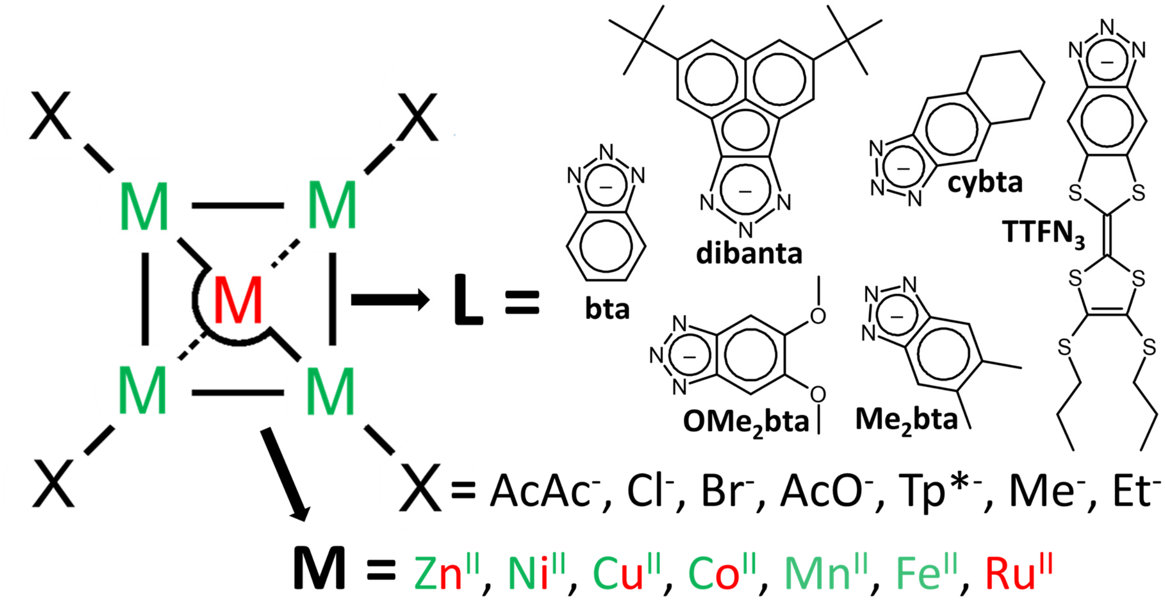

Figure 3. Lewis formulae of the various 1,2,3-triazolate ligands (L) known to form Kuratowski complexes with variable side ligands (X) and variable central (red) and peripheral (green) metal ions (M).

A tendency to form "condensed" Kuratowski complexes, sharing one peripheral metal center and thus resulting in nonanuclear complexes, was also shown with various examples in the literature.[33,37] Full condensation (sharing of all peripheral metal sites) leads to the formation of MOFs, which are to be discussed in detail in section 1.4 (Figure 10).[38]

Furthermore, their potential as molecular building blocks (MBBs) for the synthesis of coordination frameworks and MOFs from Kuratowski complexes via postsynthetic side ligand exchange with linking molecules like TCNQ[39] or dicarboxylates[40,41] to interconnect the Kuratowski SBUs has been proven in the literature.

Recently, a pentanuclear Th^{IV} complex ([$Th_5(NO_3)_8\{(py)_2C(O)_2\}_6$]), synthesized from a di(2-pyridyl)ketone ligand precursor, has been described as an unusual Kuratowski-type compound with tetravalent metal ions and coordination numbers >6.[42]

1.3. MFU-4- and MAF-Type Metal-Organic Frameworks

1.3.1. Synthesis and Structures

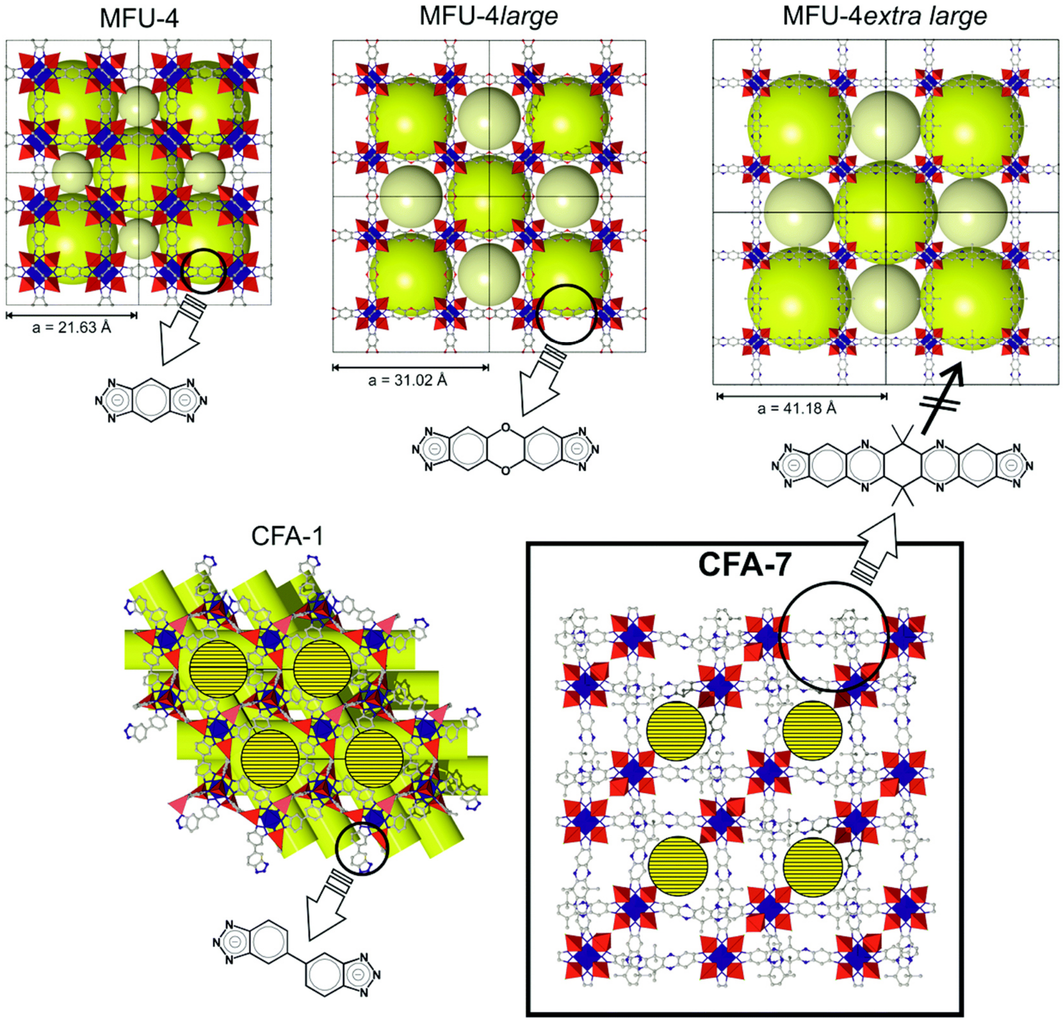

Figure 4. Size and structure comparison of **MFU-4** (top left), **MFU-4*l*** (top middle), **CFA-1** (bottom left) and **CFA-7** (top right) constructed from the **bbta^{2-}**, **btdd^{2-}**, **tqpt^{2-}** and **bibta^{2-}** ligands, respectively. Reproduced from Ref. 46 with permission from the Royal Society of Chemistry.[43]

Employing bistriazolate linkers, the Kuratowski coordination motif can be used as a SBU to construct MFU-4-type (MFU-4= **M**etal-Organic **F**ramework **U**lm University-4) MOFs extending in three dimensions. The T_d symmetry of the Kuratowski complex unit, in combination with straight ligands like the **H_2-bbta** (1*H*,5*H*-benzo(1,2-*d*:4,5-*d′*)bistriazole) and **H_2-btdd** (bis(1*H*-1,2,3-triazolo[4,5-*b*],[4′,5′-*i*])dibenzo[1,4]dioxin)) leads to the cubic **MFU-4** ($[Zn_5Cl_4(bbta)_3]$)[44] and **MFU-4*l***(arge) ($[Zn_5Cl_4(btdd)_3]$)[45] structures, respectively, featuring a six-connected net and crystallizing in the space group $Fm\bar{3}m$ (225). The Kuratowski SBUs of both frameworks feature chloride side ligands from the synthesis with $ZnCl_2$ in DMF at elevated temperatures. Furthermore, both frameworks exhibit a 3D pore system with alternating small and large pores, which are confined by the Cl^- anions and the ligand backbone, respectively. Extension of the bistriazolate linker backbone with the **H_2-tqpt** (6,6,14,14-tetramethyl-6,14-dihydroquinoxalino[2,3-*b*]phenazinebistriazole) linker and standard **MFU-4** synthesis conditions with $ZnCl_2$ and DMF resulted in the **CFA-7** ($[Zn_5Cl_4(tqpt)_3]$) framework, which exhibits a two-fold interpenetration of MFU-4-type structures that are deformed due to their interaction and flexibility of the linker (Figure 4). For the synthesis of **CFA-1** ([$Zn_5Cl_4(tqpt)_3$]) with the **H_2-bibta** (1*H*,1′*H*-5,5′-bibenzo[*d*][1,2,3]triazole) linker the procedure had to be adapted with NMF as solvent and $Zn(OAc)_2 \cdot 2H_2O$ as metal salt at 90° C.[46] The non-linear **H_2-bibta** does not allow for a cubic structure and additionally leads to the formation of two enantiomorphous crystals of the **CFA-1** structure, which are chiral due to the out-of-plane rotation of the biphenyl backbone.

MOFs built from the condensed nonanuclear Kuratowski-type complexes as SBUs were also shown to be available from in-situ synthesis with the [$Zn_9(CH_3CO_2)_6(bbtm)_6$] framework and not only from approaches using such complexes as MBBs.[41,47]

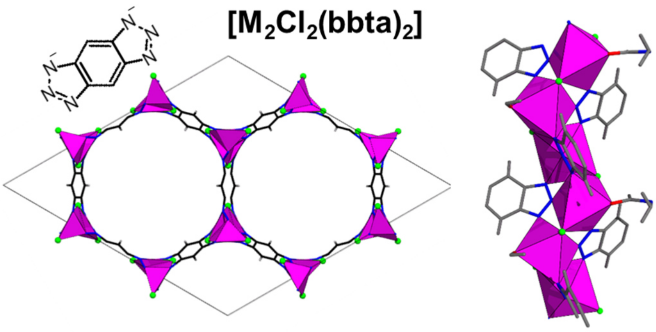

Figure 5. Structure of **[$M_2Cl_2(btdd)_2$]** (top) constructed from 1D chains of octahedrally coordinated M^{II} ions (bottom)

In the presence of alcohols and hydrochloric acid at lower temperatures, the bistriazolate linkers tend to directly form hexagonal MAF-type (Metal Azolate Framework) structures with a variety of different open shell transition metals of the general composition [$Mn_2Cl_2(L)(H_2O)_2$] (L= **bbta** (M= Mn^{II}, Fe^{II}, Co^{II}, Ni^{II}, Cu^{II}); **L= btdd** (M= Mn^{II}, Co^{II}, Ni^{II}, Fe^{II}); Figure 5).[48–50] Recently also an enantiopure MAF-type metal organic framework has been constructed from the *R*-enantiomer of the **H_2-spirta** (7,7,7′,7′-tetramethyl-6,6′,7,7′-tetrahydro-3*H*,3′*H*-5,5′-spirobi[indeno[5,6-*d*]-[1,2,3]triazole]) linker using $MnCl_2 \cdot 2H_2O$ in pure DMF (Figure 6).[51]

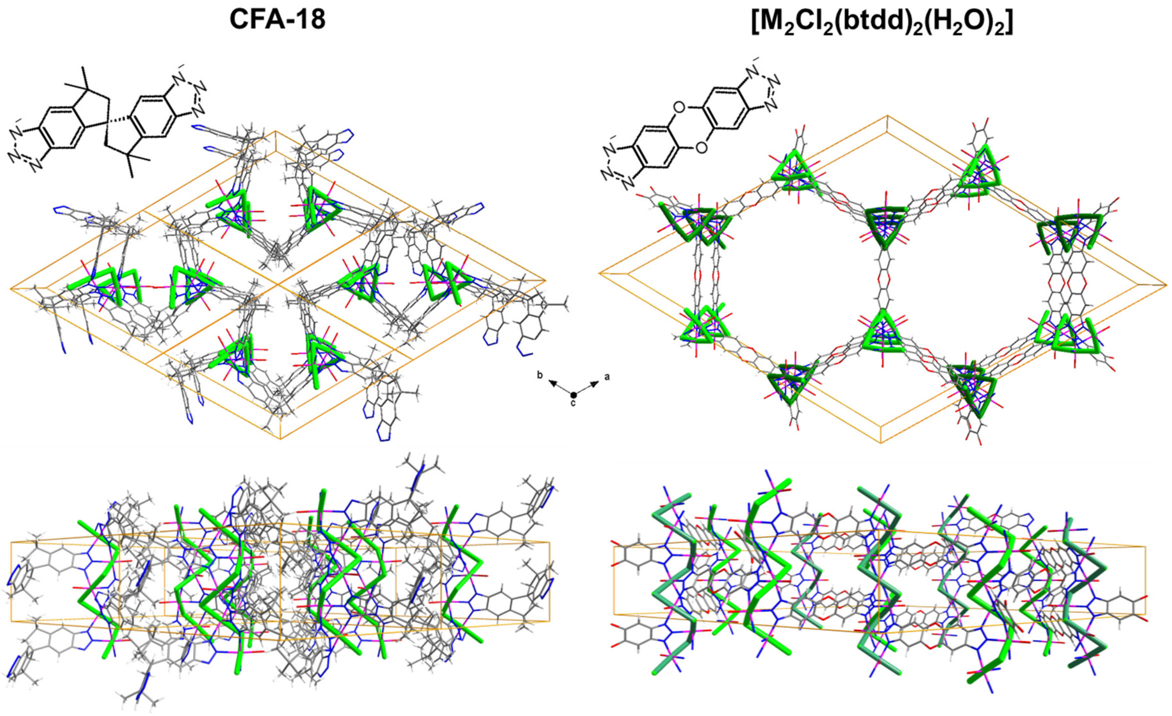

Figure 6. Structures of **CFA-18** (left) and **[$M_2Cl_2(btdd)_2(H_2O)_2$]** (right) showing that the alternating rotation of the 1D metal chains in **[$M_2Cl_2(btdd)_2(H_2O)_2$]** is unidirectional for the chiral **CFA-18**.[51]

1.3.2. Postsynthetic Modifications and Applications

For **MFU-4** the most interesting phenomena are based on the narrow pore apertures of the small pores, which are usually enclosed by eight Cl^- side ligands. A selective uptake and release of gases was observed,[52] which can be even applied for H_2/D_2 quantum sieving. [53] This selectivity was further exploited and analyzed in MOF@SAW (SAW= Surface Acoustic Wave) based sensor devices.[54,55] For such and other applications, the selective growth of **MFU-4** and **MFU-4*l*** onto micro-structured plasma polymer coatings has been developed,[56] as well as methods to control the crystal sizes.[57] In addition, **MFU-4** has recently been shown to be useful for H_2S and CO_2 separation from CH_4 in mixed-matrix membranes,[58] as well as for ammonia capture in MFU-4 coated textile fibers.[59]

A more sophisticated gas uptake phenomenon is the kinetic trapping of gases, which was first described for **MFU-4**.[60] More than 44.5 wt% of xenon gas can be loaded into the framework using high pressures and elevated temperatures to overcome the potential barrier of the small apertures in **MFU-4**, which are much smaller (2.52 Å) in comparison to the van der Waals diameter of xenon (4.4 Å). Thus, sealing the gas inside of the framework with a very slow release rate at ambient conditions, which can be significantly accelerated via thermal activation. A complete entrapment without any signs of gas release after two months at ambient conditions was observed for SF_6 entrapped in **MFU-4**.[61]

The interactions and properties of the larger **MFU-4*l*** framework filled with noble gases [62,63] and supercooled liquids[64] were also investigated in detail. In addition, in order to obtain tailored microporous semiconductors, methods to engineer the bandgap of MFU-4 type MOFs were derived from experimental measurements and DFT calculations.[65]

However, the main functionalities of MFU-4-type MOFs arise from post-synthetic exchange of the peripheral Zn^{II} ions and their Cl^- or CH_3COO^- side ligands (Figure 7), which leads to active and open metal sites (OMSs) in the frameworks. Such metal exchanges were described for all MOFs featuring Kuratowski SBUs, which exhibit pore apertures large enough for the diffusion of metal ions and solvents.[43,46,66,67]

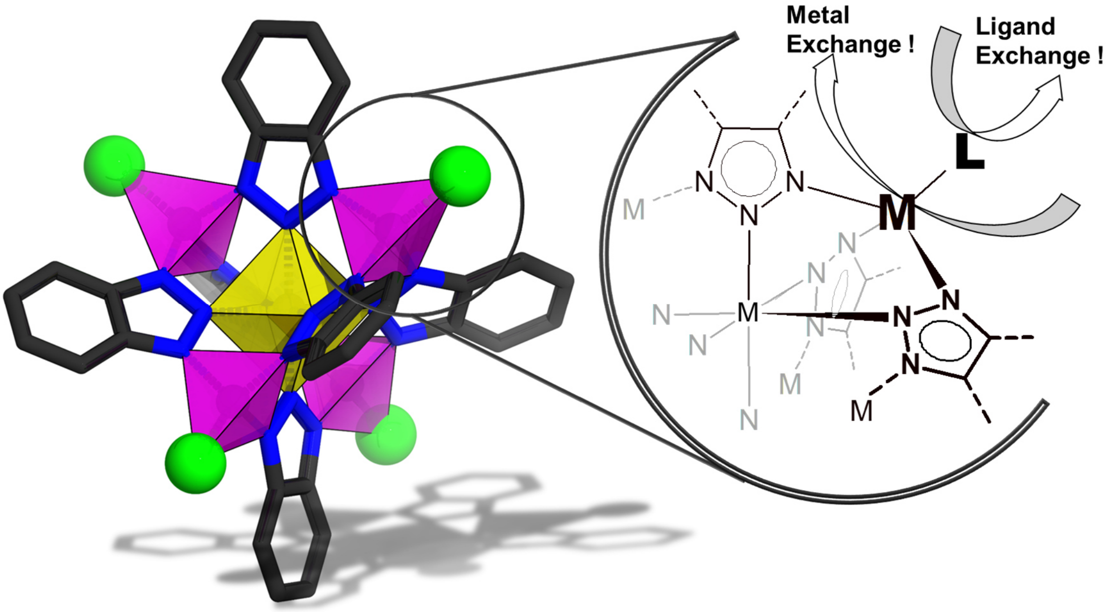

Figure 7. Schematic representation of the side ligand and metal exchange at the scorpionate-type coordination sites of the Kuratowski complex

In the case of **MFU-4**, however, direct synthesis methods with assistance of LiCl can be applied to obtain the Co and other analogues.[66] Only a post-synthetic side ligand exchange of the Cl^- with OH^- anions has been described for **MFU-4** so far.[68] The partial substitution of metal ions and side ligands is especially well characterized for **MFU-4*l***, resulting in MOFs of the general composition $[Zn_{(5-x)}M_x(L)_yCl_{(4-y)}(BTDD)_3]$ ($4 \geq x \geq 0$; $4 \geq y \geq 0$) with M= Li^{I}, Cu^{I}, Cu^{II}, Mn^{II}, Fe^{II}, Co^{II}, Ni^{II}, V^{II}, V^{IV}, Cr^{III} , Ti^{III}, Ti^{IV} [63,66,69–74] and L= NO_2^-, NO_3^-, $CF_3SO_3^-$, N_3^- ,NCO^-, $HCOO^-$, CH_3COO^-, F^-, H^-; OH^-, $(OH)_2AsO^-$.[68,70,72,75–77] Except for the arsenic loaded **MFU-4*l*** nanoparticles, established as drug delivery agents for anticancer treatment with arsenic trioxide,[77] most of these exchanges were realized for the activation and binding of small molecules. Starting from the gas-phase oxidation of CO with the **Co-MFU-4*l*** as first prove of principle application of post-synthetic metal metathesis for the introduction of active OMSs in **MFU-4*l***,[66,78] this approach was extended for various catalytic reactions. Control over the metal exchange ratio in **Co-MFU-4*l*** also results in a tuneable hydrophilicity, which could be applied for atmospheric water harvesting due to its high water adsorption capacity of 105 wt%.[79] The **Cu^{I}-MFU-4*l***, best prepared via thermal decomposition of the **Cu^{II}-MFU-4*l*-HCOO** precursor, revealed a strong binding of various small molecules like N_2 (41.6 kJmol^{-1}), O_2 (52.6 kJmol^{-1}), C_2H_4 (88 kJmol^{-1}), CH_4 (14.6 kJmol^{-1}) and H_2 (32.3 kJmol^{-1}),[69,80] which was exploited further for the capture of heavy hydrogen isotopes.[81] Thermal decomposition of the **Zn^{II}-MFU-4*l*-HCOO** results in the **Zn^{II}-MFU-4*l*-H** framework useful as a hydride transfer agent for electrophiles.[69] A comparing study of the **Cu^{I}-MFU-4*l*** with **Li^{I}-MFU-4*l***, obtained from a direct exchange reaction in LiCl solutions, revealed a preferential binding of N_2O (30.8 kJmol^{-1}) over CO_2 (15.3 kJmol^{-1}) for **Cu^{I}-MFU-4*l***, whereas **Li^{I}-MFU-4*l*** showed similar binding energies for N_2O (23.6 kJmol^{-1}) and CO_2 (22.7 kJmol^{-1}).[71] The **Li^{I}-MFU-4*l*** has also revealed high H_2 (9.4 wt %; 77 K; 100bar) and CH_4 (44 wt%; 270 K; 100 bar) uptake capacities.[82]

The **Cu^{I}-MFU-4*l*** was also applied for cyclic gas-phase heterogeneous NO disproportionation,[83] similar to the previously reported process in which **Ni^{II}-MFU-4*l*-NO$_2$** converts the toxic gases CO and NO to non-toxic CO_2 and N_2O (**Figure 8**).[72] In addition, **Cu^{I}-MFU-4*l*** is also proposed as an efficient catalyst for the conversion of CO_2 and propylene oxide into propylene carbonate.[84] **Mn^{II}-CFA-1** was introduced as a catalyst for selective cyclohexene oxidation with air.[85]

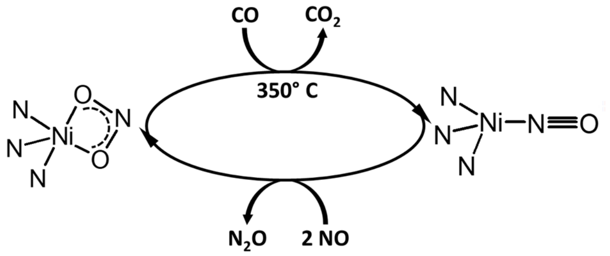

Figure 8. Reaction scheme showing the cyclic conversion of CO and NO to CO_2 and N_2O in the gas-phase heterogeneous process developed for **Ni^{II}-MFU-4*l***.[72]

Much effort has also been successfully invested into the application of **MFU-4*l*** derivatives as single-site heterogeneous catalysts for the dimerization and polymerization of olefins (**Figure 9**), which started with the selective dimerization of ethylene to 1-butene in **Ni^{II}-MFU-4*l*** surpassing the performance of commercial catalysts with a selectivity over 96% and a turnover frequency (TOF) of 41500 h^{-1}.[86] Such single-site catalytic reactions are driven by organometallic co-catalysts like MAO, MMAO-12, $AlMe_3$, or $AlEt_3$, which are expected to activate the metal sites via formation of organometallic side ligand species. Subsequently, the polymerization of ethylene and co-polymerization of ethylene and propylene with **Cr^{II}-MFU-4*l***, **Cr^{III}-MFU-4*l***, **Ti^{III}-MFU-4*l***, and **Ti^{IV}-MFU-4*l***,[73] the selective dimerization of propylene to branched hexenes with **Ni^{II}-MFU-4*l***,[87] stereoselective polymerization of 1,3-butadiene to polybutadiene (>99% 1,4-cis) with **Co^{II}-MFU-4*l***,[88] ethylene and stereoselective propylene polymerization with **V^{II}-MFU-4*l*** and **V^{IV}-MFU-4*l***,[74] and gas phase ethylene polymerization with **Cr^{III}-MFU-4*l*** were demonstrated.[89] The high selectivity of the **Co^{II}-MFU-4*l*** catalyst towards 1,4-*cis*-polybutadiene is expected to be a result of missing linker defects in the framework.[90] Especially with the use of more economical catalysts like e.g. the **Ni^{II}-CFA-1** for the dimerization of ethylene to 1-butene (87.1%, TOF= 37100 h^{-1}), the commercialization of such catalysts seems to be clearly within reach.[91] It should be kept in mind here that the steric environment of the active-sites, which is influenced by the different linker molecules in **CFA-1** and **MFU-4*l***, already has an impact on the catalysis reaction and performance.[92]

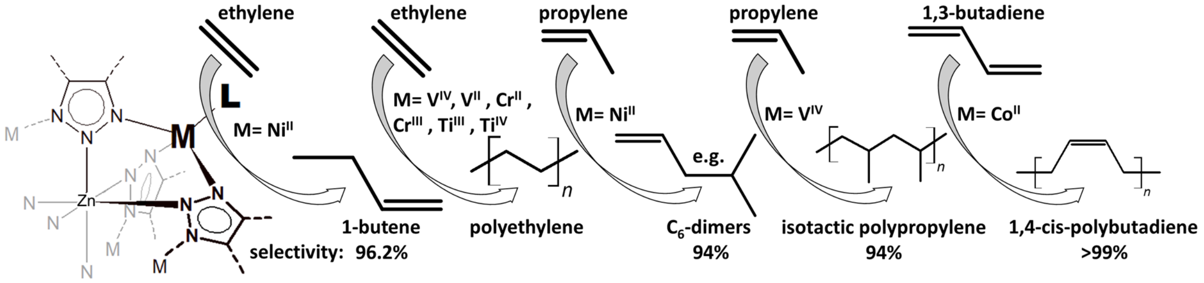

Figure 9. Schematic representation of some olefin dimerization and polymerization reactions in heterometallic MFU-4-type framework single-site catalysts.

Side ligand exchange with hydroxide anions at the Kuratowski SBUs of **Zn^{II}-MFU-4**, **Zn^{II}/Co^{II}/Ni^{II}-MFU-4*l***, **Zn^{II}/Co^{II}/Ni^{II}-CFA-1**, as well as the $[Zn_9(CH_3CO_2)_6(bbtm)_6]$ MOF has gained special interest due to a CO_2 binding mechanism, which is similar to that of carbonic anhydrase enzymes with sorption enthalpies ranging from -63 to -84 kJmol^{-1}.[47,68,76,93] Furthermore, such hydroxide functionalized SBUs were shown to be useful for the catalytic degradation of organophosphorus nerve agents.[94]

In a similar manner, hexagonal MAF-type structures synthesized from the **H$_2$-bbta** linker containing hydroxide functions from a post-synthetic oxidation step were proven to be excellent materials for the CO_2 capture from flue gases with enthalpies of adsorption up to -124 kJmol^{-1} and even applicable in humid environments.[95] While the first hexagonal MAF structure constructed from the **H$_2$-bbta** linker was employed as an alkylaromatics oxidation catalyst,[95] most of the structures constructed from the **H$_2$-btdd** linker were investigated for the sorption of gases like ammonia,[49,96] O_2,[97] CO, ethylene, and H_2.[98] Moreover, the **M$_2$Cl$_2$(BTDD)** MOFs have set records for water capture with up to 82 wt% at a relative humidity below 30%,[99] which lead to several studies for the application in atmospheric fresh water harvesting.[100] The recently reported $V_2Cl_{2.8}$(btdd) exhibits high isosteric enthalpies of adsorption for N_2 and H_2 of −56 kJmol^{-1} and −21 kJ mol^{-1} , respectively,[101] which was explored further in some in silico studies.[102]

In addition, conductivities in the order of 10^{-6} S/cm were found for the **Fe$_2$Cl$_2$(btdd)(DMF)$_2$** structure, which is several orders of magnitude higher than the usually isolating MOFs and also the counterparts synthesized from other transition metals.[48]

1.4. Other 1,2,3-Triazolate-Based Coordination Frameworks

High electrical conductivities were also observed for the $Fe(ta)_2$ MOF in contrast to a variety of isostructural $M(ta)_2$ (M= Cd^{II}, , Mn^{II}, Fe^{II}, Co^{II}, Cu^{II}, Zn^{II}) type frameworks, which are constructed via full condensation of the Kuratowski SBUs.[38,103,104] In these structures, every peripheral metal center of the Kuratowski SBU is shared between two Kuratowski units (Figure 10).

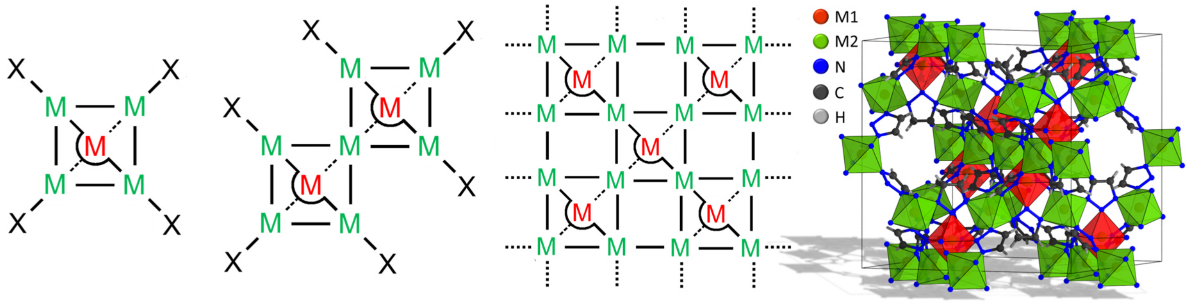

Figure 10. Condensation of Kuratowski SBUs leading from the single Kuratowski (left), over the nonanuclear complex (middle), to the $M(ta)_2$ frameworks (right).[38]

This leads to a network of metal ions in close proximity, which in the case of iron, in combination with partial oxidation to Fe^{III}, leads to an intrinsic electrical conductivity of around 7.7×10^{-5} Scm^{-1}.[103] The reason for this conductivity is still the subject of debate but most probably results from charge hopping processes assisted by the mixed valence nature of the $Fe^{II/III}(ta)_2$.[105] This was further confirmed by oxidation experiments applying thianthrenium tetrafluoroborate to obtain $Fe_{0.66}{}^{II}Fe_{0.33}{}^{III}$ $(tri)_2(BF_4)_{0.33}$ with the record conductivity of 0.3 Scm^{-1} for a 3D framework due to the increase of the charge carrier density.[106] Although the initially observed conductivity increases to 1.0×10^{-3} Scm^{-1} upon treatment of the $Fe(ta)_2$ with I_2 vapor, it is questionable if the iodine's oxidation potential is sufficient to oxidize the Fe^{II} to Fe^{III} as suggested by the authors of this study.[103] Other effects from a pore filling with iodine, or even the iodine itself, which is a fairly good conductor in the solid state with 0.01×10^{-2} Scm^{-1},[107] could be the reason for this effect. It can also be imagined that the iodine enhances the electrical contact between the single crystallites of the nanocrystalline MOF powder. Recent investigations also indicate that the contact between the crystallites plays a crucial role for the conductivity, as the conductivity of $Fe(ta)_2$ counterintuitively increases with decreasing particle size.[108] The effect of more grain boundaries seems to be overpowered by the denser packing and better arrangement of the smaller crystals, although the increased surface to bulk ratio might also increase the conductivity due to surface defects increasing the charge carrier density.

In a similar manner, a conductivity of $\sigma = 1.4(1) \times 10^{-2}$ Scm^{-1} was measured for the mixed valent $Cr_{0.67}{}^{II}Cr_{0.33}{}^{III}(ta)_2(CF_3SO_3)_{0.33}$ framework.[109] In addition, the strong coupling interactions, resulting from the narrow distances between the metal ions, also results in highly interesting magnetic phenomena in such materials. The $Cr_{0.67}{}^{II}Cr_{0.33}{}^{III}(ta)_2(CF_3SO_3)_{0.33}$ exhibits the highest ferromagnetic ordering temperature reported for a MOF at $T_C = 225$ K, which is explained by itinerant ferromagnetism in this material.[109]

Whereas most of the $M(ta)_2$ frameworks were obtained as small crystals, the literature also states single-crystal synthesis conditions for the $Cd(ta)_2$, $Mn(ta)_2$, and $Zn(ta)_2$ structures, which were prepared for detailed investigations of the pore and pocket sizes´ influence on the adsorption behavior of N_2, H_2, CO_2, and C_2H_2.[110] In contrast to the other cubic $M(ta)_2$ structures (space group $Fd\bar{3}m$ (No. 227)), the $Cu(ta)_2$, prepared from ethanol/ammonia solutions and $Cu(OH)_2$, was shown by SC-XRD to crystallize in the tetragonal space group $I4_1/amd$ (no. 141) at RT due to a Jahn-Teller distortion. In addition, the magnetic properties were investigated and a reversible phase transition to the cubic structure at temperatures above 120° C was observed.[38] $Cu(ta)_2$ prepared from DEF and $Cu(NO_3)_2$ seems to crystallize directly in the cubic space group according to the obtained powder patterns,[103] which might be explained by a large number of missing linker defects found and exploited in this structure for photocatalytic proton reduction.[111]

However, not only $M(ta)_2$-type frameworks are an interesting playground for magnetic phenomena but also the magnetic properties of e.g. other 1,2,3-triazolate-based Cu^{II} and Mn^{II} frameworks have been investigated in literature.[112,113]

2. Results

2.1. Organometallic Ligand Exchange in MFU-4*l*

As aforementioned, the side ligand at the Kuratowski SBU in **MFU-4*l*** plays a crucial role for the catalytic activity. Because organometallic side ligands are expected to occur in the literature olefin polymerization reactions due to the use of the organometallic co-catalysts like $AlMe_3$ or $AlEt_3$, we wanted to examine and characterize such side-ligand exchanges in detail for **MFU-4*l*** frameworks.

Hence, **MFU-4*l*** and **Co-MFU-4*l*** were prepared according to the literature procedures[45,66] and a variety of different routes were established for the exchange of the initial side ligands with organometallic ligands (Figure 11). This resulted in the well characterized **MFU-4*l*-L** ($[Zn_5L_xCl_{4-x}(BTDD)_3]$ ($4 \geq x > 3$; L = methanido (**MFU-4*l*-Me**), ethanido (**MFU-4*l*-Et**), *n*-butanido (**MFU-4*l*-*n*-Bu**), *tert*-butanido (**MFU-4*l*-t-Bu**), 3,3-dimethyl-1-butyn-1-ido (**MFU-4*l*-Butyne**); H_2-BTDD = bis(1*H*-1,2,3-triazolo[4,5-*b*][4′,5′-*i*])dibenzo[1,4]dioxin) and **Co-MFU-4*l*-L** ($[Zn_{1.5}Co_{3.5}Me_{3.1}Cl_{0.9}(BTDD)_3]$ (**Co-MFU-4*l*-Me**) and $[Zn_{1.4}Co_{3.6}(OH)_{3.1}Cl_{0.9}(BTDD)_3]$ (**Co-MFU-4*l*-OH**)) frameworks.

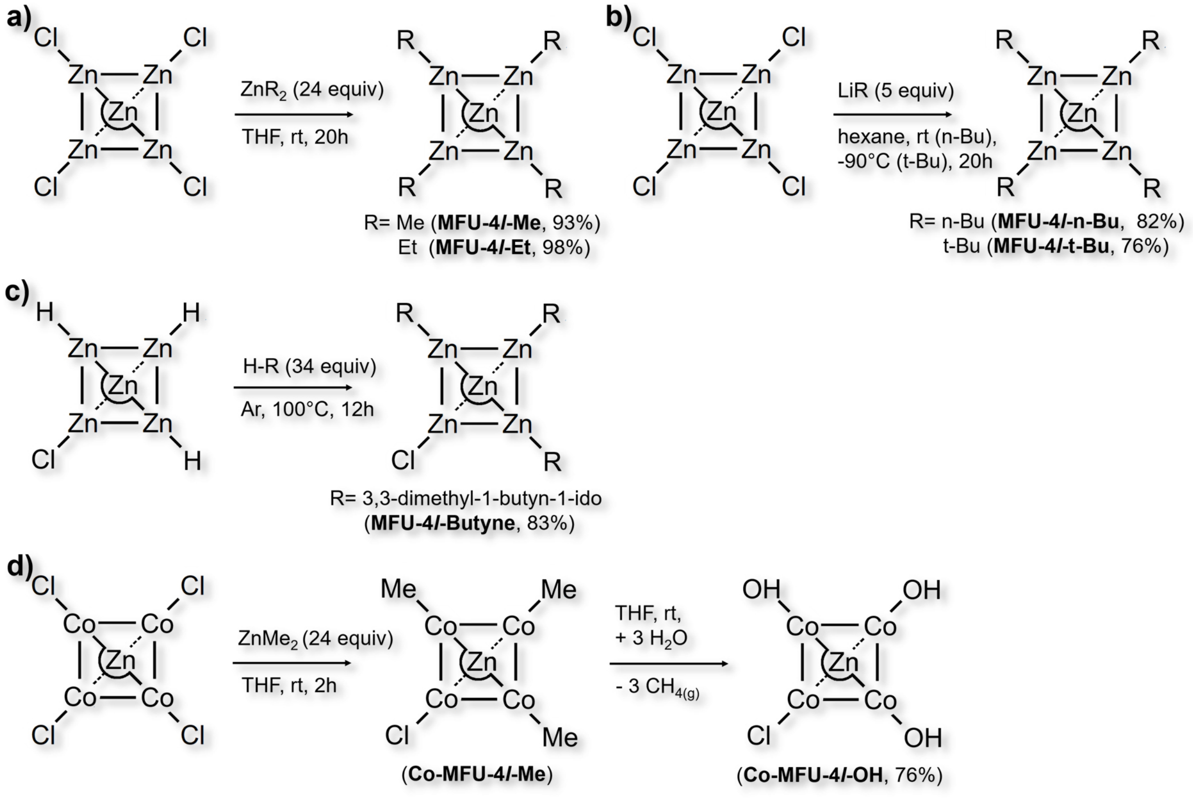

Figure 11. Schematic representation of the ligand exchange reactions at the Kuratowski SBUs resulting in the a) **MFU-4*l*-Me, MFU-4*l*-Et,** b) **MFU-4*l*-*n*-Bu, MFU-4*l*-*n*-Bu,** c) **MFU-4*l*-Butyne**, d) **Co-MFU-4*l*-Me** and **Co-MFU-4*l*-OH** frameworks

Fourier transform infrared (FT-IR) spectroscopy in conjunction with simulated spectra was established as an efficient tool for the characterization of such compounds, which showed good matches (Figure 12). This is significant here, because the insolubility of the frameworks forecloses liquid state NMR spectroscopy and MS, which is usually employed for the characterization of organometallic complexes. Evaluation of argon adsorption isotherms for the

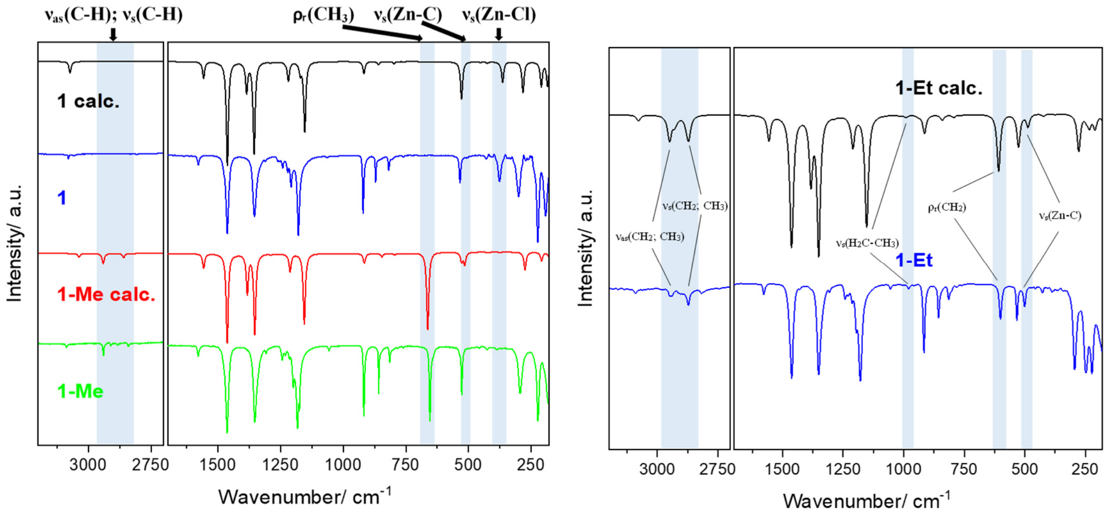

Figure 12. FT-IR spectra of **MFU-4*l***, **MFU-4*l*-Me**, and **MFU-4*l*-Et** showing the good match between measured and calculated spectra, in which the side ligand induced changes are highlighted

organometallic **MFU-4*l*** derivatives revealed BET surface areas, which are in good agreement with the expected and calculated changes, as well as pore size distributions nicely matching the expected steric demand of the respective ligands.

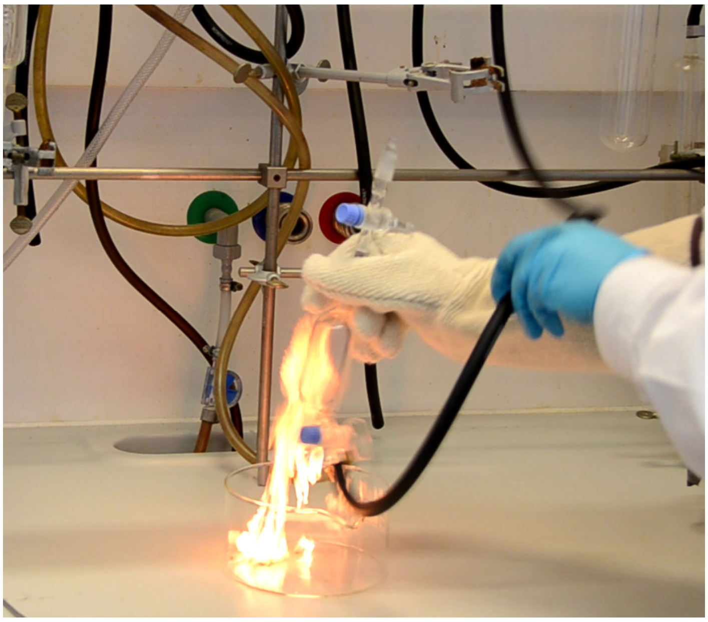

Figure 13. Combustion of approximately 25-35 mg of the highly pyrophoric material obtained from the reaction of $AlMe_3$ with the **Co-MFU-4*l*-HCOO** framework

Besides the reported procedures, $AlMe_3$ and $AlEt_3$ solutions in hexane were also tested for the ligand exchange reactions in **MFU-4*l*** derivatives. However, in addition to the ligand exchange, large amounts of residual Al were detected in the EDX spectra of the resulting compounds and it is not clear whether they are a result of metal exchange or reactant residues in the pores. For example, the tests with **Co-MFU-4*l*-HCOO** and $AlMe_3$ resulted in highly pyrophoric materials most probably due to binding of $AlMe_3$ or derivatives thereof in the pores (Figure 13). Reactions of **Co-MFU-4*l*** with $ZnMe_2$ gave better results with nearly no leftover Zn in the structures and good chloride to methanido ligand exchange ratios. The pure **Co-MFU-4*l*-Me** still exhibits a slightly pyrophoric behavior and high reactivity but is not comparable to the explosive nature of the **Co-MFU-4*l*-HCOO** and $AlMe_3$ reaction product. Quenching of the **Co-MFU-4*l*-Me** with a water/THF mixture presents a neat pathway towards the **Co-MFU-4*l*-OH** framework.

In contrast, nearly no reactivity of the various **Zn-MFU-4*l*** derivatives could be observed under controlled hydrolysis conditions or in synthetic air at elevated temperatures. Except for **MFU-4*l*-t-Bu**, the expected β-hydrogen elimination reactions of **MFU-4*l*-Et** and **MFU-4*l*-n-Bu** start only shortly before the general framework decomposition (Figure 14). Moreover, the **MFU-4*l*-t-Bu**

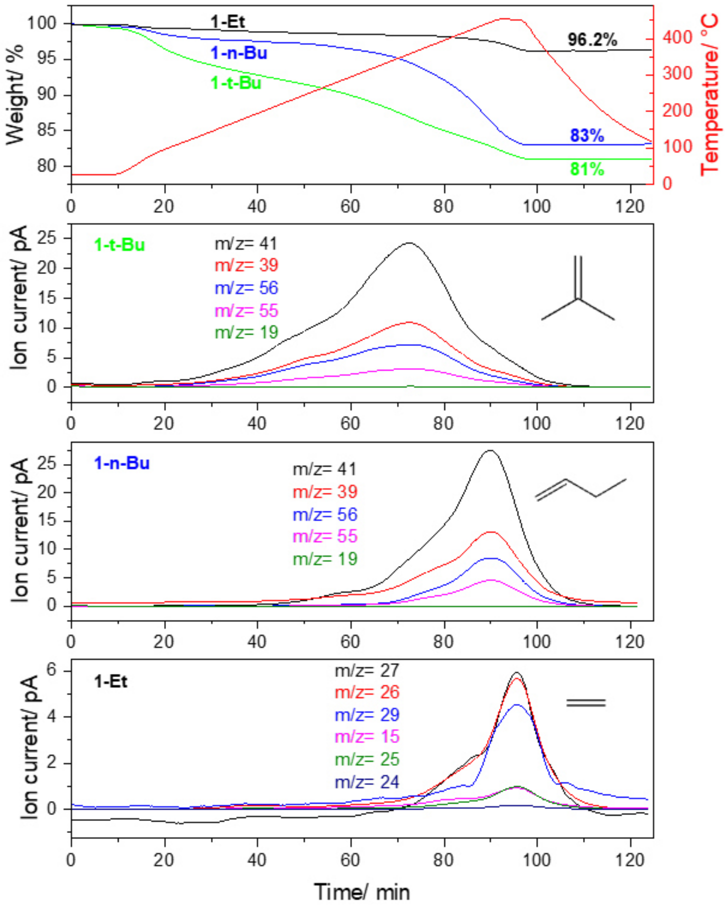

Figure 14. Simultaneous TG-MS curves of **MFU-4*l*-t-Bu**, **MFU-4*l*-n-Bu**, and **MFU-4*l*-Et** showing the evolution of the corresponding 2-methylprop-1-ene, but-1-ene, and ethene.

seems to be unstable at ambient conditions and aqueous conditions, not only hydrolyzing the t-butanido group but even completely losing its crystallinity upon water contact. Apart from that, only the **MFU-4*l*-Butyne** exhibited minor signs of a hydrolysis reaction to the **MFU-4*l*-OH**, but with retained crystallinity. DRIFTS measurements of the **Co-MFU-4*l*-OH** revealed a CO$_2$ binding

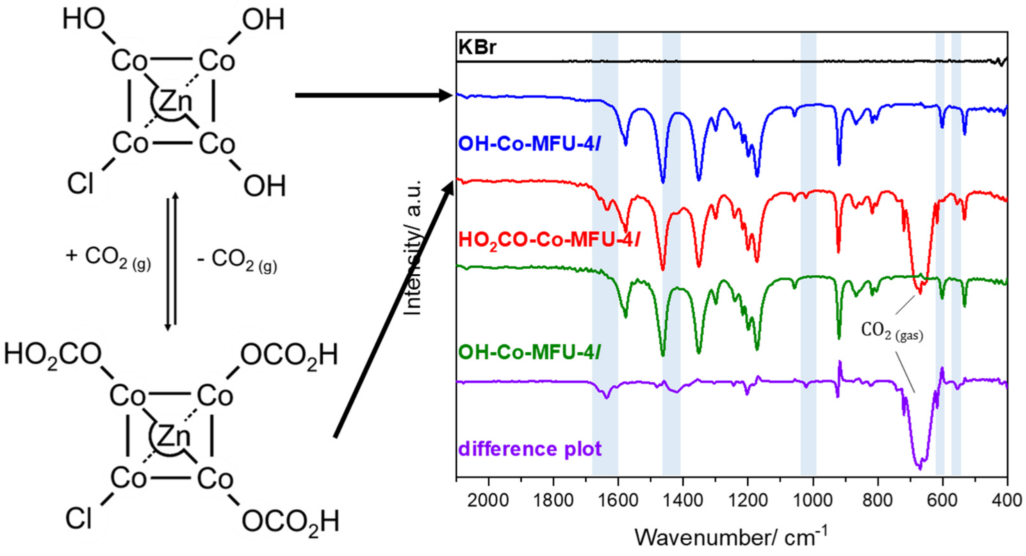

Figure 15. Schematic representation of the reversible binding of CO$_2$ at the **Co-MFU-4*l*-OH** Kuratwoski SBUs and DRIFTS measurements of **Co^{II}-MFU-4*l*-OH** showing the changes associated with the reversible formation of a bicarbonate ligand in the difference plot (pink) and the gas change sequence from nitrogen (blue) to CO$_2$ (red) to nitrogen (green) atmospheres.

mechanism similar to that of carbonic anhydrase also described for **MFU-4*l*-OH** in literature (Figure 15).[76] In such compounds, which mimic the metalloenzyme, the CO_2 is reversibly bound in the form of a monodentate bicarbonate ligand to the M^{II} ion (M^{II}-OCO_2H), which accelerates the exchange between the oxygen atoms of CO_2 and H_2O in the $CO_2 + H_2O \rightleftharpoons H_2CO_3$ equilibrium reaction. Unfortunately, time restraints and defect measurement devices prevented the measurement of CO_2 adsorption isotherms for the determination of the isosteric enthalpy of adsorption in this case. Such materials are promising candidates for future atmospheric CO_2 capture and conversion applications.

So far, first test reactions for the methylation of benzaldehyde were only conducted with the seemingly more reactive $AlMe_3$ and **Co-MFU-4*l*-HCOO** reaction product, which unfortunately did not yield the expected racemic 1-phenylethanol according to GC-MS analysis. This should be tested again for the pure **Co-MFU-4*l*-Me** because it is considered to be an interesting proof-of-principle for future asymmetric methylation approaches in chiral frameworks like **CFA-1**.[46,114] Reactions with benzoyl chloride were also tested for all organometallic **MFU-4*l*** derivatives without any signs of the expected reaction products in the GC-MS measurements, but a lot of unidentifiable signals, which could not be explained so far.

2.2. Diamine-Functionalized Kuratowski Complexes as Molecular Building Blocks for Porous Metal Hydrogen-Bonded Organic Frameworks and MOF Dyads

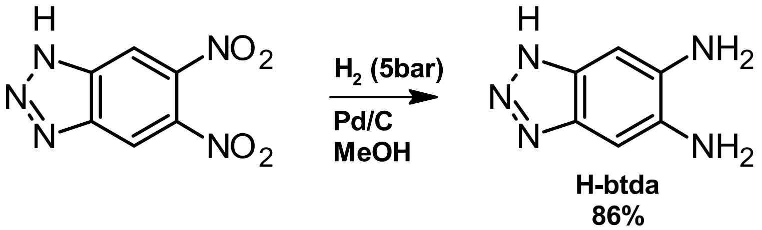

Figure 16. Synthesis of 1*H*-benzotriazole-5,6-diamine (**H-btda**) starting from 5,6-dinitro-1*H*-benzotriazole

Novel assembly strategies from pre-built complex MBBs are envisaged to further increase the variability and complexity of framework structures, which are often limited by the standard MOF synthesis strategy of direct in-situ complex formation and interconnection. Aiming to create MBBs from triazolate ligands the 1*H*-benzotriazole-5,6-diamine (**H-btda**) was prepared in the gram scale via hydrogenation from the literature known 5,6-dinitro-1*H*-benzotriazole (Figure 16).[115] The use of this ligand in standard reaction procedures with $ZnCl_2$ and 2,6-lutidine in DMF yields the expected Kuratowski complex, which features six diamine functional groups in an octahedral arrangement for further interconnection. Single crystals for the X-ray structure solution of the resulting **CFA-20-Cl** M-HOF were obtained by slow MeOH and 2,6-lutidine vapor diffusion into the DMF solution, but the use of more concentrated solutions without MeOH even yields single crystals in the mm regime (**Figure 17**).

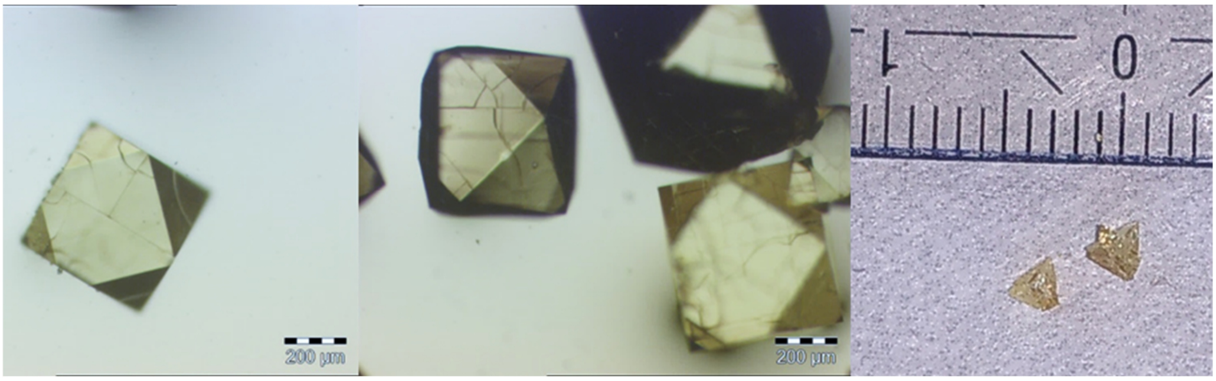

Figure 17. Single crystals of the **CFA-20-Cl** M-HOF obtained via MeOH/2,6-lutidine (left, middle) or pure 2,6-lutidine (right) vapor diffusion into the DMF solutions of the **H-btda** ligand and $ZnCl_2$.

The SC-XRD structure analysis revealed the unique potentially porous assembly of Kuratowski complexes in the space group $F\bar{4}3m$. This structure is stabilized via a hydrogen bond framework between the twelve amine functions of six complexes and a central twelve-fold hydrogen bonded chloride anion, which adapts the coordination environment of an irregular icosahedron (Figure 18). To the best of our knowledge such an unusual chloride coordination has not been observed before. Using $ZnBr_2$ in the synthesis leads to the assembly of an isostructural compound with bromide instead of chloride, whereas no Kuratowski complexes could be obtained with the ZnI_2 or ZnF_2 salts. Both structures are unstable upon solvent removal by drying or washing with MeOH, resulting in amorphous powders, which regain their crystallinity upon DMF addition (Figure 19).

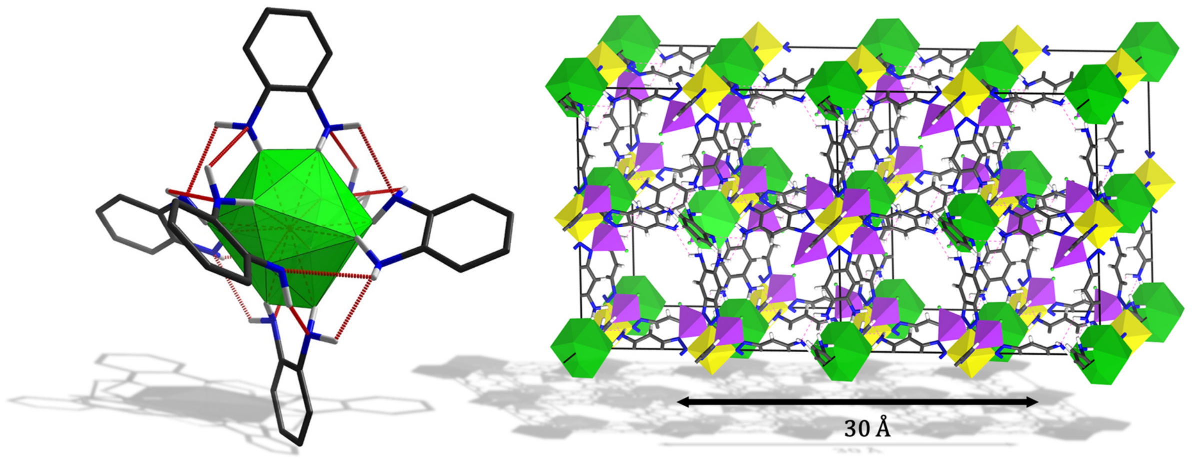

Figure 18. Simulated hydrogen bond framework around the chloride anion (left) and unit cells of **CFA-20-Cl** exhibiting the alternating Kuratowski and chloride HOF SBUs, as well as showing the potential porosity.

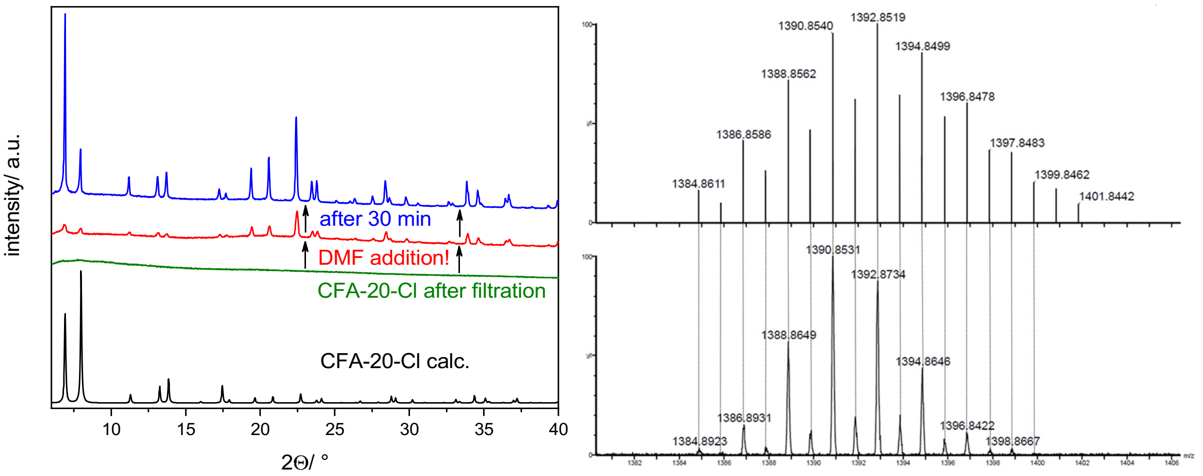

Figure 19. PXRD patterns of **CFA-20-Cl** calculated from single crystal data and measured after DMF addition (left). ESI⁻-MS isotope pattern of **CFA-20-Cl** ($[Zn_5Cl_4(btda)_6]\cdot Cl^-$: $Zn_5Cl_5C_{36}N_{30}H_{36}$) still bound to the additional chloride anion (right).

To interconnect such complexes into MOF frameworks via metal coordination at the free amine functions the peripheral metal sites were capped to prevent unwanted metal exchanges and to increase the solubility. For this purpose, a post-synthetic ligand exchange reaction similar to literature was applied,[36] exchanging the chloride side ligands with Tp and Tp*, which resulted in the assembly of the trigonal **CFA-20-Tp** ($[Zn_5Tp_4(btda)_6]$; $R3m$) and **CFA-20-Tp*** ($[Zn_5Tp^*_4(btda)_6]$; $R\bar{3}$) M-HOFs from DMF solutions via MeOH vapor diffusion. Recrystallization of **CFA-20-Tp*** from DMSO yields the variant **CFA-20-Tp*-DMSO** structure in the space group $P2_12_12_1$, which was not investigated further due to its instability upon solvent removal.

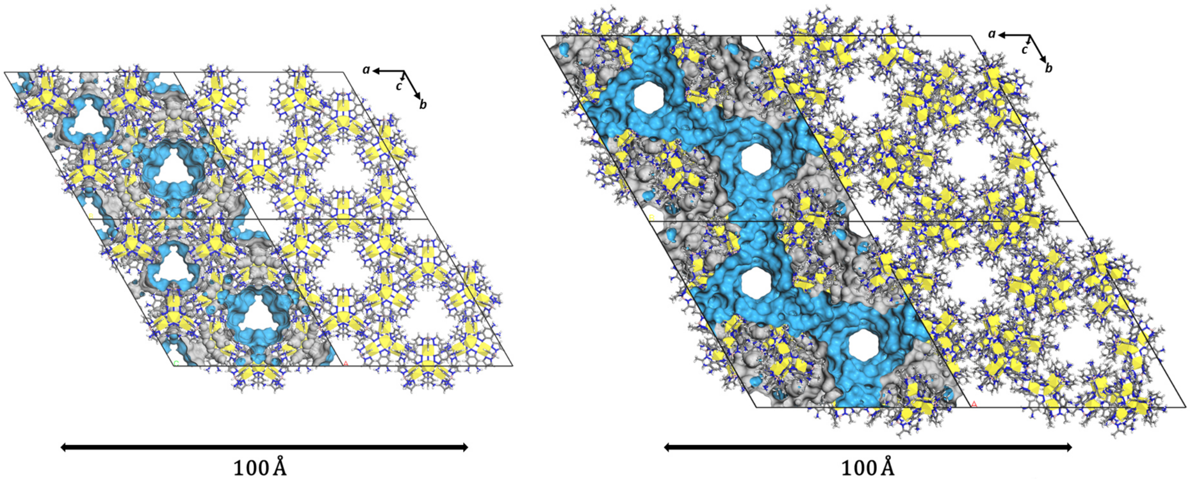

Figure 20. **CFA-20-Tp** (left) and **CFA-20-Tp*** (right) structures with plots of the Connolly surface highlighting the channel pores in the crystallographic *c*-direction

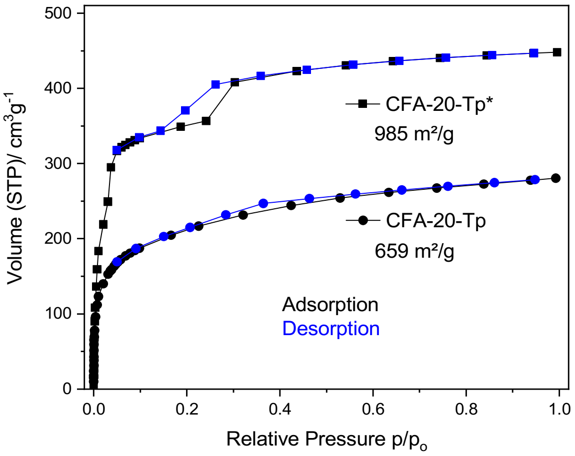

Figure 21. Argon adsorption isotherms for **CFA-20-Tp** and recrystallized **CFA-20-Tp*** at 77 K

In contrast, the **CFA-20-Tp** and **CFA-20-Tp*** structures are stable upon solvent removal and up to 100°C, revealing high specific surface areas in the argon adsorption isotherms (**Figure 21**). The recrystallization of **CFA-20-Tp*** was successfully applied to increase the initially lower surface area, emphasizing the advantage of soluble M-HOFs over MOFs. In addition to this purification, the solubility also allows for a broader variety of analysis methods in comparison to MOFs like liquid state NMR and ESI-MS, successfully applied for the characterization of those compounds. Only the **CFA-20-Tp** was not soluble enough for such characterizations, whereas the **CFA-20-Tp***, in comparison to **CFA-20-Cl**, even exhibits a good solubility in mixtures of chloroform, dichloromethane, and 1,4-dioxane with MeOH and not only DMF, DMSO, or similar solvents. Taking a detailed look at the amount and distance of possible hydrogen-bond interactions between the amine groups in the crystal structures assisted with simulations, no correlation was found between the amount or lengths of bonds and the structural stability. This leads to the conclusion that also architectural aspects might play a crucial role for permanent porosity in such materials, as the ringlike arrangement of the complexes in **CFA-20-Tp** and **CFA-20-Tp*** prevents a structure collapse towards the channel pores running along the *c*-direction of the structures.

Thus, to summarize, five new M-HOF structures were assembled and characterized, of which two even exhibit permanent porosity. The possibility for recrystallization and assembly of different M-HOF structures from other solvents underlines their potential as MBBs for future syntheses of porous framework structures. Especially the connection of the free amine functions via metal coordination seems to be a desirable aim, which could e.g. lead to MOF dyads with an

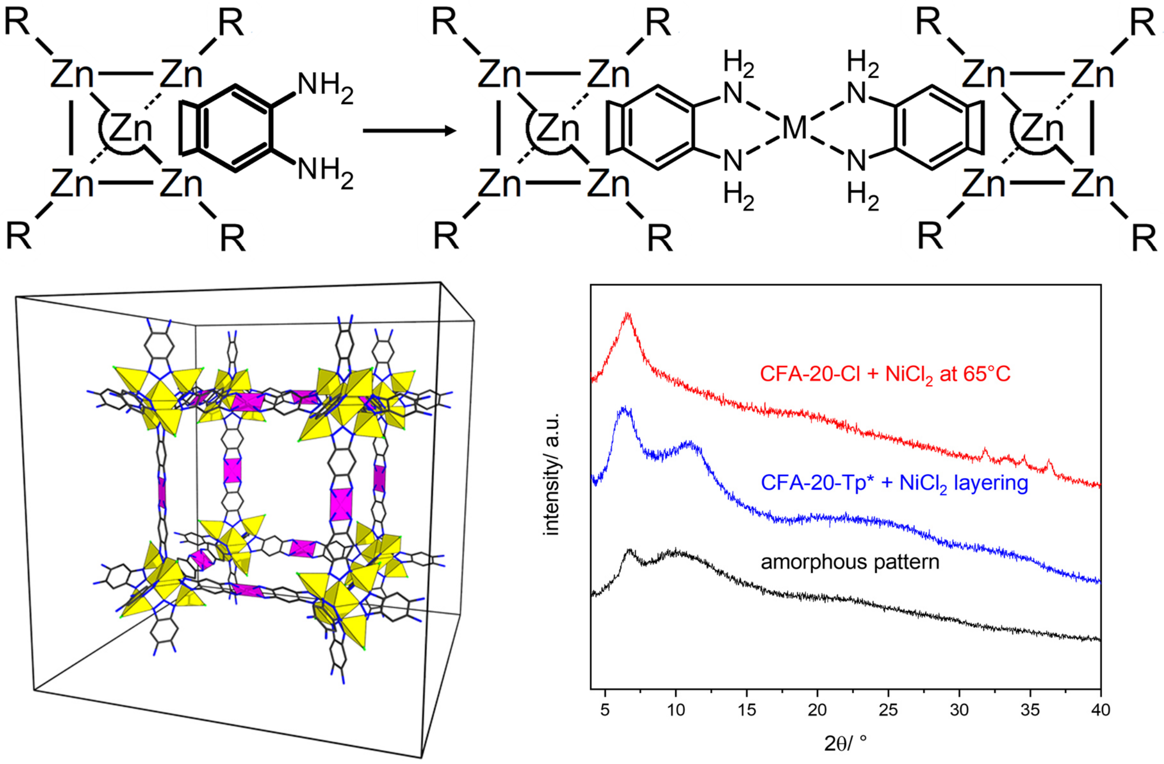

Figure 22. top: Simplified reaction scheme for the interconnection of Kuratwoski complexes via square planar metal coordination without semiquinonate formation. left: Schematic visualization of an MFU-4-type dyad structure constructed from interconnection of the Kuratowski SBUs (yellow) via square planar coordination of metal ions (purple) between the diamines leading to a cubic structure. right: Comparison of PXRD pattern of a **CFA-20-Cl** sample (heated at 65°C in an open beaker with $NiCl_2 \cdot 6H_2O$ in a solution of 0.8 mL ammonia (25%) and 5 mL of water), a CFA-20-Tp* sample (obtained from a layering approach with $NiCl_2$ in 1,4-dioxane/MeOH solutions), and an amorphous pattern, emphasizing the features below 10° 2Θ, which indicate some order in the materials with large unit cells.

MFU-4-type structure assuming a square planar coordination of metal ions like e.g. Cu^{II}, Ni^{II}, or Pt^{II} (**Figure 22**). So far, test reactions applying metal salts like $CuSO_4 \cdot 6H_2O$, $CuBr_2$, $Cu(NO_3)_2 \cdot 3H_2O$, $Cu(ClO_4)_2 \cdot 6H_2O$, $NiCl_2 \cdot 6H_2O$, $NiBr_2$, $Ni(NO_3)_2 \cdot 6H_2O$, $Ni(ClO_4)_2 \cdot 6H_2O$ or $K_2[PtCl_4]$ in DMF, DMSO, ammonia solutions, or MeOH mixtures with chloroform or 1,4-dioxane resulted mostly in precipitates without reasonable crystallinity for **CFA-20-Cl**, **CFA-20-Tp**, and **CFA-20-Tp***. Various methods from solvothermal reactions to slow diffusion via layering of metal salt solutions with complex solutions were tested. In DMF and DMSO solutions the formation of colorless $Zn(Tp^*)_2$ crystals was observed at elevated temperatures, which indicates that these synthesis conditions are not ideal for the **CFA-20-Tp*** and the **CFA-20-Cl** might be better suited for such reaction conditions, although partial exchange of the peripheral metal ions is expected to be more likely without the Tp* caps. It is expected that the equilibrium in the reaction is shifted strongly towards the highly stable and precipitating $Zn(Tp^*)_2$, whereas the ZnCl is anticipated to be more stable in the Kuratowski complex. The otherwise often dark brownish to black color of the precipitates indicates at least some coordination of the Cu or Ni ions at the amines, which could not be investigated further due to limited time during this thesis. Nonetheless, it still seems worthwhile to conduct further research into this kind of attempts because they exhibit features in the XRPD patterns that could indicate some long-range order and the formation of defective MOF nanocrystals with very poor crystallinity. Especially a layering of $NiCl_2$ and **CFA-20-Tp*** in a 1,4-dioxane/MeOH (1:1) solution and a reaction of **CFA-20-Cl** with $NiCl_2 \cdot 6H_2O$ in ammonia solution at 65°C similar to literature look promising in this regard (**Figure 22**).[116] To verify the formation of such a structure detailed analysis of the metal ratios by ICP-OES and EDX spectroscopy, elemental composition, porosity, coordination environments with X-ray absorption spectroscopy methods, and maybe also TEM and electron diffraction could be applied.

In a different approach, the already porous structures could be post-synthetically stabilized against dissolution via direct coordination of metal ions into the structures. Some preliminary experiments previously revealed in SC-XRD measurements that the **CFA-20-Tp*** M-HOF in this case can be converted into a MOF via treatment with $CuCl_2$, which leads to the coordination of CuCl moieties at its HOF SBU (**Figure 23**). Only low amounts of metal salts should be used for such conversions, because larger excess seemed to shatter the crystals and led only to amorphous products. A possibility to improve this could be the use of different metal salts because the strong interaction of the chloride anions with the amines could destabilize the structure.

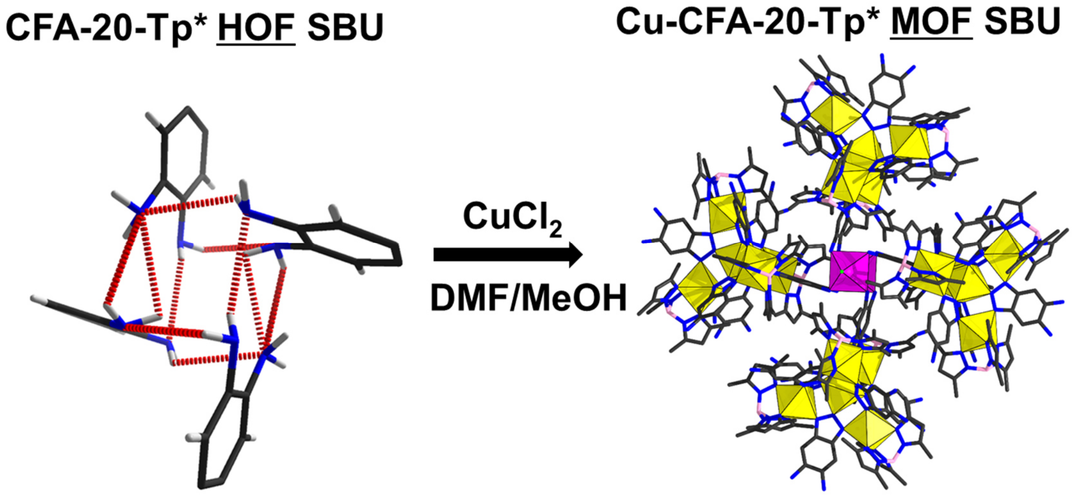

Figure 23. Reaction of the **CFA-20-Tp*** HOF SBU to a MOF SBU

2.3. Synthesis of CFA-19 and Post-Synthetic Functionalization of the Open Bibenzimidazole Coordination Sites

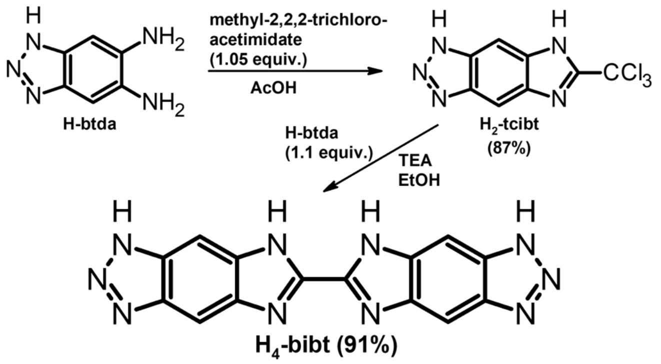

Figure 24. Synthesis of 1,1',5,5'-tetrahydro-6,6'-biimidazo[4,5-*f*]benzotriazole (**H$_4$-bibt**) via the 6-(trichloromethyl)-1,7-dihydroimidazo[4,5-*f*]benzotriazole (**H$_2$-tcibt**)·intermediate starting from 1*H*-benzotriazole-5,6-diamine (**H-btda**)

Driven by the success of the **MFU-4**, **MFU-4*l***, and **CFA-1** major efforts were invested to enhance the functionality of such MFU-4-type frameworks further. For this purpose, the novel 1,1',5,5'-tetrahydro-6,6'-biimidazo[4,5-*f*]benzotriazole (**H$_4$-bibt**) linker was envisaged and obtained in a two-step procedure starting from the **H-btda** ligand with high yields and purity (Figure 24).

In contrast to the **H$_2$-bbta** and **H$_2$-btdd**, this linker features a bibenzimidazole moiety at the backbone, which allows for additional functionalization via coordination of metal ions and complexes. It even allows for deprotonation and thus more variety and stronger binding in comparison to the commonplace bipyridines often found in literature.[117] This additional feature might also be the reason complicating the MOF formation due to unwanted interactions with the Zn salts usually employed for the synthesis of other MFU-4-type MOFs. So far, crystalline precipitates with the **H$_4$-bibt** linker were only obtained using $CoCl_2$, directly providing redox-active metal sites in the framework. Optimization of the synthesis conditions with dry DMF and 1.66 equivalents of $CoCl_2$ under argon atmosphere at 160° C gave pure phase single-crystals of the **CFA-19** MOF ([$Co_5^{II}Cl_4(H_2\text{-bibt})_3$]) (Figure 25), which crystallizes isoreticular to **MFU-4** in the cubic space group $Fm\bar{3}m$ (225). In contrast to **CFA-7** the framework does not show interpenetration, although the unit cell constant of a = 37.1738 Å is larger than in **MFU-4** (a = 21.6265 Å) and **MFU-4*l*** (a = 31.057 Å). Higher linker concentrations, alcohol impurities, and lower temperatures during the single-crystal synthesis screening also indicated the formation of the hexagonal MAF-type phase, which has not been investigated further so far.

Unfortunately, the unsaturated Co sites of the CFA-19 structure not only led to a characteristic color change from green (tetrahedrally and octahedrally coordinated Co^{II} ions) to yellow/golden (octahedrally coordinated Co^{II} ions) upon contact with polar solvents but also to a hygroscopic nature (Figure 26), which results in accumulation of water and framework degradation at a relative humidity above 30%.

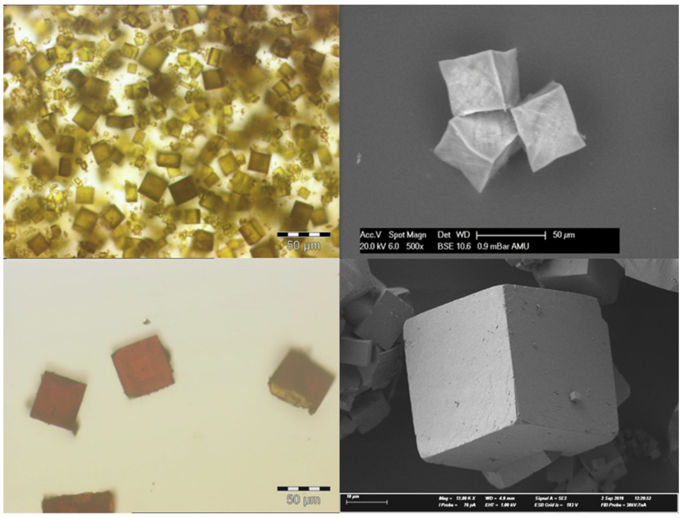

Figure 25. Optical microscopy (left) and SEM (right) images of **CFA-19** (top) and **CFA-19-Tp** (bottom), showing the shriveling of the **CFA-19** crystals after prolonged exposure to ambient conditions.

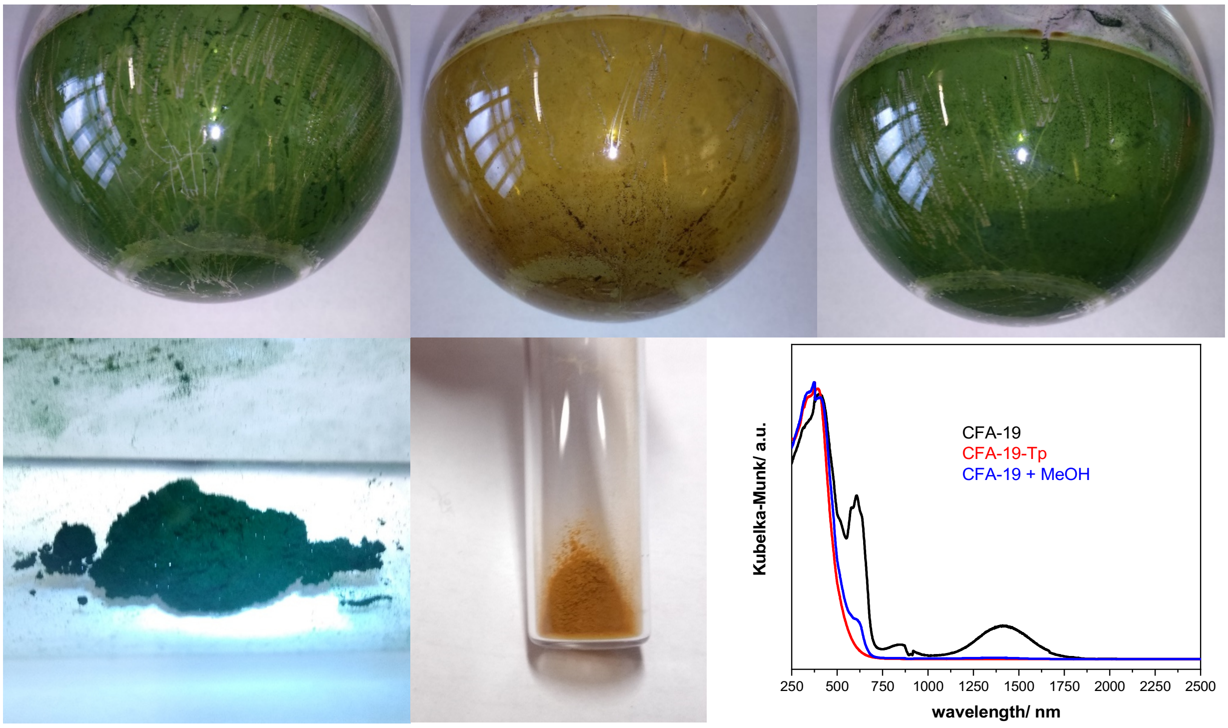

Figure 26. Top: Intense and rapid color change from green **CFA-19** (left) to golden in a MeOH atmosphere (middle) and to green after a few seconds of vacuum drying (right) as a result of the coordination environment change of the peripheral cobalt ions from tetrahedral to octahedral to tetrahedral. Bottom: Photographs of the green **CFA-19** (left), the brownish **CFA-19-Tp** (middle) and UV-VIS spectra comparison of the respective samples, showing the loss of the absorption bands associated with tetrahedrally coordinated Co^{II} ions (right).

However, the first post-synthetic treatment step exchanging the chloride side-ligands with Tp caps not only stabilizes the framework against unwanted exchange of the peripheral metal sites but also against degradation in humid environments. Therefore, the **CFA-19-Tp** was the ideal basis for the first incorporation of additional metal sites at the bibenzimidazole moieties. Treatment of **CFA-19-Tp** with excess $Re^{I}Br(CO)_5$ in DCM at 40° C resulted in a nearly complete occupation of the coordination sites in the resulting **$ReBr(CO)_3$@CFA-19-Tp** ($[Co_5^{II}Cl_{0.4}Tp_{3.6}(H_2\text{-bibt})_3\cdot(Re^{I}Br(CO)_3)_{2.8}]$) framework, in which the $Re^{I}Br(CO)_3$ moieties could be unequivocally located at the bibenzimidazole by SC-XRD structure refinement. This was a quite sophisticated task for a two-times post-synthetically modified single crystal with over 1700 atoms per unit cell. Although EDX spectra showed a similar saturation with $ReBr(CO)_3$ moieties in untreated **CFA-19**, those single crystal structures could not be reasonably refined, which might be explained by a strong bending of the linker observed upon the metal coordination in this structure, indicating that the Tp caps of the **CFA-19-Tp** also induce a structural stabilization.

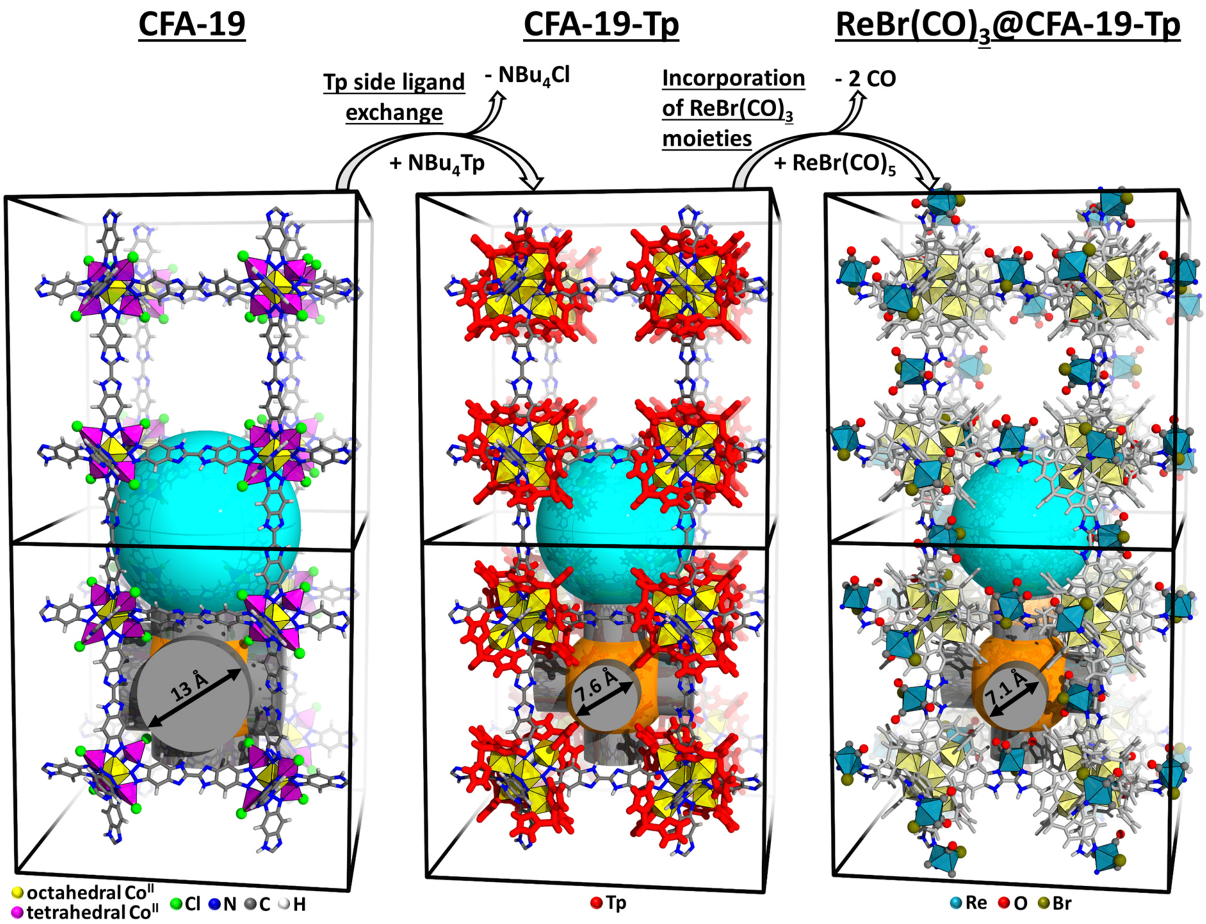

Figure 27. Post-synthetic modification of **CFA-19** towards the **CFA-19-Tp** and **ReBr(CO)$_3$@CFA-19-Tp** structures, highlighting the structure changes and channels (grey) connecting the large (blue), medium (orange), and small pores (light orange).

A similar **MnBr(CO)$_3$@CFA-19-Tp** ([Co$_5^{II}$Cl$_{0.4}$Tp$_{3.6}$(H$_2$-bibt)$_3$(Mn^{I}Br(CO)$_3$)$_3$]·3.1(Mn^{I}Br(CO)$_x$)) framework was prepared under the same conditions using Mn^{I}Br(CO)$_5$ and also solved by SC-XRD analysis. An advantage of the M^{I}Br(CO)$_3$ moieties is also the facile detection of the incorporation via the distinct IR bands around 1900 cm^{-1} (Figure 29), which are the clear fingerprint of the CO stretching vibrations. PXRD patterns and argon adsorption isotherms with

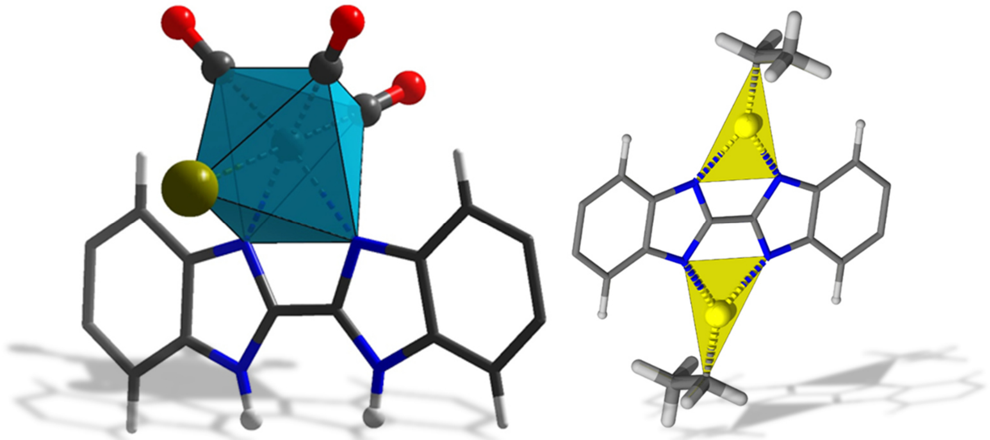

Figure 28. Detailed depiction of the ReBr(CO)$_3$ (left) and ZnEt (right) coordination moieties bound to the bibenzimidazole site in **CFA-19-Tp**

the resulting BET surface areas and pore size distributions of the compounds were also nicely aligning to the expectations and calculations, even showing the additional small pore expected to form upon introduction of the $M^{I}Br(CO)_3$ moieties (Figure 27). To unravel the full coordination potential of the bibenzimidazole sites, their deprotonation was achieved by the reaction with $ZnEt_2$ in THF, resulting in the **ZnEt@CFA-19-Tp** ($[Co_5^{II}Cl_{0.9}Tp_{3.1}(H\text{-}bibt)_{1.1}(bibt)_{1.9}\cdot(ZnEt)_{4.9}]$) framework. In contrast to the unreactive ethanido side ligands in **MFU-4*l*-Et**, the resulting ZnEt moieties exhibit a high reactivity and are unstable at ambient conditions due to the better accessibility at the bidentate coordination site. This reactivity prevented SC-XRD analysis, but the expected structure could be verified again by a combination of simulated and measured IR spectra clearly showing the symmetric and asymmetric C-H stretching vibrations of the ethanido ligand, a significant intensity decrease of the N-H stretching vibration, the Zn-C stretching vibration, as well as distinct changes of the linker bending (Figure 29).

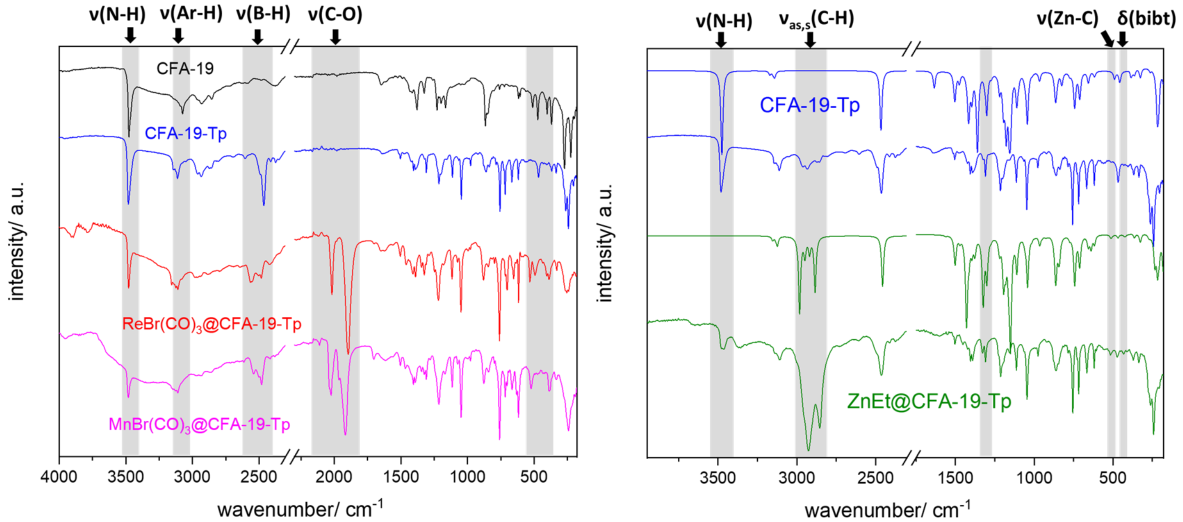

Figure 29. Left: Combined ATR-FTIR and DRIFT spectra comparison between **CFA-19** (black), **CFA-19-Tp** (blue), **$ReBr(CO)_3$@CFA-19-Tp** (red), and **$MnBr(CO)_3$@CFA-19-Tp** (pink). Right: Comparison between simulated and measured combined ATR-FTIR and DRIFT spectra of **CFA-19-Tp** (blue) and **ZnEt@CFA-19-Tp** (green).

The SC-XRD of **$MnBr(CO)_3$@CFA-19-Tp** revealed only a slightly higher occupation of the bibenzimidazole sites, although a much higher Mn and Br concentration was observed in ICP-OES and EDX measurements, which indicates some residual disordered $Mn^{I}Br(CO)_X$ complexes stuck in the structure. Despite the fact that $Mn^{I}Br(CO)_5$ sublimates easily, vacuum treatment at elevated temperatures did not significantly reduce the amount of Mn in the structure but showed a complete loss of the CO bands in the FT-IR spectra. This thermally induced cleavage of the CO ligands was also observed with a significant weight loss in the TGA curves (Figure 30), indicating a facile pathway towards highly unsaturated open Mn^{I} sites in the structure.

For similar sites, very strong dihydrogen binding energies up to 113.6 $kJmol^{-1}$ were calculated,[118] rendering them highly interesting for H_2 binding and activation, which was also shown recently for similar Mn^{I} complexes applied as hydrogenation catalysts.[119] First DRIFT spectroscopy investigations of the activation of **$MnBr(CO)_3$@CFA-19-Tp** under hydrogen atmosphere did not give away any signals of bound dihydrogen or hydride species, even when cooled down to -20° C. A major problem during this experiment was the high thermal conductivity of pure hydrogen gas, which prevents reasonable cooling to lower temperatures and also causes ice formation on the KBr windows of the sample cell. Another reason, which could have prevented the binding of dihydrogen, might be the water residues in the framework.

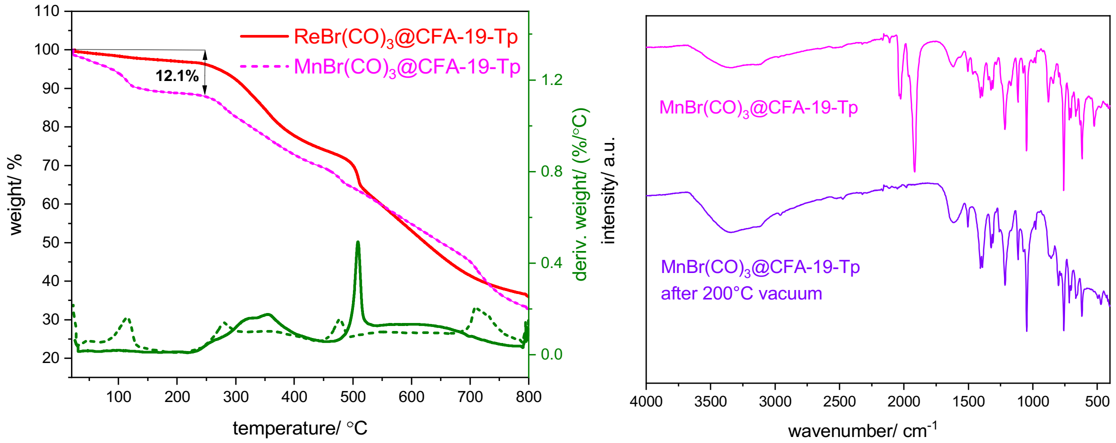

Figure 30. Left: TGA curves of **ReBr(CO)$_3$@CFA-19-Tp** (red) and **MnBr(CO)$_3$@CFA-19-Tp** (pink). Right: ATR FT-IR spectra of **MnBr(CO)$_3$@CFA-19-Tp** before (pink) and after (purple) treatment at 200° C in vacuum.

This water could directly substitute some of the CO ligands during the activation and thus deactivate the open metal sites. Vacuum treatment did not seem to be sufficient to remove the water, but other procedures like the treatment with dry solvents or drying agents could be imagined for future approaches. Furthermore, the in-situ activation and measurement of hydrogen adsorption isotherms of **MnBr(CO)$_3$@CFA-19-Tp** should provide further insights with a determination of the isosteric enthalpies of adsorption at lower temperatures. It is highly recommended to conduct such investigations as soon as the measurement device is repaired.

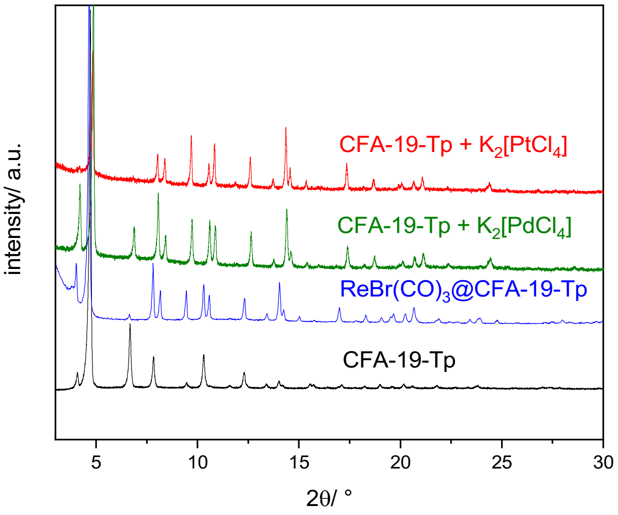

Figure 31. PXRD pattern comparison of **CFA-19-Tp** with its derivatives obtained by treatment with ReBr(CO)$_5$, K$_2$[PdCl$_4$], and K$_2$[PtCl$_4$]. The patterns of the **M^{II}Cl$_2$@CFA-19-Tp** samples were enlarged for a better comparison of the reflexes.

In some preliminary studies the incorporation of various coordination moieties was already tested. Especially the incorporation of highly coordinatively unsaturated Cu^I sites seemed to be a desirable aim. Test reactions with mesitylcopper in dry acetonitrile or THF solutions to directly deprotonate and incorporate Cu^I ions at the bibenzimidazole were unfortunately not successful so far. No significant amount of Cu could be detected in the EDX spectra of **CFA-19-Tp** frameworks treated in this manner. However, we also observed that other metal ions seem to be readily bound in the **CFA-19-Tp** structure and e.g. M^{II}Cl$_2$ (M= Pd^{II}, Pt^{II}) coordination moieties can be assumed at the bibenzimidazole from PXRD patterns of samples treated with excess K$_2$[PdCl$_4$] and K$_2$[PtCl$_4$] in water at 50° C (Figure 31). The treatment in water led to a decrease in crystallinity, which is not ideal, especially for single-crystal X-ray diffraction analyses. Therefore, complexes like cis-dichlorobis(pyridine)platinum(II) with a better solubility in organic solvents could be applied for future investigations under more gentle reaction conditions.

2.4. Magnetic Properties of a Mn(II) 1,2,3-Triazolate Coordination Framework with Ultranarrow Pores

The reaction of the 1*H*-1,2,3-triazole (**H-ta**) linker with $MnCl_2$ under solvothermal conditions in isopropyl alcohol at 210°C resulted in large single-crystal specimens of **CFA-23** (((propan-2-yl)oxidanium)$^+$[$Mn_6Cl_5(ta)_8$]$^-$) during the screening of synthesis conditions to reproduce $Mn(ta)_2$ single-crystals from literature (Figure 32).[110]

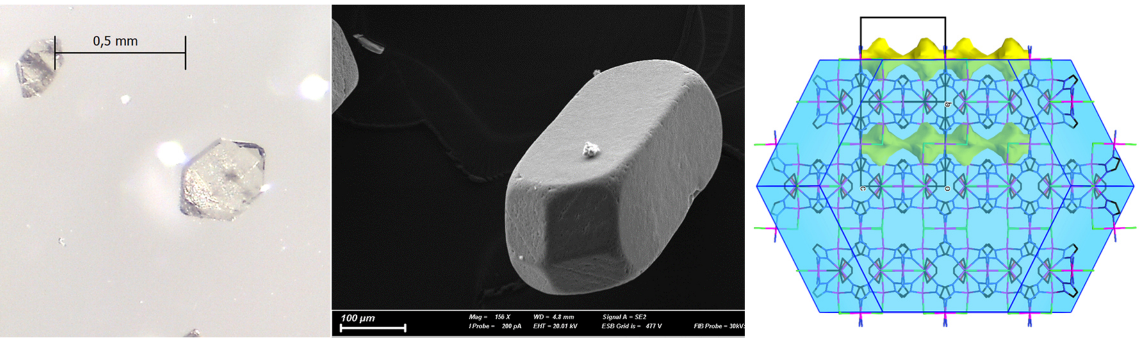

Figure 32. Optical (left) and SEM (middle) micrographs of **CFA-23** single-crystals in comparison with the crystal morphology structure plot showing the narrow pore channels (yellow) running along the *c*-direction.

Analysis of the structure revealed a two-fold interpenetration of the framework nets, which have the same SBUs and topology (***dia*** nets with point (Schläfli) symbol 6^6) as the non-interpenetrated literature compound ($H[Mn_6(bta)_8Cl_5] \cdot (H_2O)_4$) built from 1*H*-1,2,3-benzotriazole.[112] Albeit **CFA-23** crystallizes in the space group $P4_2/nnm$ (134)(a=b=14.4426(4) Å and c=10.2366(3) Å) instead of $I\bar{4}2d$ (122) like the literature compound. Another difference is the proposed counterion, which in our case could be identified as a (propan-2-yl)oxidanium$^+$ cation from the SC-XRD data, as well as a combined TGA-MS measurement detecting the expected propene as decomposition product. The Mn_4 units with a central μ_4-Cl bridge in **CFA-23** mainly differ in a smaller out-of-plane distortion of the manganese ions in comparison to the literature $H[Mn_6(bta)_8Cl_5] \cdot (H_2O)_4$. Similar SBUs without the interconnection via μ_2-Cl-Mn-μ_2-Cl bridges are a well-known structure motif of pyrazolate, triazolate, and tetrazolate MOFs in literature, in which all four Mn ions are usually in a plane with the chloride anion.[120]

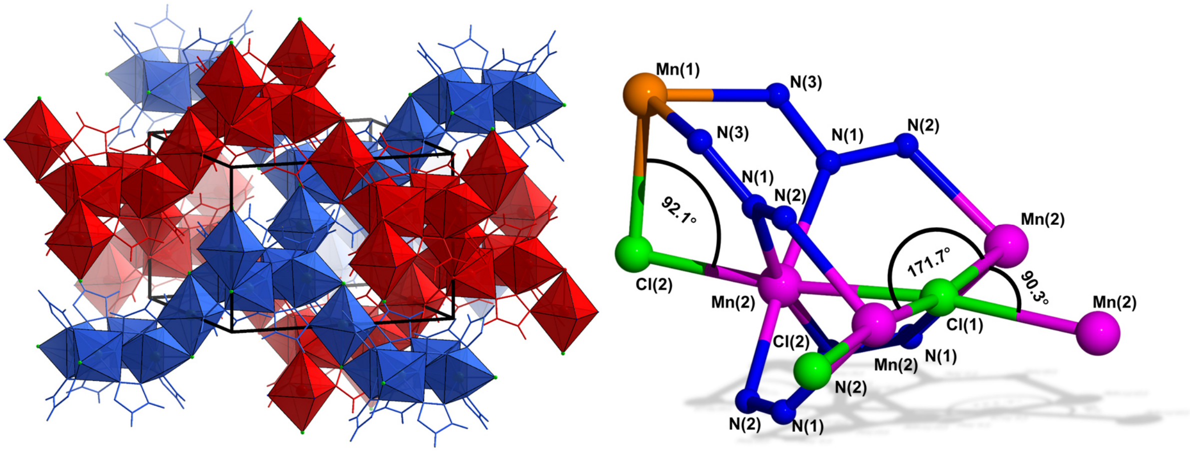

Figure 33. Structure plot visualizing the two interpenetrated networks of the CFA-23 structure (left) and plot showing the atoms and bond angles of the tetranuclear Mn_4 unit (pink) interconnected in the framework via the Mn(1) (orange) ions (right).

The ultra-narrow pore aperture of 2.72 Å in the **CFA-23** structure is expected to be the reason why no gas adsorption of H_2, CO_2 or Ar could be observed and kinetic trapping experiments at higher temperatures and pressures with Xe also failed so far. Nonetheless, testing of smaller molecules still might be successful.

Magnetic investigation of the sample showed similar properties as the spin-canted literature compound $H[Mn_6(bta)_8Cl_5]\cdot(H_2O)_4$ in general, although the increased $\chi_M T$ product of **CFA-23** with a value of 23.22 $cm^3mol^{-1}K$ in comparison to 19.24 $cm^3mol^{-1}K$ indicates weaker, but still quite large, antiferromagnetic exchange interactions. This is also in agreement with the higher Weiss temperature of $\theta_W = -67$ K in comparison to -76 K found for literature material. From this, a slightly higher frustration parameter of $f=2.4$ is obtained for **CFA-23** in comparison to the $f=1.7$ for $H[Mn_6(bta)_8Cl_5]\cdot(H_2O)_4$.

A deeper insight into the coupling between the metal ions was gained via fitting of the magnetic susceptibility with an antiferromagnetic quadratic lattice approximation and a molecular approach, indicating frustration of the antiferromagnetic tetranuclear Mn_4 unit. The match between simulation and measurement suggests that the Mn_4 units are mainly responsible for the magnetic behavior and the bridging Mn ions mostly act as mediators between those tetramers.

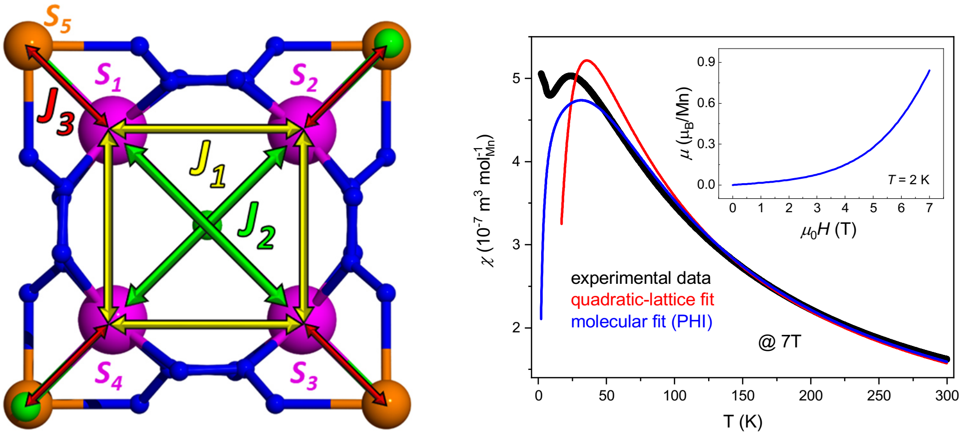

Figure 34. Depiction of the Mn_4-tetramer with the respective Mn^{II}-Mn^{II} exchange couplings J_1 (yellow), J_2 (green) and J_3 (red) in the basic (pink) and the bridging Mn^{II} ions (orange) of **CFA-23** (left). Comparison between the measured magnetic susceptibility χ in a 7 T field per Mn^{II} ion and the fits obtained from the quadratic-layer and molecular models. The isothermal magnetization M as function of the magnetic field H at 2K obtained from the molecular fit is given in the inset (right).

2.5. Cooperative Spin-Crossover Phase Transition and Adsorbate Dependent Conductivity of Fe(ta)$_2$

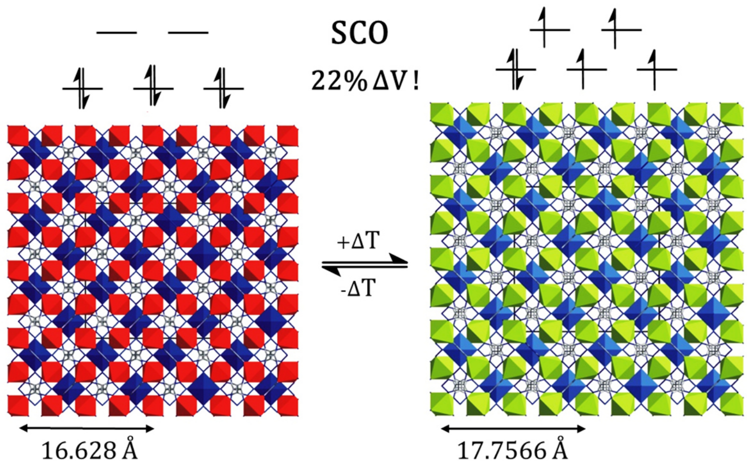

Figure 35. Visualization of the 22% volumetric expansion upon transition of the Fe(ta)$_2$ from the low- (left) to high-spin/temperature (right) phase.

Samples of Fe(ta)$_2$, well known as an electrically conductive MOF from literature,[103,106] were prepared in large quantities and analyzed accordingly via FT-IR, argon adsorption, PXRD and TGA for the investigation of its spin-crossover transition, as well as conductivity changes upon gas adsorption. VT-XRPD patterns and DSC curves of Fe(ta)$_2$ revealed a large-hysteresis phase transition accompanied by a large change of the unit cell volume, but without changes of the $Fd\bar{3}m$ (no. 227) space group. Magnetic measurements and Mössbauer spectroscopy of Fe(ta)$_2$ samples prepared with high purity FeCl$_2$ (99.999%) revealed the expected low- to high-spin transition upon heating over 290° C. Unfortunately, this is in a temperature regime where the material already shows the first signs of decomposition. This is the reason why susceptibility data was only measured up to 297° C exhibiting only an incomplete transition. Susceptibility data measured at higher temperatures gave rise to ferromagnetic impurities overshadowing the sample signals. Similar observations were made during the Mössbauer spectroscopy, where the minor decomposition products fortunately are only visible as minor impurities in the spectra, although the samples were measured for 12 h at each temperature in this case. Furthermore, the low- and high-spin Fe(ta)$_2$ structures were also investigated in silico, clearly indicating a pure low-spin phase for standard DFT calculations without spin constraints. In addition, the electronic structures of the low-spin and two possible ferro- or antiferromagnetic high-spin structures were simulated.

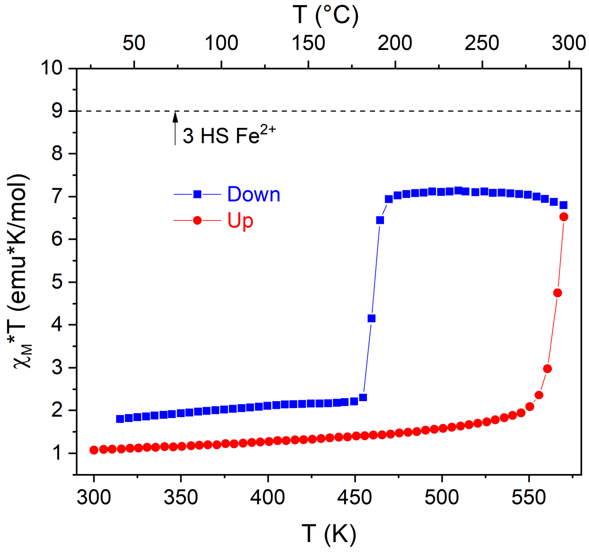

Figure 36. χ_MT representation of the molar magnetic susceptibility of Fe(ta)$_2$ (based on the $Fe_3C_{12}H_{12}N_{18}$ sum formula) upon heating to 297°C (red circles) and cooling (blue squares) showing a partial transition to the high-spin phase and a gap in the hysteresis loop.

In a different study, the changes in electrical conductivity of the Fe(ta)$_2$ MOF upon adsorption of chemically inert CO$_2$ and Ar gas, showing 2-site Langmuir-type behavior, were investigated with

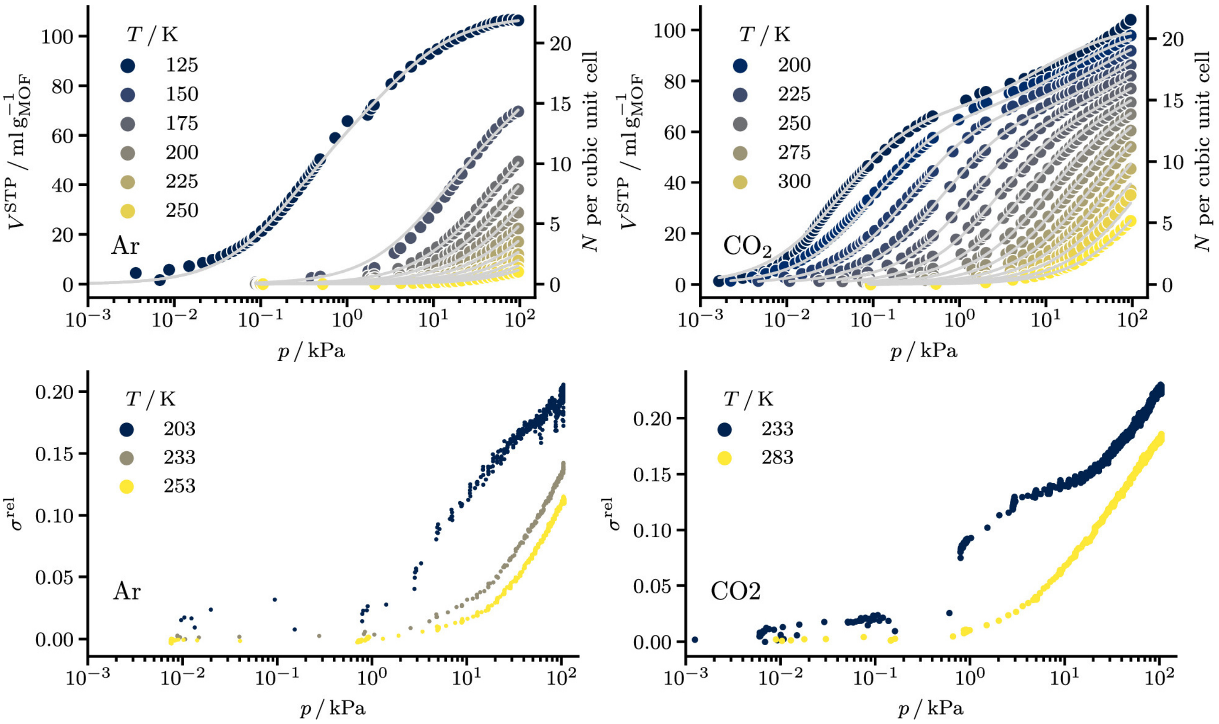

Figure 37. The Ar and CO2 adsorption isotherms measured at different temperatures (top) are matching with the curves of the relative conductivity during gas loading at similar temperatures (bottom).

a combination of theoretical methods and experiments. To evaluate the findings, detailed adsorption isotherms at various temperatures were measured and compared to simulated gas uptakes (Figure 37). In addition, the interaction between the gas and the framework was further analyzed by calculation of the isosteric enthalpies of adsorption (ΔH_{ad}) making use of the Clausius-Clapeyron equation (Eq. 1).

$$\Delta H_{ad} = R\left(\frac{\partial \ln p}{\partial\left(^{1}/_{T}\right)}\right)_{V} \qquad (1)$$

R= gas constant
p= pressure
T= temperature
V= volume

From this, the isosteric enthalpies of adsorption were determined as the slope of linear Arrhenius plots (ln$p$ vs 1/RT), which are obtained from the respective pressure and temperature pairs at constant loadings (which is equivalent to constant volumes) according to equation 2.

$$\ln p = \Delta H_{ad}\frac{1}{RT} + \ln p_0 \qquad (2)$$

In general, the obtained isotherms can be fitted well by a two adsorption-site Langmuir model, which is in accordance with the two different pores of the structure. The measured and calculated values for the adsorption, are also in a good agreement showing a similar energy of roughly -16 kJmol^{-1} for Ar in both pores. In contrast, for CO_2 a decrease of the isosteric adsorption enthalpies is observed for loadings >16 molecules per unit cell, where presumably all small pores could be occupied. This aligns well with the calculated trend of a strong adsorption energy of CO_2 in the small pores and a significantly smaller energy in the large ones. Moreover, structural investigations upon uptake of the gases at different pressures and temperatures were obtained by Le Bail fits of XRPD patterns, matching well with the simulated cell changes for similar uptake amounts.

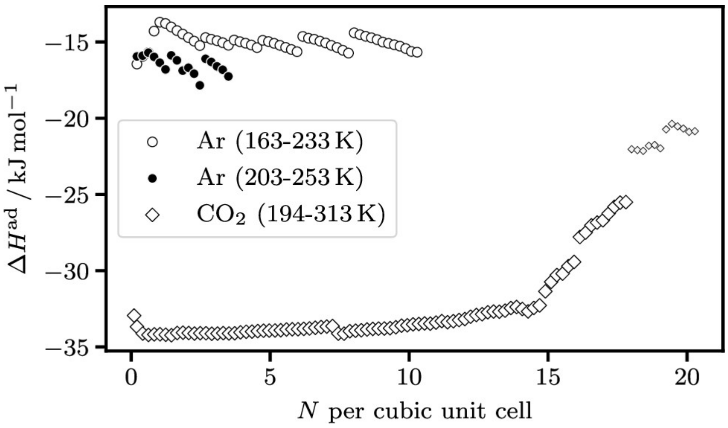

Figure 38. Isosteric enthalpies of adsorption for the unit cell loading obtained from Ar adsorption between 163-233K (empty circles) and 203-253K (full circles), as well as for CO_2 between 194-313K (cubes).

As these results showed a good agreement between theory and experiment, the observed changes in the relative conductivity upon gas uptake could also be ascribed mainly to the deformation potential from theoretical simulations of various pore loading configurations in the $Fe(ta)_2$ MOF.

3. Conclusions and Outlook

In summary, a variety of 18 new 1,2,3-triazolate-based coordination frameworks were obtained either from direct synthesis with novel ligands or post-synthetic modifications. In addition, the Fe(ta)$_2$ MOF was prepared and investigated with respect to a spin-crossover phase transition and its temperature and adsorbate dependent electrical conductivity.

The versatility and our understanding of the **MFU-4*l*** MOFs behavior during well-established literature catalysis reactions using organometallic co-catalysts was significantly enhanced from the characterization of the isolated organometallic **MFU-4*l*** MOFs obtained from post-synthetic ligand exchange reactions. Herein, FT-IR spectroscopy in combination with simulated spectra was established as a valuable characterization tool for such post-synthetic modifications in MOFs, which cannot be investigated by liquid state NMR or mass spectrometry usually applied for organometallic complexes. Whereas most of the five resulting organometallic **Zn-MFU-4*l*** MOFs exhibit a good stability at ambient and even controlled hydrolysis conditions, the pyrophoric **Co-MFU-4*l*-Me** revealed a high reactivity, which gives rise to a neat synthesis pathway towards **Co-MFU-4*l*-OH** upon hydrolysis. The Co-OH functions of **Co-MFU-4*l*-OH** were shown by DRIFTS measurements to mimic the CO$_2$ binding behavior of carbonic anhydrase enzymes, which is highly interesting for future CO$_2$ capture and conversion applications. The **Co-MFU-4*l*-Me** could also be directly tested e.g. as olefin polymerization catalyst without use of the organometallic co-catalysts or as a methylation agent.
In the future, the stability of organometallic **Zn-MFU-4*l*** derivatives could also be interesting for other types of functionalization. For example, 3,3-dimethyl-1-butyn-1-ido side ligand derivatives featuring dipolar functions instead of the methyl groups are envisaged for the introduction of dipolar rotors, which then line the apertures of the small pores in **MFU-4*l***.

In the effort to establish new synthesis strategies for MOFs and related compounds, the **CFA-20** series of five new M-HOF structures, assembled from four Kuratowski-type MBBs featuring the 1*H*-benzotriazole-5,6-diamine (**H-btda**) ligand, was successfully developed. In the porous **CFA-20-Cl** and **CFA-20-Br** structures six Kuratowski complexes arrange around a unique twelve-fold hydrogen bonded halogen anion (Cl, Br) with their amine functions. In contrast to those structures, the **CFA-20-Tp** and **CFA-20-Tp***, obtained by a ligand exchange reaction with Tp and Tp*, are even stable upon solvent removal, which gives rise to permanent porosity. This is a feature not often observed for similar materials and thus an important contribution to the small family of permanently porous M-HOFs. One advantage to MOFs is that the weaker hydrogen-bond or π-π interactions result in a good solubility of such materials. This not only allows for more characterization methods like liquid state NMR or mass spectroscopy, but also for a facile material regeneration or purification via recrystallization, as well as the assembly of new structures. This was successfully employed to increase the porosity of **CFA-20-Tp*** by recrystallization and to assemble the variant **CFA-20-Tp*-DMSO** structure.
Those complexes are envisaged as multifunctional MBBs in a variety of MOF assembly strategies. Although the synthesis attempts towards cubic MFU-4-type dyad structures with additional SBUs, in which metal ions adapt a square planar coordination from the amines of the **CFA-20**

MBBs, could not be obtained so far, we are certain that such structures are feasible applying the correct synthesis conditions. In addition, it seems worthwhile to take a more detailed look at the materials obtained in these efforts because they might already be the desired products only lacking the high crystallinity usually expected from MOFs. As proven by some preliminary experiments, the direct conversion of the M-HOF structures into MOFs via metal incorporation is another suitable method, which is worthy of further investigation. Another possibility not tested so far due to time restraints is the organic functionalization of the diamine groups. For example the reaction with 6-(trichloromethyl)-1,7-dihydroimidazo[4,5-*f*]benzotriazole (**H_2-tcibt**) could result in a Kuratowski complex with the **CFA-19** linker, which could then be applied in a MOF synthesis with $CoCl_2$ resulting in a **CFA-19** framework with alternating Co-and Zn-based SBUs (Figure 39).

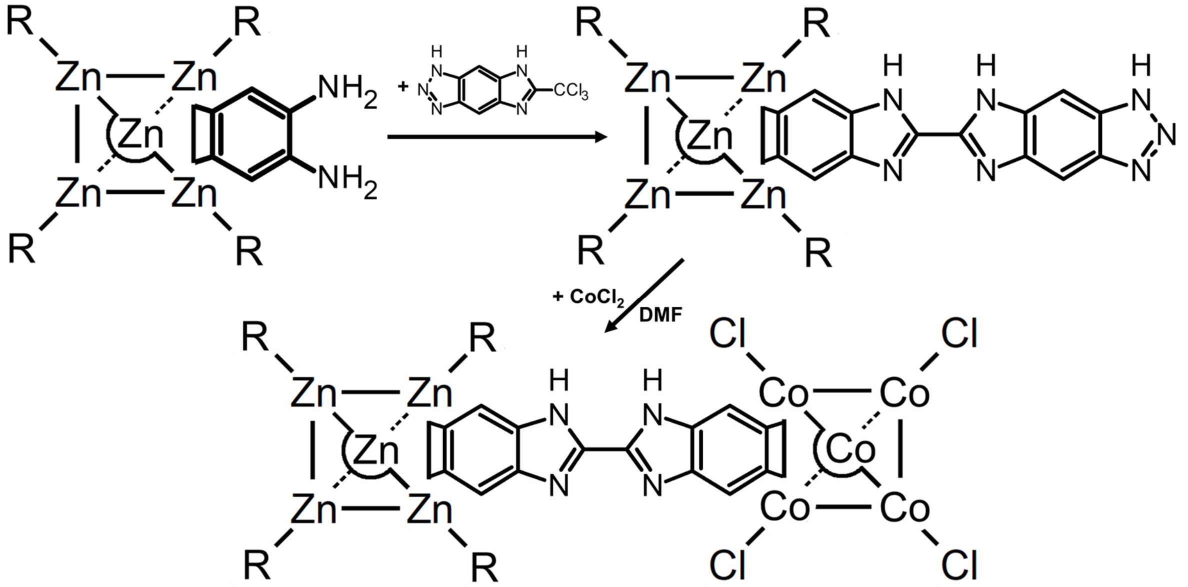

Figure 39. Schematic MOF synthesis procedure towards the proposed MOF structure with alternating Zn and Co Kuratowski SBUs applying CFA-20-type Kuratowski complex building blocks obtained from the reaction with 6-(trichloromethyl)-1,7-dihydroimidazo[4,5-*f*]benzotriazole (**H_2-tcibt**).

These results and concepts render the **CFA-20** compounds valuable MBBs for future assembly strategies towards advanced framework architectures, which are not accessible via standard MOF syntheses approaches directly applying ligands and metal salts.

Moreover, the amine rich pore linings in the **CFA-20-Tp** and **CFA-20-Tp*** frameworks demand the investigation of CO_2 capture properties, as such materials are known for strong interactions with CO_2. [16,121]

Starting from 1*H*-benzotriazole-5,6-diamine (**H-btda**) the so far most sophisticated MFU-4-type bistriazolate linker 1,1',5,5'-tetrahydro-6,6'-biimidazo[4,5-*f*]benzotriazole (**H_4-bibt**) was obtained in a two-step reaction via the 6-(trichloromethyl)-1,7-dihydroimidazo[4,5-*f*]benzotriazole (**H_2-tcibt**)·intermediate. This linker was successfully employed for the synthesis of the novel **CFA-19** MOF, which is isoreticular to **MFU-4** and, in contrast to other MFU-4-type MOFs, directly built from redox-active Co^{II} ions. It represents the largest non-interpenetrated member of the MFU-4-type MOF family. Moreover, the combination of Kuratowski SBUs and additional open bibenzimidazole coordination sites at the linker backbone potentiates the

variability of post-synthetic functionalization. Protection of the peripheral Co ions with Tp caps resulted in the stabilized **CFA-19-Tp** structure, which was successfully used for first proof-of-principle post-synthetic coordination of $M^{I}Br(CO)_3$ (M= Mn^{I}, Re^{I}) and ZnEt moieties. While both **$M^{I}Br(CO)_3$@CFA-19-Tp** frameworks could be solved by SC-XRD structure refinement, the highly reactive **ZnEt@CFA-19-Tp** was again characterized with a combination of measured and simulated IR spectra. This also revealed the deprotonation of the bibenzimidazole, which is a significant advantage regarding the binding strength of metal sites in comparison to the standard bipyridines often used in literature.[117,122] The high reactivity of the ZnEt moieties in comparison to **Zn-MFU-4*l*-Et**, which is a result from the better steric accessibility of the coordination moieties at the biimidazole, further corroborates the functionality of such bidentate sites. The **$MnBr(CO)_3$@CFA-19-Tp** should also be of special interest for further investigations on the binding or activation of small molecules, because a thermally induced cleavage of all CO ligands was observed, which should lead to highly unsaturated Mn^{I} sites. Although first attempts to identify bound hydride or dihydrogen species failed, it might only be necessary to find proper treatment, activation, and measurement procedures for this compound. Furthermore, such $M^{I}Br(CO)_3$ moieties are well known from literature as CO_2 reduction photo- and electrocatalysts,[122,123] which clearly demands further investigations in those MOFs, as well as their potential as gasotransmitters.[124] Incorporation of other moieties into the **CFA-19-Tp** scaffold, as shown in preliminary tests with $M^{II}Cl_2$ (M= Pd^{II}, Pt^{II}), should enable us to conduct the large variety of homogeneous catalysis reactions known for the respective complexes in a heterogenous fashion. The **H_4-bibt** linker could also be used for the synthesis of different structures. In this regard, hints towards the formation of a hexagonal MAF phase have been already observed during the single-crystal synthesis screenings from higher linker and metal salt concentrations.
In summary, a new series of MFU-4-type MOFs were successfully established as stable scaffolds for the post-synthetic incorporation of additional coordination moieties, which are expected to result in a variety of different applications. Next to the binding and activation of small molecules, even photocatalytic redox cascades can be envisaged for such coupled multi-metal site architectures.

The novel **CFA-23** (((propan-2-yl)oxidanium)$^{+}$[$Mn_6Cl_5(ta)_8$]$^{-}$) coordination framework was obtained from the high temperature solvothermal reaction of 1*H*-1,2,3-triazole and $MnCl_2$ in isopropyl alcohol during reaction parameter screening for $Mn(ta)_2$ single-crystal synthesis. The SC-XRD structure revealed a framework with the same topology as a literature compound synthesized from 1*H*-1,2,3-benzotriazole, but a two-fold interpenetration due to the lower steric demand of 1*H*-1,2,3-triazole. This led to some minor changes in bond angles and ultranarrow channel pores along the crystallographic *c*-direction, which so far were not even accessible for small gas molecules like H_2 or in high pressure and temperature kinetic trapping experiments. The kinetic trapping of gases in this compound still might give interesting results, because so far only larger Xe was tested, and smaller molecules could be more suitable for **CFA-23**. Moreover, this material was an ideal sample for the investigation of the structure-magnetism relations in comparison with the literature compound. The magnetic investigations revealed a behavior differing from the literature counterpart, thus, indicating that minor changes induced from interpenetration or steric linker demand might be a novel means for the adjustment of magnetic properties in future compounds. For this purpose, various derivatives of the **H-ta** ligand with cyclopentyl, methyl, ethyl, or halogenide rests can be imagined.

The Fe(ta)$_2$, which has gained large interest in literature as a rare example of a 3D framework exhibiting electrical conductivity, was prepared with high purity metal salts for the investigation of a high temperature spin-crossover phase transition. It was shown that this cooperative phase transition, investigated by VT-PXRD, Mössbauer spectroscopy, DSC, and magnetic measurements, starts around 290 °C leading to a 22% increase of the unit cell volume. With the transition to the low-spin phase starting below 210° C, this is, to the best of our knowledge, the largest hysteresis of a SCO material observed so far. The knowledge gained herein has already been established further with computational methods in literature regarding the origin of the cooperativity leading to such a large hysteresis.[125] This is expected to help us in the design of future SCO materials with adjustable transition temperatures and hysteresis loops, which are envisaged for memory device,[126] barocaloric,[127] sensor, and mechanical actuator applications.[128]

Furthermore, it was verified that the electrical conductivity of the Fe(ta)$_2$ changes upon loading with different guest molecules in the pores. To assist the sophisticated computational methods indicating a prominent influence of the deformation potential in the Bardeen–Shockley (BS) mobility, the gas loading and resulting adsorption enthalpies were determined from CO$_2$ and Ar adsorption isotherms at various temperatures for a better insight into these phenomena.

Such gas loading dependent conductivity changes in the Fe(ta)$_2$ can be utilized as an additional measurement dimension to the selective mass loadings detected with MOF@SAW-based gas sensor devices applying **MFU-4** and **MFU-4*l*** under different gas conditions.[54,55] Because such conductivity changes can also be read out from the SAW sensor signals it would significantly increase the parameters for the distinction of various gases in such devices, ultimately aiming towards application as artificial nose.

4. References

[1] a) M. M. Sabzehmeidani, S. Mahnaee, M. Ghaedi, H. Heidari, V. A. L. Roy, *Mater. Adv.* **2021**, *2*, 598; b) Y. Li, L. Li, J. Yu, *Chem* **2017**, *3*, 928; c) A. Huang, Y. He, Y. Zhou, Y. Zhou, Y. Yang, J. Zhang, L. Luo, Q. Mao, D. Hou, J. Yang, *J. Mater. Sci.* **2019**, *54*, 949.

[2] Y. Li, J. Yu, *Nat. Rev. Mater.* **2021**, *6*, 1156.

[3] a) J. Ribas Gispert, *Coordination chemistry*, Wiley-VCH, Weinheim, **2008**; b) G. A. Lawrance, *Introduction to Coordination Chemistry*, John Wiley & Sons, Ltd, Chichester, UK, **2010**; c) V. Gold, *The IUPAC Compendium of Chemical Terminology*, International Union of Pure and Applied Chemistry (IUPAC), Research Triangle Park, NC, **2019**; d) P. Schwab, M. B. France, J. W. Ziller, R. H. Grubbs, *Angew. Chem. Int. Ed. Engl.* **1995**, *34*, 2039; e) P. Schwab, R. H. Grubbs, J. W. Ziller, *J. Am. Chem. Soc.* **1996**, *118*, 100.

[4] M. Eddaoudi, J. Kim, N. Rosi, D. Vodak, J. Wachter, M. O'Keeffe, O. M. Yaghi, *Science* **2002**, *295*, 469.

[5] S. R. Batten, N. R. Champness, X.-M. Chen, J. Garcia-Martinez, S. Kitagawa, L. Öhrström, M. O’Keeffe, M. Paik Suh, J. Reedijk, *Pure Appl. Chem.* **2013**, *85*, 1715.

[6] a) O. M. Yaghi, M. O'Keeffe, N. W. Ockwig, H. K. Chae, M. Eddaoudi, J. Kim, *Nature* **2003**, *423*, 705; b) M. O'Keeffe, M. A. Peskov, S. J. Ramsden, O. M. Yaghi, *Acc. Chem. Res.* **2008**, *41*, 1782; c) M. Li, D. Li, M. O'Keeffe, O. M. Yaghi, *Chem. Rev.* **2014**, *114*, 1343.

[7] a) P. Li, M. R. Ryder, J. F. Stoddart, *Acc. Mater. Res.* **2020**, *1*, 77; b) R.-B. Lin, Y. He, P. Li, H. Wang, W. Zhou, B. Chen, *Chem. Soc. Rev.* **2019**, *48*, 1362; c) B. Wang, R.-B. Lin, Z. Zhang, S. Xiang, B. Chen, *J. Am. Chem. Soc.* **2020**, *142*, 14399; d) Z.-H. Zhu, H.-L. Wang, H.-H. Zou, F.-P. Liang, *Dalton Trans.* **2020**, *49*, 10708.

[8] a) K. Geng, T. He, R. Liu, S. Dalapati, K. T. Tan, Z. Li, S. Tao, Y. Gong, Q. Jiang, D. Jiang, *Chem. Rev.* **2020**, *120*, 8814; b) M. G. Mohamed, A. F. M. EL-Mahdy, M. G. Kotp, S.-W. Kuo, *Mater. Adv.* **2022**, *3*, 707.

[9] a) A. I. Cooper, *ACS Cent. Sci.* **2017**, *3*, 544; b) S. Lee, H. Jeong, D. Nam, M. S. Lah, W. Choe, *Chem. Soc. Rev.* **2021**, *50*, 528; c) B. D. Egleston, A. Mroz, K. E. Jelfs, R. L. Greenaway, *Chem. Sci.* **2022**, *13*, 5042.

[10] a) Chui, Lo Charmant, Orpen, Williams, *Science* **1999**, *283*, 1148; b) H. Li, M. Eddaoudi, M. O'Keeffe, O. M. Yaghi, *Nature* **1999**, *402*, 276.

[11] R. Freund, S. Canossa, S. M. Cohen, W. Yan, H. Deng, V. Guillerm, M. Eddaoudi, D. G. Madden, D. Fairen-Jimenez, H. Lyu et al., *Angew. Chem. Int. Ed.* **2021**, *60*, 23946.

[12] R. Freund, O. Zaremba, G. Arnauts, R. Ameloot, G. Skorupskii, M. Dincă, A. Bavykina, J. Gascon, A. Ejsmont, J. Goscianska et al., *Angew. Chem. Int. Ed.* **2021**, *60*, 23975.

[13] a) N. Hanikel, M. S. Prévot, F. Fathieh, E. A. Kapustin, H. Lyu, H. Wang, N. J. Diercks, T. G. Glover, O. M. Yaghi, *ACS Cent. Sci.* **2019**, *5*, 1699; b) F. Fathieh, M. J. Kalmutzki, E. A. Kapustin, P. J. Waller, J. Yang, O. M. Yaghi, *Sci. Adv.* **2018**, *4*, eaat3198; c) H. Kim, S. R. Rao, E. A. Kapustin, L. Zhao, S. Yang, O. M. Yaghi, E. N. Wang, *Nat. Commun.* **2018**, *9*; d) H. Kim, S. Yang, S. R. Rao, S. Narayanan, E. A. Kapustin, H. Furukawa, A. S. Umans, O. M. Yaghi, E. N. Wang, *Science* **2017**, *356*, 430.

[14] a) R. Ettlinger, U. Lächelt, R. Gref, P. Horcajada, T. Lammers, C. Serre, P. Couvreur, R. E. Morris, S. Wuttke, *Chem. Soc. Rev.* **2022**, *51*, 464; b) H. Bunzen, D. Jirák, *ACS Appl. Mater. Interfaces* **2022**.

[15] I. Tibbetts, G. E. Kostakis, *Molecules* **2020**, *25*.

[16] Z. Sun, Y. Liao, S. Zhao, X. Zhang, Q. Liu, X. Shi, *J. Mater. Chem. A* **2022**, *10*, 5174.

[17] M. Ding, R. W. Flaig, H.-L. Jiang, O. M. Yaghi, *Chem. Soc. Rev.* **2019**, *48*, 2783.

[18] A. Bavykina, N. Kolobov, I. S. Khan, J. A. Bau, A. Ramirez, J. Gascon, *Chem. Rev.* **2020**, *120*, 8468.

[19] P. Lanzafame, S. Perathoner, G. Centi, S. Gross, E. J. M. Hensen, *Catal. Sci. Technol.* **2017**, *7*, 5182.

[20] a) H.-Y. Li, S.-N. Zhao, S.-Q. Zang, J. Li, *Chem. Soc. Rev.* **2020**, *49*, 6364; b) H. Yuan, N. Li, W. Fan, H. Cai, D. Zhao, *Adv. Sci.* **2022**, *9*, e2104374.

[21] A. E. Thorarinsdottir, T. D. Harris, *Chem. Rev.* **2020**, *120*, 8716.

[22] a) M. G. Yamada, H. Fujita, M. Oshikawa, *Phys. Rev. Lett.* **2017**, *119*, 57202; b) Y. Misumi, A. Yamaguchi, Z. Zhang, T. Matsushita, N. Wada, M. Tsuchiizu, K. Awaga, *J. Am. Chem. Soc.* **2020**, *142*, 16513; c) J. M. Bulled, J. A. M. Paddison, A. Wildes, E. Lhotel, S. J. Cassidy, B. Pato-Doldán, L. C. Gómez-Aguirre, P. J. Saines, A. L. Goodwin, *Phys. Rev. Lett.* **2022**, *128*, 177201; d) V. Ban, R. Sibille, A. Mesbah, T. Gaudisson, T. Mazet, M. François, *Solid State Sci.* **2014**, *37*, 154; e) R. A. Murphy, L. E. Darago, M. E. Ziebel, E. A. Peterson, E. W. Zaia, M. W. Mara, D. Lussier, E. O. Velasquez, D. K. Shuh, J. J. Urban et al., *ACS Cent. Sci.* **2021**, *7*, 1317.

[23] C. R. Groom, I. J. Bruno, M. P. Lightfoot, S. C. Ward, *Acta Cryst. B* **2016**, *72*, 171.

[24] Casimir Kuratowski, *Fundamenta Mathematicae* **1930**, *15*, 271.

[25] S. Biswas, M. Tonigold, M. Speldrich, P. Kögerler, M. Weil, D. Volkmer, *Inorg. chem.* **2010**, *49*, 7424.

[26] J. H. Marshall, *Inorg. chem.* **1978**, *17*, 3711.

[27] a) R. Alsfasser, A. K. Powell, H. Vahrenkamp, S. Trofimenko, *Chem. Ber.* **1993**, *126*, 685; b) R. Alsfasser, S. Trofimenko, A. Looney, G. Parkin, H. Vahrenkamp, *Inorg. chem.* **1991**, *30*, 4098.

[28] a) V. L. Himes, A. D. Mighell, A. R. Siedle, *J. Am. Chem. Soc.* **1981**, *103*, 211; b) G. F. Kokoszka, J. Baranowski, C. Goldstein, J. Orsini, A. D. Mighell, V. L. Himes, A. R. Siedle, *J. Am. Chem. Soc.* **1983**, *105*, 5627; c) J. Handley, D. Collison, C. D. Garner, M. Helliwell, R. Docherty, J. R. Lawson, P. A. Tasker, *Angew. Chem.* **1993**, *32*, 1036; d) M. Murrie, D. Collison, C. Garner, M. Helliwell, P. A. Tasker, S. S. Turner, *Polyhedron* **1998**, *17*, 3031; e) J. WANG, *Chin. sci. bull.* **2002**, *47*, 890.

[29] a) V. Tangoulis, C. P. Raptopoulou, A. Terzis, E. G. Bakalbassis, E. Diamantopoulou, S. P. Perlepes, *Inorg. chem.* **1998**, *37*, 3142; b) E. G. Bakalbassis, E. Diamantopoulou, S. P. Perlepes, C. P. Raptopoulou, V. Tangoulis, A. Terzis, T. F. Zafiropoulos, *J. Chem. Soc., Chem. Commun.* **1995**, 1347.

[30] S. Biswas, M. Tonigold, D. Volkmer, *Z. anorg. allg. Chem.* **2008**, *634*, 2532.

[31] Y.-Y. Liu, M. Grzywa, M. Tonigold, G. Sastre, T. Schüttrigkeit, N. S. Leeson, D. Volkmer, *Dalton Trans.* **2011**, *40*, 5926.

[32] K. Knippen, D. Matuszczyk, M. Kraft, B. Bredenkötter, G. Eickerling, T. Lis, D. Volkmer, M. Stępień, *Chem. Eur. J.* **2021**.

[33] S. Biswas, M. Tonigold, H. Kelm, H.-J. Krüger, D. Volkmer, *Dalton Trans.* **2010**, *39*, 9851.

[34] L. Cui, Y.-F. Geng, C. F. Leong, Q. Ma, D. M. D'Alessandro, K. Deng, Q.-D. Zeng, J.-L. Zuo, *Sci. Rep.* **2016**, *6*, 25544.

[35] H. Bunzen, M. Grzywa, A. Kalytta-Mewes, D. Volkmer, *Dalton Trans.* **2017**, *46*, 2618.

[36] T. W. Werner, S. Reschke, H. Bunzen, H.-A. K. von Nidda, J. Deisenhofer, A. Loidl, D. Volkmer, *Inorg. chem.* **2016**, *55*, 1053.

[37] a) C. Gkioni, V. Psycharis, C. P. Raptopoulou, *Polyhedron* **2009**, *28*, 3425; b) S. Biswas, M. Tonigold, M. Speldrich, P. Kögerler, D. Volkmer, *Eur. J. Inorg. Chem.* **2009**, *2009*, 3094; c) V. Tangoulis, E. Diamantopoulou, E. G. Bakalbassisc, C. P. Raptopouloua, A. Terzisa, S. P. Perlepes, *Mol. Cryst. Liq. Cryst.* **1999**, *335*, 463.

[38] M. Grzywa, D. Denysenko, J. Hanss, E.-W. Scheidt, W. Scherer, M. Weil, D. Volkmer, *Dalton Trans.* **2012**, *41*, 4239.

[39] Y.-L. Bai, J. Tao, R.-B. Huang, L.-S. Zheng, *Angew. Chem. Int. Ed.* **2008**, *47*, 5344.

[40] a) Y.-Q. Lan, S.-L. Li, H.-L. Jiang, Q. Xu, *Chem. Eur. J.* **2012**, *18*, 8076; b) X.-L. Wang, C. Qin, S.-X. Wu, K.-Z. Shao, Y.-Q. Lan, S. Wang, D.-X. Zhu, Z.-M. Su, E.-B. Wang, *Angew. Chem.* **2009**, *121*, 5395.

[41] Y.-W. Li, K.-H. He, X.-H. Bu, *J. Mater. Chem. A* **2013**, *1*, 4186.

[42] S. T. Tsantis, P. Danelli, D. I. Tzimopoulos, C. P. Raptopoulou, V. Psycharis, S. P. Perlepes, *Inorg. chem.* **2021**, *60*, 11888.

[43] P. Schmieder, M. Grzywa, D. Denysenko, M. Hambach, D. Volkmer, *Dalton Trans.* **2015**, *44*, 13060.

[44] S. Biswas, M. Grzywa, H. P. Nayek, S. Dehnen, I. Senkovska, S. Kaskel, D. Volkmer, *Dalton Trans.* **2009**, 6487.

[45] D. Denysenko, M. Grzywa, M. Tonigold, B. Streppel, I. Krkljus, M. Hirscher, E. Mugnaioli, U. Kolb, J. Hanss, D. Volkmer, *Chem. Eur. J.* **2011**, *17*, 1837.

[46] P. Schmieder, D. Denysenko, M. Grzywa, B. Baumgärtner, I. Senkovska, S. Kaskel, G. Sastre, L. van Wüllen, D. Volkmer, *Dalton Trans.* **2013**, *42*, 10786.

[47] Q. Liu, N. Hoefer, G. Berkbigler, Z. Cui, T. Liu, A. C. Co, D. W. McComb, C. R. Wade, *Inorg. chem.* **2022**.

[48] L. Sun, C. H. Hendon, S. S. Park, Y. Tulchinsky, R. Wan, F. Wang, A. Walsh, M. Dincă, *Chem. Sci.* **2017**, *8*, 4450.

[49] A. J. Rieth, Y. Tulchinsky, M. Dincă, *J. Am. Chem. Soc.* **2016**, *138*, 9401.

[50] P.-Q. Liao, X.-Y. Li, J. Bai, C.-T. He, D.-D. Zhou, W.-X. Zhang, J.-P. Zhang, X.-M. Chen, *Chem. Eur. J.* **2014**, *20*, 11303.

[51] K. Knippen, B. Bredenkötter, L. Kanschat, M. Kraft, T. Vermeyen, W. Herrebout, K. Sugimoto, P. Bultinck, D. Volkmer, *Dalton Trans.* **2020**, 15758.

[52] G. Sastre, J. van den Bergh, F. Kapteijn, D. Denysenko, D. Volkmer, *Dalton Trans.* **2014**, *43*, 9612.

[53] J. Teufel, H. Oh, M. Hirscher, M. Wahiduzzaman, L. Zhechkov, A. Kuc, T. Heine, D. Denysenko, D. Volkmer, *Adv. Mater.* **2013**, *25*, 635.

[54] B. Paschke, A. Wixforth, D. Denysenko, D. Volkmer, *ACS Sens.* **2017**, *2*, 740.

[55] B. Paschke, D. Denysenko, B. Bredenkötter, G. Sastre, A. Wixforth, D. Volkmer, *Chem. Eur. J.* **2019**, *25*, 10803.

[56] a) A. Schaller, A. Ullrich, S. Horn, D. Volkmer, *Chem. Commun.* **2015**, *51*, 12494; b) A. Schaller, A. Ullrich, D. Volkmer, *Thin Solid Films* **2019**, *684*, 36.

[57] H. Bunzen, M. Grzywa, M. Hambach, S. Spirkl, D. Volkmer, *Cryst. Growth Des.* **2016**, *16*, 3190.

[58] Q. Qian, A. M. Wright, H. Lee, M. Dincă, Z. P. Smith, *Chem. Mater.* **2021**, *33*, 6825.

[59] R. Cao, Z. Chen, Y. Chen, K. B. Idrees, S. L. Hanna, X. Wang, T. A. Goetjen, Q. Sun, T. Islamoglu, O. K. Farha, *ACS applied materials & interfaces* **2020**, *12*, 47747.

[60] H. Bunzen, F. Kolbe, A. Kalytta-Mewes, G. Sastre, E. Brunner, D. Volkmer, *J. Am. Chem. Soc.* **2018**, *140*, 10191.

[61] H. Bunzen, A. Kalytta-Mewes, L. van Wüllen, D. Volkmer, *Beilstein J. Nanotechnol.* **2019**, *10*, 1851.

[62] a) A. Soleimani-Dorcheh, R. E. Dinnebier, A. Kuc, O. Magdysyuk, F. Adams, D. Denysenko, T. Heine, D. Volkmer, W. Donner, M. Hirscher, *Phys. Chem. Chem. Phys.* **2012**, *14*, 12892; b) A. Soleimani Dorcheh, D. Denysenko, D. Volkmer, W. Donner, M. Hirscher, *Micropor. Mesopor. Mat.* **2012**, *162*, 64.

[63] O. V. Magdysyuk, D. Denysenko, I. Weinrauch, D. Volkmer, M. Hirscher, R. E. Dinnebier, *Chem. Commun.* **2015**, *51*, 714.

[64] a) J. K. H. Fischer, P. Sippel, D. Denysenko, P. Lunkenheimer, D. Volkmer, A. Loidl, *Commun. Phys.* **2020**, *3*; b) J. K. H. Fischer, P. Sippel, D. Denysenko, P. Lunkenheimer, D. Volkmer, A. Loidl, *J. Chem. Phys.* **2015**, *143*, 154505.

[65] P. Sippel, D. Denysenko, A. Loidl, P. Lunkenheimer, G. Sastre, D. Volkmer, *Adv. Funct. Mater.* **2014**, *24*, 3885.

[66] D. Denysenko, T. Werner, M. Grzywa, A. Puls, V. Hagen, G. Eickerling, J. Jelic, K. Reuter, D. Volkmer, *Chem. Commun.* **2012**, *48*, 1236.

[67] C. K. Brozek, L. Bellarosa, T. Soejima, T. V. Clark, N. López, M. Dincă, *Chem. Eur. J.* **2014**, *20*, 6871.

[68] Z. Cai, C. E. Bien, Q. Liu, C. R. Wade, *Chem. Mater.* **2020**, *32*, 4257.

[69] D. Denysenko, M. Grzywa, J. Jelic, K. Reuter, D. Volkmer, *Angew. Chem.* **2014**, *126*, 5942.

[70] D. Denysenko, J. Jelic, K. Reuter, D. Volkmer, *Chem. Eur. J.* **2015**, *21*, 8188.

[71] D. Denysenko, J. Jelic, O. V. Magdysyuk, K. Reuter, D. Volkmer, *Microporous Mesoporous Mat.* **2015**, *216*, 146.

[72] D. Denysenko, D. Volkmer, *Faraday Discuss.* **2017**, *201*, 101.

[73] R. J. Comito, K. J. Fritzsching, B. J. Sundell, K. Schmidt-Rohr, M. Dincă, *J. Am. Chem. Soc.* **2016**, *138*, 10232.

[74] R. J. Comito, Z. Wu, G. Zhang, J. A. Lawrence, M. D. Korzyński, J. A. Kehl, J. T. Miller, M. Dincă, *Angew. Chem.* **2018**, *57*, 8135.

[75] R. Röß-Ohlenroth, B. Bredenkötter, D. Volkmer, *Organometallics* **2019**, *38*, 3444.

[76] A. M. Wright, Z. Wu, G. Zhang, J. L. Mancuso, R. J. Comito, R. W. Day, C. H. Hendon, J. T. Miller, M. Dincă, *Chem* **2018**, *4*, 2894.

[77] R. Ettlinger, M. Sönksen, M. Graf, N. Moreno, D. Denysenko, D. Volkmer, K. Kerl, H. Bunzen, *J. Mater. Chem. B* **2018**, *6*, 6481.

[78] J. Jelic, D. Denysenko, D. Volkmer, K. Reuter, *New J. Phys.* **2013**, *15*, 115004.

[79] A. M. Wright, A. J. Rieth, S. Yang, E. N. Wang, M. Dincă, *Chem. Sci.* **2018**, *9*, 3856.

[80] L. Li, Y. Yang, M. H. Mohamed, S. Zhang, G. Veser, N. L. Rosi, J. K. Johnson, *Organometallics* **2019**, *38*, 3453.

[81] I. Weinrauch, I. Savchenko, D. Denysenko, S. M. Souliou, H.-H. Kim, M. Le Tacon, L. L. Daemen, Y. Cheng, A. Mavrandonakis, A. J. Ramirez-Cuesta et al., *Nat. Commun.* **2017**, *8*, 14496.

[82] Z. Chen, M. R. Mian, S.-J. Lee, H. Chen, X. Zhang, K. O. Kirlikovali, S. Shulda, P. Melix, A. S. Rosen, P. A. Parilla et al., *Journal of the American Chemical Society* **2021**, *143*, 18838.

[83] A. M. Wright, C. Sun, M. Dincă, *J. Am. Chem. Soc.* **2021**, *143*, 681.

[84] K. Yang, J. Jiang, *J. CO2 Util.* **2022**, *63*, 102148.

[85] A. W. Stubbs, M. Dincă, *Inorg. chem.* **2019**, *58*, 13221.

[86] a) E. D. Metzger, C. K. Brozek, R. J. Comito, M. Dincă, *ACS Cent. Sci.* **2016**, *2*, 148; b) E. D. Metzger, R. J. Comito, C. H. Hendon, M. Dincă, *J. Am. Chem. Soc.* **2017**, *139*, 757.

[87] R. J. Comito, E. D. Metzger, Z. Wu, G. Zhang, C. H. Hendon, J. T. Miller, M. Dincă, *Organometallics* **2017**, *36*, 1681.

[88] R. J.-C. Dubey, R. J. Comito, Z. Wu, G. Zhang, A. J. Rieth, C. H. Hendon, J. T. Miller, M. Dincă, *J. Am. Chem. Soc.* **2017**, *139*, 12664.

[89] H. D. Park, R. J. Comito, Z. Wu, G. Zhang, N. Ricke, C. Sun, T. van Voorhis, J. T. Miller, Y. Román-Leshkov, M. Dincă, *ACS Catal.* **2020**, *10*, 3864.

[90] H. Shao, R. Pandharkar, C. J. Cramer, *Organometallics* **2022**, *41*, 169.

[91] E. D. Metzger, R. J. Comito, Z. Wu, G. Zhang, R. C. Dubey, W. Xu, J. T. Miller, M. Dincă, *ACS Sustain. Chem. Eng.* **2019**, *7*, 6654.

[92] D. E. Ortega, R. A. Matute, *Catal. Sci. Technol.* **2021**, *11*, 2422.

[93] a) C. Jin, S. Zhang, Z. Zhang, Y. Chen, *Inorganic chemistry* **2018**, *57*, 2169; b) C. E. Bien, Q. Liu, C. R. Wade, *Chem. Mater.* **2020**, *32*, 489; c) M. E. Zick, D. Cho, J. Ling, P. J. Milner, *ChemNanoMat* **2022**.

[94] a) M. R. Mian, T. Islamoglu, U. Afrin, S. Goswami, R. Cao, K. O. Kirlikovali, M. G. Hall, G. W. Peterson, O. K. Farha, *Chem. Mater.* **2020**, *32*, 6998; b) M. R. Mian, H. Chen, R. Cao, K. O. Kirlikovali, R. Q. Snurr, T. Islamoglu, O. K. Farha, *Journal of the American Chemical Society* **2021**, *143*, 9893; c) R. Cao, M. R. Mian, X. Liu, Z. Chen, M. C. Wasson, X. Wang, K. B. Idrees, K. Ma, Q. Sun, J.-R. Li et al., *ACS Materials Lett.* **2021**, *3*, 1363; d) D. Ma, Z. Cao, *J. Phys. Chem. C* **2022**.

[95] P.-Q. Liao, H. Chen, D.-D. Zhou, S.-Y. Liu, C.-T. He, Z. Rui, H. Ji, J.-P. Zhang, X.-M. Chen, *Energy Environ. Sci.* **2015**, *8*, 1011.

[96] D. W. Kim, D. W. Kang, M. Kang, D. S. Choi, H. Yun, S. Y. Kim, S. M. Lee, J.-H. Lee, C. S. Hong, *J. Am. Chem. Soc.* **2022**, *144*, 9672.

[97] A. S. Rosen, M. R. Mian, T. Islamoglu, H. Chen, O. K. Farha, J. M. Notestein, R. Q. Snurr, *J. Am. Chem. Soc.* **2020**, *142*, 4317.

[98] J. J. Oppenheim, J. L. Mancuso, A. M. Wright, A. J. Rieth, C. H. Hendon, M. Dincă, *J. Am. Chem. Soc.* **2021**, *143*, 16343.

[99] A. J. Rieth, S. Yang, E. N. Wang, M. Dincă, *ACS Cent. Sci.* **2017**, *3*, 668.

[100] a) A. J. Rieth, K. M. Hunter, M. Dincă, F. Paesani, *Nat. Commun.* **2019**, *10*, 4771; b) S. Bagi, A. M. Wright, J. Oppenheim, M. Dincă, Y. Román-Leshkov, *ACS Sustain. Chem. Eng.* **2021**, *9*, 3996.

[101] a) D. E. Jaramillo, D. A. Reed, H. Z. H. Jiang, J. Oktawiec, M. W. Mara, A. C. Forse, D. J. Lussier, R. A. Murphy, M. Cunningham, V. Colombo et al., *Nat. Mater.* **2020**, *19*, 517; b) D. E.

Jaramillo, H. Z. H. Jiang, H. A. Evans, R. Chakraborty, H. Furukawa, C. M. Brown, M. Head-Gordon, J. R. Long, *J. Am. Chem. Soc.* **2021**, *143*, 6248.

[102] H. Kwon, D.-E. Jiang, *J. Phys. Chem. Lett.* **2022**, *13*, 9129.

[103] F. Gándara, F. J. Uribe-Romo, D. K. Britt, H. Furukawa, L. Lei, R. Cheng, X. Duan, M. O'Keeffe, O. M. Yaghi, *Chem. Eur. J.* **2012**, *18*, 10595.

[104] X.-H. Zhou, Y.-H. Peng, X.-D. Du, J.-L. Zuo, X.-Z. You, *CrystEngComm* **2009**, *11*, 1964.

[105] a) L. Sun, M. G. Campbell, M. Dincă, *Angew. Chem. Int. Ed. Engl.* **2016**, *55*, 3566; b) D. D. Medina, A. Mähringer, T. Bein, *Isr. J. Chem.* **2018**, *58*, 1089; c) C. Muschielok, H. Oberhofer, *J. Chem. Phys.* **2019**, *151*, 15102; d) L. S. Xie, G. Skorupskii, M. Dincă, *Chem. Rev.* **2020**, *120*, 8536.

[106] J. G. Park, M. L. Aubrey, J. Oktawiec, K. Chakarawet, L. E. Darago, F. Grandjean, G. J. Long, J. R. Long, *J. Am. Chem. Soc.* **2018**, *140*, 8526.

[107] I. Rubinstein, E. Gileadi, *J. electroanal. chem. interfacial electrochem.* **1980**, *108*, 191.

[108] C. R. Marshall, J. P. Dvorak, L. P. Twight, L. Chen, K. Kadota, A. B. Andreeva, A. E. Overland, T. Ericson, A. F. Cozzolino, C. K. Brozek, *J. Am. Chem. Soc.* **2022**.

[109] J. G. Park, B. A. Collins, L. E. Darago, T. Runčevski, M. E. Ziebel, M. L. Aubrey, H. Z. H. Jiang, E. Velasquez, M. A. Green, J. D. Goodpaster et al., *Nat. Chem.* **2021**, *13*, 594.

[110] C.-T. He, Z.-M. Ye, Y.-T. Xu, D.-D. Zhou, H.-L. Zhou, Da Chen, J.-P. Zhang, X.-M. Chen, *Chem. Sci.* **2017**, *8*, 7560.

[111] Z.-D. Wang, Y. Zang, Z.-J. Liu, P. Peng, R. Wang, S.-Q. Zang, *Appl. Catal. B* **2021**, *288*, 119941.

[112] S.-D. Han, J.-P. Zhao, Y.-Q. Chen, S.-J. Liu, X.-H. Miao, T.-L. Hu, X.-H. Bu, *Cryst. Growth Des.* **2014**, *14*, 2.

[113] a) E.-C. Yang, Y.-Y. Zhang, Z.-Y. Liu, X.-J. Zhao, *Inorg. chem.* **2014**, *53*, 327; b) H. Bunzen, M. Grzywa, R. Aljohani, H.-A. Krug von Nidda, D. Volkmer, *Eur. J. Inorg. Chem.* **2019**, *2019*, 4471.

[114] M. Kitamura, H. Oka, R. Noyori, *Tetrahedron* **1999**, *55*, 3605.

[115] M. D. Coburn, *J. Heterocyclic Chem.* **1973**, *10*, 743.

[116] D. Sheberla, L. Sun, M. A. Blood-Forsythe, S. Er, C. R. Wade, C. K. Brozek, A. Aspuru-Guzik, M. Dincă, *J. Am. Chem. Soc.* **2014**, *136*, 8859.

[117] E. D. Bloch, D. Britt, C. Lee, C. J. Doonan, F. J. Uribe-Romo, H. Furukawa, J. R. Long, O. M. Yaghi, *J. Am. Chem. Soc.* **2010**, *132*, 14382.

[118] a) R. L. Sweany, D. Watzke, *Organometallics* **1997**, *16*, 1037; b) Y. Y. Sun, Y.-H. Kim, S. B. Zhang, *J. Am. Chem. Soc.* **2007**, *129*, 12606.

[119] F. Freitag, T. Irrgang, R. Kempe, *J. Am. Chem. Soc.* **2019**, *141*, 11677.

[120] a) M. Dincă, A. Dailly, Y. Liu, C. M. Brown, D. A. Neumann, J. R. Long, *J. Am. Chem. Soc.* **2006**, *128*, 16876; b) D. J. Xiao, M. I. Gonzalez, L. E. Darago, K. D. Vogiatzis, E. Haldoupis, L. Gagliardi, J. R. Long, *J. Am. Chem. Soc.* **2016**, *138*, 7161; c) D. Chen, W. Shi, P. Cheng, *Chem. Commun.* **2015**, *51*, 370.

[121] C. A. Trickett, A. Helal, B. A. Al-Maythalony, Z. H. Yamani, K. E. Cordova, O. M. Yaghi, *Nat. Rev. Mater.* **2017**, *2*.

[122] K. M. Choi, D. Kim, B. Rungtaweevoranit, C. A. Trickett, J. T. D. Barmanbek, A. S. Alshammari, P. Yang, O. M. Yaghi, *J. Am. Chem. Soc.* **2017**, *139*, 356.

[123] a) P. M. Stanley, C. Thomas, E. Thyrhaug, A. Urstoeger, M. Schuster, J. Hauer, B. Rieger, J. Warnan, R. A. Fischer, *ACS Catal.* **2021**, *11*, 871; b) P. M. Stanley, J. Haimerl, C. Thomas, A.

Urstoeger, M. Schuster, N. B. Shustova, A. Casini, B. Rieger, J. Warnan, R. A. Fischer, *Angew. Chem.* **2021**, *60*, 17854; c) J. Mukherjee, I. Siewert, *Eur. J. Inorg. Chem.* **2020**, *2020*, 4319.

[124] a) A. Carné-Sánchez, F. J. Carmona, C. Kim, S. Furukawa, *Chem. Commun.* **2020**, *56*, 9750; b) P. Kittikhunnatham, G. A. Leith, A. Mathur, J. K. Naglic, C. R. Martin, K. C. Park, K. McCullough, H. D. A. C. Jayaweera, R. E. Corkill, J. Lauterbach et al., *Angew. Chem. Int. Ed.* **2022**, *134*.

[125] A. B. Andreeva, K. N. Le, K. Kadota, S. Horike, C. H. Hendon, C. K. Brozek, *Chem. Mater.* **2021**, *33*, 8534.

[126] a) O. Kahn, C. J. Martinez, *Science* **1998**, *279*, 44; b) K. Senthil Kumar, M. Ruben, *Coord. Chem. Rev.* **2017**, *346*, 176.

[127] a) J. Seo, J. D. Braun, V. M. Dev, J. A. Mason, *J. Am. Chem. Soc.* **2022**, *144*, 6493; b) M. S. Reis, *Coord. Chem. Rev.* **2020**, *417*, 213357.

[128] a) M. Piedrahita-Bello, J. E. Angulo-Cervera, A. Enriquez-Cabrera, G. Molnár, B. Tondu, L. Salmon, A. Bousseksou, *Materials horizons* **2021**, *8*, 3055; b) H. J. Shepherd, I. A. Gural'skiy, C. M. Quintero, S. Tricard, L. Salmon, G. Molnár, A. Bousseksou, *Nat. Commun.* **2013**, *4*, 2607; c) G. Molnár, S. Rat, L. Salmon, W. Nicolazzi, A. Bousseksou, *Adv. Mater.* **2018**, *30*.

5. Acknowledgements

This work is dedicated to Dr. Dmytro Denysenko† (1977-2018†), our dear colleague, mentor, and father to the MFU-4*l* MOF, who supported me throughout my bachelor and master theses with his extraordinary laboratory skills and knowledge.

First, I want to thank Prof. Dr. Dirk Volkmer, who gave me the opportunity and necessary support to complete this project, always helping with good advice, new ideas, and valuable simulations.

A special thanks goes to Prof. Dr. Achim Wixforth, our dear colleague from the DFG SPP 1928 COORNET project, who was so kind to spend his well-deserved retirement time for the examination of this thesis.

I am also very grateful to all my collaborators and everyone at the chair of solid-state chemistry for all the help, the good time, and cooperation. Especially to Dr. Björn Bredenkötter, Andreas Kalytta-Mewes and Dr. Hana Bunzen for their great help and the measurements they conducted for me. I am especially grateful for SEM micrographs and EDX measurements conducted by Ralph Freund, Marcel Hirrle, and Silke Weigel, ICP-OES measurements from Romy Ettlinger and Jennifer Schnabel, as well as English language proofreading of this thesis by Sabina Berg.

At last, I want to express my deepest gratitude to my family and friends for all their help and support. Especially to my son, his mother and his grandparents for their encouragement, backup, and patience throughout the whole duration of this project.

Financial support by the DFG within the priority program SPP 1928 ("Coordination Networks: Building Blocks for Functional Systems") is gratefully acknowledged.

6. Conference Contributions

6.1. Oral Presentations

- **Organometallic MFU-4/(arge) Metal-Organic Frameworks**
  R. Röß-Ohlenroth, B. Bredenkötter, D. Volkmer
  Oral presentation at the euroMOF 2019 – 3rd International Conference on Metal Organic Frameworks and Porous Polymers, 2019, Maison de la Chimie, Paris, France

- **MFU-4-type Scaffolds Featuring Open Bidentate Bibenzimidazole Coordination Sites**
  R. Röß-Ohlenroth, D. Volkmer
  Oral presentation at the ICCC 2022 – 44th International Conference on Coordination Chemistry, 2022, Palacongressi di Rimini, Rimini, Italy

- **From Assembly of Metal Hydrogen-Bonded Organic Frameworks with Pre-Built Kuratowski SBUs towards Metal-Organic Framework Dyads**
  R. Röß-Ohlenroth, D. Volkmer
  Oral presentation at the MOF 2022 – 8th International Conference on Metal-Organic Frameworks and Open Framework Compounds, 2022, International Congress Center Dresden, Germany

6.2. Poster Presentations

- **A 1,2,3-Triazolate-Based Kuratowski-Type Precursor for Novel Metal-Organic Framework Synthesis Approaches: Linkage of Prebuilt Secondary Building Units**
  R. Röß-Ohlenroth, M. Grzywa, D. Denysenko, D. Volkmer
  Poster presentation at the docMOF 2018 – 1st European Doctoral Symposium on Metal-Organic Frameworks, 2018, Raitenhaslach, Germany

- **MFU-4-type Metal-Organic Frameworks with a Bidentate Bibenzimidazole Backbone for Postsynthetic Metalation**
  R. Röß-Ohlenroth, D. Volkmer
  Poster presentation at the euroMOF 2021– 4th International Conference on Metal Organic Frameworks and Porous Polymers, 2021, virtual event

6.3. Talks at the Seminar of the Volkmer Group

- **A 1,2,3-Triazolate-Based Kuratowski-Type Precursor for Novel Metal-Organic Framework Assembly Strategies**
  (31.01.2018)
- **Addition to the MFU-4 Family and Related Metal Azolate Frameworks**
  (20.06.2018)
- **Multi Pixel MOF@SAW Gas Sensors**
  (30.01.2019)
- **Triazolate-Based Coordination Compounds with Functional Ligands**
  (25.11.2020)
- **CFA-19 MOFs**
  (19.05.2021)
- **Steric Magneto-Structure Manipulation of M(triazolate-R)$_2$ Coordination Frameworks**
  (06.07.2022)

7. Appendix Publications

A1 **Organometallic MFU-4*l*(arge) Metal-Organic Frameworks**……………………………**A 1-88**
R. Röß-Ohlenroth, B. Bredenkötter, D. Volkmer*
Organometallics **2019**, *38*, 3444-3452
DOI: 10.1021/acs.organomet.9b00297
Reprinted with permission from the American Chemical Society. Copyright 2019
American Chemical Society.

A2 **Assembly of Porous Metal Hydrogen-Bonded Organic Frameworks from Diamine-Functionalized Kuratowski Complexes**…………………………………………………**A 89-137**
R. Röß-Ohlenroth, C. Freudig, M. Kraft, H. Bunzen, D. Volkmer*
Cryst. Growth Des. **2022**, *22*, 379-391
DOI: 10.1021/acs.cgd.1c01008
Reprinted with permission from the American Chemical Society. Copyright 2022
American Chemical Society.

A3 **Inhibition, Binding of Organometallics, and Thermally Induced CO Release in an MFU-4-Type Metal–Organic Framework Scaffold with Open Bidentate Bibenzimidazole Coordination Sites**……………………………………………………**A 139-186**
Richard Röß-Ohlenroth, Maryana Kraft, Hana Bunzen, Dirk Volkmer*
Inorg. Chem., **2022**, *61*, 16380-16389
DOI: 10.1021/acs.inorgchem.2c02394
Reprinted with permission from the American Chemical Society. Copyright 2022
American Chemical Society.

A4 **Synthesis, Thermal Stability and Magnetic Properties of an Interpenetrated Mn(II) Triazolate Coordination Framework**……………………………………………………**A 187-208**
R. Röß-Ohlenroth, M. Hirrle, M. Kraft, A. Kalytta-Mewes, A. Jesche, H.-A. Krug von Nidda, D. Volkmer*
Z. Anorg. Allg. Chem. **2022**, *648*, e202200153
DOI: 10.1002/zaac.202200153
Reprinted with permission from Wiley-VCH GmbH under the CC BY-NC-ND 4.0 license. Copyright © 2022 The Authors. Zeitschrift für anorganische und allgemeine Chemie published by Wiley-VCH GmbH.

A5 Cooperative Large-Hysteresis Spin-Crossover Transition in the Iron(II) Triazolate $[Fe(ta)_2]$ Metal–Organic Framework……………………………………………………………A 209-229

M. Grzywa, R. Röß-Ohlenroth, C. Muschielok, H. Oberhofer, A. Błachowski, J. Żukrowski, D. Vieweg, H.-A. Krug von Nidda, D. Volkmer*
Inorg. Chem. 2020, *59*, 10501-10511
DOI: 10.1021/acs.inorgchem.0c00814
Reprinted with permission from the American Chemical Society. Copyright 2020 American Chemical Society.

A6 Combining Theory and Experiments to Study the Influence of Gas Sorption on the Conductivity Properties of Metal-Organic Frameworks………………………………A 231-261

C. Muschielok, A. Reiner, R. Röß-Ohlenroth, A. Kalytta-Mewes, D. Volkmer, A. Wixforth, H. Oberhofer*
ACS Appl. Mater. Interfaces, 2022, *14*, 29, 33662–33674
DOI: 10.1021/acsami.2c05127
Reprinted with permission from the American Chemical Society. Copyright 2022 American Chemical Society.

ORGANOMETALLICS
Article
Cite This: *Organometallics* 2019, 38, 3444−3452
pubs.acs.org/Organometallics

Organometallic MFU-4*l*(arge) Metal−Organic Frameworks

Richard Röß-Ohlenroth, Björn Bredenkötter, and Dirk Volkmer*

Chair of Solid State and Materials Chemistry, Institute of Physics, University of Augsburg, Universitätsstraße 1, 86159 Augsburg, Germany

Supporting Information

ABSTRACT: Ligand exchange reactions at the Kuratowski-type secondary building unit in MFU-4*l*(arge) metal−organic frameworks (MOFs) result in organometallic porous compounds with metal−carbon bonds of the general formula $[Zn_5L_xCl_{4-x}(BTDD)_3]$ ($4 \geq x > 3$; L = methanido, ethanido, *n*-butanido, *tert*-butanido, 3,3-dimethyl-1-butyn-1-ido; H_2-BTDD = bis(1*H*-1,2,3-triazolo[4,5-*b*][4′,5′-*i*])dibenzo[1,4]-dioxin) and $[Zn_{1.5}Co_{3.5}Me_{3.1}Cl_{0.9}(BTDD)_3]$. The compounds were characterized by FT-IR, EDX spectroscopy, X-ray powder diffraction (XRPD), and argon adsorption measurements. VT-XRPD, TGA, and TG-MS measurements were applied to investigate the thermal and oxidative stability of the organometallic Zn-MFU-4*l* derivatives. The hydrolytic stability of all compounds was examined, and a conversion of the methanide to hydroxide ligands is observed in the cobalt-containing compound. DRIFTS measurements of the resulting framework with the composition $[Zn_{1.4}Co_{3.6}(OH)_{3.1}Cl_{0.9}(BTDD)_3]$ revealed a mechanism of carbon dioxide binding similar to that of carbonic anhydrase.

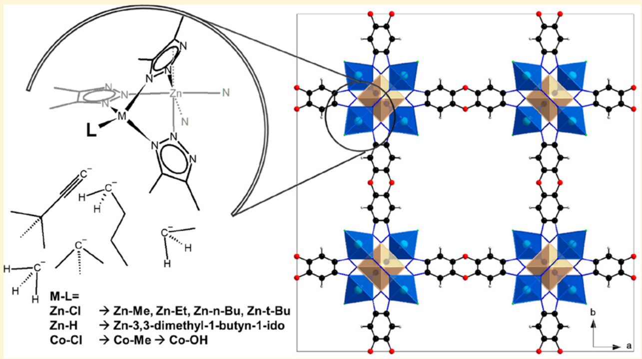

INTRODUCTION

Postsynthetic metal and ligand exchange at the pentanuclear Kuratowski-type[1] secondary building unit (SBU) of MFU-4-type MOFs has emerged as a versatile approach toward functional and catalytically active frameworks.[2−17] The bistriazolate-linked SBUs of the parent MFU-4-type MOFs usually feature one central Zn^{2+} ion, octahedrally coordinated by nitrogen, and four peripheral Zn^{2+} ions which are tetrahedrally coordinated, each of which thus resembles mononuclear scorpionate complexes consisting of a tris(pyrazolyl)borate (TP) ligand, the metal center, and a chloride anion.[2,18,19] Postsynthetic exchange of the peripheral Zn^{2+} ions and chloride ligands has been investigated intensively for MFU-4*l*, leading to a large variety of compounds with the general composition $[Zn_{5-x}M_x(L)_yCl_{4-y}(BTDD)_3]$ ($4 \geq x \geq 0$; $4 \geq y \geq 0$; M = Mn^{II}, Fe^{II}, Co^{II}, Ni^{II}, Cu^{II}, V^{II}; L = NO_2^-, NO_3^-, $CF_3SO_3^-$, N_3^-, NCO^-, $HCOO^-$, CH_3COO^-, F^-,H^-; H_2-BTDD = bis(1*H*-1,2,3-triazolo[4,5-*b*][4′,5′-*i*])dibenzo-[1,4]dioxin)).[2−4,6,8,15] Metal exchange has also been reported to occur with mono (Li^I, Cu^I)-,[5,7,9] tri (Cr^{III}, Ti^{III})-, or even tetravalent (Ti^{IV}, V^{IV}) metal ions.[11,15]

Of these, especially the Ni^{II}- and Co^{II}-MFU-4*l* derivatives have been investigated regarding the heterogeneous selective dimerization of ethylene and propylene, as well as stereoselective heterogeneous diene polymerization.[10,12−14] A synthetically more economical alternative to MFU-4*l* is the chiral CFA-1 ($[Zn_5(OAc)_4(BIBTA)_3]$; H_2-BIBTA = 1*H*,1′*H*-5,5′-bibenzo[*d*][1,2,3]triazole), which also features Kuratowski-type SBUs.[20] A partially Ni^{II} exchanged derivative of CFA-1 has recently shown selective heterogeneous ethylene dimerization similar to that of the Ni^{II}-MFU-4*l* derivative, advancing toward industrial applicability.[17]

Although these heterogeneous catalytic reactions involve the use of organometallic cocatalysts such as MAO, MMAO-12, $AlMe_3$, or $AlEt_3$ in order to activate the metal sites, so far, no MFU-4-type MOF with typical C-donor organometallic ligands has been characterized in full detail. With the well-established chemistry of organometallic scorpionate complexes taken into account,[21] the recently described structures of highly stable organometallic Kuratowski complexes $[Zn_5L_4(Me_2bta)_6]$ (L = methanido, ethanido; H-Me_2bta = 5,6-dimethylbenzotriazole)[22] provided further impetus for us to investigate organometallic MFU-4*l* frameworks.

For this, ligand exchange procedures for Zn-MFU-4*l* $[Zn_5Cl_4(BTDD)_3]$ (**1**), leading to frameworks of the general composition $[Zn_5L_xCl_{4-x}(BTDD)_3]$ ($4 \geq x > 3$; L = methanido (**1-Me**), ethanido (**1-Et**), *n*-butanido (**1-*n*-Bu**), *tert*-butanido (**1-t-Bu**), 3,3-dimethyl-1-butyn-1-ido (**1-Butyne**); H_2-BTDD = bis(1*H*-1,2,3-triazolo[4,5-*b*][4′,5′-*i*])-dibenzo[1,4]dioxin), were developed. An interesting characteristic of the new organometallic Zn-MFU-4*l* derivatives is their high stability, allowing in most cases for easy handling and analytical characterization under ambient conditions, making them ideal model compounds. In fact, **1-Me**, **1-Et**, and **1-**

Special Issue: Organometallic Chemistry within Metal-Organic Frameworks

Received: May 5, 2019
Published: July 29, 2019

DOI: 10.1021/acs.organomet.9b00297

Butyne exhibit an extraordinary stability against thermal and oxidative degradation, which even surpasses that of the corresponding methanide and ethanide Kuratowski complexes.[22] The ligand exchange with methanide in Co-MFU-4*l* $[Zn_{1.3}Co_{3.7}Cl_4(BTDD)_3]$ (**2**) leads to the more reactive $[Zn_{1.5}Co_{3.5}Me_{3.1}Cl_{0.9}(BTDD)_3]$ (**2-Me**), which readily reacts with air and moisture under ambient conditions. The hydrolysis reaction of **2-Me** yielded $[Zn_{1.4}Co_{3.6}(OH)_{3.1}Cl_{0.9}(BTDD)_3]$ (**2-OH**), which represents a cobalt analogue to a recently published structural mimic of carbonic anhydrase, $[Zn_5OH_4(BTDD)_3]$ (**1-OH**).[16]

A major challenge for the characterization of the organometallic MOFs is their insolubility, which excludes common characterization techniques such as solution NMR and mass spectrometry often used for organometallic complexes. However, we were able to employ Fourier transform infrared (FT-IR) spectroscopy in conjunction with simulated spectra as a suitable characterization technique for the derivatives of **1**.

■ RESULTS AND DISCUSSION

Synthesis and Characterization. Although the reaction of dialkylzinc with 5,6-dimethylbenzotriazole ($H\text{-}Me_2bta$) has recently been introduced as a neat synthesis pathway toward organometallic Kuratowski complexes of the composition $[Zn_5L_4(Me_2bta)_6]$ (L= methanido, ethanido), the low solubility of the H_2-BTDD linker in suitably inert solvents (e.g., hexane, tetrahydrofuran, diglyme) prohibited similar synthesis approaches for the corresponding organometallic frameworks **1-Me** and **1-Et.**[22]

However, postsynthetic organometallic ligand exchange was found to be a suitable method. **1-Me** and **1-Et** were obtained by treatment of **1** with 24 equiv (alkyl:Cl ratio 12:1) of the respective dialkylzinc in dry tetrahydrofuran under an argon atmosphere at room temperature (Scheme 1a), achieving nearly complete exchange of the chloride ligands with methanide or ethanide (Table 1). The same reaction conditions with hexane as the solvent decreased the exchange rate, while the use of trimethyl- or triethylaluminum in hexane showed substantial aluminum residues.

The Co-MFU-4*l* derivative **2-Me** was obtained under conditions similar to those for **1-Me** (Scheme 1b). The reaction time was decreased to 2 h, and only dry tetrahydrofuran was used for washing due to the compound's reactivity with water. **2-Me** can be directly converted to **2-OH** by a second washing step with a mixture of water and tetrahydrofuran, leading to the evolution of gaseous methane, which was confirmed by mass spectrometry (Figure S54).

Ligand exchange in **1** is also observed for the reaction with 5 equiv of *n*- and *t*-BuLi in dry hexane (Scheme 2a). In this case, however, the use of dry tetrahydrofuran as the solvent showed no ligand exchange, even when conducted at −90 °C.

Inspired by a procedure from the literature, we obtained **1-Butyne** from a dehydrogenation reaction of the Zn-MFU-4*l*-hydride ($[Zn_5H_{3.2}Cl_{0.8}(BTDD)_3]$ (**1-H**)) with an alkyne compound (Scheme 2b).[23] Instead of phenylacetylene, 3,3-dimethyl-1-butyne was used for the reaction due to otherwise expected steric hindrance within the framework. Due to the low boiling point of 3,3-dimethyl-1-butyne, a solvent-free reaction was developed, in which **1-H** and excess 3,3-dimethyl-1-butyne were sealed under an argon atmosphere in a closed vessel and heated to 100 °C. The excess 3,3-dimethyl-1-butyne was easily removed under vacuum.

Scheme 1. Ligand Exchange Reactions Occurring at the Kuratowski-SBUs in MFU-4*l* Leading to (a) 1-Me and 1-Et, (b) 2-Me, and (c) 2-OH

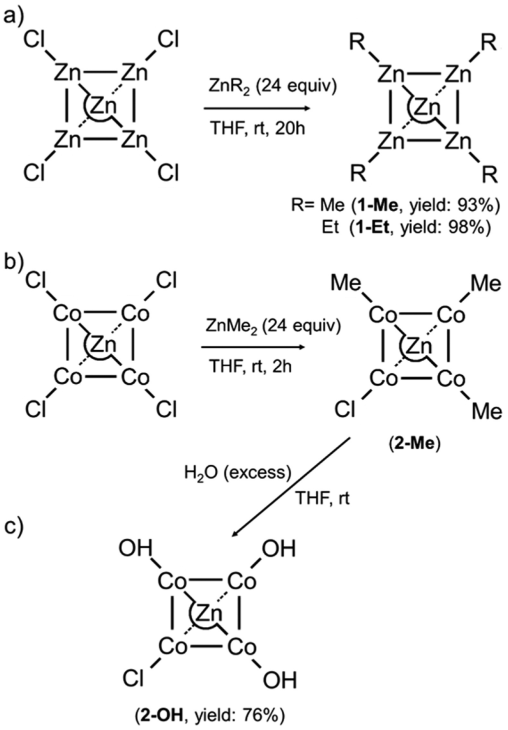

Table 1. Zn:Cl Ratios and Sum Formula of the Compounds Derived from EDX Data and Normalized to the Content of One Kuratowski SBU

compound	Zn	Cl	sum formula
1	5	4.2	$[Zn_5Cl_{4.2}(BTDD)_3]$
1-Me	5	0.1	$[Zn_5Me_{3.9}Cl_{0.1}(BTDD)_3]$
1-Et	5	0.1	$[Zn_5Et_{3.9}Cl_{0.1}(BTDD)_3]$
1-n-Bu	5	0.1	$[Zn_5\textit{n}\text{-}Bu_{3.9}Cl_{0.1}(BTDD)_3]$
1-t-Bu	5	0.3	$[Zn_5\textit{t}\text{-}Bu_{3.7}Cl_{0.3}(BTDD)_3]$
1-H	5	0.8	$[Zn_5H_{3.2}Cl_{0.8}(BTDD)_3]$
1-Butyne	5	0.8	$[Zn_5(\text{3,3-dimethyl-1-butyn-1-ido})_{3.2}Cl_{0.8}(BTDD)_3]$

Scheme 2. Ligand Exchange Occurring at the Kuratowski-SBUs in MFU-4*l* Leading to (a) 1-n-Bu and 1-t-Bu and (b) 1-Butyne

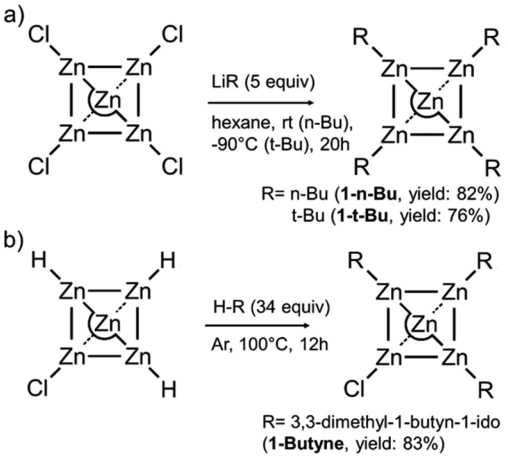

XRPD, EDX, and ICP-OES. X-ray powder diffraction (XRPD) patterns of the compounds are in good agreement with the calculated patterns (Figures S13−S19) and showed that high crystallinity is retained upon ligand exchange procedures. Only **1-t-Bu** showed a broadening and significant intensity decrease of the reflections (Figure S17).

The Zn:Co:Cl ratios were determined by energy dispersive X-ray (EDX) spectroscopy and are given with the resulting sum formulas in Table 2. The exchange ratio achieved for **1-Me** and **1-Et** is better than we would expect from a statistical point of view (expected Zn:Cl ratio 5:0.3 for the applied alkyl:Cl ratio of 12:1 and obtained 5:0.1 for **1-Me** and **1-Et**), indicating a shift of the reaction equilibrium to the more stable products. A high exchange of chloride ligands is also achieved for **1-n-Bu** and **1-t-Bu**, but inductively coupled plasma optical emission spectrometry (ICP-OES) measurements gave Zn:Li ratios of 5:0.4 for **1-n-Bu** and 5:2.9 for **1-t-Bu**. Therefore, the partial substitution of the peripheral zinc ions with lithium, already described in the literature,[5] cannot be ruled out, especially for **1-t-Bu**. Moreover, this could indicate a reaction of *t*-BuLi with the linker, leading to the framework degradation observed for **1-t-Bu**. The Zn:Cl ratio of **1-Butyne** remained unchanged with respect to the **1-H** precursor.

Table 2. Zn:Co:Cl Ratios and Sum Formula of the Compounds Derived from EDX Data and Normalized to the Content of One Kuratowski SBU

compound	Zn	Co	Cl	sum formula
2	1.3	3.7	4.0	$[Zn_{1.3}Co_{3.7}Cl_4(BTDD)_3]$
2-Me	1.5	3.5	0.9	$[Zn_{1.5}Co_{3.5}Me_{3.1}Cl_{0.9}(BTDD)_3]$
2-OH	1.4	3.6	0.9	$[Zn_{1.4}Co_{3.6}(OH)_{3.1}Cl_{0.9}(BTDD)_3]$

The Co-MFU-4*l* derivative **2-Me** shows a lower exchange ratio, leading to a residual of 0.9 chloride anion, which results in at least 2.6 Co-Me groups per Kuratowski SBU. Although the lower cobalt contents of **2-Me** and **2-OH** are expected to be due to a minor metal exchange from cobalt to zinc, amorphous residues of zinc byproducts cannot be ruled out completely. The batch of **2-Me** converted to **2-OH** shows a similar Zn:Co:Cl ratio and at least 2.7 Co-OH groups per Kuratowski SBU. Additional ICP-OES measurements of the Zn:Co ratios are in good agreement with the obtained EDX data.

IR Spectroscopy. Although a large variety of organometallic divalent zinc and cobalt scorpionate complexes have been described in the literature, no assignments of M−C stretching modes were found for comparison. A reason for this might be the large number of bands observed in the fingerprint region of such compounds, preventing the assignment.[22,24] A comparison of calculated and measured attenuated total reflection Fourier transform infrared spectra (ATR FT-IR) resulted in good matches for compounds **1** and **1-Me** (Figure 1). All IR bands of the calculated spectrum of **1** can be found in the measurement. The fingerprint region of compound **1-Me** clearly shows the loss of the symmetrical Zn−Cl stretching vibration at 377 cm^{-1} and a new strong band at 654 cm^{-1}, nicely matching the calculated hydrogen rocking vibration of the methyl group. The symmetrical Zn−C stretching vibration expected at around 515 cm^{-1} from the calculation is not directly visible in the measured spectrum. However, the intensity increase and shift of the phenyl ring stretching vibration from 534 cm^{-1} in **1** to 527 cm^{-1} in **1-Me** indicate a superposition of both bands. This superposition is further confirmed by the small shoulder visible at 534 cm^{-1} in a magnification of this band (Figure S5). The additional band at 2940 cm^{-1} can be attributed to the asymmetric C−H stretching of the methyl group. The symmetric stretching vibration is most probably visible at 2840 cm^{-1}, but two very weak signals are also observed at 2911 and 2883 cm^{-1}.

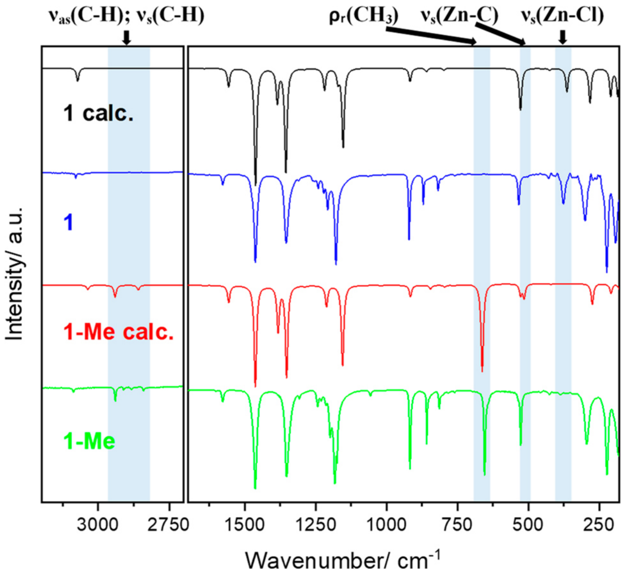

Figure 1. Comparison of calculated and measured IR spectra (ATR FT-IR) of compounds **1** and **1-Me**.

Similar to **1-Me,** the measured spectra of **1-Et**, **1-n-Bu**, and **1-Butyne** neatly match the calculations and can be found in the Supporting Information with the relevant vibrations assigned (Figures S1−S4). The ligand exchange in **1-Butyne** is further confirmed by the loss of all bands assigned to the Zn−H species of **1-H** (Figure S6). A DRIFT spectrum had to be taken for the observation of the weak C≡C stretching vibration at 2127 cm^{-1} in **1-Butyne** (Figure S7). The spectrum of **1-t-Bu** also shows the expected symmetric and asymmetric C−H stretching bands and indeed no characteristic bands are expected in the fingerprint region (Figure S3). However, the measured spectrum suffers from significant broadening of the bands in the fingerprint region and a strong background in the far-infrared region, indicating the framework's degradation.

Since IR calculations for the derivatives of **2** were not possible, simple scorpionate model complexes of the composition [M(Tp)L] (L = Cl$^-$, Me$^-$, OH$^-$; M = Zn^{II}, Co^{II}) were used (Figures S10−S12). The comparison of the relevant bands between the cobalt and zinc derivatives in those spectra matched well with the shifts observed in the experimental IR spectra (Table S1). The IR spectrum of **2-Me** had to be measured under an argon atmosphere and clearly shows the expected Co−C stretching vibration at 518 cm^{-1} next to the phenyl ring stretching vibration at 532 cm^{-1} (Figure S8). This shift to a lower wavenumber is consistent with the calculated values of 523 cm^{-1} for [Co(Tp)Me] and 539 cm^{-1} for [Zn(Tp)Me]. The hydrogen rocking vibration is visible at 569 cm^{-1}, which nicely matches the calculated shift to lower wavenumbers (Table S1). The larger shift between the calculated and measured wavenumbers for **1-Me** and **2-Me** can be explained by the interaction of the methyl group with the linker molecule observed in the simulations for **1-Me**, which showed a direct match of the bands. The C−H

DOI: 10.1021/acs.organomet.9b00297
Organometallics 2019, 38, 3444−3452

stretching vibration of the methyl group is observed at 2906 cm^{-1}. These vibrations at 518, 569, and 2906 cm^{-1} disappear directly under ambient conditions and convert to a band at 602 cm^{-1} after treatment with water (Figure S8). This indicates the formation of **2-OH**, as the Co−O stretching vibration is expected in this region (Table S1). Additionally, a small permanent band is present in **2-Me** and **2-OH** at 655 cm^{-1} corresponding to the hydrogen rocking vibration of residual Zn−CH_3 groups. The very weak bands of the O−H stretching and bending modes calculated for **1-OH** at 3670 and 758 cm^{-1}, respectively, are observed in the literature spectrum at approximately 3700 and 700 cm^{-1},[16] but they were not observable in **2-OH**. The background noise in our measurements above 3500 cm^{-1} was, even in the DRIFTS measurements, too strong to observe the weak O−H stretching vibration. The O−H bending vibration expected below 689 cm^{-1} from the complex simulation might be too weak for observation, as the calculation indicates a lower intensity and **2-OH** holds a lower loading with O−H groups in comparison to **1-OH** from the literature.

Argon Adsorption Analysis. The porosity was investigated by argon adsorption measurements at 77 K, showing the characteristic type 1 isotherm behavior of microporous solids and high BET surface areas (Table 3 and Figures S24 and S25). Nonlocal density functional theory (NLDFT) pore size distributions of all compounds were calculated by implementation of a carbon equilibrium kernel for argon adsorption at 77 K based on a slit pore model (Figures S26−S33).[26,27] In general, the new derivatives of **1** follow the expected and calculated trend to smaller pores and lower BET surfaces with increasing ligand size and weight (Table 3). MFU-4-type frameworks feature two different pores,[18] from which the smaller pore is limited by the side ligands. Compounds **1** and **1-Me** are indistinguishable with regard to pore size distribution and BET surface area (Table 3), whereas **1-Et** already exhibits a decrease of over 400 m^2 g^{-1} and a shift to smaller pore widths. In comparison to **1-Me**, the BET surface area of **1-Butyne** is decreased to 2978 m^2 g^{-1} and a large shift of 2.8 Å to a smaller pore width for the first maximum of the pore size distribution is observed. This is in fair agreement with the expected reduction of free volume in the small pores of compound **1-Butyne** (Figure 2). **1-n-Bu** and especially **1-t-Bu** show lower BET surfaces of 2898 and 2486 m^2 g^{-1}, respectively, which can be explained by the framework degradation observed in the XRPD pattern and IR spectrum of **1-t-Bu**, as well as lithium residues in both frameworks. No changes in BET surface area and pore size distribution were observed for **2-OH** in comparison with **2**, although a slightly higher BET surface area is expected for **2-OH**.

Table 3. Comparison of Measured and Calculated Argon BET Surface Areas and Pore Size Distribution Maxima of the Compounds

	BET SSA			
compound	measd (m^2 g^{-1})	calcd[a] (m^2 g^{-1})	calcd[a] (m^2 cm^{-3})	pore size distribution max (Å)
1	4147	4384	2313	13.6
1-Me	4114	4704	2332	13.6
1-Et	3677	4474	2321	12.9
1-n-Bu	2898	3867	2190	10.8
1-t-Bu	2486	3898	2201	13.0
1-Butyne	2978	3364	2037	10.8
2	3824	4475	2313	13.6
2-OH	3790	4855	2367	13.6

[a] Surface areas were calculated with iRASPA software[25]

Thermal and Oxidative Stability. The thermal and oxidative stabilities were investigated by thermogravimetric analysis (TGA) under nitrogen and synthetic air gas flows. Variable-temperature XRPD (VT-XRPD) measurements were conducted in a sealed glass capillary under an argon atmosphere. Those measurements revealed a surprisingly high stability for **1-Me** under inert conditions, which showed no loss of weight or crystallinity up to temperatures of 400 °C and decreasing reflection intensities starting from temperatures ≥450 °C (Figure 3). **1-Butyne** is similarly stable, but a slight decrease in crystallinity is already observed in the VT-XRPD pattern at 400 °C (Figure S23).

For **1-Et** the onset of the weight loss at approximately 400 °C (Figure 3) is in accordance with the loss of crystallinity in the VT-XRPD measurement (Figure S20). **1-n-Bu** is crystalline up to 350 °C (Figure S21) but shows an onset of the weight loss at around 150 °C (Figure 3). **1-t-Bu**, in contrast, is not even stable at room temperature, as indicated by the weight loss in the 5 min isothermal step at the beginning of the TGA curves (Figure 3). Furthermore, a continuous loss of crystallinity can be observed in the VT-XRPD pattern from 30 to 400 °C (Figure S22). The TGA curves under synthetic air show very similar behavior for all compounds with the decomposition steps shifted about approximately 100 °C to lower temperatures (Figure 3).

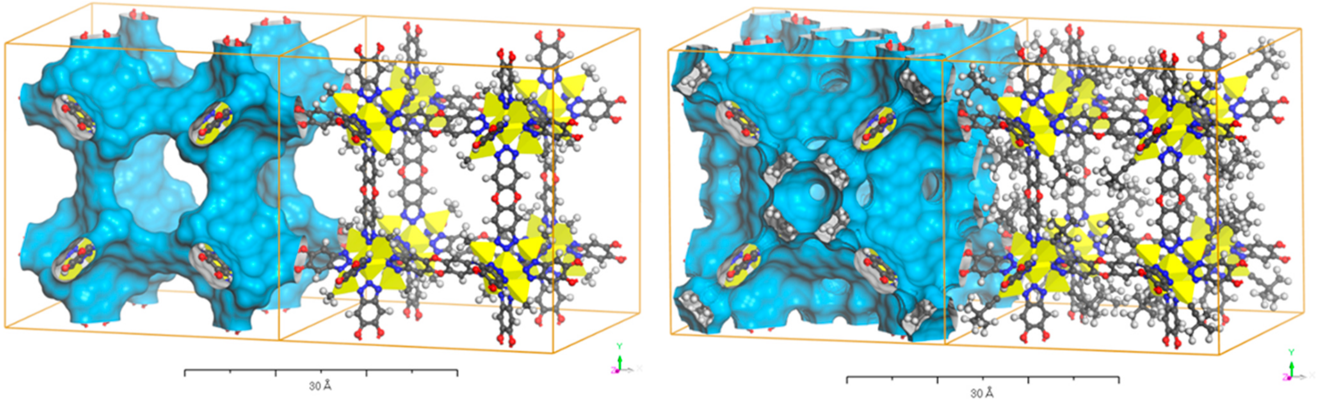

Figure 2. Conventional unit cells of **1-Me** and **1-Butyne** with plots of the Connolly surface created with BIOVIA Materials Studio 2019.

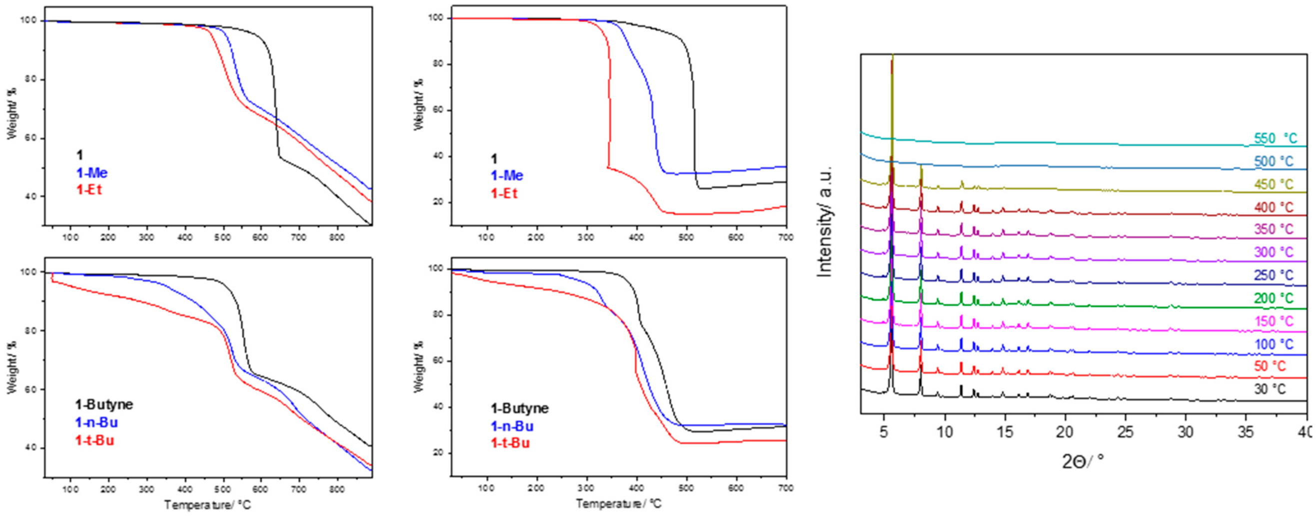

Figure 3. TGA curves of **1**, **1-Me**, **1-Et**, **1-Butyne**, **1-n-Bu**, and **1-t-Bu** obtained under nitrogen (left) and synthetic air (middle) gas flows. Exemplary VT-XRPD pattern of **1-Me** (right).

The decomposition process of **1-Et**, **1-n-Bu**, and **1-t-Bu** was further characterized by thermogravimetric analysis coupled with mass spectrometry (TG-MS), with regard to an expected β-hydrogen elimination. Indeed, evolution of the corresponding 2-methylprop-1-ene, but-1-ene, and ethane was observed in the mass spectra (Figure 4). **1-t-Bu** already lost small amounts of 2-methylprop-1-ene in the isothermal step and reached a lower baseline value after decomposition. The 2-methylprop-1-ene concentration reached its maximum after 73 min at a temperature of 360 °C and a total weight loss of 19 wt % is observed (calculated for [$Zn_5Bu_4(BTDD)_3$]: 16.65 wt %). For **1-n-Bu** the first signs of but-1-ene evolution can be seen at around 200 °C and the maximum is reached at 445 °C. The total weight loss is 17%, but about 2% of this loss could be attributed to residual solvents at the beginning of the curve, also observed for **1-t-Bu**. The onset of the β-hydride elimination in **1-Et** is at 350 °C and reaches its maximum at 450 °C but only shows partial reaction with a total weight loss of 4% (calculated for [$Zn_5Et_4(BTDD)_3$]: 9.1%). This result is surprising, as this starting point for the β-hydride elimination in the **1-Et** framework surpasses that of the ethanide Kuratowski complex by approximately 100 °C and is already in the region of the framework decomposition observed in the VT-XRPD (Figure S20).[22] IR spectra after the measurements also show this partial conversion to the hydride for **1-Et**, but no signs of hydrides could be found for **1-n-Bu** and **1-t-Bu** (Figure S41). Therefore, especially in **1-t-Bu**, which readily loses crystallinity even at low temperatures, other decomposition pathways can be expected to occur simultaneously.

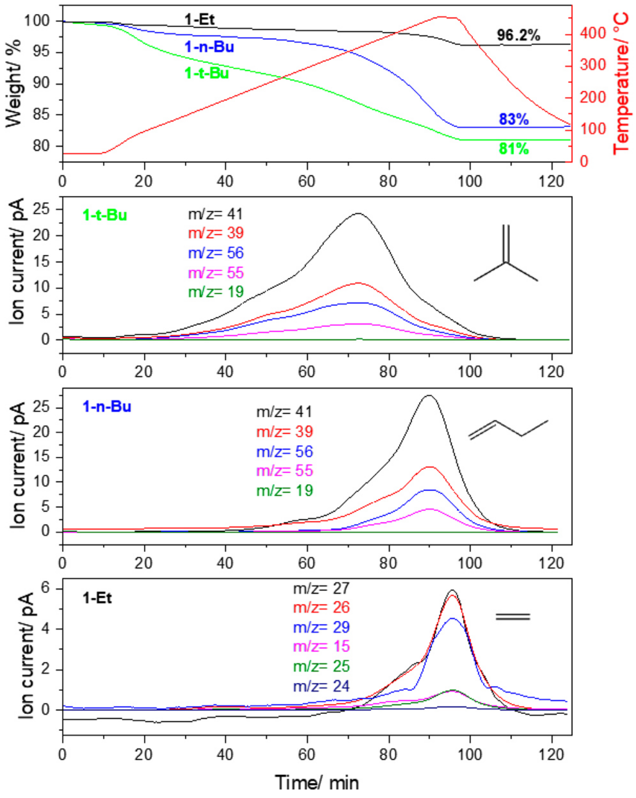

Figure 4. TG-curves and simultaneous MS signals of **1-t-Bu**, **1-n-Bu**, and **1-Et** showing the evolution of the corresponding 2-methylprop-1-ene, but-1-ene, and ethane.

Long-Term and Hydrolytic Stability. For long-term stability tests, the compounds were examined after storage over 4 weeks under ambient conditions in standard capped vials. Except for **1-t-Bu**, which completely lost its crystallinity, no signs of degradation were visible for the other Zn-MFU-4*l* compounds in the IR spectra and XRPD patterns (Figures S52 and S53). The sensitivity to moisture was tested by suspension of the compounds in a mixture of 5% water in tetrahydrofuran for 96 h in total and an analysis step after 24 h. **1-Me**, **1-Et**, and **1-n-Bu** seem to be completely inert toward the applied moisture, as no signs of degradation are visible in the IR spectra and XRPD patterns (Figures S42−S51). However, the position of the C−O stretching vibration overlaps with the CH_2 rocking and Zn−C stretching vibrations of **1-n-Bu**, making it hard to differentiate these compounds. **1-t-Bu** already lost all crystallinity after 24 h. **1-Butyne** developed increasing bands at 700 and 593 cm^{-1}, characteristic for the Zn−OH group (derived from the calculated spectrum of **1-OH** and literature for the band at 700 cm^{-1}),[16] and showed a decrease of the bands at 738 and 464 cm^{-1} (Figure S46), indicating a hydrolysis reaction. It retained good crystallinity with only small shifts of reflection intensities at 4.8, 12.3 and

12.6° 2θ, further confirming the partial ligand exchange (Figure S51).

A very different behavior was observed for the pyrophoric Co-MFU-4*l* derivative **2-Me**, which directly changed color from deep blue to green-brown upon the slightest contact with air. The hydrolysis reaction occurs immediately upon contact with moisture, yielding blue-purple **2-OH** with no changes in crystallinity or porosity with regard to those of **2**. The Co−OH function in **2-OH** was further investigated by DRIFTS measurements, showing the same reversible formation of a bicarbonate species with carbon dioxide as its zinc analogue **1-OH** (Figure 5).[16]

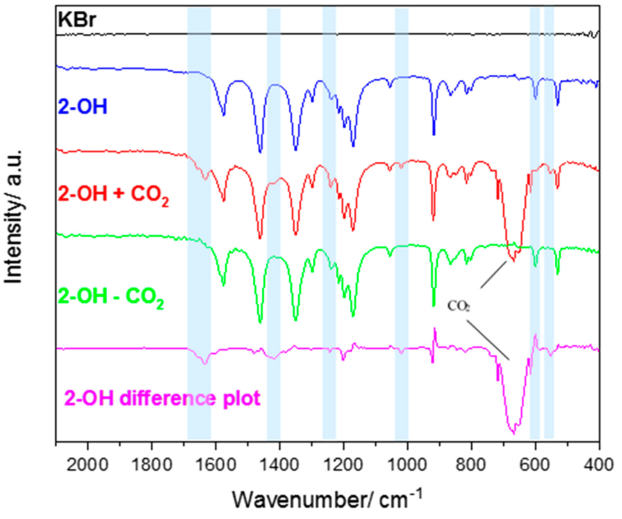

Figure 5. Sequence of DRIFTS measurements of **2-OH** under nitrogen (blue), carbon dioxide (red), and nitrogen (green) atmospheres with the difference plot (pink) showing the reversible formation of a bicarbonate ligand.

The asymmetric and symmetric O═C−O stretching vibrations observed for **1-OH** at 1660 and 1245 cm^{-1} are visible at 1636 and 1244 cm^{-1} in **2-OH**.[16] The bands at 1423 and 1021 cm^{-1} are also in good agreement with the reported stretching and bending vibrations of C−OH at 1423 and 1018 cm^{-1}.[16] Additionally, the Co−OH stretching vibration at 602 cm^{-1} vanishes upon bicarbonate formation and a new band at 555 cm^{-1} occurs, which could be attributed to a Co−OC vibration.

■ CONCLUSION

Ligand exchange and dehydrogenation reactions were successfully employed for the synthesis of the first organometallic MFU-4*l* derivatives with a defined stoichiometric structure, which could be fully characterized in this initial study. The IR spectra measured for the derivatives of **1** neatly fitted the simulations, proving IR to be a valuable tool for the identification of organometallic ligands in MFU-4*l* metal organic frameworks. XRPD and argon adsorption measurements confirmed that all compounds, except for **1-t-Bu**, retained high crystallinity and porosities matching the expected trends for bulky ligands. Exceptionally high thermal as well as high oxidative and hydrolytic stabilities were observed for **1-Me** and **1-Et**. Indeed, their thermal stability significantly exceeds that of the organometallic Kuratowski complexes [$Zn_5L_4(Me_2bta)_6$] (L = methanido, ethanido).[22] This could be explained by an interaction between the Kuratowski complexes, which is inhibited owing to the long distances between these SBUs in the rigid structure of MFU-4*l*. The investigations of the expected β-hydride elimination reactions of **1-Et**, **1-n-Bu**, and **1-t-Bu** indicate additional decomposition processes, especially for **1-n-Bu** and **1-t-Bu**. Hydrolytic stabilities reported for bulky (Ttz$^{t\text{Bu},\text{Me}}$)ZnR (R = Me, Et) and (Tp$^{\text{Ph}}$)ZnR (R = Me,Et,t-Bu) compounds show the same behavior as for our compounds, even reporting a disintegration instead of hydrolysis of the (Tp$^{\text{Ph}}$)Zn-t-Bu complex.[28,29] The slow but steady hydrolysis reaction of **1-Butyne** proved it to be the only reactive species of the derivatives of **1** without simultaneous framework degradation, making it suitable for reactions. It also underlines the functionality of **1-H**, which could be employed for reactions similar to the coupling of terminal alkynes and hydrosilanes reported in the literature.[23]

As expected from similar scorpionate complexes,[30,31] the principal study for organometallic ligand exchanges in Co-MFU-4*l* (**2**) has been proven to be a suitable approach toward compounds with a higher reactivity, although further simulations and measurements are necessary for a better understanding of the differences observed between the cobalt and zinc MFU-4*l* frameworks. The reactivity of **2-Me** was confirmed by the fast hydrolysis reaction yielding **2-OH**, which showed the same carbonic anhydrase mimicking behavior as the reported **1-OH**.[16] Usually the formation of carbonato-bridged binuclear complexes is observed for the reaction of scorpionate Co−OH complexes with carbon dioxide, which is not possible in the rigid MOF structure.[32−34] This could enable reactions not possible for the molecular complexes.

■ EXPERIMENTAL SECTION

General Methods. All syntheses were carried out under an argon atmosphere using common Schlenk line techniques. The chemicals were of reagent grade and were used as obtained from the commercial supplier. Dry and inhibitor-free tetrahydrofuran and dry hexane fraction were obtained from Acros Organics. *Caution*! Compound **2-Me** is pyrophoric!

A Bruker Equinox 55 FT-IR spectrometer was used to obtain the Fourier transform infrared (FT-IR) spectra in the range 4000−180 cm^{-1} with the PLATINUM ATR unit and a KBr (4000−500 cm^{-1}) or Si (500−180 cm^{-1}) beam splitter. The spectra were combined at 500 cm^{-1} from the two measurements. Diffuse reflectance infrared Fourier transform (DRIFT) spectra in the range 4000−400 cm^{-1} were collected on the same instrument equipped with a Harrick praying mantis reaction chamber and KBr as reference. **2-OH** was activated in situ under a nitrogen gas flow at 100 °C for 1 h prior to DRIFTS measurements. Compound **2-Me** was measured with an Agilent Cary 630 FTIR spectrometer equipped with a Diamond ATR unit in an argon-filled glovebag in the range of 4000−400 cm^{-1}. The signals were labeled strong (s), medium (m), and weak (w); the vibrational modes ν_s, ν_{as}, δ, and ρ_r denote symmetrical stretching, asymmetrical stretching, and bending and rocking vibrations, respectively. Thermogravimetric analysis (TGA) data were recorded on a TA Instruments Q500 device in the temperature range of 25−900 °C under a nitrogen or synthetic air gas flow with a heating rate of 10 K min^{-1} and starting after a 5 min isothermal step.

TGA-MS analysis was performed with a Netzsch STA 409 C thermobalance connected via Skimmer coupling to a Balzers QMG 421 mass spectrometer. The temperature range was 20−450 °C with a heating rate of 5 K min^{-1} under a nitrogen atmosphere for compounds **1-n-Bu** and **1-t-Bu** and under an argon atmosphere for compound **1-Et**.

X-ray powder diffraction patterns were measured at room temperature in the 4−40° 2θ range with a Seifert XRD 3003 TT powder diffractometer with a Meteor1D detector using Cu Kα_1 radiation.

The variable-temperature XRPD data were collected in the 2θ range of 3−60°, with 0.02° steps and an interval of 2 s per step, using a Bruker A8 Advance diffractometer equipped with a LYNXEYE 1-D detector in transmittance Bragg−Brentano geometry employing a Göbel mirror and Cu Kα_1 radiation. The samples were heated using an MRI TCPU1 oven, applying a heating rate of 3 °C/min and a 1 min isothermal step before each measurement.

Energy dispersive X-ray spectroscopy (EDX) with a Philips XL 30 FEG instrument with an EDAX SiLi detector was used to determine the Zn:Co:Cl ratios in squares of at least 5×5 μm, while the lithium and Zn:Co contents were measured by ICP-OES with the Vista MPX of VARIAN. *Caution*! Spontaneous combustion was observed for **1-n-Bu** when it was dissolved in fuming nitric acid for the measurements!

Argon adsorption isotherms were obtained in the range $5.00 \times 10^{-5} \leq p/p_0 \leq 1.00$ at 77.3 K with a Quantachrome Autosorb-I ASI-CP-8 instrument. The samples were dried for 20 h under vacuum at ambient temperature prior to the measurements. The evolution of methane during a synthesis of **2-OH** was verified by connection of the reaction headspace into the gas line of a BelCat-B catalyst analyzer (Bel Japan, Inc.), which was coupled with an OmniStar GSD 320 mass spectrometer (Pfeiffer Vacuum).

1, **2** (ICP-OES Zn:Co ratio 1.2:3.8), and **1-H** were prepared according to the previously reported procedures.[2−4] **1** and **2** were activated directly before use in Schlenk flasks under vacuum (>0.2 mbar) for 20 h at 180 and 150 °C, respectively, cooled to room temperature, and flushed with argon. Synthesis yields were calculated for a complete ligand exchange.

Computational Simulations. In order to simulate the crystal structures and vibrational properties of the organometallic MFU-4*l* derivatives, first-principles DFT+D lattice geometry optimizations were performed with the CASTEP code,[35] PBE-GGA, and norm-conserving plane-wave pseudopotentials (energy cutoff: 830 eV) employing a semiempirical dispersion correction for nonbonding interactions according to the scheme suggested by Tkatchenko and Scheffler.[36,37]

The final lattice parameters and selected properties of the fully converged cells are shown in Tables S2 and S3. CIF files of the geometry-converged unit cells of the compounds displayed in Tables S2 and S3 are provided as detailed at the end of the paper.

Phonon frequencies were obtained via CASTEP DFPT linear response calculations[38] at the Γ points of the converged primitive cell geometries. Tabulated values for calculated IR frequencies including their intensities are shown in the Supporting Information. It should be noted that some negative (virtual) frequencies have been obtained in DFPT calculations for **1-Et**, **1-n-Bu**, **1-t-Bu**, and **1-Butyne**, which so far we have been unable to avoid by changing different parameter settings (i.e., DFT grid resolution, convergence tolerance, etc.). Owing to the large number of atoms in the primitive cells, the use of hybrid functionals proved to be impracticable. Thus, it was decided to discard negative frequencies for the aforementioned cells in which they occurred in order to retain consistency in phonon frequency calculations for all systems. Moreover, this pragmatic approach can be justified on the basis of the very good match between calculated and experimental IR frequencies.

The calculated and measured IR spectra were compared and fitted with SpecDis version 1.71 software.[39] Scaling factors of 1.004−1.006 and γ values (Lorentzian line shape) between 5 and 11 were applied to the spectra in the range 1800−180 cm^{-1}. The intensity in the range 700−180 cm^{-1} was multiplied by a factor of 10−15 for the calculated spectra. Between 2800 and 3200 cm^{-1} scaling factors of 0.97−0.988 were applied to the calculated spectra and the experimental spectra magnified by a factor of 2−4.

DFT calculations on mononuclear model complexes of the type [M(Tp)X], where M = Co^{II}, Zn^{II} and X = CH_3^-, OH$^-$, Cl$^-$, were performed with the DMol3 program.[40,41] Geometry optimizations were performed with the B3LYP hybrid functional and a numerical all-electron basis set (DNP, double numerical plus polarization including a polarization p function on all hydrogen atoms). For all Co^{II} complexes spin-polarized calculations have been performed. Subsequent to geometry optimization the Hessians of all compound were computed by finite differences of analytic first derivatives. Calculated IR spectra and selected frequencies are displayed in Figures S10−S12 and Tables S1 and S11−S16. The spectra were fitted with the SpecDis version 1.71 software.[39] Frequency calculations of model complexes were required, because the current CASTEP version does not support DFPT calculations for spin-polarized 3D periodic cells. The use of smaller model complexes for simulating localized vibrations of ligands bound to the metal centers of Kuratowski-type coordination units has been thoroughly analyzed and described in a previous report.[42]

Syntheses. *[$Zn_5Me_{3.9}Cl_{0.1}(BTDD)_3$]* ***(1-Me)***. Activated **1** (100 mg, 0.08 mmol) was suspended in 8 mL of dry and inhibitor-free tetrahydrofuran under an argon atmosphere. Then dimethylzinc (1 M in hexane, 1.9 mL, 1.9 mmol) was added dropwise and the mixture stirred for 20 h. The product was filtered under an argon atmosphere with a Schlenk frit, washed three times with 4 mL of dry tetrahydrofuran, methanol, and dichloromethane, respectively, and dried under vacuum for 2 h to obtain a white powder (87.2 mg, 93%). FT-IR (ATR) 4000−180 cm^{-1}: 3087 (w), 2940 (w), 2911 (w), 2883 (w), 2840 (w), 1578 (w), 1463 (s), 1353 (s), 1308 (w), 1243 (w), 1231 (w), 1214 (w), 1199 (m), 1182 (s), 1175 (s), 1057 (w), 917 (s), 858 (m), 814 (w), 760 (w), 654 (s), 527 (m), 294 (s), 223 (s), 181 (s). EDX Zn/Cl ratio: 5:0.1. BET surface area (Ar, 77.3 K): 4114 m^2 g^{-1}.

[$Zn_5Et_{3.9}Cl_{0.1}(BTDD)_3$] ***(1-Et)***. Activated **1** (100 mg, 0.08 mmol) was suspended in 8 mL of dry and inhibitor-free tetrahydrofuran under an argon atmosphere. Then diethylzinc (1 M in hexane, 1.9 mL, 1.9 mmol) was added dropwise and the mixture stirred for 20 h. The product was filtered under an argon atmosphere with a Schlenk frit, washed three times with 4 mL of dry tetrahydrofuran, methanol, and dichloromethane, respectively, and dried under vacuum for 2 h to obtain a white powder (96.5 mg, 98%). FT-IR (ATR) 4000−180 cm^{-1}: 3091 (w), 2943 (w), 2871 (w), 1578 (w), 1463 (s), 1351 (s), 1307 (w), 1242 (w), 1229 (w), 1213 (w), 1196 (m), 1180 (s), 1055 (w), 980 (w), 917 (s), 856 (m), 815 (w), 782 (w), 601 (m), 533 (w), 501 (w), 427 (w), 387 (w), 294 (s), 248 (s), 223 (s). EDX Zn/Cl ratio: 5:0.1. BET surface area (Ar, 77.3 K): 3677 m^2 g^{-1}.

[Zn_5-n-$Bu_{3.9}Cl_{0.1}(BTDD)_3$] ***(1-n-Bu)***. Activated **1** (100 mg, 0.08 mmol) was suspended in 8 mL of dry hexane under an argon atmosphere. Then *n*-butyllithium (1.6 M in *n*-hexane, 0.25 mL, 0.4 mmol) was added dropwise and the mixture stirred for 20 h. The product was filtered under an argon atmosphere with a Schlenk frit, washed three times with 4 mL of dry hexane, methanol, and dichloromethane, respectively, and dried under vacuum at 100 °C for 2 h to obtain a white powder (91.6 mg, 82%). FT-IR (ATR) 4000−180 cm^{-1}: 2955 (w), 2921 (w), 2872 (w), 1577 (w), 1462 (s), 1348 (s), 1239 (w), 1179 (s), 1407 (w), 915 (m), 854 (m), 813 (w), 780 (w), 609 (w), 532 (m), 427 (w), 378 (w), 296 (m), 224 (s). EDX Zn/Cl ratio: 5:0.1. ICP-OES Zn/Li ratio: 5:0.4. BET surface area (Ar, 77.3 K): 2898 m^2 g^{-1}.

[Zn_5-t-$Bu_{3.7}Cl_{0.3}(BTDD)_3$] ***(1-t-Bu)***. Activated **1** (100 mg, 0.08 mmol) was suspended in 8 mL of dry hexane under an argon atmosphere and cooled to −90 °C in a liquid nitrogen cooled ethanol bath. Then *tert*-butyllithium (1.7 M in *n*-pentane, 0.23 mL, 0.4 mmol) was added dropwise and the mixture stirred for 20 h. The product was filtered under an argon atmosphere with a Schlenk frit, washed three times with 4 mL of dry tetrahydrofuran, methanol, and dichloromethane, respectively, and dried under vacuum for 2 h to obtain a beige powder (84.9 mg, 76%). FT-IR (ATR) 4000−180 cm^{-1}: 2955 (w), 2816 (w), 1635 (w), 1574 (w), 1459 (s), 1341 (s), 1293 (w), 1174 (s), 1027 (m), 914 (m), 848 (m), 805 (m), 776 (w), 675 (w), 529 (m), 424 (w), 286 (w), 222 (s). EDX Zn/Cl ratio: 5:0.3. ICP-OES Zn/Li ratio: 5:2.9. BET surface area (Ar, 77.3 K): 2486 m^2 g^{-1}.

[Zn_5(3,3-dimethyl-1-butyn-1-ido)$_{3.2}Cl_{0.8}(BTDD)_3$] ***(1-Butyne)***. Freshly prepared **1-H** (100 mg, 0.09 mmol) and 3,3-dimethyl-1-butyne (0.25 mL, 3.04 mmol) were sealed in a 38 mL ACE pressure tube and heated to 100 °C for 12 h in a drying oven. The solid was collected and dried under vacuum for 2 h to obtain a beige powder (106.6 mg, 83%). FT-IR (KBr) 4000−180 cm^{-1}: 2969 (w), 1577 (w), 1461 (s), 1351 (s), 1237 (w), 1206 (w), 1181 (s), 1062 (w), 919

(m), 868 (m), 816 (m), 759 (w), 738 (w), 533 (w), 464 (w), 429 (w), 420 (w), 311 (m), 250 (s), 222 (m). EDX Zn/Cl ratio: 5:0.8. BET surface area (Ar, 77.3 K): 2978 m^2 g^{-1}.

[Zn$_{1.5}$Co$_{3.5}$Me$_{3.1}$Cl$_{0.9}$(BTDD)$_3$] ***(2-Me).*** Activated **2** (50 mg, 0.04 mmol) was suspended in 4 mL of dry and inhibitor-free tetrahydrofuran an under argon atmosphere. Then dimethylzinc (1 M in hexane, 0.98 mL, 0.98 mmol) was added dropwise and the mixture stirred for 2 h. The product was filtered under an argon atmosphere with a Schlenk frit, washed three times with 4 mL of dry tetrahydrofuran, and dried under vacuum for 2 h to obtain a blue powder. FT-IR (ATR) 4000−400 cm^{-1}: 2906 (w), 1576 (m), 1460 (s), 1348 (s), 1238 (w), 1195 (m), 1172 (s), 1055 (w), 959 (w), 917 (s), 858 (m), 803 (w), 688 (w), 655 (w), 602 (w), 569 (m), 533 (m), 518 (m), 423 (w). EDX Zn/Co/Cl ratio: 1.5:3.5:0.9. ICP-OES Zn/Co ratio: 1.55:3.45.

[Zn$_{1.4}$Co$_{3.6}$(OH)$_{3.1}$Cl$_{0.9}$(BTDD)$_3$] ***(2-OH).*** Freshly prepared **2-Me** was washed three times with 3 mL of a 19/1 tetrahydrofuran/water solution, methanol, and dichloromethane, respectively, and dried under vacuum for 2 h to obtain a blue-purple powder (42.8 mg, 76%). FT-IR (ATR) 4000−180 cm^{-1}: 3084 (w), 1578 (w), 1461 (s), 1350 (s), 1300 (w), 1240 (w), 1199 (w), 1171 (s), 1057 (w), 919 (m), 866 (w), 817 (w), 804 (w), 602 (w), 532 (m), 383 (w), 304 (s), 225 (s). EDX Zn/Co/Cl ratio: 1.4:3.6:0.9. ICP-OES Zn/Co ratio: 1.4:3.6. BET surface area (Ar, 77.3 K): 3790 m^2 g^{-1}.

Water Stability Tests. Five milligram portions of **1-Me**, **1-Et**, **1-n-Bu**, **1-t-Bu**, and **1-Butyne** were suspended and stirred in 0.3 mL of a 5% water solution in tetrahydrofuran under ambient conditions. After 24 h the solvent was removed under reduced pressure and the samples were dried under vacuum overnight. Subsequent to IR spectra and XRPD measurements, the samples were subjected to the same procedure with a reaction time of 72 h.

■ ASSOCIATED CONTENT

Ⓢ Supporting Information

The Supporting Information is available free of charge on the ACS Publications website at DOI: 10.1021/acs.organomet.9b00297.

IR spectra, lattice parameters and selected properties of the fully converged cells, values for calculated IR frequencies, XRPD pattern, VT-XRPD pattern, argon adsorption isotherms, NLDFT pore size distribution plots, plots of the unit cells with Connolly surfaces, IR spectra and XRPD pattern of the stability tests, the mass spectrum of the methane detection, and EDX data (PDF)

Geometry-converged unit cells of the compounds displayed in Tables S2 and S3 (ZIP)

■ AUTHOR INFORMATION

Corresponding Author

*E-mail: dirk.volkmer@physik.uni-augsburg.de.

ORCID

Dirk Volkmer: 0000-0002-8105-2157

Notes

The authors declare no competing financial interest.

■ ACKNOWLEDGMENTS

This manuscript is dedicated to Dr. Dmytro Denysenko, who sadly passed away far too soon, on July 1, 2018. He was and remains an inspiration to us all. Financial support from the DFG (SPP 1928 COORNETs: Coordination Networks: Building Blocks for Functional Systems) is gratefully acknowledged. The authors are grateful for the English proofreading by Patrizia del Forno. R.R.-O. is grateful for the technical advice and support provided by Andreas Kalytta-Mewes, as well as help from Romy Ettlinger, Katharina Schmitz, and Martin Schäfer.

■ REFERENCES

(1) Biswas, S.; Tonigold, M.; Speldrich, M.; Kögerler, P.; Weil, M.; Volkmer, D. Syntheses and magnetostructural investigations on Kuratowski-type homo- and heteropentanuclear coordination compounds MZn$_4$Cl$_4$(L)$_6$ (M(II) = Zn, Fe, Co, Ni, or Cu; L = 5,6-dimethyl-1,2,3-benzotriazolate) represented by the nonplanar K$_{3,3}$ graph. *Inorg. Chem.* **2010**, *49*, 7424−7434.

(2) Denysenko, D.; Grzywa, M.; Tonigold, M.; Streppel, B.; Krkljus, I.; Hirscher, M.; Mugnaioli, E.; Kolb, U.; Hanss, J.; Volkmer, D. Elucidating gating effects for hydrogen sorption in MFU-4-type triazolate-based metal-organic frameworks featuring different pore sizes. *Chem. - Eur. J.* **2011**, *17*, 1837−1848.

(3) Denysenko, D.; Werner, T.; Grzywa, M.; Puls, A.; Hagen, V.; Eickerling, G.; Jelic, J.; Reuter, K.; Volkmer, D. Reversible gas-phase redox processes catalyzed by Co-exchanged MFU-4*l*(arge). *Chem. Commun.* **2012**, *48*, 1236−1238.

(4) Denysenko, D.; Grzywa, M.; Jelic, J.; Reuter, K.; Volkmer, D. Scorpionate-Type Coordination in MFU-4*l* Metal-Organic Frameworks: Small-Molecule Binding and Activation upon the Thermally Activated Formation of Open Metal Sites. *Angew. Chem.* **2014**, *126*, 5942−5946.

(5) Denysenko, D.; Jelic, J.; Magdysyuk, O. V.; Reuter, K.; Volkmer, D. Elucidating Lewis acidity of metal sites in MFU-4l metal-organic frameworks: N$_2$O and CO$_2$ adsorption in MFU-4*l*, CuI-MFU-4*l* and Li-MFU-4*l*. *Microporous Mesoporous Mater.* **2015**, *216*, 146−150.

(6) Denysenko, D.; Jelic, J.; Reuter, K.; Volkmer, D. Postsynthetic Metal and Ligand Exchange in MFU-4l: A Screening Approach toward Functional Metal-Organic Frameworks Comprising Single-Site Active Centers. *Chem. - Eur. J.* **2015**, *21*, 8188−8199.

(7) Magdysyuk, O. V.; Denysenko, D.; Weinrauch, I.; Volkmer, D.; Hirscher, M.; Dinnebier, R. E. Formation of a quasi-solid structure by intercalated noble gas atoms in pores of Cu(I)-MFU-4l metal-organic framework. *Chem. Commun.* **2015**, *51*, 714−717.

(8) Denysenko, D.; Volkmer, D. Cyclic gas-phase heterogeneous process in a metal-organic framework involving a nickel nitrosyl complex. *Faraday Discuss.* **2017**, *201*, 101−112.

(9) Weinrauch, I.; Savchenko, I.; Denysenko, D.; Souliou, S. M.; Kim, H.-H.; Le Tacon, M.; Daemen, L. L.; Cheng, Y.; Mavrandonakis, A.; Ramirez-Cuesta, A. J.; et al. Capture of heavy hydrogen isotopes in a metal-organic framework with active Cu(I) sites. *Nat. Commun.* **2017**, *8*, 14496.

(10) Metzger, E. D.; Brozek, C. K.; Comito, R. J.; Dincă, M. Selective Dimerization of Ethylene to 1-Butene with a Porous Catalyst. *ACS Cent. Sci.* **2016**, *2*, 148−153.

(11) Comito, R. J.; Fritzsching, K. J.; Sundell, B. J.; Schmidt-Rohr, K.; Dincă, M. Single-Site Heterogeneous Catalysts for Olefin Polymerization Enabled by Cation Exchange in a Metal-Organic Framework. *J. Am. Chem. Soc.* **2016**, *138*, 10232−10237.

(12) Dubey, R. J.-C.; Comito, R. J.; Wu, Z.; Zhang, G.; Rieth, A. J.; Hendon, C. H.; Miller, J. T.; Dincă, M. Highly Stereoselective Heterogeneous Diene Polymerization by Co-MFU-4*l*: A Single-Site Catalyst Prepared by Cation Exchange. *J. Am. Chem. Soc.* **2017**, *139*, 12664−12669.

(13) Comito, R. J.; Metzger, E. D.; Wu, Z.; Zhang, G.; Hendon, C. H.; Miller, J. T.; Dincă, M. Selective Dimerization of Propylene with Ni-MFU-4*l*. *Organometallics* **2017**, *36*, 1681−1683.

(14) Metzger, E. D.; Comito, R. J.; Hendon, C. H.; Dincă, M. Mechanism of Single-Site Molecule-Like Catalytic Ethylene Dimerization in Ni-MFU-4*l*. *J. Am. Chem. Soc.* **2017**, *139*, 757−762.

(15) Comito, R. J.; Wu, Z.; Zhang, G.; Lawrence, J. A.; Korzyński, M. D.; Kehl, J. A.; Miller, J. T.; Dincă, M. Stabilized Vanadium Catalyst for Olefin Polymerization by Site Isolation in a Metal-Organic Framework. *Angew. Chem., Int. Ed.* **2018**, *57*, 8135−8139.

(16) Wright, A. M.; Wu, Z.; Zhang, G.; Mancuso, J. L.; Comito, R. J.; Day, R. W.; Hendon, C. H.; Miller, J. T.; Dincă, M. A Structural

A 9

Mimic of Carbonic Anhydrase in a Metal-Organic Framework. *Chem.* **2018**, *4*, 2894−2901.

(17) Metzger, E. D.; Comito, R. J.; Wu, Z.; Zhang, G.; Dubey, R. C.; Xu, W.; Miller, J. T.; Dincă, M. Highly Selective Heterogeneous Ethylene Dimerization with a Scalable and Chemically Robust MOF Catalyst. *ACS Sustainable Chem. Eng.* **2019**, *7*, 6654−6661.

(18) Biswas, S.; Grzywa, M.; Nayek, H. P.; Dehnen, S.; Senkovska, I.; Kaskel, S.; Volkmer, D. A cubic coordination framework constructed from benzobistriazolate ligands and zinc ions having selective gas sorption properties. *Dalton Trans.* **2009**, 6487−6495.

(19) Biswas, S.; Tonigold, M.; Volkmer, D. Homo- and Heteropentanuclear Coordination Compounds with Td Symmetry - the Solid State Structures of $[MZn_4(L)_4(L')_6]$ (M = Co II or Zn; L = chloride or acac; L′ = 1,2,3-benzotriazolate). *Z. Anorg. Allg. Chem.* **2008**, *634*, 2532−2538.

(20) Schmieder, P.; Denysenko, D.; Grzywa, M.; Baumgärtner, B.; Senkovska, I.; Kaskel, S.; Sastre, G.; van Wüllen, L.; Volkmer, D. CFA-1: The first chiral metal-organic framework containing Kuratowski-type secondary building units. *Dalton Trans.* **2013**, *42*, 10786−10797.

(21) Pettinari, C.; Pettinari, R.; Marchetti, F. Golden Jubilee for Scorpionates. *Adv. Organomet. Chem.* **2016**, *65*, 175−260.

(22) Bunzen, H.; Grzywa, M.; Kalytta-Mewes, A.; Volkmer, D. One-pot synthesis of ultrastable pentanuclear alkylzinc complexes. *Dalton Trans.* **2017**, *46*, 2618−2625.

(23) Kahnes, M.; Görls, H.; Westerhausen, M. Synthesis of Dinuclear Zinc Alkynyls and Their Use in Catalytic Silicon−Carbon Bond Formation. *Organometallics* **2010**, *29*, 3490−3499.

(24) Reinig, R. R.; Fought, E. L.; Ellern, A.; Windus, T. L.; Sadow, A. D. Rapid and ordered carbonylation and oxygenation of a cobalt(II) methyl. *Chem. Commun.* **2017**, *53*, 11020−11023.

(25) Dubbeldam, D.; Calero, S.; Vlugt, T. J.H. iRASPA: GPU-accelerated visualization software for materials scientists. *Mol. Simul.* **2018**, *44*, 653−676.

(26) Jagiello, J.; Thommes, M. Comparison of DFT characterization methods based on N_2, Ar, CO_2, and H_2 adsorption applied to carbons with various pore size distributions. *Carbon* **2004**, *42*, 1227−1232.

(27) Ravikovitch, P. I.; Neimark, A. V. Characterization of nanoporous materials from adsorption and desorption isotherms. *Colloids Surf., A* **2001**, *187−188*, 11−21.

(28) Alsfasser, R.; Powell, A. K.; Vahrenkamp, H.; Trofimenko, S. Monofunktionelle tetraedrische Zink-Komplexe L^3ZnX [L^3=Tris-(pyrazolyl)borat]. *Chem. Ber.* **1993**, *126*, 685−694.

(29) Kumar, M.; Papish, E. T.; Zeller, M.; Hunter, A. D. New alkylzinc complexes with bulky tris(triazolyl)borate ligands: Surprising water stability and reactivity. *Dalton Trans.* **2010**, *39*, 59−61.

(30) Yoshimitsu, S.-i.; Hikichi, S.; Akita, M. Synthesis and Characterization of Coordinatively Unsaturated Alkynyl- and Aryl-Cobalt Complexes with 15 Valence Electrons, Tp iPr_2 Co−R, Bearing the Hydrotris(3,5-diisopropylpyrazolyl)borato Ligand (Tp iPr_2). *Organometallics* **2002**, *21*, 3762−3773.

(31) Kunishita, A.; Gianetti, T. L.; Arnold, J. Structures, Physicochemical Properties, and Reactivities of Cobalt(II) Complexes Supported by a Homoscorpionate (Tris(pyrazolyl)borate) Ligand $Tp^{Ph,Me}$. *Organometallics* **2012**, *31*, 372−380.

(32) Singh, U. P.; Babbar, P.; Tyagi, P.; Weyhermüller, T. A mononuclear cobalt(II) hydroxo complex: Synthesis, molecular structure, and reactivity studies. *Transition Met. Chem.* **2008**, *33*, 931−940.

(33) Kitajima, N.; Hikichi, S.; Tanaka, M.; Morooka, Y. Fixation of atmospheric carbon dioxide by a series of hydroxo complexes of divalent metal ions and the implication for the catalytic role of metal ion in carbonic anhydrase. Synthesis, characterization, and molecular structure of $[LM(OH)]_n$ (n = 1 or 2) and LM(.mu.-CO_3)ML (M(II) = Mn, Fe, Co, Ni, Cu, Zn; L = HB(3,5-iso-Pr_2pz)$_3$). *J. Am. Chem. Soc.* **1993**, *115*, 5496−5508.

(34) Bergquist, C.; Fillebeen, T.; Morlok, M. M.; Parkin, G. Protonation and reactivity towards carbon dioxide of the mononuclear tetrahedral zinc and cobalt hydroxide complexes, $Tp^{(Bu)t(,Me)}$ZnOH and $Tp^{(Bu)t(,Me)}$CoOH: Comparison of the reactivity of the metal hydroxide function in synthetic analogues of carbonic anhydrase. *J. Am. Chem. Soc.* **2003**, *125*, 6189−6199.

(35) Clark, S. J.; Segall, M. D.; Pickard, C. J.; Hasnip, P. J.; Probert, M. I. J.; Refson, K.; Payne, M. C. First principles methods using CASTEP. *Z. Kristallogr. - Cryst. Mater.* **2005**, *220*, 191.

(36) Tkatchenko, A.; Scheffler, M. Accurate molecular van der Waals interactions from ground-state electron density and free-atom reference data. *Phys. Rev. Lett.* **2009**, *102*, 73005.

(37) McNellis, E. R.; Meyer, J.; Reuter, K. Azobenzene at coinage metal surfaces: Role of dispersive van der Waals interactions. *Phys. Rev. B: Condens. Matter Mater. Phys.* **2009**, *80*, 1.

(38) Refson, K.; Tulip, P. R.; Clark, S. J. Variational density-functional perturbation theory for dielectrics and lattice dynamics. *Phys. Rev. B: Condens. Matter Mater. Phys.* **2006**, *73*, R4954.

(39) Bruhn, T.; Schaumlöffel, A.; Hemberger, Y.; Bringmann, G. SpecDis: Quantifying the comparison of calculated and experimental electronic circular dichroism spectra. *Chirality* **2013**, *25*, 243−249.

(40) Delley, B. From molecules to solids with the DMol3 approach. *J. Chem. Phys.* **2000**, *113*, 7756−7764.

(41) Delley, B. An all-electron numerical method for solving the local density functional for polyatomic molecules. *J. Chem. Phys.* **1990**, *92*, 508−517.

(42) Jelic, J.; Denysenko, D.; Volkmer, D.; Reuter, K. Computational screening study towards redox-active metal-organic frameworks. *New J. Phys.* **2013**, *15*, 115004.

Supporting Information

Organometallic MFU-4*l*(arge) metal-organic frameworks

Richard Röß-Ohlenroth, Björn Bredenkötter and Dirk Volkmer*

Chair of Solid State and Materials Chemistry, Institute of Physics, University of Augsburg, Universitätsstraße 1, 86159 Augsburg, Germany

TABLE OF CONTENTS

A 11

IR spectra

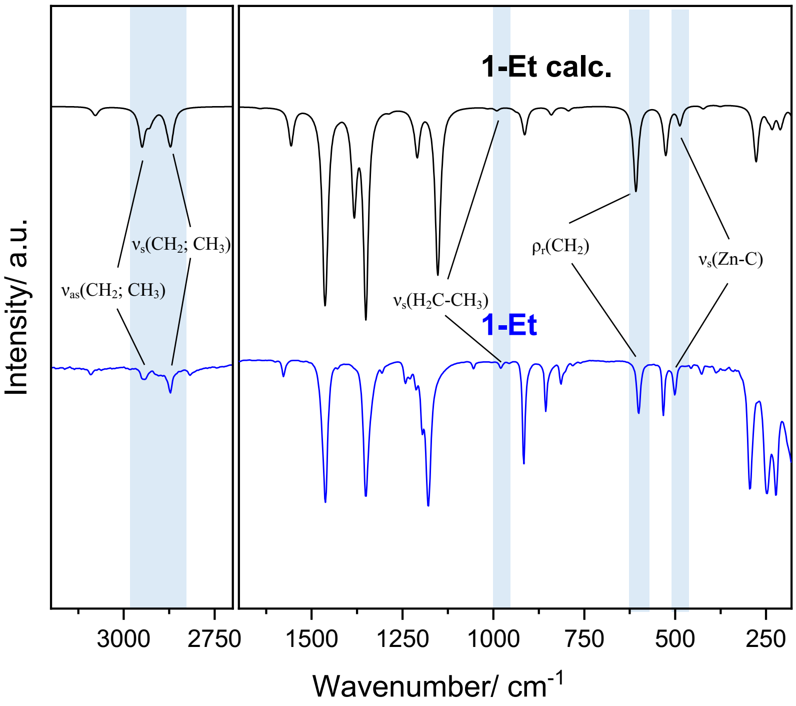

Figure S 1. calculated (black) and measured (blue) IR spectra of **1-Et**

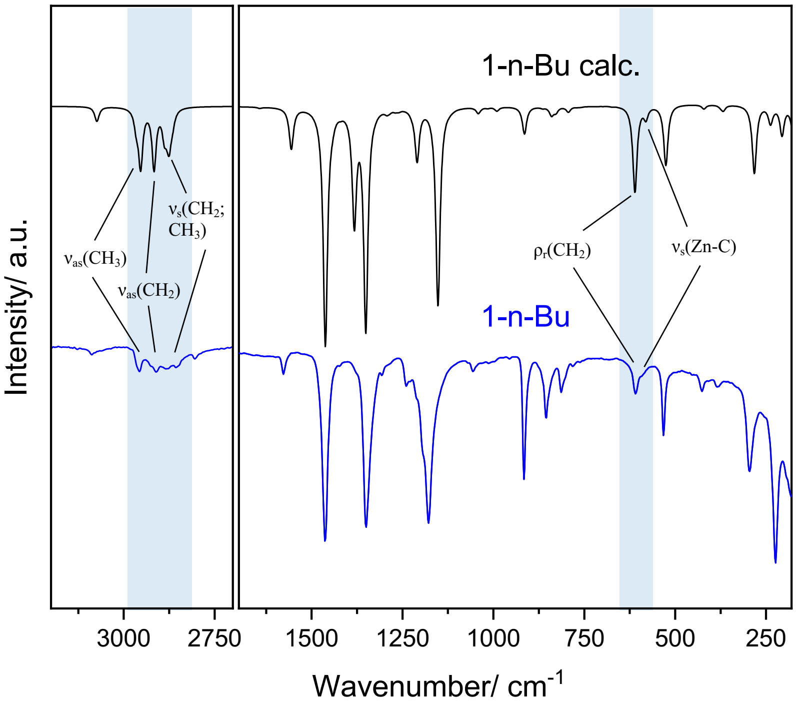

Figure S 2. calculated (black) and measured (blue) IR spectra of **1-n-Bu**

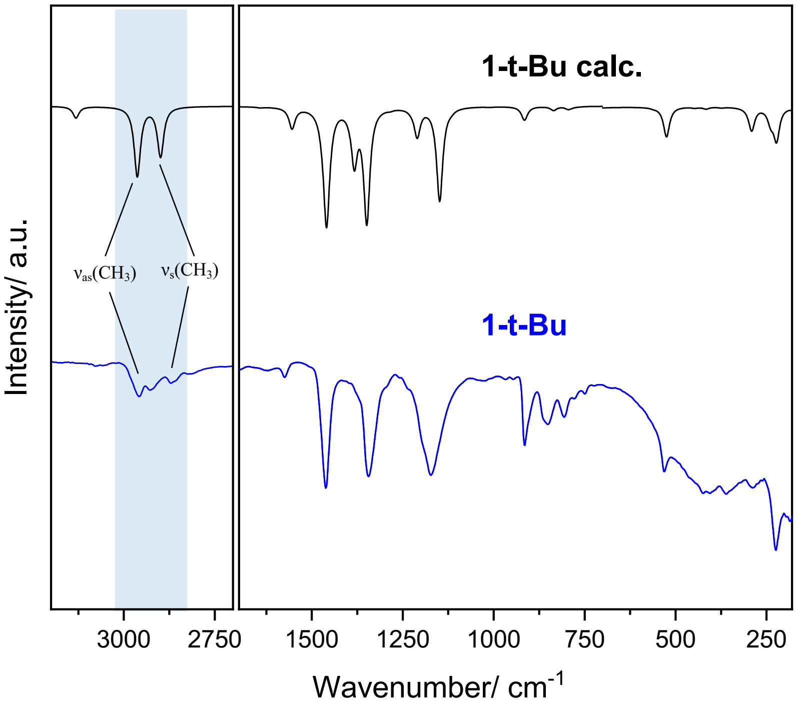

Figure S 3. calculated (black) and measured (blue) IR spectra of **1-t-Bu**

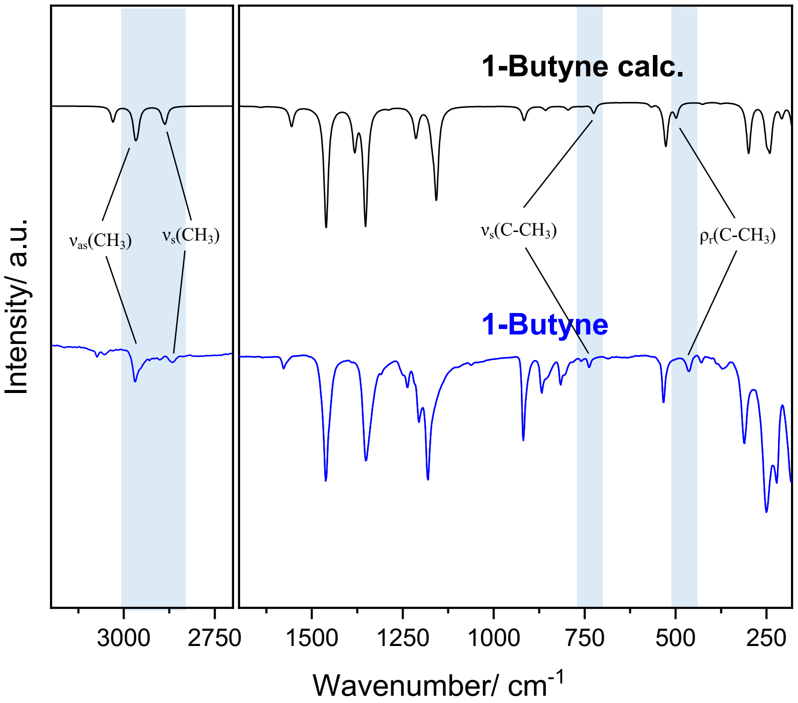

Figure S 4. calculated (black) and measured (blue) IR spectra of **1-Butyne**

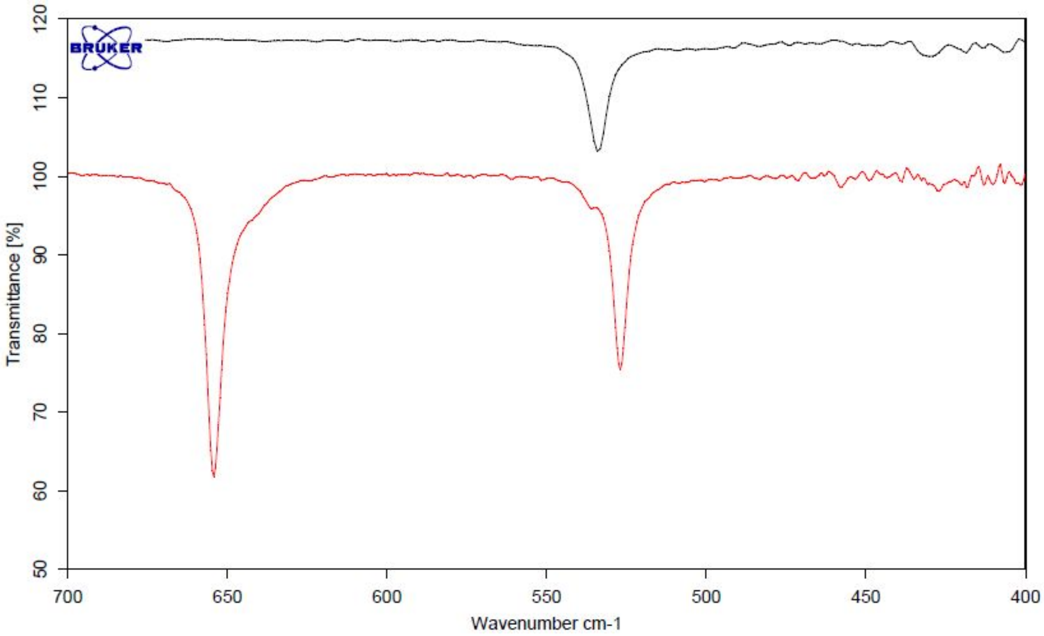

Figure S 5: magnification of the IR spectra of compound **1** (black) and compound **1-Me** (red) showing a small shoulder at 534 cm^{-1}

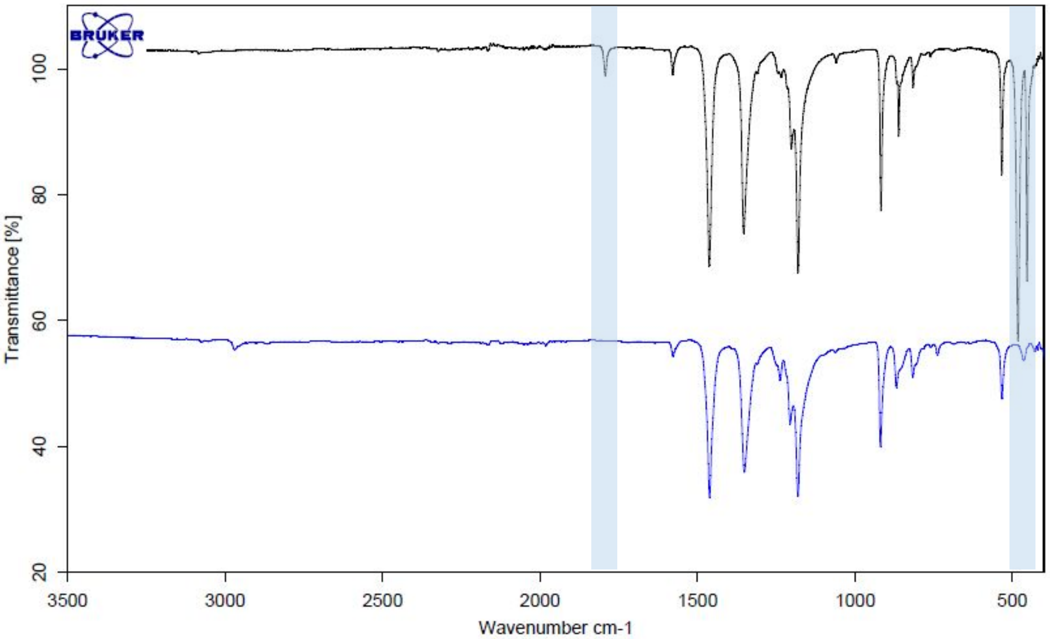

Figure S 6. comparison of the IR spectra of **1-H** (black) and **1-Butyne** (blue)

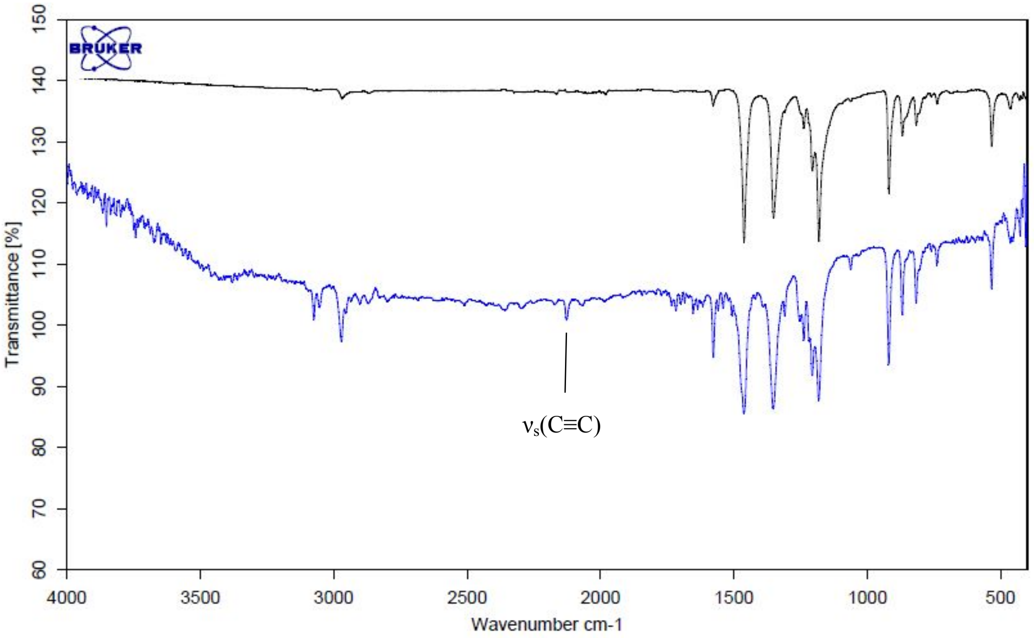

Figure S 7. comparison of ATR IR (black) and DRIFT (blue) spectra of **1-Butyne** with the C≡C stretch at 2127 cm^{-1}

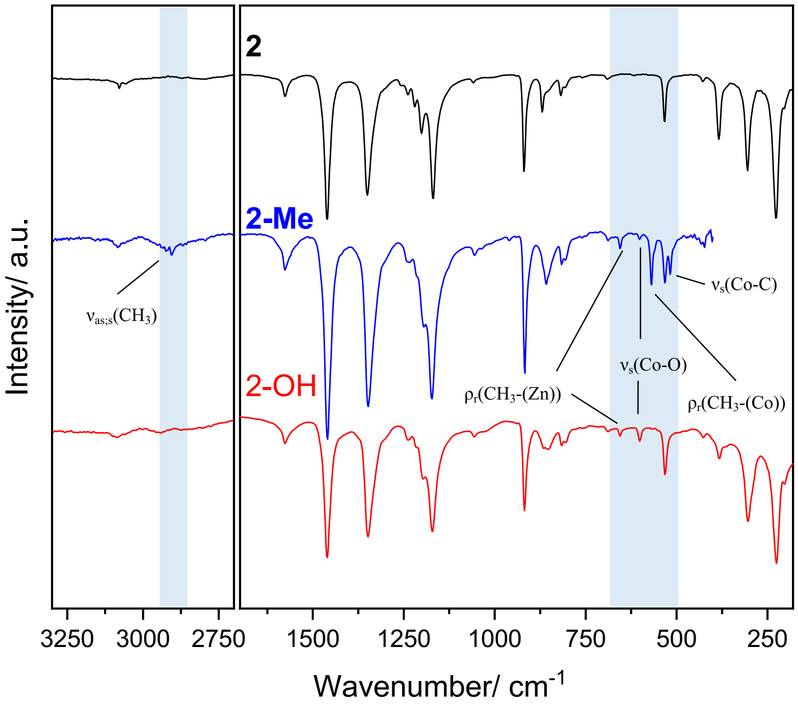

Figure S 8. comparison of ATR- IR spectra of **2** (black), **2-Me** (blue) and **2-OH** (red)

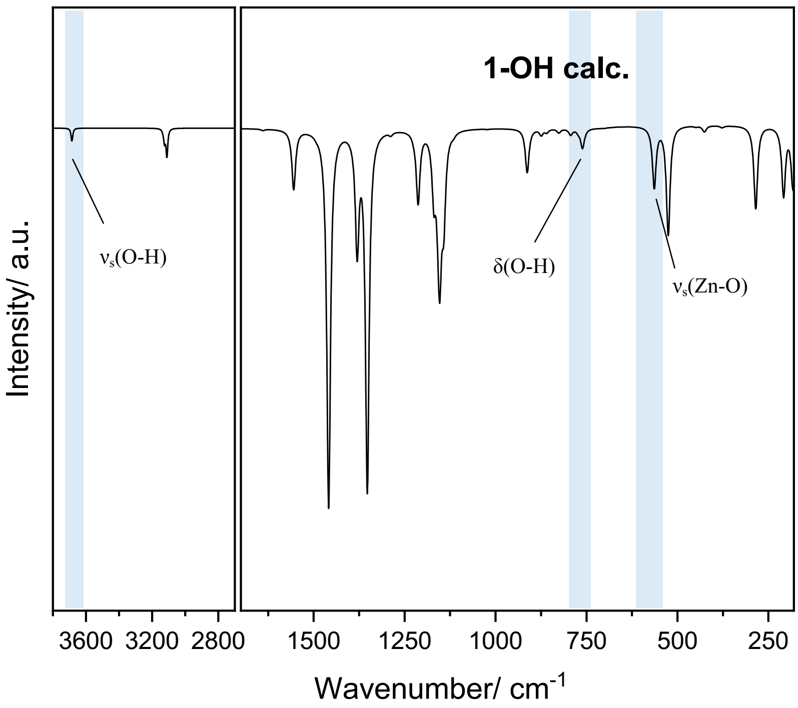

Figure S 9. calculated IR spectrum of **1-OH**

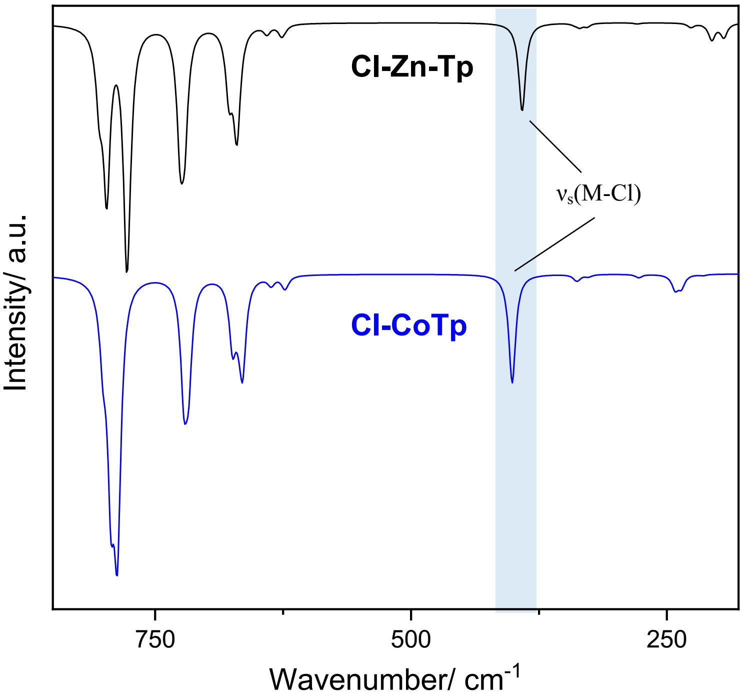

Figure S 10. calculated IR spectra of **TpZn-Cl** (black) and **TpCo-Cl** (blue)

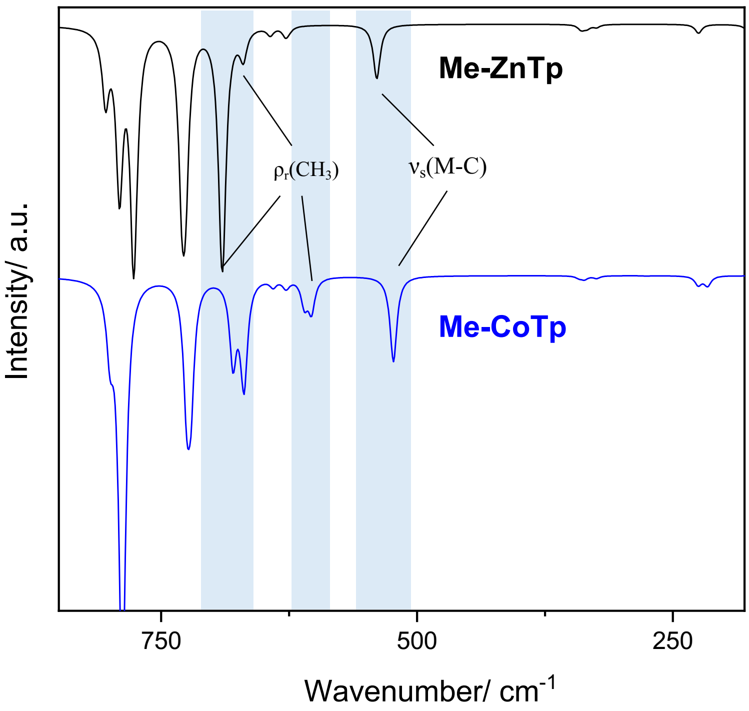

Figure S 11. calculated IR spectra of **TpZn-Me** (black) and **TpCo-Me** (blue)

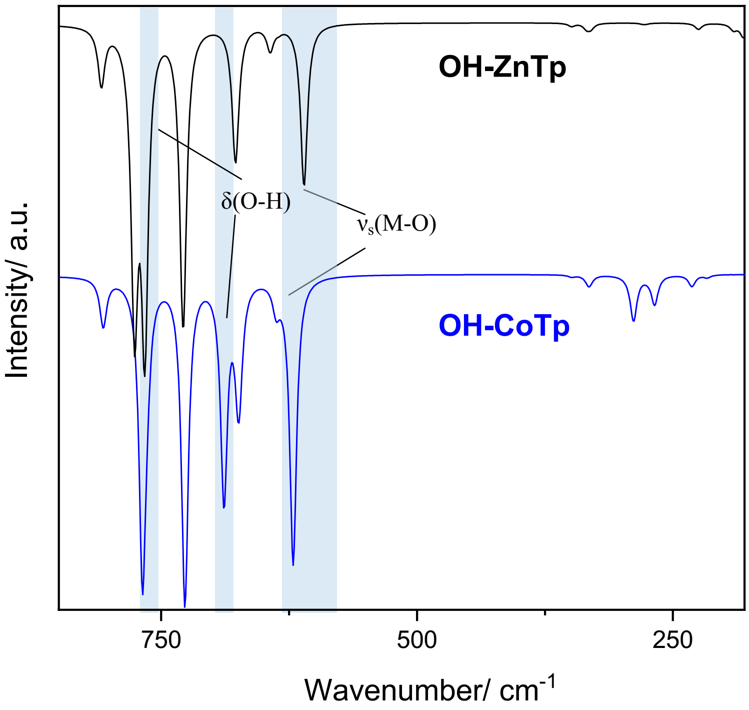

Figure S 12. calculated IR spectra of **TpZn-OH** (black) and **TpCo-OH** (blue)

Table S 1: comparison of vibrational modes calculated for the different Tp model complexes

vibrational mode	Cl-ZnTp	Cl-CoTp	Me-ZnTp	Me-CoTp	OH-ZnTp	OH-CoTp
ν_s(Cl-M) calc.	391	401				
ν_s(Cl-M) meas.	377	384				
ν_s(C-M) calc.			539	523		
ν_s(C-M) meas.			527	518		
ρ_r(CH_3) calc.			670/689/692	603/610		
ρ_r(CH_3) meas.			654	569		
ν_s(O-M) calc.					610	621
ν_s(O-M) meas.					593*	602
δ(O-H) calc.					766	689
δ(O-H) meas.					~700*	/

* the experimental value of the ν_s(O-M) band was taken from the hydrolysis reaction of **1-Butyne** and the experimental value of δ(O-H) was taken from the literature spectrum of **1-OH** (Wright, A. M.; Wu, Z.; Zhang, G.; Mancuso, J. L.; Comito, R. J.; Day, R. W.; Hendon, C. H.; Miller, J. T.; Dincă, M. A Structural Mimic of Carbonic Anhydrase in a Metal-Organic Framework. *Chem* **2018**, *4*, 2894–2901.)

Calculated cell constants, IR frequencies and character tables

Table S 2. Calculated cell constants of 1, 1-Me, 1-Et and 1-t-Bu (conventional cells)

Compound	**1**	**1-Me**	**1-Et**	**1-t-Bu**
Formula	[$Zn_5Cl_4(BTDD)_3$]	[$Zn_5Me_4(BTDD)_3$]	[$Zn_5Et_4(BTDD)_3$]	[Zn_5t-$Bu_4(BTDD)_3$]
Crystal system:	cubic	cubic	tetragonal	cubic
Space group:	Fm-3m (no. 225)	Fm-3m (no. 225)	I4/M (no. 87)	Fm-3m (no. 225)
Cell formula:	$C_{288}H_{96}N_{144}O_{48}Cl_{32}Zn_{40}$	$C_{320}H_{192}N_{144}O_{48}Zn_{40}$	$C_{176}H_{128}N_{72}O_{24}Zn_{20}$	$C_{416}H_{384}N_{144}O_{48}Zn_{40}$
Conv. cell parameters				
a [Å]	31.668629	31.620124	22.375551	31.654098
b [Å]			22.375551	
c [Å]			31.600247	
α [°]	(90)	(90)	(90)	(90)
β [°]				
γ [°]				
V [Å^3]	31760.5	31614.8	15821.1	31716.8

Table S 3. Calculated cell constants of 1-n-Bu, 1-Butyne and 1-OH (conventional cells)

Compound	**1-n-Bu**	**1-Butyne**	**1-OH**
Formula	[Zn_5n-$Bu_4(BTDD)_3$]	[Zn_5(3,3-dimethyl-1-butyn-1-ido)$_4$($BTDD)_3$]	[$Zn_5(OH)_4(BTDD)_3$]
Crystal system:	tetragonal	cubic	tetragonal
Space group:	I4/M (no. 87)	Fm-3m (no. 225)	I4/M (no. 87)
Cell formula:	$C_{208}H_{192}N_{72}O_{24}Zn_{20}$	$C_{480}H_{384}N_{144}O_{48}Zn_{40}$	$C_{144}H_{64}N_{72}O_{40}Zn_{20}$
Conv. cell parameters			
a [Å]	22.36022	31.640318	22.399589
b [Å]	22.36022		22.399589
c [Å]	31.628509		31.578374
α [°]	(90)	(90)	(90)
β [°]			
γ [°]			
V [Å^3]	15813.6	31675.4	15844.2

Table S 4. IR frequencies, intensities and character table of compound 1 (Cl-Zn-MFU-4l)

Frequency [cm^{-1}]	irrep.	IR intensity active [(D/A)^{2}amu^{-1}]
32.894860	a	3.992E-4
55.084090	a	1.53311
102.13623	a	0.12421
120.95248	a	0.19715
122.33643	a	0.71706
143.13764	a	0.41785
183.55971	a	9.97636
208.37055	a	8.77739
280.95781	a	8.26548
361.76801	a	4.325
375.75319	a	0.10102
422.44650	a	0.27398
449.62893	a	0.08508
524.64671	a	5.36609
643.97605	a	0.01627
753.14337	a	0.50493
769.90977	a	0.07421
792.90027	a	2.98554
854.20172	a	4.25043
911.68202	a	14.92528
1020.22129	a	0.0226
1116.52009	a	0.0696
1146.38588	a	68.97363
1164.30888	a	10.51414
1211.53856	a	17.87553
1224.12174	a	0.90809
1282.77647	a	0.70524

1347.30257	a	77.02319
1377.04288	a	24.19024
1453.35727	a	80.6978
1487.57613	a	0.2835
1547.73978	a	12.03212
1633.65194	a	0.32953
3116.20791	a	2.69223
3117.03982	a	1.46675

```
+      Character table from group theory analysis of eigenvectors        +
+                        Point Group =  32, Oh                          +
+ .......................................................................... +
+  Rep  Mul |   E   2   3  2'   4   I m_h  -3 m_v  -4                    +
+           | ----------------------------------------                   +
+ a T1u  36 |   3  -1   0  -1   1  -3   1   0   1  -1                    +
+ b T2u  26 |   3  -1   0   1  -1  -3   1   0  -1   1                    +
+ c T1g  26 |   3  -1   0  -1   1   3  -1   0  -1   1                    +
+ d T2g  35 |   3  -1   0   1  -1   3  -1   0   1  -1                    +
+ e Eu   19 |   2   2  -1   0   0  -2  -2   1   0   0                    +
+ f Eg   20 |   2   2  -1   0   0   2   2  -1   0   0                    +
+ g A2g   6 |   1   1   1  -1  -1   1   1   1  -1  -1                    +
+ h A1u   5 |   1   1   1   1   1  -1  -1  -1  -1  -1                    +
+ i A2u  14 |   1   1   1  -1  -1  -1  -1  -1   1   1                    +
+ j A1g  14 |   1   1   1   1   1   1   1   1   1   1                    +
```

Table S 5. IR frequencies, intensities and character table of compound 1-Me (Me-Zn-MFU-4l)

Frequency [cm^{-1}]	irrep.	IR intensity active [(D/A)^{2}amu^{-1}]
34.042030	a	0.00303
88.287960	a	0.47202
106.84843	a	0.28183
118.16901	a	0.52061
125.12451	a	6.26E-5
139.80272	a	0.42553
172.32199	a	10.32667
207.28962	a	5.58035
272.78407	a	9.12688
371.91726	a	0.14187
418.94759	a	0.2226
442.93507	a	0.0028
512.07053	a	3.31096
524.46350	a	2.51659
649.88238	a	0.18372
658.83425	a	16.00613
754.76533	a	0.43313
766.39303	a	0.19058
790.26083	a	2.07242
840.05233	a	4.4451

910.35150	a	12.60655
1012.44093	a	0.44103
1109.35623	a	0.0493
1138.78058	a	1.23095
1148.30378	a	69.47605
1152.9256	a	0.0213
1204.59985	a	17.28364
1219.05284	a	0.44971
1280.21836	a	0.80433
1344.55347	a	67.95273
1374.29975	a	32.66437
1419.87821	a	0.38656
1454.01892	a	69.2978
1483.18776	a	0.14922
1547.44781	a	10.87564
1632.93858	a	0.2465
2941.50063	a	1.60885
3025.59708	a	3.91356
3123.81482	a	0.16478
3124.7879	a	1.20541

```
+ ........................................................................ +
+      Character table from group theory analysis of eigenvectors          +
+                      Point Group =  32, Oh                       +
+ ........................................................................ +
+  Rep  Mul |   E   2   3  2'   4   I  m_h  -3  m_v  -4                  +
+           | ----------------------------------------                   +
+ a T1u  41 |   3  -1   0  -1   1  -3   1   0   1  -1                    +
+ b T2u  30 |   3  -1   0   1  -1  -3   1   0  -1   1                    +
+ c T1g  30 |   3  -1   0  -1   1   3  -1   0  -1   1                    +
+ d A2g   7 |   1   1   1  -1  -1   1   1   1  -1  -1                    +
+ e T2g  40 |   3  -1   0   1  -1   3  -1   0   1  -1                    +
+ f Eu   22 |   2   2  -1   0   0  -2  -2   1   0   0                    +
+ g Eg   23 |   2   2  -1   0   0   2   2  -1   0   0                    +
+ h A1u   6 |   1   1   1   1   1  -1  -1  -1  -1  -1                    +
+ i A2u  16 |   1   1   1  -1  -1  -1  -1  -1   1   1                    +
+ j A1g  16 |   1   1   1   1   1   1   1   1   1   1                    +
```

Table S 6. IR frequencies, intensities and character table of compound 1-Et (Et-Zn-MFU-4l)

Frequency [cm^{-1}]	irrep.	IR intensity active [(D/A)^{2}amu^{-1}]
-16.36009	a	0.00279
-13.86184	c	5.049E-4
-0.039870	a	0.00325
15.684140	c	0.00317
31.070100	a	0.02861
42.589700	c	0.03445
50.312680	a	0.1552

A 21

62.167003	c	0.0015
68.294070	a	0.08767
68.529680	c	0.28876
76.675830	a	0.01243
97.032980	c	0.02593
99.757940	a	0.03794
104.31889	c	0.02993
114.29990	a	0.44802
117.14455	c	0.29615
119.83204	a	0.0448
121.16799	c	0.01454
123.86927	a	0.01922
131.19097	c	0.19469
134.80505	a	0.26819
136.73622	c	0.1944
136.80758	a	0.11876
142.95107	c	0.1822
144.47146	a	0.03066
155.65218	c	0.01671
165.77947	a	7.60591
170.63615	c	7.94288
177.05667	a	0.00839
201.40302	c	0.71638
201.52519	a	0.43887
206.82205	a	2.46736
210.61483	c	6.78815
231.69102	a	7.05689
236.40364	c	0.31512
243.66968	a	2.81762
275.35991	c	12.14457
276.68691	a	6.55264
336.23920	c	0.00242
345.49171	a	0.00274
351.04602	c	0.00174
371.83571	a	0.00469
373.79506	c	0.15466
374.44427	a	0.16186
419.77832	a	0.04517
420.11034	c	0.49184
421.39282	a	0.24929
428.65551	a	0.00113
443.43490	a	0.00527
444.04981	c	1.969E-4
484.47854	a	3.15185
484.74913	c	0.45624
518.08147	c	0.02229
523.09008	a	4.2491
523.35268	c	4.43117

A 22

604.45527	a	4.36098
605.09076	c	8.7314
645.20918	a	0.00181
650.01519	c	0.00963
650.10178	a	0.01105
671.52466	c	0.02496
671.90672	a	0.0072
671.91557	c	9.84E-5
735.14805	c	0.01864
735.47360	a	3.955E-4
736.54781	c	7.618E-4
753.80430	c	9.702E-4
754.86881	a	0.26304
755.52095	c	0.31526
764.74971	a	0.00485
766.33841	a	0.25911
766.65659	c	0.22484
787.15649	a	0.02624
789.55941	a	2.30682
789.58118	c	2.2269
828.40634	c	0.46198
829.10679	a	0.06936
829.38330	c	0.08275
834.95700	a	0.7867
836.63235	a	2.83478
836.83281	c	4.79784
907.49687	a	1.33739
907.64972	c	3.87561
908.93582	c	0.06154
909.75120	c	10.30931
909.95780	a	12.82848
934.03269	c	1.42672
934.05692	a	0.71303
985.57828	c	1.74655
985.64093	a	1.34545
1010.00286	c	0.50552
1010.98201	c	1.04E-5
1012.01758	a	0.54338
1105.56405	a	0.01581
1108.53669	a	0.17207
1108.66674	c	0.18144
1137.12175	a	0.79843
1141.23523	c	4.44447
1143.72124	a	20.3453
1145.76544	c	9.68339
1147.45689	c	55.70565
1148.07846	a	48.21784
1155.03858	a	1.7292

A 23

1155.21221	c	0.62507
1201.3874	c	3.006E-4
1202.87212	c	17.28885
1203.90449	a	18.04861
1214.99979	a	0.41555
1216.9889	c	1.48525
1218.49351	a	0.41608
1220.40674	c	0.00657
1220.51631	a	0.06416
1276.93851	a	0.03501
1279.89698	a	0.7352
1280.4288	c	0.76018
1341.46051	c	0.08244
1343.57615	c	70.06569
1344.33085	a	71.21909
1365.97254	c	0.66798
1366.39871	a	0.67331
1374.97576	c	2.77752
1375.88125	a	31.69425
1376.08367	c	29.70678
1418.59353	c	0.06576
1418.83007	a	1.07511
1445.42708	c	0.0096
1445.66847	a	0.07922
1449.87156	c	11.4812
1452.09763	a	24.00144
1453.56107	c	16.11523
1456.7555	a	44.16431
1457.60099	c	40.52009
1481.37045	a	7.953E-4
1483.22476	a	0.1141
1483.45445	c	0.13249
1548.16079	c	0.24793
1548.28775	c	10.81931
1548.83243	a	11.03724
1633.01567	a	0.00424
1633.8983	c	0.34357
1634.0685	a	0.25128
2917.55656	c	8.92866
2918.03399	a	5.00808
2927.86728	a	2.94003
2927.89855	c	0.2344
2963.3595	a	0.32677
2963.37782	c	0.65861
2976.27968	c	0.25557
2976.32824	a	4.69847
2997.58114	c	9.55389
2997.73067	a	4.77191

3125.45591	a	0.46717
3125.46872	c	0.17177
3127.86216	c	0.18795
3127.88577	a	1.0374
3128.68119	a	0.11381
3129.72909	c	1.2976

```
+ ........................................................................... +
+        Character table from group theory analysis of eigenvectors           +
+                         Point Group =  11, C4h                              +
+ ........................................................................... +
+  Rep  Mul |    E   2   4   4   I m_h  -4  -4                                +
+           | --------------------------------                                +
+ a Eu   80 |    2  -2   0   0  -2   2   0   0                                +
+ b Bu   77 |    1   1  -1  -1  -1  -1   1   1                                +
+ c Au   78 |    1   1   1   1  -1  -1  -1  -1                                +
+ d Ag   78 |    1   1   1   1   1   1   1   1                                +
+ e Eg   79 |    2  -2   0   0   2  -2   0   0                                +
+ f Bg   79 |    1   1  -1  -1   1   1  -1  -1                                +
```

Table S 7. IR frequencies, intensities and character table of compound 1-n-Bu (n-Bu-Zn-MFU-4l)

Frequency [cm^{-1}]	irrep.	IR intensity active [(D/A)^{2}amu^{-1}]
-26.08441	c	1E-7
-20.13527	b	4.608E-4
-12.01736	c	0.03339
-0.050110	b	2.36E-5
-0.030020	c	2.052E-4
16.717770	b	0.01048
29.419680	c	0.00557
34.755930	b	0.02442
37.808340	b	0.01152
41.480760	c	7.719E-4
60.328180	c	9E-7
70.366090	b	3.097E-4
78.045600	b	0.00624
90.858540	c	0.00766
95.287800	b	0.01565
102.89242	c	0.04695
111.14536	b	0.11059
112.60853	c	0.0425
113.89218	b	0.33123
114.16359	c	0.42857
120.74590	c	9.492E-4
124.15434	c	0.00371
125.60024	b	0.05763
128.94614	b	0.03918

A 25

134.38882	b	0.07523
137.98393	c	0.05878
140.67240	b	0.03926
143.98965	b	0.00178
144.24553	c	0.08436
148.08254	c	0.10869
154.19469	b	0.30043
168.61122	c	1.73712
170.75142	c	8.5334
172.95464	b	8.9622
176.91608	b	0.82895
204.71540	c	5.99469
205.38068	b	5.53691
226.43434	c	0.2902
235.50499	b	2.47404
236.34360	c	1.90258
238.40077	b	1.71884
249.81398	b	0.027
280.42674	c	11.60172
281.24395	b	8.09302
334.97562	c	0.00538
343.70508	b	0.01402
348.88144	c	0.00717
364.38291	c	0.01046
365.75022	b	1.17857
369.62745	b	0.02461
372.49408	b	0.20441
372.94310	c	0.16829
418.17727	b	0.11235
418.92221	b	0.14078
419.01249	c	0.54046
427.49707	b	0.00581
442.32018	b	5.406E-4
442.85493	c	0.00357
518.37022	c	0.00525
522.86685	c	4.596
523.20170	b	4.71753
577.57881	c	0.01528
577.62862	b	1.63773
607.21009	b	3.57568
607.78207	c	7.92565
644.78075	b	0.00172
649.50481	c	0.00657
649.70227	b	0.01254
670.36165	c	0.03179
671.02250	c	0.02585
671.10320	b	0.01091
711.96017	c	0.12498

A 26

712.59152	b	0.07651
733.24696	c	0.01438
734.61275	c	0.04797
734.76441	b	0.00319
754.25972	c	3.622E-4
755.33332	b	0.28639
755.42673	c	0.35584
764.50486	b	0.01342
766.13844	b	0.30146
766.48654	c	0.3062
787.51531	b	0.01754
789.83596	c	2.808
789.93696	b	2.72857
823.43336	c	3.85582
824.85188	b	1.13639
827.48129	c	0.00895
828.63702	c	0.08334
828.75803	b	0.08984
833.70549	b	1.16203
836.15923	b	1.87739
836.41558	c	5.09641
856.94331	c	0.04382
860.45207	b	1.04287
908.86706	c	0.0238
909.87513	c	11.71171
910.01301	b	12.45877
983.60062	c	0.21714
984.75644	b	1.04733
985.83333	c	1.96302
986.09221	b	0.06745
1010.14052	c	0.01238
1010.3833	c	0.34092
1011.22633	b	0.40511
1027.51086	c	0.03753
1027.83861	b	0.03032
1035.57622	c	2.85588
1037.43795	b	1.97307
1105.73833	b	0.01496
1107.98282	c	0.1348
1108.09312	b	0.29355
1116.08308	c	0.08365
1117.2027	b	0.54299
1137.53994	b	0.31275
1142.26342	c	1.66926
1146.43893	b	61.27776
1146.63028	c	67.28066
1148.99682	c	1.39269
1149.18604	b	9.29218

A 27

1180.52024	c	6.47E-5
1181.70062	b	0.01329
1201.67073	c	0.02
1203.24486	c	17.2473
1204.20333	b	17.56105
1216.53137	b	0.05599
1218.15869	b	0.65111
1218.23886	c	0.9587
1253.80234	c	0.83704
1254.73404	b	0.25359
1262.76376	c	0.35745
1263.67768	b	0.70272
1276.63203	b	0.01174
1279.82627	b	0.73976
1280.10794	c	0.42827
1286.57392	c	1.40038
1287.19154	b	0.55303
1317.76852	c	0.2304
1319.02293	b	0.48545
1342.19249	c	7.548E-4
1343.42124	c	65.57666
1344.93063	b	67.77155
1354.19343	c	0.26979
1359.64614	b	0.19666
1374.87988	c	3.28666
1375.23374	c	29.01128
1375.90534	b	33.22723
1412.69701	c	0.01952
1412.92609	b	1.07201
1426.76624	c	0.00692
1428.07442	b	0.22958
1435.58719	c	2.87229
1440.50767	c	0.6494
1442.80215	b	0.11842
1452.32203	b	0.89803
1452.90664	c	1.23713
1453.26795	c	2.18237
1454.39252	c	61.45922
1455.42659	b	65.80834
1457.86667	b	0.55151
1481.23078	b	0.01158
1483.57371	b	0.12221
1484.07166	c	0.17353
1547.48002	c	10.6292
1547.95789	c	0.04373
1548.62385	b	10.82123
1632.81581	b	0.04544
1634.39618	b	0.21089

1634.73124	c	0.32776
2908.23158	c	0.20689
2908.32547	b	0.06199
2915.64711	c	0.24099
2915.68564	b	2.93825
2924.22217	c	0.33354
2924.49487	b	7.83268
2929.79462	b	2.54726
2929.85452	c	0.88185
2937.22577	c	2.77939
2939.04455	b	4.06534
2954.07821	c	0.04997
2954.21678	b	0.01363
2966.96536	c	11.24283
2967.17896	b	5.10989
3004.1519	c	13.30617
3006.99029	b	2.54929
3014.15562	c	0.93483
3017.24873	b	3.58677
3123.92304	b	0.63255
3123.93665	c	0.25017
3127.1080	b	0.2902
3127.68639	c	0.70812
3127.71398	b	0.92028
3128.16719	c	1.1443

```
+ .......................................................................... +
+       Character table from group theory analysis of eigenvectors          +
+                         Point Group =  11, C4h                            +
+ .......................................................................... +
+  Rep  Mul |   E   2   4   4   I m_h  -4  -4                               +
+           | --------------------------------                              +
+ a Bu   95 |   1   1  -1  -1  -1  -1   1   1                               +
+ b Eu   98 |   2  -2   0   0  -2   2   0   0                               +
+ c Au   96 |   1   1   1   1  -1  -1  -1  -1                               +
+ d Eg   97 |   2  -2   0   0   2  -2   0   0                               +
+ e Ag   96 |   1   1   1   1   1   1   1   1                               +
+ f Bg   97 |   1   1  -1  -1   1   1  -1  -1                               +
```

Table S 8. IR frequencies, intensities and character table of compound 1-t-Bu (t-Bu-Zn-MFU-4l)

Frequency [cm^{-1}]	irrep.	IR intensity active [$(D/A)^2amu^{-1}$]
-248.11773	e	0.03011
-0.044870	e	0.00133
31.981010	e	0.15665
41.192170	e	0.11234

A 29

88.756210	e	0.04599
112.57819	e	6.92E-4
118.74090	e	0.38938
131.61839	e	0.28431
159.08433	e	6.13
198.06292	e	0.05446
221.42675	e	12.60237
237.53582	e	4.70851
289.65222	e	6.94671
372.48134	e	0.16938
414.59646	e	0.4046
440.36504	e	0.01074
445.54998	e	0.17841
522.80195	e	4.93568
558.08789	e	0.10577
648.79242	e	0.00123
755.90973	e	0.16095
765.93597	e	0.21657
779.35754	e	0.65248
791.59728	e	3.03568
831.95182	e	4.0142
906.55915	e	0.79492
911.97107	e	12.28211
1002.35367	e	0.0844
1009.17554	e	0.30685
1087.33406	e	0.0252
1109.1485	e	0.61321
1114.3897	e	0.78178
1143.1315	e	47.76632
1145.3901	e	23.72045
1205.38862	e	20.33803
1221.61114	e	0.89352
1279.34981	e	0.75395
1343.31428	e	71.39405
1350.5260	e	2.33193
1377.60454	e	32.88048
1391.66585	e	0.77297
1433.76263	e	0.11046
1445.79066	e	3.39561
1453.70541	e	66.74923
1465.26733	e	3.91801
1483.48192	e	0.18579
1548.02779	e	11.62202
1634.96717	e	0.39054
2909.48777	e	10.56534
2913.62416	e	4.65597
2972.21039	e	5.55537
2975.29708	e	8.54165

2976.25487	e	6.5196
3143.5259	e	1.39806
3144.5096	e	1.76775

```
+ ........................................................................... +
+       Character table from group theory analysis of eigenvectors          +
+                         Point Group =  32, Oh                             +
+ ........................................................................... +
+  Rep  Mul |    E   2   3  2'   4   I  m_h  -3  m_v  -4                     +
+           | ----------------------------------------                       +
+ a A1u  10 |    1   1   1   1   1  -1  -1  -1  -1  -1                      +
+ b A2g  11 |    1   1   1  -1  -1   1   1   1  -1  -1                      +
+ c T1g  43 |    3  -1   0  -1   1   3  -1   0  -1   1                      +
+ d T2u  43 |    3  -1   0   1  -1  -3   1   0  -1   1                      +
+ e T1u  55 |    3  -1   0  -1   1  -3   1   0   1  -1                      +
+ f T2g  54 |    3  -1   0   1  -1   3  -1   0   1  -1                      +
+ g Eu   31 |    2   2  -1   0   0  -2  -2   1   0   0                      +
+ h Eg   32 |    2   2  -1   0   0   2   2  -1   0   0                      +
+ i A2u  21 |    1   1   1  -1  -1  -1  -1  -1   1   1                      +
+ j A1g  21 |    1   1   1   1   1   1   1   1   1   1                      +
```

Table S 9. IR frequencies, intensities and character table of compound 1-Butyne (3,3-dimethyl-1-butyn-1-ido - Zn-MFU-4l)

Frequency [cm^{-1}]	irrep.	IR intensity active [(D/A)^{2}amu^{-1}]
-293.22742	g	0.04999
-0.039840	g	1.9E-6
34.008160	g	0.00224
36.622490	g	0.00173
88.810070	g	0.45719
103.26434	g	0.70105
118.27575	g	0.01058
120.95890	g	0.62348
141.95280	g	0.18038
175.60924	g	9.63458
206.75762	g	3.39399
238.56296	g	8.82555
248.02208	g	6.29526
297.48927	g	9.07389
374.21250	g	0.1702
408.59645	g	0.01817
423.01471	g	0.23627
447.28602	g	0.0286
495.37216	g	1.48306
523.68929	g	4.46848
563.22197	g	0.32522
648.07949	g	0.01724

A 31

720.62715	g	0.73661
753.23212	g	0.47611
768.49233	g	0.11787
790.83283	g	3.96132
852.41011	g	3.73903
897.77027	g	0.34714
902.86782	g	0.04667
910.86714	g	12.60985
994.14498	g	0.15317
1019.12518	g	0.18399
1113.10527	g	4.636E-4
1123.49505	g	0.40838
1150.64512	g	61.45621
1161.9854	g	14.57682
1203.29713	g	4.87779
1207.24468	g	16.08881
1221.91145	g	1.09945
1280.81074	g	0.98059
1343.91279	g	45.33296
1344.70817	g	25.37954
1373.86558	g	23.05694
1386.99184	g	0.12826
1430.11726	g	0.34809
1451.20696	g	25.36557
1452.13747	g	41.57653
1461.09677	g	0.49318
1483.61543	g	0.28079
1546.29108	g	10.21771
1631.17765	g	0.44588
2110.0103	g	4.50191
2965.78934	g	3.80197
2972.79593	g	1.98721
3044.10023	g	4.67568
3050.70679	g	3.41457
3052.07734	g	3.20682
3113.55449	g	2.79079
3114.44029	g	1.24829

```
+ .......................................................................... +
+        Character table from group theory analysis of eigenvectors           +
+                         Point Group =  32, Oh                        +
+ .......................................................................... +
+  Rep  Mul |    E   2   3  2'   4   I m_h  -3 m_v  -4                    +
+           | ----------------------------------------                    +
+ a A1u  10 |    1   1   1   1   1  -1  -1  -1  -1  -1                    +
+ b T1g  45 |    3  -1   0  -1   1   3  -1   0  -1   1                   +
+ c T2u  45 |    3  -1   0   1  -1  -3   1   0  -1   1                   +
+ d A2g  11 |    1   1   1  -1  -1   1   1   1  -1  -1                    +
```

```
+ e Eu   33 |   2  2  -1  0  0  -2  -2  1  0  0              +
+ f T2g  58 |   3  -1  0  1  -1  3  -1  0  1  -1              +
+ g T1u  59 |   3  -1  0  -1  1  -3  1  0  1  -1              +
+ h Eg   34 |   2  2  -1  0  0  2  2  -1  0  0              +
+ i A2u  23 |   1  1  1  -1  -1  -1  -1  -1  1  1              +
+ j A1g  23 |   1  1  1  1  1  1  1  1  1  1              +
```

Table S 10. IR frequencies, intensities and character table of compound 1-OH (OH-Zn-MFU-4l)

Frequency [cm^{-1}]	irrep.	IR intensity active [(D/A)^{2}amu^{-1}]
26.408890	b	0.0084
30.105060	a	0.1251
32.420850	b	0.02688
33.074600	b	0.0198
56.650540	a	1.62996
59.128720	a	4.71669
61.064560	b	1.67428
75.495270	b	0.44774
87.491400	a	0.00263
87.599200	b	0.85126
100.68319	a	0.83921
103.93091	b	0.42388
115.69073	a	0.09658
119.37407	b	0.35269
120.67738	a	1.02376
120.99578	b	0.97216
124.75941	a	0.1488
134.35087	b	0.19008
140.80807	b	0.05741
143.37311	a	0.00416
146.57183	b	0.60058
146.74472	a	3.72568
149.51944	a	0.0033
153.95444	b	0.00834
176.87477	a	0.31303
178.54930	b	6.46199
179.75192	b	5.05808
183.08609	a	10.28033
206.86236	a	10.77488
207.90021	b	8.40547
253.73700	b	0.03345
283.24538	a	8.84757
284.01141	b	8.09036
334.32268	a	0.00216
344.29021	b	0.00261
350.10046	a	0.01756
373.75129	b	0.03156
375.22348	a	0.16331

A 33

377.62556	b	0.11964
423.12925	b	0.16671
423.61562	a	0.51183
426.70759	b	0.19113
432.74230	b	0.00558
447.75798	a	0.07268
448.16400	b	0.05796
518.56208	a	0.00212
522.52872	b	6.16538
524.01951	a	5.98862
561.37431	a	2.96012
561.62231	b	3.26888
641.51577	b	9.41E-5
645.91004	a	0.00233
646.30280	b	0.00854
674.40816	a	0.01125
674.54993	b	0.00167
678.49751	a	0.00459
735.04319	a	0.00545
735.27715	b	0.00778
738.35358	a	0.01428
751.15658	a	0.28606
752.25998	b	0.55782
753.39902	a	0.18872
758.06616	b	8.07785
758.15454	a	6.21847
767.29839	b	0.064
769.18833	b	0.97514
769.26514	a	1.01082
787.28269	b	0.3214
790.60096	b	2.16929
790.68926	a	1.98685
822.58854	b	0.98652
822.71082	a	1.89594
847.32758	a	0.01327
855.95682	b	2.39399
870.72247	b	1.52968
871.04208	a	2.5122
907.60586	a	0.06467
908.90457	b	13.83952
909.96624	a	14.25363
1017.48124	a	0.01683
1018.35615	b	0.17002
1018.39045	a	0.0791
1109.87411	b	0.93571
1112.60444	a	0.23033
1113.86406	b	0.37348
1135.99553	a	6.48955

A 34

1138.17358	b	34.44489
1148.80424	a	63.50102
1153.88155	b	17.65148
1164.87492	a	7.57035
1164.97059	b	21.03142
1204.95068	a	0.07453
1207.37768	b	17.35846
1208.7458	a	17.14012
1218.24811	b	0.05791
1219.70892	a	0.56462
1220.2427	b	0.5856
1279.82189	b	0.07407
1282.86342	a	0.68063
1283.16766	b	0.7539
1344.20883	a	0.15611
1347.08098	a	77.24793
1347.23421	b	75.67266
1374.36902	a	1.58426
1374.69351	a	21.90366
1375.11055	b	24.51734
1450.47682	a	0.61783
1452.85887	a	74.74349
1453.06527	b	74.06206
1485.14063	b	0.06653
1487.09791	a	0.22
1487.26794	b	0.27617
1548.17102	a	11.06278
1548.2711	a	0.01096
1548.99554	b	11.13985
1631.78011	b	0.0295
1633.10914	b	0.24048
1633.22045	a	0.22334
3098.40454	b	3.04946
3098.42817	a	2.017
3112.0860	b	0.57848
3112.97947	a	1.84947
3122.63527	a	0.00485
3122.63888	b	0.28198
3670.45711	b	1.34535
3670.45834	a	0.67152

```
+ ........................................................................... +
+        Character table from group theory analysis of eigenvectors           +
+                        Point Group =  11, C4h                       +
+ ........................................................................... +
+  Rep  Mul |    E   2   4   4   I m_h  -4  -4                         +
+           | --------------------------------                        +
```

```
+ a Au   63 |    1   1   1   1  -1  -1  -1  -1                    +
+ b Eu   65 |    2  -2   0   0  -2   2   0   0                    +
+ c Bu   62 |    1   1  -1  -1  -1  -1   1   1                    +
+ d Eg   64 |    2  -2   0   0   2  -2   0   0                    +
+ e Ag   63 |    1   1   1   1   1   1   1   1                    +
+ f Bg   64 |    1   1  -1  -1   1   1  -1  -1                    +
```

Table S 11. IR frequencies and intensities of Cl-ZnTp

Frequency [cm^{-1}]	IR intensity active [$km\ mol^{-1}$]
20.8	1.7
53.7	2.21
64.9	0.49
66.3	3.35
83	1.29
139.7	2.51
144.6	0.49
163.9	2.36
178.6	0.28
194.3	25.26
206.1	27.7
226.5	6.44
278.2	0.79
279.2	0.64
327.8	3.74
335.3	4.15
340.1	1.32
391.4	77.93
622.7	1.19
626.4	6.24
640.8	4.71
669.8	45.06
671.5	11.76
677.8	32.28
721.2	45.77
725.5	50.66
775	16.93
777.8	95.54
797.3	69.55
804.5	28.18
875.4	0
876.6	0.05
882.5	0.25
910.2	1.67
911.7	4.67
924.5	1.05

942.1	0.08
942.6	0
947.5	1.34
997	31.31
997.4	23.94
1003.9	19.53
1069.7	158.5
1071.1	149.46
1086.6	23.2
1102	1.02
1102.6	1.5
1118.1	1.63
1140	73.41
1142.1	68.51
1218.2	52.96
1218.4	43.28
1222.2	51.51
1224.2	26.93
1228.4	6.8
1238.7	6.31
1342.5	74.98
1343.9	92.69
1344.2	17.62
1422.6	17.49
1423.8	17.15
1443.1	109.64
1463.1	2.39
1467.8	1.87
1478	6.29
1548.8	63.5
1550.4	56.12
1555.9	4.3
2599.6	126.51
3274.1	0.21
3281.3	0.06
3281.5	0.22
3293.1	0.57
3294.9	0.4
3295.1	0.24
3310.1	0.35
3310.4	0.85
3310.7	0.52

Table S 12. IR frequencies and intensities of Cl-CoTp

Frequency [cm^{-1}]	IR intensity active [km mol^{-1}]
21.9	2.54

A 37

52.1	1.7
54	1.96
61.9	1.37
80.3	0.37
140.8	1.05
144.8	0.42
163.5	0.73
179.1	0.02
214.6	1.82
235.8	17.68
241.9	19.91
277.4	2.27
277.6	1.81
326.6	2.37
336.9	3.06
338.6	4.02
401.1	93.38
621	1.43
623.5	6.25
636.7	4.77
664.6	46.1
668.9	9.67
674.4	31.97
717.4	42.91
721.9	48.98
784.1	7.27
787	101.37
793.2	79.19
800.8	26.07
871.2	0.03
872.1	0
879.5	0.44
911.1	0.76
912.6	2.48
921.2	1.33
941.1	0.26
942.4	0.2
946.8	0.87
996.4	27.23
996.5	22.07
1000.7	12.86
1066.5	139.94
1068.3	153.19
1085	15.38
1101.3	2.51
1101.4	1.88
1116.5	1.07
1136.3	78.61

1138.9	72.84
1208	50.85
1211.7	65.48
1218.3	7.53
1220.9	12.42
1223.5	11.94
1236.1	7.78
1334.6	65.74
1337.8	23.91
1337.9	96.72
1421	19.37
1421.1	19.48
1442.2	109.16
1465.4	2.6
1466.4	2.13
1474.3	8.67
1546.7	51.01
1548.3	56.23
1552.7	1.6
2592.7	126.96
3264.7	0.13
3265.4	0.06
3265.7	0.12
3275.5	0.11
3275.9	0.1
3276.8	0.31
3291.1	0.46
3299.5	0.93
3299.6	0.48

Table S 13. IR frequencies and intensities of Me-ZnTp

Frequency [cm^{-1}]	IR intensity active [km mol^{-1}]
-114.8	0.41
0	0.09
0	0.19
0	0.07
0	0.04
0	0.12
0	0.07
26.9	0.78
54.8	0.66
75.5	0.25
79.4	2.49
123.4	1.3
134.7	0.94

A 39

142.4	0
164	10.42
164	15.77
173.3	18.7
177.4	2.51
224.9	13.64
274.9	0.03
275.8	0.08
324.7	3.08
334	3.87
339.5	5.33
539.3	34.59
624.8	1.4
628.3	5.61
643.4	4.39
669.6	13.99
673.1	1.32
678	0.34
689.4	73.53
691.5	55.91
726.2	62.99
729.7	64.32
774.2	12.93
777	96.75
790.7	69.42
804.3	29.28
869.5	0.01
870.7	0.03
879.3	0.37
905.7	1.44
907.1	4.4
919.6	1.58
942.7	0.04
943	0.11
947.8	1.87
994.1	31.32
994.5	21.69
1003.7	21.87
1067.8	145.94
1070.1	134.07
1085.3	26.34
1101.5	2.42
1103.6	2.33
1117.6	1.25
1141.9	81.4
1143	72.04
1205	4.83
1218.5	0.33

1219.9	13.56
1224.3	93.31
1224.7	58.39
1232.4	6.12
1237.8	8.48
1339.1	38.92
1341	46.96
1341.7	89.82
1422.2	19.95
1424.5	21.43
1442.8	101.55
1461.6	3.4
1466.1	2.11
1472.3	0.09
1475.1	1.38
1475.7	4.53
1547.8	63.88
1550	47.81
1555.8	9.7
2593.6	133.47
3032.9	49.51
3098.2	26.09
3104.1	25.36
3272.5	1.37
3279.2	0.36
3279.4	2.14
3292.8	1.56
3295.7	0.89
3295.8	0.87
3311.3	0.69
3311.9	2.21
3312	1.25

Table S 14. IR frequencies and intensities of Me-CoTp

Frequency [cm^{-1}]	IR intensity active [km mol^{-1}]
-29	0.77
0	0.03
0	0.16
0	0.12
0	0.29
0	0.03
0	0.06
37.4	1.29
58.5	0.74
79.2	0.5
82.4	0

A 41

140	0.57
140.2	0.08
147.1	0.47
167.1	0.46
184.1	0.47
215.8	12.34
217.1	3.66
225.2	13.81
275.1	0.09
275.9	0.29
324.5	2.69
336.4	3.55
341.5	2.18
523	56.46
603.1	18.75
610	14.87
625.8	0.89
628.3	4.64
640.6	4.17
668.9	51.59
672.3	5.87
679.8	40.89
720.9	48.25
724.9	53.14
783.7	0.03
787.4	101.55
788.6	82.95
799.9	25.99
869.9	0.11
870.8	0.05
878.6	0.54
910.2	0.59
911.5	2.82
917.9	2.11
942.6	0.15
942.9	0.09
947.3	0.7
993.7	21.45
993.7	22.97
999.9	17.19
1066.2	128.03
1066.7	141.11
1083.1	13.52
1101.5	4.46
1103	1.6
1116	0.48
1138.2	87.77
1139.8	78.87

1176.2	2.12
1209.5	35.72
1213.7	57.55
1219.3	14.01
1219.4	19.86
1224.5	12.31
1235.9	10.77
1330.4	46.52
1333.7	36.65
1334.8	92.49
1420.5	22.68
1422.2	25.63
1441.6	95.43
1452.6	0.63
1455.8	0.93
1463.4	3.41
1464.8	2.17
1471.8	8.11
1546.8	54.26
1547.1	46.91
1551.6	0.36
2582.2	136.28
3005.8	49.71
3074.2	36.57
3076.9	36.43
3256.1	0.96
3258.2	0.29
3258.5	1.48
3272.3	1.14
3272.7	0.51
3273	0.31
3287.5	0.93
3294.6	2.19
3294.6	1.01

Table S 15. IR frequencies and intensities of OH-ZnTp

Frequency [cm^{-1}]	IR intensity active [$km\ mol^{-1}$]
36.4	3.59
70	2.62
70.7	3.02
84.1	7.04
109.9	0
149.3	72.91
149.5	31.77
154	2.23
163.9	1.25

A 43

180.6	17.67
181.7	7.84
190.8	11.08
225	9.48
275	0.59
278.8	1.68
330.2	5.47
334.2	5.48
349	3.2
610.4	91.48
635	1.8
643.1	4.89
643.7	8.07
673.6	0.41
677	30.67
677.6	39.16
728.1	72.49
728.9	71.3
765.3	37.98
766.3	102.8
775.8	91.68
776.6	36.07
808.4	24.06
868.4	0.29
869.8	1.49
884	0.23
916.5	0.4
917.5	4.61
933.3	6.57
938.8	0.17
940.4	0.06
944.8	1.66
995.5	19.86
998.3	29.06
998.9	14.68
1073.4	143.15
1074.8	141.28
1088.8	19.94
1099.4	13.11
1108.2	4.05
1115.4	2.67
1141	69.27
1152.3	78.09
1220.8	6.89
1222	4.19
1222.1	69.42
1224.8	87.44
1229.2	13.67

1237.1	1.97
1342.4	22.46
1343.3	91.53
1343.8	59.58
1421.4	22.84
1421.5	23
1440.2	100.64
1459.5	8.05
1466.8	3.03
1475.6	5.15
1543.7	63.1
1543.8	62.42
1549.7	0.28
2585.6	125.07
3279	0.01
3279	0.83
3281.7	0.07
3288.7	1.15
3288.8	0.83
3289.9	0.4
3303.4	0.89
3303.4	1.89
3305.4	0.96
3868	22.96

Table S 16. IR frequencies and intensities of OH-CoTp

Frequency [cm^{-1}]	IR intensity active [km mol^{-1}]
45.5	0.14
52	4.34
70.4	1.37
77.7	1.74
108.4	0.32
142.6	0.14
152.5	0.03
166.5	0.72
189.3	0.23
210.5	0.13
216.4	4.54
231.4	17.45
267.8	37.43
275.3	1.56
288.4	54.58
330.9	4.56
332.5	8.01
348.8	2.02
621	159.01

A 45

631.2	1.39
636.9	4.46
637.9	10.25
672.9	9.48
673.6	26.27
675.1	33.37
688.6	110.07
726.5	68.37
727	86.74
763.5	20.26
768	79.62
768.6	53.77
806.6	20.65
863.5	0.03
865	1.07
871.8	0.02
907.2	0.48
908.3	5.64
930.3	6.19
938.3	0.55
940.3	0.14
944.4	1.18
993	21.38
993.7	12.44
995.9	13.73
1068.5	127.72
1070.3	123.86
1085.5	14.69
1100.4	15.52
1105.3	6.77
1112.8	1.23
1140.9	73.78
1148.9	81.97
1216.5	61.7
1218.4	68.55
1219.8	10.91
1220.9	8.04
1222.8	10.11
1232.3	0.88
1333.7	19.53
1334.6	88.25
1339.6	62.42
1419.8	26.65
1421.8	29.54
1440.4	93.29
1459	7.19
1464.6	3.82
1471.5	7.33

1541.9	53.23
1542.7	52.33
1547.6	1.51
2575.4	127.8
3263.6	0.29
3263.9	0.2
3268.6	0.04
3272.8	0.45
3276	1.77
3276	0.03
3287.6	0.86
3287.8	2.19
3300.5	1.52
3848.1	39.2

XRPD patterns

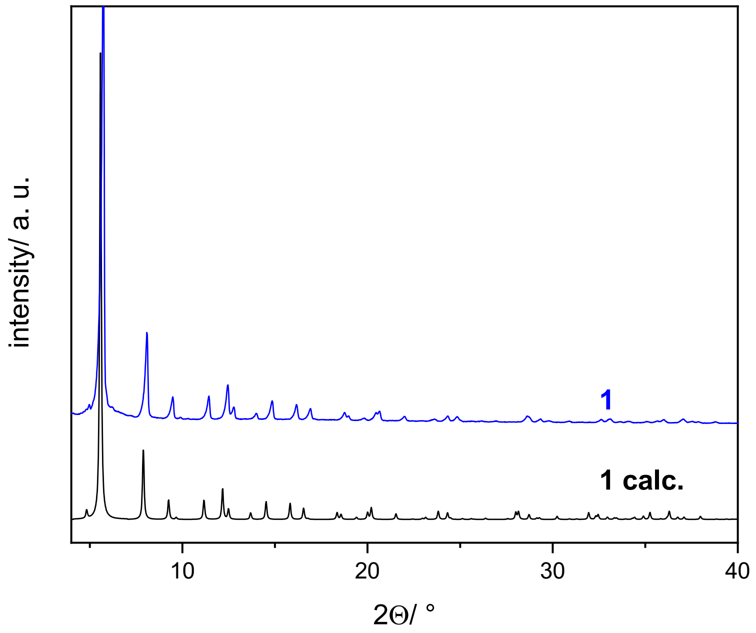

Figure S 13. measured (blue) and calculated (black) XRPD pattern of **1**

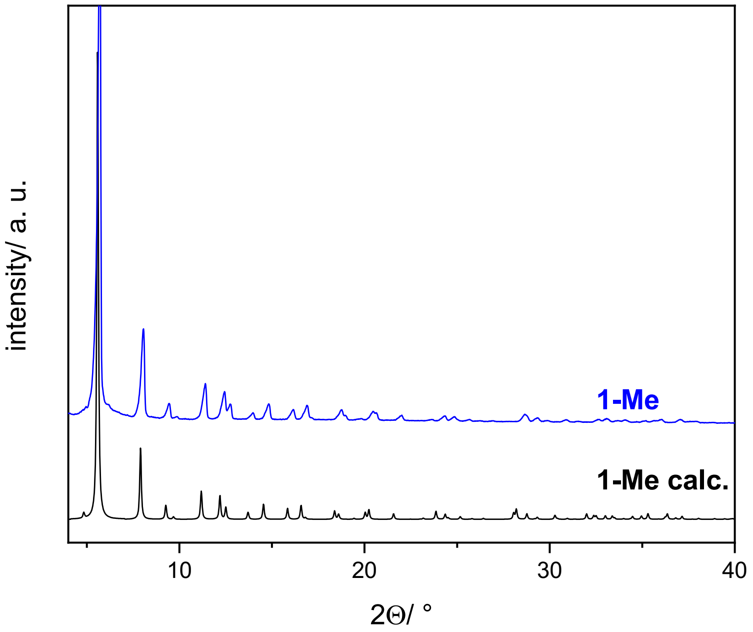

Figure S 14. measured (blue) and calculated (black) XRPD pattern of **1-Me**

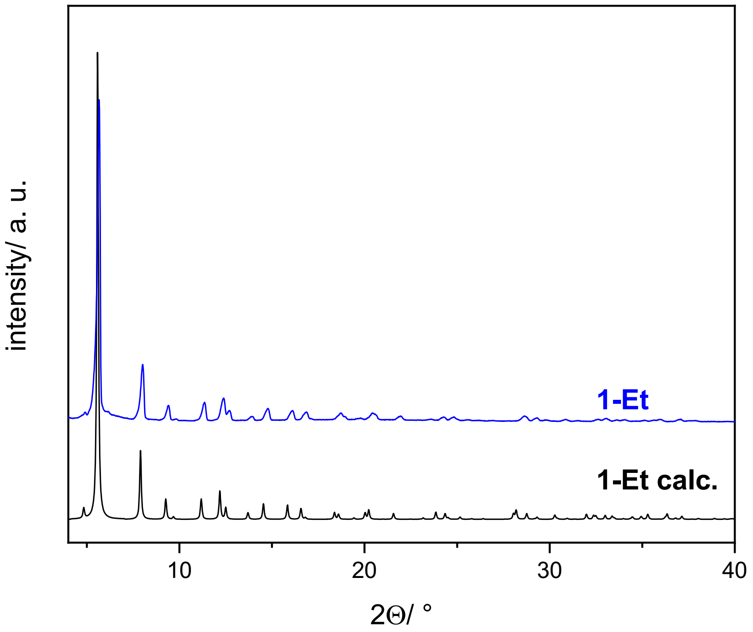

Figure S 15. measured (blue) and calculated (black) XRPD pattern of **1-Et**

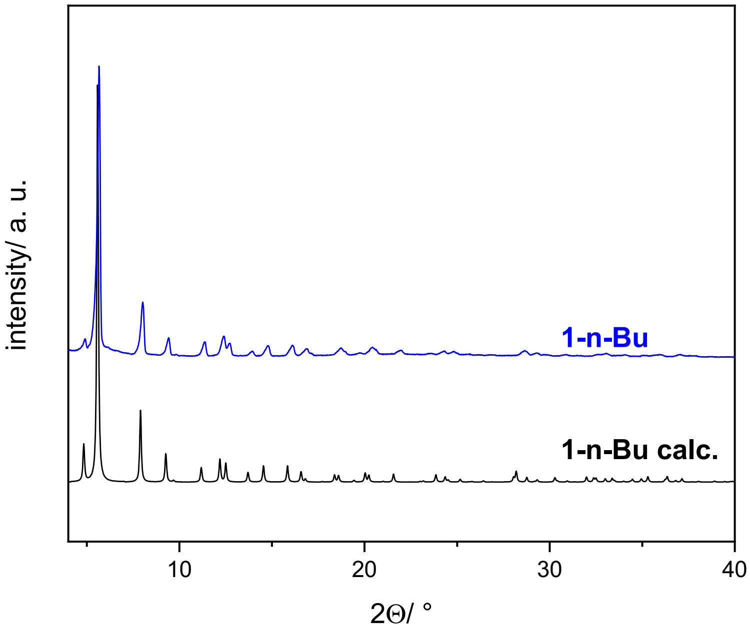

Figure S 16. measured (blue) and calculated (black) XRPD pattern of **1-n-Bu**

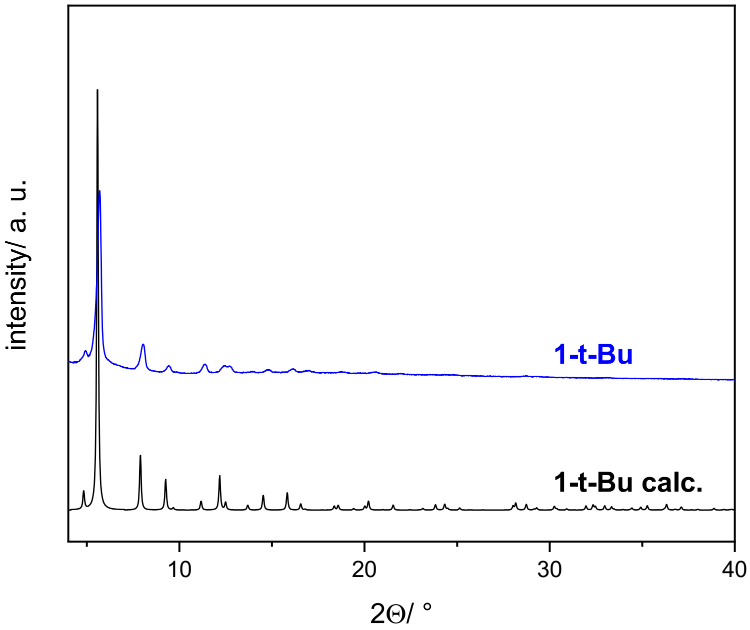

Figure S 17. measured (blue) and calculated (black) XRPD pattern of **1-t-Bu**

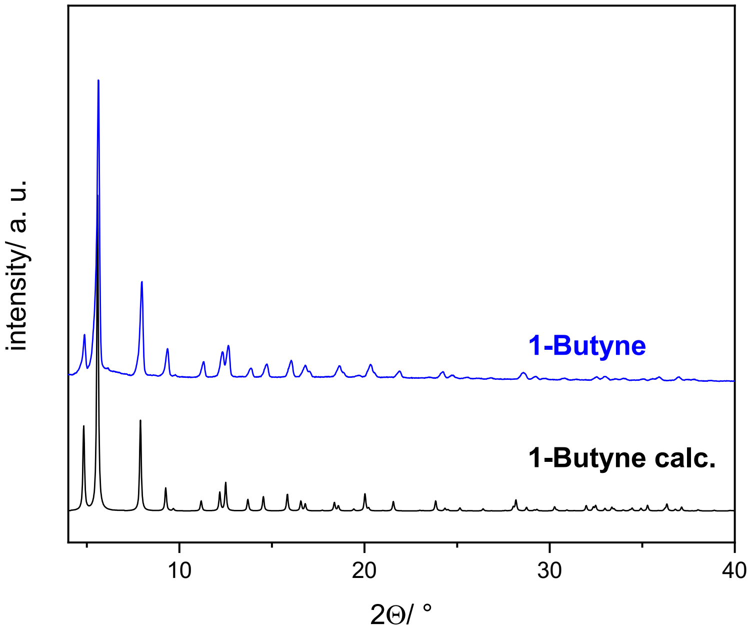

Figure S 18. measured (blue) and calculated (black) XRPD pattern of **1-Butyne**

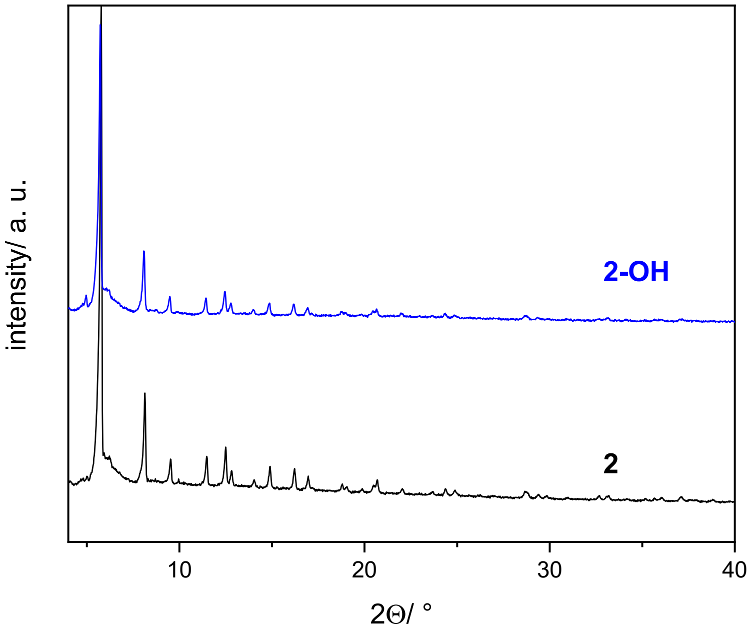

Figure S 19. comparison of the measured XRPD pattern of **2** (black) and **2-OH** (blue)

VT-XRPD measurements

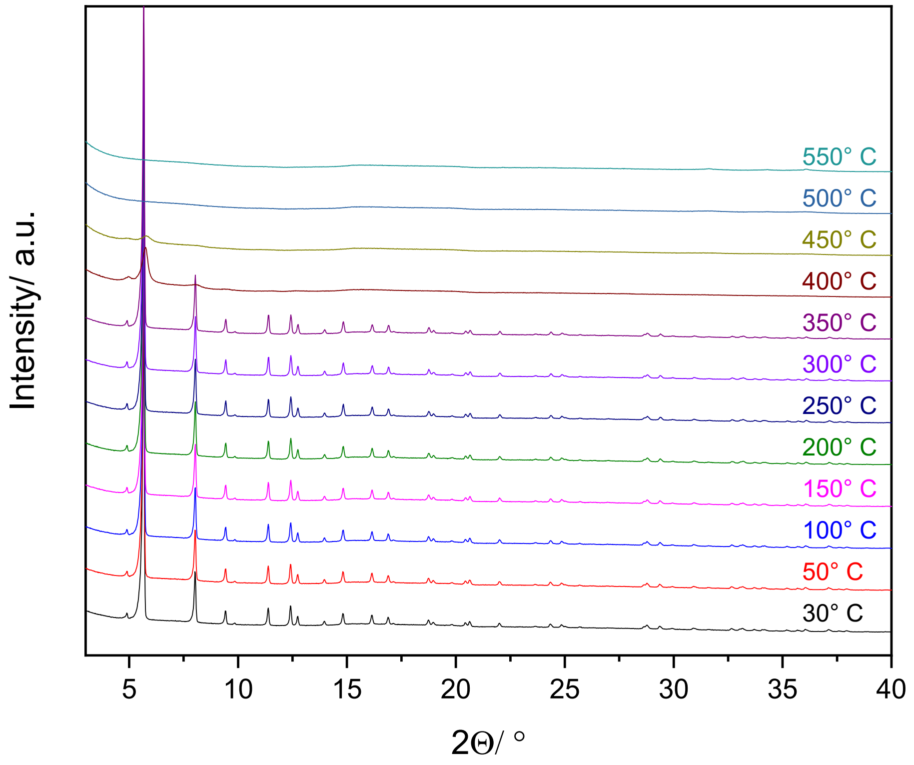

Figure S20. VT-XRPD of **1-Et**

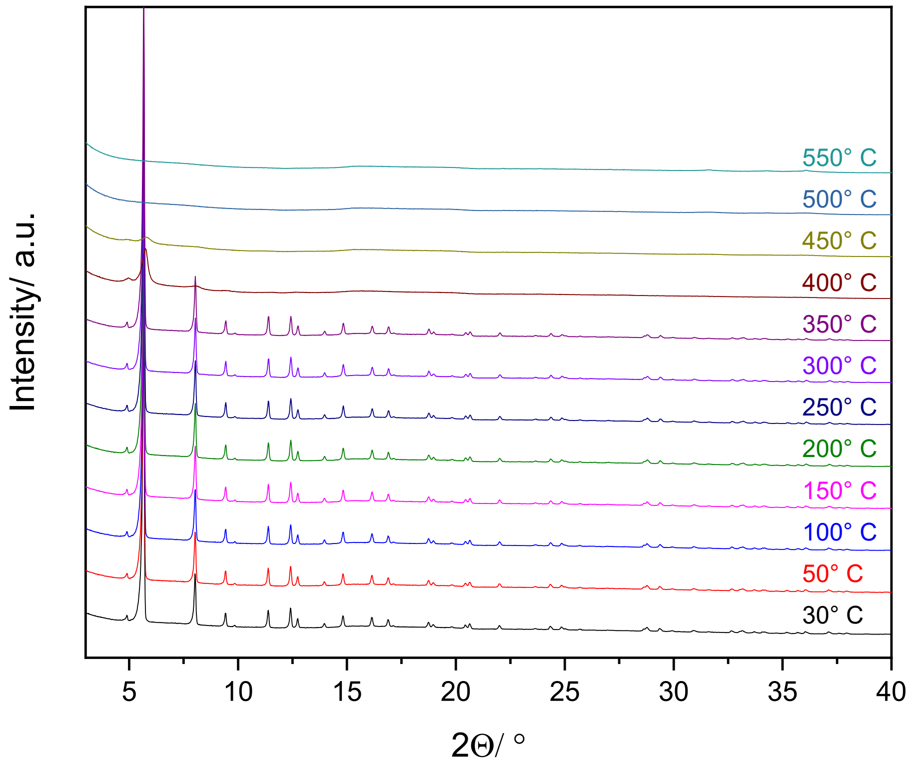

Figure S 21. VT-XRPD of **1-n-Bu**

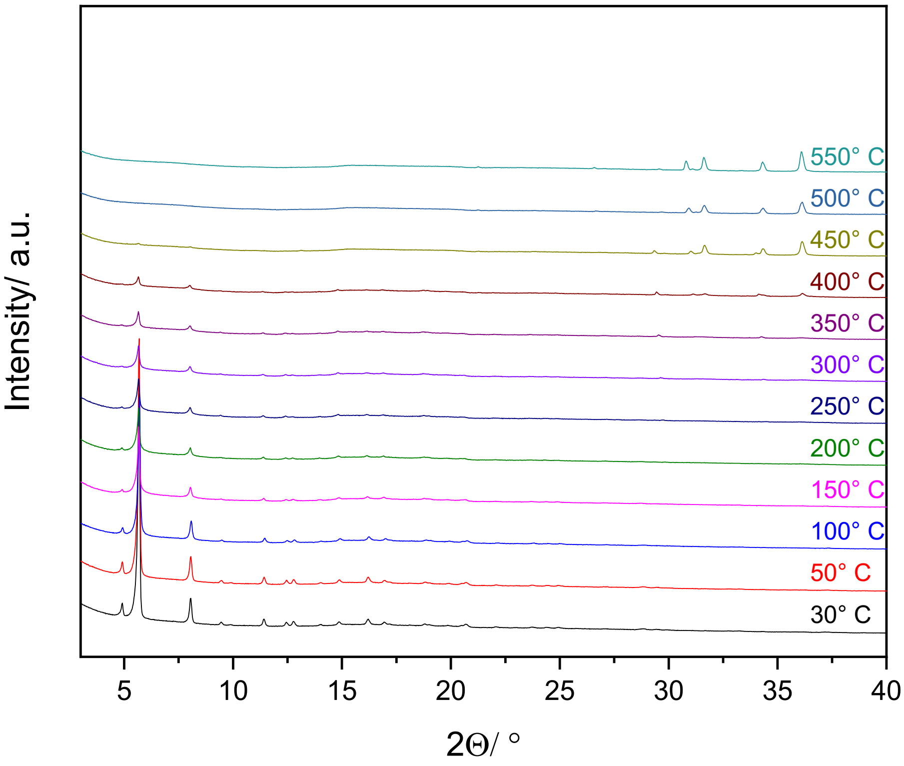

Figure S 22. VT-XRPD of **1-t-Bu**

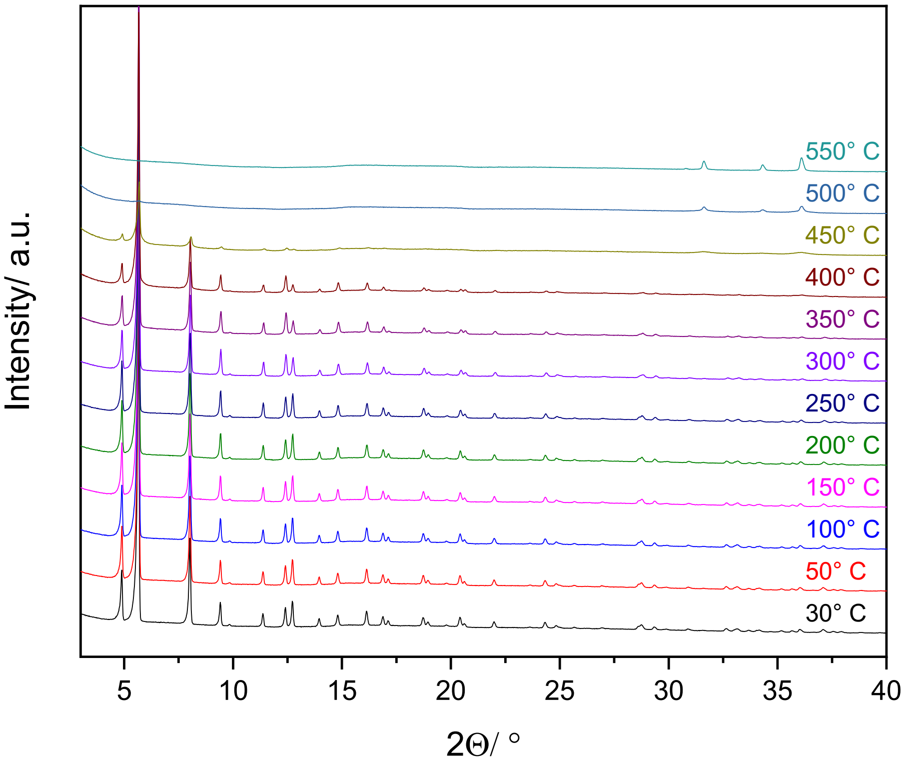

Figure S 23. VT-XRPD of **1-Butyne**

Argon Adsorption isotherms and NLDFT pore size distributions

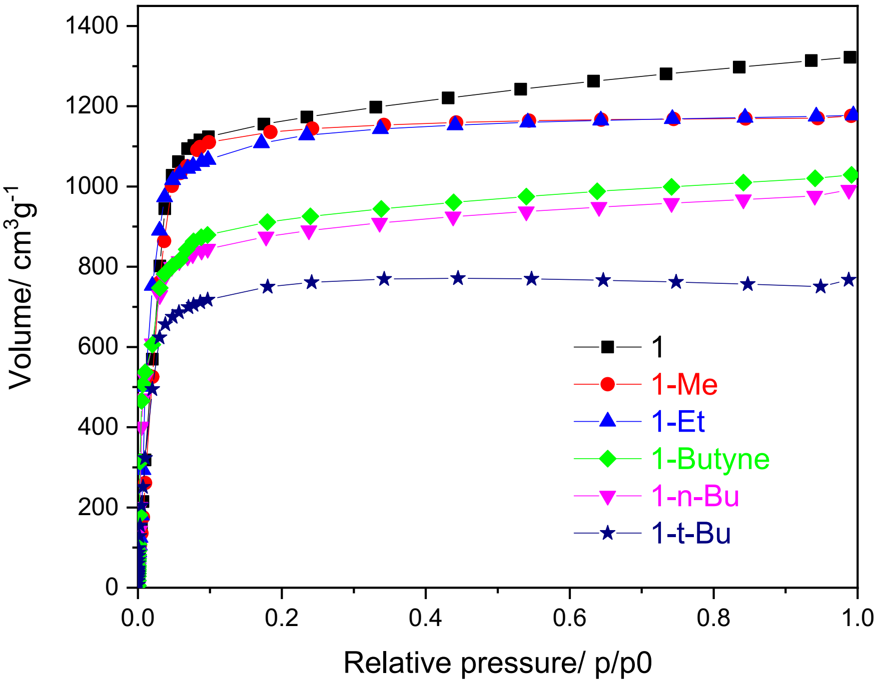

Figure S 24. Argon adsorption isotherms measured at 77K for **1** (black; 4147 m²g⁻¹), **1-Me** (red, 4114 m²g⁻¹), **1-Et** (blue, 3677 m²g⁻¹), **1-Butyne** (green, 2978 m²g⁻¹), **1-n-Bu** (pink, 2898 m²g⁻¹), **1-t-Bu** (dark blue, 2486 m²g⁻¹).

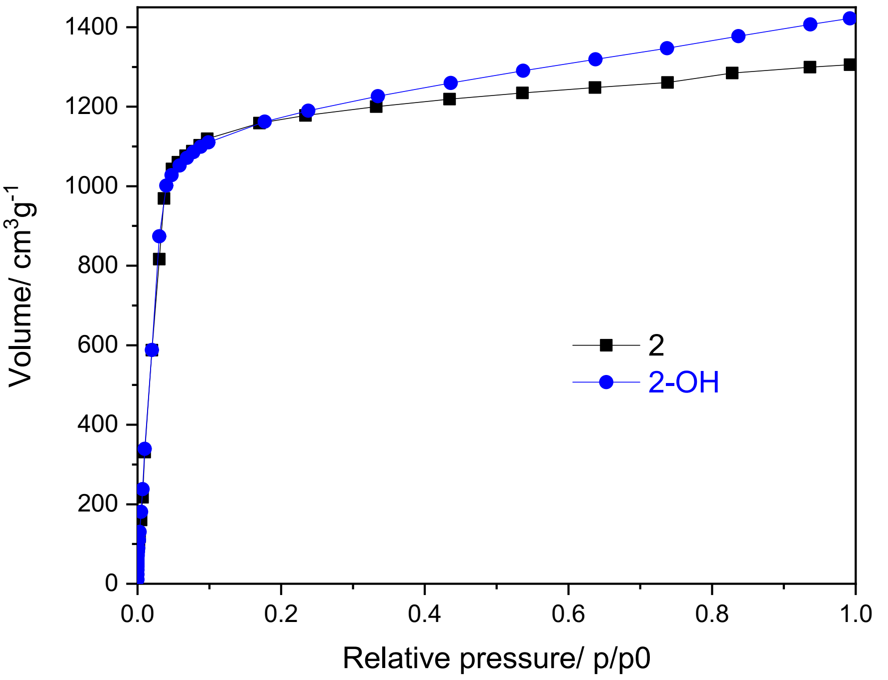

Figure S 25. Argon adsorption isotherms measured at 77K for **2** (black; 3824 m²g⁻¹) and **2-Me** (blue, 3790 m²g⁻¹).

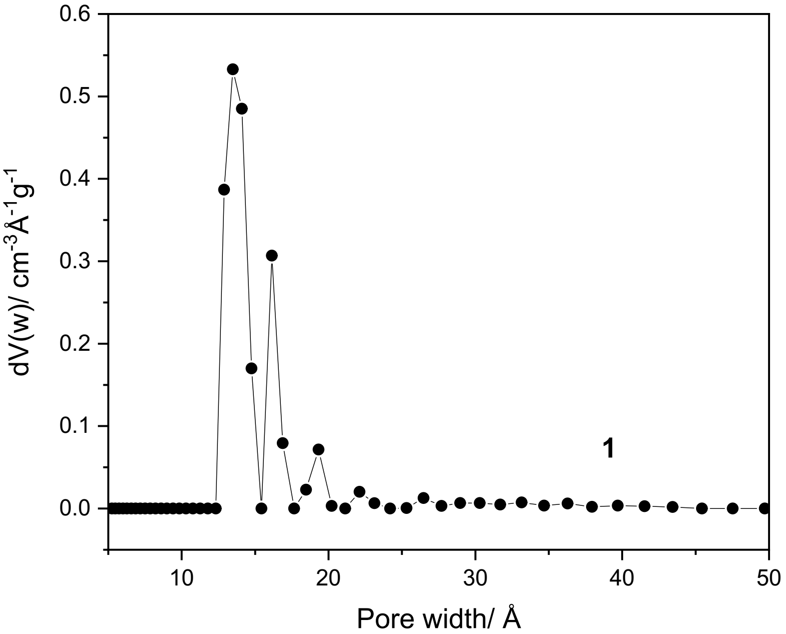

Figure S 26. NLDFT pore size distribution of **1** calculated from the argon adsorption isotherm.

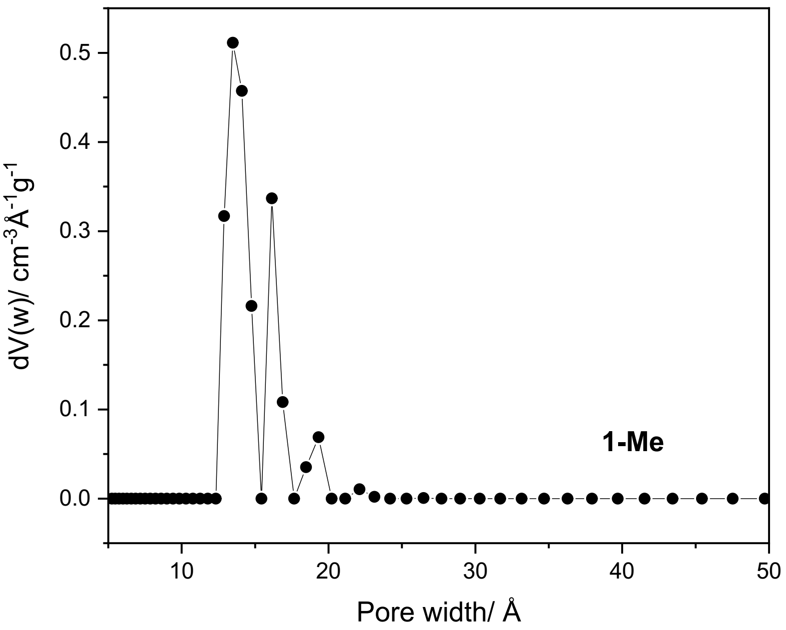

Figure S 27. NLDFT pore size distribution of **1-Me** calculated from the argon adsorption isotherm.

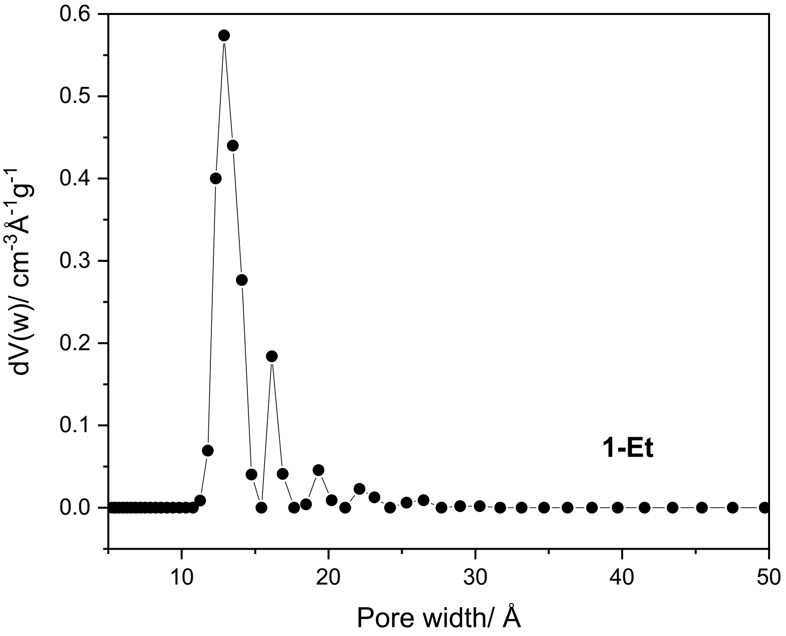

Figure S 28. NLDFT pore size distribution of **1-Et** calculated from the argon adsorption isotherm.

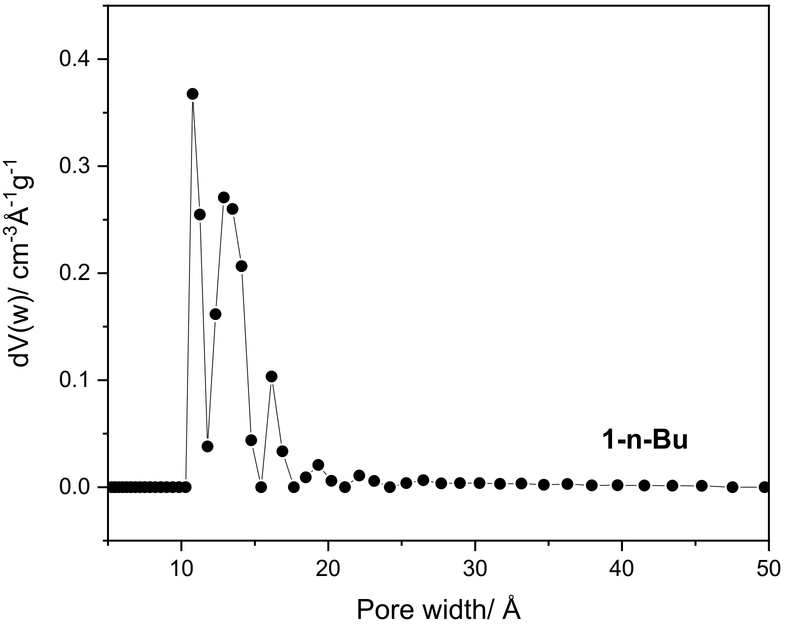

Figure S 29. NLDFT pore size distribution of **1-n-Bu** calculated from the argon adsorption isotherm.

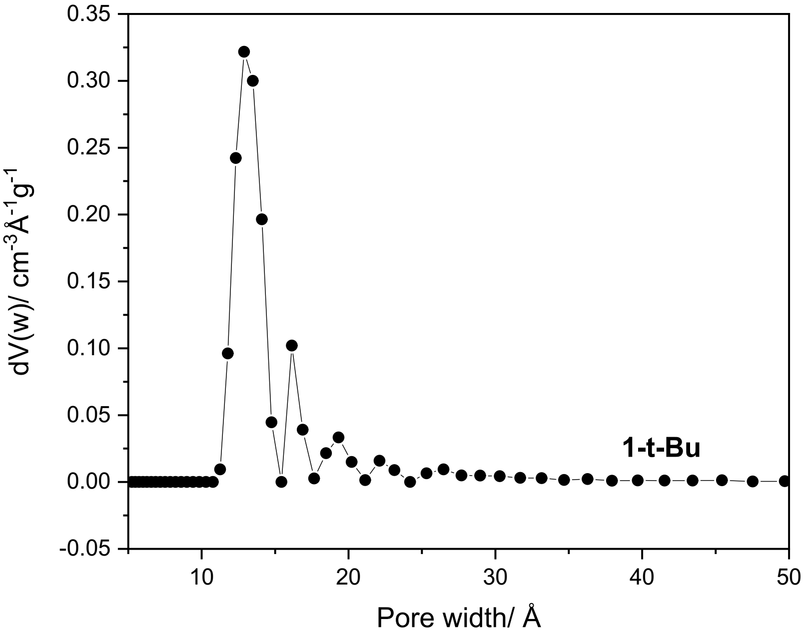

Figure S 30. NLDFT pore size distribution of **1-t-Bu** calculated from the argon adsorption isotherm.

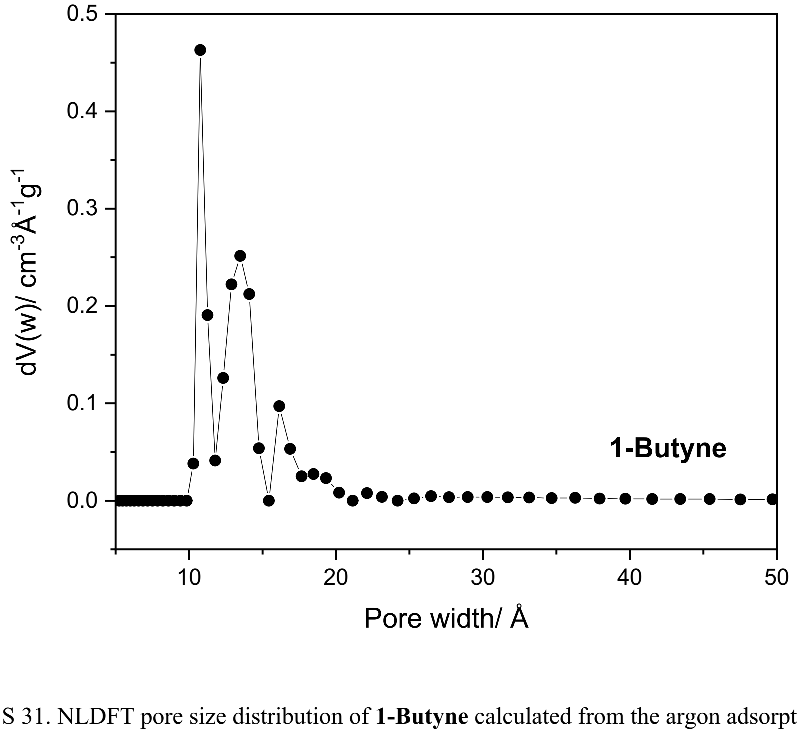

Figure S 31. NLDFT pore size distribution of **1-Butyne** calculated from the argon adsorption isotherm.

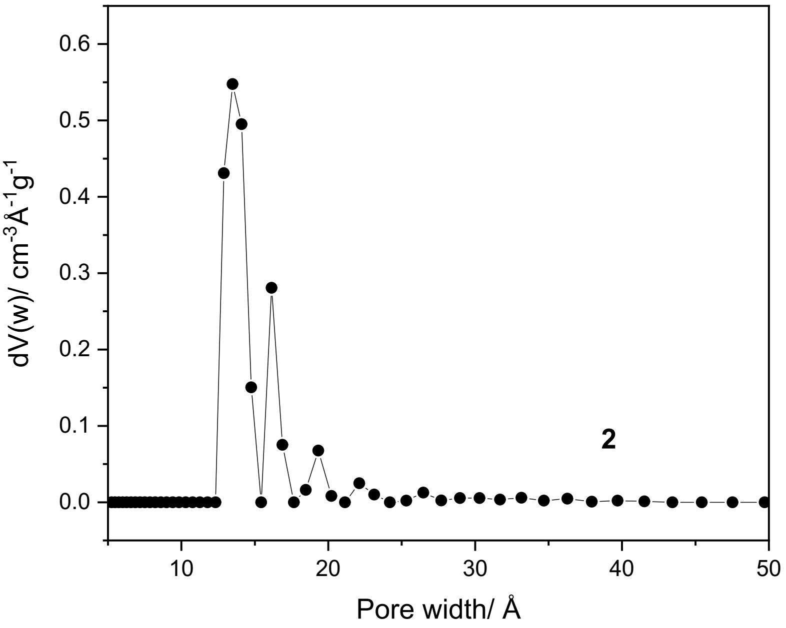

Figure S 32. NLDFT pore size distribution of **2** calculated from the argon adsorption isotherm.

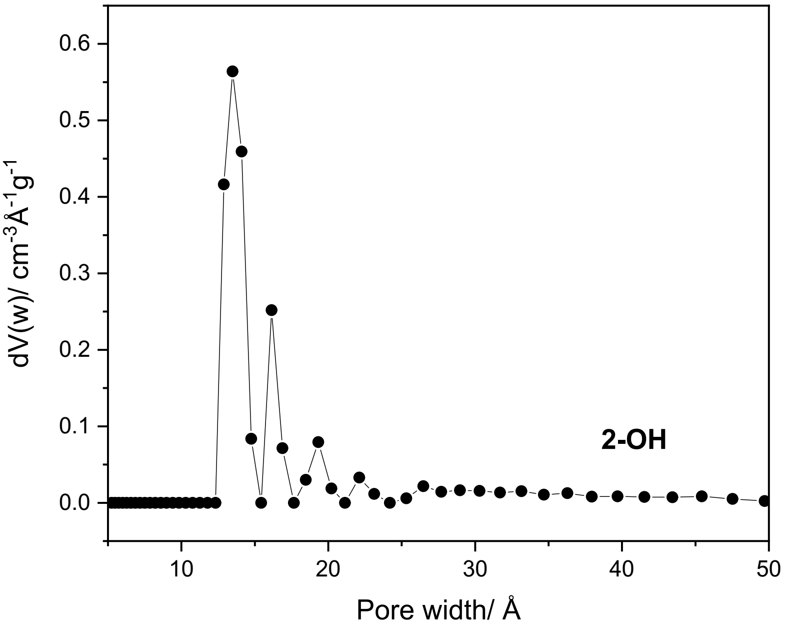

Figure S 33. NLDFT pore size distribution of **2-OH** calculated from the argon adsorption isotherm.

Connolly surface plots and conventional unit cells of the compounds

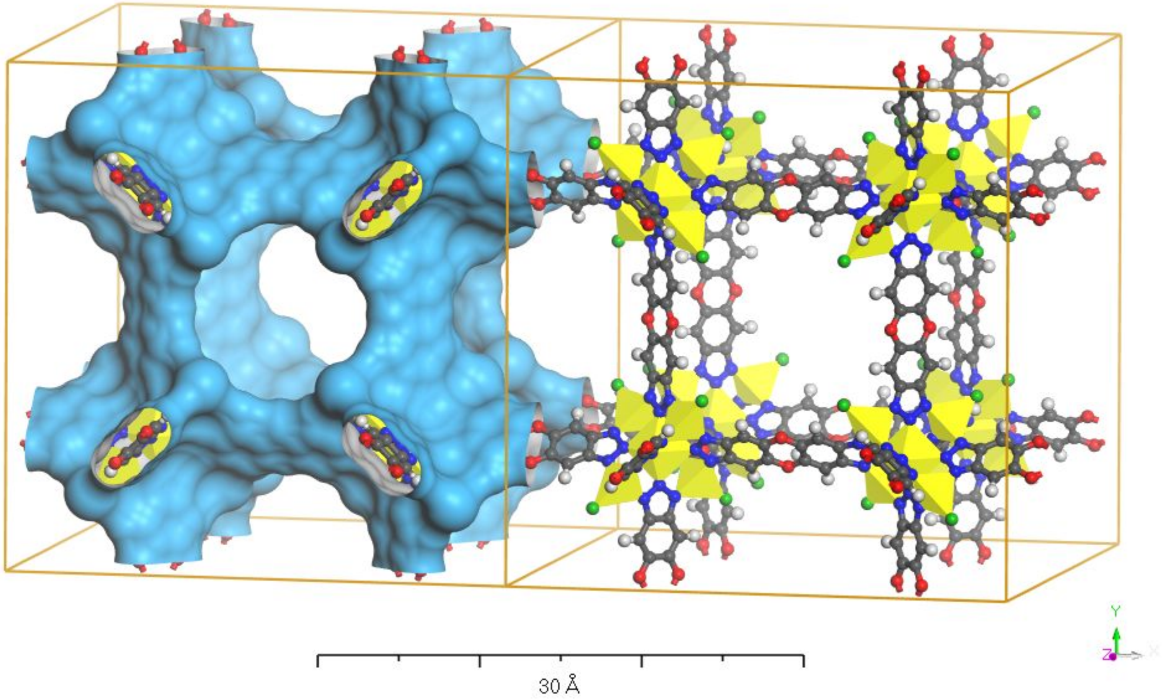

Figure S 34. Conventional unit cell of **1** and the Connolly surface plotted with BIOVIA Materials Studio 2019

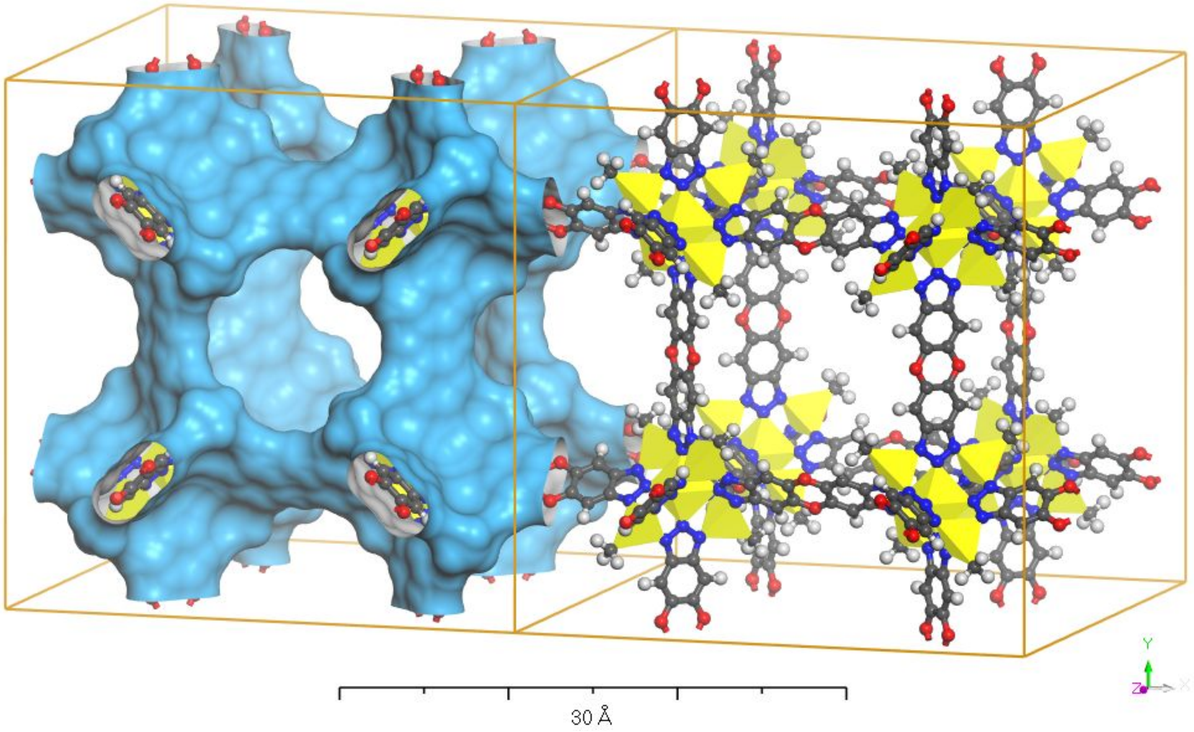

Figure S 35. Conventional unit cell of **1-Me** and the Connolly surface plotted with BIOVIA Materials Studio 2019

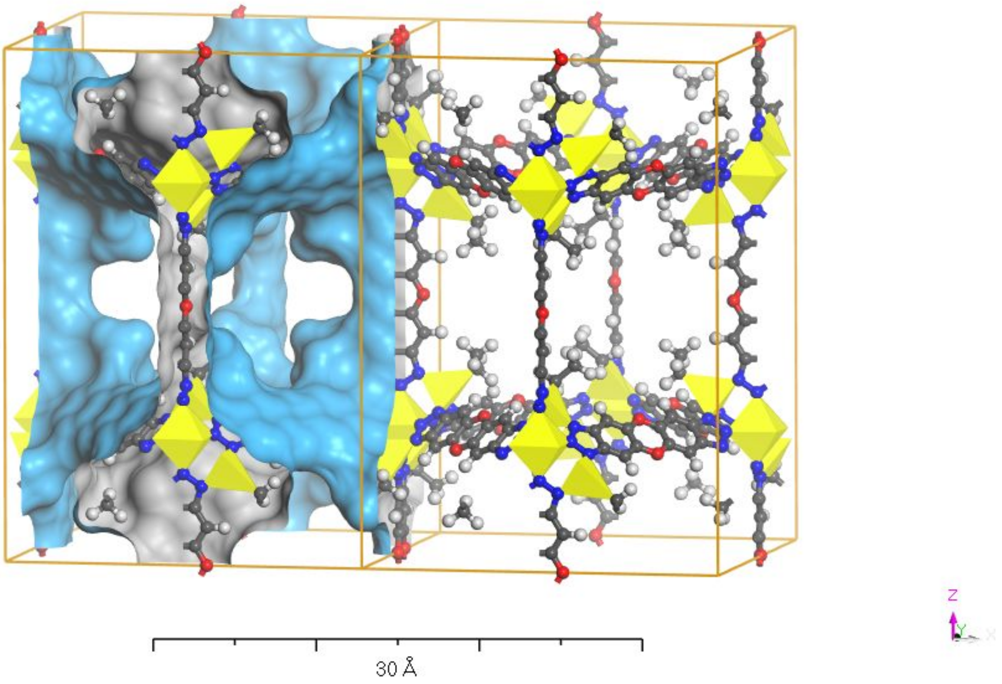

Figure S 36. Conventional unit cell of **1-Et** and the Connolly surface plotted with BIOVIA Materials Studio 2019

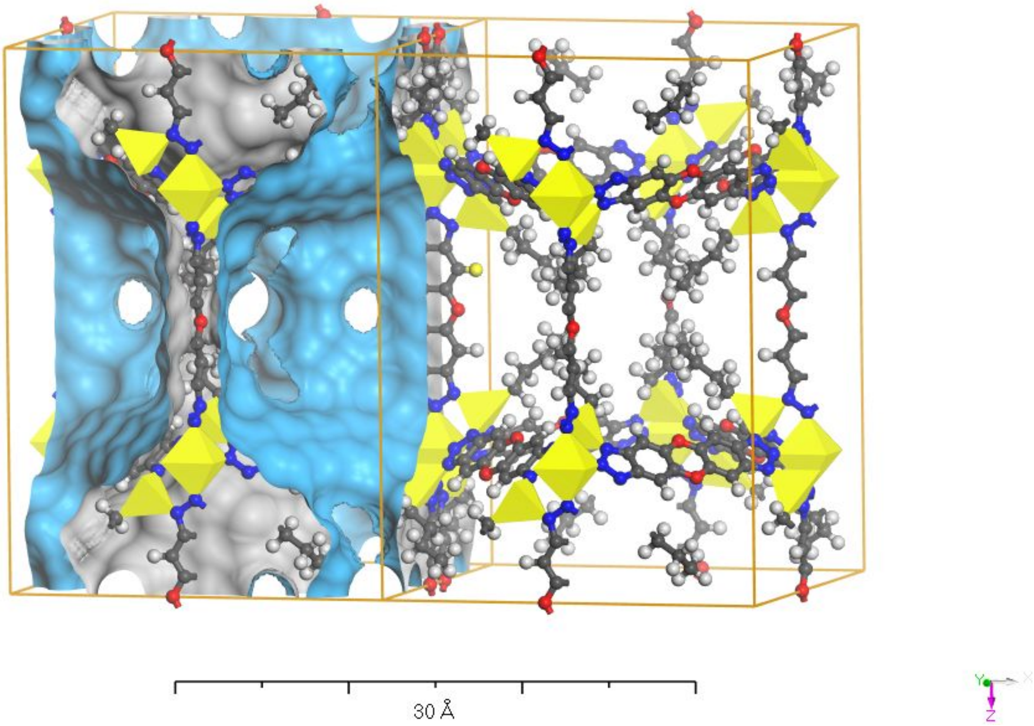

Figure S 37. Conventional unit cell of **1-n-Bu** and the Connolly surface plotted with BIOVIA Materials Studio 2019

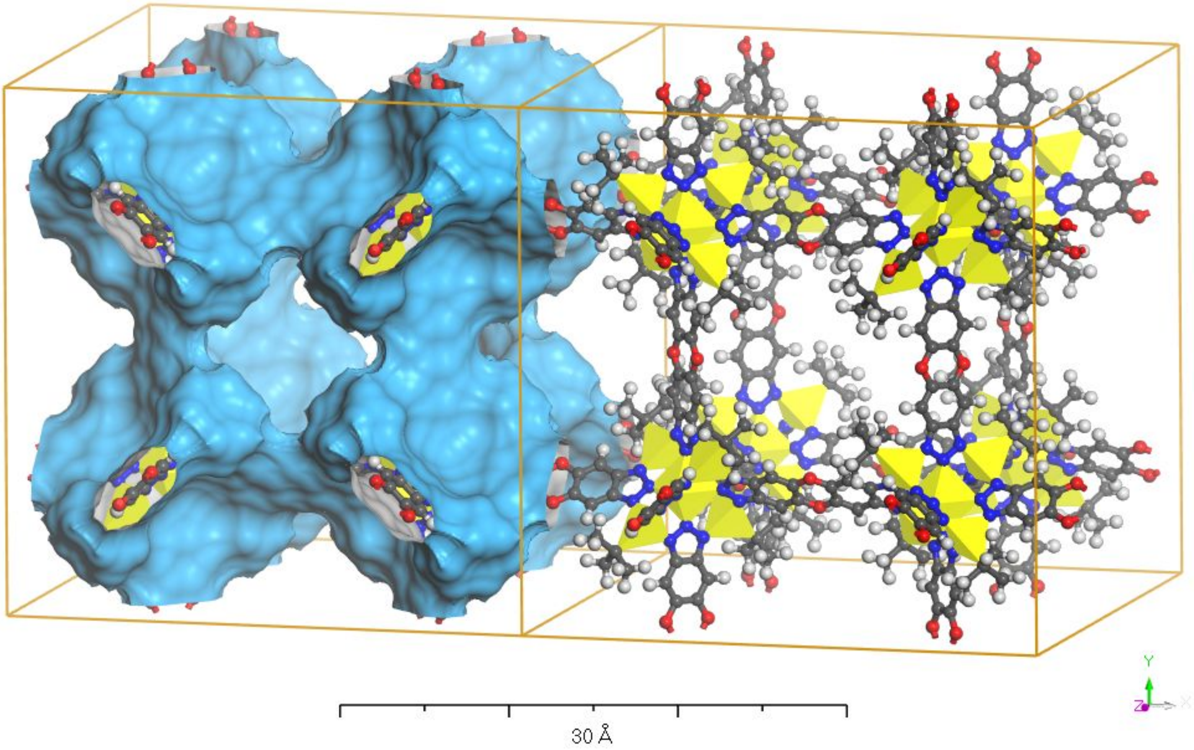

Figure S 38. Conventional unit cell of **1-t-Bu** and the Connolly surface plotted with BIOVIA Materials Studio 2019

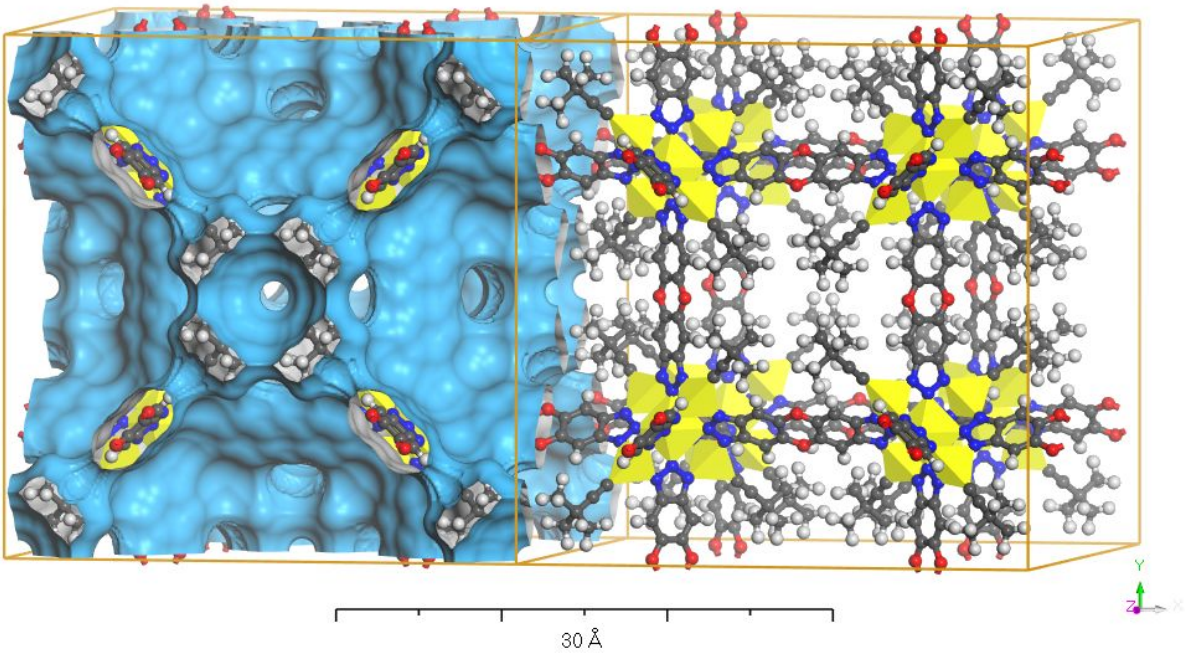

Figure S 39. Conventional unit cell of **1-Butyne** and the Connolly surface plotted with BIOVIA Materials Studio 2019

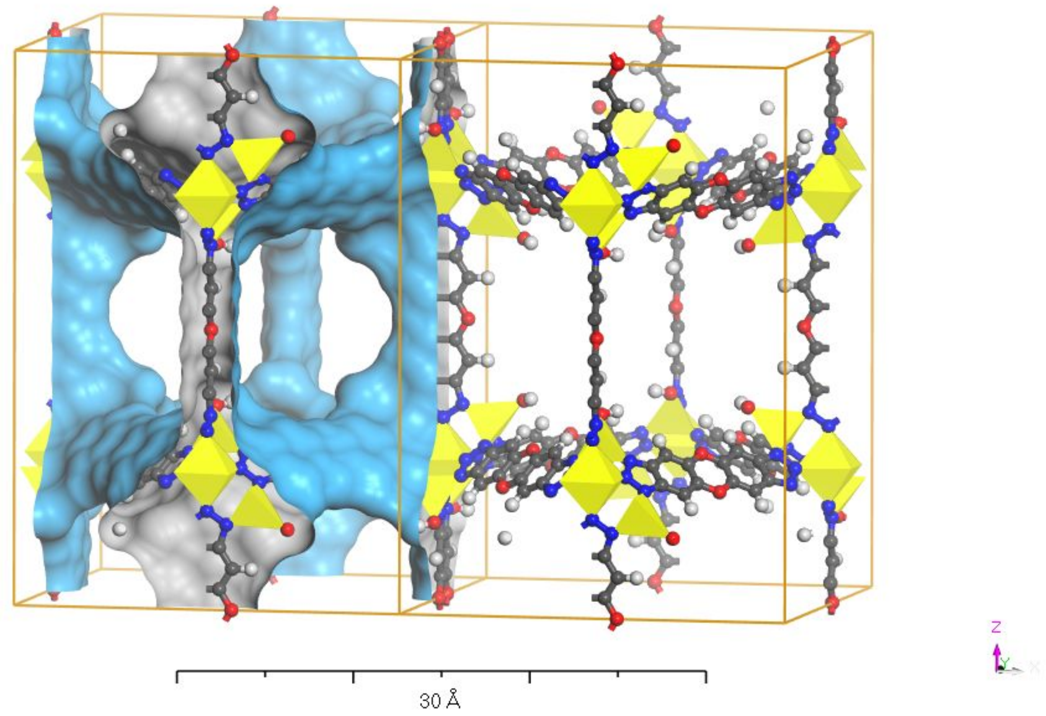

Figure S 40. Conventional unit cell of **1-OH** and the Connolly surface plotted with BIOVIA Materials Studio 2019

Stability tests

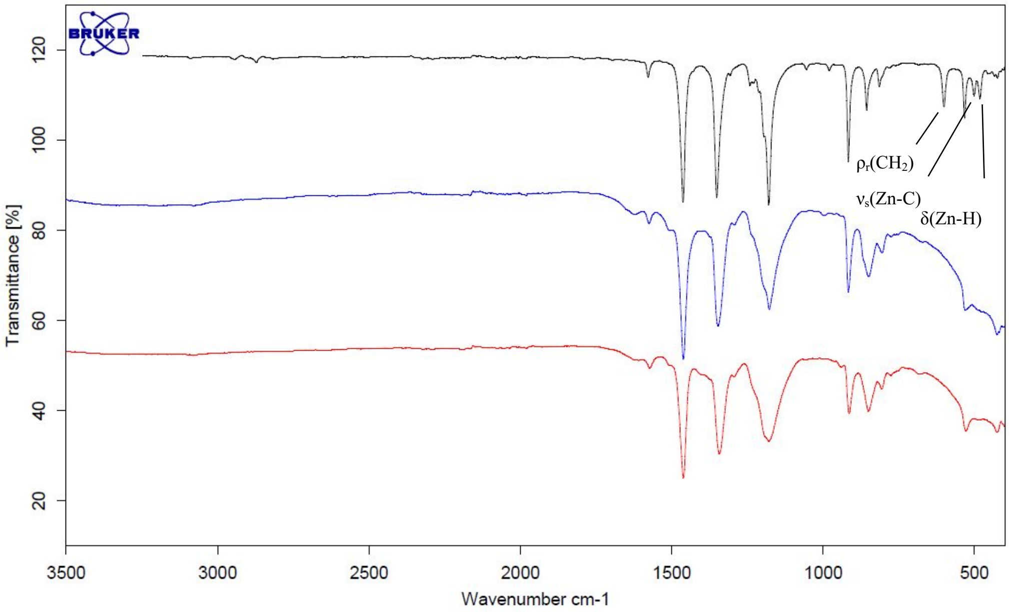

Figure S 41. IR spectra of **1-Et** (black), **1-n-Bu** (blue) and **1-t-Bu** (red) after the TG-MS measurements

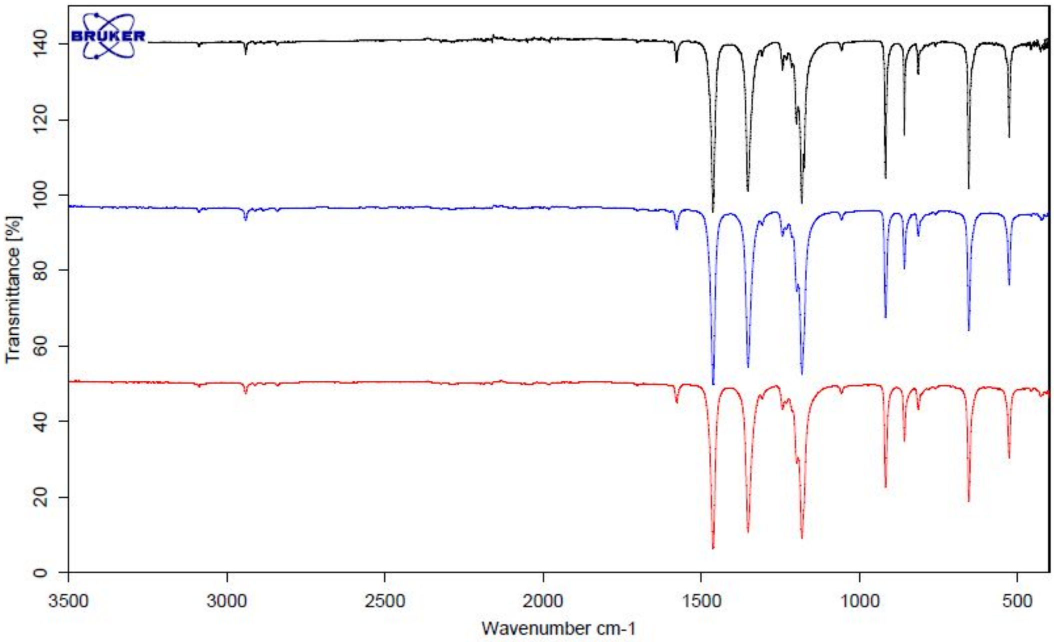

Figure S 42. ATR-IR spectra of **1-Me** (black) after stirring in a 1:19 water/tetrahydrofuran mixture for 24h (blue) and 96h (red)

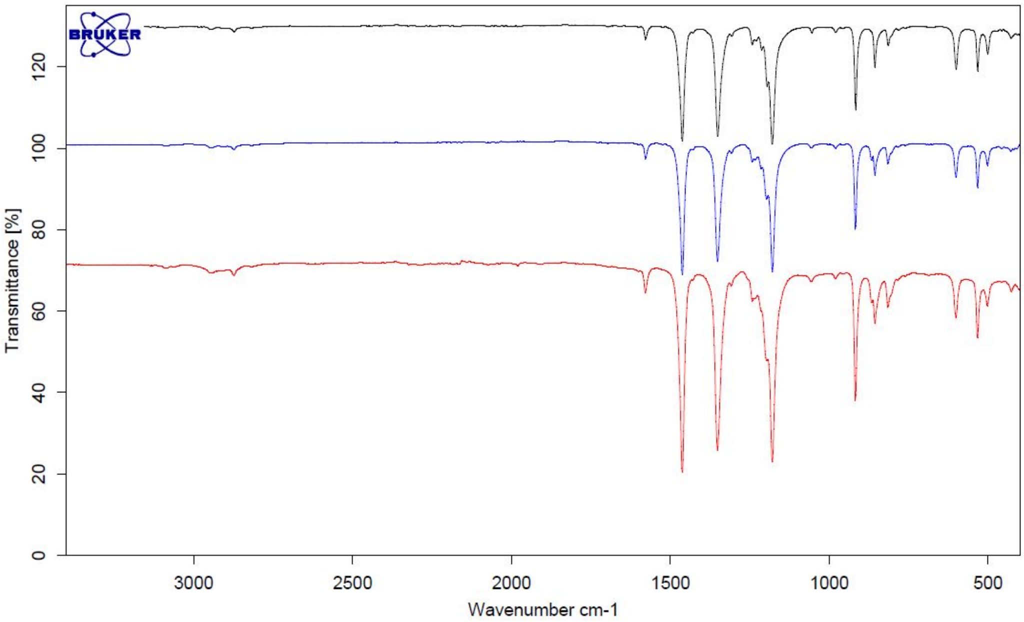

Figure S 43. ATR-IR spectra of **1-Et** (black) after stirring in a 1:19 water/tetrahydrofuran mixture for 24h (blue) and 96h (red)

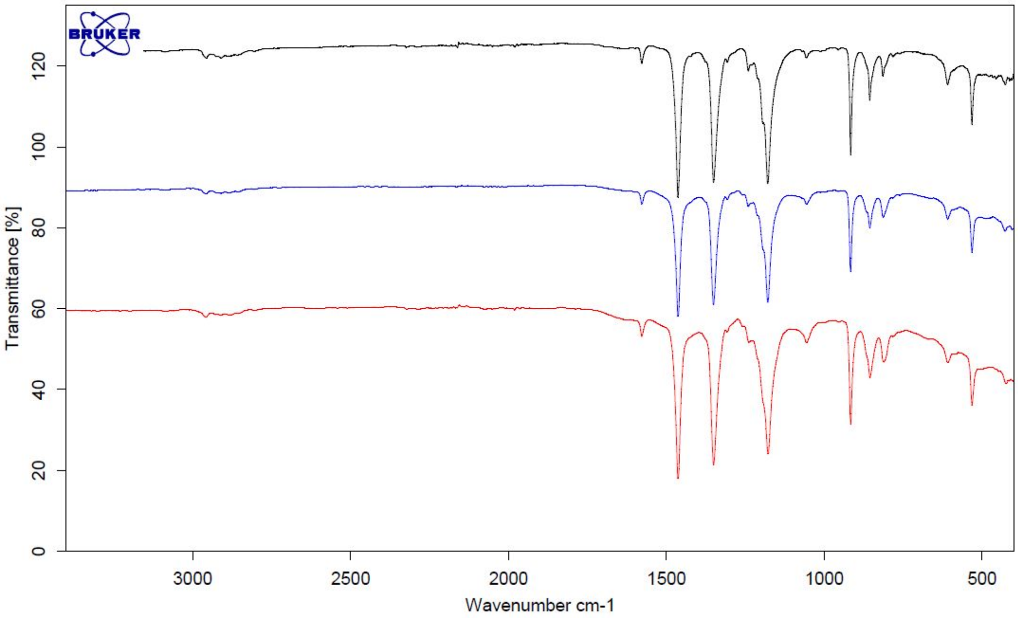

Figure S 44. ATR-IR spectra of **1-n-Bu** (black) after stirring in a 1:19 water/tetrahydrofuran mixture for 24h (blue) and 96h (red)

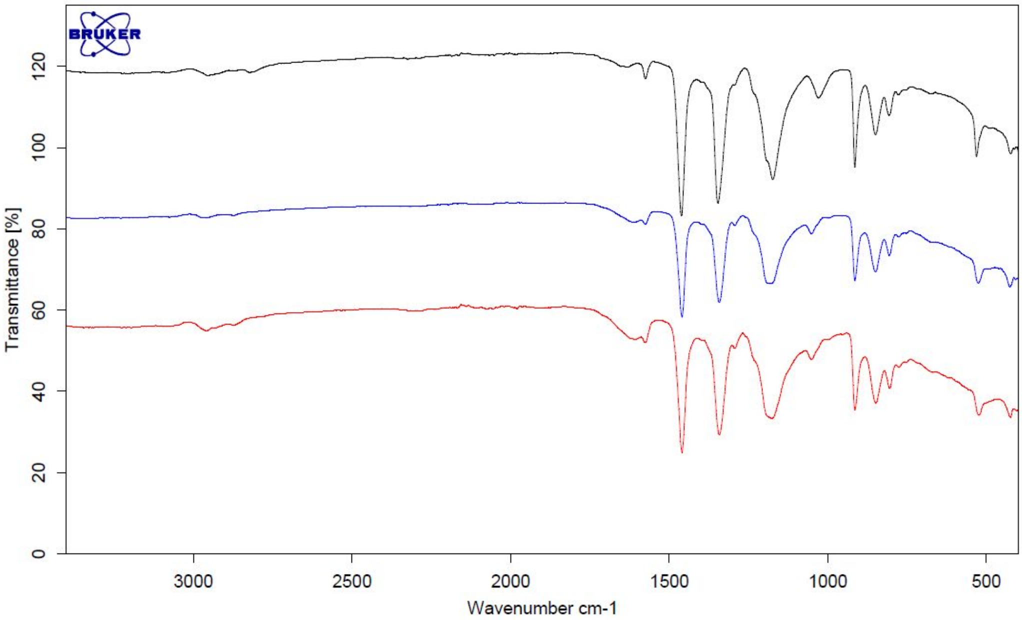

Figure S 45. ATR-IR spectra of **1-t-Bu** (black) after stirring in a 1:19 water/tetrahydrofuran mixture for 24h (blue) and 96h (red)

A 63

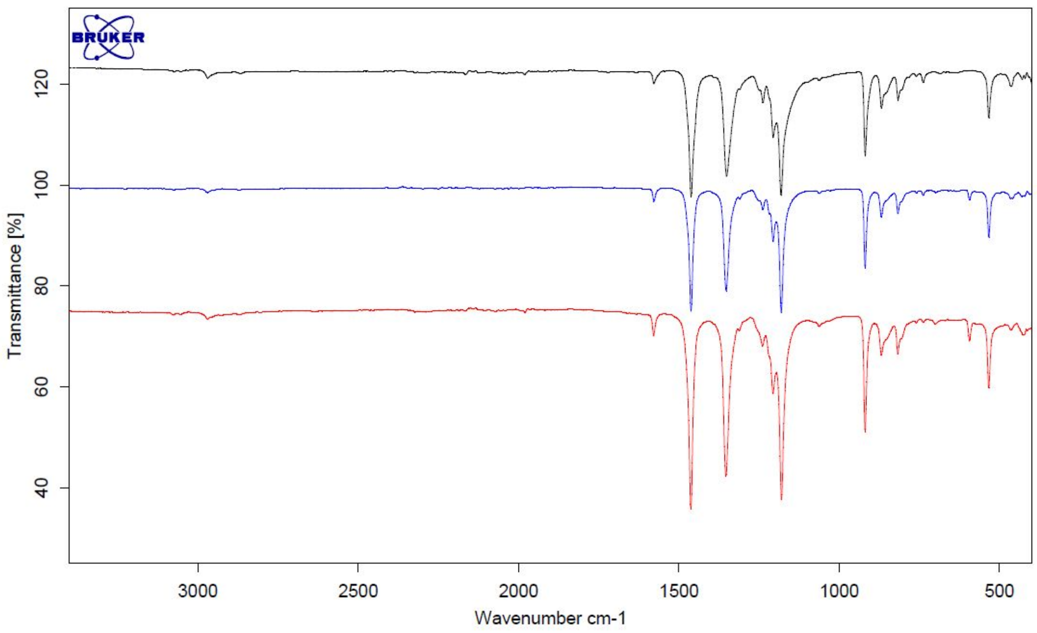

Figure S 46. ATR-IR spectra of **1-Butyne** (black) after stirring in a 1:19 water/tetrahydrofuran mixture for 24h (blue) and 96h (red)

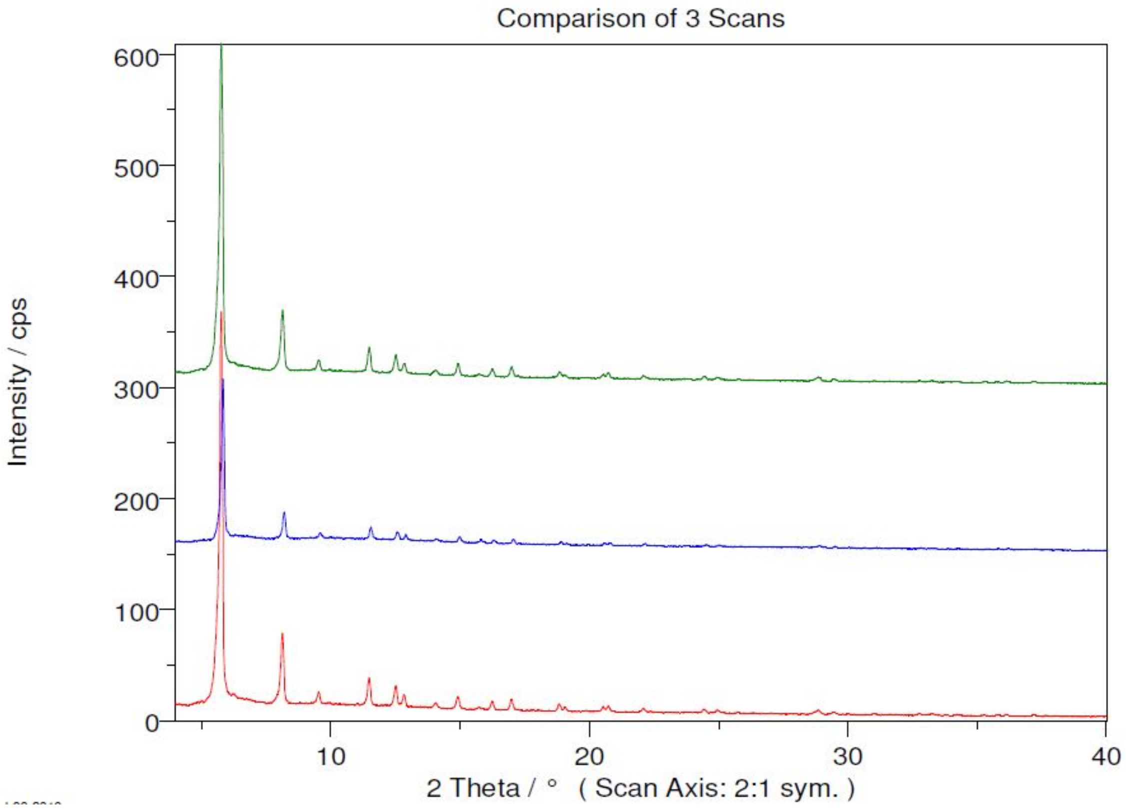

Figure S 47. XRPD pattern of **1-Me** (red) after stirring in a 1:19 water/tetrahydrofuran mixture for 24h (blue) and 96h (green)

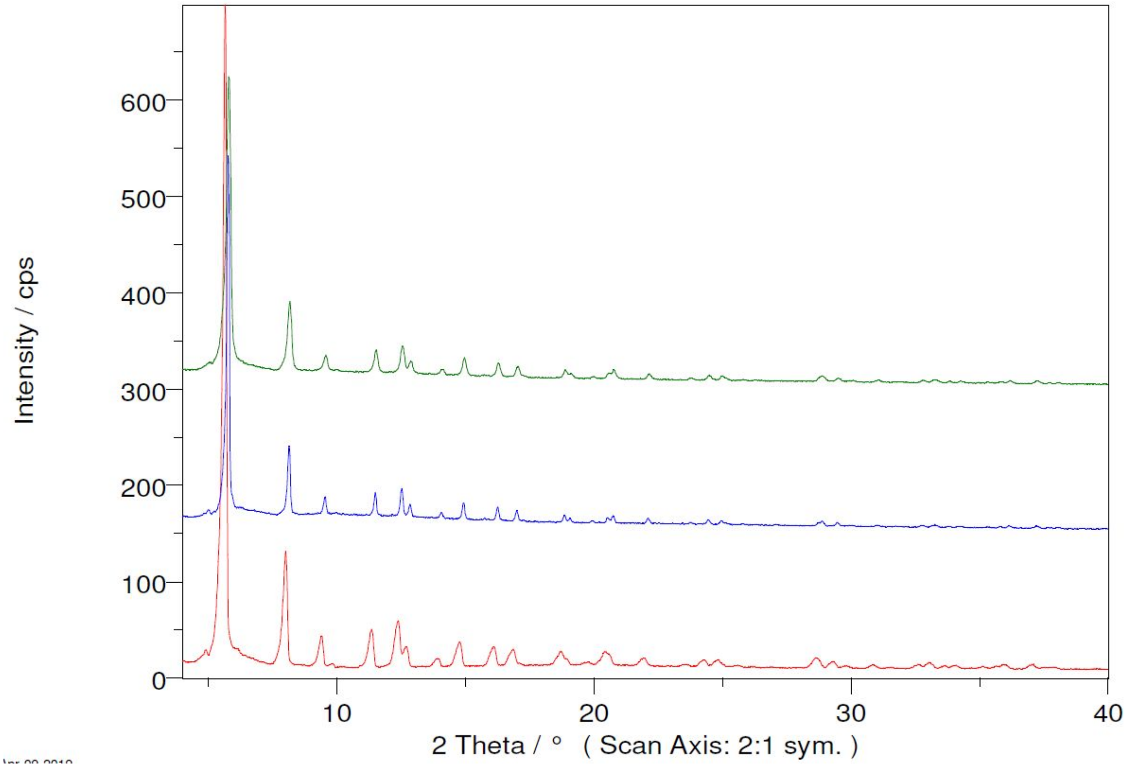

Figure S 48. XRPD pattern of **1-Et** (red) after stirring in a 1:19 water/tetrahydrofuran mixture for 24h (blue) and 96h (green)

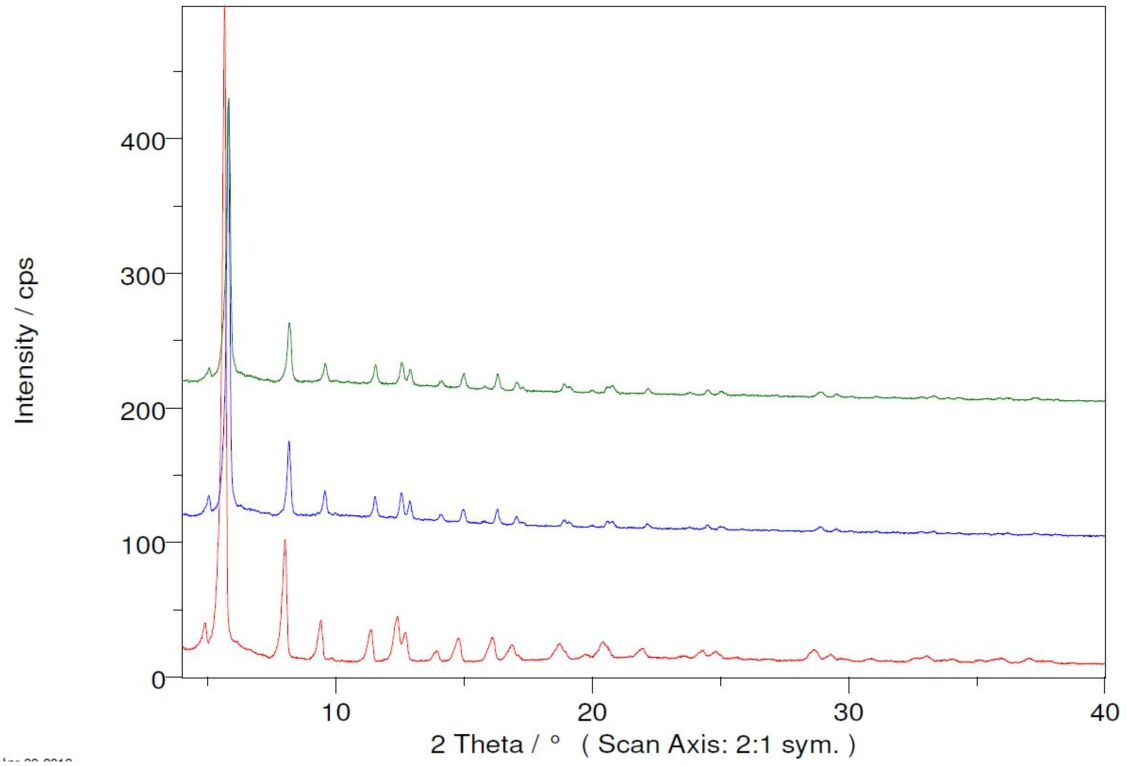

Figure S 49. XRPD pattern of **1-n-Bu** (red) after stirring in a 1:19 water/tetrahydrofuran mixture for 24h (blue) and 96h (green)

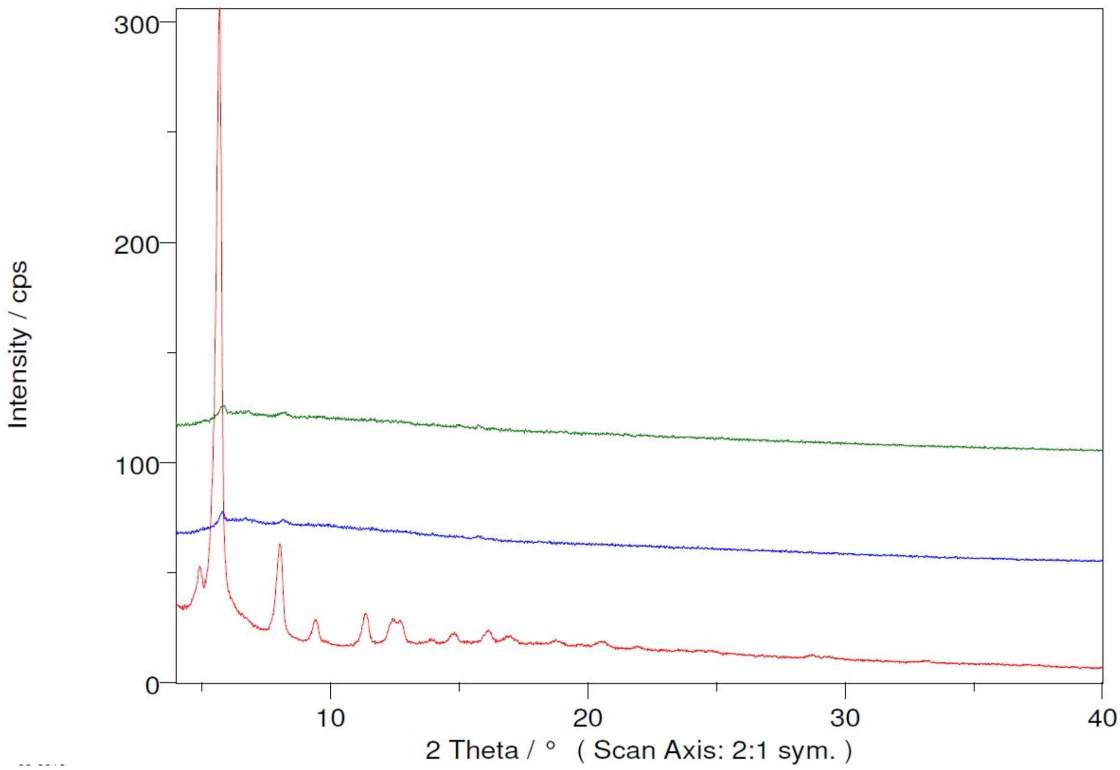

Figure S 50. XRPD pattern of **1-t-Bu** (red) after stirring in a 1:19 water/tetrahydrofuran mixture for 24h (blue) and 96h (green)

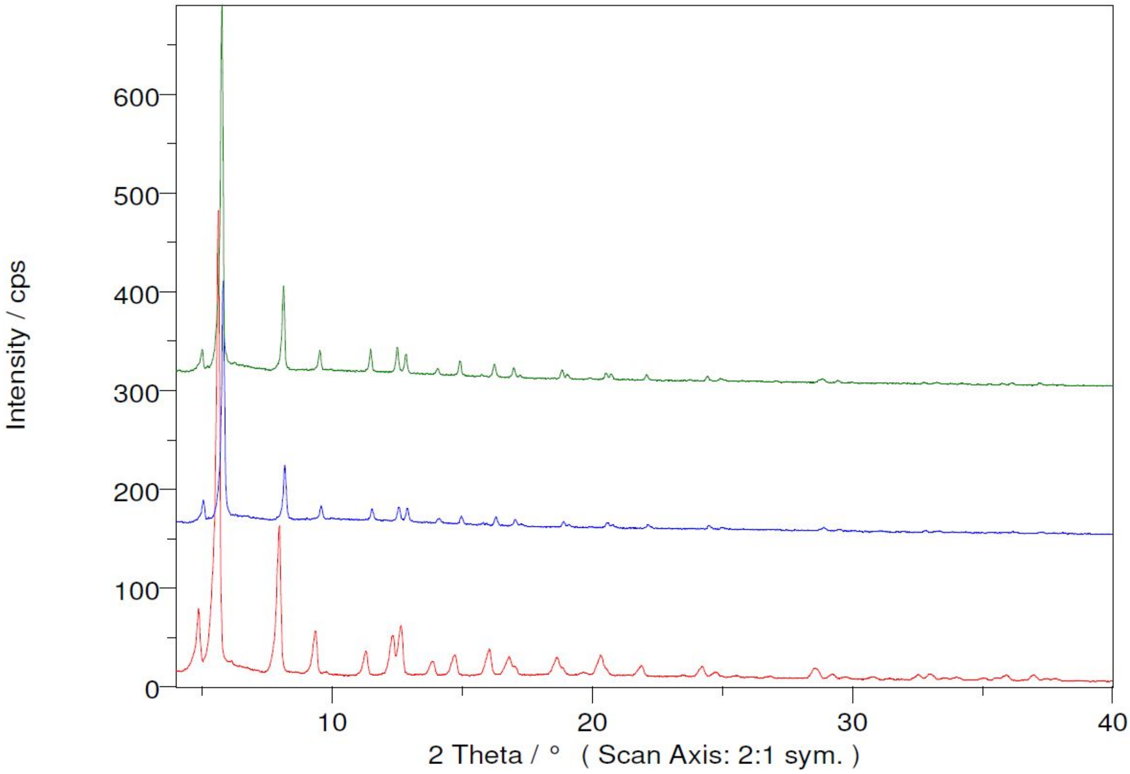

Figure S 51. XRPD pattern of **1-Butyne** (red) after stirring in a 1:19 water/tetrahydrofuran mixture for 24h (blue) and 96h (green)

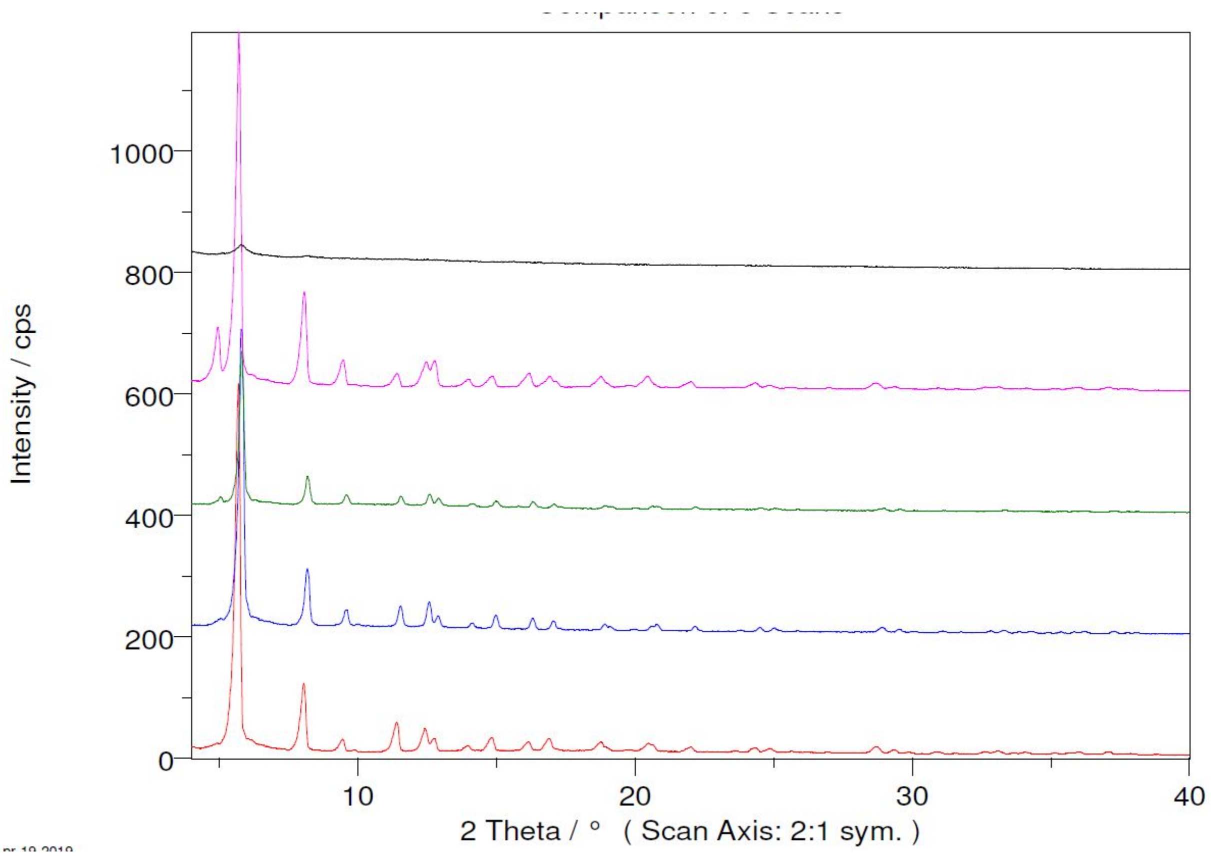

Figure S 52. XRPD pattern after approximately 1 month of storage for **1-Me** (red), **1-Et** (blue), **1-n-Bu** (green), **1-Butyne** (pink) and **1-t-Bu** (black)

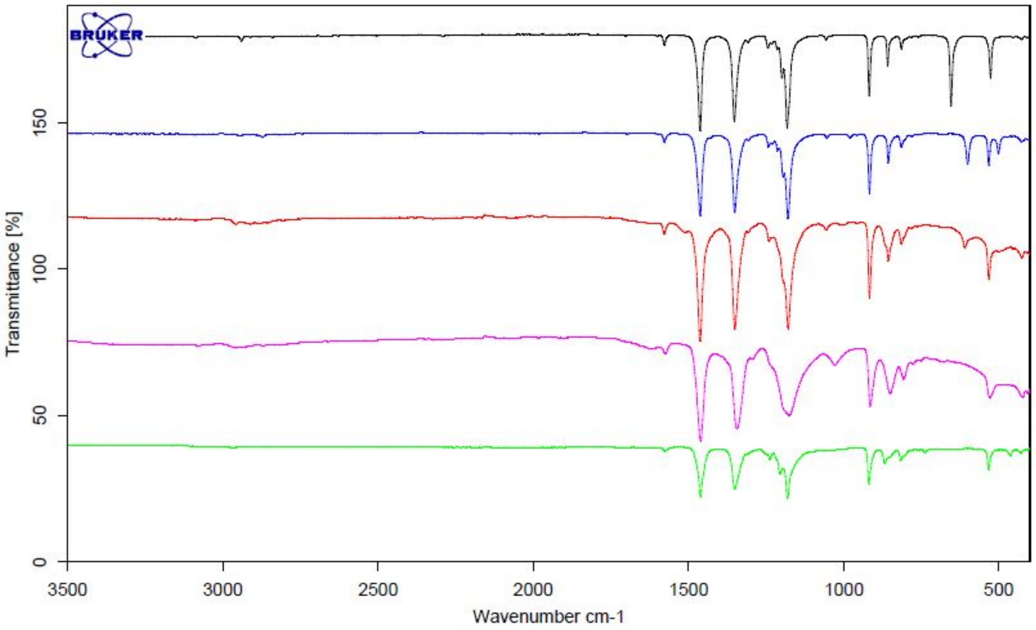

Figure S 53. ATR-IR spectra after approximately 1 month of storage for **1-Me** (black), **1-Et** (blue), **1-n-Bu** (red), **1-t-Bu** (pink) and **1-Butyne** (green)

MS data for the hydrolysis reaction of 2-Me

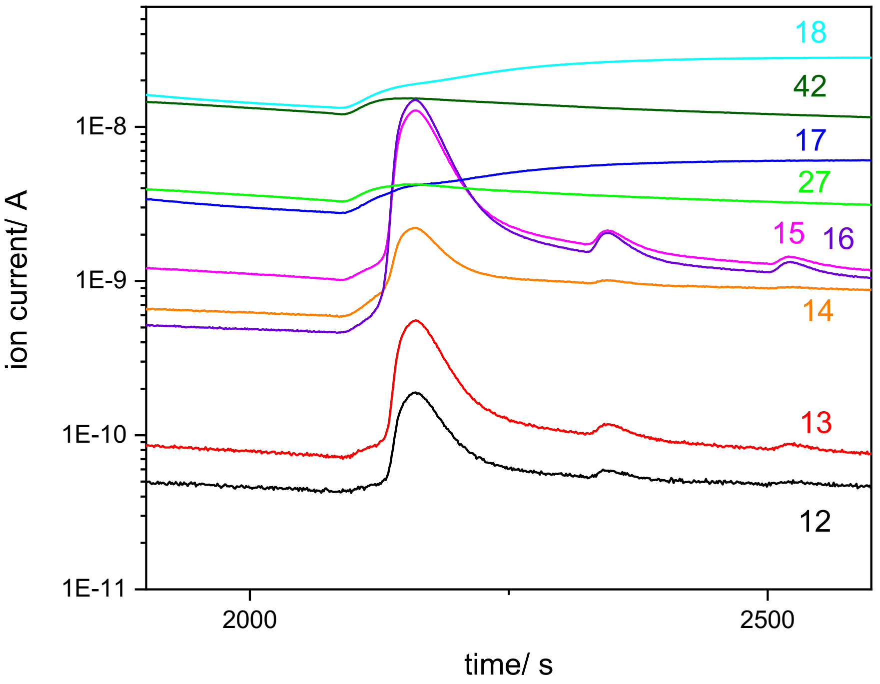

Figure S 54: mass spectrometry data showing the evolution of methane during the hydrolysis reaction of 2-Me resulting in compound 2-OH, methane: 12 m/z (black); 13 m/z (red); 14 m/z (orange); 15 m/z (pink); 16 m/z (purple), water: 16 m/z (purple); 17 m/z (dark blue); 18 m/z (light blue), THF: 42 m/z (dark green); 27 m/z (light green)

EDX data

Table S 17: Summary of the collected EDX data

compound	Zn%	Co%	Cl%	average ratios		
				Zn	Co	Cl
1	54.76	/	45.24		/	
	53.97	/	46.03	5.00	/	4.198
1-Me	97.97	/	2.03		/	
	97.70	/	2.30	5.00	/	0.111
1-Et	98.48	/	1.52		/	
	99.06	/	0.94		/	
	98.21	/	1.79	5.00	/	0.072
1-n-Bu	98.50	/	1.50		/	
	98.16	/	1.84	5.00	/	0.085
1-t-Bu	95.53	/	4.47		/	
	94.89	/	5.11	5.00	/	0.252
1-H	86.82	/	13.18	5.00	/	0.759
1-Butyne	86.84	/	13.16		/	
	87.04	/	12.96	5.00	/	0.751
2	13.99	41.91	44.10			
	15.09	40.46	44.45	1.305	3.695	3.973
2-Me	26.16	59.11	14.72			
	26.60	58.40	15.00	1.549	3.451	0.873
2-OH	24.15	60.35	15.50			
	23.86	60.91	15.23	1.418	3.582	0.908

A 69

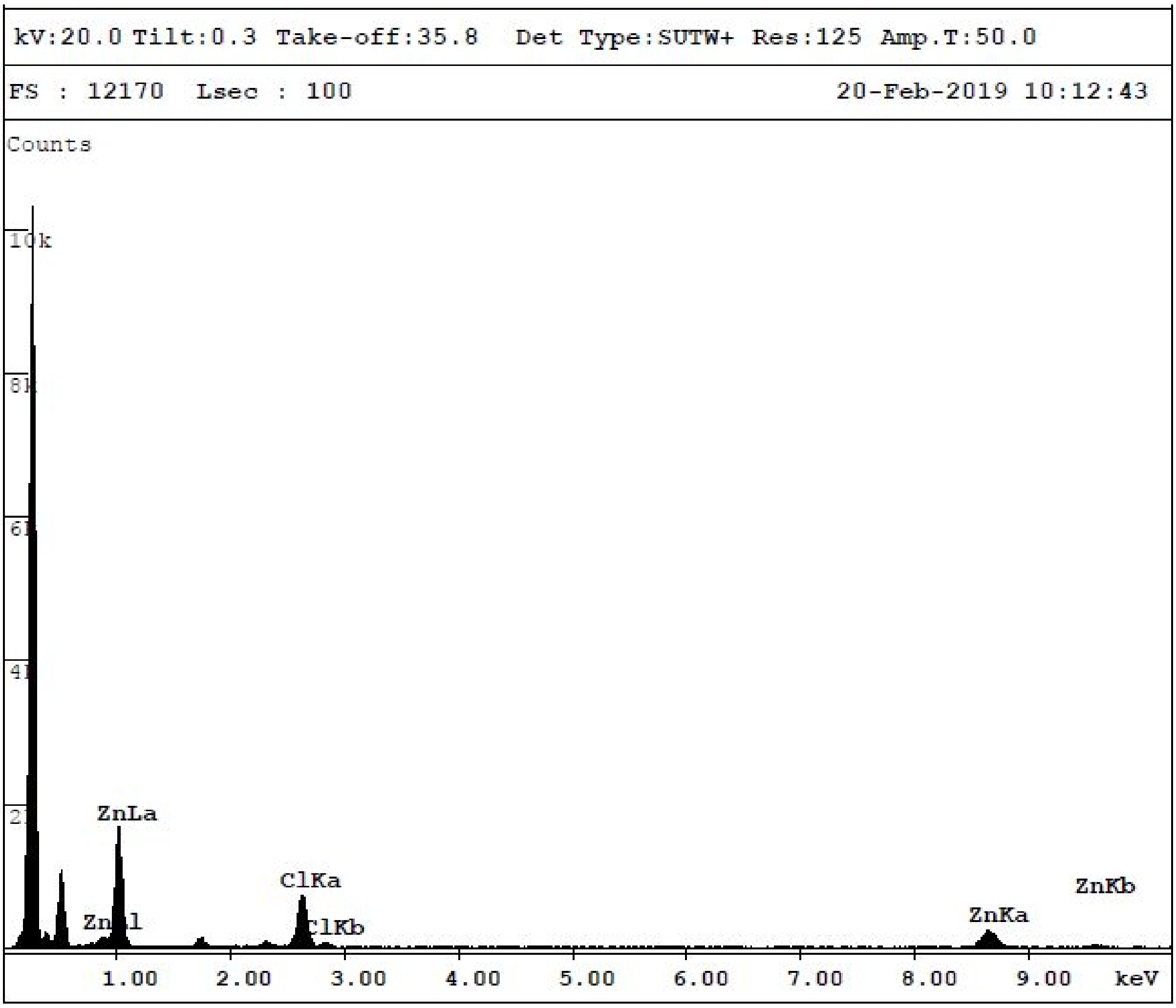

```
kV:20.0 Tilt:0.3  Take-off:35.8   Det Type:SUTW+  Res:125  Amp.T:50.0
FS  :  12170   Lsec  :  100                            20-Feb-2019 10:12:43
```

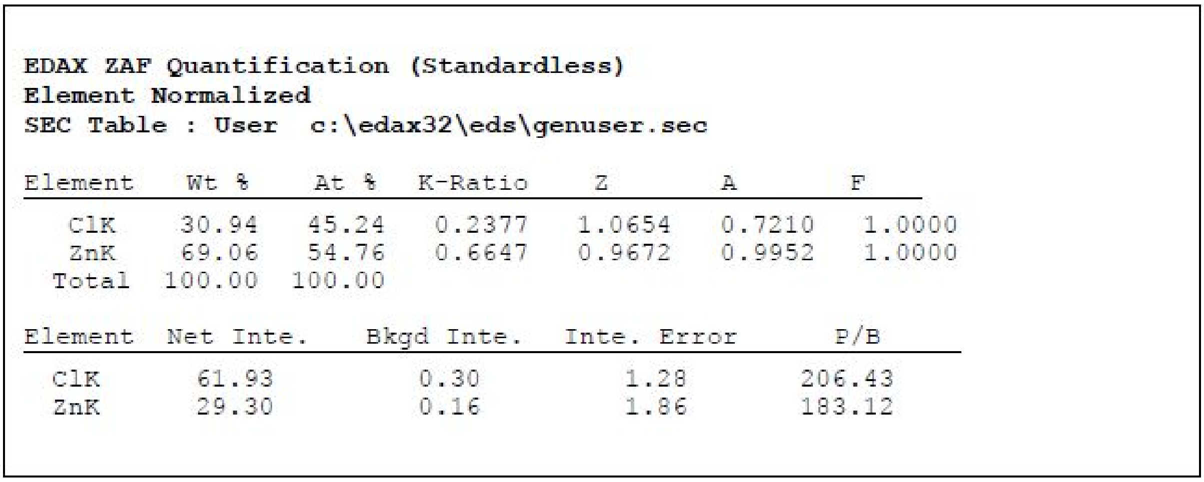

```
EDAX ZAF Quantification (Standardless)
Element Normalized
SEC Table : User  c:\edax32\eds\genuser.sec

Element    Wt %     At %   K-Ratio     Z         A         F
   ClK    30.94    45.24   0.2377   1.0654   0.7210   1.0000
   ZnK    69.06    54.76   0.6647   0.9672   0.9952   1.0000
 Total   100.00   100.00

Element   Net Inte.    Bkgd Inte.    Inte. Error      P/B
  ClK       61.93         0.30          1.28        206.43
  ZnK       29.30         0.16          1.86        183.12
```

Figure S 55: EDX spectrum and data of **1**

A 70

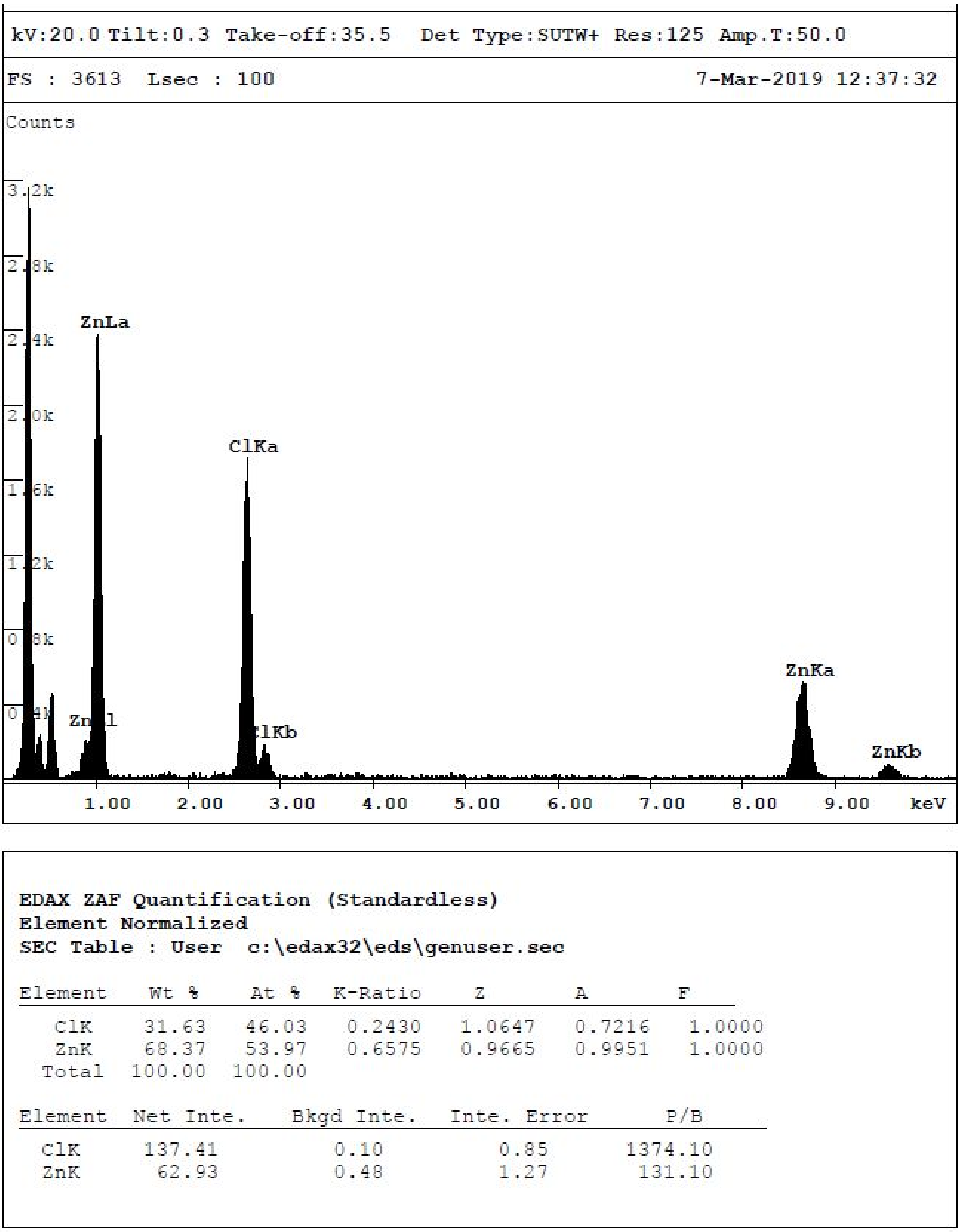

```
kV:20.0 Tilt:0.3 Take-off:35.5   Det Type:SUTW+ Res:125 Amp.T:50.0
FS : 3613  Lsec : 100                              7-Mar-2019 12:37:32
```

```
EDAX ZAF Quantification (Standardless)
Element Normalized
SEC Table : User  c:\edax32\eds\genuser.sec

Element     Wt %     At %   K-Ratio     Z        A        F
   ClK     31.63    46.03   0.2430   1.0647   0.7216   1.0000
   ZnK     68.37    53.97   0.6575   0.9665   0.9951   1.0000
  Total   100.00   100.00

Element   Net Inte.    Bkgd Inte.   Inte. Error       P/B
  ClK      137.41         0.10          0.85       1374.10
  ZnK       62.93         0.48          1.27        131.10
```

Figure S 56: EDX spectrum and data of **1**

A 71

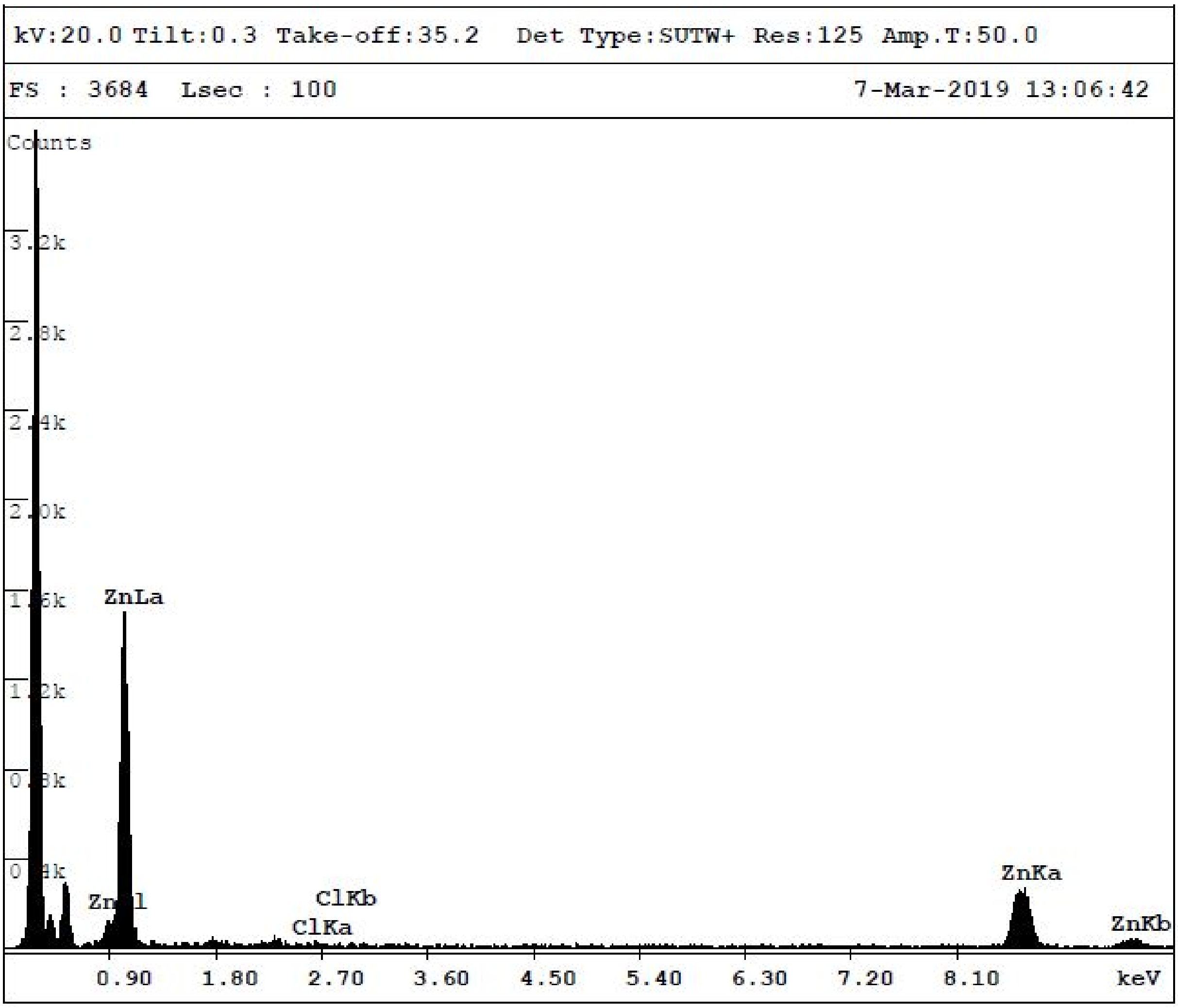

```
kV:20.0 Tilt:0.3  Take-off:35.2   Det Type:SUTW+  Res:125  Amp.T:50.0
FS : 3684   Lsec : 100                               7-Mar-2019 13:06:42
```

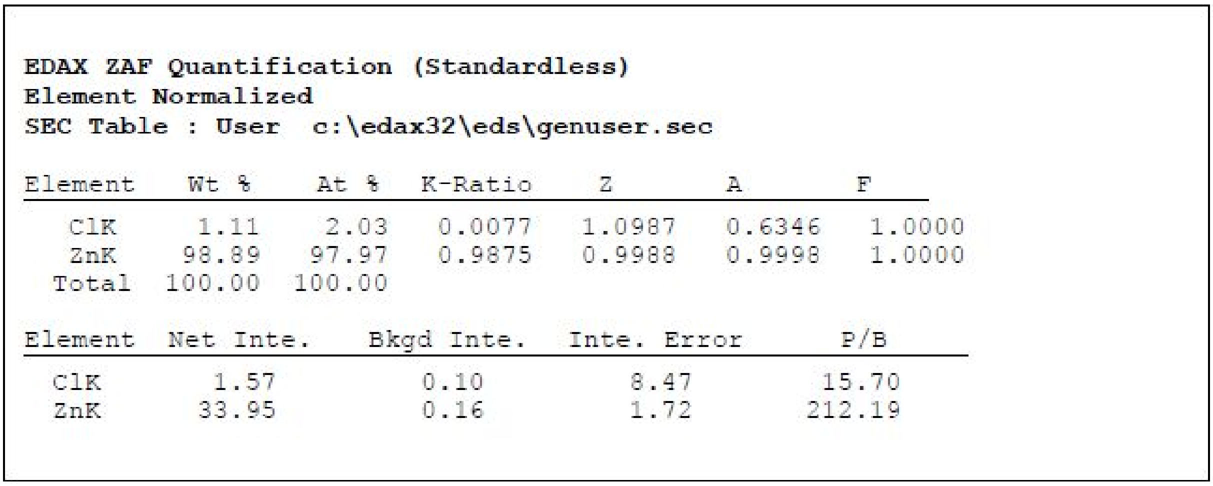

```
EDAX ZAF Quantification (Standardless)
Element Normalized
SEC Table : User   c:\edax32\eds\genuser.sec

Element     Wt %      At %   K-Ratio     Z         A         F
  ClK       1.11      2.03   0.0077   1.0987    0.6346    1.0000
  ZnK      98.89     97.97   0.9875   0.9988    0.9998    1.0000
 Total    100.00    100.00

Element   Net Inte.    Bkgd Inte.   Inte. Error      P/B
 ClK        1.57          0.10          8.47        15.70
 ZnK       33.95          0.16          1.72       212.19
```

Figure S 57: EDX spectrum and data of ***1-Me***

A 72

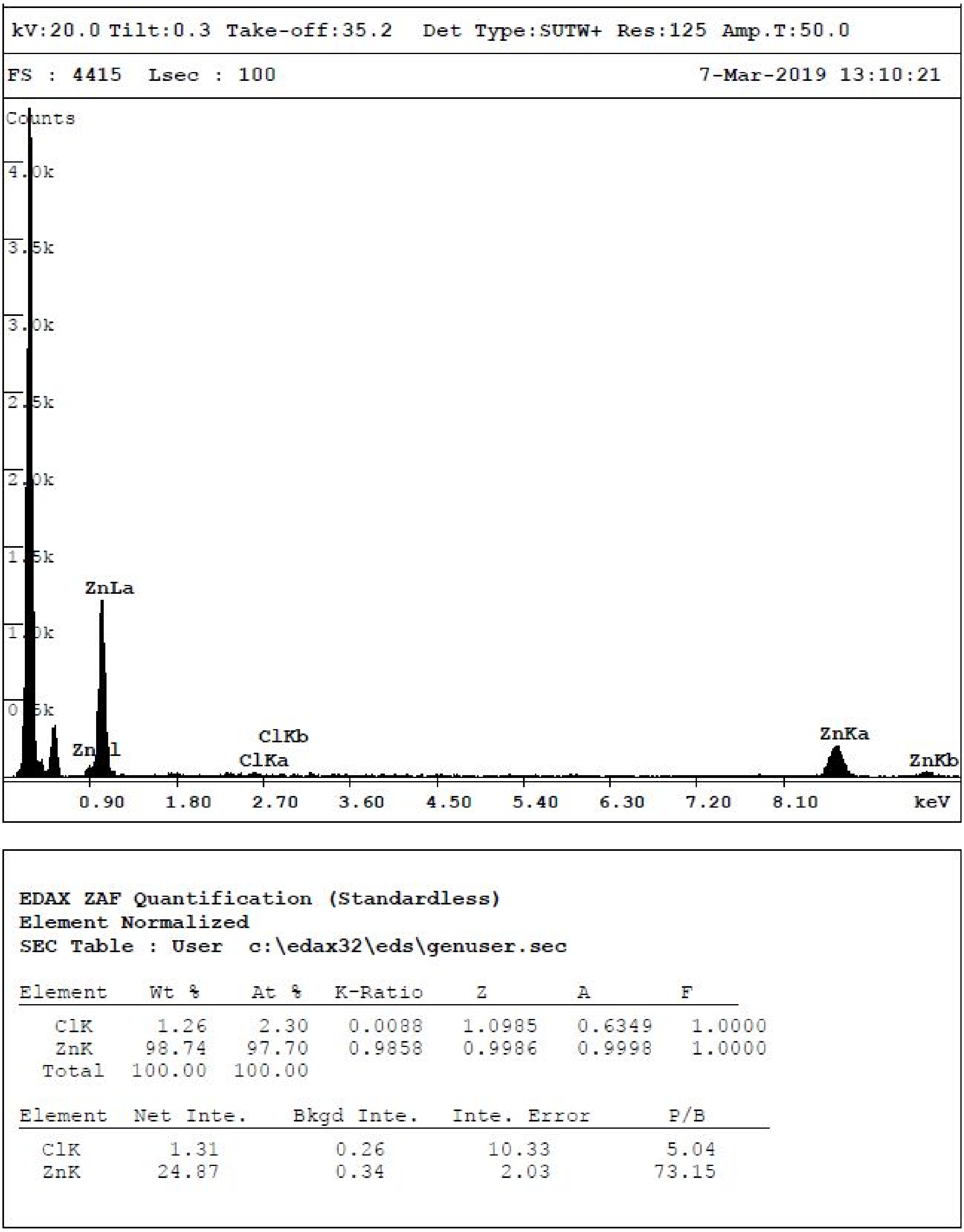

```
kV:20.0 Tilt:0.3  Take-off:35.2   Det Type:SUTW+  Res:125  Amp.T:50.0
FS :  4415   Lsec :  100                            7-Mar-2019 13:10:21
```

```
EDAX ZAF Quantification (Standardless)
Element Normalized
SEC Table : User   c:\edax32\eds\genuser.sec

Element     Wt %      At %   K-Ratio      Z          A          F
   ClK      1.26      2.30    0.0088    1.0985    0.6349    1.0000
   ZnK     98.74     97.70    0.9858    0.9986    0.9998    1.0000
  Total   100.00    100.00

Element   Net Inte.    Bkgd Inte.    Inte. Error        P/B
  ClK        1.31           0.26         10.33          5.04
  ZnK       24.87           0.34          2.03         73.15
```

Figure S 58: EDX spectrum and data of **1-Me**

A 73

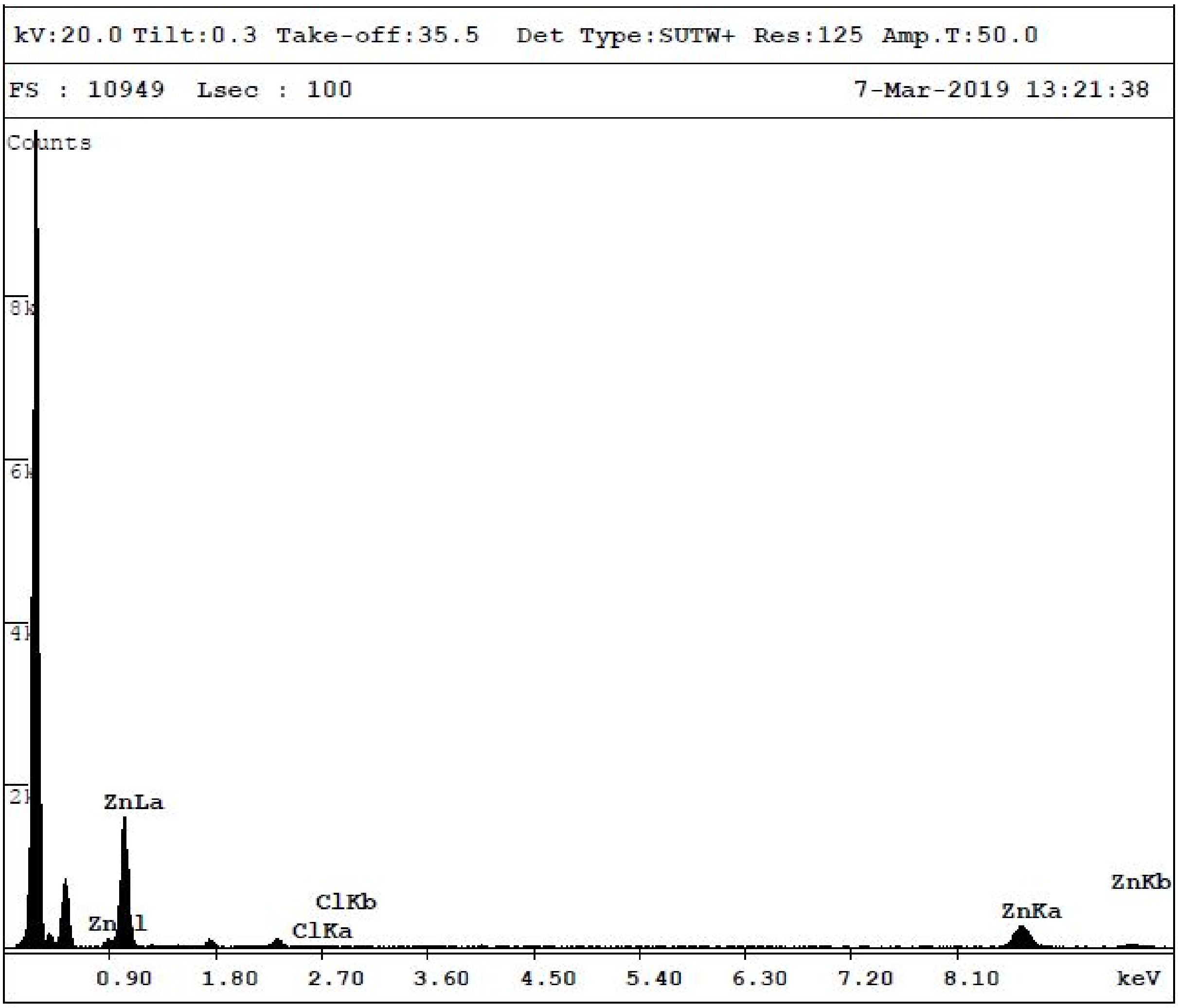

```
kV:20.0 Tilt:0.3  Take-off:35.5   Det Type:SUTW+  Res:125  Amp.T:50.0
FS :  10949   Lsec :  100                            7-Mar-2019 13:21:38
```

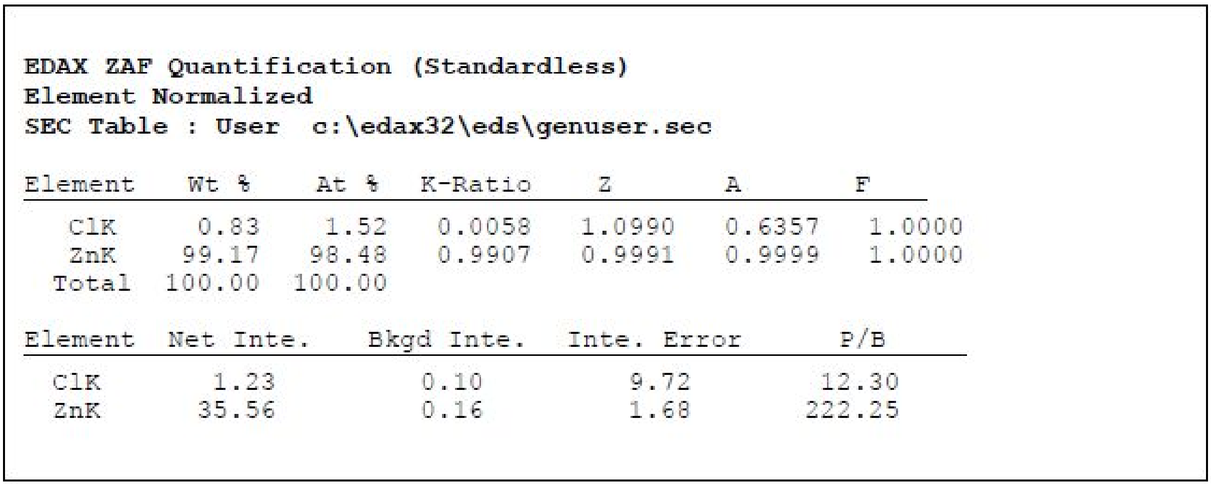

```
EDAX ZAF Quantification (Standardless)
Element Normalized
SEC Table : User  c:\edax32\eds\genuser.sec

Element     Wt %     At %   K-Ratio      Z        A        F
  ClK       0.83     1.52   0.0058   1.0990   0.6357   1.0000
  ZnK      99.17    98.48   0.9907   0.9991   0.9999   1.0000
 Total    100.00   100.00

Element   Net Inte.    Bkgd Inte.   Inte. Error       P/B
 ClK         1.23          0.10          9.72        12.30
 ZnK        35.56          0.16          1.68       222.25
```

Figure S 59: EDX spectrum and data of **1-Et**

A 74

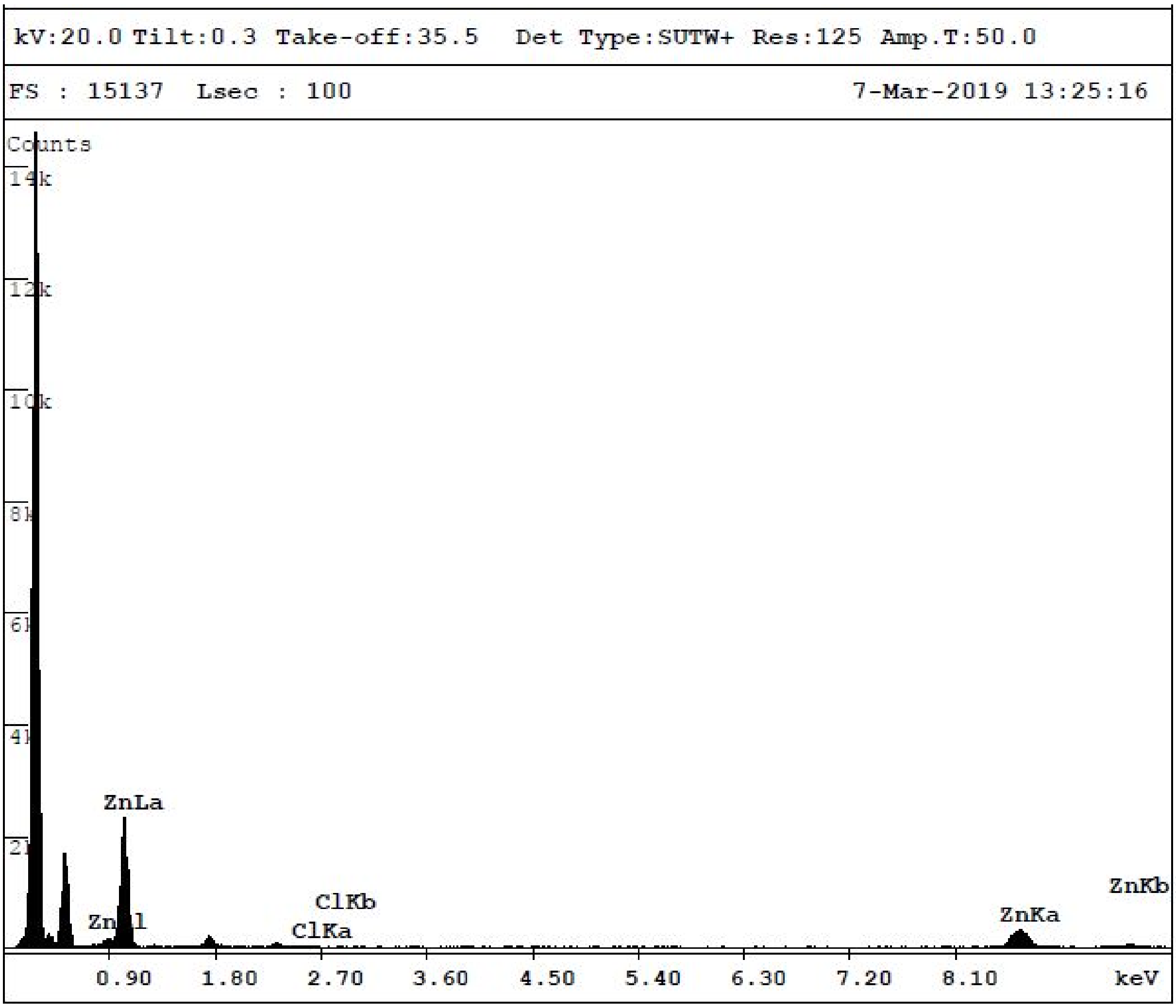

```
kV:20.0 Tilt:0.3  Take-off:35.5   Det Type:SUTW+  Res:125  Amp.T:50.0
FS : 15137   Lsec : 100                              7-Mar-2019 13:25:16
```

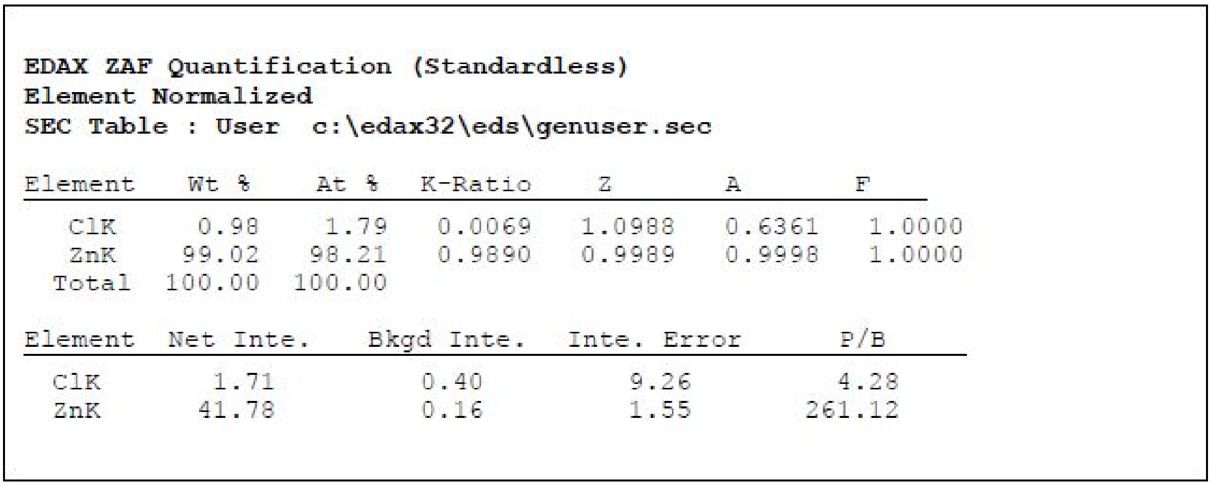

```
EDAX ZAF Quantification (Standardless)
Element Normalized
SEC Table : User  c:\edax32\eds\genuser.sec

Element     Wt %      At %   K-Ratio      Z          A          F
   ClK      0.98      1.79   0.0069   1.0988    0.6361    1.0000
   ZnK     99.02     98.21   0.9890   0.9989    0.9998    1.0000
  Total   100.00    100.00

Element   Net Inte.     Bkgd Inte.    Inte. Error        P/B
  ClK         1.71           0.40           9.26           4.28
  ZnK        41.78           0.16           1.55         261.12
```

Figure S 60: EDX spectrum and data of ***1-Et***

A 75

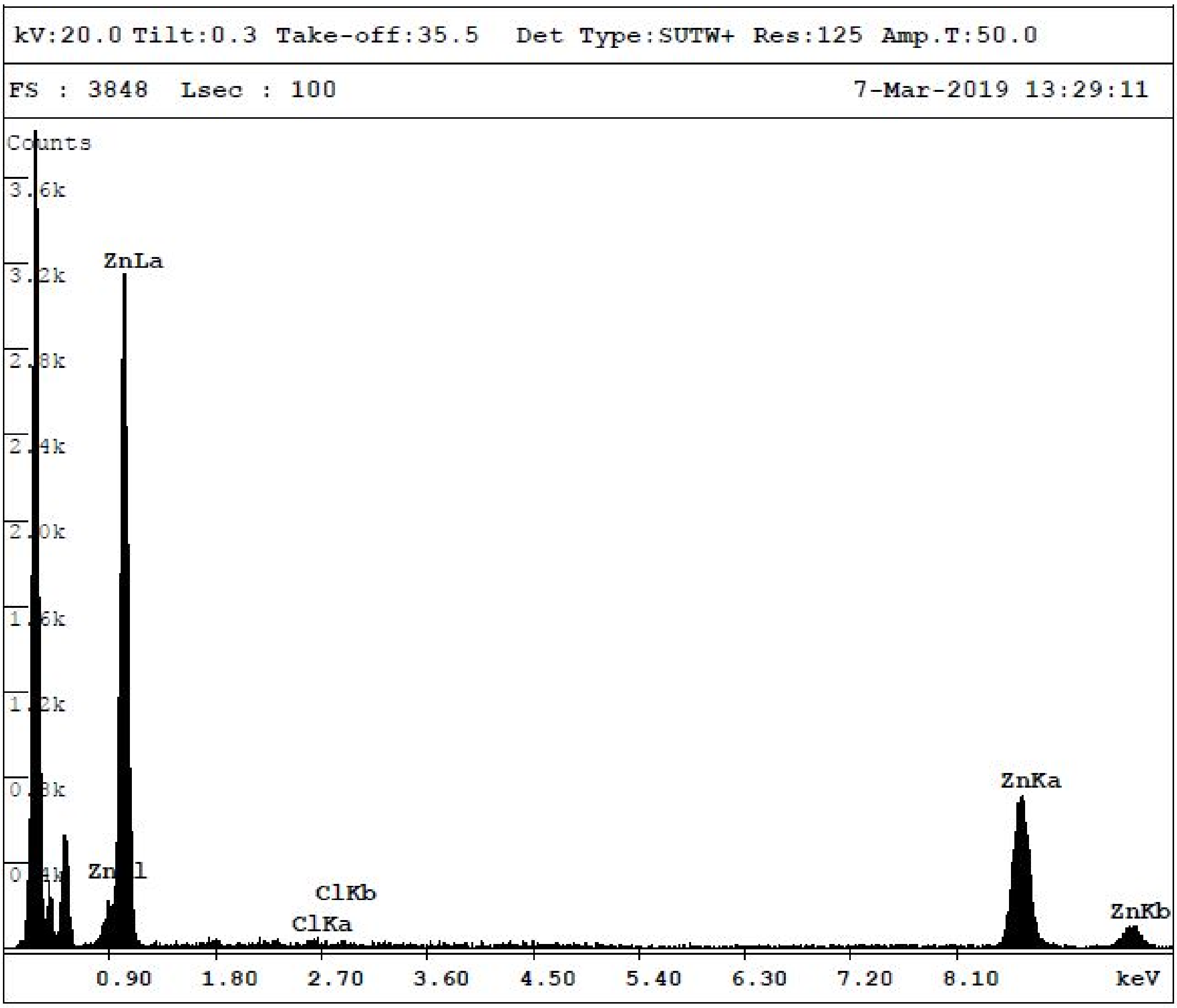

```
kV:20.0 Tilt:0.3  Take-off:35.5   Det Type:SUTW+  Res:125  Amp.T:50.0
FS :  3848   Lsec :  100                          7-Mar-2019 13:29:11
```

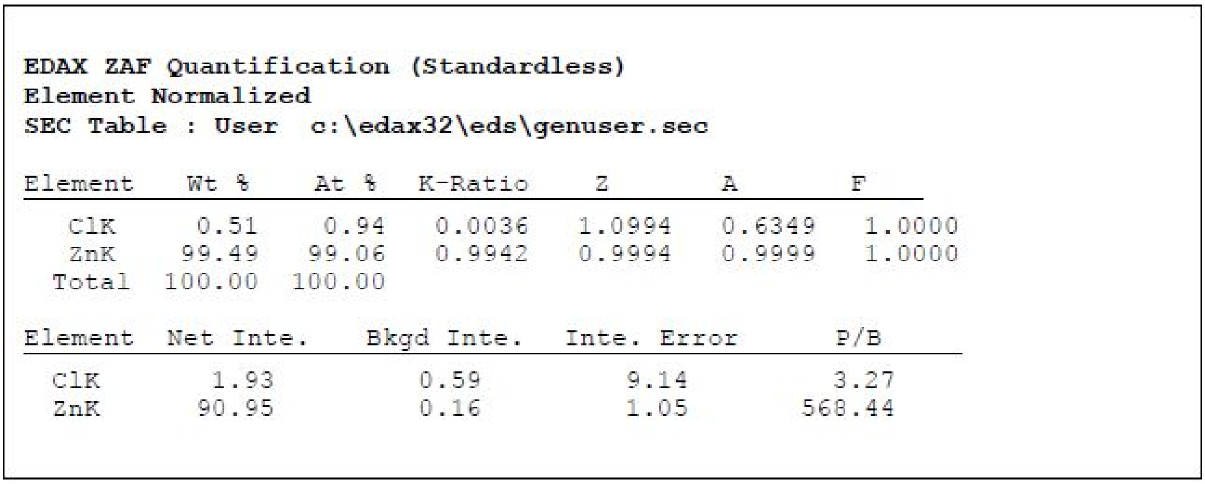

```
EDAX ZAF Quantification (Standardless)
Element Normalized
SEC Table : User  c:\edax32\eds\genuser.sec

Element     Wt %     At %   K-Ratio      Z          A          F
   ClK      0.51     0.94   0.0036   1.0994   0.6349   1.0000
   ZnK     99.49    99.06   0.9942   0.9994   0.9999   1.0000
  Total   100.00   100.00

Element   Net Inte.    Bkgd Inte.   Inte. Error        P/B
  ClK        1.93          0.59          9.14          3.27
  ZnK       90.95          0.16          1.05        568.44
```

Figure S 61: EDX spectrum and data of **1-Et**

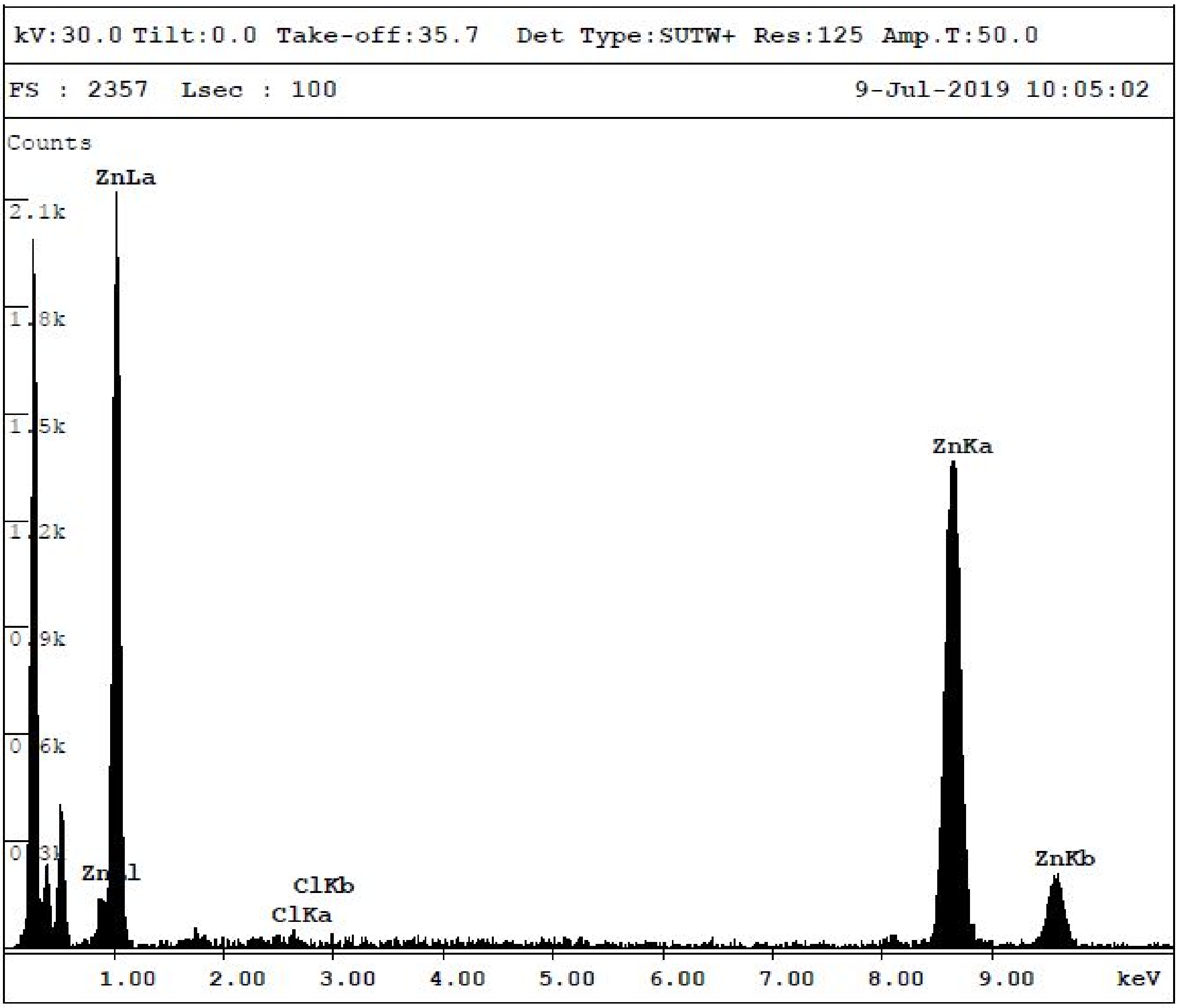

```
kV:30.0 Tilt:0.0  Take-off:35.7   Det Type:SUTW+  Res:125  Amp.T:50.0
FS  :  2357   Lsec  :  100                           9-Jul-2019 10:05:02
```

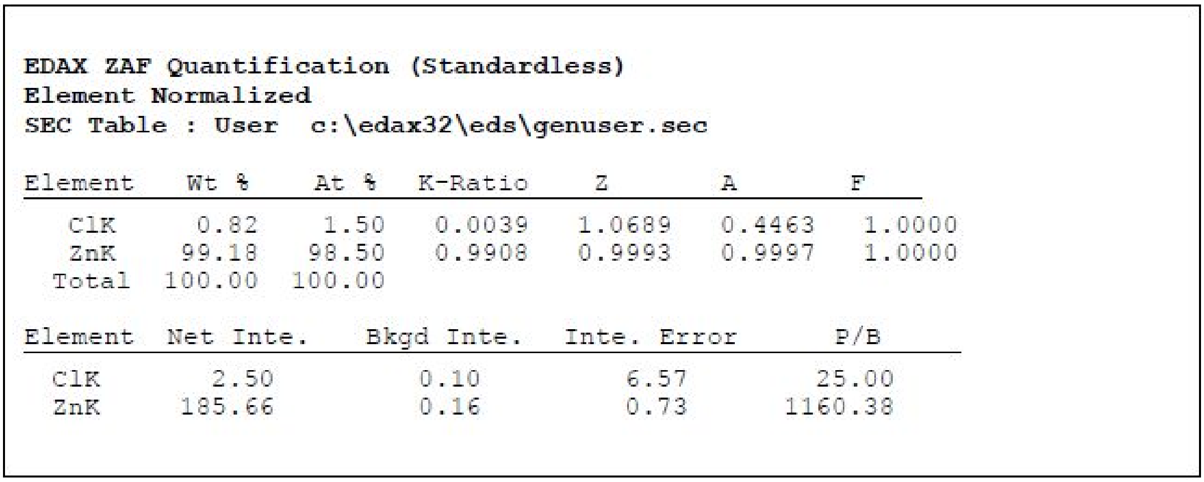

```
EDAX ZAF Quantification (Standardless)
Element Normalized
SEC Table : User  c:\edax32\eds\genuser.sec

Element    Wt %     At %   K-Ratio     Z        A        F
   ClK     0.82     1.50   0.0039   1.0689   0.4463   1.0000
   ZnK    99.18    98.50   0.9908   0.9993   0.9997   1.0000
  Total  100.00   100.00

Element   Net Inte.    Bkgd Inte.   Inte. Error        P/B
  ClK       2.50          0.10          6.57          25.00
  ZnK     185.66          0.16          0.73        1160.38
```

Figure S 62: EDX spectrum and data of **1-n-Bu**

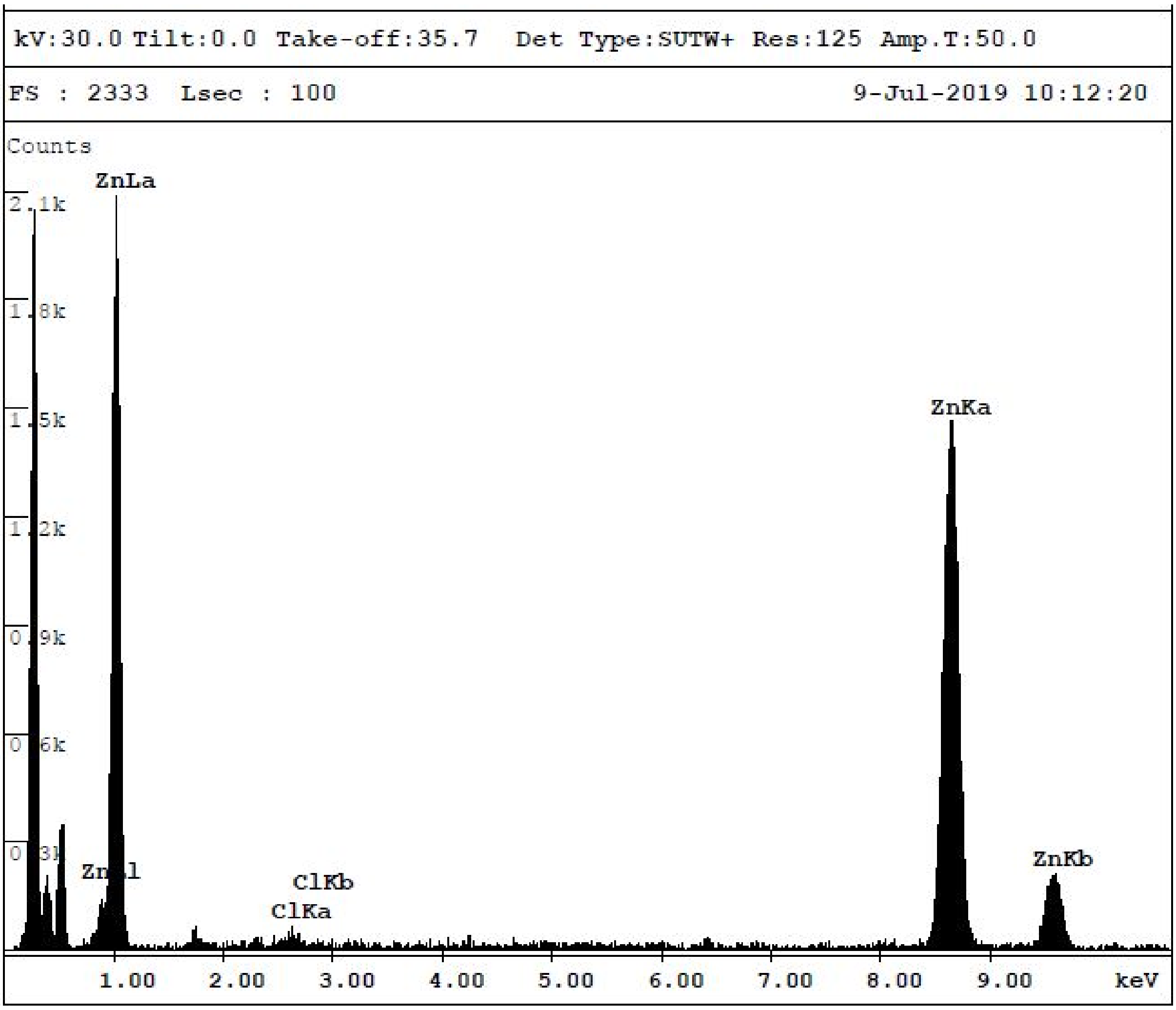

```
kV:30.0 Tilt:0.0  Take-off:35.7   Det Type:SUTW+  Res:125  Amp.T:50.0
FS : 2333   Lsec : 100                            9-Jul-2019 10:12:20
```

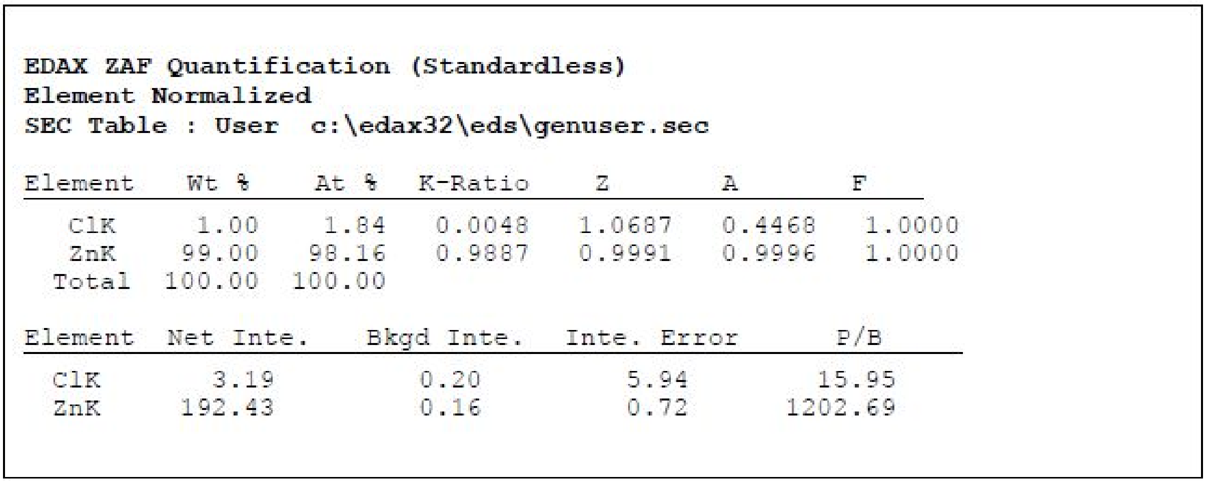

```
EDAX ZAF Quantification (Standardless)
Element Normalized
SEC Table : User  c:\edax32\eds\genuser.sec

Element    Wt %     At %   K-Ratio      Z        A        F
   ClK      1.00     1.84   0.0048   1.0687   0.4468   1.0000
   ZnK     99.00    98.16   0.9887   0.9991   0.9996   1.0000
  Total   100.00   100.00

Element   Net Inte.    Bkgd Inte.    Inte. Error       P/B
  ClK        3.19         0.20           5.94         15.95
  ZnK      192.43         0.16           0.72       1202.69
```

Figure S 63: EDX spectrum and data of **1-n-Bu**

A 78

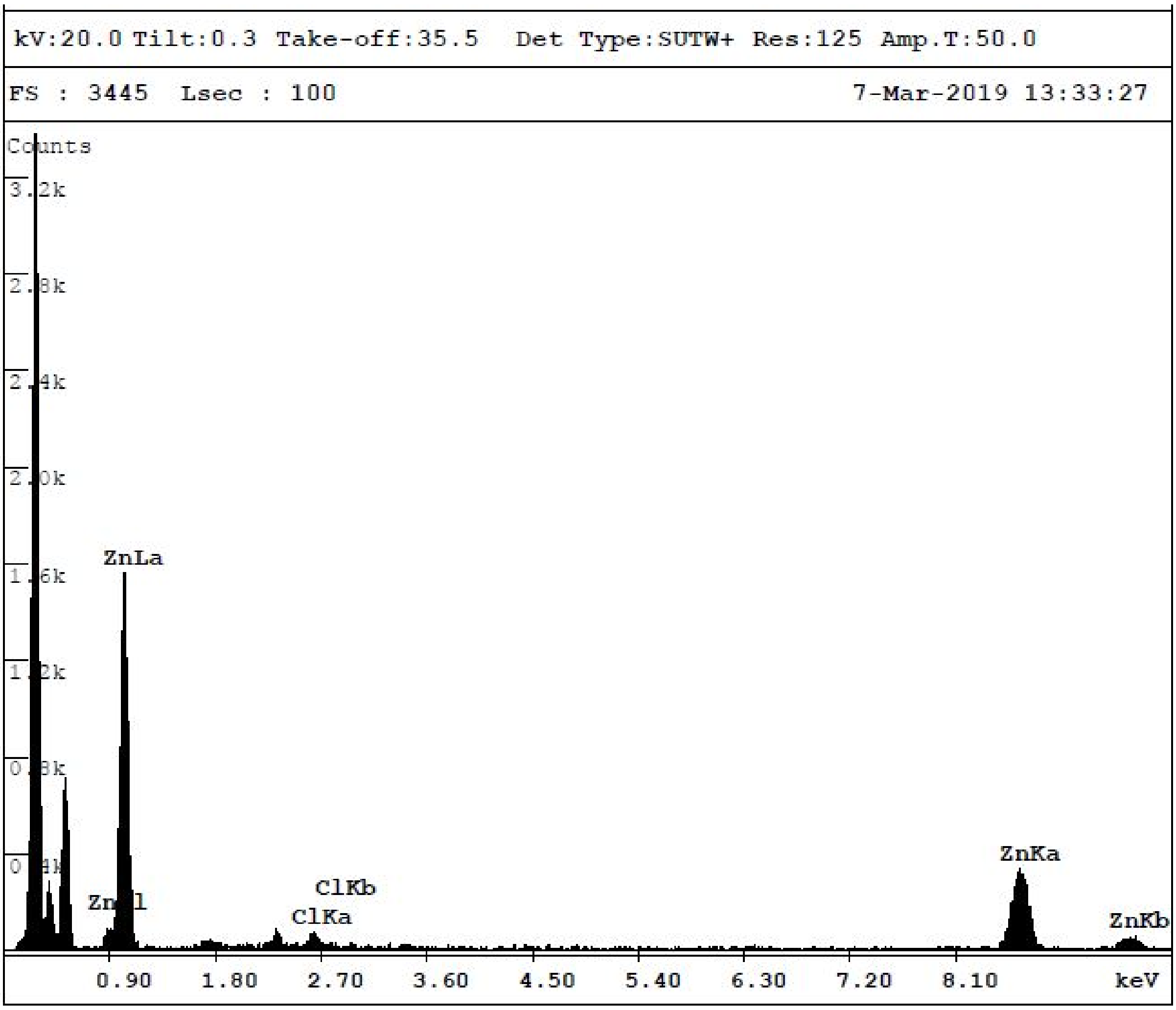

```
EDAX ZAF Quantification (Standardless)
Element Normalized
SEC Table : User  c:\edax32\eds\genuser.sec

Element    Wt %     At %   K-Ratio     Z       A       F
   ClK      2.48     4.47   0.0174   1.0971  0.6399  1.0000
   ZnK     97.52    95.53   0.9722   0.9972  0.9996  1.0000
  Total   100.00   100.00

Element   Net Inte.   Bkgd Inte.  Inte. Error    P/B
  ClK       4.50         0.48         5.19        9.38
  ZnK      42.62         0.16         1.54      266.37
```

Figure S 64: EDX spectrum and data of ***1-t-Bu***

A 79

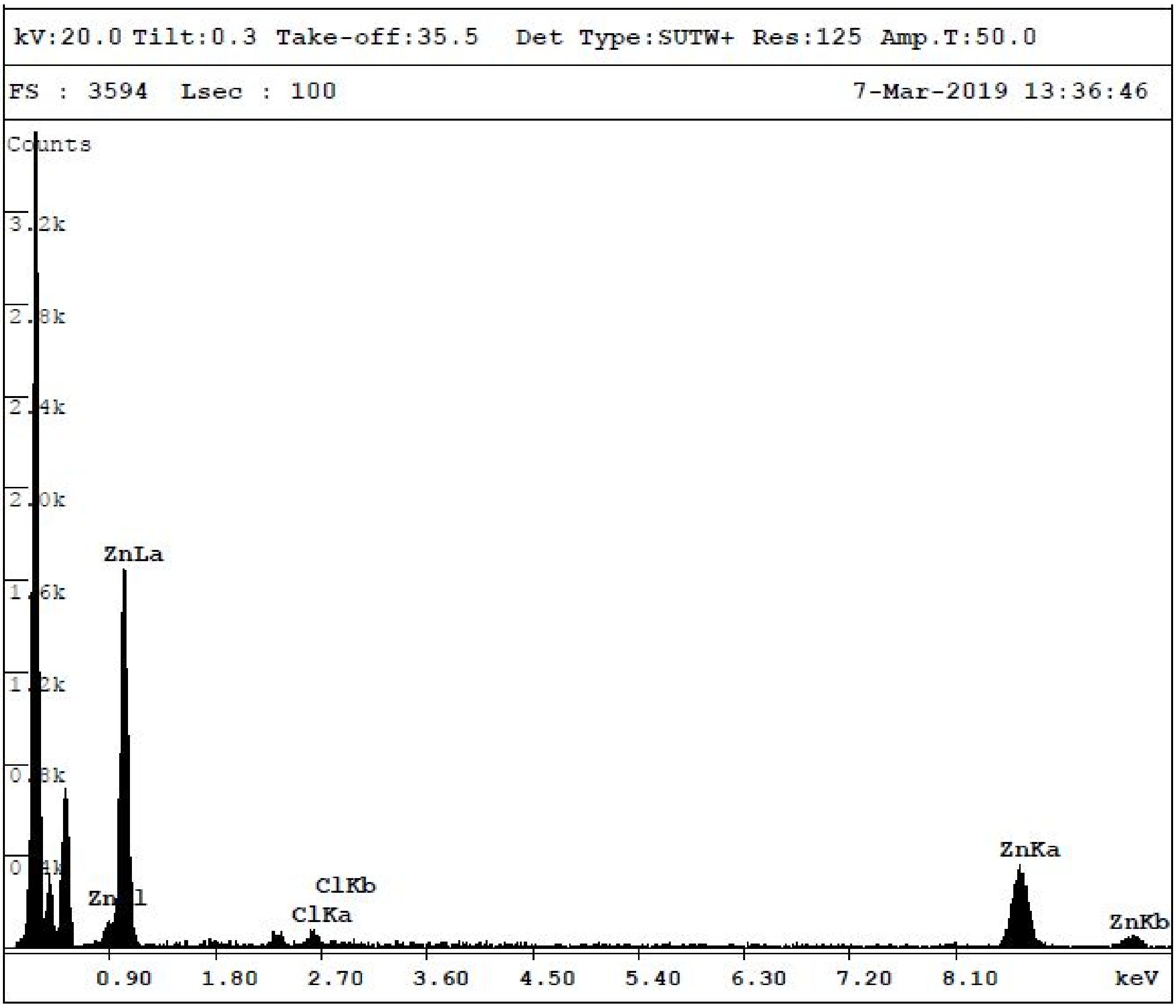

```
kV:20.0 Tilt:0.3  Take-off:35.5   Det Type:SUTW+  Res:125  Amp.T:50.0
FS :  3594   Lsec :  100                          7-Mar-2019 13:36:46
```

```
EDAX ZAF Quantification (Standardless)
Element Normalized
SEC Table : User  c:\edax32\eds\genuser.sec

Element    Wt %     At %    K-Ratio      Z         A         F
   ClK      2.83     5.11    0.0199   1.0967    0.6408    1.0000
   ZnK     97.17    94.89    0.9682   0.9968    0.9996    1.0000
 Total    100.00   100.00

Element   Net Inte.    Bkgd Inte.   Inte. Error        P/B
  ClK        5.22          0.30          4.62        17.40
  ZnK       42.94          0.16          1.53       268.37
```

Figure S 65: EDX spectrum and data of **1-t-Bu**

A 80

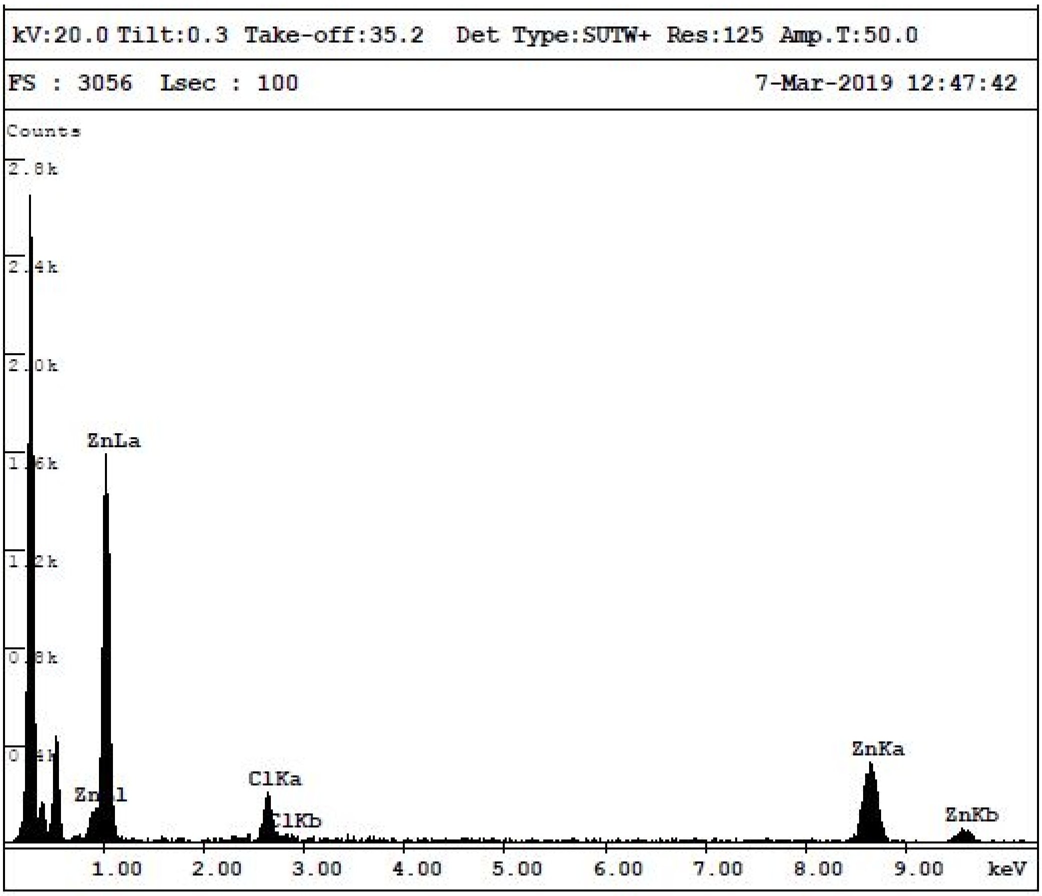

```
kV:20.0 Tilt:0.3 Take-off:35.2   Det Type:SUTW+ Res:125 Amp.T:50.0
FS : 3056   Lsec : 100                              7-Mar-2019 12:47:42
```

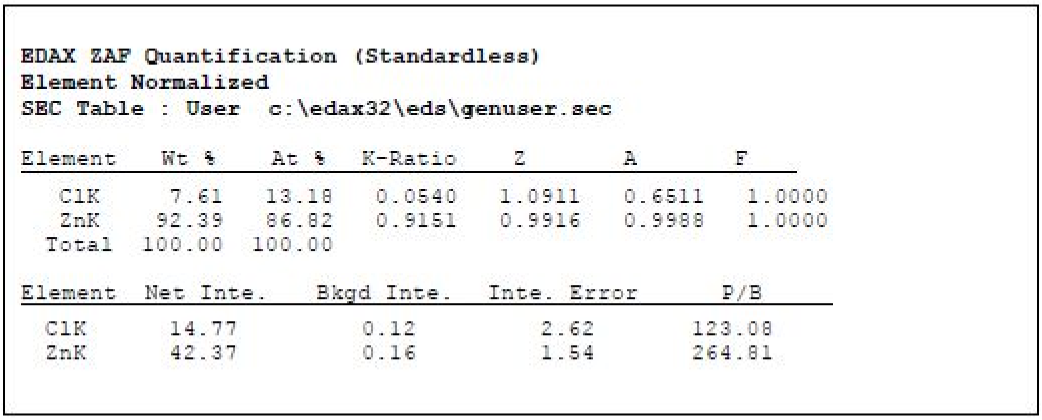

```
EDAX ZAF Quantification (Standardless)
Element Normalized
SEC Table : User   c:\edax32\eds\genuser.sec

Element    Wt %     At %   K-Ratio     Z        A        F
  ClK      7.61    13.18    0.0540   1.0911   0.6511   1.0000
  ZnK     92.39    86.82    0.9151   0.9916   0.9988   1.0000
 Total   100.00   100.00

Element  Net Inte.   Bkgd Inte.   Inte. Error      P/B
 ClK       14.77         0.12          2.62       123.08
 ZnK       42.37         0.16          1.54       264.81
```

Figure S 66: EDX spectrum and data of **1-H**

A 81

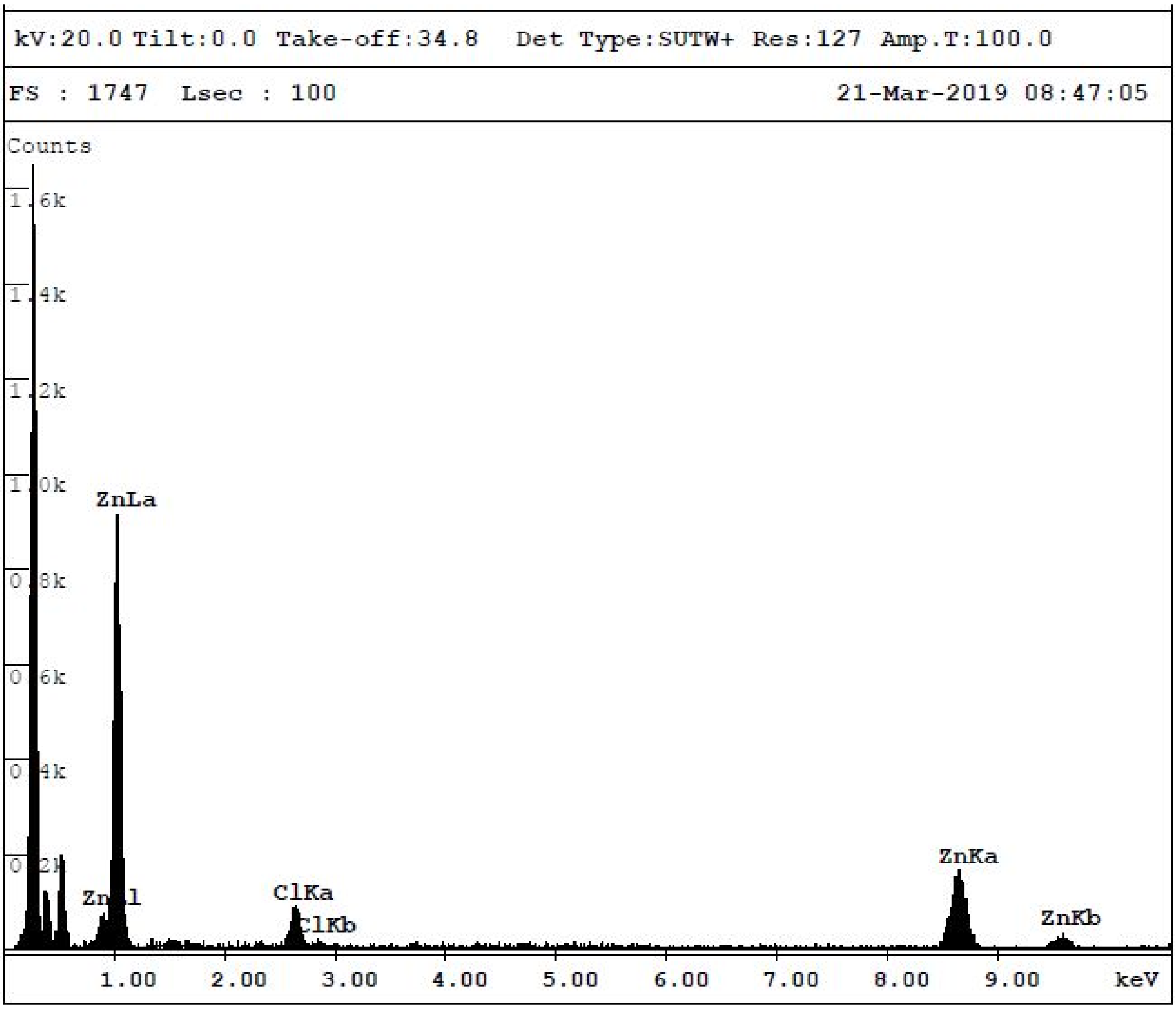

```
kV:20.0 Tilt:0.0  Take-off:34.8   Det Type:SUTW+  Res:127  Amp.T:100.0
FS :  1747   Lsec :  100                              21-Mar-2019 08:47:05
```

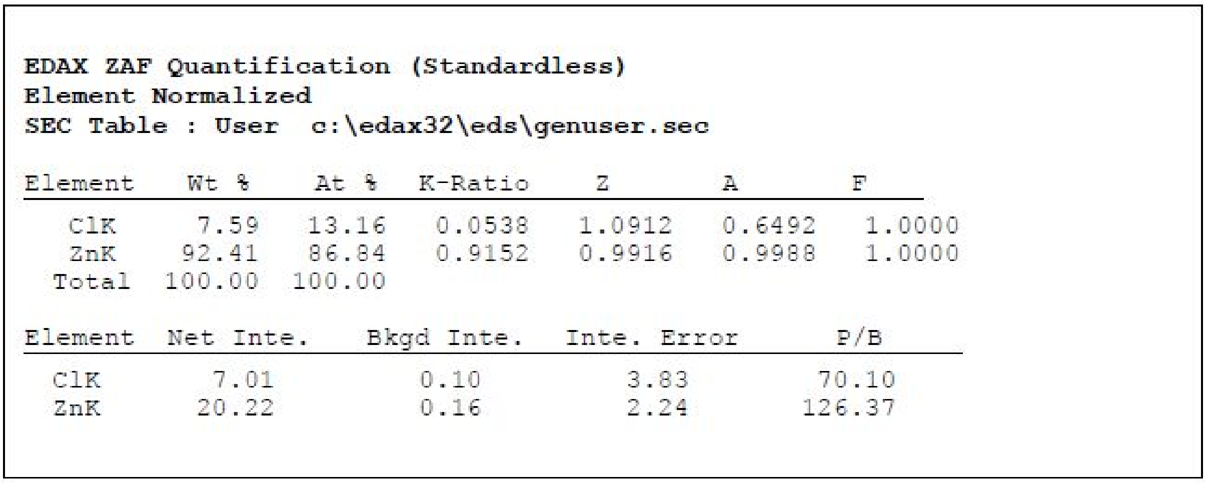

```
EDAX ZAF Quantification (Standardless)
Element Normalized
SEC Table : User  c:\edax32\eds\genuser.sec

Element    Wt %     At %   K-Ratio     Z        A        F
   ClK      7.59    13.16   0.0538   1.0912   0.6492   1.0000
   ZnK     92.41    86.84   0.9152   0.9916   0.9988   1.0000
  Total   100.00   100.00

Element  Net Inte.    Bkgd Inte.    Inte. Error      P/B
  ClK       7.01         0.10           3.83        70.10
  ZnK      20.22         0.16           2.24       126.37
```

Figure S 67: EDX spectrum and data of ***1-Butyne***

A 82

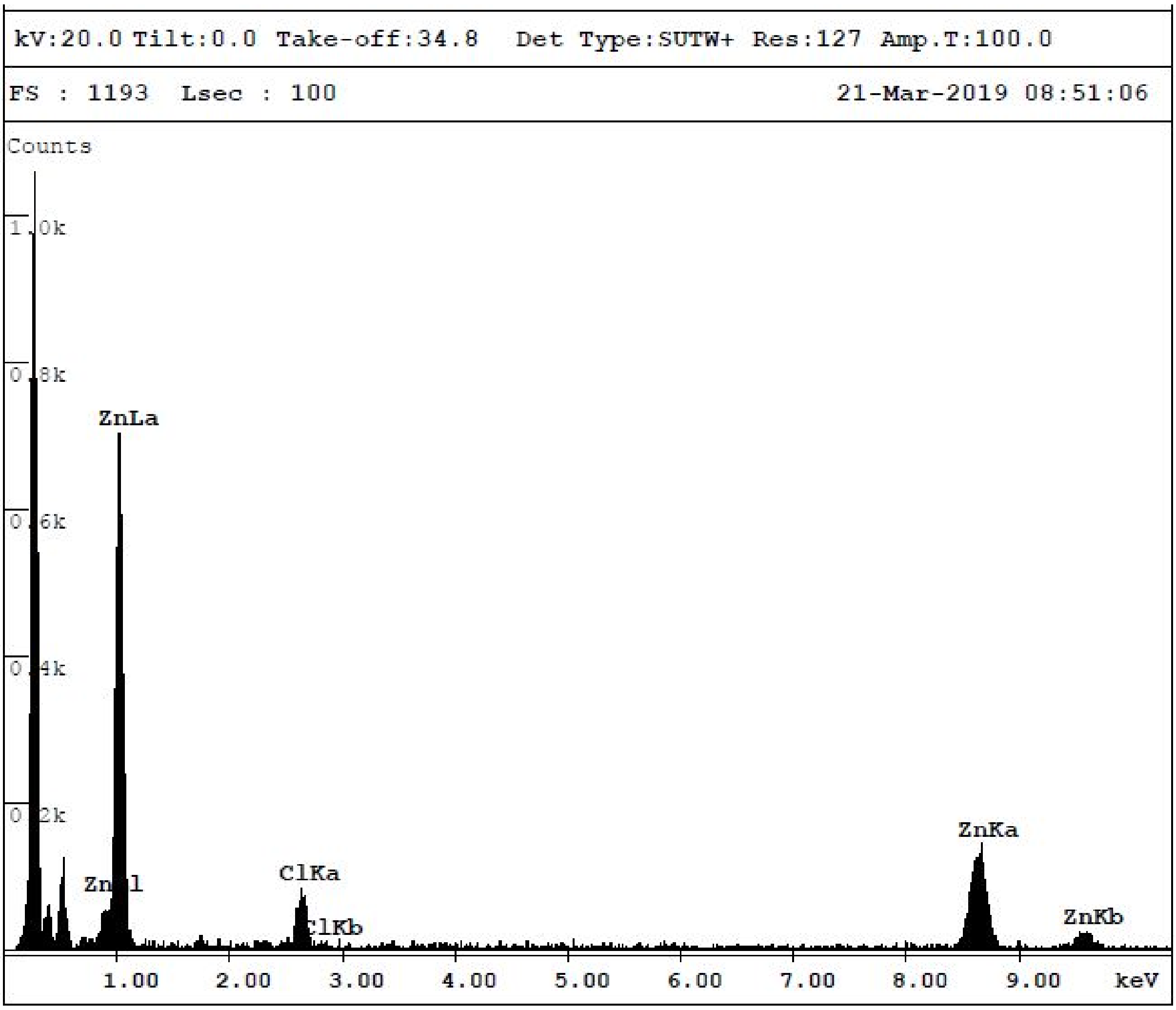

```
kV:20.0 Tilt:0.0  Take-off:34.8   Det Type:SUTW+  Res:127  Amp.T:100.0
FS : 1193   Lsec : 100                                21-Mar-2019 08:51:06
```

```
EDAX ZAF Quantification (Standardless)
Element Normalized
SEC Table : User  c:\edax32\eds\genuser.sec

Element    Wt %      At %    K-Ratio      Z          A          F
   ClK      7.47    12.96    0.0529    1.0913    0.6489    1.0000
   ZnK     92.53    87.04    0.9166    0.9918    0.9988    1.0000
  Total   100.00   100.00

Element   Net Inte.    Bkgd Inte.   Inte. Error       P/B
  ClK        6.17         0.10          4.09         61.70
  ZnK       18.11         0.16          2.37        113.19
```

Figure S 68: EDX spectrum and data of **1-Butyne**

A 83

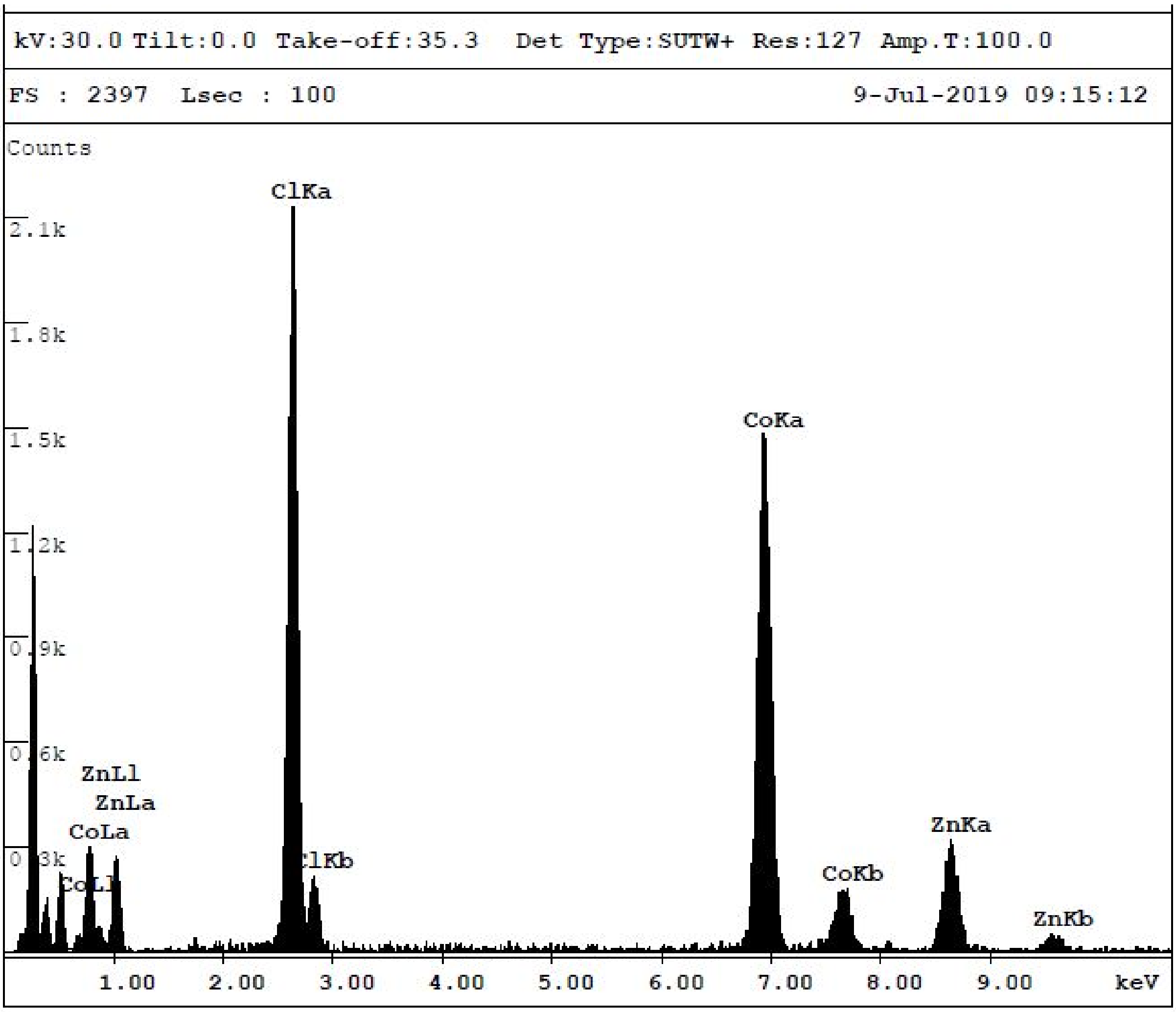

```
kV:30.0 Tilt:0.0  Take-off:35.3   Det Type:SUTW+  Res:127  Amp.T:100.0
FS : 2397   Lsec : 100                              9-Jul-2019 09:15:12
```

```
EDAX ZAF Quantification (Standardless)
Element Normalized
SEC Table : User  c:\edax32\eds\genuser.sec

Element    Wt %      At %   K-Ratio      Z          A          F
   ClK    31.60     44.10    0.2038   1.0447     0.6145     1.0046
   CoK    49.92     41.91    0.4851   0.9761     0.9657     1.0311
   ZnK    18.49     13.99    0.1601   0.9710     0.8921     1.0000
  Total  100.00    100.00

Element  Net Inte.    Bkgd Inte.   Inte. Error       P/B
  ClK     170.15          0.10          0.77       1701.50
  CoK     176.42          0.15          0.75       1176.13
  ZnK      39.18          0.16          1.60        244.88
```

Figure S 69: EDX spectrum and data of ***2***

A 84

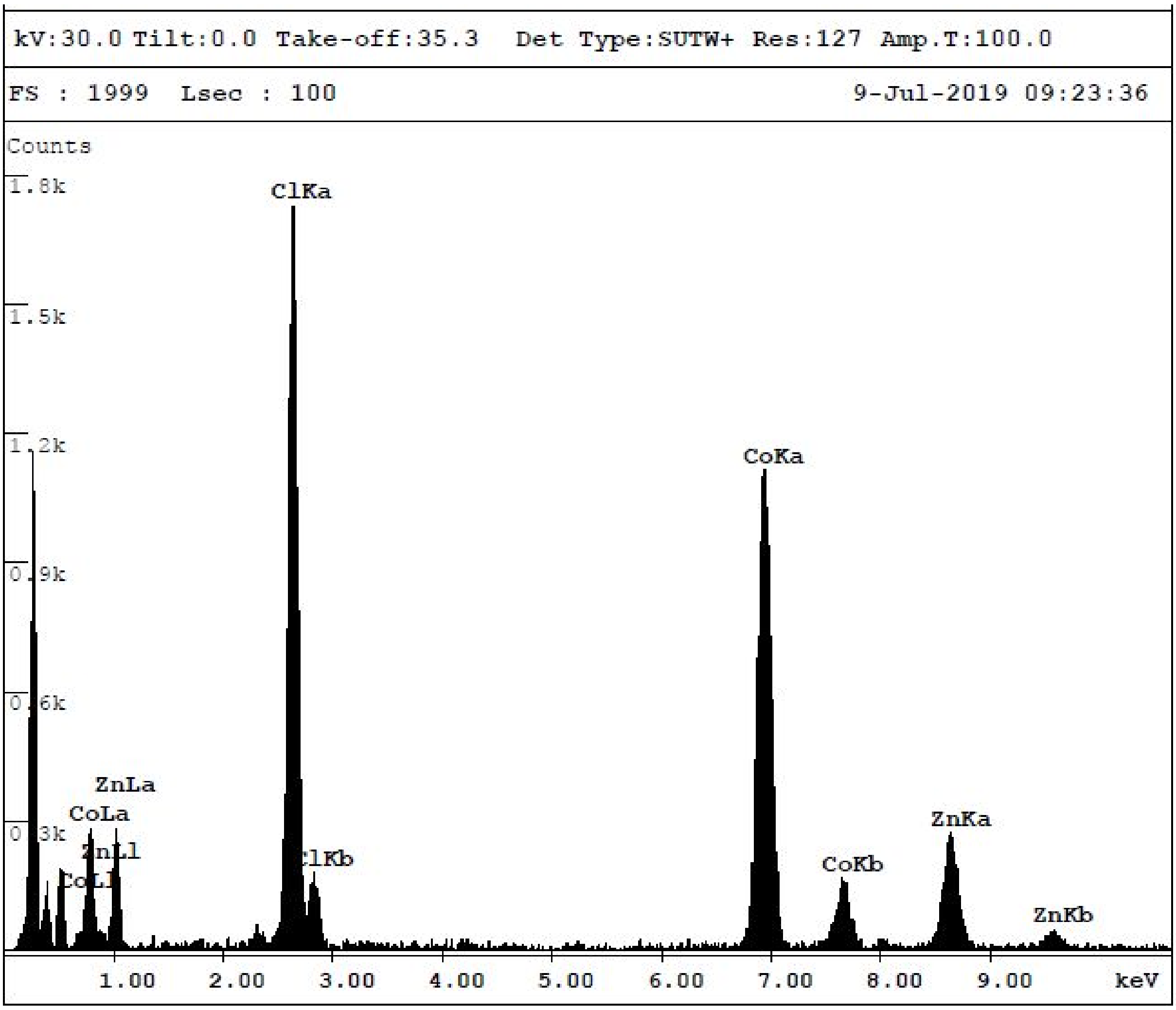

```
kV:30.0 Tilt:0.0  Take-off:35.3   Det Type:SUTW+  Res:127  Amp.T:100.0
FS : 1999   Lsec : 100                          9-Jul-2019 09:23:36
```

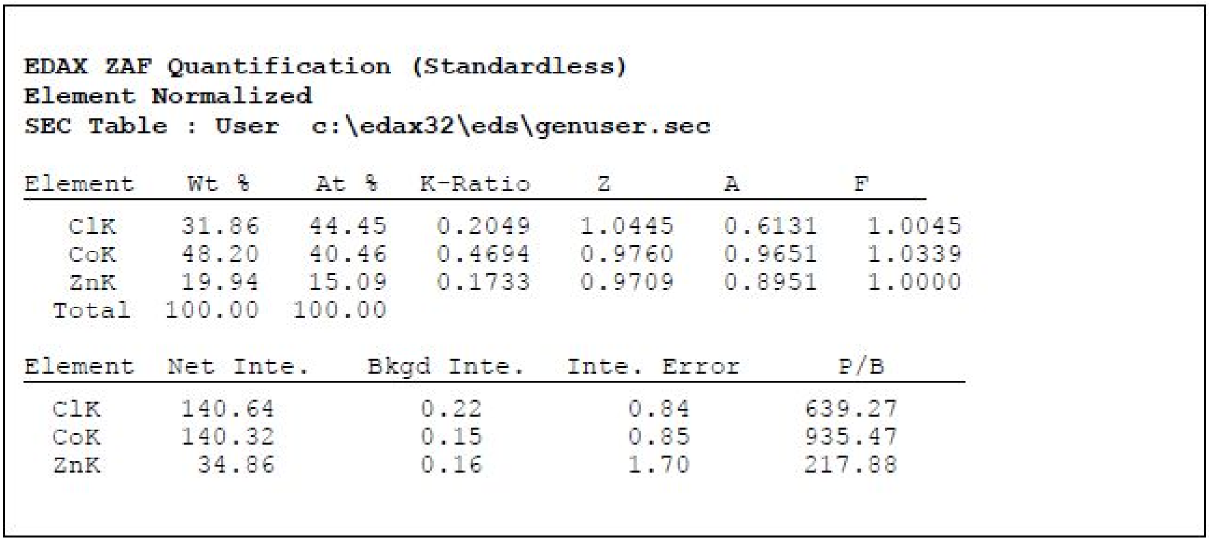

```
EDAX ZAF Quantification (Standardless)
Element Normalized
SEC Table : User  c:\edax32\eds\genuser.sec

Element     Wt %    At %   K-Ratio      Z        A        F
   ClK     31.86   44.45   0.2049   1.0445   0.6131   1.0045
   CoK     48.20   40.46   0.4694   0.9760   0.9651   1.0339
   ZnK     19.94   15.09   0.1733   0.9709   0.8951   1.0000
 Total    100.00  100.00

Element   Net Inte.    Bkgd Inte.   Inte. Error      P/B
  ClK      140.64          0.22          0.84       639.27
  CoK      140.32          0.15          0.85       935.47
  ZnK       34.86          0.16          1.70       217.88
```

Figure S 70: EDX spectrum and data of **2**

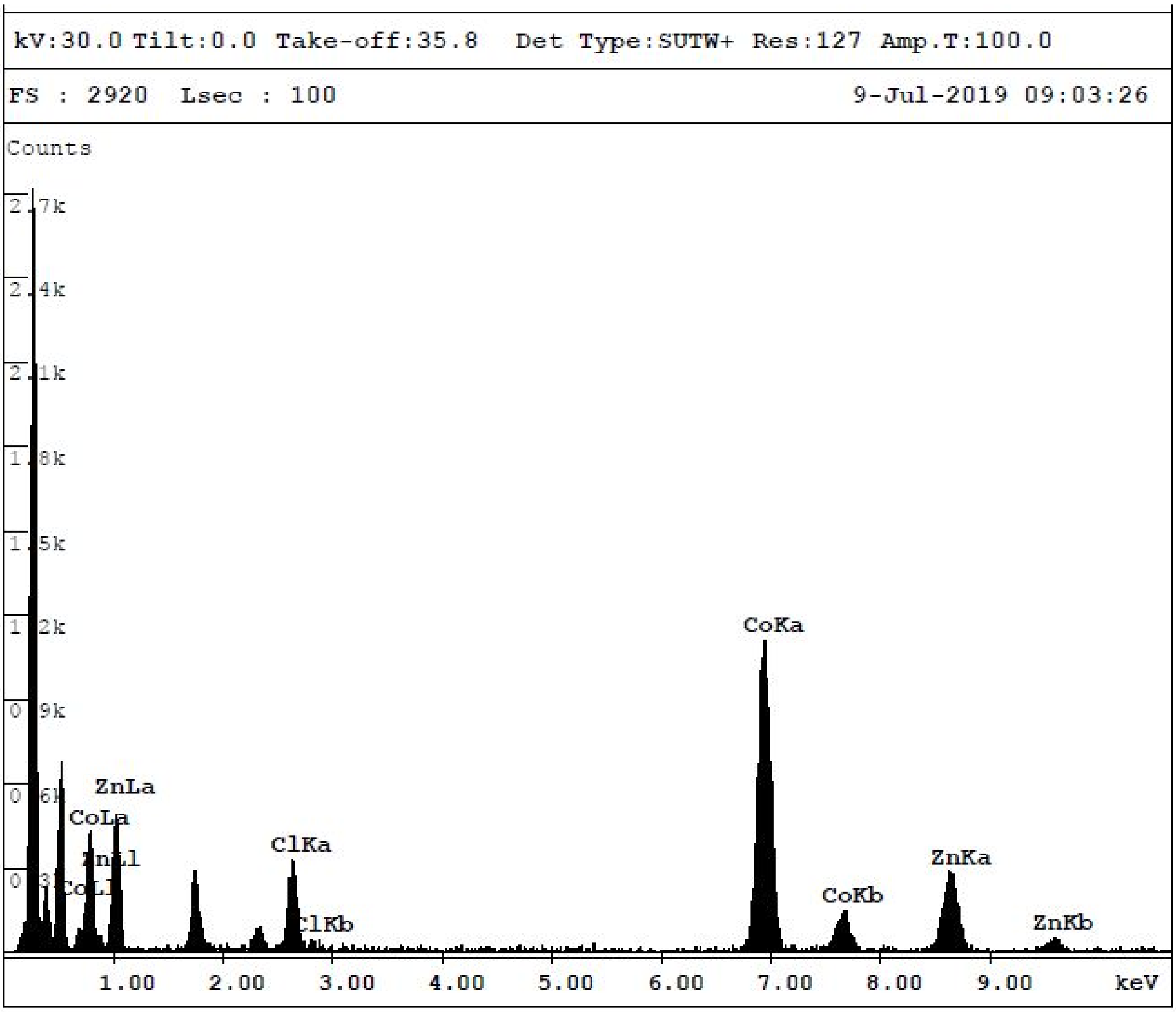

```
kV:30.0 Tilt:0.0  Take-off:35.8   Det Type:SUTW+  Res:127  Amp.T:100.0
FS : 2920   Lsec : 100                              9-Jul-2019 09:03:26
```

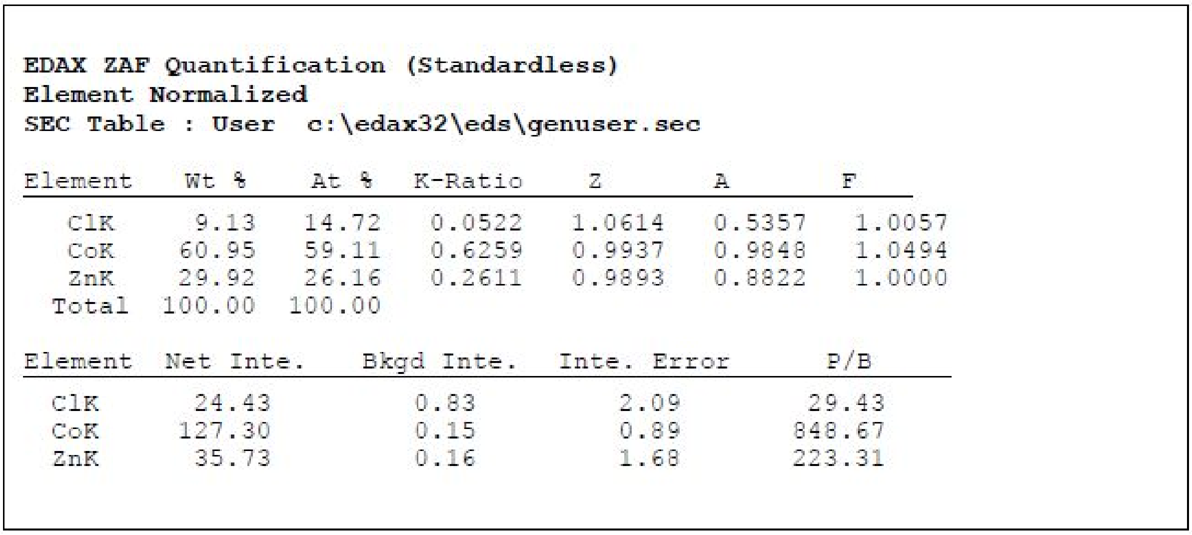

```
EDAX ZAF Quantification (Standardless)
Element Normalized
SEC Table : User   c:\edax32\eds\genuser.sec

Element    Wt %     At %   K-Ratio      Z         A         F
   ClK      9.13    14.72   0.0522   1.0614   0.5357   1.0057
   CoK     60.95    59.11   0.6259   0.9937   0.9848   1.0494
   ZnK     29.92    26.16   0.2611   0.9893   0.8822   1.0000
  Total   100.00   100.00

Element  Net Inte.    Bkgd Inte.   Inte. Error      P/B
  ClK      24.43          0.83          2.09        29.43
  CoK     127.30          0.15          0.89       848.67
  ZnK      35.73          0.16          1.68       223.31
```

Figure S 71: EDX spectrum and data of **2-Me**

A 86

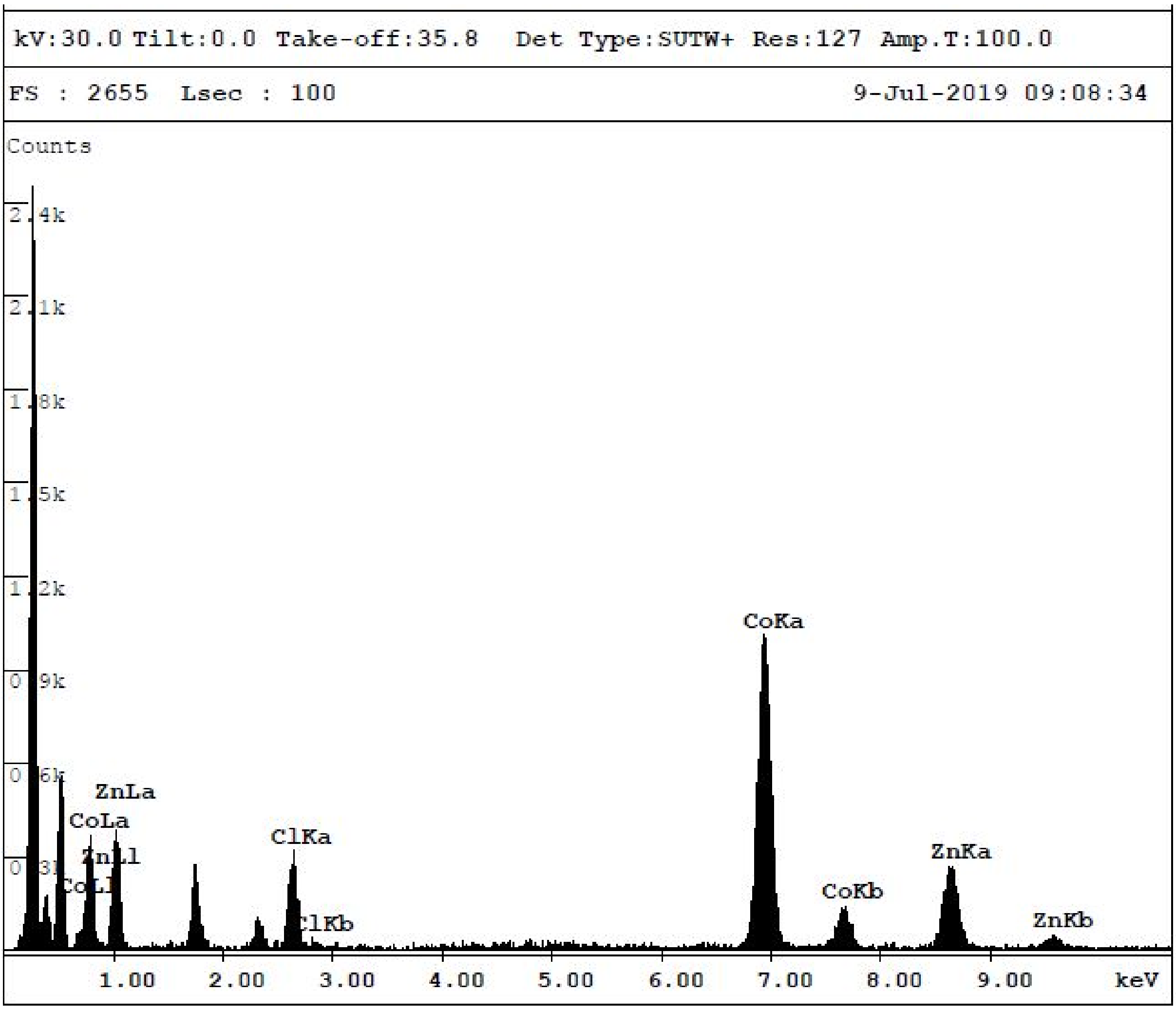

```
kV:30.0 Tilt:0.0  Take-off:35.8   Det Type:SUTW+  Res:127  Amp.T:100.0
FS : 2655   Lsec : 100                               9-Jul-2019 09:08:34
```

```
EDAX ZAF Quantification (Standardless)
Element Normalized
SEC Table : User  c:\edax32\eds\genuser.sec

Element    Wt %     At %   K-Ratio     Z          A         F
   ClK      9.31    15.00   0.0532   1.0613    0.5355    1.0056
   CoK     60.25    58.40   0.6192   0.9936    0.9845    1.0505
   ZnK     30.44    26.60   0.2660   0.9892    0.8834    1.0000
 Total   100.00   100.00

Element   Net Inte.    Bkgd Inte.   Inte. Error       P/B
  ClK       23.36         0.10          2.08        233.60
  CoK      118.15         0.30          0.92        393.83
  ZnK       34.14         0.16          1.72        213.38
```

Figure S 72: EDX spectrum and data of **2-Me**

A 87

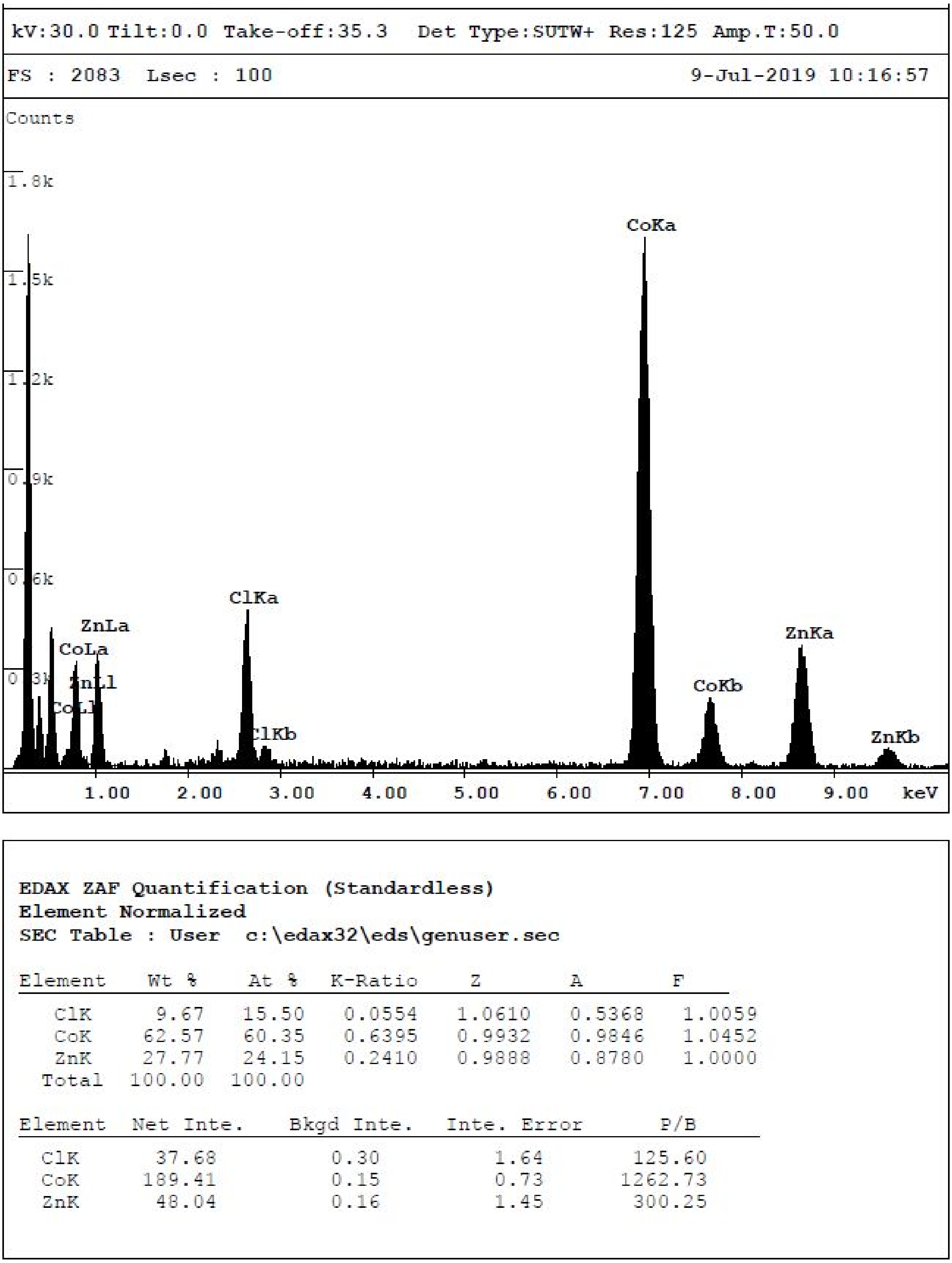

```
kV:30.0 Tilt:0.0  Take-off:35.3   Det Type:SUTW+  Res:125  Amp.T:50.0
FS : 2083   Lsec : 100                              9-Jul-2019 10:16:57
```

```
EDAX ZAF Quantification (Standardless)
Element Normalized
SEC Table : User  c:\edax32\eds\genuser.sec

Element    Wt %     At %   K-Ratio      Z        A        F
   ClK      9.67    15.50   0.0554   1.0610   0.5368   1.0059
   CoK     62.57    60.35   0.6395   0.9932   0.9846   1.0452
   ZnK     27.77    24.15   0.2410   0.9888   0.8780   1.0000
  Total   100.00   100.00

Element  Net Inte.    Bkgd Inte.    Inte. Error      P/B
  ClK       37.68          0.30          1.64       125.60
  CoK      189.41          0.15          0.73      1262.73
  ZnK       48.04          0.16          1.45       300.25
```

Figure S 73: EDX spectrum and data of **2-OH**

A 88

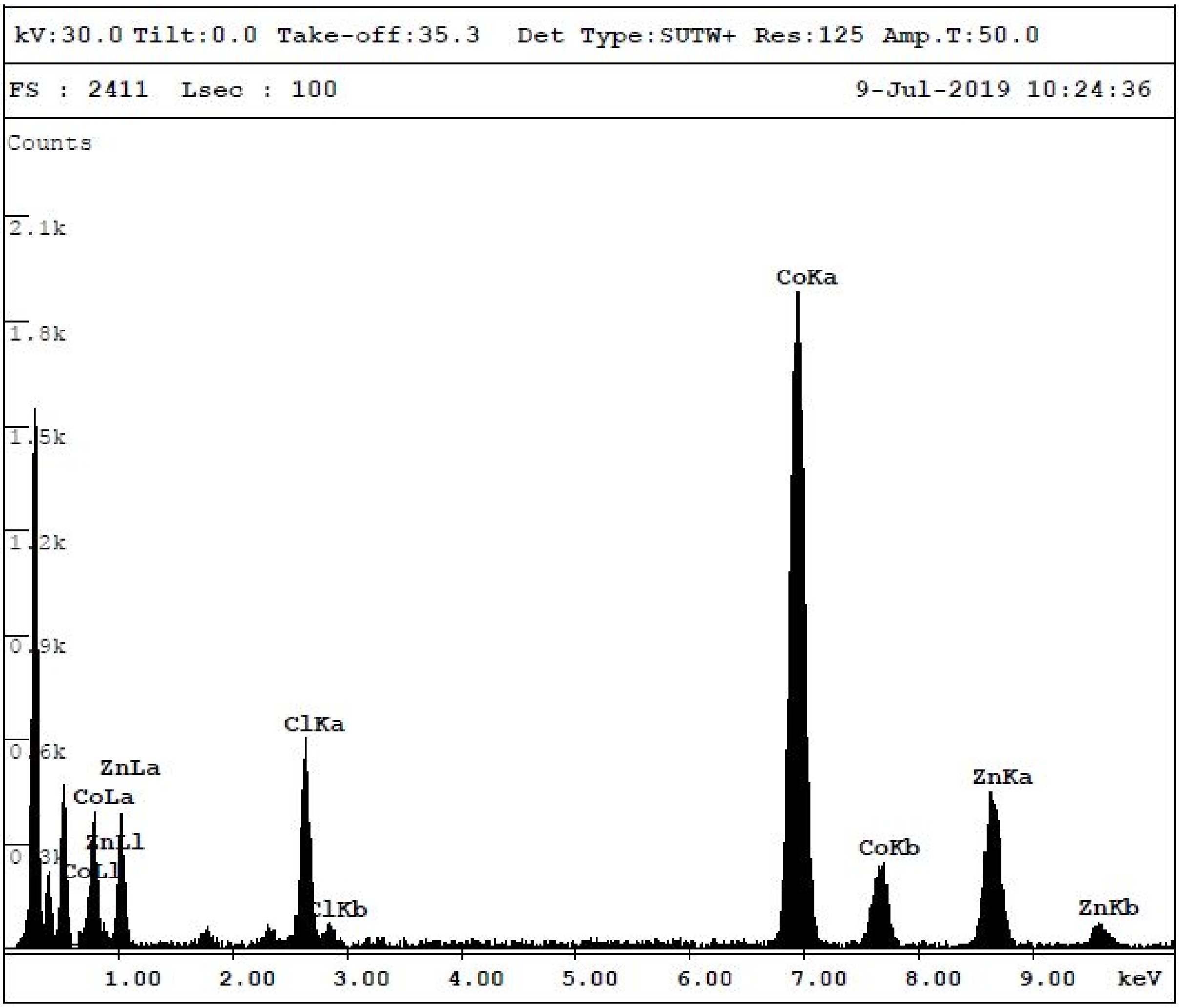

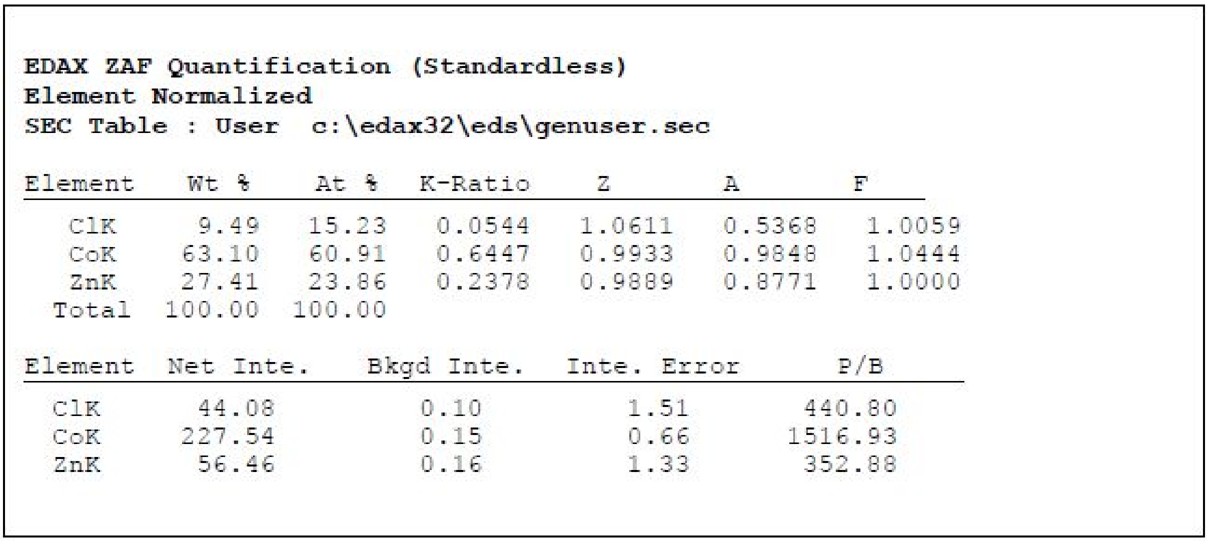

```
EDAX ZAF Quantification (Standardless)
Element Normalized
SEC Table : User  c:\edax32\eds\genuser.sec

Element    Wt %     At %   K-Ratio     Z          A          F
   ClK      9.49    15.23   0.0544   1.0611    0.5368    1.0059
   CoK     63.10    60.91   0.6447   0.9933    0.9848    1.0444
   ZnK     27.41    23.86   0.2378   0.9889    0.8771    1.0000
  Total   100.00   100.00

Element  Net Inte.    Bkgd Inte.   Inte. Error        P/B
  ClK      44.08          0.10          1.51        440.80
  CoK     227.54          0.15          0.66       1516.93
  ZnK      56.46          0.16          1.33        352.88
```

Figure S 74: EDX spectrum and data of **2-OH**

CRYSTAL GROWTH & DESIGN

pubs.acs.org/crystal Article

Assembly of Porous Metal Hydrogen-Bonded Organic Frameworks from Diamine-Functionalized Kuratowski Complexes

Richard Röß-Ohlenroth, Corbinian Freudig, Maryana Kraft, Hana Bunzen, and Dirk Volkmer*

Cite This: *Cryst. Growth Des.* 2022, 22, 379−391

Read Online

ACCESS | Metrics & More | Article Recommendations | Supporting Information

ABSTRACT: In comparison to the vast field of porous materials, research into hydrogen-bonded organic frameworks (HOFs)—and especially the subclass of metal hydrogen-bonded organic frameworks (M-HOFs), with only very few structures showing permanent porosity thus far—is still in its infancy. Herein, Kuratowski coordination units, which are well-known from various complexes and metal−organic frameworks, were applied to advance this field of research with the synthesis and characterization of a novel series of M-HOFs. Synthesis of Kuratowski complexes with the 1*H*-benzotriazole-5,6-diamine (**H-btda**) ligand resulted in molecular building blocks, which initially assemble into **CFA-20-Cl** and **CFA-20-Br** M-HOFs ($(2,6\text{-lutidinium})^+[Zn_5X_4(btda)_6X]^-\cdot n(DMF)$; X = Cl, Br; CFA-20 = Coordination Framework Augsburg University-20, DMF = *N*,*N*-dimethylformamide). Both frameworks are isostructurally stabilized via a unique hydrogen bond framework between 12 amine functional groups of six **btda** ligands and a central 12-fold hydrogen bonded halogen anion, which adapts the coordination of an irregular icosahedron. Postsynthetic ligand exchange at the Kuratowski complex of **CFA-20-Cl** performed with Tp and Tp* ligands resulted in permanently porous **CFA-20-Tp** and **CFA-20-Tp*** M-HOFs ($[Zn_5Y_4(btda)_6]$; Y = Tp (trispyrazolylborate), Tp* (tris(3,5-dimethyl-1-pyrazolyl)borate)), which, thus, constitute an important addition to the meager subclass of permanently porous M-HOFs. Crystallization of the soluble complex of **CFA-20-Tp*** from dimethylsulfoxide (DMSO) was additionally shown to result in a variant **CFA-20-Tp*-DMSO** M-HOF structure.

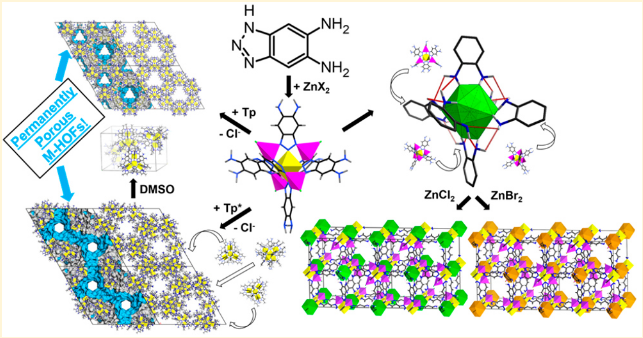

■ INTRODUCTION

After metal−organic frameworks (MOFs) and covalent organic frameworks (COFs), hydrogen-bonded organic frameworks (HOFs) have recently gained increasing interest as functional and porous materials, which allow for processing, regeneration, and recrystallization from solution, because of the reversibility of hydrogen bond formation.[1−4] Although HOFs are usually constructed from pure organic building blocks, metal hydrogen-bonded organic frameworks (M-HOFs), assembled from metal complexes, have been recently defined as a novel subclass of HOFs,[5] of which only a few examples with permanent porosity are known thus far.[5−13] The porosity of M-HOFs can hereby originate from the pores of preformed metal−organic cages (MOC), intermolecular voids, or even both.[12,13] Herein, the assembly, structures, and properties of M-HOFs constructed from complexes featuring the unique Kuratowski-type coordination motif were examined in detail.

The Kuratowski-type coordination unit has a T_d point group symmetry and consists of a central divalent metal ion, which is octahedrally coordinated by the central N atom of the six triazolate ligands and enclosed by a tetrahedron composed of four peripheral metal ions (see Figure 1).[14] Depending on the nature and valency of those peripheral metal sites, they can adopt a coordination number from three to six, based on the

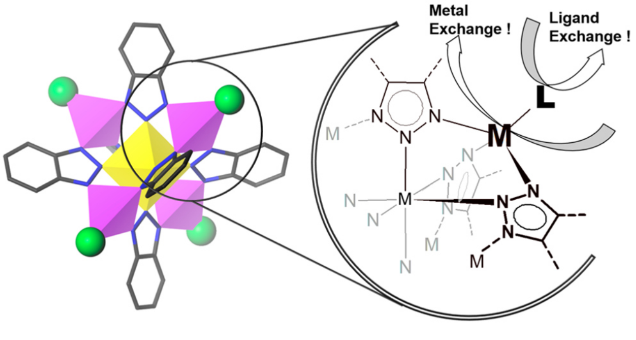

Figure 1. Standard $[M_5Cl_4(bta)_6]$-Kuratowski SBU (bta = benzotriazolate) with the central octahedrally coordinated (yellow) and the four exchangeable peripheral tetrahedrally coordinated metal ions (purple), as well as the exchangeable chloride side ligand (green).

Received: September 1, 2021
Revised: December 1, 2021
Published: December 16, 2021

ACS Publications

https://doi.org/10.1021/acs.cgd.1c01008

scorpionate-type coordination from three lateral triazolate N atoms and exchangeable side ligands. Therefore, each of the peripheral metal centers resembles the coordination in mononuclear tris(pyrazolyl)borate (TP) complexes. After the first investigations on triazolate-based pentanuclear complexes such as $[Cu_5(acac)_4(bta)_6]$ (acac = acetylacetonate; bta = benzotriazolate) with varying side ligands, valences, or metal ions in the last century,[15−21] an increasing variety of complexes and MOFs featuring Kuratowski-type coordination units have been discovered and investigated in recent years.[14,22−30]

In particular, postsynthetic metal and ligand exchange at the Kuratwoski secondary building units (SBUs) of MFU-4-type MOFs gives rise to an increasing variety of applications, such as CO_2 binding,[31−35] catalytic reactions,[36−43] kinetic trapping of gases,[44,45] H_2/D_2 quantum sieving,[46,47] and drug delivery.[48] In addition, some complexes and MOFs composed of condensed Kuratowski units have been found to exhibit fascinating physical phenomena, such as Jahn−Teller phase transitions,[49] spin-crossover transitions,[50,51] and electronic conductivity.[52]

Kuratowski-type complexes also reveal great potential for MOF synthesis via molecular building block (MBB) approaches connecting the prebuilt SBUs via ligand exchange with dicarboxylate bridges at the peripheral zinc ions.[53,54] To date, the main research in the synthesis of novel Kuratowski complexes has centered on the properties of different metal ions and side ligands, choosing triazolate ligands such as 1*H*-1,2,3-benzotriazole (**H-bta**), 5,6-dimethyl-1*H*-1,2,3-benzotriazole (**H-Me$_2$bta**), and 5,6-dimethoxy-1*H*-1,2,3-benzotriazole (**H-OMe$_2$bta**), mostly because of solubility, commercial availability, or ligand field strength.[26,50] We are aware of only one example of a tetrathiafulvalene-functionalized redox-active ligand.[55] However, we believe that an additional functionalization of the triazole ligand greatly increases the potential of such complexes and could also enable the synthesis of M-HOFs, which (to the best of our knowledge) have never been prepared from any Kuratowski complexes thus far. Therefore, herein, we synthesized the 1*H*-benzotriazole-5,6-diamine (**H-btda**) ligand and investigated it as a building block not only to prepare new Kuratowski complexes but also to unlock its potential as a precursor to form M-HOFs. Overall, we report five new potentially porous frameworks, which are assembled from Kuratowski complexes and are stabilized via hydrogen bond interactions of the free amine functional groups of the **btda$^-$** ligands, namely, **CFA-20-Cl** and **CFA-20-Br** ((2,6-lutidinium)$^+$[Zn$_5$X$_4$(btda)$_6$X]$^-$·*n*(DMF); X = Cl, Br)), **CFA-20-Tp** ([Zn$_5$Tp$_4$(btda)$_6$]) and **CFA-20-Tp*** ([Zn$_5$Tp*$_4$(btda)$_6$]) with scorpionate Tp or Tp* (Tp = trispyrazolylborate; Tp*= (tris(3,5-dimethyl-1-pyrazolyl)-borate) ligands, and the **CFA-20-Tp*-DMSO** structure obtained by crystallization of **CFA-20-Tp*** from DMSO. **CFA-20-Tp** and **CFA-20-Tp*** proved to be the most stable structures, even revealing permanent porosity.

■ EXPERIMENTAL SECTION

General Materials and Methods. All chemicals were of reagent grade and used as obtained from the commercial supplier. 5,6-Dinitro-1*H*-benzotriazole was synthesized starting from *o*-phenylenediamine, following literature procedures.[56−58] Nbu$_4$Tp and Nbu$_4$Tp* were obtained via the metathesis reaction of tetrabutylammonium chloride and commercially available Tp and Tp* potassium salts in dry THF, similar to the literature.[28] Silanized snap cap glass vials were obtained by treatment with a 5% v/v solution of dichlorodimethylsilane in DCM for several minutes followed by rinsing with DCM. Fourier-transform infrared spectra (FT-IR) were recorded with a Bruker Equinox 55 FT-IR spectrometer utilizing a PLATINUM ATR unit and a KBr beam splitter in the wavenumber range from 4000−400 cm^{-1}, and the measured signals were labeled strong (s), medium (m), weak (w) and broad (br). A TA Instruments Q500 device was used to obtain the thermogravimetric analysis (TGA) data in a temperature range of 25−800 °C under a nitrogen atmosphere with a heating rate of 5 C min^{-1} starting after a 5 min isothermal step. Powder X-ray diffraction patterns (PXRD) were collected at room temperature in the 3°−40° 2θ range with a Seifert XRD 3003 TT powder diffractometer with a Meteor1D detector and Cu Kα_1 radiation. An Empyrean (PANalytical) diffractometer equipped with a Bragg−Brentano^{HD} mirror, PIXcel^{3D} 2 × 2 detector, Cu Kα_1 radiation and XRK 900 reactor chamber was used to collect the VT-PXRD pattern in the 2θ range of 2°−40° with a step size of 0.026° and a measurement time of 1323 s for each pattern. The samples were heated at a rate of 5 °C min^{-1} with a 30 min isothermal step prior to measurement under a nitrogen atmosphere. X-ray single-crystal diffraction data were collected using a Bruker D8 Venture diffractometer (Mo Kα radiation, λ = 0.71073 Å) equipped with a low-temperature device on crystals directly picked from the mother liquor. The raw data frames were integrated and corrected for absorption effects using the Bruker SAINT[59] and SADABS[60] software packages. Structure solutions were obtained by direct methods and structure refinement using SHELXT 2014/5[61] and SHELXL 2018/3.[62] All nonhydrogen atoms were refined anisotropically. Hydrogen atoms were placed at idealized positions and refined using a riding model. In **CFA-20-Tp**, hydrogen atoms of NH$_2$ groups were refined at randomly occupied positions corresponding to the sp^3-hybridization state of N atoms with a 2/3 occupancy factor. In the **CFA-20-Cl**, **CFA-20-Br**, **CFA-20-Tp***, and **CFA-20-Tp*-DMSO** structures, part or all of the NH$_2$ groups were placed corresponding to the sp^3-hybridization state of the N atoms at positions selected according to the result of quantum mechanical simulations of the cut-out HOF SBUs. Energy-dispersive X-ray spectra (EDX) were obtained with a Philips XL 30 FEG equipped with an EDAX SiLi detector and used to determine the Zn:Cl ratios. Argon adsorption isotherms for the samples were measured after a 3 h vacuum treatment in the range $5.00 \times 10^{-5} \leq p/p_0 \leq 1.00$ at 77.3 K with a Quantachrome Autosorb-I ASI-CP-8 instrument. BET surface areas that are in accordance with the criteria suggested by Rouquerol et al.,[63] as well as nonlocal density functional theory (NLDFT) pore size distributions via implementation of a carbon equilibrium kernel for argon adsorption at 77 K based on a slit pore model, were obtained with Autosorb-I software.[64,65] Molecular masses were measured with a Q-Tof Ultima mass spectrometer (Micromass) equipped with an ESI source. Mass spectra were calibrated using phosphoric acid. The composition of the ions was verified by a comparison of the experimental and theoretical mass values. Elemental analyses were conducted on a Vario EL III instrument from Elementar Analysensysteme GmbH.

Synthesis of 1*H*-benzotriazole-5,6-diamine (H-btda). 5,6-Dinitro-1*H*-benzotriazole (6.00 g, 28.7 mmol) and 10% Pd/C (6.00 g, 50 wt % water content) were stirred vigorously in 250 mL of MeOH under a hydrogen atmosphere (5 bar) overnight. The catalyst was removed by double filtration and washed with 100 mL of MeOH. The solvent was removed under reduced pressure, and the resulting light brown solid was dried under vacuum overnight (3.66 g, 86%). melting point (mp): 197−200 °C with partial decomposition ^{1}H NMR (400 MHz, DMSO-d_6, 20 °C): δ = 14.46 (s, 1H, N−H), 6.80 (s, 2H, Ar−H), 4.91 ppm (s, 4H, NH2) ^{1}H NMR (400 MHz, D$_2$SO$_4$, 20 °C): δ = 8.69 (s, 2H, Ar−H) ppm; ^{13}C NMR (100 MHz, D$_2$SO$_4$, 20 °C): δ = 133.82, 126.43, 115.81 ppm; FT-IR (ATR cm^{-1}): 3392 (w), 3367 (w), 3323 (w), 3079 (br), 2989 (w), 2909 (w), 2809 (w), 1641 (m), 1587 (m), 1513 (vw), 1487 (s), 1425 (vw), 1406 (w), 1337 (s), 1303 (w), 1260 (w), 1215 (s), 1189 (vw), 1172 (w), 1058 (s), 998 (m), 978 (vw), 886 (vw), 853 (vw), 809 (s, br), 630 (w), 582 (br), 448 (m), 433 (w); HRMS (ESI$^-$) *m*/*z* calcd for $C_6H_6N_5-$ = 148.0629 [M−H]$^-$; found: 148.0623.

Synthesis of [Zn$_5$Cl$_4$(btda)$_6$]·HCl (CFA-20-Cl Complex). **H-btda** (1.00 g, 6.7 mmol) and ZnCl$_2$ (1.53 g, 11.2 mmol) were dissolved under argon atmosphere in 15 mL of DMF. Then, 2,6-lutidine (1.17 mL, 10.1 mmol) was added dropwise to the mixture and stirred for 3 h, already showing some precipitate. More product was precipitated via slow addition of 30 mL of MeOH. Filtration and washing with copious amounts of MeOH gave the product as a beige amorphous powder after vacuum drying (0.88 g, 56%). ^{1}H NMR (400 MHz, DMSO-d_6, 20 °C): $\delta = 7.17$ (s, 12H), 5.43 (s, 24H); ESI$^-$-MS: expected: $[M-H]^- = 1392.85$ m/z; found: $[M-H]^- = 1392.87$ m/z; FT-IR (ATR, 4000−400 cm^{-1}): 3322 (m), 1638 (m), 1572 (m), 1481 (s), 1346 (m), 1273 (w), 1215 (m), 1161 (s), 1052 (w), 875 (w), 836 (m), 735 (w), 596 (w), 501 (m), 471 (m), 427 (m); EDX Zn/Cl ratio: expected 5/5 and measured 5/4.94.

Synthesis of [$Zn_5Br_4(btda)_6$]·HBr (CFA-20-Br Complex). **H-btda** (100 mg, 0.67 mmol) and $ZnBr_2$ (126 mg, 0.56 mmol) were dissolved under an argon atmosphere in 1.5 mL of DMF. Then, 2,6-lutidine (0.12 mL, 1.0 mmol) was added dropwise to the mixture and stirred for 3 h. The product was precipitated via slow addition of 3 mL of MeOH. Filtration and washing with copious amounts of MeOH gave the product as a white amorphous powder after vacuum drying (87 mg, 48%). ^{1}H NMR (400 MHz, DMSO-d_6, 20 °C): $\delta = 7.28$ (s, 12H), 5.44 (s, 24H); ESI$^-$-MS: expected: $[M-H]^- = 1614.60$ m/z; found: $[M-H]^- = 1614.57$ m/z; FT-IR (ATR, 4000−400 cm^{-1}): 3336 (br), 1639 (m), 1573 (m), 1484 (s), 1386 (w), 1348 (m), 1317 (w), 1274 (w), 1216 (m), 1164 (s), 1096 (w), 1053 (w), 876 (m), 839 (m), 736 (w), 659 (br), 605 (br), 502 (m), 472 (m), 428 (m); EDX Zn/Br ratio: expected 5/5 and measured 5/5.11.

Single-Crystal Synthesis of (2,6-Lutidinium)$^+$-[$Zn_5X_4(btda)_6X$]$^-$·*n*(DMF) (CFA-20-Cl and CFA-20-Br M-HOFs). **H-btda** (10.0 mg, 0.067 mmol) and ZnX_2 ($ZnCl_2$: 7.6 mg, $ZnBr_2$: 12.6 mg, 0.056 mmol) were dissolved in 0.5 mL of DMF in a silanized 3-mL snap cap vial. This vial was placed into a 20-mL snap cap vial filled with 6 mL of methanol and 0.5 mL of 2,6-lutidine, purged with argon, and then capped. The single crystals formed within a few days.

Synthesis of [$Zn_5Tp_4(btda)_6$] (CFA-20-Tp). The **CFA-20-Cl** complex (100 mg, 0.07 mmol) was dissolved in 6 mL of DMF, and NBu_4Tp (270 mg, 0.59 mmol) dissolved in 4 mL of DMF was added dropwise under an argon atmosphere. The solution was stirred for 1 h, and the product precipitated via slow addition of 10 mL MeOH over 2 h. Filtration and washing with copious amounts of MeOH gave the product as a white powder after vacuum drying (120 mg, 81%). FT-IR (ATR, 4000−400 cm^{-1}): 2453 (w), 1642 (w), 1575 (w), 1501 (m), 1478 (m), 1402 (m), 1391 (w), 1337 (w), 1306 (m), 1267 (w), 1210 (m), 1189 (m), 1172 (m), 1111 (m), 1062 (w), 1043 (s), 974 (w), 874 (w), 846 (m), 809 (w), 753 (m), 717 (s), 664 (s), 621 (m), 495 (w), 466 (w), 439 (w); EDX Zn/Cl ratio: expected 5/0 and measured 5/0.06; elemental analysis calcd (%) for $C_{72}H_{76}B_4N_{55}Zn_5$: C 41.82, H 3.70, N 36.57; found: C 41.61, H 3.94, N 35.97.

[$Zn_5Tp^*_4(btda)_6$] (CFA-20-Tp*). The **CFA-20-Cl** complex (0.70 g, 0.5 mmol) was dissolved in 75 mL of DMF, and NBu_4Tp^* (2.20 g, 4.1 mmol) dissolved in 15 mL of DMF was added dropwise under an argon atmosphere. The solution was stirred for 2 h, and the product precipitated via slow addition of 100 mL H_2O. Filtration and washing with copious amounts of MeOH gave the product as a white powder after vacuum drying (0.90 g, 75%). ^{1}H NMR (400 MHz, DMSO-d_6, 20 °C): $\delta = 5.33$ (s, 12H), 4.88 (s, 12H), 3.25 (s, 24H), 2.54 (s, 36H), 0.19 (s, 36 H); ESI$^+$-MS: expected: $[M-(btda)]^+ = 2256.75$ m/z; found: $[M-(btda)]^+ = 2256.75$ m/z; FT-IR (ATR, 4000−400 cm^{-1}): 2924 (w), 2505 (w), 1576 (w), 1542 (m), 1476 (m), 1444 (w), 1414 (m), 1378 (w), 1334 (w), 1268 (w), 1202 (w), 1185 (w), 1170 (m), 1064 (m), 1037 (m), 979 (w), 845 (m), 806 (m), 771 (m), 694 (w), 642 (m), 608 (w), 494 (w), 462 (m), 441 (w); EDX Zn/Cl ratio: expected 5/0 and measured 5/0.21; elemental analysis calcd (%) for $C_{96}H_{124}B_4N_{54}Zn_5$: C 47.95, H 5.20, N 31.45; found: C 47.76, H 5.46, N 31.30.

Single-Crystal Synthesis of CFA-20-Tp and CFA-20-Tp*. Approximately 0.5 mL of the reaction solutions were transferred into a silanized 3-mL snap cap glass vial, which was placed open into a 20 mL snap cap glass vial filled with 5 mL of MeOH, purged with argon, and then capped. For **CFA-19-Tp**, the small inner glass vial was capped with a punctured snap cap to slow the crystallization.

Recrystallization of CFA-20-Tp*. Twenty milligrams of **CFA-20-Tp*** was dissolved in 0.2 mL of DMF and transferred into a silanized 3-mL snap cap glass vial through a 2-μm PTFE syringe filter. This glass vial was placed open into a 20-mL snap cap glass vial filled with 4 mL of MeOH, purged with argon, and then capped. After 24 h, the colorless crystals were washed three times with 2 mL of MeOH via decantation and dried under vacuum (11.8 mg, 59%).

Single-Crystal Synthesis of CFA-20-Tp*-DMSO. **CFA-20-Tp*** dissolved in DMSO (~30 mg/mL) was filtered through a 2-μm PTFE syringe filter. A drop of this solution was placed on a microscope slide for slow evaporation/water diffusion under ambient conditions until crystals formed. Too fast (high humidity) or slow precipitation can be countered via moderate heating (30−60 °C) of the microscope slide.

■ RESULTS AND DISCUSSION

Synthesis and Characterization. The 1*H*-benzotriazole-5,6-diamine (**H-btda**) ligand was synthesized on a gram scale via hydrogenation of 5,6-dinitro-1*H*-benzotriazole,[57] which was found to require high dilution and large amounts of Pd/C catalyst to obtain the product with high purity and yields as a light brown powder (see Scheme S1 and Figure S6 in the Supporting Information). The ligand can be stored under inert gas for several months without noticeable changes, and handling in air for short periods appears to present no problem, whereas degradation of the compound is indicated by a slow color change to darker brown upon prolonged storage under ambient conditions. Single crystals of the **CFA-20-Cl** M-HOF structure suitable for single-crystal X-ray diffraction were obtained via slow 2,6-lutidine and MeOH diffusion into solutions of **H-btda** and $ZnCl_2$ in DMF using silanized glass vials (Figure S1 in the Supporting Information). After the determination of its unique structure, similar synthesis attempts with other zinc salts were tested, resulting in the isostructural **CFA-20-Br** M-HOF when $ZnBr_2$ was used (Figure S2 in the Supporting Information). For ZnI_2, no precipitates were obtained, not even when much higher metal and ligand concentrations were used. For the case of ZnF_2, the solubility of the metal salt is too low for reasonable synthesis attempts. Employing other salts, such as $Zn(OAc)_2$, resulted in different structures and materials, which are beyond the scope of this study. The bulk material of both M-HOF compounds can be readily precipitated with MeOH from reaction solutions of **H-btda**, the corresponding metal salt, and 2,6-lutidine.

DMF and 2,6-lutidine residues can be removed by extensive washing with MeOH, yielding an amorphous powder better described as [$Zn_5X_4(btda)_6$]·HX (X = Cl, Br) complexes featuring one amine hydrohalogenide per formula unit, which cannot be recrystallized into the initial M-HOF structures. However, the **CFA-20-Cl** and **CFA-20-Br** complexes were both observed in the ESI$^-$ mass spectra as the deprotonated negatively charged [$Zn_5X_4(btda)_6$]·X$^-$ complexes and neatly match the expected isotope patterns (see Figure 2, as well as Schemes S34−S36 in the Supporting Information).

The complexes were additionally characterized by ^{1}H NMR spectroscopy, clearly showing a shift of the aromatic and amine protons, in comparison to the pure **H-btda** ligand, as well as the loss of the triazolate proton signal (Figures S25, S28, and S30 in the Supporting Information). **CFA-20-Cl** and **CFA-20-Br** M-HOFs can be obtained as crystalline bulk materials if the washing procedure with MeOH is skipped and the sample is soaked with DMF prior to the PXRD measurements. After several minutes, the obtained patterns are in fair agreement with the patterns calculated from the single-crystal data (see Figure 3, as well as Figure S44 in the Supporting Information),

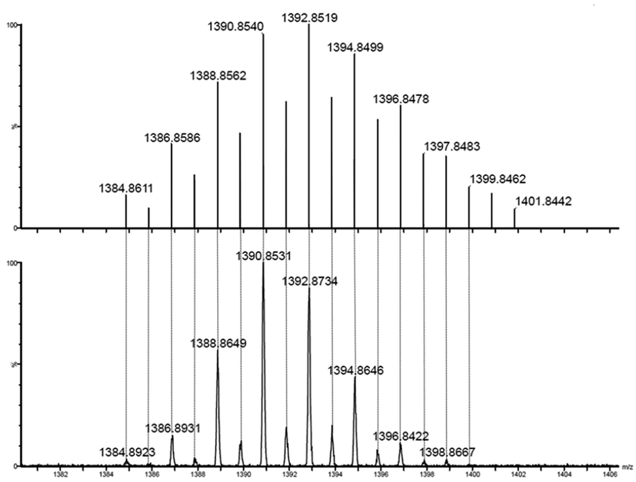

Figure 2. Simulated (top) and measured (bottom) ESI$^-$-MS isotope patterns for the deprotonated Kuratowski complex **CFA-20-Cl** ($[Zn_5Cl_4(btda)_6]\cdot Cl^-$: $Zn_5Cl_5C_{36}N_{30}H_{36}$).

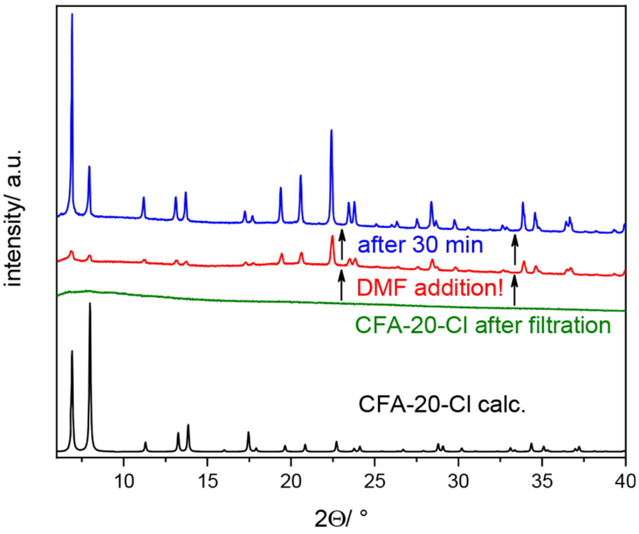

Figure 3. Calculated (black) and measured PXRD pattern for the **CFA-20-Cl** sample filtered without washing (green), directly (red) and 30 min after addition of DMF to the sample (blue).

indicating a slow recrystallization of partially dissolved compound upon DMF evaporation. After further evaporation of the DMF under ambient conditions, the structure collapses and turns amorphous again. The ^{1}H NMR data for the nonwashed and dried **CFA-20-Cl** sample still shows at least seven DMF molecules and one 2,6-lutidine, which is expected to be protonated and liable for the charge balance in the solvated M-HOF structures (see Figure S29 in the Supporting Information).

Exchange of the chloride side ligands at the Kuratowski complexes of **CFA-20-Cl** dissolved in DMF using the tetrabutylammonium salts of Tp and Tp* (NBu_4Tp, NBu_4Tp^*) resulted in **CFA-20-Tp** ($[Zn_5Tp_4(btda)_6]$) and **CFA-20-Tp*** ($[Zn_5Tp^*_4(btda)_6]$) M-HOFs after precipitation with methanol or water, respectively (Scheme 1). Single crystals suitable for single-crystal X-ray diffraction of both compounds were grown directly via slow methanol vapor diffusion into parts of the reaction solutions placed in silanized glass vials (see Figures S3 and S4 in the Supporting Information). **CFA-20-Tp*** single crystals can also be recrystallized similarly from the product redissolved in DMF. The **CFA-20-Tp*** complex can be detected by mass spectrometry (ESI+) as a $[Zn_5Tp^*_4(btda)_5]^+$ complex (see Figures S37 and S38 in the Supporting Information) and shows a fitting ^{1}H NMR spectrum (Figures S31 and S32 in the Supporting Information). In contrast to **CFA-20-Tp***, which readily dissolves in DMF, DMSO, and mixtures of MeOH with $CHCl_3$ or 1,4-dioxane, the lower solubility of **CFA-20-Tp** prevented useful NMR or ESI-MS characterization. However, the PXRD patterns for both compounds neatly match the pattern calculated from the single-crystal X-ray diffraction data, showing pure phase products and no loss of crystallinity upon removal of DMF and MeOH (see Figures S45 and S46 in the Supporting Information). The typical B−H stretching vibration of the scorpionate ligand can also be observed in the IR spectra for **CFA-20-Tp** and **CFA-20-Tp*** at 2453 and 2505 cm^{-1}, respectively.[66,67] In addition, **CFA-20-Tp*** shows symmetric and asymmetric stretching vibrations of methyl groups at and above 2924 cm^{-1}. The symmetric and asymmetric stretching vibrations of the amines are visible in the spectra for the **H-btda** ligand, **CFA-20-Cl**, and **CFA-20-Br** between 3300−3400 cm^{-1} but are only faint for **CFA-20-Tp** and **CFA-20-Tp*** (see Figures S39−S43 in the Supporting Information). EDX spectroscopy for all compounds gave results that are in fair agreement with the expected Zn:X (X = Cl, Br) ratios, and only the ratio of 5:0.2 for **CFA-20-Tp*** indicated small impurities (Figures S55−S58 in the Supporting Information), which might be located anywhere in this amine-rich structure and does not necessarily indicate a partially incomplete ligand exchange. Elemental analysis of both compounds is also in fair agreement with the expected values, although a small deviation is observed for **CFA-20-Tp**, which is most probably caused by minor solvent residues.

The crystallization process for the M−HOFs is strongly dependent on the solvents used; for example, crystallization from DMSO results in a completely different **CFA-20-Tp*-DMSO** structure (see Figure S5 in the Supporting Information). In contrast to **CFA-20-Tp***, this structure is again not stable upon solvent removal via evaporation or MeOH exchange, and was, therefore, not investigated further than the single-crystal X-ray structure analysis. Generally, the stability of the structures can already be estimated from the mechanical properties of the crystals, which showed that **CFA-20-Tp*-DMSO** crumbles upon the slightest touch, whereas significantly more force is needed to shatter the **CFA-20-Tp*** crystals. All M-HOFs and complexes described herein were observed to darken under ambient conditions; therefore, inert conditions are recommended for prolonged storage.

Crystal Structures. Single-crystal X-ray diffraction of **CFA-20-Cl** (100 K) and **CFA-20-Br** (150 K) revealed that both frameworks crystallize in the cubic space group $F\bar{4}3m$ (216) (a = 22.1260(3) and 22.3580(17) Å, respectively). Both are constructed from Kuratowski complexes with the **btda**$^-$ ligand, exhibiting distinct bond distances (Table 1) such as the tetrahedrally coordinated N2−Zn2 bond (**CFA-20-Cl**: 2.005(2); **CFA-20-Br**: 2.019(8)) or the octahedral N1−Zn1 bond (**CFA-20-Cl**: 2.174(2); **CFA-20-Br**: 2.198(9)), which are in good agreement with literature values for Kuratowski complexes such as 2.024 and 2.183 Å, respectively.[14] The Kuratowski complexes are arranged in a fcc-type lattice with halogen anions in the octahedral voids (see Figure 4b, as well as Figure S7 in the Supporting Information). The structure can

Scheme 1. Synthesis of CFA-20-Cl Starting from (a) the 1*H*-Benzotriazole-5,6-diamine (H-btda) Ligand, as Well as (b) 3D and (c) 2D Representation of the Ligand Exchange Reactions of the Chloride at the Kuratowski SBU,[14] Leading to an Octahedral Coordination of All Zinc Ions Employing (d) the Tp/Tp* Ligands

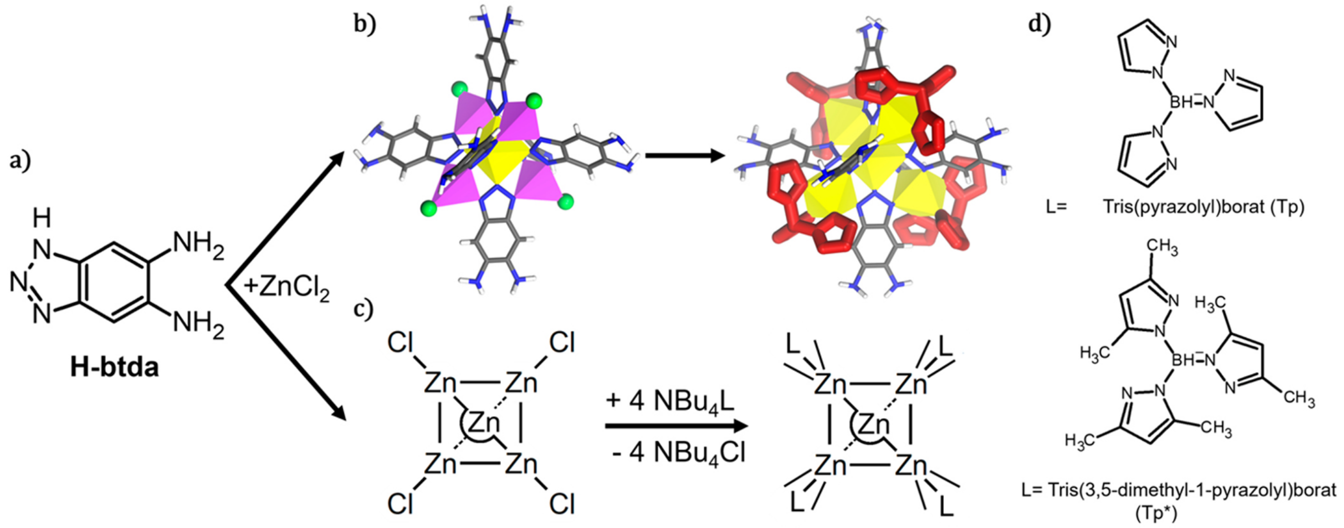

also be described as an MFU-4-type network in which every second Kuratwoski SBU is exchanged with a negatively charged halogen anion, resulting in a negatively charged framework. Similar to MFU-4 frameworks, the structure exhibits two different alternating pores, of which the small pore is confined by four chloride side ligands of the Kuratowski SBU and the large pore is confined by the benzene rings of the **btda**⁻ ligand.[22,23]

The solvent-accessible void volumes were calculated using PLATON/SQUEEZE software to be 6684 Å^3 (61.7% of the unit cell volume of 10832 Å^3) and 6862 Å^3 (61.4% of the unit cell volume of 11176 Å^3) for **CFA-20-Cl** and **CFA-20-Br**, respectively.[68] The residual electron density can account for at least one 2,6-lutidine and six (**CFA-20-Cl**; 1263 electron counts/cell) or eight (**CFA-20-Br**; 1615 electron counts/cell) DMF molecules per formula unit within the frameworks. The structures are stabilized due to the formation of a unique hydrogen bond framework between the 12 surrounding amines and the central halogen anion, which adapts the coordination geometry of an irregular icosahedron, because of the acceptance of 12 N−H···Cl hydrogen bonds (Figure 4a) and can be considered as a HOF SBU. As hydrogen atoms of the amine groups cannot be localized from single-crystal X-ray diffraction data, quantum mechanical DFT calculations were used to unravel the structure of this unusual coordination motif. For the halogenide-centered hydrogen-bridged building units, smaller cluster models were extracted from the single crystal data. The organic **btda**⁻ ligands were replaced by 1,2-phenylenediamine moieties, and the geometry of the resulting hydrogen-bonded building unit was optimized under symmetry constraints (*D*2 point group symmetry) by dispersion-corrected DFT (DFT-D) calculations (TURBOMOLE, B3LYP functional, D4 dispersion, def-2 TZVPP basis set).[69,70] A DFT frequency calculation, employing density functional perturbation theory, was performed for the converged structure, which showed the absence of negative vibrational frequencies. Similar symmetry-constrained DFT-D calculations were also performed for other hydrogen bond motifs of the HOF structures described in the manuscript and in the Supporting Information. Taking the amine hydrogen

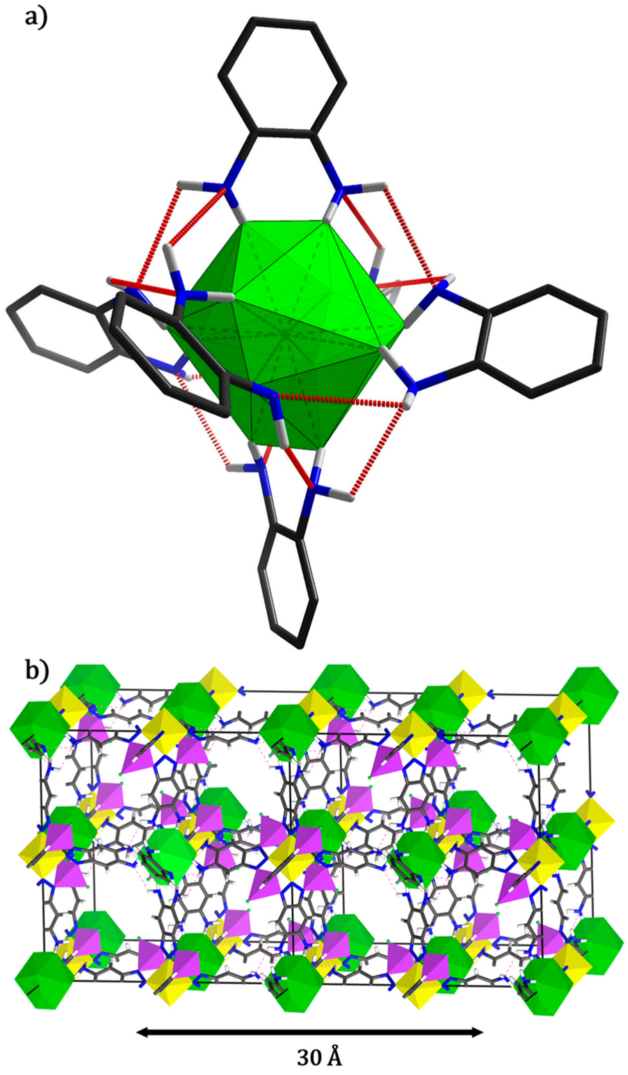

Figure 4. (a) Simulated hydrogen bond framework and (b) unit cells of **CFA-20-Cl** showing the alternating SBUs and potential porosity.

atoms into account, the $F\bar{4}3m$ (No. 216) space group must be reduced to $F23$ (No. 196) to prevent splitting of the hydrogen positions due to symmetry, although both hydrogen bond cluster variants should be present as a statistical distribution in the structure. An sp^3 hybridization of the amines appears to be clearly favored and is also supported by their large N3−C3 bond distances of 1.423 Å (**CFA-20-Cl**) and 1.418 Å (**CFA-20-Br**), indicating strong pyramidalization according to the literature, which states average distances of 1.355 Å for sp^2 hybridized amines, 1.395 Å for sp^3 hybridized amines and 1.465 Å for ammonium salts.[71] In fact, the data indicate a pyramidalization degree between that of sp^3 hybridization and ammonium cation known from the literature,[72] which is due to the 12 additional hydrogen bonds between the neighboring amines themselves, each acting as a hydrogen bond donor and acceptor (Figure 4a). Although charge balance for the negatively charged framework is most likely achieved due to residual protonated 2,6-lutidine in the pores, which is also visible in the NMR spectra for a nonwashed bulk sample (Figure S20 in the Supporting Information), the formation of ammonium cations among the 12 surrounding amines cannot be ruled out, especially due to the deprotonated hydrohalogenide complexes of $[\mathrm{Zn_5X_4(btda)_6}]\cdot\mathrm{X^-}$ (X = Cl, Br) observed in the ESI$^-$ mass spectra for the 2,6-lutidine- and DMF-free complex samples. The contribution of such a charge balancing ammonium cation to the mean pyramidalization is expected to be rather small due to the 1:11 ammonium cation to amine ratio, but it might lead to an energetically unfavorable disturbance in the hydrogen bond framework. The N3···Cl2 and N3···Br2 distances of 3.498 and 3.581 Å can be considered long in contrast to the mean N···X distances reported in the literature,[73] indicating a moderate to low hydrogen bond strength, as well as intermolecular N3···N3 (e.g.: N3(x,y,z)···N3($x,{}^3/_2-y,{}^3/_2-z$); N3(x,y,z)···N3(${}^3/_2-x,y,{}^3/_2-z$)) distances of 3.155 and 3.311 Å for **CFA-20-Cl** and **CFA-20-Br**, respectively.[74] However, the sheer number of 24 hydrogen bonds appears to compensate for it. A direct evaluation and comparison of the bond strengths/lengths between both frameworks is aggravated, if not permitted, by the different measurement temperatures, as well as the different ion radii of the chloride and bromide anions. Some additional electron density, most likely from water molecules, was also found in the vicinity of those hydrogen bond frameworks but could not be reasonably refined.

Table 1. Distinct Bond Distances of CFA-20-Cl and CFA-20-Br

bond	CFA-20-Cl [Å]	CFA-20-Br [Å]
N1−N2	1.350(2)	1.357(9)
N1−Zn1	2.174(2)	2.198(9)
N2−Zn2	2.005(2)	2.019(8)
X1-Zn2	2.1846(13)	2.310(3)
N2−C1	1.339(3)	1.331(12)
N3−C3	1.423(4)	1.418(13)

Nonetheless, this is an indication for additional interactions with solvent or water molecules necessary for framework stabilization. No similar equivalent 12-fold hydrogen-bonded chloride or bromide anions were found in the literature, but various samples for chlorides and bromides bound in cryptands by protonated secondary and tertiary amines are known. The different N···Cl distances of such compounds range from 3.048 Å (2-fold),[75] 3.059−3.847 Å (2-fold),[76] and 3.197−3.941 Å (6-fold)[77] if only distances below 4.5 Å are considered. The type of encapsulated halogen anion appears to play a crucial role in the coordination motif, as chloride anions often enforce a 2-fold coordination, as shown by the equidistant N···Cl distance of 3.048 Å, which turns into four N···Br distances of 3.471−3.998 Å with an encapsulated bromine, although water molecules and halogen anions outside of the cryptands also affect such structures.[78] 12-fold hydrogen-bonded chlorides were only found in the single-crystal structure of a hexaaminobenzene (HAB) derivative, which is described as (HAB)Cl$_2$ ($\mathrm{C_6H_{12}Cl_2N_6}$). However, from our understanding, it should contain two ammonium cations due to charge balance reasons, which is supported by the two long C−N bond distances of 1.455 Å per hexaaminobenzene ring, indicating ammonium cations at those positions.[79] In this structure, the two different chlorides are each surrounded by 12 amines with two times six different N···Cl distances ranging from 3.204−3.555 Å (Cl1) and 3.054−4.180 Å (Cl2), which results in an average distance of 3.529 Å neatly comparable to the distance of 3.498 Å found in **CFA-20-Cl**. Regarding the lower coordination numbers or nonequivalent N···Cl distances in the literature for chloride and bromide anions, we conclude that symmetry and crystal packing effects, resulting from the high symmetry and stiffness of the Kuratowski complex units, play a crucial role in the equidistant 12-fold hydrogen bonded halogen anions found in the **CFA-20-Cl** and **CFA-20-Br** structures.

Single-crystal X-ray diffraction for **CFA-20-Tp** (250 K) and **CFA-20-Tp*** (150 K) revealed that the compounds crystallized in similar trigonal space groups $R3m$ (No. 160) (a = 41.7591(12) Å and c = 16.7108(7) Å) and $R\bar{3}$ (No. 148) (a = 53.131(14) Å and c = 31.196(9) Å), respectively (Figures 5a and 5b). Both frameworks exhibit the expected Kuratowski complexes, in which all the chloride side ligands are exchanged with Tp- and Tp*-ligands, resulting in an octahedral coordination environment for all Zn ions. Hereby, a large increase in the unit cell lengths is observed for **CFA-20-Tp*** due to its sterically more demanding complex SBU. The **CFA-20-Tp** and **CFA-20-Tp*** complexes assemble into three- and six-membered rings, respectively, which are stacked in the crystallographic c-direction with a staggered abcabc pattern (see Figures 5c−f). An alternating orientation of the complexes in the six-membered rings of **CFA-20-Tp***, although very similar to one diamine function pointing directly into the ring center, leads to a chair conformation. **CFA-20-Tp** can be similarly described with six-membered rings in a more distinct chair conformation, where every complex unit is shared in two six-membered rings. These ring structures and their stacking lead to the creation of pore channels in the c-direction of both frameworks, which show an alternating channel diameter. In the larger **CFA-20-Tp*** framework structure, the pore channels are interconnected into a 3D pore network (see Figure S8 in the Supporting Information). Solvent-accessible void volumes of 6202 Å^3 (24.6% of the unit cell volume of 25236.5 Å^3) and 31604 Å^3 (41.4% of the unit-cell volume of 76266 Å^3) were calculated with PLATON/SQUEEZE software for **CFA-20-Tp** and **CFA-20-Tp***, respectively.[68] For **CFA-20-Tp**, one DMF molecule per complex can be refined in the structure, although approximately eight additional DMF molecules per formula unit can be calculated to be present in the pore channels from the residual electron density (2850 electron counts/cell), which appears to be concentrated in the vicinity of the open

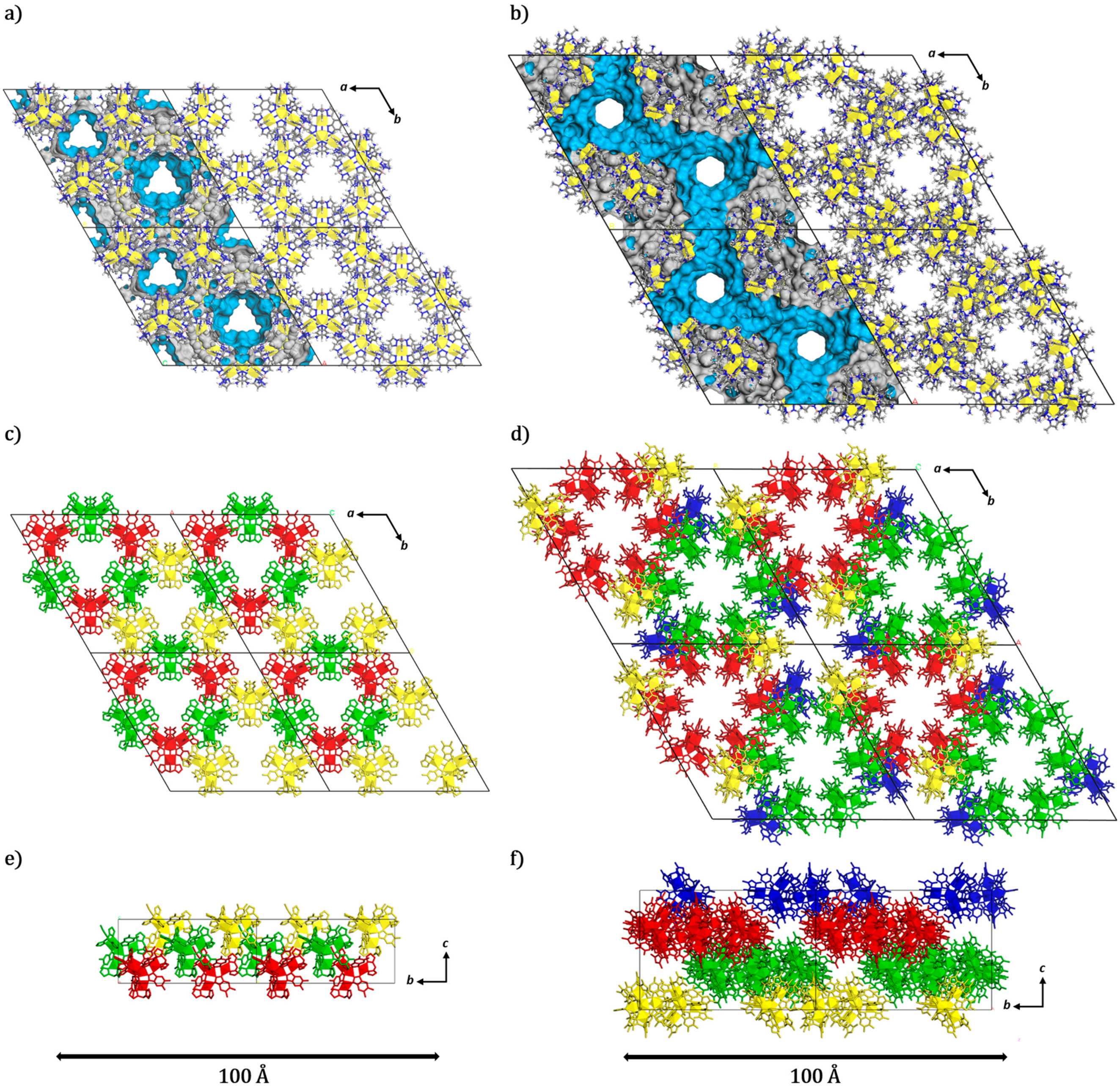

Figure 5. Comparison of the permanently porous **CFA-20-Tp** and **CFA-20-Tp*** structures showing plots of (a, b) the Connolly surfaces created with BIOVIA Materials Studio 2021 (viewed along the *c*-direction) and colored complexes illustrating the stacking pattern for the ring motifs consisting of three and six complexes in (c, e) **CFA-20-Tp** (view along the *c*- and *a*-directions) and (d, f) **CFA-20-Tp*** (view along the *c*- and *a*-direction), respectively.[80]

diamine functions. However, those electron densities cannot be assigned to certain molecules, and, in reality, a mixture of DMF, water, and MeOH should be present. The additional electron density in the pores of **CFA-20-Tp*** (6274 electron counts/cell) can be assigned to approximately nine DMF molecules per Kuratowski unit, although water and MeOH should also be present. Both structures are also expected to be stabilized via hydrogen bond interactions between the amines, which is supported by the N−C bond distances ranging between 1.388−1.423 Å and 1.402−1.445 Å for **CFA-20-Tp** and **CFA-20-Tp***, respectively, again indicating strong pyramidalization and sp^3 hybridization according to the literature.[71] Because of the complex entanglement of the Kuratowski units with their amine functions and additional solvent molecules in the solvated crystals, the hydrogen bond systems supporting the structures cannot be unraveled completely. However, in **CFA-20-Tp***, two opposing diamine functions of four complex building units are held together in a pseudocubic arrangement with intermolecular N···N distances in the range of 3.249−3.326 Å, indicating strong to moderate interaction strengths also present in the desolvated structure (Figures S12 and S13 in the Supporting Information).[74] An arrangement of the hydrogen atoms fitting the symmetry of the initial structure solution was chosen to illustrate this HOF SBU, although different arrangements can be imagined.

Table 2. Crystal Data and Structure Refinement for CFA-20-Cl, CFA-20-Br, CFA-20-Tp, CFA-20-Tp* and CFA-20-Tp*-DMSO

compound	CFA-20-Cl	CFA-20-Br	CFA-20-Tp	CFA-20-Tp*	CFA-20-Tp*-DMSO
empirical formula	$C_{36}H_{36}Cl_5N_{30}Zn_5$	$C_{36}H_{36}Br_5N_{30}Zn_5$	$C_{75}H_{83}B_4N_{55}OZn_5$	$C_{96}H_{124}B_4N_{54}Zn_5$	$C_{96}H_{124}B_4N_{54}Zn_5$
formula	$C_{36}H_{36}Cl_5N_{30}Zn_5$	$C_{36}H_{36}Br_5N_{30}Zn_5$	$C_{72}H_{76}B_4N_{54}Zn_5\cdot C_3H_7NO$	$C_{96}H_{124}B_4N_{54}Zn_5$	$C_{96}H_{124}B_4N_{54}Zn_5$
formula weight (g mol^{-1})	1393.05	1615.35	2141.05	2404.57	2404.57
temperature (K)	100 (2)	150 (2)	250(2)	150(2)	150(2)
wavelength (Å)	0.71073	0.71073	0.71073	0.71073	0.71073
crystal system	Cubic	Cubic	Trigonal	Trigonal	Orthorhombic
space group	*F*-43 *m*	*F*-43 *m*	*R*3 *m*	*R*-3	$P2_12_12_1$
a (Å)	22.1260(3)	22.3580(17)	41.7591(12)	53.131(14)	20.5247(8)
b (Å)	22.1260(3)	22.3580(17)	41.7591(12)	53.131(14)	22.8524(9)
c (Å)	22.1260(3)	22.3580(17)	16.7108(7)	31.196(9)	30.6569(13)
volume (Å^3)	10832.0(4)	11176(3)	25236.5(18)	76266(45)	14379.3(10)
Z	4	4	9	18	4
D_g (g cm^{-3})	0.854	0.960	1.268	0.942	1.111
μ (mm^{-1})	1.245	2.875	1.118	0.745	0.878
F(000)	2788	3148	9864	22464	4992
crystal size (mm^3)	0.18 × 0.18 × 0.18	0.08 × 0.08 × 0.05	0.06 × 0.06 × 0.04	0.2 × 0.1 × 0.08	0.1 × 0.1 × 0.06
Θ range	2.604°–27.454°	2.577°–24.697°	2.368°–23.498°	2.300°–19.601°	2.14°–22.528°
reflectonss collected	81200	24476	92093	216794	209692
independent reflections	1279 [*R*(int) = 0.0343]	996 [*R*(int) = 0.1209]	8660 [*R*(int) = 0.1565]	14822 [*R*(int) = 0.1044]	18808 [*R*(int) = 0.0567]
completeness	99.6%	99.6%	99.9	99.2	99.7
data/restraints/parameters	1279/0/44	996/0/44	8660/106/700	14822/162/1468	18808/21/1456
goodness of fit on F^2	1.178	1.180	1.116	1.050	1.051
final R indices [$I > 2\text{sigma}(I)$]	R1 = 0.0178, wR2 = 0.0476	R1 = 0.0359, wR2 = 0.0834	R1 = 0.0800, wR2 = 0.1536	R1 = 0.0652, wR2 = 0.1751	R1 = 0.0348, wR2 = 0.0825
R indices (all data)	R1 = 0.0196, wR2 = 0.0497	R1 = 0.0746, wR2 = 0.1064	R1 = 0.1002, wR2 = 0.1626	R1 = 0.0841, wR2 = 0.1919	R1 = 0.0431, wR2 = 0.0886
Flack parameter	0.489(19)	0.06(5)	0.011(12)	–	−0.003(3)
largest diff. peak and hole/e.Å^{-3}	0.179 and −0.197	0.318 and −0.274	0.690 and −0.632	0.535 and −0.389	0.417 and −0.287
CCDC No.	2102233	2102234	2102235	2102236	2102237

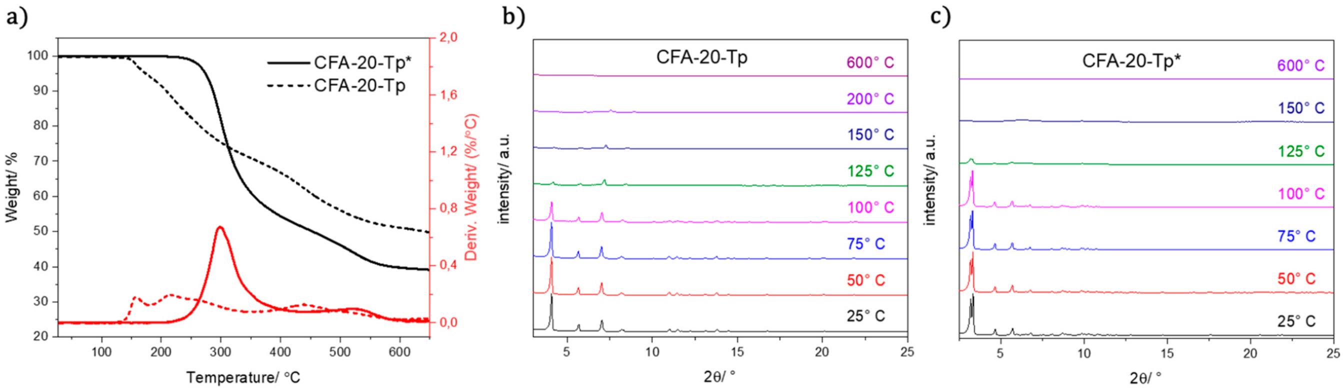

Figure 6. (a) TGA curves and VT-PXRD patterns for (b) **CFA-20-Tp** and (c) **CFA-20-Tp***.

Of the four residual diamine functions for each complex, one directly points into the *c*-channel pore and three line the pores interconnecting the channels in the *c*-direction with N···N distances larger than 4.44 Å. As no distinct positions of these hydrogen atoms can be expected or determined, they were added to the amines in the structures, assuming sp^3 hybridization with occupancy factors of 2/3. In contrast to **CFA-20-Tp***, all amines of **CFA-20-Tp**, except for N9, appear to participate at least in weak hydrogen bond interactions that should still be present in the desolvated structure. In the structure, all amines and their hydrogen atoms were also added with sp^3-hybridization and occupancy factors of 2/3 because the N···N distances in the range of 3.147–3.708 Å are distributed in large rings around the pore channels (see Figure S11 and Table S1 in the Supporting Information), and weaker bonds can already be considered to be of a more dynamic nature.

The **CFA-20-Tp*-DMSO** structure, which was also solved using single-crystal X-ray diffraction, crystallizes in the orthorhombic space group $P2_12_12_1$ (No. 19) (a = 20.5247(8) Å, b = 22.8524(9) Å, c = 30.6569(13) Å). The structure consists of the same Kuratowski SBU as **CFA-20-Tp*** but in a different arrangement (Figure S9 in the Supporting Information). This structure also exhibits a 3D-pore system with large pores, and a solvent accessible void volume of 4416 Å^3 (30.7% of the unit cell volume of 14379.3 Å^3) was determined with PLATON/SQUEEZE.[68] Herein, the pores should be mostly filled with DMSO, which can be calculated to be ~9 DMSO molecules per Kuratowski unit from the residual electron density (1473 electron counts/cell), but water should also be present in this structure. The structure shows two different HOF SBUs in which all amines take part with N···N distances in the range of 3.024−3.823 Å (Table S3 in the Supporting Information), which indicates considerably more interaction in comparison to the initial **CFA-20-Tp*** structure. Hydrogen atoms were placed with the assistance of quantum mechanical simulations for the cut-out HOF SBUs (see Figure S14 in the Supporting Information).

Thermal Stability. The TGA curves for the **CFA-20-Cl** and **CFA-20-Br** complexes showed 2 and 4 wt % mass losses at 150 °C (Figure S47 in the Supporting Information), respectively, which can be mainly attributed to the loss of residual water and solvents also visible in the NMR spectra (see Figures S29 and 30 in the Supporting Information). The onset of decomposition at ~330 °C for the **CFA-20-Br** complex is slightly lower than that at 370 °C for the **CFA-20-Cl** complex. The TGA curve for **CFA-20-Tp*** shows no initial weight loss prior to the decomposition onset at 220 °C. This is unexpected for **CFA-20-Tp***, because VT-PXRD experiments reveal an almost complete loss of crystallinity already above 125 °C (Figure 6). For **CFA-20-Tp**, the decomposition onset at 125 °C is in better agreement with the starting decrease in reflex intensities at 100 °C and a nearly complete loss of crystallinity at 125 °C.

Argon Adsorption Analysis and Porosity. Although a high potential porosity and surface areas are found in the crystal structures of **CFA-20-Cl** (2628 m^2/g), **CFA-20-Br** (2313 m^2/g), and **CFA-20-Tp*-DMSO** (1156 m^2/g) using iRASPA software,[81] they are not stable enough to show permanent porosity upon solvent removal. However, the **CFA-20-Tp** and **CFA-20-Tp*** frameworks were found to be stable upon washing with MeOH and solvent removal in vacuum at room temperature (RT), giving rise to permanent porosities, which were investigated by argon adsorption measurements at 77 K. The isotherm for **CFA-20-Tp** shows typical type I behavior for microporous solids, and the BET surface area was determined to be 659 m^2/g (see Figure 7, as well as Figure S48 in the Supporting Information), which is in good agreement with the theoretical value of 689 m^2/g, calculated using the iRASPA software for the structure without the DMF molecule.[81] The NLDFT pore size distribution shows two main maxima at values of 5 and 12.5 Å (Figure S49 in the Supporting Information), which are in fair agreement with the alternating diameters for the channel pores in the *c*-direction of this structure. The surface area of **CFA-20-Tp*** was calculated with iRASPA to be 1240 m^2/g,[81] but a BET surface area of only 682 m^2/g was determined from the argon adsorption isotherm of the initial sample (see Figures S50 and S51 in the Supporting Information). This low surface area can be explained by the fast precipitation method with water, resulting in a large number of defects in the structure. Therefore, a sample slowly recrystallized from DMF was tested, resulting in a BET surface area of 985 m^2/g, which is in better agreement with the expected value (see Figure 7, as well as Figure S52 in the Supporting Information).

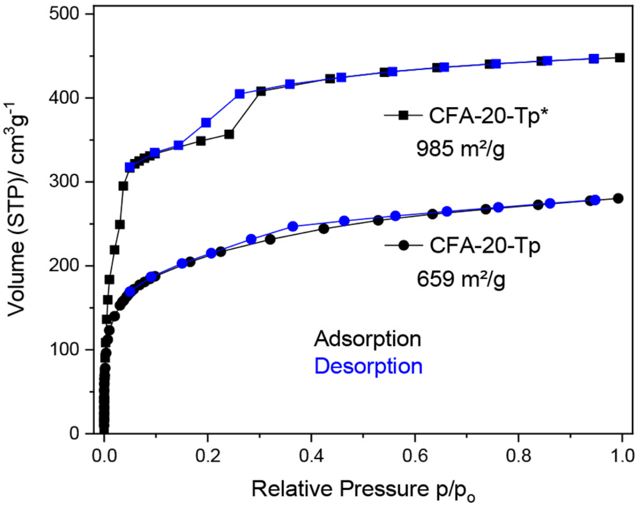

Figure 7. Argon adsorption and desorption isotherms for **CFA-20-Tp** and the recrystallized **CFA-20-Tp*** sample, together with the calculated values for the BET surface area.

The NLDFT pore size distributions for both **CFA-20-Tp*** samples exhibit the same maxima at ~5.4 and 14 Å, which are in fair agreement with the bottlenecks and interconnections of the channels in the *c*-direction, as well as some smaller and broader features between 20−30 Å (see Figures S53 and S54 in the Supporting Information). The main difference in the distributions is the significantly larger peak size and area at 14 Å for the recrystallized **CFA-20-Tp*** sample, corroborating a blocking of the large pores in the initial **CFA-20-Tp*** sample via disordered complexes or impurities. The adsorption isotherm for recrystallized **CFA-20-Tp*** follows type IV behavior with a distinct hysteresis between 0.15−0.3 p/p_0, and a small hysteretic feature also visible between 0.25−6 p/p_0 for **CFA-20-Tp**, which is often observed in soft porous materials.[82−85] Generally, as already known for more-stable MOFs, solvent exchange and activation procedures might play a crucial role in the permanent porosity of such compounds, and, thus, leave further room for improvement.[86] Especially, given the different amount of hydrogen bonds in the **CFA-20-Tp*** (two of six diamines partaking in hydrogen bonds) and **CFA-20-Tp*-DMSO** (all diamines partaking in hydrogen bonds) structures, we also conclude that permanent porosity in such M-HOFs can significantly be dependent on the packing and arrangement of the MBBs within the structure and not mainly on the strength or amount of hydrogen bonds. The ring motifs in the structures of **CFA-20-Tp** and **CFA-20-Tp*** can additionally prevent collapse or structural rearrangement toward the channel pores in the *c*-direction from an architectural statics point of view, similar to the force distribution exploited in arch bridges or the thermal expansion phenomenon of rings, which only allows for enlargement of the hole diameter. Nonetheless, the presence of hydrogen bonds in the structures, as well as their influence on the assembly and arrangement process, demand classification as M-HOFs and not only as porous molecular crystals.[5,87]

■ CONCLUSION

The **H-btda** ligand was successfully prepared on the gram scale and applied for the synthesis of several novel Kuratowski complexes. It was shown that the additional diamine functionality of this ligand results in hydrogen bond interactions, which readily gives rise to a variety of different M-HOF structures. The **CFA-20-Cl** and **CFA-20-Br** structures obtained directly from the complex synthesis were investigated in detail to unravel the unique hydrogen bond framework system, consisting of a central halogen anion and 12 surrounding amines, stabilizing the potentially porous M-HOFs. In addition, post-synthetic ligand exchange of the chloride side ligands at the Kuratwoski unit with scorpionate Tp and Tp* ligands results in two similar M−HOF structures—**CFA-20-Tp** and **CFA-20-Tp***—which are proven to exhibit permanent porosity, and, thus, prove to be a valuable addition to this small material subclass. Moreover, the analysis of the argon adsorption isotherms is in fair agreement with the pore systems expected from the crystal structures. Hereby, the possibility for recrystallization of such M−HOFs was successfully utilized to improve the initially lower surface area of **CFA-20-Tp***, highlighting the advantage of reversible hydrogen bond formation in comparison to insoluble MOFs. In addition, the solubility of the **CFA-20-Tp*** complex was successfully exploited further for the synthesis of the **CFA-20-Tp*-DMSO** structure via crystallization from DMSO, emphasizing its functionality as an MBB. Although this structure does not exhibit permanent porosity, this approach could be pushed further with the use of sterically demanding solvents, which should induce larger pores and different structures. Regarding the affinity of the **CFA-20** complexes for the formation of porous framework structures, as well as the versatile reactions of diamine functions, the complexes can also be envisaged as suitable MBBs for future synthesis strategies via covalent bond formation or metal coordination at the amine functions, leading to more robust framework structures with additional functionalities. Hereof, for example, square planar coordination of metal ions with two diamine functions, similar to the literature MOFs,[88,89] might yield MFU-4 analogous structures with additional metal centers. In particular, the **CFA-20-Tp*** complex is expected to be the perfect candidate for such investigations, because of its sterically shielded Kuratwoski unit and good solubility.

■ ASSOCIATED CONTENT

Supporting Information

The Supporting Information is available free of charge at https://pubs.acs.org/doi/10.1021/acs.cgd.1c01008.

> Optical microscopy images and pictures, additional crystal structure plots and data, ^{1}H NMR spectra, ESI-MS data, IR spectra, PXRD pattern, TGA curves, argon adsorption data and EDX spectra (PDF)

Accession Codes

CCDC 2102233−2102237 contains the supplementary crystallographic data for this publication. These data can be obtained free of charge via www.ccdc.cam.ac.uk/data_request/cif, or by emailing data_request@ccdc.cam.ac.uk, or by contacting The Cambridge Crystallographic Data Centre, 12 Union Road, Cambridge CB2 1EZ, UK; fax: + 44 1223 336033.

■ AUTHOR INFORMATION

Corresponding Author

Dirk Volkmer − *Chair of Solid State and Materials Chemistry, Institute of Physics, University of Augsburg, 86159 Augsburg, Germany*; orcid.org/0000-0002-8105-2157; Email: dirk.volkmer@physik.uni-augsburg.de

Authors

Richard Röß-Ohlenroth − *Chair of Solid State and Materials Chemistry, Institute of Physics, University of Augsburg, 86159 Augsburg, Germany*

Corbinian Freudig − *Chair of Solid State and Materials Chemistry, Institute of Physics, University of Augsburg, 86159 Augsburg, Germany*

Maryana Kraft − *Chair of Solid State and Materials Chemistry, Institute of Physics, University of Augsburg, 86159 Augsburg, Germany*

Hana Bunzen − *Chair of Solid State and Materials Chemistry, Institute of Physics, University of Augsburg, 86159 Augsburg, Germany*

Complete contact information is available at: https://pubs.acs.org/10.1021/acs.cgd.1c01008

Notes

The authors declare no competing financial interest.

■ ACKNOWLEDGMENTS

Financial support from the DFG (SPP 1928 COORNETs: Coordination Networks: Building Blocks for Functional Systems) is gratefully acknowledged. The authors are grateful to Dr. M. Grzywa for the preliminary SC-XRD investigation of CFA-20-Cl.

■ REFERENCES

(1) Li, P.; Ryder, M. R.; Stoddart, J. F. Hydrogen-Bonded Organic Frameworks: A Rising Class of Porous Molecular Materials. *Acc. Mater. Res.* **2020**, *1* (1), 77−87.

(2) Lin, R.-B.; He, Y.; Li, P.; Wang, H.; Zhou, W.; Chen, B. Multifunctional porous hydrogen-bonded organic framework materials. *Chem. Soc. Rev.* **2019**, *48* (5), 1362−1389.

(3) Luo, J.; Wang, J.-W.; Zhang, J.-H.; Lai, S.; Zhong, D.-C. Hydrogen-bonded organic frameworks: design, structures and potential applications. *CrystEngComm* **2018**, *20* (39), 5884−5898.

(4) Hisaki, I.; Xin, C.; Takahashi, K.; Nakamura, T. Designing Hydrogen-Bonded Organic Frameworks (HOFs) with Permanent Porosity. *Angew. Chem., Int. Ed.* **2019**, *58* (33), 11160−11170.

(5) Zhu, Z.-H.; Wang, H.-L.; Zou, H.-H.; Liang, F.-P. Metal hydrogen-bonded organic frameworks: structure and performance. *Dalton Trans.* **2020**, *49* (31), 10708−10723.

(6) Bao, Z.; Xie, D.; Chang, G.; Wu, H.; Li, L.; Zhou, W.; Wang, H.; Zhang, Z.; Xing, H.; Yang, Q.; Zaworotko, M. J.; Ren, Q.; Chen, B. Fine Tuning and Specific Binding Sites with a Porous Hydrogen-Bonded Metal-Complex Framework for Gas Selective Separations. *J. Am. Chem. Soc.* **2018**, *140* (13), 4596−4603.

(7) Gong, W.; Chu, D.; Jiang, H.; Chen, X.; Cui, Y.; Liu, Y. Permanent porous hydrogen-bonded frameworks with two types of Brønsted acid sites for heterogeneous asymmetric catalysis. *Nat. Commun.* **2019**, *10* (1), 600.

(8) Nugent, P. S.; Rhodus, V. L.; Pham, T.; Forrest, K.; Wojtas, L.; Space, B.; Zaworotko, M. J. A robust molecular porous material with high CO_2 uptake and selectivity. *J. Am. Chem. Soc.* **2013**, *135* (30), 10950−10953.

(9) Peng, J.-M.; Wang, H.-L.; Zhu, Z.-H.; Liu, Z.-Y.; Zou, H.-H.; Liang, F.-P. Substituents lead to differences in the formation of a series of dysprosium hydrogen-bonded organic frameworks with high stability and acid stimulus−response luminescence properties. *J. Mater. Chem. C* **2021**, *9* (29), 9319−9330.

(10) Roques, N.; Mouchaham, G.; Duhayon, C.; Brandès, S.; Tachon, A.; Weber, G.; Bellat, J. P.; Sutter, J.-P. A robust nanoporous supramolecular metal-organic framework based on ionic hydrogen bonds. *Chem. - Eur. J.* **2014**, *20* (37), 11690−11694.

(11) Wang, H.-L.; Ma, X.-F.; Zhu, Z.-H.; Zhang, Y.-Q.; Zou, H.-H.; Liang, F.-P. A series of dysprosium-based hydrogen-bonded organic

frameworks (Dy−HOFs): thermally triggered off → on conversion of a single-ion magnet. *Inorg. Chem. Front.* **2019**, *6* (10), 2906−2913.

(12) Zhang, H.-X.; Yan, X.; Chen, Y.-X.; Zhang, S.-H.; Li, T.; Han, W.-K.; Bao, L.-Y.; Shen, R.; Gu, Z.-G. A zeolite supramolecular framework with LTA topology based on a tetrahedral metal-organic cage. *Chem. Commun.* **2019**, *55* (8), 1120−1123.

(13) Zhou, M.; Liu, G.; Ju, Z.; Su, K.; Du, S.; Tan, Y.; Yuan, D. Hydrogen-Bonded Framework Isomers Based on Zr-Metal Organic Cage: Connectivity, Stability, and Porosity. *Cryst. Growth Des.* **2020**, *20* (6), 4127−4134.

(14) Biswas, S.; Tonigold, M.; Speldrich, M.; Kögerler, P.; Weil, M.; Volkmer, D. Syntheses and magnetostructural investigations on Kuratowski-type homo- and heteropentanuclear coordination compounds $MZn_4Cl_4(L)_6$ (M(II) = Zn, Fe, Co, Ni, or Cu; L = 5,6-dimethyl-1,2,3-benzotriazolate) represented by the nonplanar K(3,3) graph. *Inorg. Chem.* **2010**, *49* (16), 7424−7434.

(15) Marshall, J. H. Preparation and characterization of tetrakis(2,4-pentanedionato)hexakis(benzotriazolato)pentacopper(II). *Inorg. Chem.* **1978**, *17* (12), 3711−3713.

(16) Himes, V. L.; Mighell, A. D.; Siedle, A. R. Synthesis and structure of $Cu_5(BTA)_6(t\text{-}C_4H_9NC)_4$, a mixed-valent copper-nitrogen cluster containing η^3-benzotriazolate. *J. Am. Chem. Soc.* **1981**, *103* (1), 211−212.

(17) Kokoszka, G. F.; Baranowski, J.; Goldstein, C.; Orsini, J.; Mighell, A. D.; Himes, V. L.; Siedle, A. R. Two-dimensional dynamical Jahn-Teller effects in a mixed-valence benzotriazolato copper cluster, $Cu_5(BTA)_6(RNC)_4$. *J. Am. Chem. Soc.* **1983**, *105* (17), 5627−5633.

(18) Handley, J.; Collison, D.; Garner, C. D.; Helliwell, M.; Docherty, R.; Lawson, J. R.; Tasker, P. A. Hexakis(benzotriazolato)-tetrakis(2,4-pentanedionato)pentacopper(II): A Model for Corrosion Inhibition. *Angew. Chem., Int. Ed. Engl.* **1993**, *32* (7), 1036−1038.

(19) Murrie, M.; Collison, D.; Garner, C.; Helliwell, M.; Tasker, P. A.; Turner, S. S. Synthesis structure magnetic properties of $[Cu_5(bta)_6L_4]$ (bta = benzotriazolate;L = β-diketonate) Clusters. *Polyhedron* **1998**, *17* (17), 3031−3043.

(20) Bakalbassis, E. G.; Diamantopoulou, E.; Perlepes, S. P.; Raptopoulou, C. P.; Tangoulis, V.; Terzis, A.; Zafiropoulos, T. F. Benzotriazolate-mediated assembly of the discrete asymmetric pentanuclear nickel complex $[Ni_5(OH)(bta)_5(acac)_4(H_2O)_4]$(Hbta = benzotriazole, Hacac = pentane-2,4-dione). *J. Chem. Soc., Chem. Commun.* **1995**, No. 13, 1347.

(21) Tangoulis, V.; Raptopoulou, C. P.; Terzis, A.; Bakalbassis, E. G.; Diamantopoulou, E.; Perlepes, S. P. Polynuclear Nickel(II) Complexes: Preparation, Characterization, Magnetic Properties, and Quantum-Chemical Study of $[Ni_5(OH)(Rbta)_5(acac)_4(H_2O)_4]$ (RbtaH = Benzotriazole and 5,6-Dimethylbenzotriazole). *Inorg. Chem.* **1998**, *37* (13), 3142−3153.

(22) Denysenko, D.; Grzywa, M.; Tonigold, M.; Streppel, B.; Krkljus, I.; Hirscher, M.; Mugnaioli, E.; Kolb, U.; Hanss, J.; Volkmer, D. Elucidating gating effects for hydrogen sorption in MFU-4-type triazolate-based metal-organic frameworks featuring different pore sizes. *Chem. - Eur. J.* **2011**, *17* (6), 1837−1848.

(23) Biswas, S.; Grzywa, M.; Nayek, H. P.; Dehnen, S.; Senkovska, I.; Kaskel, S.; Volkmer, D. A cubic coordination framework constructed from benzobistriazolate ligands and zinc ions having selective gas sorption properties. *Dalton Trans.* **2009**, No. 33, 6487−6495.

(24) Schmieder, P.; Denysenko, D.; Grzywa, M.; Baumgärtner, B.; Senkovska, I.; Kaskel, S.; Sastre, G.; van Wüllen, L.; Volkmer, D. CFA-1:The first chiral metal-organic framework containing Kuratowski-type secondary building units. *Dalton Trans.* **2013**, *42* (30), 10786−10797.

(25) Schmieder, P.; Grzywa, M.; Denysenko, D.; Hambach, M.; Volkmer, D. CFA-7:An interpenetrated metal-organic framework of the MFU-4 family. *Dalton Trans.* **2015**, *44* (29), 13060−13070.

(26) Biswas, S.; Tonigold, M.; Volkmer, D. Homo- and Heteropentanuclear Coordination Compounds with Td Symmetry - the Solid State Structures of $[MZn_4(L)_4(L')_6]$(M = Co II or Zn; L = chloride or acac; L′ = 1,2,3-benzotriazolate). *Z. Anorg. Allg. Chem.* **2008**, *634* (14), 2532−2538.

(27) Liu, Y.-Y.; Grzywa, M.; Tonigold, M.; Sastre, G.; Schüttrigkeit, T.; Leeson, N. S.; Volkmer, D. Photophysical properties of Kuratowski-type coordination compounds $M(II)Zn_4Cl_4(Me_2bta)_6$ (M(II) = Zn or Ru) featuring long-lived excited electronic states. *Dalton Trans.* **2011**, *40* (22), 5926−5938.

(28) Werner, T. W.; Reschke, S.; Bunzen, H.; von Nidda, H.-A. K.; Deisenhofer, J.; Loidl, A.; Volkmer, D. $Co_5Tp^*{}_4(Me_2bta)_6$:A Highly Symmetrical Pentanuclear Kuratowski Complex Featuring Tris-(pyrazolyl)borate and Benzotriazolate Ligands. *Inorg. Chem.* **2016**, *55* (3), 1053−1060.

(29) Bunzen, H.; Grzywa, M.; Kalytta-Mewes, A.; Volkmer, D. One-pot synthesis of ultrastable pentanuclear alkylzinc complexes. *Dalton Trans.* **2017**, *46* (8), 2618−2625.

(30) WANG, J. Synthesis and structure of $Cu_5(BTA)_6(TTA)_4\cdot 5DMF$, a copper-nitrogen cluster containing η^3-benzotriazolate. *Chin. Sci. Bull.* **2002**, *47* (11), 890.

(31) Röß-Ohlenroth, R.; Bredenkötter, B.; Volkmer, D. Organometallic MFU-4*l* (arge) Metal−Organic Frameworks. *Organometallics* **2019**, *38* (18), 3444−3452.

(32) Jin, C.; Zhang, S.; Zhang, Z.; Chen, Y. Mimic Carbonic Anhydrase Using Metal-Organic Frameworks for CO_2 Capture and Conversion. *Inorg. Chem.* **2018**, *57* (4), 2169−2174.

(33) Cai, Z.; Bien, C. E.; Liu, Q.; Wade, C. R. Insights into CO 2 Adsorption in M−OH Functionalized MOFs. *Chem. Mater.* **2020**, *32* (10), 4257−4264.

(34) Bien, C. E.; Liu, Q.; Wade, C. R. Assessing the Role of Metal Identity on CO_2 Adsorption in MOFs Containing M−OH Functional Groups. *Chem. Mater.* **2020**, *32* (1), 489−497.

(35) Wright, A. M.; Wu, Z.; Zhang, G.; Mancuso, J. L.; Comito, R. J.; Day, R. W.; Hendon, C. H.; Miller, J. T.; Dincă, M. A Structural Mimic of Carbonic Anhydrase in a Metal-Organic Framework. *Chem.* **2018**, *4* (12), 2894−2901.

(36) Denysenko, D.; Werner, T.; Grzywa, M.; Puls, A.; Hagen, V.; Eickerling, G.; Jelic, J.; Reuter, K.; Volkmer, D. Reversible gas-phase redox processes catalyzed by Co-exchanged MFU-4l(arge). *Chem. Commun.* **2012**, *48* (9), 1236−1238.

(37) Denysenko, D.; Jelic, J.; Reuter, K.; Volkmer, D. Postsynthetic Metal and Ligand Exchange in MFU-4l:A Screening Approach toward Functional Metal-Organic Frameworks Comprising Single-Site Active Centers. *Chem. - Eur. J.* **2015**, *21* (22), 8188−8199.

(38) Denysenko, D.; Jelic, J.; Magdysyuk, O. V.; Reuter, K.; Volkmer, D. Elucidating Lewis acidity of metal sites in MFU-4l metal-organic frameworks:N_2O and CO_2 adsorption in MFU-4l, CuI-MFU-4l and Li-MFU-4l. *Microporous Mesoporous Mater.* **2015**, *216*, 146−150.

(39) Denysenko, D.; Grzywa, M.; Jelic, J.; Reuter, K.; Volkmer, D. Scorpionate-Type Coordination in MFU-4 *l* Metal-Organic Frameworks:Small-Molecule Binding and Activation upon the Thermally Activated Formation of Open Metal Sites. *Angew. Chem.* **2014**, *126* (23), 5942−5946.

(40) Denysenko, D.; Volkmer, D. Cyclic gas-phase heterogeneous process in a metal-organic framework involving a nickel nitrosyl complex. *Faraday Discuss.* **2017**, *201*, 101−112.

(41) Comito, R. J.; Fritzsching, K. J.; Sundell, B. J.; Schmidt-Rohr, K.; Dincă, M. Single-Site Heterogeneous Catalysts for Olefin Polymerization Enabled by Cation Exchange in a Metal-Organic Framework. *J. Am. Chem. Soc.* **2016**, *138* (32), 10232−10237.

(42) Metzger, E. D.; Comito, R. J.; Wu, Z.; Zhang, G.; Dubey, R. C.; Xu, W.; Miller, J. T.; Dincă, M. Highly Selective Heterogeneous Ethylene Dimerization with a Scalable and Chemically Robust MOF Catalyst. *ACS Sustainable Chem. Eng.* **2019**, *7* (7), 6654−6661.

(43) Metzger, E. D.; Comito, R. J.; Hendon, C. H.; Dincă, M. Mechanism of Single-Site Molecule-Like Catalytic Ethylene Dimerization in Ni-MFU-4l. *J. Am. Chem. Soc.* **2017**, *139* (2), 757−762.

(44) Bunzen, H.; Kolbe, F.; Kalytta-Mewes, A.; Sastre, G.; Brunner, E.; Volkmer, D. Achieving Large Volumetric Gas Storage Capacity in Metal-Organic Frameworks by Kinetic Trapping: A Case Study of

Xenon Loading in MFU-4. *J. Am. Chem. Soc.* **2018**, *140* (32), 10191−10197.

(45) Bunzen, H.; Kalytta-Mewes, A.; van Wüllen, L.; Volkmer, D. Long-term entrapment and temperature-controlled-release of SF6 gas in metal-organic frameworks (MOFs). *Beilstein J. Nanotechnol.* **2019**, *10*, 1851−1859.

(46) Teufel, J.; Oh, H.; Hirscher, M.; Wahiduzzaman, M.; Zhechkov, L.; Kuc, A.; Heine, T.; Denysenko, D.; Volkmer, D. MFU-4 – a metal-organic framework for highly effective H(2)/D(2) separation. *Adv. Mater.* **2013**, *25* (4), 635−639.

(47) Weinrauch, I.; Savchenko, I.; Denysenko, D.; Souliou, S. M.; Kim, H.-H.; Le Tacon, M.; Daemen, L. L.; Cheng, Y.; Mavrandonakis, A.; Ramirez-Cuesta, A. J.; Volkmer, D.; Schütz, G.; Hirscher, M.; Heine, T. Capture of heavy hydrogen isotopes in a metal-organic framework with active Cu(I) sites. *Nat. Commun.* **2017**, *8*, 14496.

(48) Ettlinger, R.; Sönksen, M.; Graf, M.; Moreno, N.; Denysenko, D.; Volkmer, D.; Kerl, K.; Bunzen, H. Metal-organic framework nanoparticles for arsenic trioxide drug delivery. *J. Mater. Chem. B* **2018**, *6* (40), 6481−6489.

(49) Grzywa, M.; Denysenko, D.; Hanss, J.; Scheidt, E.-W.; Scherer, W.; Weil, M.; Volkmer, D. CuN$_6$ Jahn-Teller centers in coordination frameworks comprising fully condensed Kuratowski-type secondary building units: phase transitions and magneto-structural correlations. *Dalton Trans.* **2012**, *41* (14), 4239−4248.

(50) Biswas, S.; Tonigold, M.; Kelm, H.; Krüger, H.-J.; Volkmer, D. Thermal spin-crossover in the M$_3$Zn$_6$Cl$_6$L$_{12}$ (M = Zn, Fe(II); L = 5,6-dimethoxy-1,2,3-benzotriazolate) system: structural, electrochemical, Mössbauer, and UV-Vis spectroscopic studies. *Dalton Trans.* **2010**, *39* (41), 9851−9859.

(51) Grzywa, M.; Röß-Ohlenroth, R.; Muschielok, C.; Oberhofer, H.; Błachowski, A.; Żukrowski, J.; Vieweg, D.; von Nidda, H.-A. K.; Volkmer, D. Cooperative Large-Hysteresis Spin-Crossover Transition in the Iron(II) Triazolate Fe(ta)$_2$ Metal-Organic Framework. *Inorg. Chem.* **2020**, *59* (15), 10501−10511.

(52) Gándara, F.; Uribe-Romo, F. J.; Britt, D. K.; Furukawa, H.; Lei, L.; Cheng, R.; Duan, X.; O'Keeffe, M.; Yaghi, O. M. Porous, conductive metal-triazolates and their structural elucidation by the charge-flipping method. *Chem. - Eur. J.* **2012**, *18* (34), 10595−10601.

(53) Lan, Y.-Q.; Li, S.-L.; Jiang, H.-L.; Xu, Q. Tailor-made metal-organic frameworks from functionalized molecular building blocks and length-adjustable organic linkers by stepwise synthesis. *Chem. - Eur. J.* **2012**, *18* (26), 8076−8083.

(54) Li, Y.-W.; He, K.-H.; Bu, X.-H. Bottom-up assembly of a porous MOF based on nanosized nonanuclear zinc precursors for highly selective gas adsorption. *J. Mater. Chem. A* **2013**, *1* (13), 4186.

(55) Cui, L.; Geng, Y.-F.; Leong, C. F.; Ma, Q.; D'Alessandro, D. M.; Deng, K.; Zeng, Q.-D.; Zuo, J.-L. Synthesis, properties and surface self-assembly of a pentanuclear cluster based on the new π-conjugated TTF-triazole ligand. *Sci. Rep.* **2016**, *6*, 25544.

(56) Cheeseman, G. W. H. 223. Quinoxalines and related compounds. Part VI. Substitution of 2,3-dihydroxyquinoxaline and its 1,4-dimethyl derivative. *J. Chem. Soc.* **1962**, 1170.

(57) Coburn, M. D. Nitro derivatives of 1-picrylbenzotriazole. *J. Heterocycl. Chem.* **1973**, *10* (5), 743−746.

(58) Rombouts, J. A.; Ravensbergen, J.; Frese, R. N.; Kennis, J. T. M.; Ehlers, A. W.; Slootweg, J. C.; Ruijter, E.; Lammertsma, K.; Orru, R. V. A. Synthesis and photophysics of a red-light absorbing supramolecular chromophore system. *Chem. - Eur. J.* **2014**, *20* (33), 10285−10291.

(59) SAINT; Bruker Analytical X-Ray Systems, Inc., Madison, WI, 2015.

(60) Krause, L.; Herbst-Irmer, R.; Sheldrick, G. M.; Stalke, D. Comparison of silver and molybdenum microfocus X-ray sources for single-crystal structure determination. *J. Appl. Crystallogr.* **2015**, *48* (1), 3−10.

(61) Sheldrick, G. M. SHELXT - integrated space-group and crystal-structure determination. *Acta Crystallogr., Sect. A: Found. Adv.* **2015**, *71* (1), 3−8.

(62) Sheldrick, G. M. Crystal structure refinement with SHELXL. *Acta Crystallogr., Sect. C: Struct. Chem.* **2015**, *71* (1), 3−8.

(63) Rouquerol, F. *Adsorption by Powders and Porous Solids: Principles, Methodology and Applications*, 2nd Edition; Academic Press, 2014.

(64) Jagiello, J.; Thommes, M. Comparison of DFT characterization methods based on N$_2$, Ar, CO$_2$, and H$_2$ adsorption applied to carbons with various pore size distributions. *Carbon* **2004**, *42* (7), 1227−1232.

(65) Ravikovitch, P. I.; Neimark, A. V. Characterization of nanoporous materials from adsorption and desorption isotherms. *Colloids Surf., A* **2001**, *187−188*, 11−21.

(66) Gondzik, S.; Bläser, D.; Wölper, C.; Schulz, S. Novel synthetic pathway for new Zn-Zn-bonded compounds from dizincocene. *Chem. - Eur. J.* **2010**, *16* (46), 13599−13602.

(67) Gioia Lobbia, G.; Bovio, B.; Santini, C.; Pettinari, C.; Marchetti, F. First-row transition and group 12 element bis[poly[4-methyl-1H-pyrazol-1-yl)borate]] derivatives. X-ray crystal structure of Zn[HB(4-Mepz)3]2·CHCl3. *Polyhedron* **1997**, *16* (4), 671−680.

(68) Spek, A. L. Single-crystal structure validation with the program PLATON. *J. Appl. Crystallogr.* **2003**, *36* (1), 7−13.

(69) Caldeweyher, E.; Bannwarth, C.; Grimme, S. Extension of the D3 dispersion coefficient model. *J. Chem. Phys.* **2017**, *147* (3), 034112.

(70) *TURBOMOLE rev. V7.5.0*; TURBOMOLE GmbH, Karlsruhe, Germany, 2020.

(71) Allen, F. H.; Kennard, O.; Watson, D. G.; Brammer, L.; Orpen, A. G.; Taylor, R. Tables of bond lengths determined by X-ray and neutron diffraction. Part 1. Bond lengths in organic compounds. *J. Chem. Soc., Perkin Trans. 2* **1987**, No. 12, S1.

(72) Stolić, I.; Bajić, M.; Matković-Čalogović, D. Effect of Hydrogen Bonding on the Pyramidalization of the Amino Group:Structure of 3,4-diaminobenzamidinium Chloride. *Croat. Chem. Acta* **2013**, *86* (2), 193−199.

(73) Steiner, T. Hydrogen-Bond Distances to Halide Ions in Organic and Organometallic Crystal Structures: Up-to-date Database Study. *Acta Crystallogr., Sect. B: Struct. Sci.* **1998**, *54* (4), 456−463.

(74) Jeffrey, G. A. *An introduction to hydrogen bonding*; Topics in Physical Chemistry Series; Oxford University Press, 1997.

(75) Saeed, M. A.; Fronczek, F. R.; Hossain, M. A. Encapsulated chloride coordinating with two in-in protons of bridgehead amines in an octaprotonated azacryptand. *Chem. Commun.* **2009**, No. 42, 6409−6411.

(76) Lakshminarayanan, P. S.; Suresh, E.; Ghosh, P. A hybrid water-chloride structure with discrete undecameric water moieties self-assembled in a heptaprotonated octaamino cryptand. *Angew. Chem., Int. Ed.* **2006**, *45* (23), 3807−3811.

(77) Inoue, Y.; Kanbara, T.; Yamamoto, T. Preparation of a new receptor for anions, macrocyclic polythiolactam—structure and high anion-binding ability. *Tetrahedron Lett.* **2003**, *44* (28), 5167−5169.

(78) Haque, S. A.; Saeed, M. A.; Jahan, A.; Wang, J.; Leszczynski, J.; Hossain, M. A. Experimental and Theoretical Aspects of Anion Complexes with a Thiophene-Based Cryptand. *Comments Inorg. Chem.* **2016**, *36* (6), 305−326.

(79) Eberle, B.; Kaifer, E.; Himmel, H.-J. A Stable Hexakis-(guanidino)benzene: Realization of the Strongest Neutral Organic Four-Electron Donor. *Angew. Chem., Int. Ed.* **2017**, *56* (12), 3360−3363.

(80) *BIOVIA Materials Studio 2021 (21.1.1.8)*; Dassault Systèmes, 2019.

(81) Dubbeldam, D.; Calero, S.; Vlugt, T. J. iRASPA:GPU-accelerated visualization software for materials scientists. *Mol. Simul.* **2018**, *44* (8), 653−676.

(82) Chen, B.; Liang, C.; Yang, J.; Contreras, D. S.; Clancy, Y. L.; Lobkovsky, E. B.; Yaghi, O. M.; Dai, S. A microporous metal-organic framework for gas-chromatographic separation of alkanes. *Angew. Chem., Int. Ed.* **2006**, *45* (9), 1390−1393.

(83) Horike, S.; Shimomura, S.; Kitagawa, S. Soft porous crystals. *Nat. Chem.* **2009**, *1* (9), 695−704.. (Published online: Nov. 23, 2009.)

(84) He, Y.; Xiang, S.; Chen, B. A microporous hydrogen-bonded organic framework for highly selective C_2H_2/C_2H_4 separation at ambient temperature. *J. Am. Chem. Soc.* **2011**, *133* (37), 14570–14573.

(85) Rahman, S.; Arami-Niya, A.; Yang, X.; Xiao, G.; Li, G.; May, E. F. Temperature dependence of adsorption hysteresis in flexible metal organic frameworks. *Commun. Chem.* **2020**, *3* (1), DOI: 10.1038/s42004-020-00429-3.

(86) Howarth, A. J.; Peters, A. W.; Vermeulen, N. A.; Wang, T. C.; Hupp, J. T.; Farha, O. K. Best Practices for the Synthesis, Activation, and Characterization of Metal–Organic Frameworks. *Chem. Mater.* **2017**, *29* (1), 26–39.

(87) Cooper, A. I. Porous Molecular Solids and Liquids. *ACS Cent. Sci.* **2017**, *3* (6), 544–553.

(88) Feng, D.; Lei, T.; Lukatskaya, M. R.; Park, J.; Huang, Z.; Lee, M.; Shaw, L.; Chen, S.; Yakovenko, A. A.; Kulkarni, A.; Xiao, J.; Fredrickson, K.; Tok, J. B.; Zou, X.; Cui, Y.; Bao, Z. Robust and conductive two-dimensional metal–organic frameworks with exceptionally high volumetric and areal capacitance. *Nat. Energy* **2018**, *3* (1), 30–36.

(89) Sheberla, D.; Sun, L.; Blood-Forsythe, M. A.; Er, S.; Wade, C. R.; Brozek, C. K.; Aspuru-Guzik, A.; Dincă, M. High electrical conductivity in Ni_3(2,3,6,7,10,11-hexaiminotriphenylene)$_2$, a semiconducting metal-organic graphene analogue. *J. Am. Chem. Soc.* **2014**, *136* (25), 8859–8862.

Supporting Information

Assembly of Porous Metal Hydrogen-Bonded Organic Frameworks from Diamine-Functionalized Kuratowski Complexes

Richard Röß-Ohlenroth, Corbinian Freudig, Maryana Kraft, Hana Bunzen and Dirk Volkmer*

Chair of Solid State and Materials Chemistry, Institute of Physics, University of Augsburg, Universitätsstraße 1, 86159 Augsburg, Germany

TABLE OF CONTENTS

Optical microscopy images and sample photograph

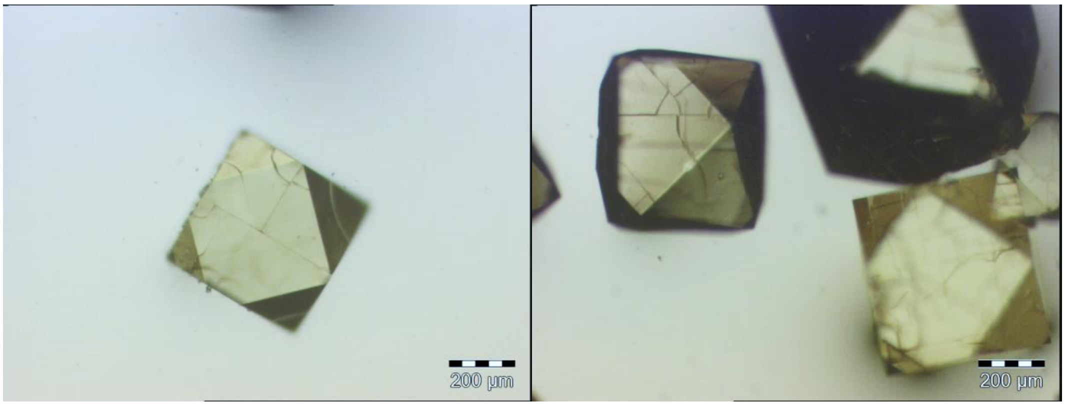

Figure S 1. Optical microscopy images of **CFA-20-Cl** single crystals

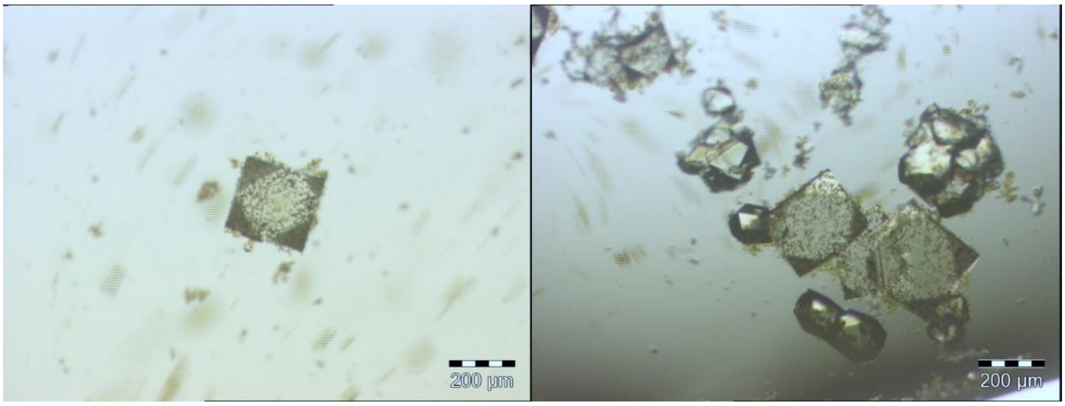

Figure S 2. Optical microscopy images of **CFA-20-Br** single crystals

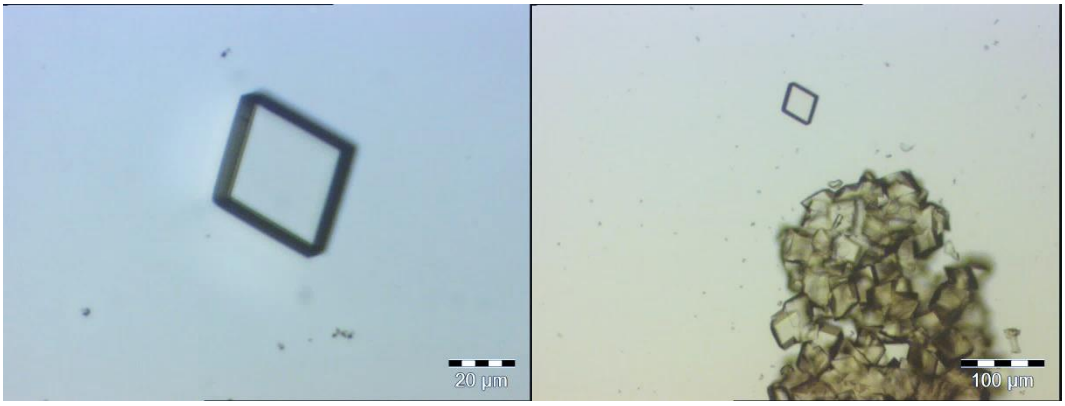

Figure S 3. Optical microscopy images of **CFA-20-Tp** single crystals

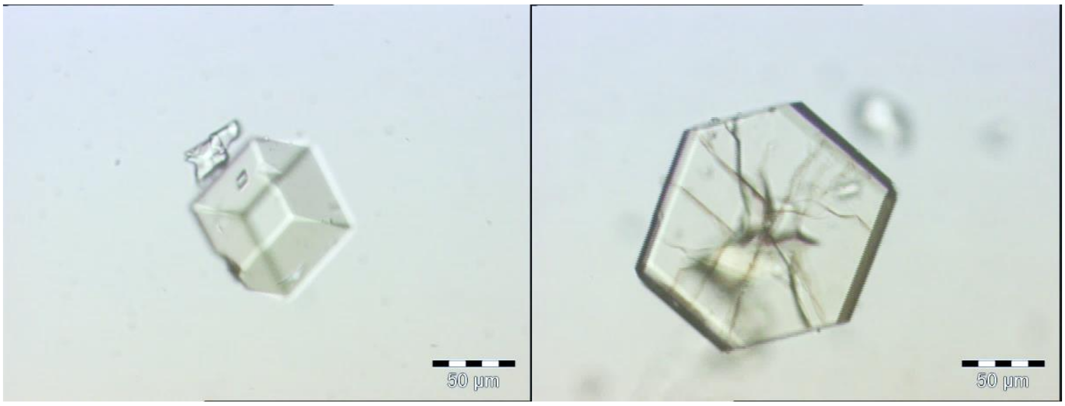

Figure S 4. Optical microscopy images of **CFA-20-Tp*** single crystals

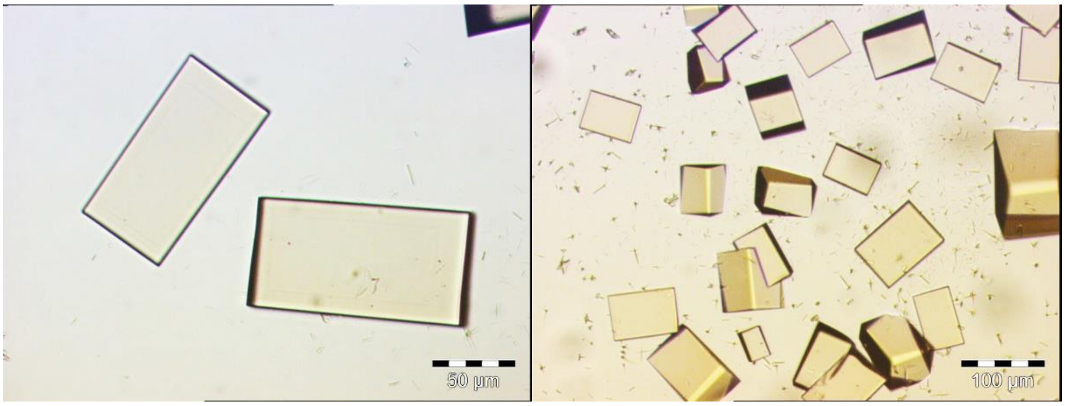

Figure S 5. Optical microscopy images of **CFA-20-Tp*-DMSO** single crystals

Figure S 6. A photograph of a **H-btda** ligand sample

Crystal structure plots

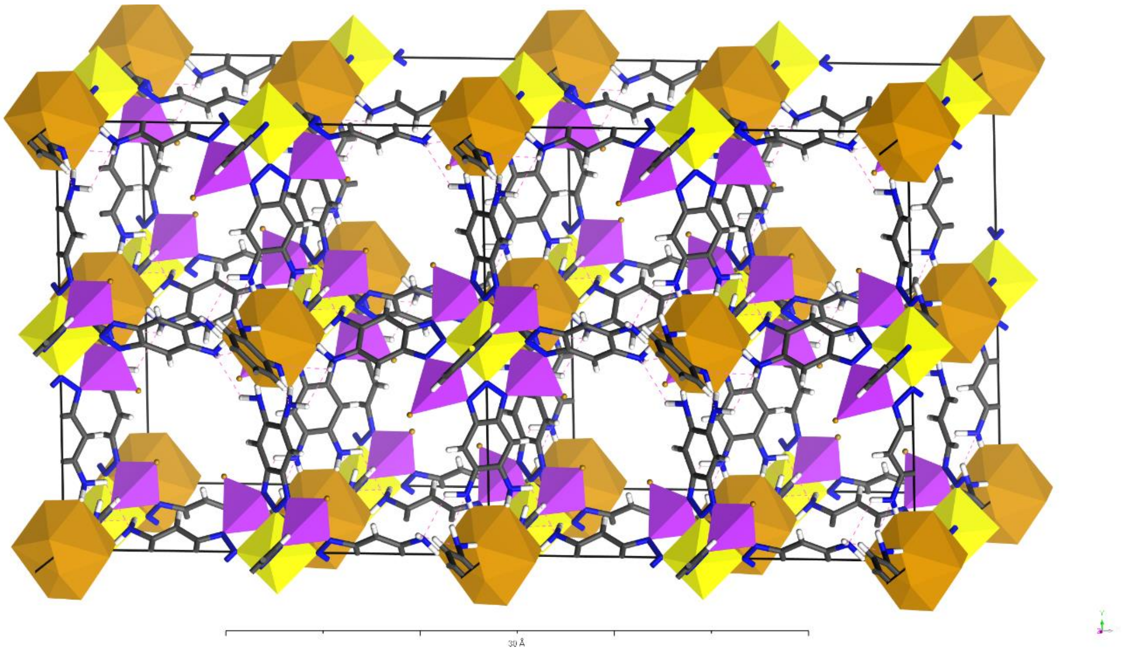

Figure S 7. Crystal structure of **CFA-20-Br**

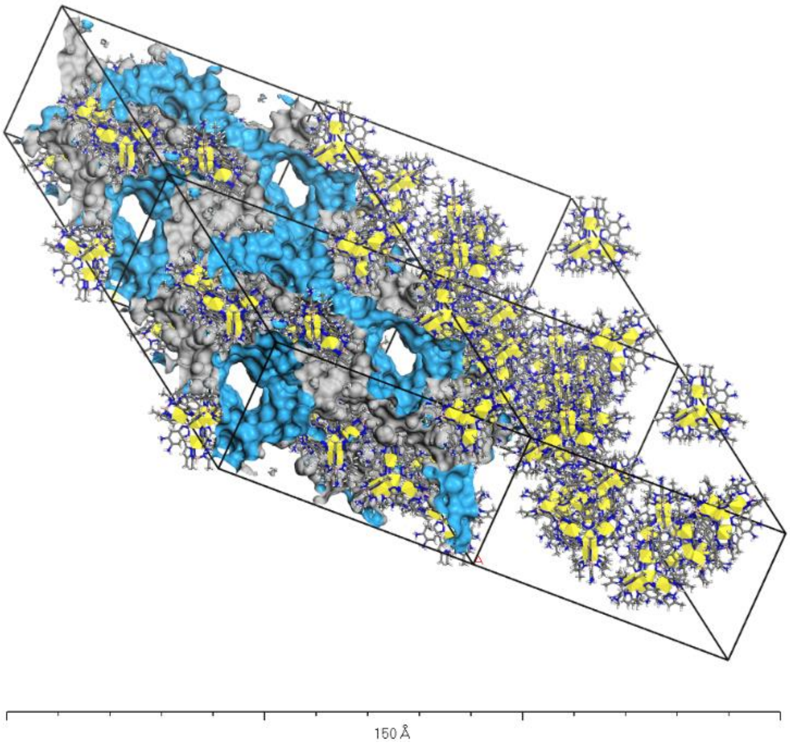

Figure S 8. View along the interconnecting pores of the **CFA-20-Tp*** structure with a plot of the Connolly surface created with BIOVIA Materials Studio 2019[1]

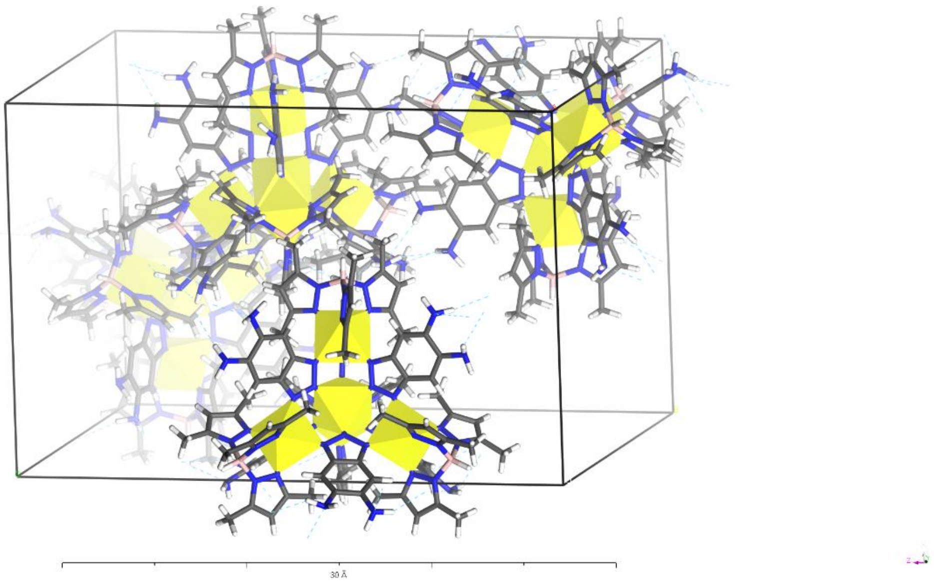

Figure S 9. Crystal structure of **CFA-20-Tp*-DMSO**

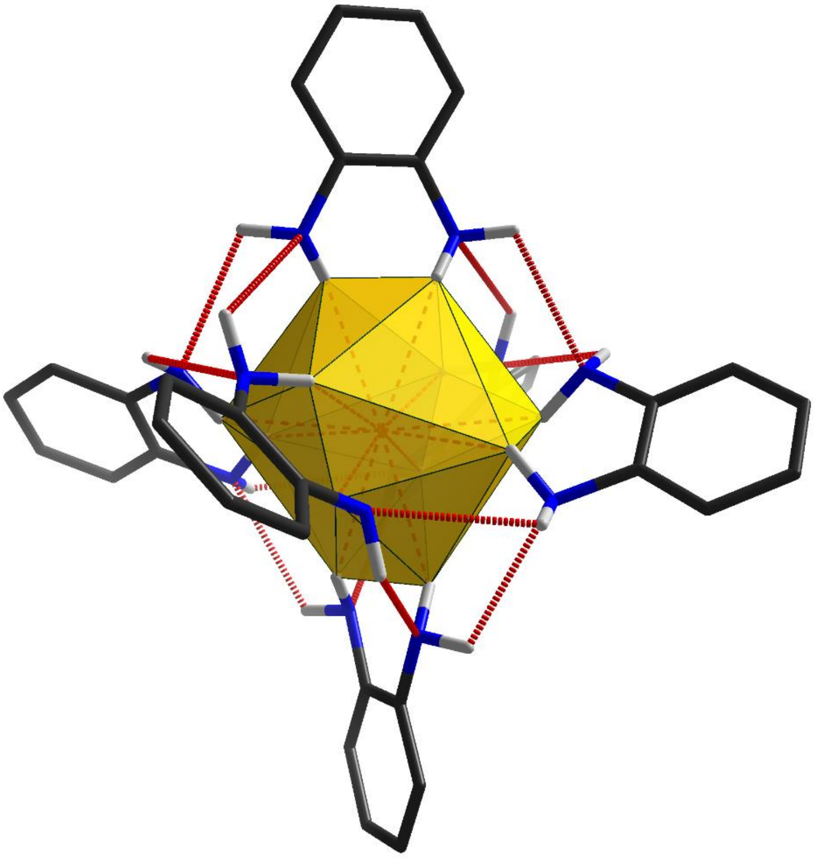

Figure S 10. Simulated hydrogen bond framework of **CFA-20-Br**

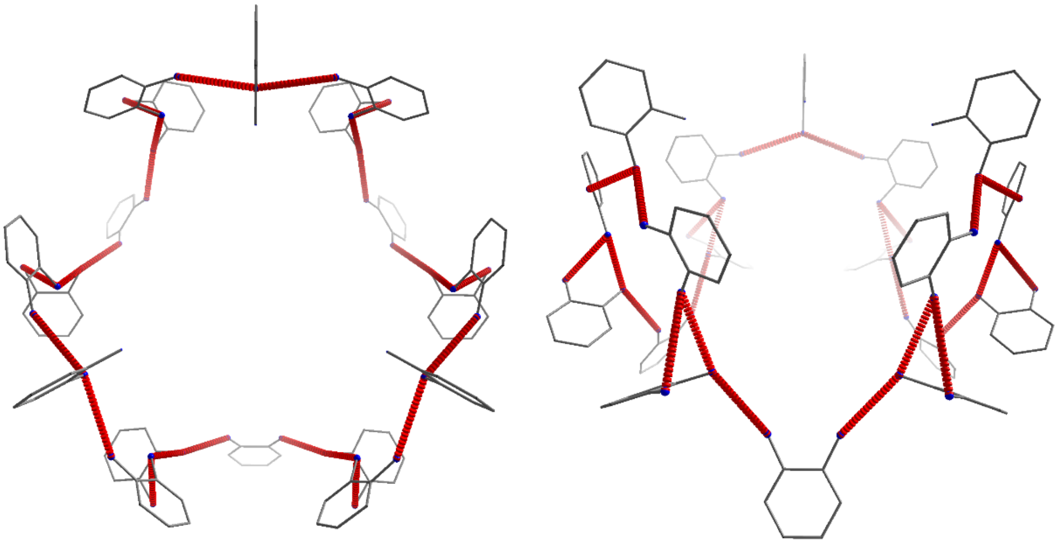

Figure S 11. View along the *c*-direction (left) and sideways (right) of the close contacts (red) of the amines in **CFA-20-Tp**

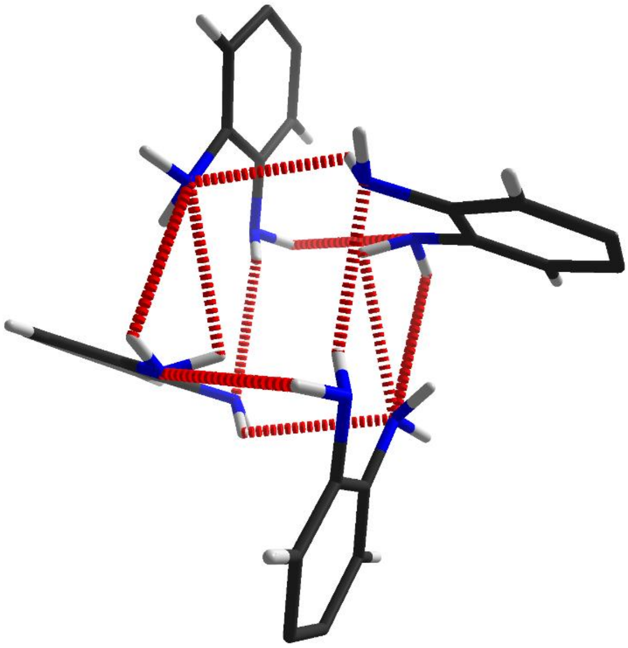

Figure S 12. Cube-like HOF SBU in **CFA-20-Tp*** showing the intermolecular hydrogen bonds (red)

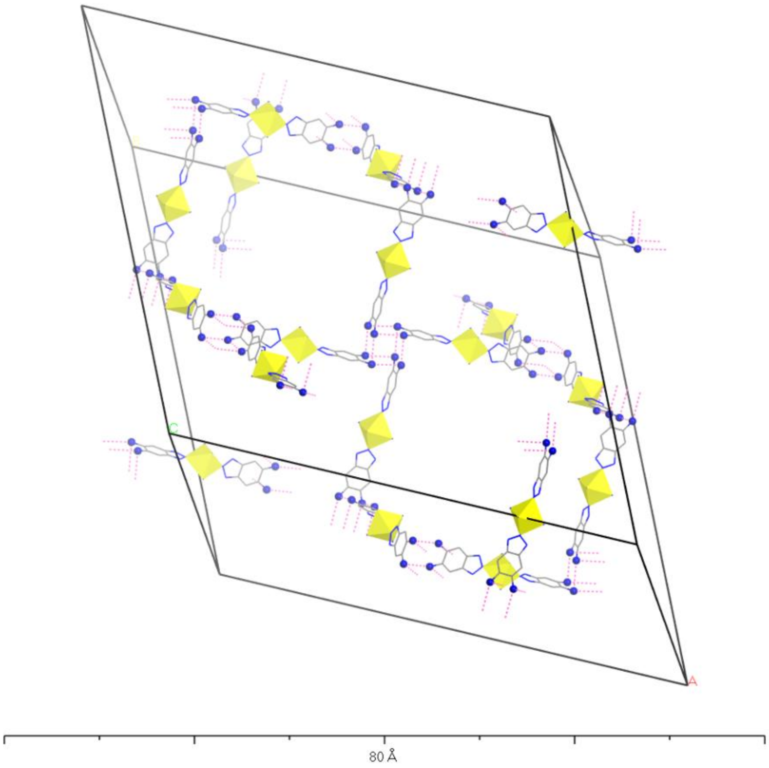

Figure S 13. Reduced **CFA-20-Tp*** structure showing the connection network of the cube-like HOF SBUs between the complex building units

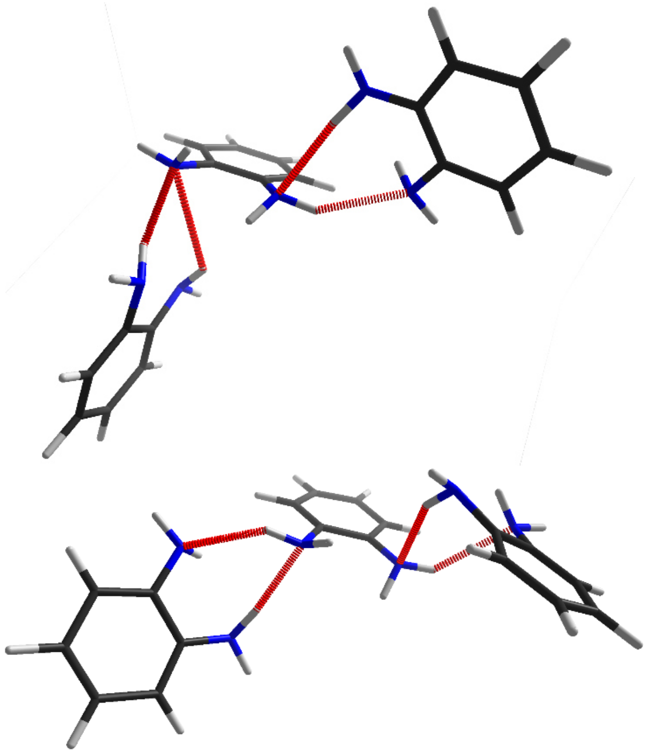

Figure S 14. HOF SBUs in **CFA-20-Tp*** showing the intermolecular hydrogen bonds (red)

N···N distance tables

Note here that literature considers the strength of hydrogen bonds according to the donor-acceptor distances as strong (2.2-2.5 Å), medium (2.5-3.2 Å) and weak (3.2-4.0 Å).[2]

Table S 1. N···N distances indicating hydrogen bond interactions for **CFA-20-Tp**

N···N	Distance [Å]
N4···N14	3.147
N18···N14	3.367
N4···N15	3.616
N5···N10	3.708

Table S 2. N···N distances indicating hydrogen bond interactions for **CFA-20-Tp***

N···N	Distance [Å]
N42···N26	3.224
N42···N37	3.273
N39···N37	3.294
N39···N26	3.312

Table S 3. N···N distances indicating hydrogen bond interactions for **CFA-20-Tp*-DMSO**

N···N	Distance [Å]
N12···N42	3.024
N40···N53	3.103
N40···N52	3.163
N48···N1	3.180
N51···N5	3.222
N10···N42	3.252
N51···N6	3.381
N48···N54	3.505
N51···N1	3.763
N51···N54	3.823

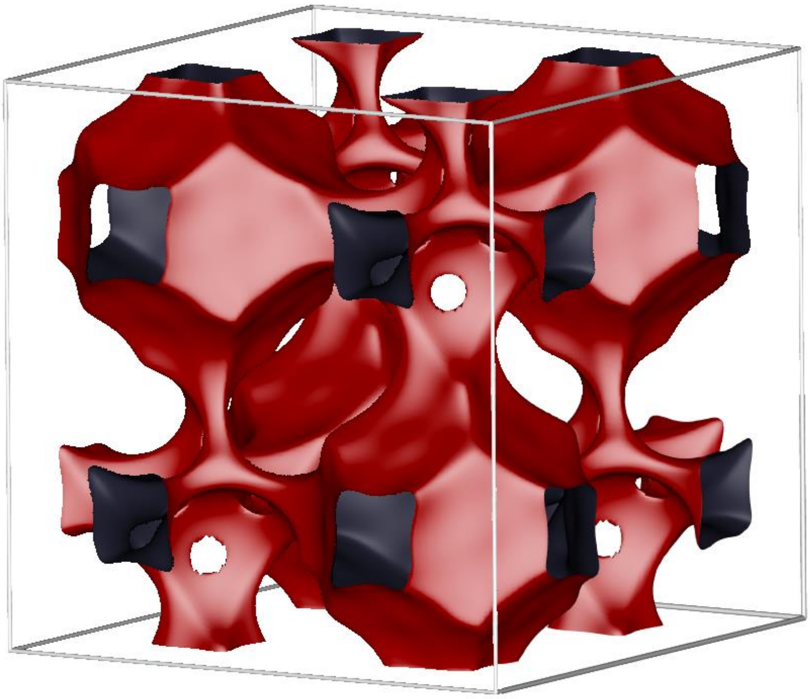

Figure S 15. Plot of the argon adsorption surface using iRASPA software[3], visualizing the alternating pores in the **CFA-20-Cl** framework

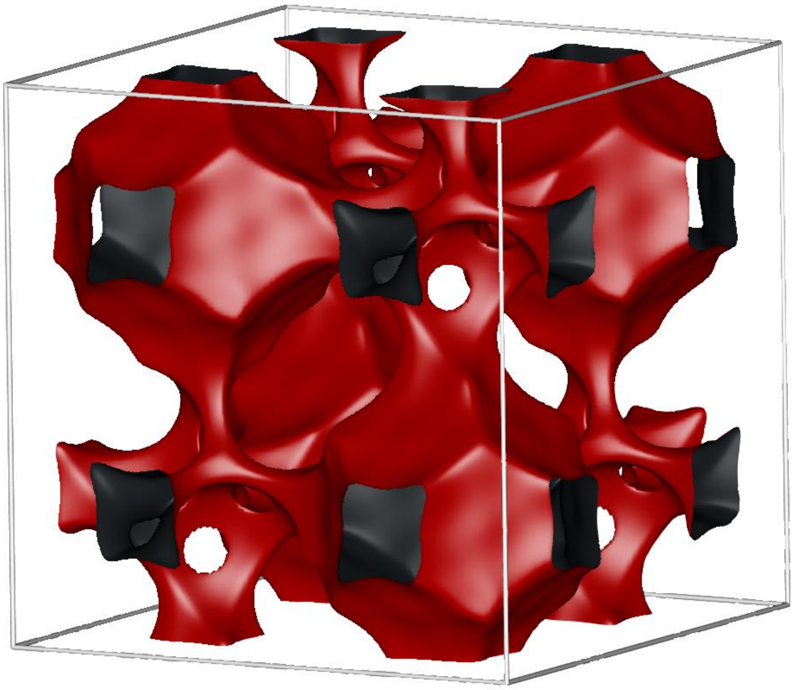

Figure S 16. Plot of the argon adsorption surface using iRASPA software[3], visualizing the alternating pores in the **CFA-20-Br** framework

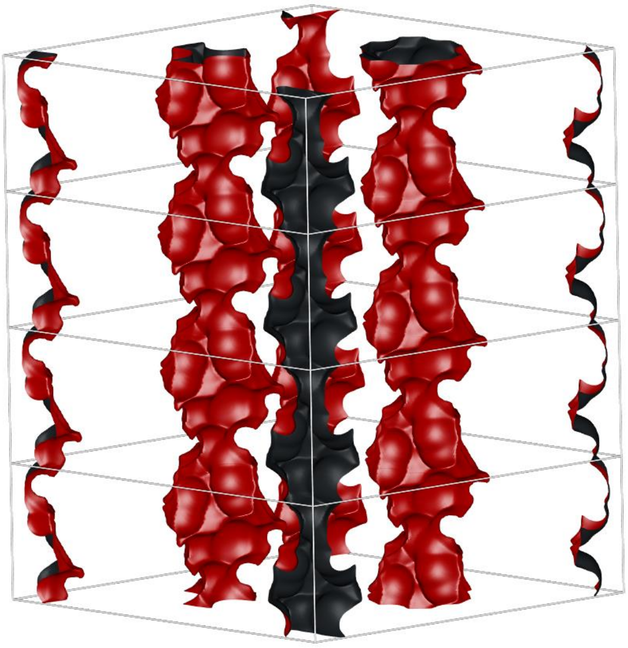

Figure S 17. Plot of the argon adsorption surface using iRASPA software[3], visualizing the channel pores in the c-direction of the **CFA-20-Tp** framework

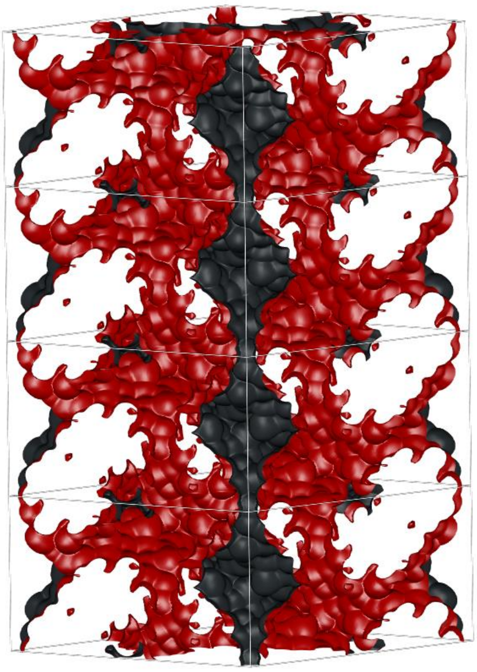

Figure S 18. Plot of the argon adsorption surface using iRASPA software[3], visualizing the 3D pore network of the **CFA-20-Tp*** framework

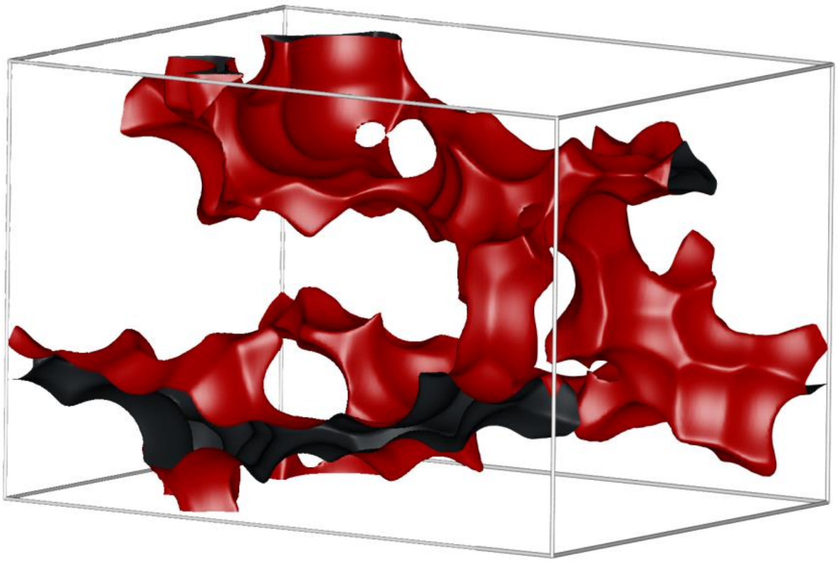

Figure S 19. Plot of the argon adsorption surface using iRASPA software[3], visualizing the 3D pore network of the **CFA-20-Tp*-DMSO** framework

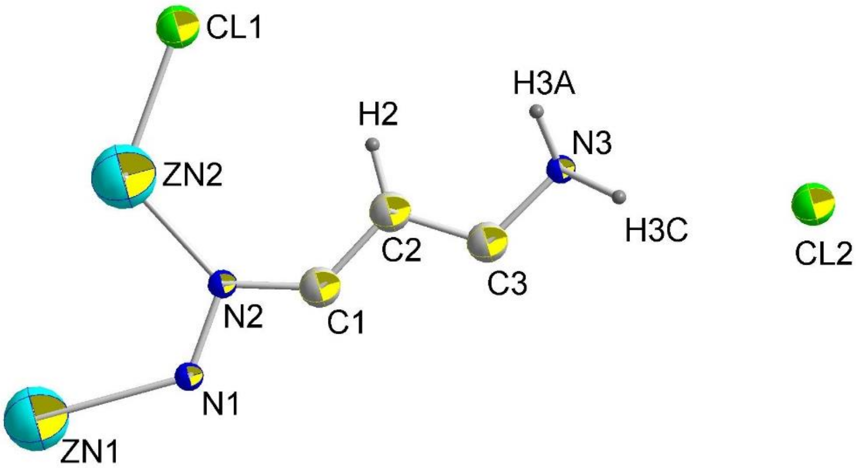

Figure S 20. ORTEP-Style plot of the asymmetric unit of **CFA-20-Cl** with a 50% probability for the thermal ellipsoids.

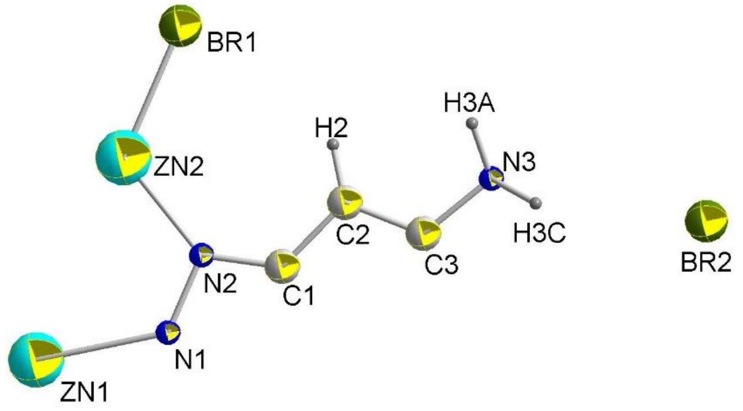

Figure S 21. ORTEP-Style plot of the asymmetric unit of **CFA-20-Br** with a 50% probability for the thermal ellipsoids.

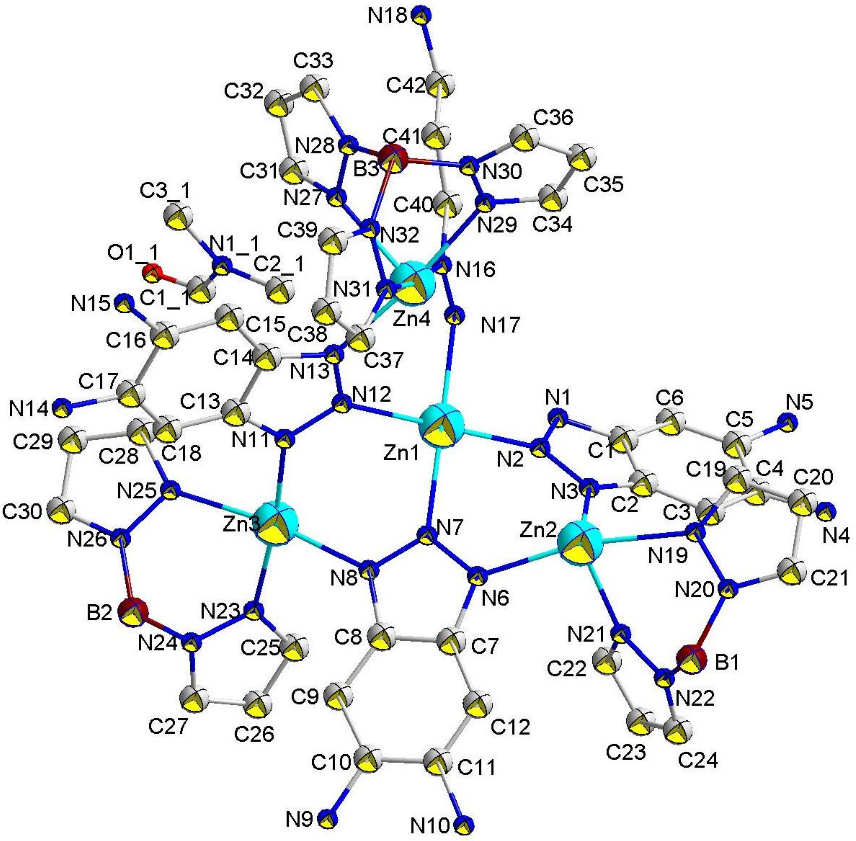

Figure S 22. ORTEP-Style plot of the asymmetric unit of **CFA-20-Tp** with a 50% probability for the thermal ellipsoids. Hydrogen atoms have been omitted for clarity.

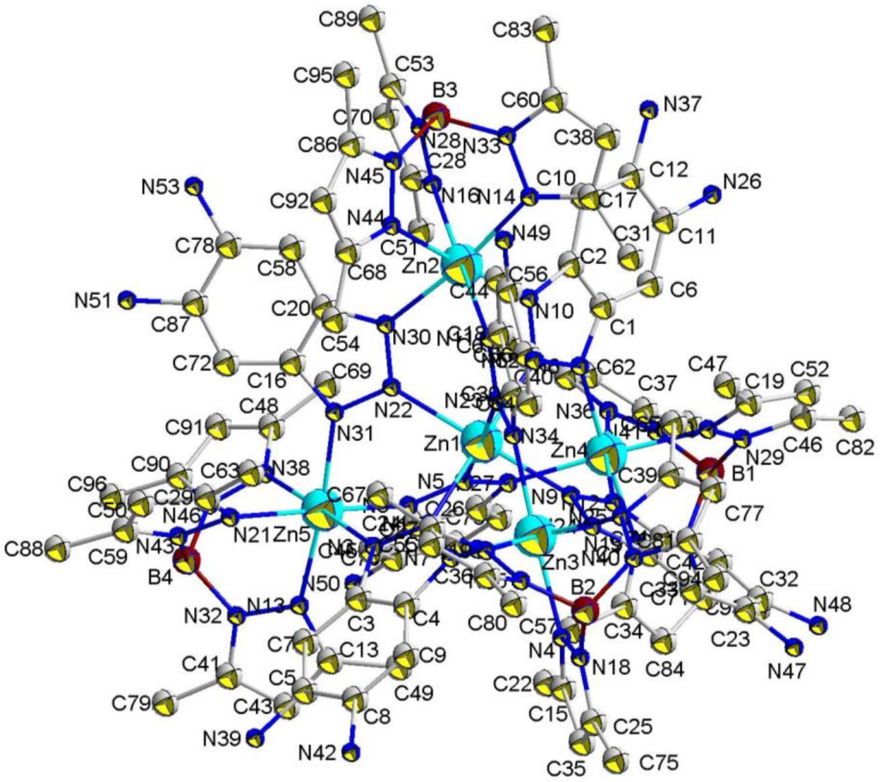

Figure S 23. ORTEP-Style plot of the asymmetric unit of **CFA-20-Tp*** with a 50% probability for the thermal ellipsoids. Hydrogen atoms have been omitted for clarity.

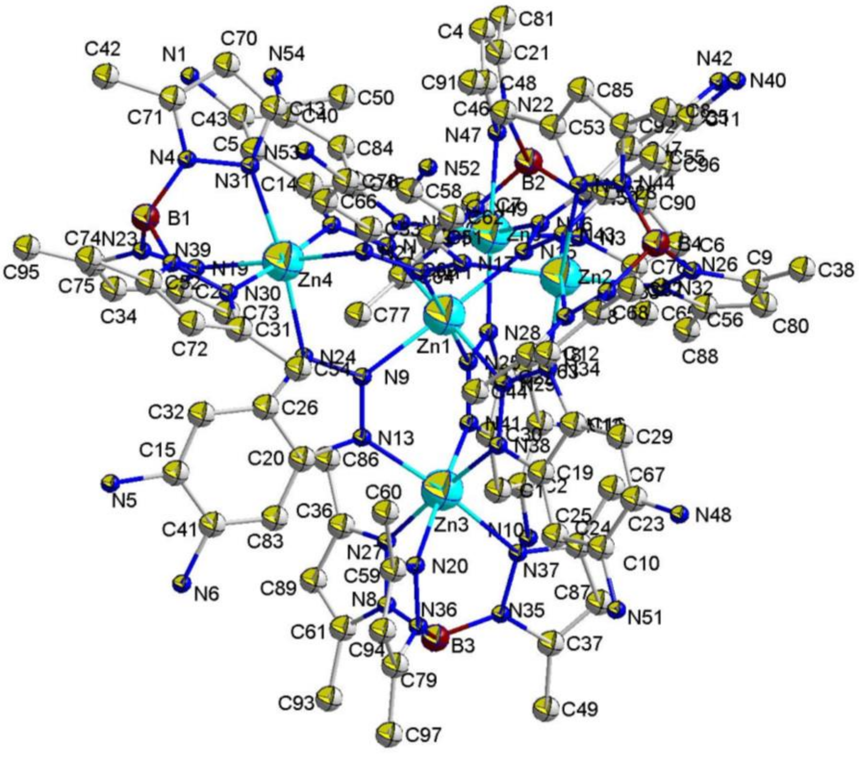

Figure S 24. ORTEP-Style plot of the asymmetric unit of **CFA-20-Tp*-DMSO** with a 50% probability for the thermal ellipsoids. Hydrogen atoms have been omitted for clarity.

Synthesis Scheme

Scheme S 1. Synthesis of the 1*H*-benzotriazole-5,6-diamine (**H-btda**) ligand

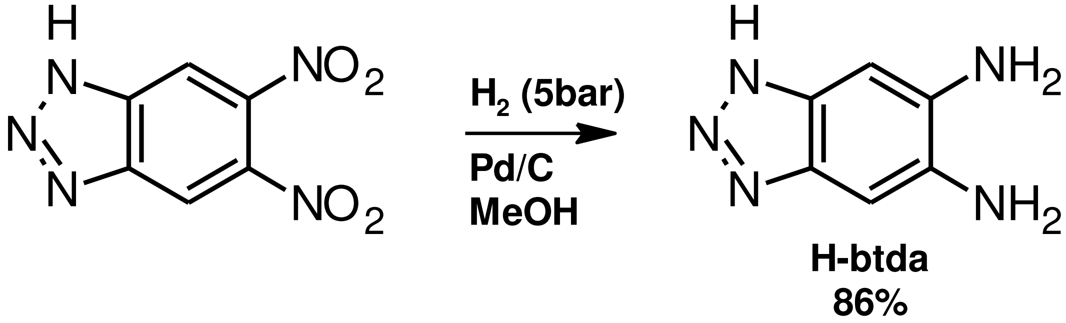

NMR spectra

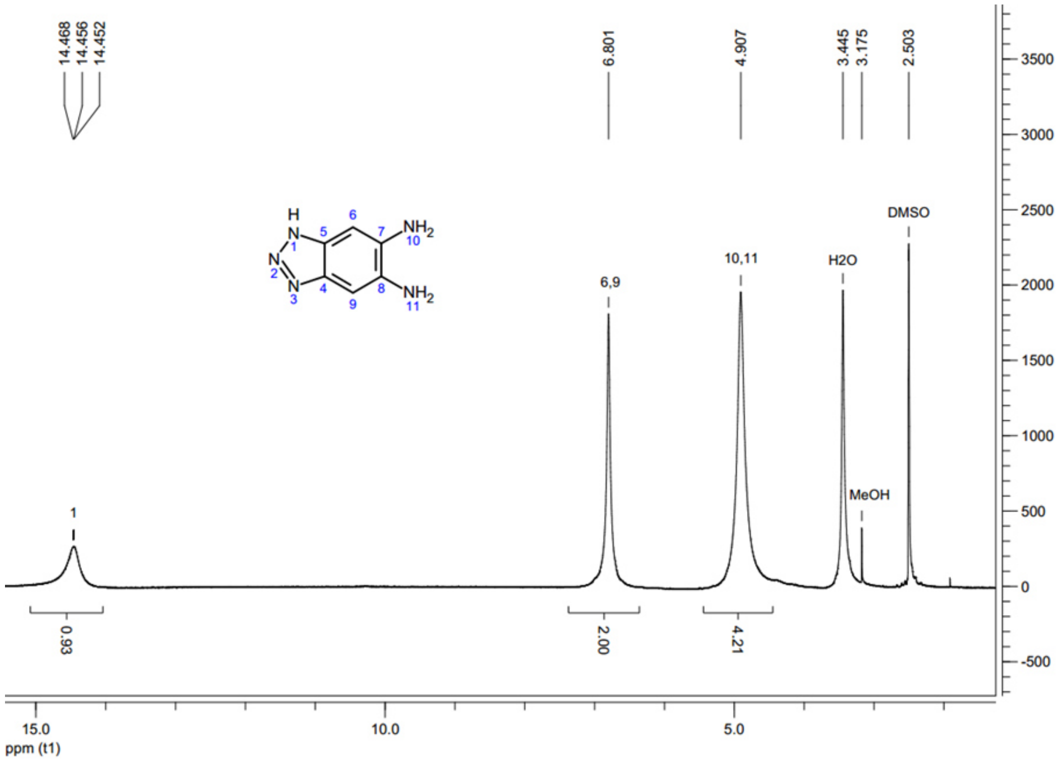

Figure S 25. ^{1}H-NMR spectrum of **H-btda** in DMSO-d6

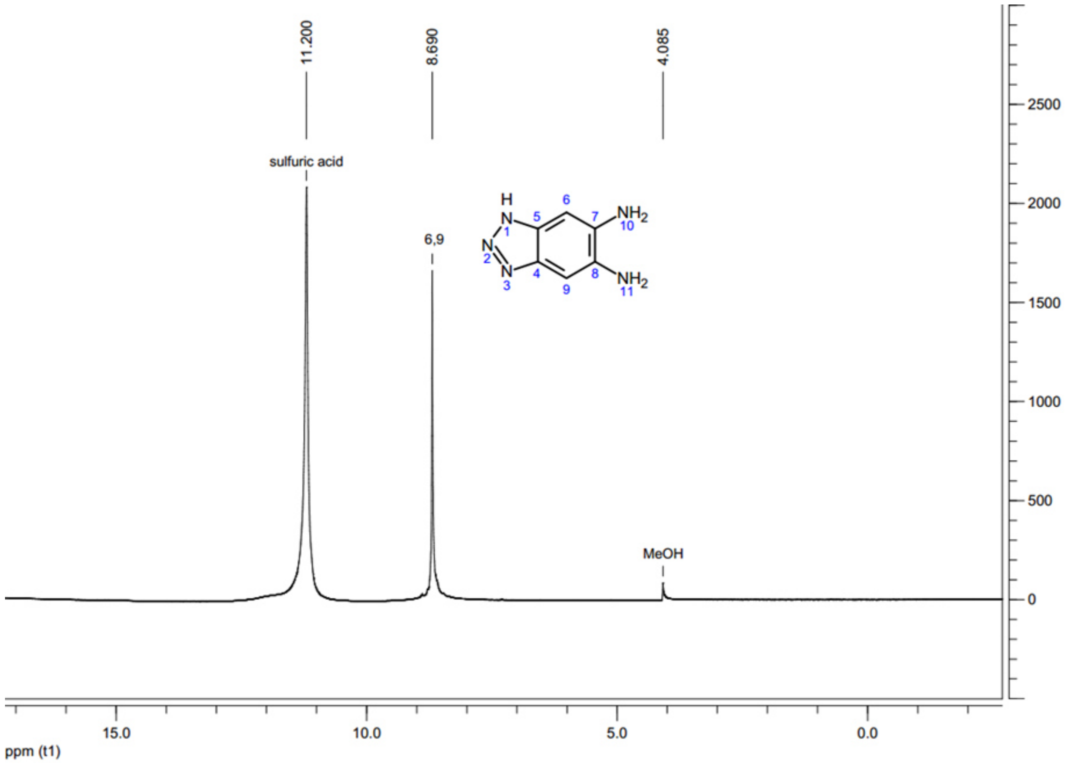

Figure S 26. ^{1}H-NMR spectrum of **H-btda** in D_2SO_4

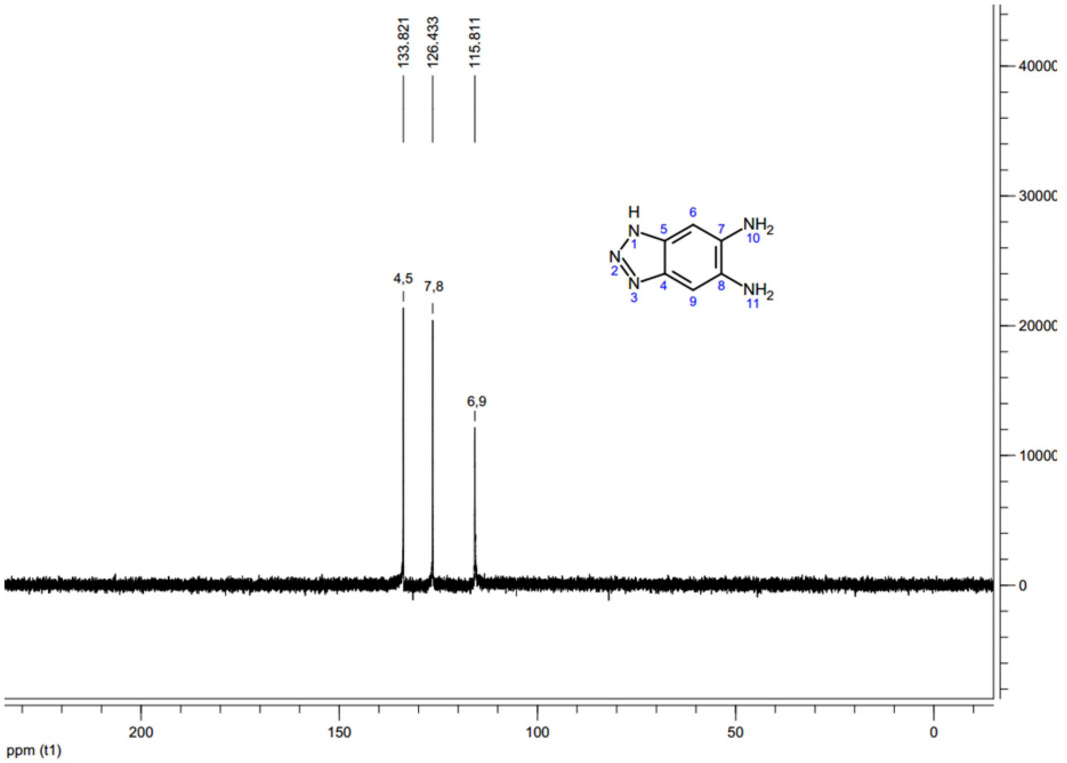

Figure S 27. ^{13}C-NMR spectrum of **H-btda** in D_2SO_4

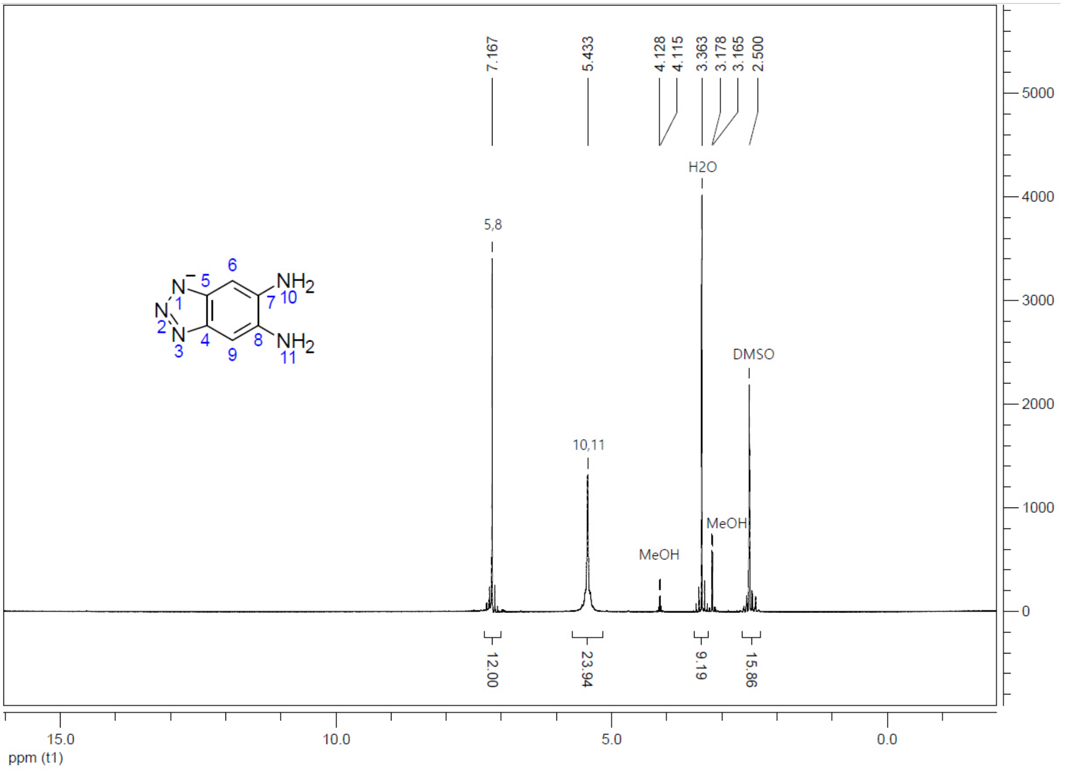

Figure S 28. ^{1}H-NMR spectrum of **CFA-20-Cl** in DMSO-d6

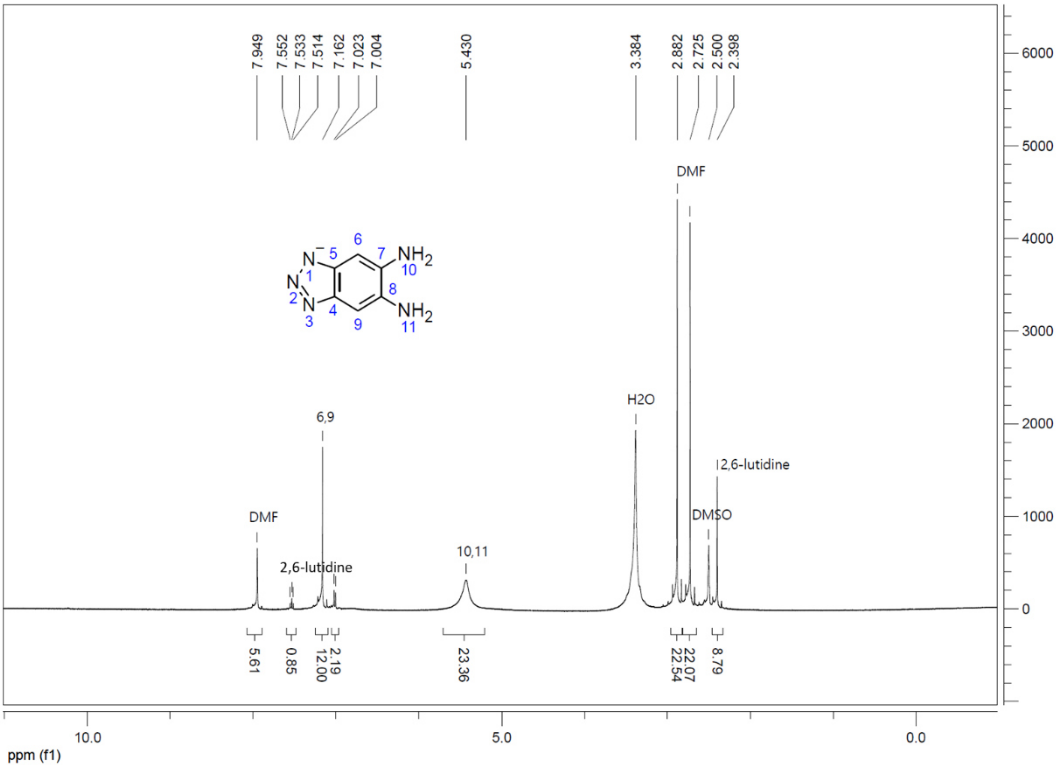

Figure S 29. ^{1}H-NMR spectrum of nonwashed **CFA-20-Cl** in DMSO-d6

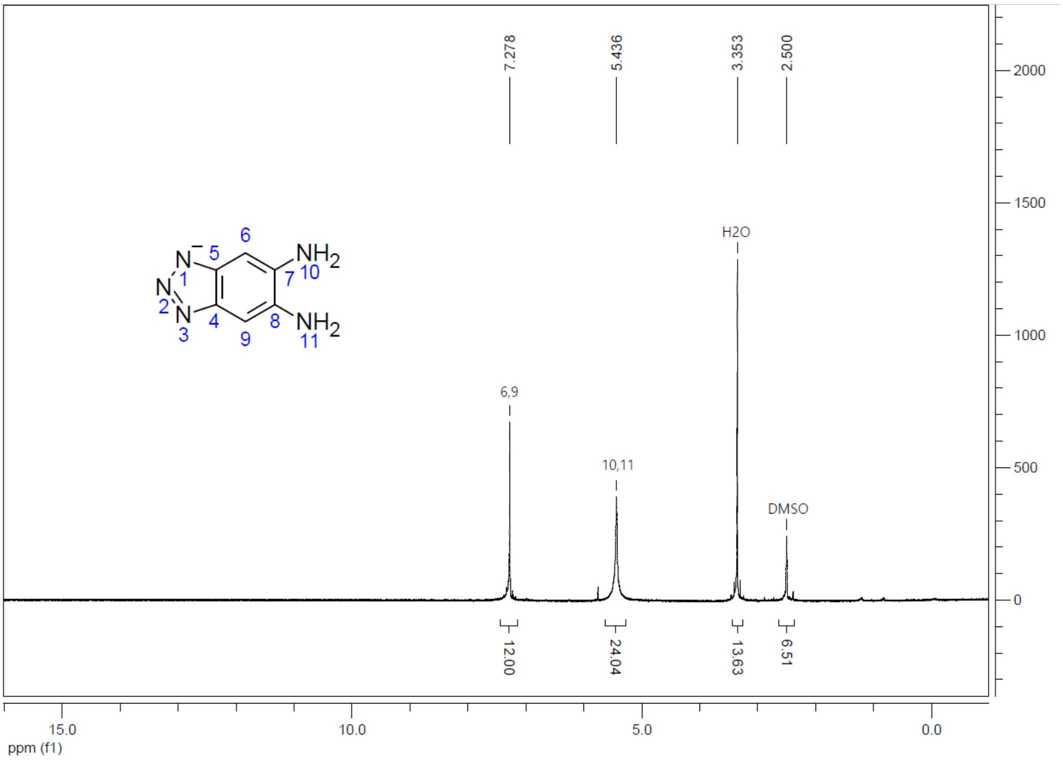

Figure S 30. ^{1}H-NMR spectrum of **CFA-20-Br** in DMSO-d6

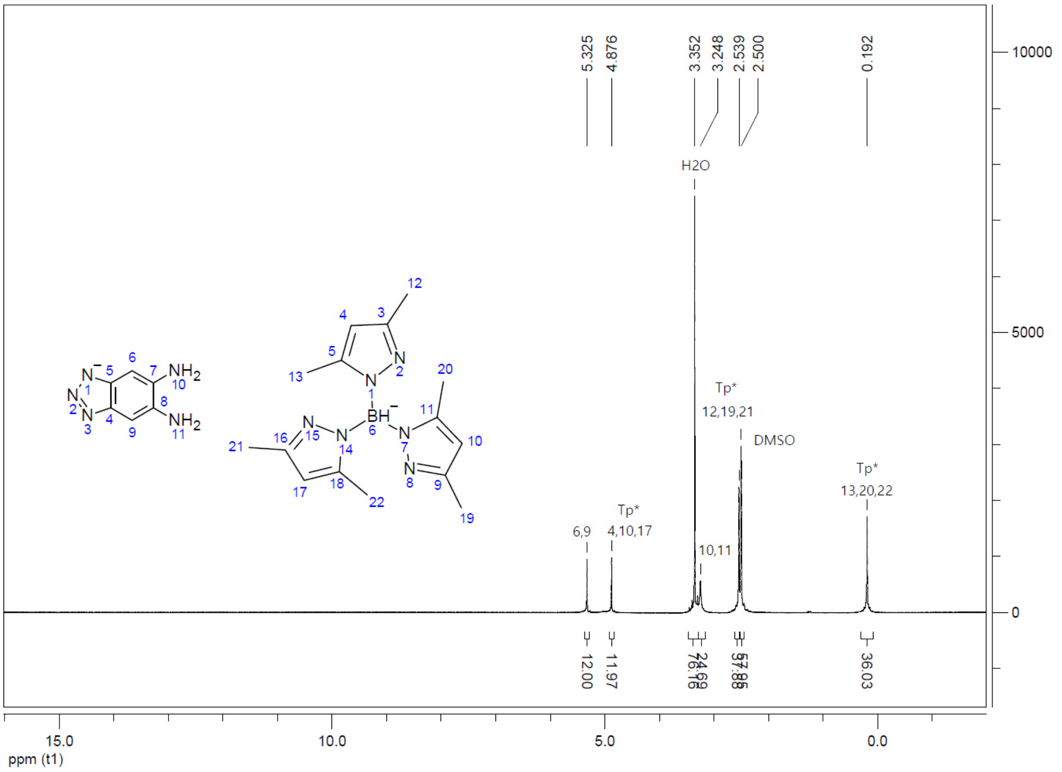

Figure S 31. ^{1}H-NMR spectrum of **CFA-20-Tp*** in DMSO-d6

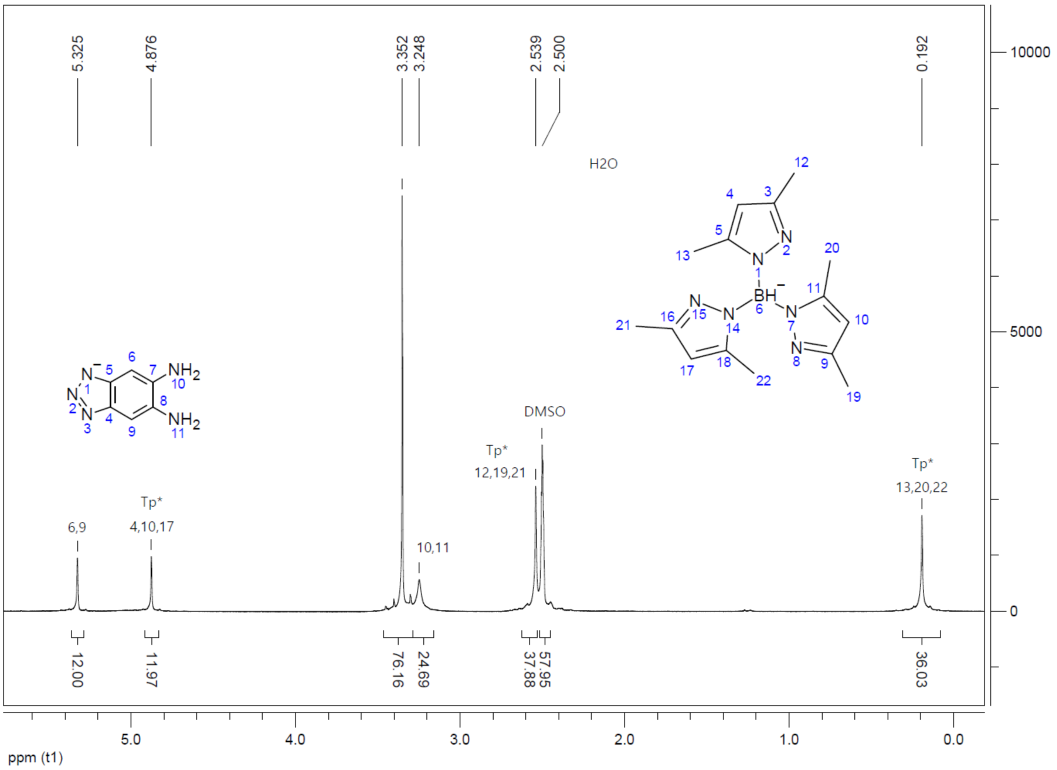

Figure S 32. Enlarged ^{1}H-NMR spectrum of **CFA-20-Tp*** in DMSO-d6

ESI-MS data

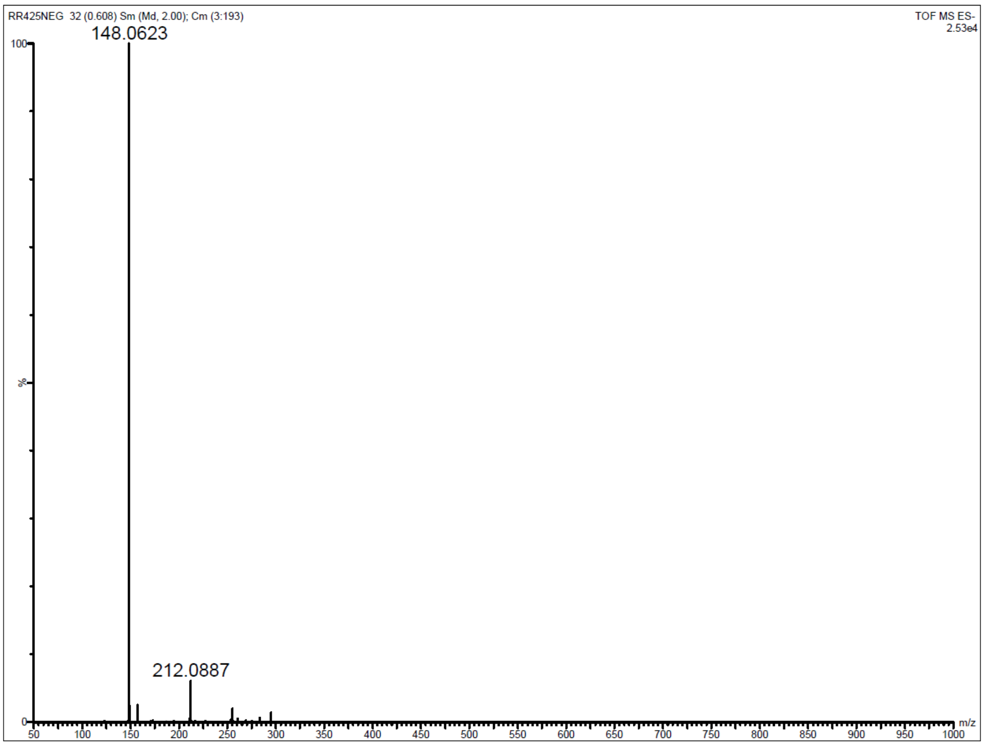

Figure S 33. High-resolution ESI$^-$-MS spectrum of the **H-btda** ligand; m/z calcd for $(C_6H_6N_5)^-$ = 148.0629 [M-H]$^-$; found: 148.0623 m/z

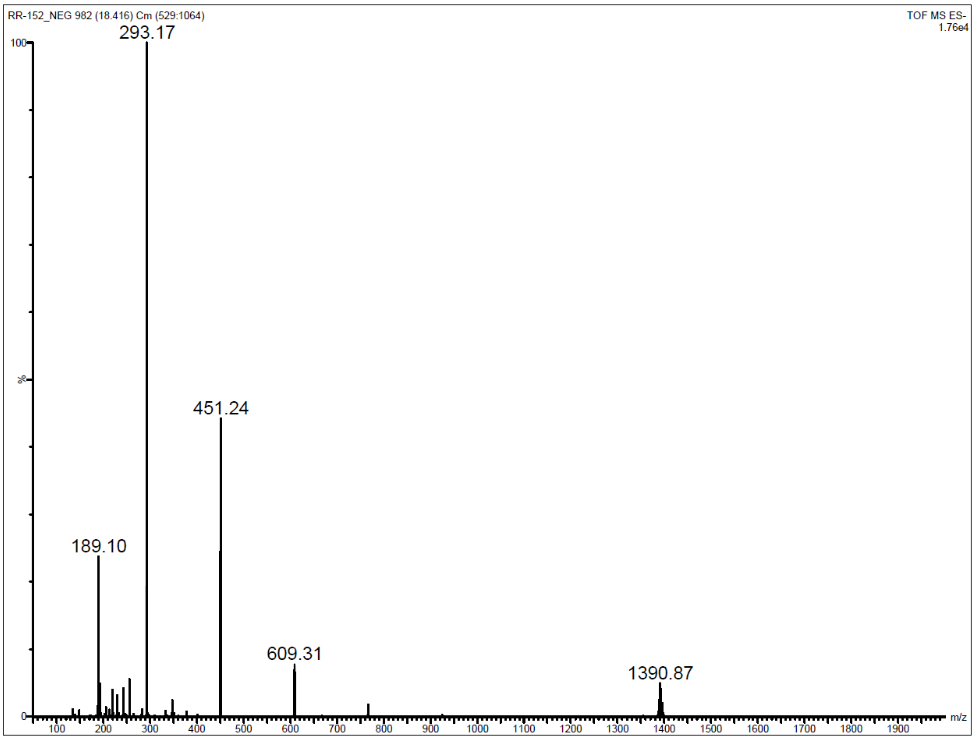

Figure S 34. ESI$^-$-MS spectrum of **CFA-20-Cl**; m/z calcd for [M-H]$^-$ = 1392.85 m/z; found: 1392.87 m/z

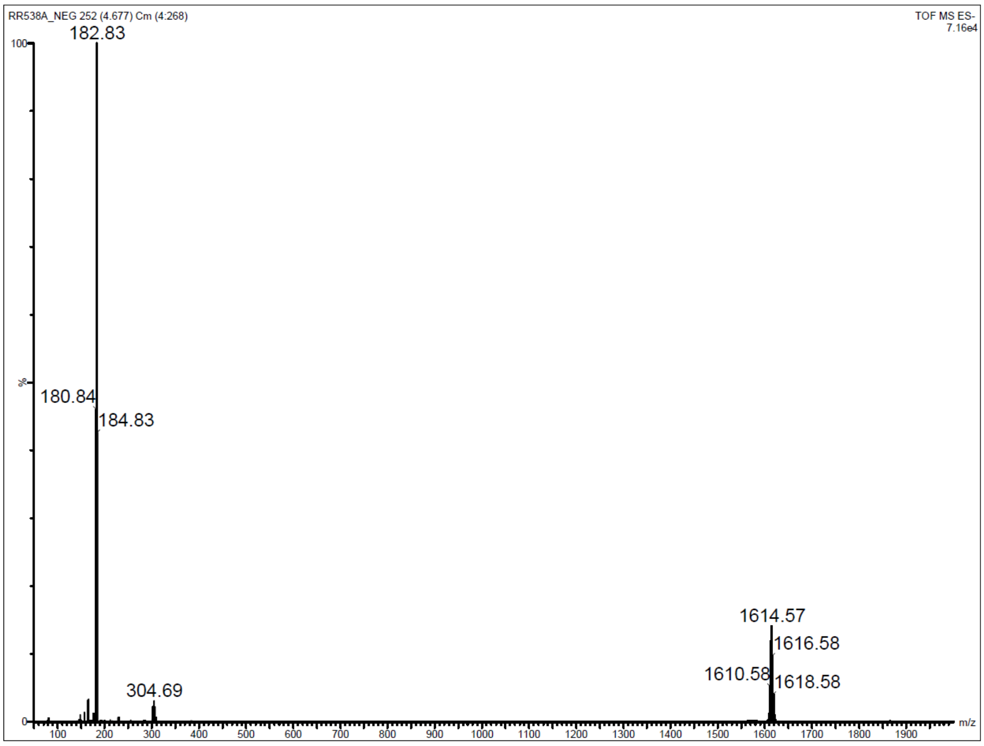

Figure S 35. ESI$^-$-MS spectrum of **CFA-20-Br**; m/z calcd for $[M-H]^-$ = 1614.60 m/z; found: 1614.57 m/z

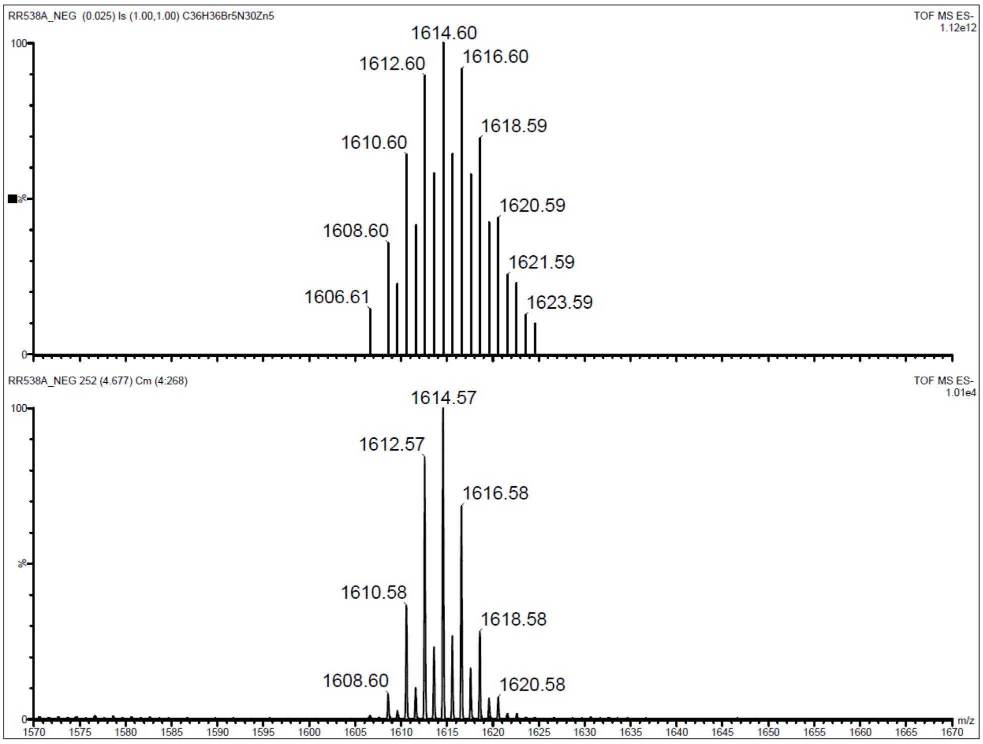

Figure S 36. ESI$^-$-MS spectra calculated for $[M-H]^-$ ($Zn_5Br_5C_{36}N_{30}H_{36}$) (top) and measured for **CFA-20-Br** (bottom)

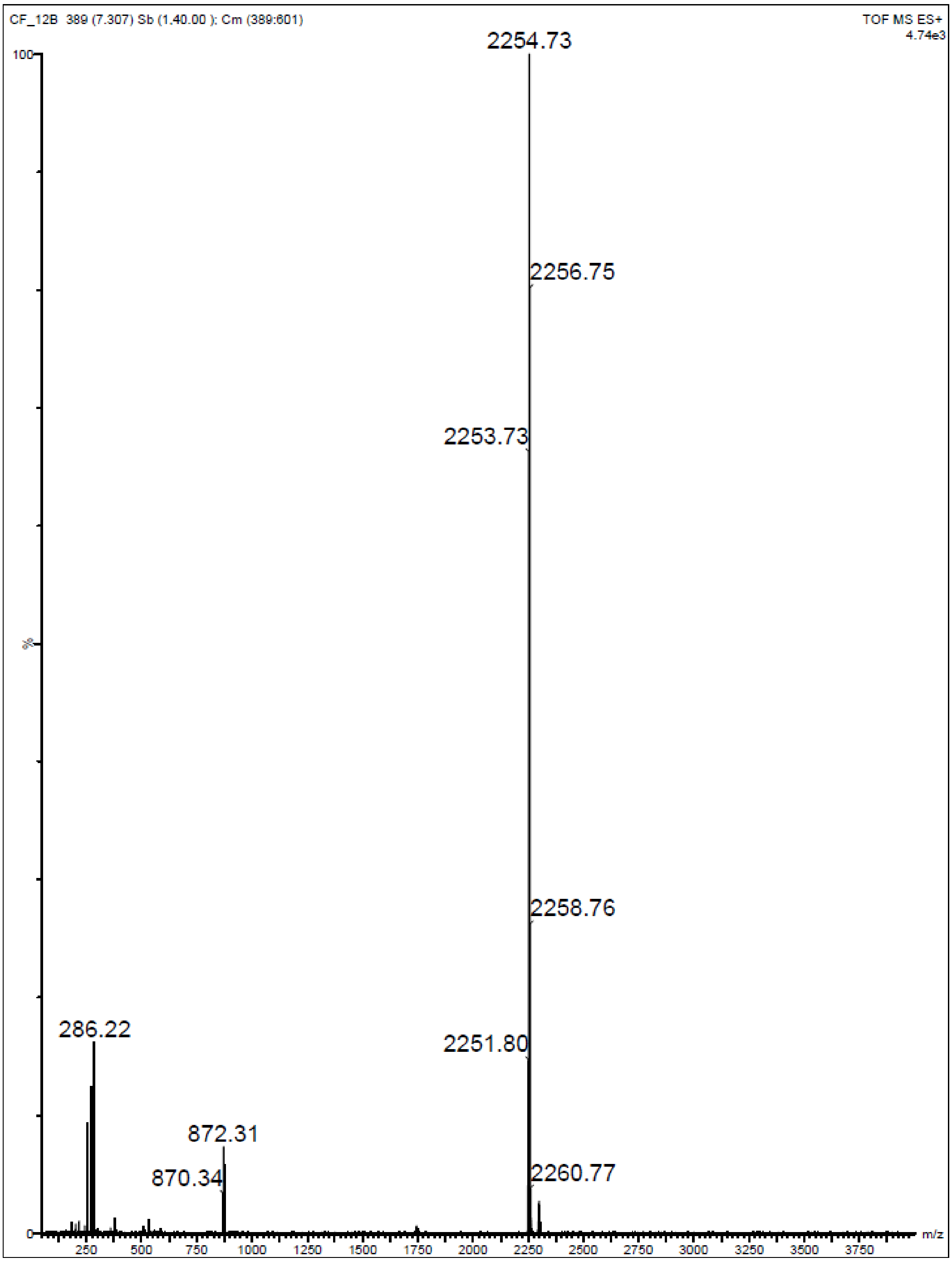

Figure S 37. ESI$^+$-MS spectrum of **CFA-20-Tp***; m/z calcd for $[M\text{-}(btda)]^+ = 2256.75$; found: 2256.75 m/z

A 123

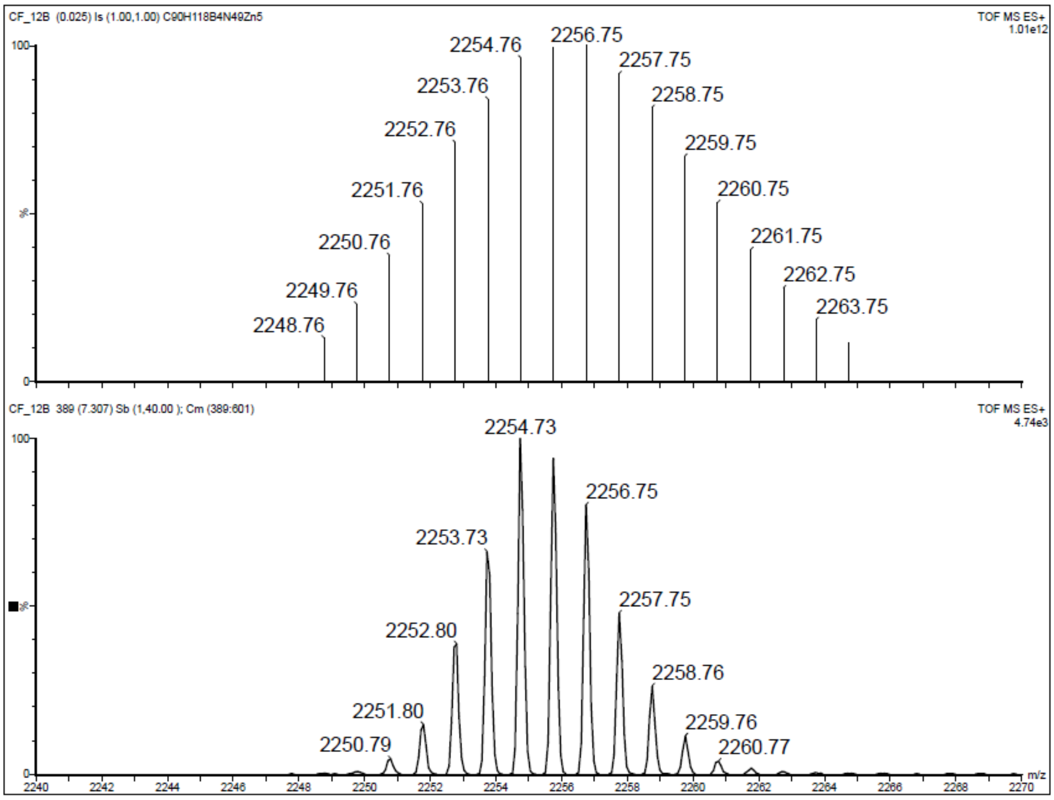

Figure S 38. ESI$^+$-MS spectra calculated for [M-(btda)$^-$]$^+$ ($C_{90}H_{118}B_4N_{49}Zn_5$) (top) and measured for **CFA-20-Tp*** (bottom)

A 124

IR spectra

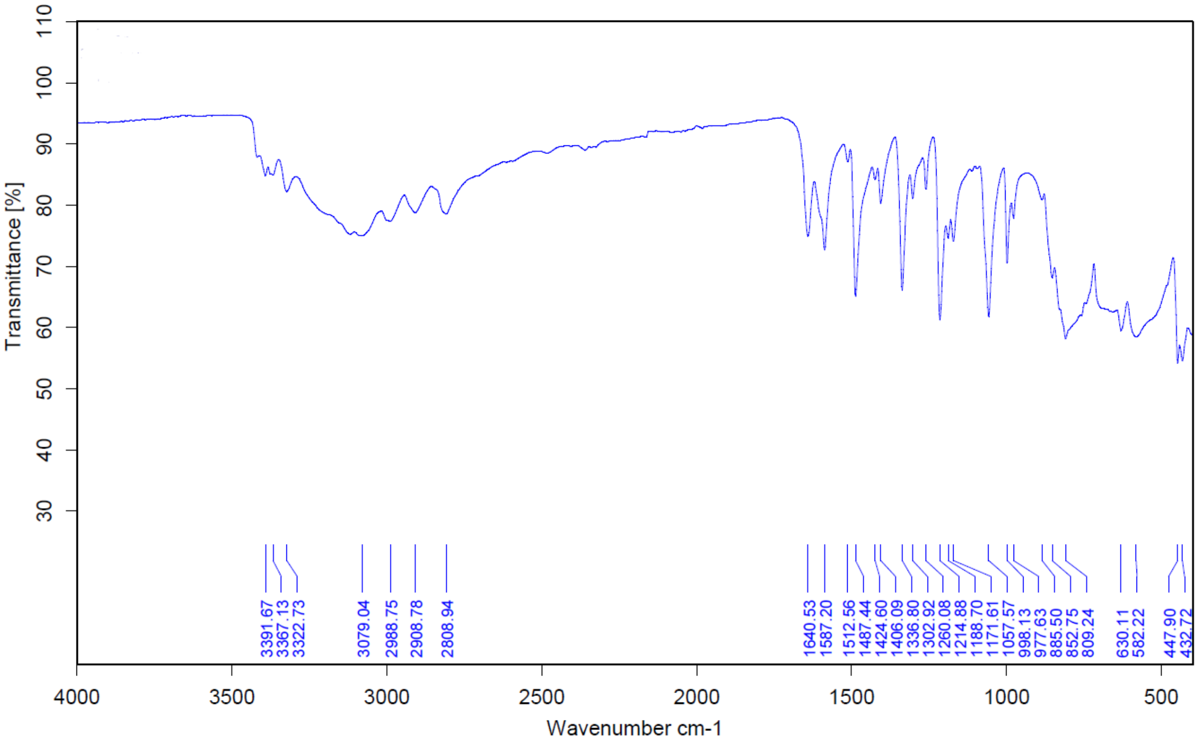

Figure S 39. IR spectrum of the **H-btda** ligand

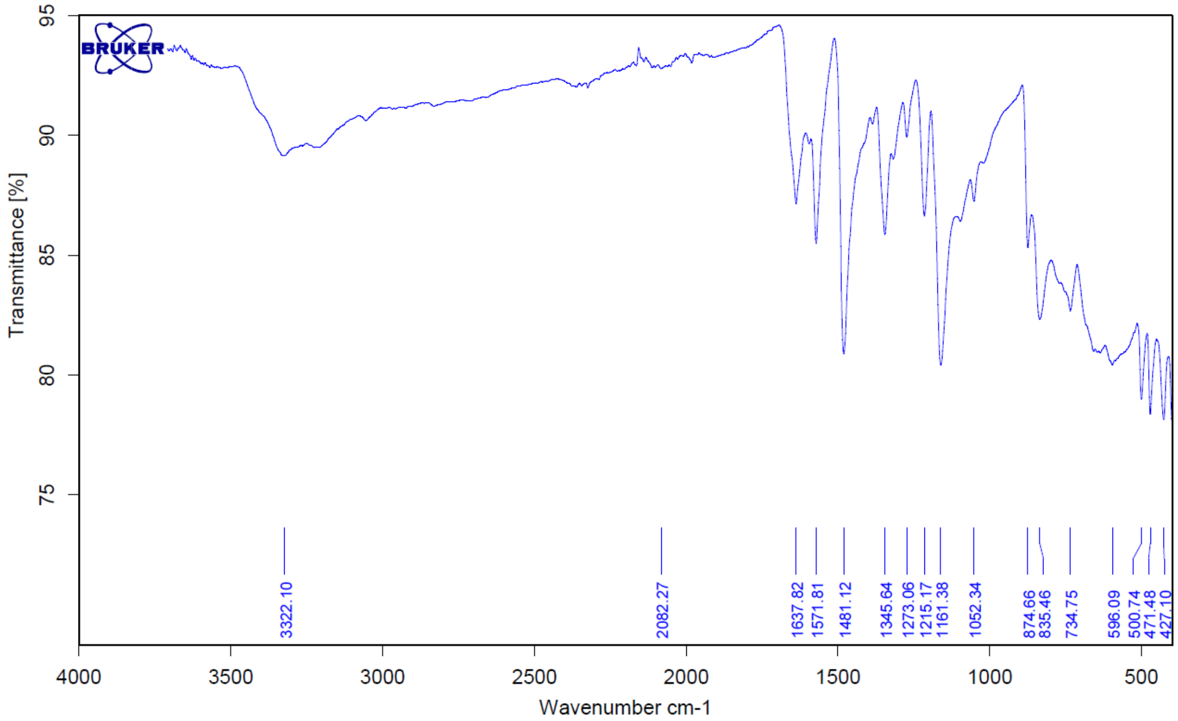

Figure S 40. IR spectrum of **CFA-20-Cl**

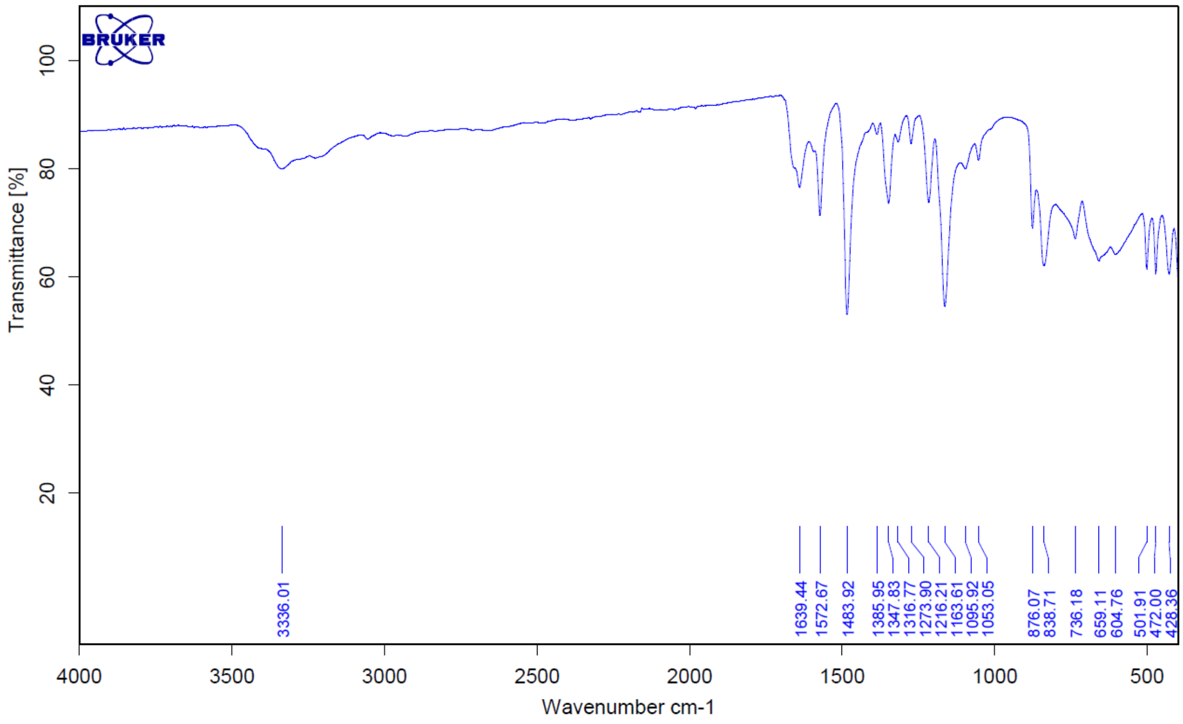

Figure S 41. IR spectrum of **CFA-20-Br**

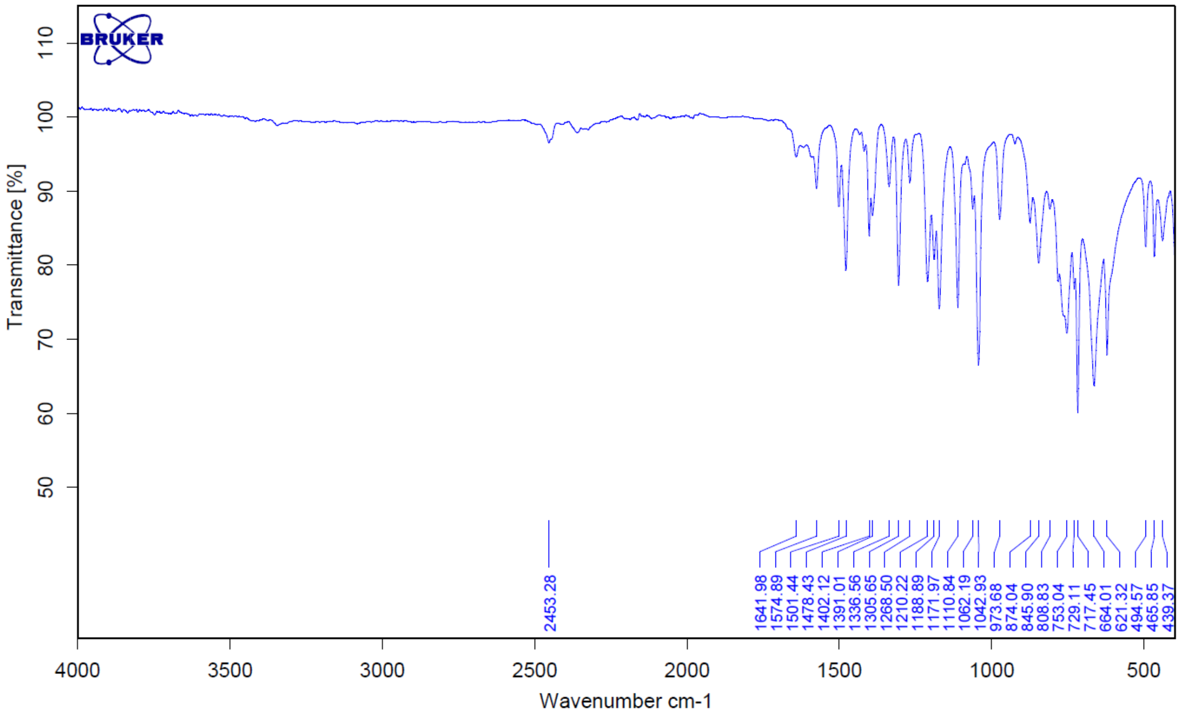

Figure S 42. IR spectrum of **CFA-20-Tp**

A 126

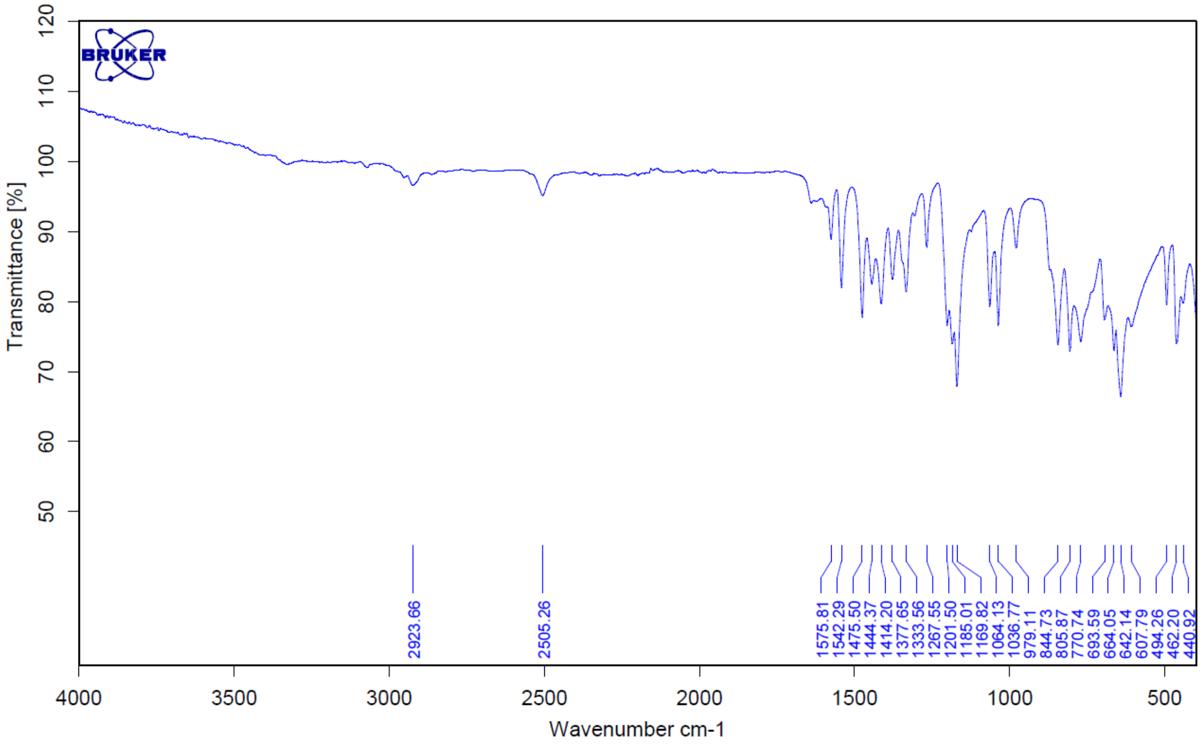

Figure S 43. IR spectrum of **CFA-20-Tp***

XRPD pattern

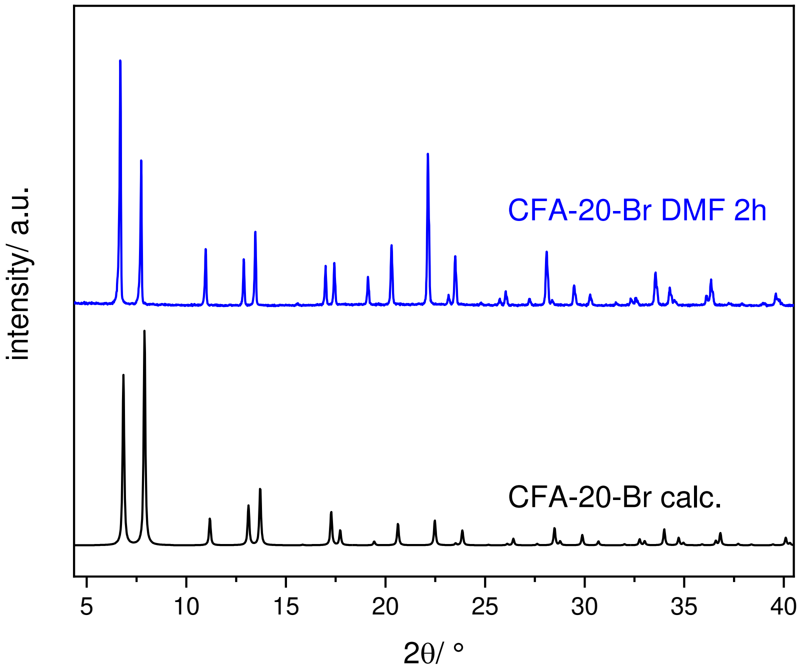

Figure S 44. Calculated (black) and measured (blue) XRPD patterns for **CFA-20-Br** 2 h after DMF addition to the sample

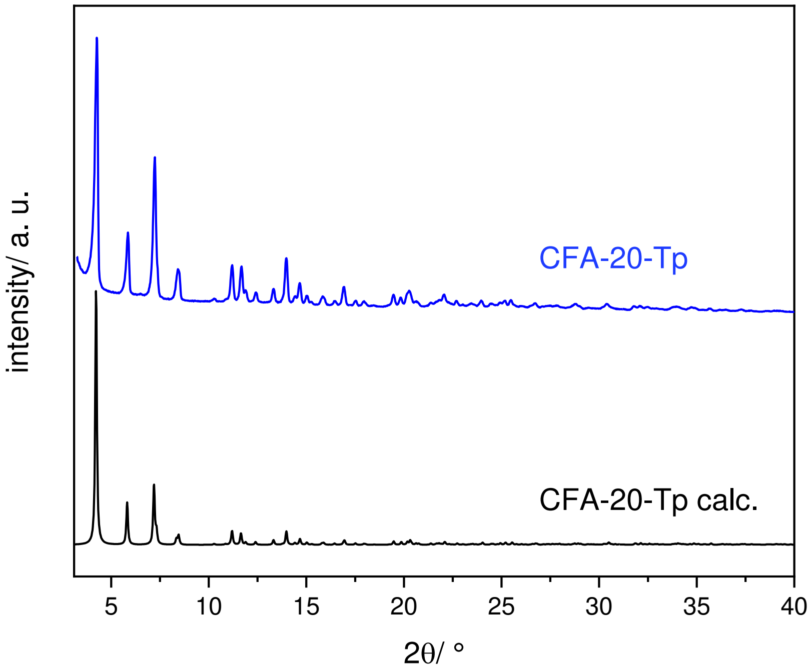

Figure S 45. Calculated (black) and measured (blue) XRPD patterns for **CFA-20-Tp**

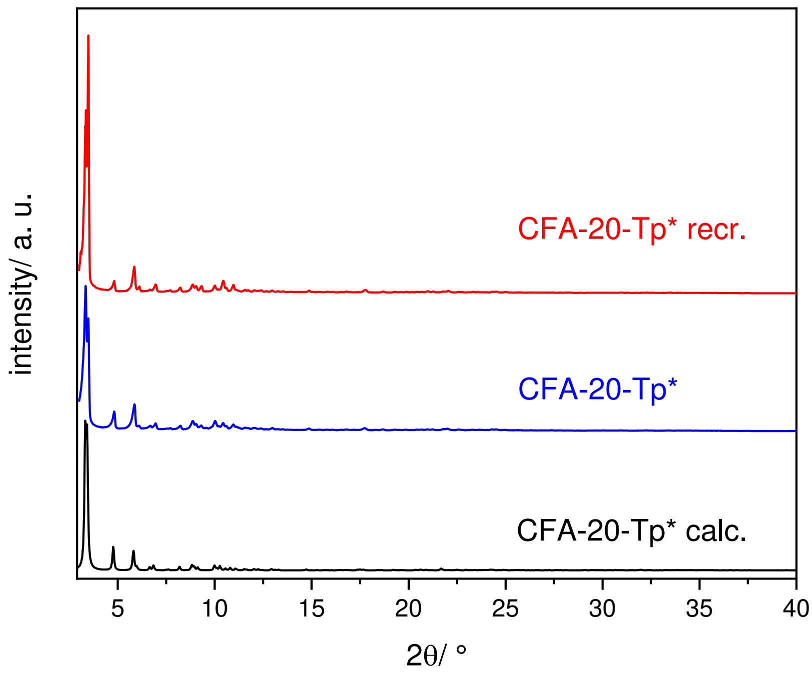

Figure S 46. Calculated (black) and measured XRPD patterns for **CFA-20-Tp*** (blue) and the recrystallized sample of **CFA-20-Tp*** (red)

TGA curves

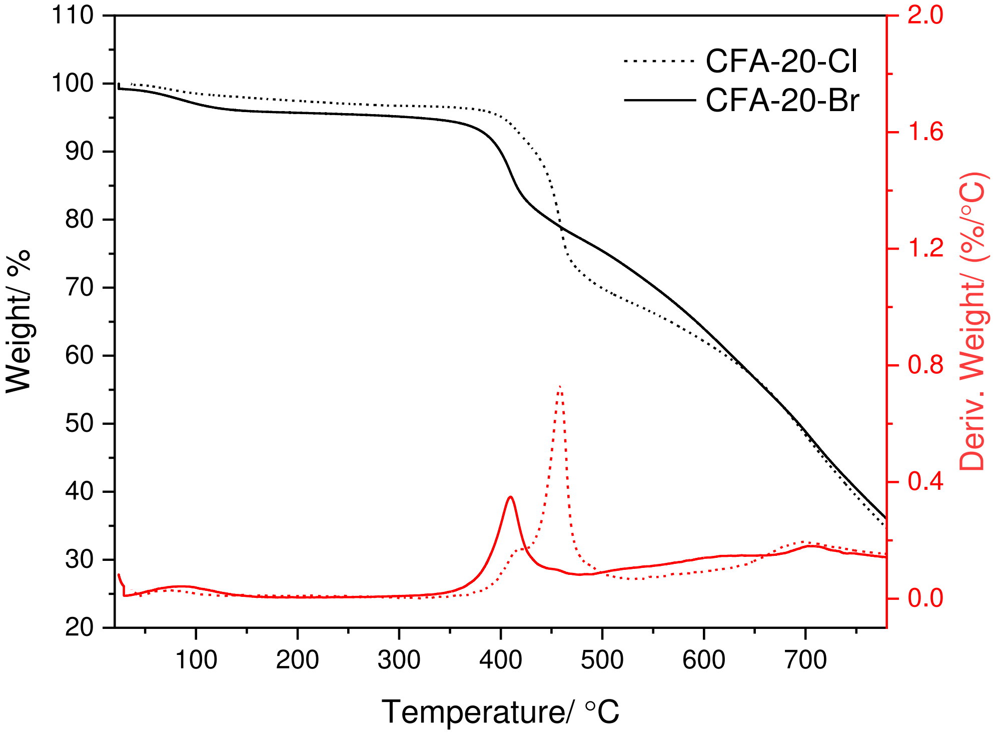

Figure S 47. TGA data for **CFA-20-Cl** (dotted lines) and **CFA-20-Br** (solid lines)

Argon adsorption data

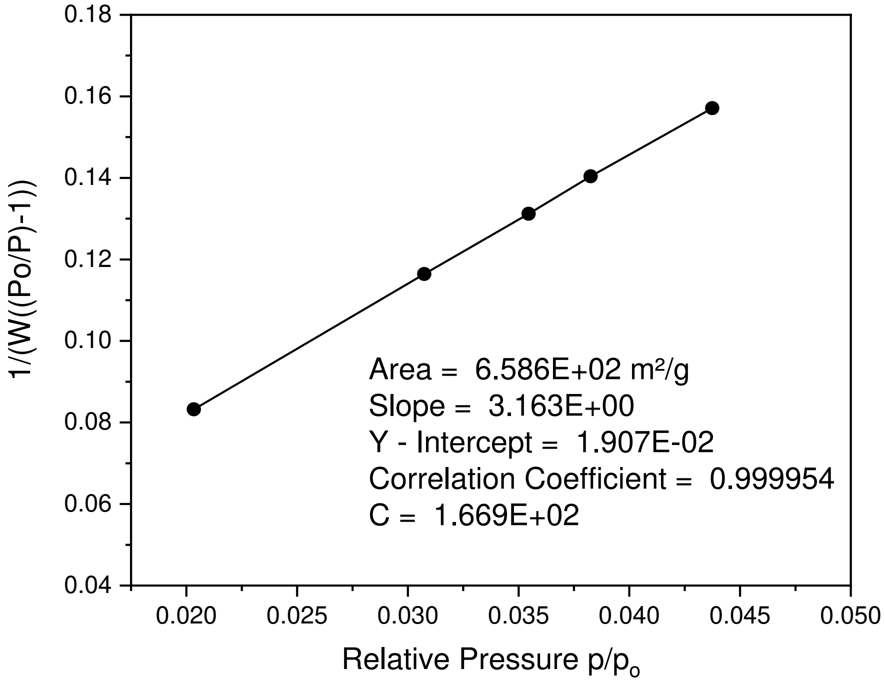

Figure S 48. BET plot for the surface area determination of **CFA-20-Tp**

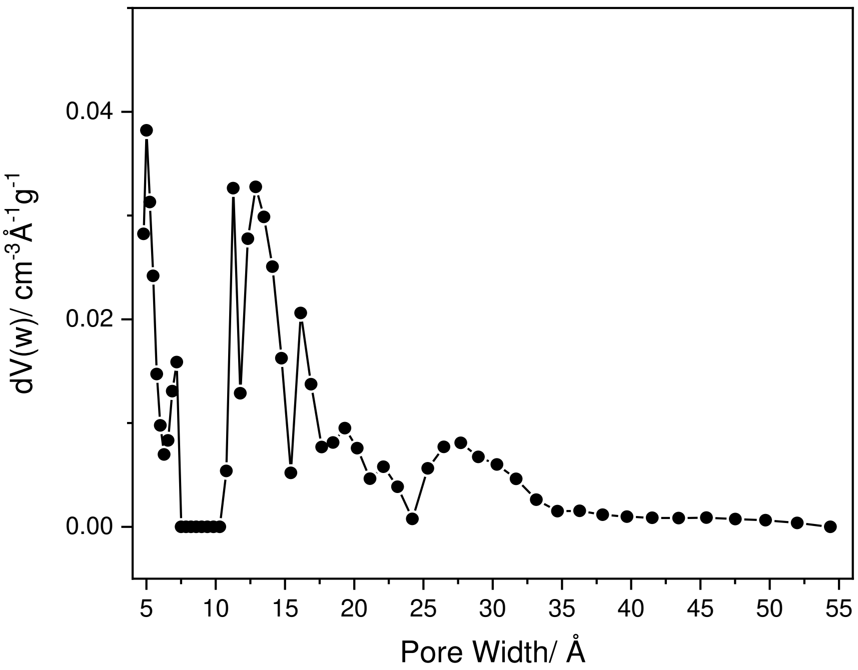

Figure S 49. NLDFT pore size distribution of **CFA-20-Tp** calculated from the argon adsorption isotherm

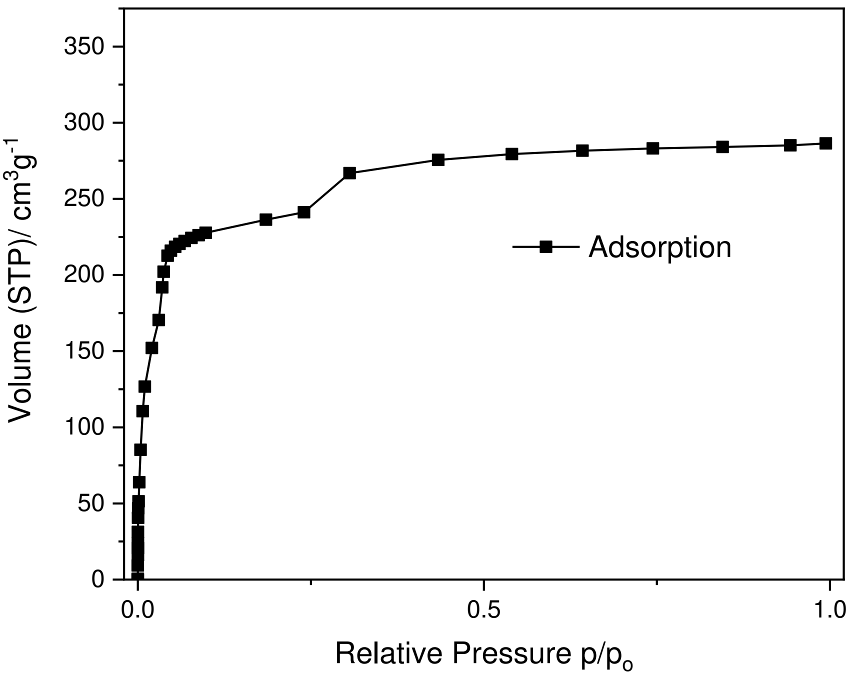

Figure S 50. Argon adsorption isotherm measured at 77 K for **CFA-20-Tp***

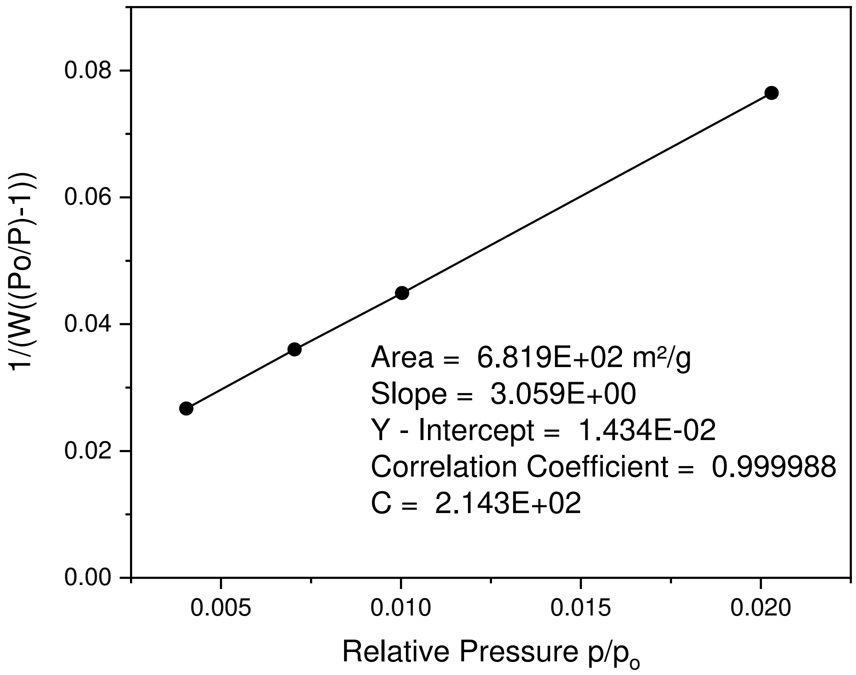

Figure S 51. BET plot for the surface area determination of **CFA-20-Tp***

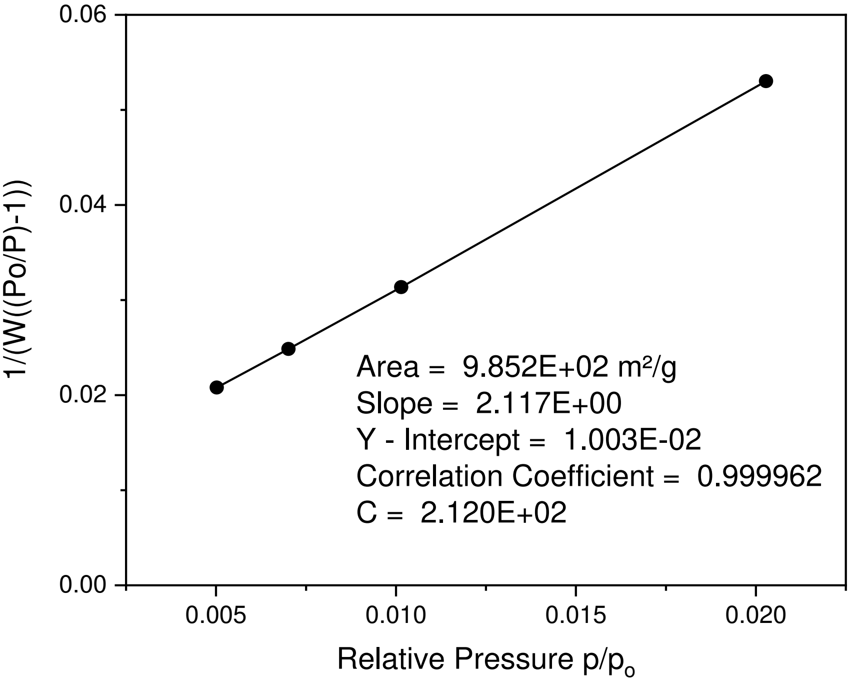

Figure S 52. BET plot for the determination of the surface area of the recrystallized **CFA-20-Tp*** sample

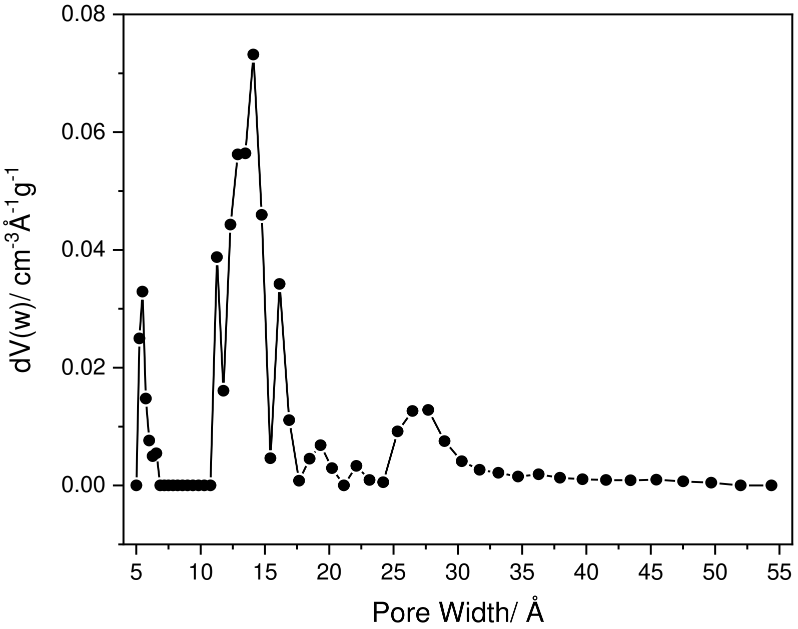

Figure S 53. NLDFT pore size distribution of **CFA-20-Tp*** calculated from the argon adsorption isotherm

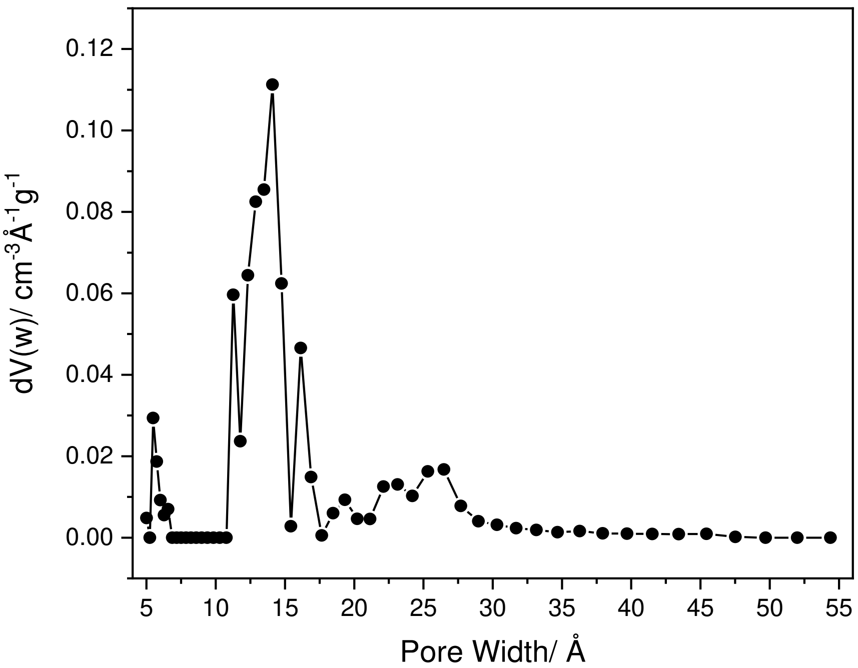

Figure S 54. NLDFT pore size distribution for the recrystallized **CFA-20-Tp*** sample calculated from the argon adsorption isotherm

A 134

EDX Data

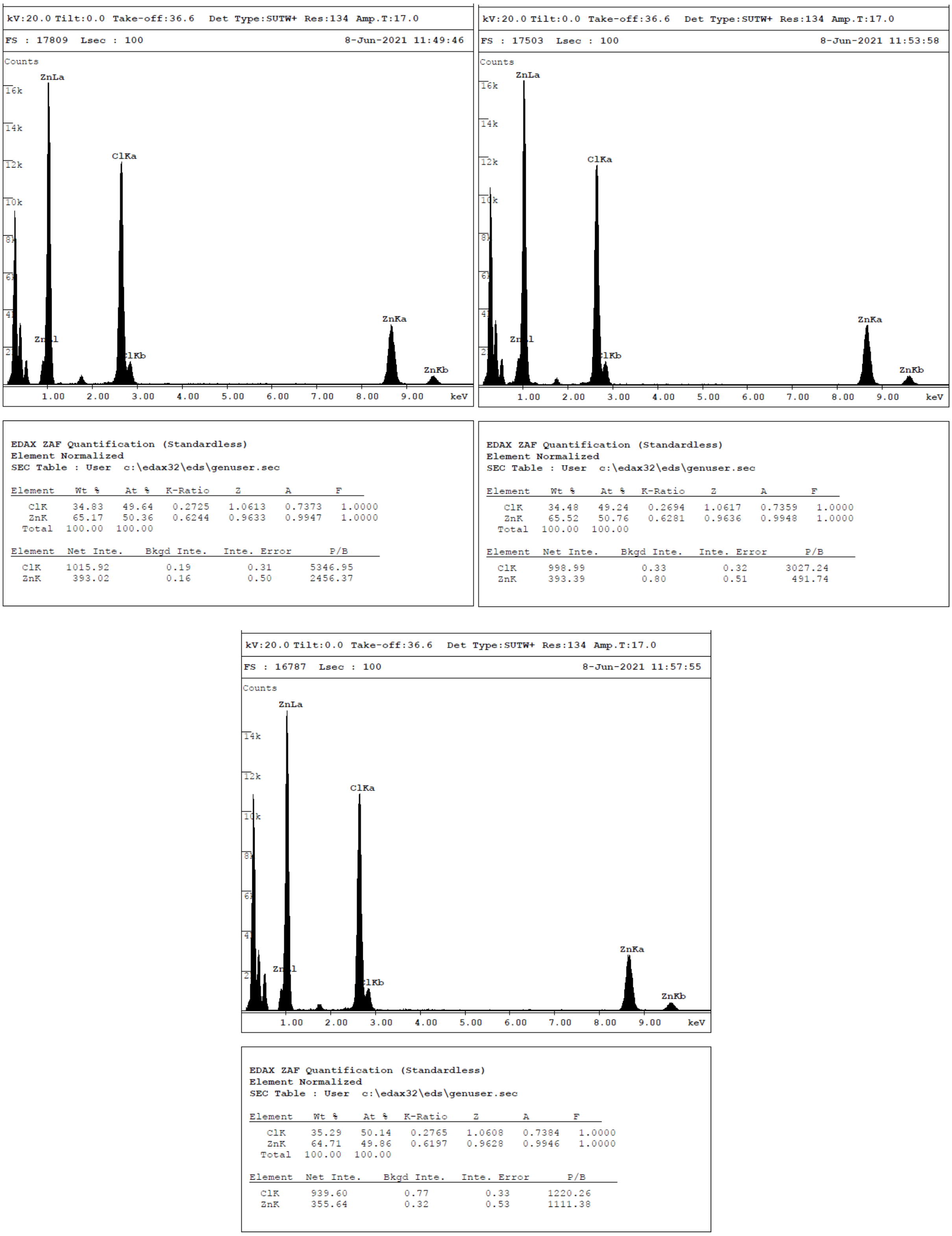

```
kV:20.0 Tilt:0.0  Take-off:36.6  Det Type:SUTW+ Res:134 Amp.T:17.0
FS : 17809  Lsec : 100                              8-Jun-2021 11:49:46
```

```
EDAX ZAF Quantification (Standardless)
Element Normalized
SEC Table : User  c:\edax32\eds\genuser.sec

Element   Wt %    At %   K-Ratio    Z        A        F
   ClK   34.83   49.64   0.2725   1.0613   0.7373   1.0000
   ZnK   65.17   50.36   0.6244   0.9633   0.9947   1.0000
 Total  100.00  100.00

Element  Net Inte.    Bkgd Inte.   Inte. Error      P/B
  ClK    1015.92         0.19          0.31       5346.95
  ZnK     393.02         0.16          0.50       2456.37
```

```
kV:20.0 Tilt:0.0  Take-off:36.6  Det Type:SUTW+ Res:134 Amp.T:17.0
FS : 17503  Lsec : 100                              8-Jun-2021 11:53:58
```

```
EDAX ZAF Quantification (Standardless)
Element Normalized
SEC Table : User  c:\edax32\eds\genuser.sec

Element   Wt %    At %   K-Ratio    Z        A        F
   ClK   34.48   49.24   0.2694   1.0617   0.7359   1.0000
   ZnK   65.52   50.76   0.6281   0.9636   0.9948   1.0000
 Total  100.00  100.00

Element  Net Inte.    Bkgd Inte.   Inte. Error      P/B
  ClK     998.99         0.33          0.32       3027.24
  ZnK     393.39         0.80          0.51        491.74
```

```
kV:20.0 Tilt:0.0  Take-off:36.6  Det Type:SUTW+ Res:134 Amp.T:17.0
FS : 16787  Lsec : 100                              8-Jun-2021 11:57:55
```

```
EDAX ZAF Quantification (Standardless)
Element Normalized
SEC Table : User  c:\edax32\eds\genuser.sec

Element   Wt %    At %   K-Ratio    Z        A        F
   ClK   35.29   50.14   0.2765   1.0608   0.7384   1.0000
   ZnK   64.71   49.86   0.6197   0.9628   0.9946   1.0000
 Total  100.00  100.00

Element  Net Inte.    Bkgd Inte.   Inte. Error      P/B
  ClK     939.60         0.77          0.33       1220.26
  ZnK     355.64         0.32          0.53       1111.38
```

Figure S 55. EDX spectra for **CFA-20-Cl**

A 135

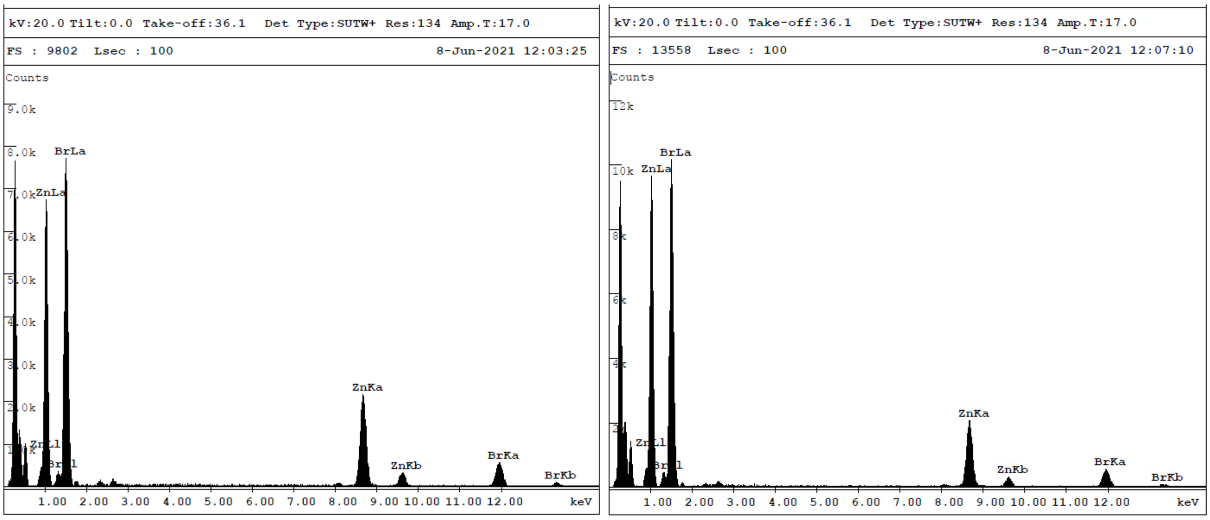

```
EDAX ZAF Quantification (Standardless)
Element Normalized
SEC Table : User  c:\edax32\eds\genuser.sec

Element   Wt %    At %   K-Ratio     Z         A         F
   ZnK    44.40   49.40   0.4775   1.0343   0.9943   1.0456
   BrK    55.60   50.60   0.5310   0.9699   0.9847   1.0000
  Total  100.00  100.00

Element  Net Inte.    Bkgd Inte.   Inte. Error      P/B
  ZnK     270.45         0.26         0.61       1040.19
  BrK      80.93         1.56         1.13         51.88
```

```
EDAX ZAF Quantification (Standardless)
Element Normalized
SEC Table : User  c:\edax32\eds\genuser.sec

Element   Wt %    At %   K-Ratio     Z         A         F
   ZnK    44.37   49.37   0.4771   1.0343   0.9943   1.0456
   BrK    55.63   50.63   0.5313   0.9699   0.9847   1.0000
  Total  100.00  100.00

Element  Net Inte.    Bkgd Inte.   Inte. Error      P/B
  ZnK     265.37         0.16         0.61       1658.56
  BrK      79.52         0.19         1.12        418.53
```

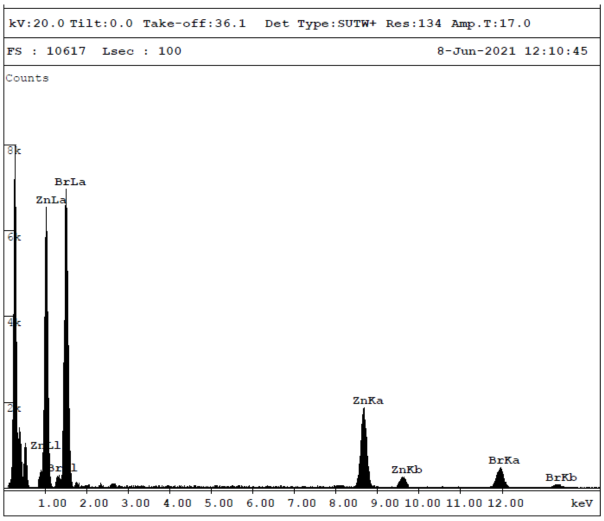

```
EDAX ZAF Quantification (Standardless)
Element Normalized
SEC Table : User  c:\edax32\eds\genuser.sec

Element   Wt %    At %   K-Ratio     Z         A         F
   ZnK    44.67   49.67   0.4801   1.0341   0.9943   1.0453
   BrK    55.33   50.33   0.5283   0.9697   0.9846   1.0000
  Total  100.00  100.00

Element  Net Inte.    Bkgd Inte.   Inte. Error      P/B
  ZnK     250.31         0.16         0.63       1564.44
  BrK      74.12         0.38         1.17        195.05
```

Figure S 56. EDX spectra for **CFA-20-Br**

A 136

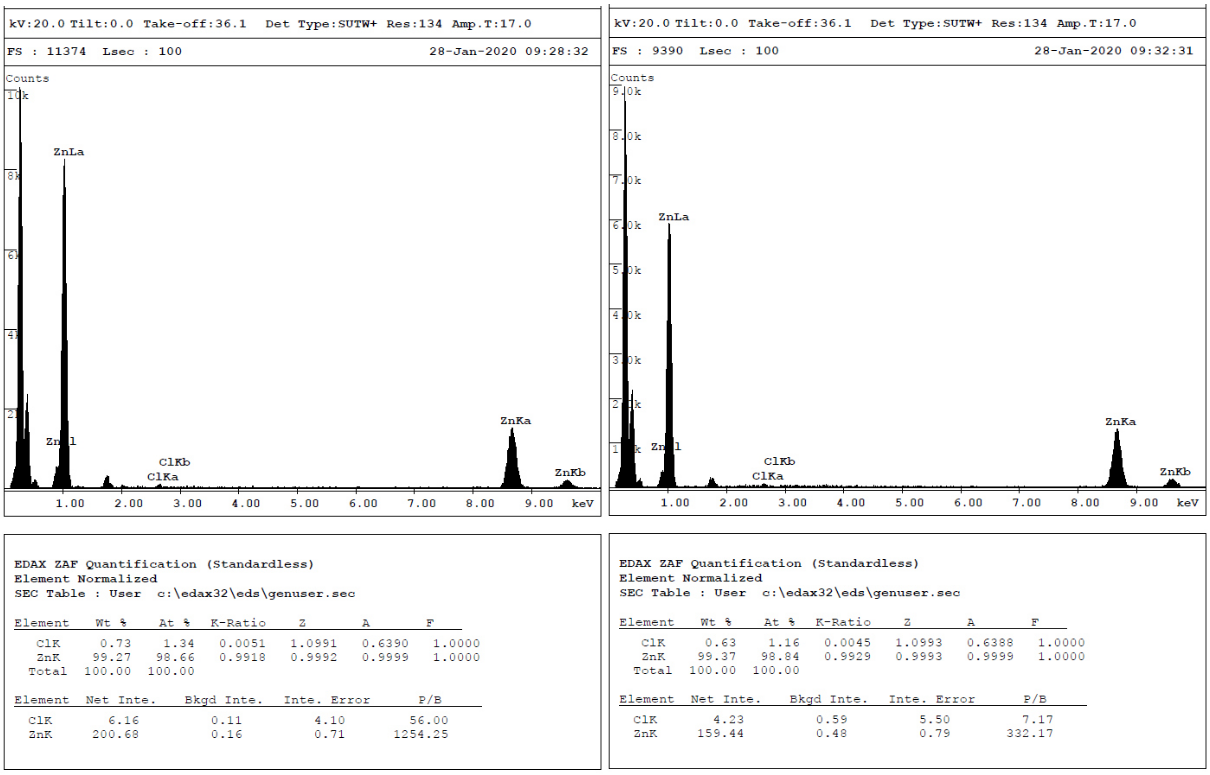

```
kV:20.0 Tilt:0.0 Take-off:36.1  Det Type:SUTW+ Res:134 Amp.T:17.0
FS : 11374  Lsec : 100                       28-Jan-2020 09:28:32

EDAX ZAF Quantification (Standardless)
Element Normalized
SEC Table : User  c:\edax32\eds\genuser.sec

Element   Wt %    At %   K-Ratio     Z       A       F
   ClK    0.73    1.34   0.0051   1.0991  0.6390  1.0000
   ZnK   99.27   98.66   0.9918   0.9992  0.9999  1.0000
  Total  100.00  100.00

Element  Net Inte.    Bkgd Inte.    Inte. Error     P/B
  ClK      6.16          0.11          4.10        56.00
  ZnK    200.68          0.16          0.71      1254.25
```

```
kV:20.0 Tilt:0.0 Take-off:36.1  Det Type:SUTW+ Res:134 Amp.T:17.0
FS : 9390  Lsec : 100                        28-Jan-2020 09:32:31

EDAX ZAF Quantification (Standardless)
Element Normalized
SEC Table : User  c:\edax32\eds\genuser.sec

Element   Wt %    At %   K-Ratio     Z       A       F
   ClK    0.63    1.16   0.0045   1.0993  0.6388  1.0000
   ZnK   99.37   98.84   0.9929   0.9993  0.9999  1.0000
  Total  100.00  100.00

Element  Net Inte.    Bkgd Inte.    Inte. Error     P/B
  ClK      4.23          0.59          5.50         7.17
  ZnK    159.44          0.48          0.79       332.17
```

Figure S 57. EDX spectra for **CFA-20-Tp**

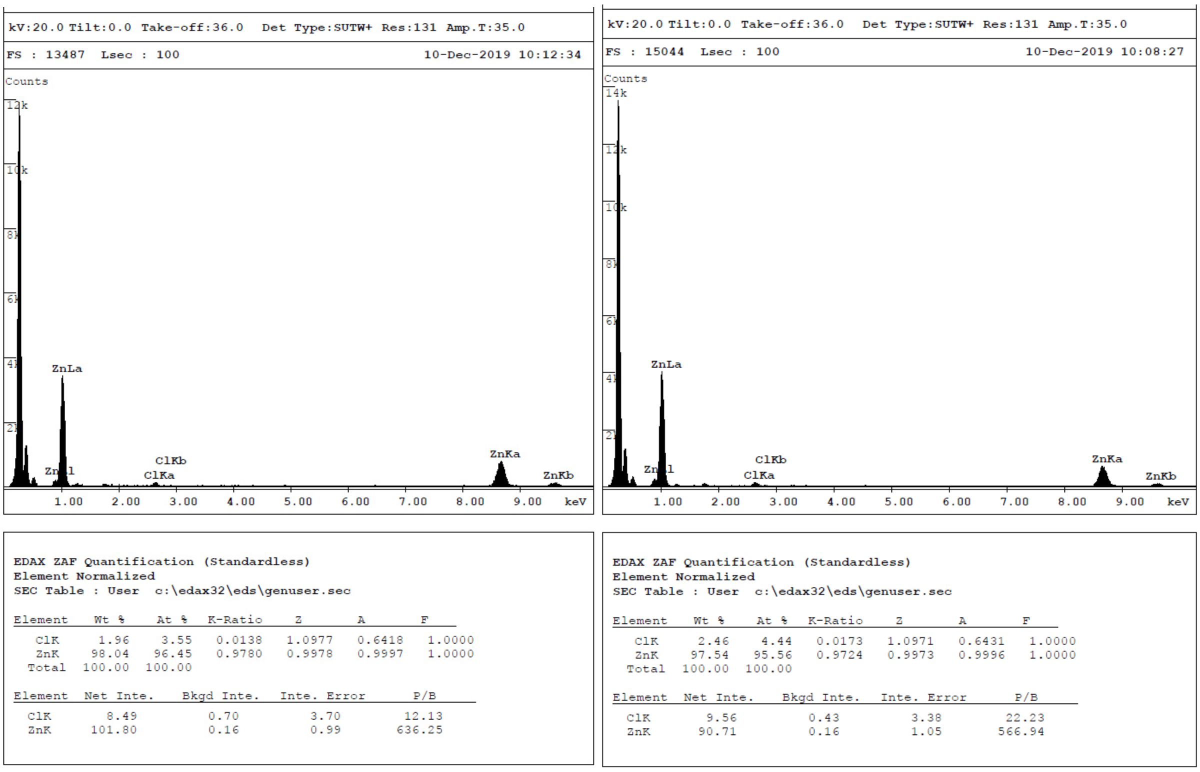

```
kV:20.0 Tilt:0.0 Take-off:36.0  Det Type:SUTW+ Res:131 Amp.T:35.0
FS : 13487  Lsec : 100                       10-Dec-2019 10:12:34

EDAX ZAF Quantification (Standardless)
Element Normalized
SEC Table : User  c:\edax32\eds\genuser.sec

Element   Wt %    At %   K-Ratio     Z       A       F
   ClK    1.96    3.55   0.0138   1.0977  0.6418  1.0000
   ZnK   98.04   96.45   0.9780   0.9978  0.9997  1.0000
  Total  100.00  100.00

Element  Net Inte.    Bkgd Inte.    Inte. Error     P/B
  ClK      8.49          0.70          3.70        12.13
  ZnK    101.80          0.16          0.99       636.25
```

```
kV:20.0 Tilt:0.0 Take-off:36.0  Det Type:SUTW+ Res:131 Amp.T:35.0
FS : 15044  Lsec : 100                       10-Dec-2019 10:08:27

EDAX ZAF Quantification (Standardless)
Element Normalized
SEC Table : User  c:\edax32\eds\genuser.sec

Element   Wt %    At %   K-Ratio     Z       A       F
   ClK    2.46    4.44   0.0173   1.0971  0.6431  1.0000
   ZnK   97.54   95.56   0.9724   0.9973  0.9996  1.0000
  Total  100.00  100.00

Element  Net Inte.    Bkgd Inte.    Inte. Error     P/B
  ClK      9.56          0.43          3.38        22.23
  ZnK     90.71          0.16          1.05       566.94
```

Figure S 58. EDX spectra for **CFA-20-Tp***

References

(1) *BIOVIA Materials Studio 2021 (21.1.1.8)*; (c) 2019 Dassault Systèmes.

(2) Jeffrey, G. A. *An introduction to hydrogen bonding*; Topics in physical chemistry; Oxford Univ. Press, 1997.

(3) Dubbeldam, D.; Calero, S.; Vlugt, T. J. iRASPA:GPU-accelerated visualization software for materials scientists. *Molecular Simulation* **2018**, *44* (8), 653–676. DOI: 10.1080/08927022.2018.1426855.

Inorganic Chemistry

pubs.acs.org/IC

Article

Inhibition, Binding of Organometallics, and Thermally Induced CO Release in an MFU-4-Type Metal–Organic Framework Scaffold with Open Bidentate Bibenzimidazole Coordination Sites

Richard Röß-Ohlenroth, Maryana Kraft, Hana Bunzen, and Dirk Volkmer*

Cite This: *Inorg. Chem.* 2022, 61, 16380−16389

Read Online

ABSTRACT: Triazolate-based MFU-4-type metal−organic frameworks are promising candidates for various applications, of which heterogeneous catalysis has emerged as a hot topic owing to the facile post-synthetic metal and ligand exchange in Kuratowski secondary building units (SBUs). Herein, we present the largest non-interpenetrated isoreticular MFU-4-type framework **CFA-19** ($[Co_5^{II}Cl_4(H_2\text{-bibt})_3]$; H_4-bibt = 1,1′,5,5′-tetrahydro-6,6′-biimidazo[4,5-*f*]-benzotriazole; CFA-19 = Coordination Framework Augsburg University-19) and the **CFA-19-Tp** derivative featuring trispyrazolylborate inhibited SBUs as a scaffold with open bibenzimidazole coordination sites at the backbone of the **H_4-bibt** linker. The proof-of-principle incorporation of accessible $M^IBr(CO)_3$ (M = Re, Mn) sites in **CFA-19-Tp** was revealed by single-crystal X-ray diffraction, and a thermally induced CO release was observed for $MnBr(CO)_3$. Deprotonation of bibenzimidazole was also achieved by the reaction with $ZnEt_2$.

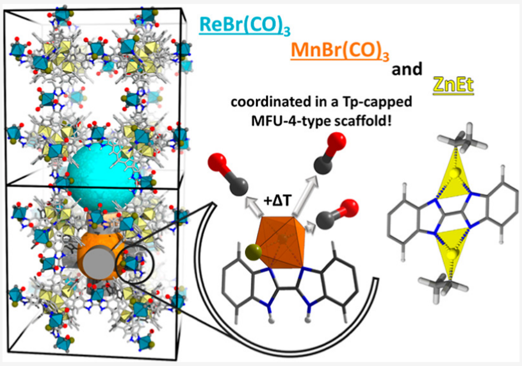

■ INTRODUCTION

Although the secondary building units (SBUs) are the main source of functional coordination moieties in most metal−organic frameworks (MOFs), the incorporation of guest molecules at additional binding sites represents another possibility, whose potential has recently been unlocked and demonstrated in various catalytic applications.[1−10] To achieve further enhancement, it is desirable to combine both approaches within the same framework.

For this purpose, MFU-4-[11−14] and MAF-type[15−17] MOFs represent a functional and robust foundation to build upon. Comprised of bistriazolate ligands, these have gained increasing interest owing to the readily modifiable open metal sites (OMSs) of their SBUs and their applications in catalysis,[18] gas separation, adsorption and trapping,[15,16,19−25] sensing,[26,27] and drug delivery.[28] In particular, post-synthetic metal and ligand exchange in MFU-4-type frameworks, such as **MFU-4*l*** ($[Zn_5Cl_4(BTDD)_3]$; H_2-BTDD = bis(1*H*-1,2,3-triazolo-[4,5-*b*],[4′,5′-*i*])dibenzo-[1,4]-dioxin),[14] has emerged as a facile pathway toward a wide variety of OMSs. This is enabled by the so-called Kuratowski SBU (Figure S8), which consists of a central octahedral nitrogen-coordinated divalent metal ion and four exchangeable peripheral metal ions. These peripheral metal ions are coordinated by three triazolate nitrogen atoms, adopting a coordination geometry similar to that of mononuclear scorpionate trispyrazolylborate (Tp) complexes with mono-, bi-, or tridentate side ligands.[11,29] In particular, partial or complete exchange of peripheral metal ions with Li^I, Cu^I, Cu^{II}, Mn^{II}, Fe^{II}, Co^{II}, Ni^{II}, V^{II}, V^{IV}, Cr^{III}, Ti^{III}, and Ti^{IV} has been reported for MFU-4*l*,[14,30−37] leading to its application as a heterogeneous catalyst in gas and liquid phases.[30,35,36,38−41] Another promising example is the chiral and more economical **CFA-1** ($[Zn_5Cl_4(bibta)_3]$, H_2-bibta = 1*H*,1′*H*-5,5′-bibenzo[*d*][1,2,3]triazole),[12] which is moving toward commercialization as a heterogeneous catalyst for ethylene dimerization via partial Ni^{II} substitution in Kuratowski SBUs.[42] In addition to the nature of the peripheral metal ion, the coordination number and type of side ligand also play a crucial role in the activity of OMSs in such catalytic reactions, as can be deduced from the necessity of organometallic co-catalysts such as $AlMe_3$ or $AlEt_3$. Recently, we employed infrared (IR) spectra simulations to characterize some MFU-4*l* frameworks with organometallic C-donor ligands (e.g., methanido, ethanido, *n*-butanido, *tert*-butanido, and 3,3-dimethyl-1-butyn-1-ido)[43] that are expected to occur during such catalytic reactions. This series was added to previously characterized side ligands such as NO_2^-, NO_3^-, $CF_3SO_3^-$, N_3^-, NCO^-, $HCOO^-$, CH_3COO^-, F^-, H^-, OH^-,[32,35,43−45] and $OAs(OH)_2$.[28] However, the scorpionate-

Received: July 8, 2022
Published: October 5, 2022

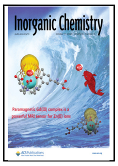

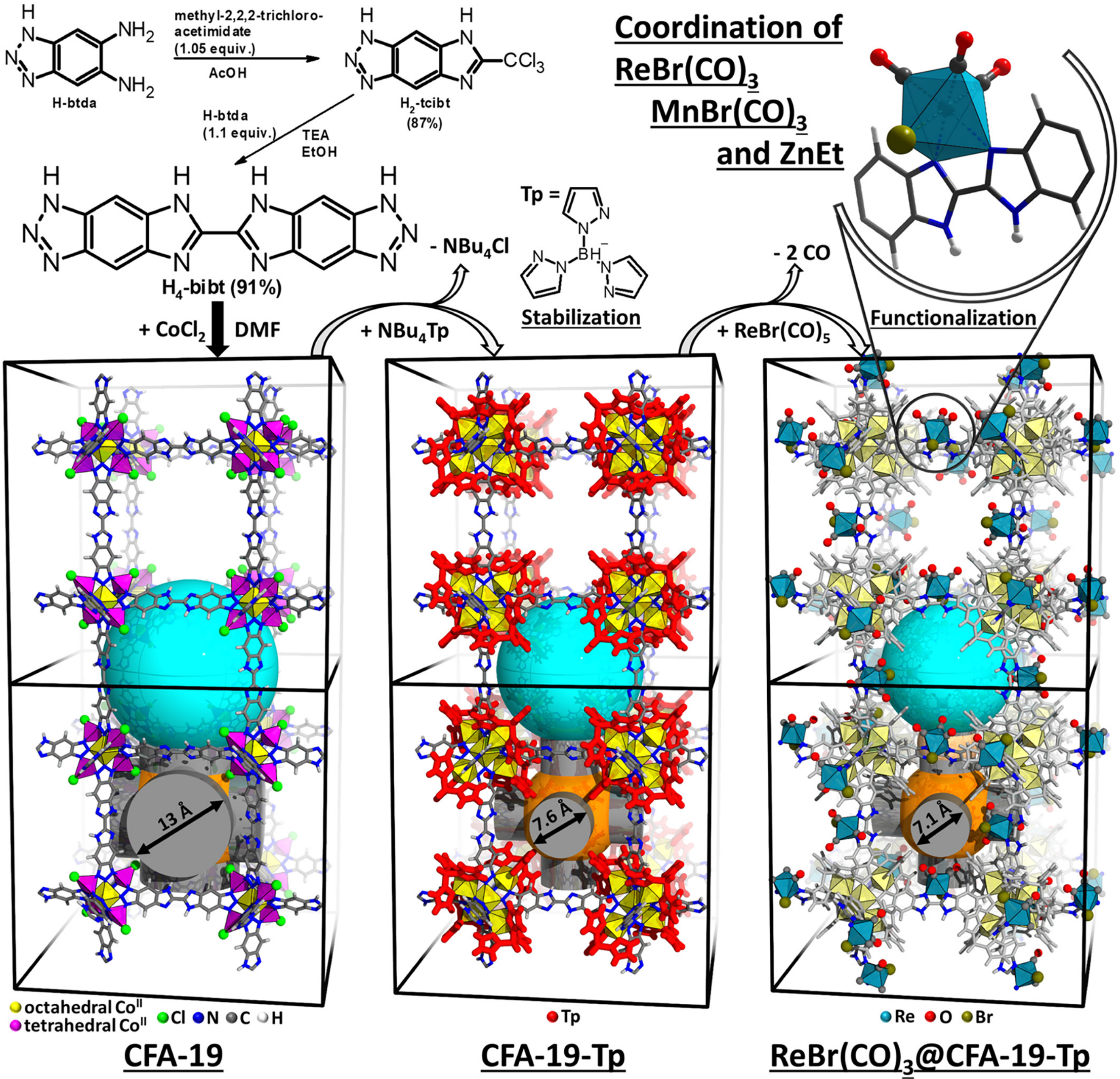

Figure 1. Synthesis and idealized structures of 1,1′,5,5′-tetrahydro-6,6′-biimidazo[4,5-*f*]benzotriazole (**H_4-bibt**), **CFA-19**, **CFA-19-Tp**, and **$ReBr(CO)_3$@CFA-19-Tp** exhibiting the large (blue) and medium (orange) pores with connecting channels (gray) as well as a third smaller pore (light orange) in the **$ReBr(CO)_3$@CFA-19-Tp** structure.

type coordination of OMSs in the Kuratowski SBU restricts the number of accessible coordination sites to three and includes a linker-dependent steric limitation that impacts the catalytic performance.[46]

In line with our ongoing efforts to extend the functionality and variability of such frameworks, we developed and applied the novel **H_4-bibt** (1,1′,5,5′-tetrahydro-6,6′-biimidazo[4,5-*f*]benzotriazole) bistriazolate linker in the synthesis of the **CFA-19** MOF ([$Co_5^{II}Cl_4(H_2\text{-bibt})_3$]) and the first Tp ligand-exchanged MFU-type MOF **CFA-19-Tp** ([$Co_5^{II}Cl_{0.4}Tp_{3.6}(H_2\text{-bibt})_3$]) featuring an isoreticular structure to **MFU-4** and additional open bidentate bibenzimidazole coordination sites at the linker backbone. Thus, enabling the post-synthetic coordination of, for example, $M^{I}Br(CO)_3$ (M = Re, Mn) units at the bibenzimidazole moiety, which resulted in the **$ReBr(CO)_3$@CFA-19-Tp** ([$Co_5^{II}Cl_{0.4}Tp_{3.6}(H_2\text{-bibt})_3\cdot(Re^{I}Br(CO)_3)_{2.8}$]) and **$MnBr(CO)_3$@CFA-19-Tp** ([$Co_5^{II}Cl_{0.4}Tp_{3.6}(H_2\text{-bibt})_3(Mn^{I}Br(CO)_3)_3]\cdot 3.1(Mn^{I}Br(CO)_X)$) frameworks. A thermally induced CO release was observed for **$MnBr(CO)_3$@CFA-19-Tp**. Similar CO-releasing frameworks are mostly investigated as drug delivery systems for CO[47−50] but also the simultaneous use as catalysts and delivery vehicles for such toxic gases is an attractive approach for catalytic applications.[51]

In contrast to the bipyridines often used in the literature,[52] the bibenzimidazole moiety allows for deprotonation, as demonstrated by the reaction of **CFA-19-Tp** with $ZnEt_2$

(**ZnEt@CFA-19-Tp**; $[Co_5^{II}Cl_{0.9}Tp_{3.1}(H\text{-}bibt)_{1\cdot1}(bibt)_{1.9}\cdot(ZnEt)_{4.9}]$).

■ RESULTS AND DISCUSSION

Starting from 1*H*-benzotriazole-5,6-diamine (**H-btda**),[53] the **H_4-bibt** linker was obtained with a good yield by adapting the standard procedures for bibenzimidazole synthesis in a two-step reaction (Figure 1).[54,55] The orange/brownish **H_4-bibt** linker shows strong absorption bands in the ultraviolet (UV) region, some absorption between 400-550 nm, and a fluorescence emission maximum at 400 nm (Figures S41 and S45). Contrary to our expectations, the use of this novel bistriazolate linker for MFU-4-type MOF synthesis did not yield any crystalline material using zinc salts, whereas the use of $CoCl_2$ readily produced crystalline precipitates over a wide temperature range between 120 and 160 °C in *N*,*N*-dimethylformamide (DMF). Optimization of the synthesis conditions with anhydrous DMF at 160 °C in an argon atmosphere and a cobalt-to-linker ratio of 1.66 resulted in cubic single crystals of **CFA-19** suitable for single-crystal X-ray diffraction (SC-XRD) (Figures S14 and 15). SC-XRD analysis revealed a structure isoreticular to **MFU-4** that was exclusively built from cobalt ions, which directly implements redox-active OMSs. To date, this has only been achieved for a Kuratowski complex and **MFU-4**.[30,56] Other MFU-4-type MOFs require a post-synthetic metal exchange procedure to incorporate cobalt ions, which only exchanges the peripheral metal sites of the Kuratowski SBU.[12,13,30] If the hydrogen atoms at the bibenzimidazole moiety of the linker are omitted or a statistical distribution is assumed, then **CFA-19** crystallizes isoreticular to **MFU-4** in the cubic space group $Fm\bar{3}m$ (225).[11] With a unit cell constant of a = 37.1738 Å (**MFU-4**: a = 21.6265 Å; **MFU-4*l***: a = 31.057 Å), it is also the largest MFU-4-type framework without interpenetration (Table S1), which was observed for the **CFA-7 framework.**[13] In the first post-synthetic structure modification step, the chloride side ligands of the Kuratowski SBUs were exchanged with scorpionate trispyrazolylborate (Tp) ligands, similar to previously reported complexes.[53] This resulted in **CFA-19-Tp**, which is stabilized against the unwanted exchange of the peripheral cobalt ions. The **CFA-19-Tp** SC-XRD structure retains the $Fm\bar{3}m$ (225) space group and shows the complete exchange between the chloride side ligands and scorpionate Tp-ligands, leading to an octahedral coordination environment of peripheral cobalt ions along with a characteristic color change from green to orange/brown (Figure S52). In the second post-synthetic modification, **CFA-19-Tp** single crystals were treated with excess $M^IBr(CO)_5$ (M = Re, Mn) at 40 °C in dichloromethane, resulting in the **$ReBr(CO)_3$@CFA-19-Tp** and **$MnBr(CO)_3$@CFA-19-Tp** structures. SC-XRD analysis revealed that both frameworks still exhibited the $Fm\bar{3}m$ (225) space group but with additional statistically distributed $MBr(CO)_3$ fragments coordinated at the bibenzimidazole backbone of the **H_2-bibt** linker. The $ReBr(CO)_3$ sites showed an occupancy of approximately 50%. This is in agreement with the expected statistical distribution of the $ReBr(CO)_3$ fragments, of which only one should be coordinated on either side of the still protonated bibenzimidazole, similar to the complex $(bbimH_2)Re(CO)_3Br$ ($bbimH_2$ = 2,2′-bibenzimidazole) in the literature.[57] SC-XRD measurement of **$MnBr(CO)_3$@CFA-19-Tp** revealed a similar structure with a slightly higher occupation of coordination sites and an incomplete Tp ligand exchange, which is in fair agreement with the chloride residues in the bulk materials. SC-XRD of the **CFA-19-Tp** and $ZnEt_2$ reaction was not performed because of the sample reactivity.

The phase purity of the bulk materials was confirmed by powder XRD (PXRD) (Figure 2), and closely matched the patterns calculated from the SC-XRD data. **CFA-19** was unstable under ambient conditions and variable humidity PXRD showed a loss of crystallinity at humidity levels above 30% at RT (Figures S23 and S24), leading to irreversibly shriveled "crystals", as shown by environmental scanning electron microscopy (SEM) (Figure S14). In contrast, **CFA-19-Tp** showed no structural changes under ambient conditions, even after suspension in a methanol/water mixture (1:1) for 3 days. In pure water, only a slight loss of crystallinity was observed after 3 days (Figure S25). Therefore, **CFA-19-Tp** is easier to handle than **CFA-19** and allows for a larger variety of treatment conditions, in addition to its expected stability against unwanted exchange of peripheral metal ions. The Tp ligand exchange in **CFA-19-Tp** was verified by energy-dispersive X-ray spectroscopy (EDX), which showed a large decrease in chloride content (Figures S46 and S47). For **$ReBr(CO)_3$@CFA-19-Tp**, **$MnBr(CO)_3$@CFA-19-Tp**, and **ZnEt@CFA-19-Tp**, the EDX analysis results agreed with the metal-to-metal ratios obtained from inductively coupled

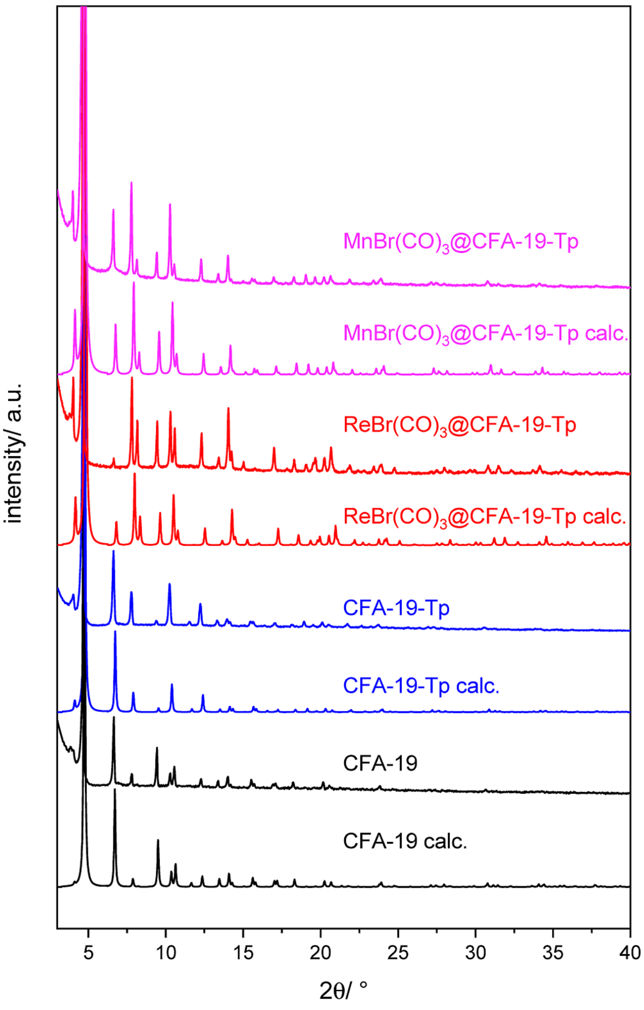

Figure 2. PXRD patterns measured (top) and calculated from the SC data (bottom) of **CFA-19** (black), **CFA-19-Tp** (blue), **$ReBr(CO)_3$@CFA-19-Tp** (red), and **$MnBr(CO)_3$@CFA-19-Tp** (pink).

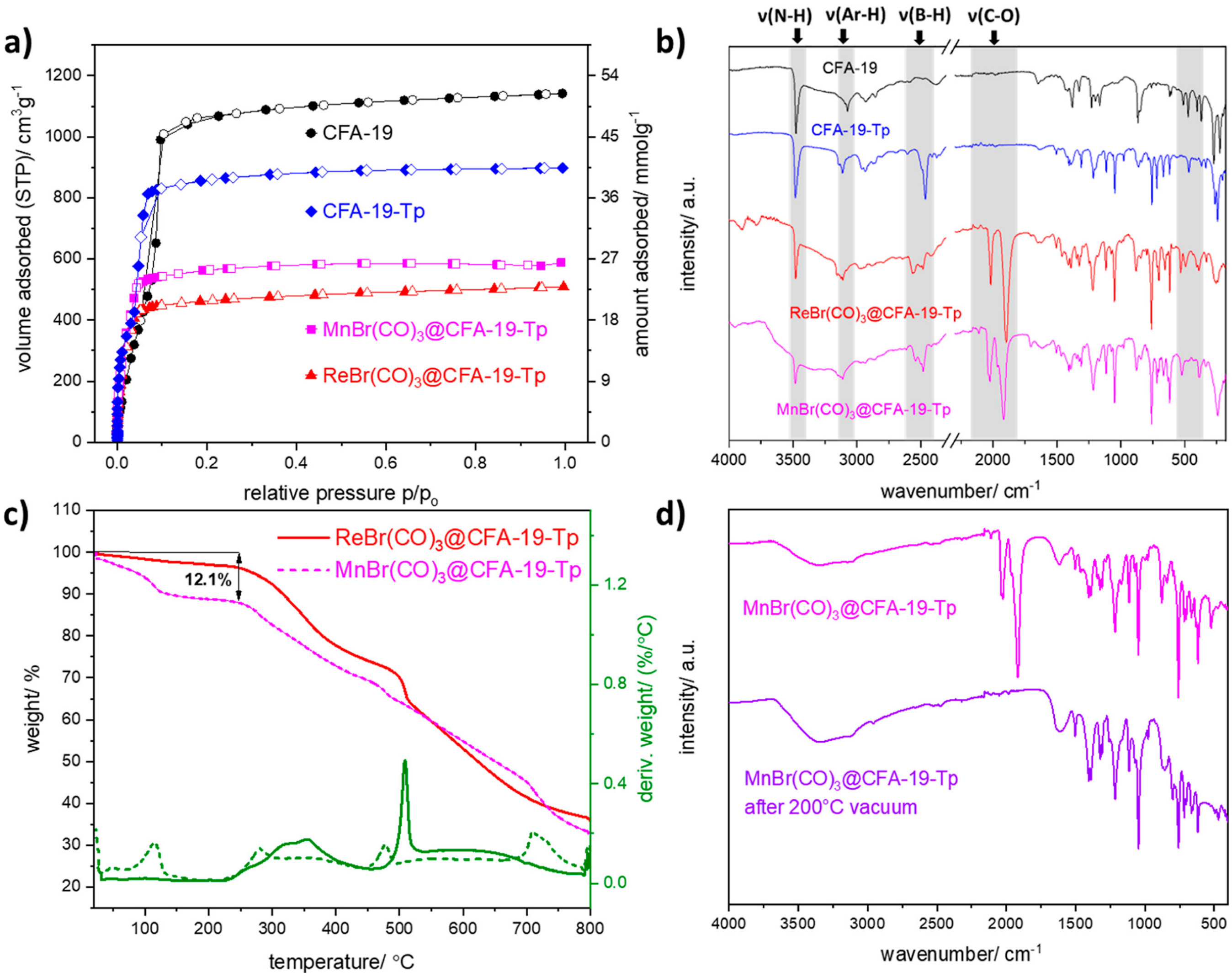

Figure 3. (a) Argon adsorption and desorption isotherms and (b) combined attenuated total reflectance (ATR-IR) (2300−180 cm^{-1}) and DRIFT (4000−2300 cm^{-1}) spectra of **CFA-19** (black), **CFA-19-Tp** (blue), **ReBr(CO)$_3$@CFA-19-Tp** (red), and **MnBr(CO)$_3$@CFA-19-Tp** (pink). (c) TGA curves of **ReBr(CO)$_3$@CFA-19-Tp** (straight line) and **MnBr(CO)$_3$@CFA-19-Tp** (dotted line) showing a mass loss of ca. 12% for **MnBr(CO)$_3$@CFA-19-Tp** associated with the loss of the CO molecules and some residual MnBr(CO)$_5$. This is also seen in the (d) IR spectra comparison of **MnBr(CO)$_3$@CFA-19-Tp** heated to 200 °C in vacuum for 1 h.

plasma atomic emission spectroscopy (ICP-OES). Higher Mn and Br contents were observed only in **MnBr(CO)$_3$@CFA-19-Tp** compared with the SC-XRD data, indicating a higher occupation of coordination sites or MnBr(CO)$_5$ residues. High porosities and pore size distributions (Figures 3a and S27−S32), which are in agreement with the different post-synthetic framework modifications, were obtained for **CFA-19** (3316 m^2 g^{-1}), **CFA-19-Tp** (2097 m^2 g^{-1}), **ReBr(CO)$_3$@CFA-19-Tp** (1917 m^2 g^{-1}), and **MnBr(CO)$_3$@CFA-19- Tp** (1924 m^2 g^{-1}). The CO stretching vibrations observed in the Fourier transform infrared spectra of **ReBr(CO)$_3$@CFA-19-Tp** (2017 and 1895 cm^{-1}) and **MnBr(CO)$_3$@CFA-19-Tp** (2111, 2024, and 1917 cm^{-1}) agreed with those of similar complexes known in the literature (Figure 3b).[57,58] Variable-temperature PXRD (VT-PXRD) patterns (Figures S17−S20) and thermogravimetric analysis (TGA) (Figures 3c and S26) reveal the high-temperature stability of all compounds in a nitrogen atmosphere, except for **MnBr(CO)$_3$@CFA-19-Tp**, which showed a 12% weight loss before 200 °C and a slight change in patterns (Figures 3c and S21). These can be attributed to the cleavage of all CO ligands and the loss of minor MnBr(CO)$_5$ residues, which were also observed in the IR spectra (Figure 3d). Only a minor loss of Mn was detected by EDX analysis of a sample heated in vacuum at 200 °C, verifying that most of the Mn remained in the framework as the Co/Mn ratio changed from 5:5.9 to 5:5.2. This indicates that OMSs can be thermally generated in the **MnBr(CO)$_3$@CFA-19-Tp** structure.

To further unlock the potential of the bibenzimidazole coordination site in **CFA-19-Tp**, ZnEt$_2$ was used in a proof-of-principle coordination and deprotonation study, which showed a Co/Zn ratio of ca. 5:5 and a crystalline PXRD pattern after quenching (Figure S16). Deprotonation was verified by the diffuse reflectance infrared Fourier transform (DRIFT) spectra of the freshly prepared and in situ activated sample, which showed the significant decrease in the bibenzimidazole N−H stretching vibration intensity, in addition to the CH$_2$, CH$_3$, and Zn−C stretching vibrations simulated for the expected coordination moiety after THF removal (Figures 4 and S6). Treatment of the sample with a water/THF mixture and

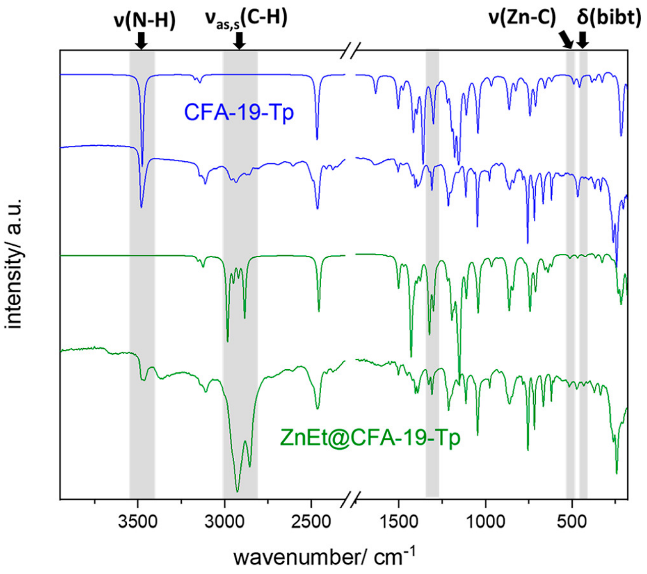

Figure 4. DRIFT (left) and ATR FT-IR spectra (right) comparison of calculated (top) and measured (bottom) IR spectra of **CFA-19-Tp** and **ZnEt@CFA-19-Tp**.

storage under ambient conditions revealed a higher reactivity compared with the inert Kuratowski SBUs featuring ethanido ligands in a tetrahedral scorpionate-type coordination environment reported in the literature (Figures S39 and S40).[43,59] This result is expected because of the more accessible OMSs at the bidentate bibenzimidazole.

■ CONCLUSIONS

In summary, the development of the novel **H_4-bibt** (1,1′,5,5′-tetrahydro-6,6′-biimidazo[4,5-*f*]benzotriazole) linker and its organic building block precursor **H_2-tcibt** (6-(trichloromethyl)-1,7-dihydroimidazo[4,5-*f*]benzotriazole) opens up great opportunities for synthesizing various complexes and MOF structures with potentially attractive properties, which, so far, has culminated in the synthesis of the novel **CFA-19** and **CFA-19-Tp** MOFs. In particular, **CFA-19-Tp** features a stable and versatile template for post-synthetic modifications via metalation of the bibenzimidazole linker backbone. This was proven with the **$ReBr(CO)_3$@CFA-19-Tp** and **$MnBr(CO)_3$@CFA-19-Tp** structures, in which the coordination fragments were unequivocally located at the bibenzimidazole coordination sites by SC-XRD. Thermal analysis and IR spectroscopy revealed the thermally induced loss of all coordinated CO molecules, and hence the creation of OMSs upon heating of **$MnBr(CO)_3$@CFA-19-Tp**. Such framework architectures are envisaged for a variety of applications, given that similar coordination compounds have promising applications in catalysis,[60] as CO-releasing molecules for medical applications,[61,62] and in photo- and electrocatalytic CO_2 reduction.[5,7,63,64] This is also the field being investigated for **CFA-19** derivatives as well as the activation of small molecules. The potential for deprotonation of the bibenzimidazole moieties, and thus the stronger binding of coordination fragments, was demonstrated by the reaction with $ZnEt_2$. The accessibility of this coordination site leads to the increased reactivity of organometallic ZnEt fragments compared with Kuratowski-type organozinc compounds.[43,59] As SC-XRD analysis is not always applicable, IR spectroscopy in conjunction with simulated spectra were proven to be valuable tools for characterizing post-synthetic modifications and may even facilitate future in situ observations.

■ EXPERIMENTAL SECTION

Materials. DMF (Acros, extra dry, 99.8%), THF (Alfa Aesar, 99.8%, anhydrous, unstabilized), *n*-hexane (Alfa Aesar, anhydrous), $CoCl_2$ (Alfa Aesar, 97%), $ZnEt_2$ (Sigma-Aldrich, 1 M in hexanes), and potassium tris(1-pyrazolyl)borohydride (TCI, 97%) were used as received from the commercial supplier. DCM (VWR, technical grade) was distilled and stored over molecular sieves prior to use.

ATR and DRIFT Infrared Spectroscopy. Fourier transform infrared (FT-IR) spectra in the range of 4000−180 cm^{-1} were measured with a Bruker Equinox 55 FT-IR spectrometer equipped with a PLATINUM ATR unit and a KBr (4000−400 cm^{-1}) or Si (4000−180 cm^{-1}) beam splitter. A Harrick praying mantis reaction chamber was used in the measurement of DRIFT spectra in the range of 4000−400 cm^{-1} on the same instrument with KBr as a reference. Each spectrum was obtained as the accumulation of 32 scans with a 4 cm^{-1} resolution, unless stated otherwise. The signals were labeled very strong (vs), strong (s), medium (m), weak (w), very weak (vw), and broad (br). The vibration modes are symmetrical stretching (ν_s), asymmetrical stretching (ν_{as}), bending (δ), and rocking (ρ_r) vibrations. For DRIFT measurements, the powdered KBr background was first heated at 300 °C in an argon gas stream prior to the measurements. The samples were directly sprinkled and dispersed onto the KBr background because mixing in a mortar appeared to have a negative influence on the samples. The fresh **ZnEt@CFA-19-Tp** sample was directly injected as the THF suspension into the KBr via a syringe and activated in situ.

TG Analysis. TGA data were obtained in a nitrogen atmosphere at a heating rate of 5 K min^{-1} after a 5 min isothermal step with a TA Instruments Q500 thermogravimetric analyzer in the temperature range of 25−800 °C. The samples were briefly dried in vacuum prior to the measurement without heating.

Argon Adsorption Measurements. Argon adsorption isotherms were measured on a Quantachrome Autosorb-I ASI-CP-8 instrument at 77.3 K in the range of $5.00 \times 10^{-5} \leq p/p_0 \leq 1.00$. The Brunauer−Emmett−Teller (BET) specific surface areas were determined by considering the criteria proposed by Rouquerol et al.[65] The nonlocal density functional theory (NLDFT) pore size distributions were determined by implementing a carbon equilibrium kernel based on a slit pore model for argon adsorption at 77 K in Autosorb-1 software.[66,67]

EDX and SEM Analysis. SEM micrographs were taken on a Zeiss Crossbeam 550 and a Philips XL 30 FEG scanning electron microscope, which was also used for energy-dispersive X-ray spectroscopy (EDX) with an EDAX SiLi detector on sample squares of at least 5 × 5 μm and an operating voltage of 20 kV. For **$ReBr(CO)_3$@CFA-19-Tp,** a carbon-coated sample and the analytical silicon drift detector from Oxford Instruments at the Zeiss Crossbeam 550 were used for the EDX measurement. The EDX of **ZnEt@CFA-19-Tp** was obtained with a Thermo Scientific Prisma ESEM with a standard LVD detector.

PXRD. PXRD patterns were collected with a Malvern Panalytical Empyrean diffractometer equipped with a Bragg−Brentano^{HD} mirror and a PIXcel^{3D} 2 × 2 detector. VT-PXRD patterns were collected in the range of 2−40° 2θ using the XRK 900 reactor chamber, 0.026° steps, and a measurement time of 1884 s for each pattern. The samples were heated with 25 °C steps, a rate of 5 °C/min, and with a 30 min isothermal step prior to each measurement in a nitrogen atmosphere. PXRD data on humidity were recorded by the same instrument using a CHC + chamber and a proUmid modular humidity generator in the range of 3−30° 2θ with an angular step width of 0.013° 2θ and a measurement time of 1005 s for each pattern.

Electrospray Ionization Mass Spectrometry. The molecular mass was measured with a Micromass Q-Tof Ultima mass spectrometer equipped with an electrospray ionization mass (ESI) source. The samples were dissolved in methanol and injected into the

ESI source at a flow rate of 6−10 μL/min. The measurements were carried out in the negative ESI mode. The capillary voltage was set as 2.8−3.6 kV, while the cone voltage was set as 50−120 V. The collision energy was set as 6.0−15.0 eV. The spectra are the average spectra collected within 2 min. The mass spectra were calibrated using phosphoric acid. The ion composition was verified by the comparison between experimental and theoretical mass values.

Nuclear Magnetic Resonance Spectroscopy. ^{1}H nuclear magnetic resonance (NMR) (400 MHz) and ^{13}C NMR (100 MHz) spectra were obtained by a Mercury plus 400 high-resolution system (Fa. Varian Deutschland GmbH). The chemical shifts were reported in ppm relative to the solvent signal.

UV−Visible Spectroscopy. Solid-state UV−visible (vis) samples were measured by a Perkin Elmer Lamda 750s spectrometer equipped with a 60 mm integration sphere detector on a Spectralon background. The liquid sample of **H_4-bibt** in DMF was measured by the same instrument using the STD detector module.

ICP-OES Analysis. A VARIAN Vista MPX ICP-OES was used to analyze at least two samples per compound. For each sample, approximately 3−4 mg were digested in a mixture of 2 mL of nitric acid (65%) and 0.5 mL of H_2O_2 (30%). A CEM Discover S microwave was used for heating at 150 °C for 30 min and then diluted with 3.5 mL of water prior to measurement.

SC-XRD and Refinement. SC-XRD data for all the structures in this study were collected by a Bruker D8 Venture diffractometer equipped with a low-temperature device. The raw data frames were integrated and corrected for absorption effects using the Bruker SAINT[68] and SADABS[69] software packages. The structure solution by direct methods and structure refinement by full matrix least-square techniques against F^2 were performed using SHELXT 2014/5[70] and SHELXL 2018/3.[71] All nonhydrogen atoms in the structures described in this paper, except for **ReBr(CO)$_3$@CFA-19-Tp**, were refined anisotropically. It was not possible to refine the solvent molecules in the voids; hence, the SQUEEZE[72] procedure was applied to all the data. **CFA-19**: the hydrogen atoms were placed at idealized positions and refined with fixed thermal parameters using a riding model. The occupancy of N−H hydrogen was set at 0.5. The occupancy of the chloride Cl1 position was refined at 0.58(1) coupled with a 0.42(1) occupancy for O1. The Co3 position was refined with an 0.262(8) occupancy. **ReBr(CO)$_3$@CFA-19-Tp**: because the electron density at the Br position was found to be lower than expected for Br atoms, it was refined as a Br/CO mixture with occupancies of 0.19(1)/0.31(1), respectively. These atoms can only be isotropically refined. The total occupancy of the resulting complex $Re(CO)_{4.24}Br_{0.76}$ was set at 50%. Hydrogen atoms, except for N−H, were included in the final refinement cycles using a riding model with constrained Uiso parameters. **MnBr(CO)$_3$@CFA-19-Tp:** the statistical mixture of Tp-ligand/Cl^- coordinated to CO_2 was refined with occupancies of 0.779(9) and 0.221(9), respectively. The occupancy for $Mn(CO)_3Br$ was refined at 0.581(7). Multiple DFIX restraints were applied to the distances in $Mn(CO)_3Br$. Hydrogen atoms, except for N−H, were placed at idealized positions and refined with fixed thermal parameters using a riding model. Complete crystallographic data for the structures reported in this paper have been deposited in the CIF format at the Cambridge Crystallographic Data Center as supplementary publication no. 2169269−2169272.

Syntheses. The linker was obtained by a two-step synthesis, in which 1*H*-benzotriazole-5,6-diamine[53] was synthesized according to procedures in the literature, starting from *o*-phenylenediamine.[73−75]

NBu_4Tp was prepared via the metathesis reaction of NBu_4Cl (1.7 g, 5.8 mol) and KTp (1.46, 5.8 mol) for 3 h in 50 mL of dry THF, similar to the procedure reported for NBu4Tp*.[56] Filtration, followed by the removal of the solvent at a reduced pressure and vacuum drying for 1 h yielded a white powder (2.39 g, 90.5%) as the product.

6-(Trichloromethyl)-1,7-dihydroimidazo[4,5-*f*]benzotriazole·0.5 AcOH (H_2-tcibt·0.5 AcOH). 1*H*-Benzotriazole-5,6-diamine (2 g, 13.4 mmol) was dissolved in acetic acid (50 mL) followed by the dropwise addition of methyl-2,2,2-trichloroacetimidate (1.74 mL, 2.48 g, 14.1 mmol) to the solution. The mixture was stirred for 1 h at room temperature. The yellow precipitate was collected via filtration and washed with 250 mL of water. After drying in vacuum overnight, a yellow powder (3.58 g, 87%) was obtained as the product.

mp > 190 °C decomposition.

^{1}H NMR (400 MHz, TFA-*d*$_1$, 20 °C): δ 9.63 (s, 2H, Ar−H).

^{13}C NMR (100 MHz, TFA-*d*$_1$, 20 °C): δ 158.2, 136.5, 136.2, 103.9, 84.5.

FT-IR (ATR 4000−400 cm^{-1}): 1708 (w,br), 1641 (vw), 1598 (w), 1543 (vw), 1503 (w), 1472 (w), 1419 (m), 1374 (w), 1328 (w), 1271 (w), 1227 (s), 1168 (w), 1032 (s), 995 (m), 891 (m), 841 (s), 829 (s), 771 (w), 754 (vw), 718 (vw), 672 (vs), 648 (vw), 489 (m), 433 (m), 409 (w).

HRMS (ESI$^-$) *m*/*z* calcd. for $C_8H_3Cl_3N_5^-$, 273.9460 [M − H]$^-$; found, 273.9445.

1,1′,5,5′-Tetrahydro-6,6′-biimidazo[4,5-*f*]benzotriazole (H_4-bibt). H_2-tcibt·0.5 AcOH (2 g, 6.5 mmol) and **H-btda** (1.08 g, 7.2 mmol) were suspended in 60 mL of EtOH in an argon atmosphere, and TEA (10 mL, 7.3 g, 72.1 mmol) was added. The mixture was then stirred for 24 h at room temperature. The brown precipitate was filtered and washed three times with EtOH (3 × 50 mL) and MeOH (3 × 50 mL). The product was further purified by EtOH Soxhlet extraction for 6 h and then dried in vacuum at 120 °C overnight. An orange/brown powder (1.87 g, 91%) was obtained as the product.

mp > 300 °C.

^{1}H NMR (400 MHz, D_2SO_4, 20 °C): δ 9.60 (s, 4H, Ar−H).

^{13}C NMR (100 MHz, D_2SO_4, 20 °C): δ 137.4, 133.7, 133.2, 103.1.

FT-IR (ATR 4000−400 cm^{-1}): 1638 (w), 1459 (vw), 1420 (m), 1372 (m), 1326 (m), 1276 (w), 1223 (s), 1103 (m, br), 101 6(w), 983 (s), 926 (w), 823 (s, br), 710 (w), 570 (w), 450 (m), 410 (s);

HRMS (ESI) *m*/*z* calcd. for $C_{14}H_7N_{10}^-$: 315.0861 [M − H]$^-$; found, 315.0862.

Bulk Synthesis of [$Co_5Cl_4(H_2$-bibt)$_3$] (CFA-19). **H_4-bibt** (400 mg, 1.26 mmol) was dissolved in 200 mL of dry DMF in an ACE round-bottomed pressure flask (400 mL inner volume, sealed with a silicone o-ring) in an argon atmosphere in an ultrasonic bath. After complete dissolution, $CoCl_2$ (295 mg, 2.27 mmol) was added, and argon was rigorously bubbled through the reaction mixture for 10 min. The resulting mixture was capped and heated at 160 °C in an oven for 3 days with a heating and cooling rate of 1 °C/min. The sample was transferred to a Schlenk flask fitted with a septum, and the solvent was exchanged via decantation three times with 40 mL of dry DMF, dry THF, and dry hexane fraction for 2 days each. After drying in vacuum (10^{-2} bar) at 250 °C for 5 h, dark green crystals (228 mg, 39%) were obtained as the product.

FT-IR (ATR 4000−180 cm^{-1}): 3480 (vw), 1646 (br, m), 1379 (m), 1325 (m), 1229 (m), 1198 (w), 1165 (m), 866 (s), 759 (vw), 617 (2), 511 (m) 273 (vs), 225 (vs).

Ar(77 K)-BET surface: 3316 m^2 g^{-1} EDX Co/Cl ratio: 5:4.0.

Bulk Synthesis of [$Co_5Cl_{0.4}Tp_{3.6}(H_2$-bibt)$_3$] (CFA-19-Tp). CFA-19 (220 mg, 0.16 mmol) was suspended in a NBu_4Tp solution (601 mg, 1.32 mmol) in 70 mL of dry DCM. After 12 h, the NBu_4Tp solution was replaced and left to stand for another 12 h. Filtration; washing with 50 mL of DCM, MeOH, and DCM; and drying in vacuum overnight yielded brown crystals (307 mg, 92%) as the product.

FT-IR (ATR 4000−180 cm^{-1}): 2470 (vw, br), 1633 (w, br), 1504 (w), 1405 (m), 1391 (m), 1309 (m), 1214 (s, br), 1113 (m), 1047 (s), 977 (w), 860 (m, br), 756 (s), 718 (s), 667 (m), 619 (m), 467 (m), 369 (w), 335 (w), 263 (s), 243 (vs), 205 (w).

Ar(77 K)-BET surface: 2097 m^2 g^{-1}.

EDX Co/Cl ratio: 5:0.4.

Bulk Synthesis of [$Co_5Cl_{0.4}Tp_{3.6}(H_2$-bibt)$_3$·(ReBr(CO)$_3$)$_{2.8}$] (ReBr(CO)$_3$@CFA-19-Tp). CFA-19-Tp (50 mg, 0.024 mmol) was suspended in 10 mL of dry DCM with $ReBr(CO)_5$ (232 mg, 0.571 mmol) in an ACE pressure tube (40 ml inner volume, sealed with a silicone o-ring) and heated at 40 °C for 3 days. After washing three times with 10 mL of dry DCM, two times with dry *n*-hexane via centrifugation/decantation, and vacuum drying at 130 °C for 1 h, a brown powder (68 mg, 93%) was obtained as the product.

FT-IR (ATR 4000−180 cm^{-1}): 2017 (s), 1895 (vs), 1622 (w, br), 1505 (w), 1461 (w), 1409 (m), 1390 (m), 1324 (m), 1219 (s), 1116 (m), 1049 (s), 880 (m), 798 (w), 760 (s), 703 (m), 654 (m), 617 (s), 532 (m), 494 (w), 389 (m), 331 (w), 255 (m, br).

Ar(77 K)-BET surface: 1917 m^2 g^{-1}.

EDX Co/Cl/Br/Re ratio: 5:0.9:3.2:2.7.

ICP-OES: Co/Re ratio: 5:2.83.

Bulk Synthesis of $[Co_5Tp_4(H_2\text{-bibt})_3(MnBr(CO)_3)_3]\cdot 3.1(MnBr(CO)_X)$ ($MnBr(CO)_3$@CFA-19-Tp). **CFA-19-Tp** (20 mg, 0.0096 mmol) was suspended in 10 mL of dry DCM with $MnBr(CO)_5$ (93 mg, 0.339 mmol) in an ACE pressure tube (40 mL inner volume, sealed with a silicone o-ring) and heated at 40 °C for 2 days. Filtration and washing three times with 7.5 mL of dry DCM, followed by vacuum drying for 4 h yielded a brown powder (25 mg, 81%) as the product.

FT-IR (ATR 4000−180 cm^{-1}): 2111 (vw), 2024 (s), 1917 (vs), 1703 (w), 1616 (w, br), 1504 (w), 1406 (w), 1392 (w), 1309 (w), 1215 (s), 1114 (m), 1048 (s), 878 (m), 759 (s), 717 (w), 666 (w), 618 (m), 5223 (w), 388 (w), 242 (s, br).

Ar(77 K)-BET surface: 1924 m^2 g^{-1}.

EDX Co/Cl/Br/Mn ratio: 5:0.6:6.5:5.9; after vacuum drying at 200 °C for 1 h: 5:0.4:5.7:5.2.

ICP-OES: Co/Mn ratio: 5:6.11.

Bulk Synthesis of $[Co_5Cl_{0.9}Tp_{3.1}(H\text{-bibt})_{1.1}(bibt)_{1.9}\cdot(ZnEt)_{4.9}]$ (ZnEt@CFA-19-Tp). **CFA-19-Tp** (30 mg, 0.0144 mmol) was dried at 200 °C in vacuum for 1 h, suspended in 10 mL of dry THF in an argon atmosphere, followed by the dropwise addition of $ZnEt_2$ (1 mL, 1 mmol). The reaction mixture was stirred for 1 h, and the solvent was removed and exchanged three times with 10 mL of dry THF via a syringe. After IR measurements, the sample was quenched with 5 mL of 5% v/v water in THF, and a brown powder was obtained after vacuum drying.

FT-IR (ATR 4000−180 cm^{-1}): 2472 (vw), 1599 (vw, br), 1503 (w), 1452 (w), 1404 (m), 1391 (m), 1327 (w), 1309 (m), 1212 (s, br), 1156 (m), 1113 (w), 1045 (s), 967 (w), 861 (m, br), 785 (vs), 718 (s), 666 (m), 620 (m), 516 (w), 474 (w), 432 (vw), 372 (w), 336 (w), 262 (m), 243 (vs).

EDX Co/Cl/Zn ratio: 5:0.9:5.1.

ICP-OES: Co/Zn ratio: 5:4.92.

SC Synthesis of $[Co_5Cl_4(H_2\text{-bibt})_3]$ (CFA-19). **H_4-bibt** (10 mg, 0.032 mmol) was dissolved in 5 mL of dry DMF in a Schott Duran culture tube (16 × 160 mm, screw cap) in an argon atmosphere in an ultrasonic bath. After complete dissolution, a 1 M $CoCl_2$ solution in dry DMF (53 μL, 0.053 mmol) was added, and the mixture was rigorously bubbled with argon for 10 min. The resulting mixture was capped and heated at 160 °C in an oven for 3 days with a heating and cooling rate of 1 °C/min. Suitable crystals for SC-XRD were obtained directly from the reaction solution.

SC Synthesis of $[Co_5Cl_{0.4}Tp_{3.6}\ (H_2\text{-bibt})_3]$ (CFA-19-Tp). A small sample from the SC synthesis was washed three times with 5 mL of dry DMF and dry DCM, and treated with a NBu_4Tp solution (50 mg in 5 mL dry DCM) overnight. The solution was decanted and the brown/yellow crystals were washed twice with 5 mL of dry DCM while keeping them continuously wetted with the solvent.

SC Synthesis of $[Co_5Cl_{0.4}Tp_{3.6}(H_2\text{-bibt})_3\cdot(ReBr(CO)_3)_{2.8}]$ ($ReBr(CO)_3$@CFA-19-Tp). A few dried **CFA-19-Tp** single crystals were suspended in 1 mL of DCM with $ReBr(CO)_5$ (20 mg, 0.049 mmol) in a Schott Duran culture tube and heated at 40 °C in a heating block for 3 days. The brown crystals were washed three times with 5 mL of dry DCM and two times with 5 mL of dry *n*-hexane, while keeping them continuously wetted with the solvent.

SC Synthesis of $[Co_5Tp_4(H_2\text{-bibt})_3(MnBr(CO)_3)_3]\cdot n(MnBr(CO)_X)$ ($MnBr(CO)_3$@CFA-19-Tp). A few dried **CFA-19-Tp** single crystals were suspended in 1 mL of DCM with $MnBr(CO)_5$ (20 mg, 0.073 mmol) in a Schott Duran culture tube and heated at 40 °C in a heating block for 3 days. The brown crystals were washed once with 2 mL of dry DCM, while keeping them continuously wetted with the solvent.

■ ASSOCIATED CONTENT

SI Supporting Information

The Supporting Information is available free of charge at https://pubs.acs.org/doi/10.1021/acs.inorgchem.2c02394.

> Detailed discussions of the crystal structures, composition, adsorption analysis, IR spectroscopy and stability; optical and electron microscopy images, PXRD patterns, VT-PXRD patterns, TGA curves, argon adsorption analysis data, NMR spectra, UV-vis spectra, IR spectra, fluorescence spectrum, EDX spectra, and sample photographs (PDF)

Accession Codes

CCDC 2169269−2169272 contain the supplementary crystallographic data for this paper. These data can be obtained free of charge via www.ccdc.cam.ac.uk/data_request/cif, or by emailing data_request@ccdc.cam.ac.uk, or by contacting The Cambridge Crystallographic Data Centre, 12 Union Road, Cambridge CB2 1EZ, UK; fax: +44 1223 336033.

■ AUTHOR INFORMATION

Corresponding Author

Dirk Volkmer − *Chair of Solid State and Materials Chemistry, Institute of Physics, University of Augsburg, D-86159 Augsburg, Germany;* orcid.org/0000-0002-8105-2157; Email: dirk.volkmer@physik.uni-augsburg.de

Authors

Richard Röß-Ohlenroth − *Chair of Solid State and Materials Chemistry, Institute of Physics, University of Augsburg, D-86159 Augsburg, Germany*

Maryana Kraft − *Chair of Solid State and Materials Chemistry, Institute of Physics, University of Augsburg, D-86159 Augsburg, Germany*

Hana Bunzen − *Chair of Solid State and Materials Chemistry, Institute of Physics, University of Augsburg, D-86159 Augsburg, Germany;* orcid.org/0000-0003-1824-0291

Complete contact information is available at: https://pubs.acs.org/10.1021/acs.inorgchem.2c02394

Author Contributions

The manuscript was written through contributions of all authors.

Notes

The authors declare no competing financial interest.

■ ACKNOWLEDGMENTS

Financial support by the Deutsche Forschungsgemeinschaft (DFG) via SPP 1928 COORNETs: Coordination Networks: Building Blocks for Functional Systems is gratefully acknowledged. R.R.-O. is grateful for SEM micrographs and EDX measurements conducted by Ralph Freund, Marcel Hirrle and Silke Weigel.

■ REFERENCES

(1) Baek, J.; Rungtaweevoranit, B.; Pei, X.; Park, M.; Fakra, S. C.; Liu, Y.-S.; Matheu, R.; Alshmimri, S. A.; Alshehri, S.; Trickett, C. A.; Somorjai, G. A.; Yaghi, O. M. Bioinspired Metal-Organic Framework Catalysts for Selective Methane Oxidation to Methanol. *J. Am. Chem. Soc.* **2018**, *140*, 18208−18216.

(2) Ji, S.; Chen, Y.; Zhao, S.; Chen, W.; Shi, L.; Wang, Y.; Dong, J.; Li, Z.; Li, F.; Chen, C.; Peng, Q.; Li, J.; Wang, D.; Li, Y. Atomically Dispersed Ruthenium Species Inside Metal-Organic Frameworks:

Combining the High Activity of Atomic Sites and the Molecular Sieving Effect of MOFs. *Angew. Chem.* **2019**, *58*, 4271−4275.

(3) Quan, Y.; Song, Y.; Shi, W.; Xu, Z.; Chen, J. S.; Jiang, X.; Wang, C.; Lin, W. Metal-Organic Framework with Dual Active Sites in Engineered Mesopores for Bioinspired Synergistic Catalysis. *J. Am. Chem. Soc.* **2020**, *142*, 8602−8607.

(4) Song, Y.; Feng, X.; Chen, J. S.; Brzezinski, C.; Xu, Z.; Lin, W. Multistep Engineering of Synergistic Catalysts in a Metal-Organic Framework for Tandem C-O Bond Cleavage. *J. Am. Chem. Soc.* **2020**, *142*, 4872−4882.

(5) Stanley, P. M.; Haimerl, J.; Thomas, C.; Urstoeger, A.; Schuster, M.; Shustova, N. B.; Casini, A.; Rieger, B.; Warnan, J.; Fischer, R. A. Host-Guest Interactions in a Metal-Organic Framework Isoreticular Series for Molecular Photocatalytic CO_2 Reduction. *Angew. Chem.* **2021**, *60*, 17854−17860.

(6) Sun, C.; Skorupskii, G.; Dou, J.-H.; Wright, A. M.; Dincă, M. Reversible Metalation and Catalysis with a Scorpionate-like Metallo-ligand in a Metal-Organic Framework. *J. Am. Chem. Soc.* **2018**, *140*, 17394−17398.

(7) Stanley, P. M.; Thomas, C.; Thyrhaug, E.; Urstoeger, A.; Schuster, M.; Hauer, J.; Rieger, B.; Warnan, J.; Fischer, R. A. Entrapped Molecular Photocatalyst and Photosensitizer in Metal−Organic Framework Nanoreactors for Enhanced Solar CO_2 Reduction. *ACS Catal.* **2021**, *11*, 871−882.

(8) Lee, J. S.; Kapustin, E. A.; Pei, X.; Llopis, S.; Yaghi, O. M.; Toste, F. D. Architectural Stabilization of a Gold(III) Catalyst in Metal-Organic Frameworks. *Chem* **2020**, *6*, 142−152.

(9) Zhu, Y.-Y.; Lan, G.; Fan, Y.; Veroneau, S. S.; Song, Y.; Micheroni, D.; Lin, W. Merging Photoredox and Organometallic Catalysts in a Metal-Organic Framework Significantly Boosts Photocatalytic Activities. *Angew. Chem.* **2018**, *57*, 14090−14094.

(10) Zhang, L.; Yuan, S.; Feng, L.; Guo, B.; Qin, J.-S.; Xu, B.; Lollar, C.; Sun, D.; Zhou, H.-C. Pore-Environment Engineering with Multiple Metal Sites in Rare-Earth Porphyrinic Metal-Organic Frameworks. *Angew. Chem., Int. Ed. Engl.* **2018**, *57*, 5095−5099.

(11) Biswas, S.; Grzywa, M.; Nayek, H. P.; Dehnen, S.; Senkovska, I.; Kaskel, S.; Volkmer, D. A cubic coordination framework constructed from benzobistriazolate ligands and zinc ions having selective gas sorption properties. *Dalton Trans.* **2009**, 6487−6495.

(12) Schmieder, P.; Denysenko, D.; Grzywa, M.; Baumgärtner, B.; Senkovska, I.; Kaskel, S.; Sastre, G.; van Wüllen, L.; Volkmer, D. CFA-1: The first chiral metal-organic framework containing Kuratowski-type secondary building units. *Dalton Trans.* **2013**, *42*, 10786−10797.

(13) Schmieder, P.; Grzywa, M.; Denysenko, D.; Hambach, M.; Volkmer, D. CFA-7: An interpenetrated metal-organic framework of the MFU-4 family. *Dalton Trans.* **2015**, *44*, 13060−13070.

(14) Denysenko, D.; Grzywa, M.; Tonigold, M.; Streppel, B.; Krkljus, I.; Hirscher, M.; Mugnaioli, E.; Kolb, U.; Hanss, J.; Volkmer, D. Elucidating gating effects for hydrogen sorption in MFU-4-type triazolate-based metal-organic frameworks featuring different pore sizes. *Chem. - Eur. J.* **2011**, *17*, 1837−1848.

(15) Liao, P.-Q.; Chen, H.; Zhou, D.-D.; Liu, S.-Y.; He, C.-T.; Rui, Z.; Ji, H.; Zhang, J.-P.; Chen, X.-M. Monodentate hydroxide as a super strong yet reversible active site for CO_2 capture from high-humidity flue gas. *Energy Environ. Sci.* **2015**, *8*, 1011−1016.

(16) Rieth, A. J.; Tulchinsky, Y.; Dincă, M. High and Reversible Ammonia Uptake in Mesoporous Azolate Metal-Organic Frameworks with Open Mn, Co, and Ni Sites. *J. Am. Chem. Soc.* **2016**, *138*, 9401−9404.

(17) Knippen, K.; Bredenkötter, B.; Kanschat, L.; Kraft, M.; Vermeyen, T.; Herrebout, W.; Sugimoto, K.; Bultinck, P.; Volkmer, D. CFA-18: a homochiral metal-organic framework (MOF) constructed from rigid enantiopure bistriazolate linker molecules. *Dalton Trans.* **2020**, *49*, 15758−15768.

(18) Bour, J. R.; Wright, A. M.; He, X.; Dincă, M. Bioinspired chemistry at MOF secondary building units. *Chem. Sci.* **2020**, *11*, 1728−1737.

(19) Weinrauch, I.; Savchenko, I.; Denysenko, D.; Souliou, S. M.; Kim, H.-H.; Le Tacon, M.; Daemen, L. L.; Cheng, Y.; Mavrandonakis, A.; Ramirez-Cuesta, A. J.; Volkmer, D.; Schütz, G.; Hirscher, M.; Heine, T. Capture of heavy hydrogen isotopes in a metal-organic framework with active Cu(I) sites. *Nat. Commun.* **2017**, *8*, 14496.

(20) Oppenheim, J. J.; Mancuso, J. L.; Wright, A. M.; Rieth, A. J.; Hendon, C. H.; Dincă, M. Divergent Adsorption Behavior Controlled by Primary Coordination Sphere Anions in the Metal-Organic Framework Ni_2X_2BTDD. *J. Am. Chem. Soc.* **2021**, *143*, 16343−16347.

(21) Teufel, J.; Oh, H.; Hirscher, M.; Wahiduzzaman, M.; Zhechkov, L.; Kuc, A.; Heine, T.; Denysenko, D.; Volkmer, D. MFU-4 – a metal-organic framework for highly effective H_2/D_2 separation. *Adv. Mater.* **2013**, *25*, 635−639.

(22) Bunzen, H.; Kolbe, F.; Kalytta-Mewes, A.; Sastre, G.; Brunner, E.; Volkmer, D. Achieving Large Volumetric Gas Storage Capacity in Metal-Organic Frameworks by Kinetic Trapping: A Case Study of Xenon Loading in MFU-4. *J. Am. Chem. Soc.* **2018**, *140*, 10191−10197.

(23) Bien, C. E.; Liu, Q.; Wade, C. R. Assessing the Role of Metal Identity on CO_2 Adsorption in MOFs Containing M−OH Functional Groups. *Chem. Mater.* **2020**, *32*, 489−497.

(24) Chen, Z.; Mian, M. R.; Lee, S.-J.; Chen, H.; Zhang, X.; Kirlikovali, K. O.; Shulda, S.; Melix, P.; Rosen, A. S.; Parilla, P. A.; Gennett, T.; Snurr, R. Q.; Islamoglu, T.; Yildirim, T.; Farha, O. K. Fine-Tuning a Robust Metal-Organic Framework toward Enhanced Clean Energy Gas Storage. *J. Am. Chem. Soc.* **2021**, *143*, 18838−18843.

(25) Cao, R.; Mian, M. R.; Liu, X.; Chen, Z.; Wasson, M. C.; Wang, X.; Idrees, K. B.; Ma, K.; Sun, Q.; Li, J.-R.; Islamoglu, T.; Farha, O. K. Benign Synthesis and Modification of a Zn−Azolate Metal−Organic Framework for Enhanced Ammonia Uptake and Catalytic Hydrolysis of an Organophosphorus Chemical. *ACS Mater. Lett.* **2021**, *3*, 1363−1368.

(26) Paschke, B.; Wixforth, A.; Denysenko, D.; Volkmer, D. Fast Surface Acoustic Wave-Based Sensors to Investigate the Kinetics of Gas Uptake in Ultra-Microporous Frameworks. *ACS Sens.* **2017**, *2*, 740−747.

(27) Paschke, B.; Denysenko, D.; Bredenkötter, B.; Sastre, G.; Wixforth, A.; Volkmer, D. Dynamic Studies on Kinetic H_2/D_2 Quantum Sieving in a Narrow Pore Metal-Organic Framework Grown on a Sensor Chip. *Chem. - Eur. J.* **2019**, *25*, 10803−10807.

(28) Ettlinger, R.; Sönksen, M.; Graf, M.; Moreno, N.; Denysenko, D.; Volkmer, D.; Kerl, K.; Bunzen, H. Metal-organic framework nanoparticles for arsenic trioxide drug delivery. *J. Mater. Chem. B* **2018**, *6*, 6481−6489.

(29) Biswas, S.; Tonigold, M.; Volkmer, D. Homo- and Heteropentanuclear Coordination Compounds with Td Symmetry - the Solid State Structures of $[MZn_4(L)_4(L')_6]$ (M = Co^{II} or Zn; L = chloride or acac; L′ = 1,2,3-benzotriazolate). *Z. Anorg. Allg. Chem.* **2008**, *634*, 2532−2538.

(30) Denysenko, D.; Werner, T.; Grzywa, M.; Puls, A.; Hagen, V.; Eickerling, G.; Jelic, J.; Reuter, K.; Volkmer, D. Reversible gas-phase redox processes catalyzed by Co-exchanged MFU-4l(arge). *Chem. Commun.* **2012**, *48*, 1236−1238.

(31) Denysenko, D.; Grzywa, M.; Jelic, J.; Reuter, K.; Volkmer, D. Scorpionate-Type Coordination in MFU-4*l* Metal-Organic Frameworks:Small-Molecule Binding and Activation upon the Thermally Activated Formation of Open Metal Sites. *Angew. Chem.* **2014**, *126*, 5942−5946.

(32) Denysenko, D.; Jelic, J.; Reuter, K.; Volkmer, D. Postsynthetic Metal and Ligand Exchange in MFU-4*l*: A Screening Approach toward Functional Metal-Organic Frameworks Comprising Single-Site Active Centers. *Chem. - Eur. J.* **2015**, *21*, 8188−8199.

(33) Denysenko, D.; Jelic, J.; Magdysyuk, O. V.; Reuter, K.; Volkmer, D. Elucidating Lewis acidity of metal sites in MFU-4l metal-organic frameworks: N_2O and CO_2 adsorption in MFU-4l, Cu^I-MFU-4l and Li-MFU-4*l*. *Microporous Mesoporous Mater.* **2015**, *216*, 146−150.

(34) Magdysyuk, O. V.; Denysenko, D.; Weinrauch, I.; Volkmer, D.; Hirscher, M.; Dinnebier, R. E. Formation of a quasi-solid structure by

intercalated noble gas atoms in pores of Cu(I)-MFU-4*l* metal-organic framework. *Chem. Commun.* **2015**, *51*, 714−717.

(35) Denysenko, D.; Volkmer, D. Cyclic gas-phase heterogeneous process in a metal-organic framework involving a nickel nitrosyl complex. *Faraday Discuss.* **2017**, *201*, 101−112.

(36) Comito, R. J.; Fritzsching, K. J.; Sundell, B. J.; Schmidt-Rohr, K.; Dincă, M. Single-Site Heterogeneous Catalysts for Olefin Polymerization Enabled by Cation Exchange in a Metal-Organic Framework. *J. Am. Chem. Soc.* **2016**, *138*, 10232−10237.

(37) Comito, R. J.; Wu, Z.; Zhang, G.; Lawrence, J. A.; Korzyński, M. D.; Kehl, J. A.; Miller, J. T.; Dincă, M. Stabilized Vanadium Catalyst for Olefin Polymerization by Site Isolation in a Metal-Organic Framework. *Angew. Chem.* **2018**, *57*, 8135−8139.

(38) Park, H. D.; Comito, R. J.; Wu, Z.; Zhang, G.; Ricke, N.; Sun, C.; Van Voorhis, T.; Miller, J. T.; Román-Leshkov, Y.; Dincă, M. Gas-Phase Ethylene Polymerization by Single-Site Cr Centers in a Metal−Organic Framework. *ACS Catal.* **2020**, *10*, 3864−3870.

(39) Metzger, E. D.; Comito, R. J.; Hendon, C. H.; Dincă, M. Mechanism of Single-Site Molecule-Like Catalytic Ethylene Dimerization in Ni-MFU-4l. *J. Am. Chem. Soc.* **2017**, *139*, 757−762.

(40) Mian, M. R.; Chen, H.; Cao, R.; Kirlikovali, K. O.; Snurr, R. Q.; Islamoglu, T.; Farha, O. K. Insights into Catalytic Hydrolysis of Organophosphonates at M-OH Sites of Azolate-Based Metal Organic Frameworks. *J. Am. Chem. Soc.* **2021**, *143*, 9893−9900.

(41) Mian, M. R.; Islamoglu, T.; Afrin, U.; Goswami, S.; Cao, R.; Kirlikovali, K. O.; Hall, M. G.; Peterson, G. W.; Farha, O. K. Catalytic Degradation of an Organophosphorus Agent at Zn−OH Sites in a Metal−Organic Framework. *Chem. Mater.* **2020**, *32*, 6998−7004.

(42) Metzger, E. D.; Comito, R. J.; Wu, Z.; Zhang, G.; Dubey, R. C.; Xu, W.; Miller, J. T.; Dincă, M. Highly Selective Heterogeneous Ethylene Dimerization with a Scalable and Chemically Robust MOF Catalyst. *ACS Sustainable Chem. Eng.* **2019**, *7*, 6654−6661.

(43) Röß-Ohlenroth, R.; Bredenkötter, B.; Volkmer, D. Organometallic MFU-4*l*(arge) Metal−Organic Frameworks. *Organometallics* **2019**, *38*, 3444−3452.

(44) Wright, A. M.; Wu, Z.; Zhang, G.; Mancuso, J. L.; Comito, R. J.; Day, R. W.; Hendon, C. H.; Miller, J. T.; Dincă, M. A Structural Mimic of Carbonic Anhydrase in a Metal-Organic Framework. *Chem* **2018**, *4*, 2894−2901.

(45) Cai, Z.; Bien, C. E.; Liu, Q.; Wade, C. R. Insights into CO_2 Adsorption in M−OH Functionalized MOFs. *Chem. Mater.* **2020**, *32*, 4257−4264.

(46) Ortega, D. E.; Matute, R. A. Influence of linkers on the Kuratowski-type secondary building unit in nickel single-site MOFs for ethylene oligomerization catalysis: a computational study. *Catal. Sci. Technol.* **2021**, *11*, 2422−2432.

(47) Carné-Sánchez, A.; Carmona, F. J.; Kim, C.; Furukawa, S. Porous materials as carriers of gasotransmitters towards gas biology and therapeutic applications. *Chem. Commun.* **2020**, *56*, 9750−9766.

(48) Ma, M.; Noei, H.; Mienert, B.; Niesel, J.; Bill, E.; Muhler, M.; Fischer, R. A.; Wang, Y.; Schatzschneider, U.; Metzler-Nolte, N. Iron metal-organic frameworks MIL-88B and NH_2-MIL-88B for the loading and delivery of the gasotransmitter carbon monoxide. *Chem. - Eur. J.* **2013**, *19*, 6785−6790.

(49) Diring, S.; Carné-Sánchez, A.; Zhang, J.; Ikemura, S.; Kim, C.; Inaba, H.; Kitagawa, S.; Furukawa, S. Light responsive metal-organic frameworks as controllable CO-releasing cell culture substrates. *Chem. Sci.* **2017**, *8*, 2381−2386.

(50) Carmona, F. J.; Rojas, S.; Romão, C. C.; Navarro, J. A. R.; Barea, E.; Maldonado, C. R. One-pot preparation of a novel CO-releasing material based on a CO-releasing molecule@metal-organic framework system. *Chem. Commun.* **2017**, *53*, 6581−6584.

(51) Kittikhunnatham, P.; Leith, G. A.; Mathur, A.; Naglic, J. K.; Martin, C. R.; Park, K. C.; McCullough, K.; Jayaweera, H. D. A. C.; Corkill, R. E.; Lauterbach, J.; Karakalos, S. G.; Smith, M. D.; Garashchuk, S.; Chen, D. A.; Shustova, N. B. A Metal-Organic Framework (MOF)-Based Multifunctional Cargo Vehicle for Reactive-Gas Delivery and Catalysis. *Angew. Chem., Int. Ed.* **2022**, *134*, No. e202113909.

(52) Bloch, E. D.; Britt, D.; Lee, C.; Doonan, C. J.; Uribe-Romo, F. J.; Furukawa, H.; Long, J. R.; Yaghi, O. M. Metal insertion in a microporous metal-organic framework lined with 2,2′-bipyridine. *J. Am. Chem. Soc.* **2010**, *132*, 14382−14384.

(53) Röß-Ohlenroth, R.; Freudig, C.; Kraft, M.; Bunzen, H.; Volkmer, D. Assembly of Porous Metal Hydrogen-Bonded Organic Frameworks from Diamine-Functionalized Kuratowski Complexes. *Cryst. Growth Des.* **2022**, *22*, 379−391.

(54) Yin, J.; Elsenbaumer, R. L. Efficient synthesis and characterization of novel bibenzimidazole oligomers and polymers as potential conjugated chelating ligands. *J. Org. Chem.* **2005**, *70*, 9436−9446.

(55) Baggi, G.; Loeb, S. J. Rotationally Active Ligands: Dialing-Up the Co-conformations of a 2Rotaxane for Metal Ion Binding. *Angew. Chem.* **2016**, *55*, 12533−12537.

(56) Werner, T. W.; Reschke, S.; Bunzen, H.; von Nidda, H.-A. K.; Deisenhofer, J.; Loidl, A.; Volkmer, D. $Co_5Tp^*{}_4(Me_2bta)_6$: A Highly Symmetrical Pentanuclear Kuratowski Complex Featuring Tris(pyrazolyl)borate and Benzotriazolate Ligands. *Inorg. Chem.* **2016**, *55*, 1053−1060.

(57) Rau, S.; Görls, H. Solid state structure of a rhenium bibenzimidazole complex. *J. Coord. Chem.* **2004**, *57*, 1587−1590.

(58) Hu, M.; Yan, Y.; Zhu, B.; Chang, F.; Yu, S.; Alatan, G. A series of Mn(I) photo-activated carbon monoxide-releasing molecules with benzimidazole coligands: synthesis, structural characterization, CO releasing properties and biological activity evaluation. *RSC Adv.* **2019**, *9*, 20505−20512.

(59) Bunzen, H.; Grzywa, M.; Kalytta-Mewes, A.; Volkmer, D. One-pot synthesis of ultrastable pentanuclear alkylzinc complexes. *Dalton Trans.* **2017**, *46*, 2618−2625.

(60) Hevia, E.; Miguel, D.; Pérez, J.; Riera, V. Synthesis and Reactivity of New (Methoxy)methyl Complexes of Manganese(I) and Rhenium(I). *Organometallics* **2006**, *25*, 4909−4912.

(61) Ling, K.; Men, F.; Wang, W.-C.; Zhou, Y.-Q.; Zhang, H.-W.; Ye, D.-W. Carbon Monoxide and Its Controlled Release: Therapeutic Application, Detection, and Development of Carbon Monoxide Releasing Molecules (CORMs). *J. Med. Chem.* **2018**, *61*, 2611−2635.

(62) Pierri, A. E.; Pallaoro, A.; Wu, G.; Ford, P. C. A luminescent and biocompatible photoCORM. *J. Am. Chem. Soc.* **2012**, *134*, 18197−18200.

(63) Mukherjee, J.; Siewert, I. Manganese and Rhenium Tricarbonyl Complexes Equipped with Proton Relays in the Electrochemical CO 2 Reduction Reaction. *Eur. J. Inorg. Chem.* **2020**, *2020*, 4319−4333.

(64) Choi, K. M.; Kim, D.; Rungtaweevoranit, B.; Trickett, C. A.; Barmanbek, J. T. D.; Alshammari, A. S.; Yang, P.; Yaghi, O. M. Plasmon-Enhanced Photocatalytic CO_2 Conversion within Metal-Organic Frameworks under Visible Light. *J. Am. Chem. Soc.* **2017**, *139*, 356−362.

(65) Rouquerol, F. *Adsorption by Powders and Porous Solids: Principles, Methodology and Applications*, 2nd ed.; Academic Press, 2014.

(66) Jagiello, J.; Thommes, M. Comparison of DFT characterization methods based on N_2, Ar, CO_2, and H_2 adsorption applied to carbons with various pore size distributions. *Carbon* **2004**, *42*, 1227−1232.

(67) Ravikovitch, P. I.; Neimark, A. V. Characterization of nanoporous materials from adsorption and desorption isotherms. *Colloids Surf., A* **2001**, *187−188*, 11−21.

(68) *SAINT*; Bruker Analytical X-Ray Systems Inc: Madison, WI, 2015.

(69) Krause, L.; Herbst-Irmer, R.; Sheldrick, G. M.; Stalke, D. Comparison of silver and molybdenum microfocus X-ray sources for single-crystal structure determination. *J. Appl. Crystallogr.* **2015**, *48*, 3−10.

(70) Sheldrick, G. M. SHELXT - integrated space-group and crystal-structure determination. *Acta Crystallogr., Sect. A: Found. Crystallogr.* **2015**, *71*, 3−8.

(71) Sheldrick, G. M. Crystal structure refinement with SHELXL. *Acta Crystallogr., Sect. C: Struct. Chem.* **2015**, *71*, 3−8.

(72) Spek, A. L. Structure validation in chemical crystallography. *Acta Crystallogr., Sect. D: Biol. Crystallogr.* **2009**, *65*, 148−155.

(73) Rombouts, J. A.; Ravensbergen, J.; Frese, R. N.; Kennis, J. T. M.; Ehlers, A. W.; Slootweg, J. C.; Ruijter, E.; Lammertsma, K.; Orru, R. V. A. Synthesis and photophysics of a red-light absorbing supramolecular chromophore system. *Chem. - Eur. J.* **2014**, *20*, 10285−10291.
(74) Cheeseman, G. W. H. 223. Quinoxalines and related compounds. Part VI. Substitution of 2,3-dihydroxyquinoxaline and its 1,4-dimethyl derivative. *J. Chem. Soc.* **1962**, 1170.
(75) Coburn, M. D. Nitro derivatives of 1-picrylbenzotriazole. *J. Heterocycl. Chem.* **1973**, *10*, 743−746.

https://doi.org/10.1021/acs.inorgchem.2c02394
Inorg. Chem. 2022, 61, 16380−16389

Supporting Information

Inhibition, Binding of Organometallics, and Thermally Induced CO Release in an MFU-4-Type Metal–Organic Framework Scaffold with Open Bidentate Bibenzimidazole Coordination Sites

Richard Röß-Ohlenroth, Maryana Kraft, Hana Bunzen, Dirk Volkmer*

Chair of Solid State and Materials Chemistry, Institute of Physics, University of Augsburg, Universitätsstraße 1,
86159 Augsburg, Germany

*Corresponding Author
E-mail: dirk.volkmer@physik.uni-augsburg.de

Table of Contents

Detailed Structure descriptions and discussion

CFA-19:

As the **CFA-19** single-crystal was picked directly from the DMF reaction solution, residual electron density was localized at the bibenzimidazole group. This may be attributed to the partial occupation of this coordination site by residual cobalt ions from the reaction solution, which should be removed during the washing procedure. The peripheral cobalt metal sites of the Kuratowski SBU do not show the typical tetrahedral coordination by three nitrogen atoms and one chloride anion, but a statistical intermediate between the tetrahedral and octahedral coordination with additional neutral ligands, most probably DMF or water from the reaction solution. The additional side ligands are expected to be absent from the activated structure, which can be deduced from the reversible color change effect from green to gold upon the addition of MeOH or other polar solvents. This is due to the change from a tetrahedral to an octahedral coordination environment, which was previously observed in the literature (Figure S42, 53).[1] The typical bond distances of **CFA-19**, such as Co1-N1 (2.183(8) Å), Co2-N2 (2.027(6) Å), and Co2-Cl (2.091(6) Å), are in fair agreement with the values obtained for **Co-MFU-4** (2.290(2), 1.965(7), 2.014(8) Å), ***Co-MFU-4l*** (Zn-N, 2.009(9), 2.00(5) Å), and the $[Co_5Cl_4(Me_2bta)_6]$ complex (2.186(3), 2.0007(16), 2.2192(6) Å).[2]

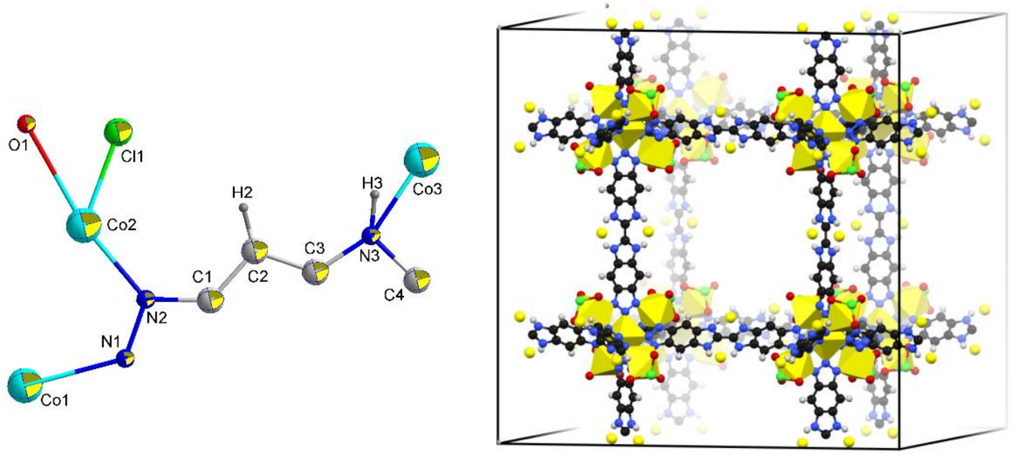

Figure S1. ORTEP-style plot of the asymmetric unit with a 50% probability for thermal ellipsoids (left) and packing plot of the **CFA-19** SC-XRD structure (right)

CFA-19-Tp:

A more distinct single-crystal structure solution was obtained for **CFA-19-Tp**, in which the chloride side ligands were exchanged post-synthetically with Tp-ligands by the suspension of DMF and DCM washed single-crystals in a solution of NBU_4Tp in DCM. **CFA-19-Tp** retains the $Fm\bar{3}m$ (225) space group, but does not exhibit any residual electron density at the bibenzimidazole coordination site, as well as the complete exchange of the chloride side ligands with the scorpionate Tp-ligands. This leads to an octahedral coordination environment of the peripheral cobalt ions, which is also visible by the orange/brown color of the material in contrast to the dark green color of **CFA-19** (Figure S52). This is in good agreement with the optical observations and UV/VIS spectra reported in the literature for $[Co_5Tp^*_4(Me_2bta)_6]$ and $[Co_5Cl_4(Me_2bta)_6]$ complexes.[1] The Co2-N4 bond distance of **CFA-19-Tp** (2.051(14) Å) slightly differs from the Co2-N6/N8/N10 distances of 2.201(4), 2.170(4), and 2.161(4) Å in the $[Co_5Tp^*_4(Me_2bta)_6]$ complex.[1]

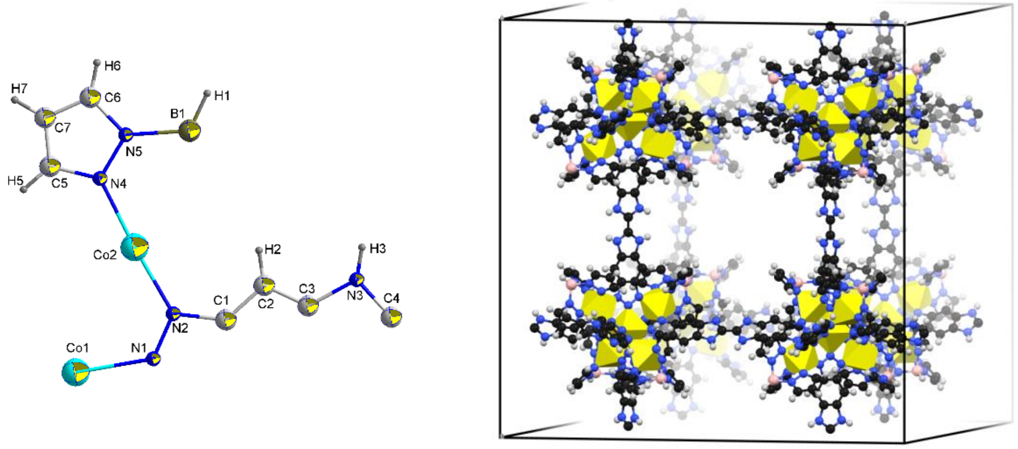

Figure S2. ORTEP-style plot of the asymmetric unit with a 50% probability for thermal ellipsoids (left) and packing plot of the **CFA-19-Tp** SC-XRD structure (right)

ReBr(CO)$_3$@CFA-19-Tp:

For the **ReBr(CO)$_3$@CFA-19-Tp** single-crystal, no changes with respect to **CFA-19-Tp** were observed, except for the additional ReBr(CO)$_3$ fragments. It still crystallizes in the space group $Fm\bar{3}m$ (225) but with a slightly smaller unit cell size. A statistically distributed coordination site occupation of ca. 50% with ReBr(CO)$_3$ fragments was found, which is in fair agreement with the Co:Re:Br ratios obtained from EDX and ICP-OES measurements. The Re-N5 (2.136(10) Å), Re-Br (2.564(14) Å), and Re-C8/C9 (1.92(2)/ 1.89(7) Å) distances in **ReBr(CO)$_3$@CFA-19-Tp** are similar to the corresponding distances of Re-N1 (2.194(3) Å), Re-N2 (2.190(3) Å), and Re-Br (2.6320(4) Å) Re-C15/C16/C17 (1.907(4), 1.932(4), 1.934(5) Å) in the literature for the (bbimH$_2$)Re(CO)$_3$Br (bbimH$_2$= 2,2´-bibenzimidazole) complex.[3]

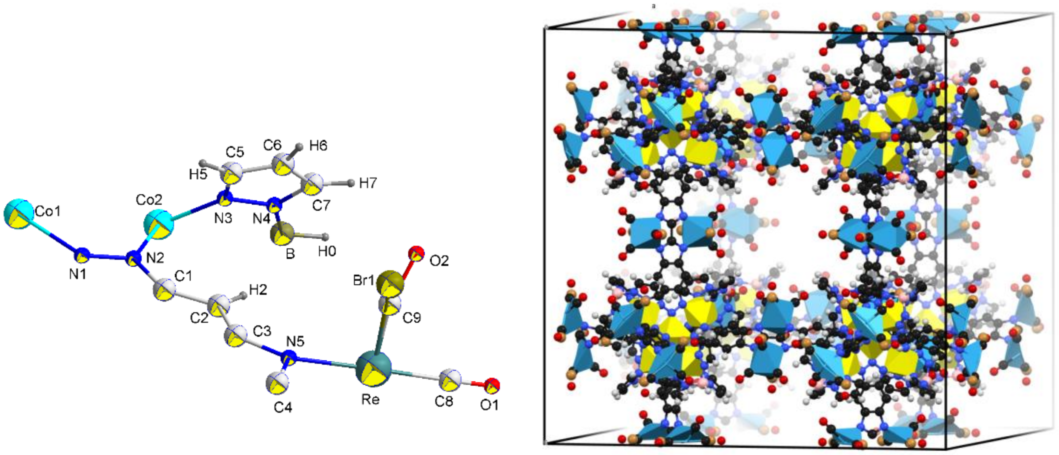

Figure S3. ORTEP-style plot of the asymmetric unit with a 50% probability for the thermal ellipsoids (left) and packing plot of the **ReBr(CO)$_3$CFA-19** SC-XRD structure (right)

MnBr(CO)$_3$@CFA-19-Tp:

The **MnBr(CO)$_3$@CFA-19-Tp** single-crystal structure was also solved in the $Fm\bar{3}m$ (225) space group, which exhibited a unit cell size similar to that of **CFA-19-Tp**. A coordination site occupation of ca. 60% with MnBr(CO)$_3$ fragments was observed, which is lower than that expected from the EDX and ICP-OES data, which indicated 80% or higher. In addition, this single-crystal showed only partial Tp ligand exchange with approximately one chloride anion left per Kuratowski SBU. However, partial exchange with bromide anions cannot be ruled out, which may lead to the slight overestimation of the chloride occupation. This is in fair agreement with the EDX data of bulk materials showing some leftover chloride and bromide. Defects or blocked pores in some crystals could prevent a complete ligand exchange with the bulky Tp ligands in some crystals. However, the Mn1-N5 (2.086(8) Å), Mn1-Br (2.62(3) Å), and Mn-C9/C10 (1.882(15), 1.77(2) Å) bond distances of the MnBr(CO)$_3$ fragment in **MnBr(CO)$_3$@CFA-19-Tp** are in fair agreement with the corresponding Mn2-N1 (2.082(3) Å), Mn2-N4 (2.066(3) Å), Mn2-Br1 (2.5701(11) Å), and Mn2-C15/C16/C17 (1.803(5), 1.813(5),1.799(6) Å) distances in the literature for the [MnBr(CO)$_3$(2,2′-bibenzimidazole)] complex.[4]

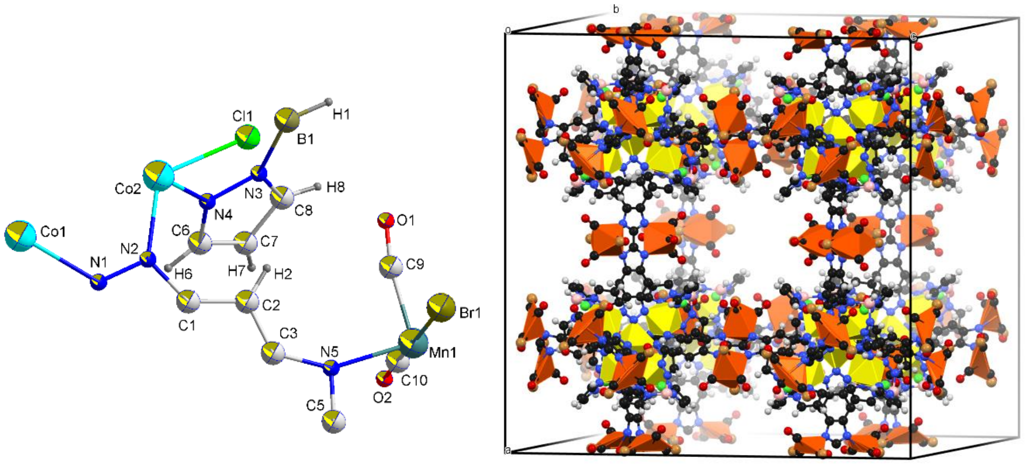

Figure S4. ORTEP-style plot of the asymmetric unit with a 50% probability for thermal ellipsoids (left) and packing plot of the **MnBr(CO)$_3$CFA-19** SC-XRD structure (right)

Table S1. Crystal Data and Structural Refinement for **CFA-19**, **CFA-19-Tp**, **$ReBr(CO)_3$@CFA-19-Tp**, and **$MnBr(CO)_3$@CFA-19-Tp**

Compound]	**CFA-19**	**CFA-19-Tp**	**$ReBr(CO)_3$@CFA-19-Tp**	**$MnBr(CO)_3$@CFA-19-Tp**
empirical formula	$C_{42}H_{18}Cl_{2.32}Co_{6.57}N_{30}O_{5.04}$	$C_{78}H_{58}B_4Co_5N_{54}$	$C_{87.70}H_{52}B_4Br_{2.30}Co_5N_{54}O_{9.70}Re_3$	$C_{80.52}H_{43.17}B_{3.12}Br_{3.49}Cl_{0.88}Co_5Mn_{3.49}N_{48.70}$
formula				
formula weight (g mol^{-1})	1493.21	2089.67	3097.84	2690.81
temperature (K)	250(2)	250(2)	150(2)	150(2)
wavelength (Å)	1.54178	1.54178	1.54178	0.71073
crystal system	Cubic	Cubic	Cubic	Cubic
space group	*F*m-3m	*F*m-3m	*F*m-3m	*F*m-3m
a (Å)	a = 37.1738(18)	a = 37.0540(19)	a = 36.6657(9)	a = 36.9245(7)
volume (Å^3)	51370(7)	50875(8)	49292(4)	50344(3)
Z	8	8	8	8
D_g (g cm^{-3})	0.386	0.546	0.835	0.710
μ (mm^{-1})	3.604	2.729	6.105	1.086
F(000)	5898	8472	11955	10608
crystal size (mm^3)	0.06 x 0.05 x 0.05	0.05 x 0.05 x 0.05	0.05 x 0.05 x 0.05	0.06 x 0.06 x 0.06
Θ range	2.377° - 48.491°.	2.385° - 35.838°.	2.087° - 72.604°.	2.206° to 21.946°.
reflections collected	42747	10563	137927	158811
independent reflections	1292 [R(int) = 0.3032]	647 [R(int) = 0.0781]	2449 [R(int) = 0.1236]	1579 [R(int) = 0.1413]
completeness	99.8 %	99.5 %	99.9 %	99.7 %
data/restraints/parameters	1292 / 6 / 58	647 / 94 / 77	2449 / 18 / 102	1579 / 22 / 115
goodness of fit on F^2	1.085	1.431	1.079	1.146
final R indices [$I > 2\text{sigma}(I)$]	R1 = 0.0774, wR2 = 0.2331	R1 = 0.0902, wR2 = 0.2943	R1 = 0.0836, wR2 = 0.2746	R1 = 0.0688, wR2 = 0.1906
R indices (all data)	R1 = 0.1229, wR2 = 0.2676	R1 = 0.0997, wR2 = 0.3026	R1 = 0.1077, wR2 = 0.3156	R1 = 0.0949, wR2 = 0.2257
Flack parameter	-	0.000045(16)	-	-
largest diff. peak and hole/e.Å^{-3}	0.452 and -0.268	0.565 and -0.263	0.797 and -0.803	0.736 and -0.346
CCDC No.	2169270	2169269	2169271	2169272

Material composition

The expected sum formulas of the compounds describe the activated state. These were derived from the single-crystal structures, EDX, and ICP-OES data (Figure S46-51). The cobalt content of the structures was assumed to be 5 to determine the ratios.

The exchange of chloride anions was confirmed by EDX measurements, which showed the change in the cobalt to chloride ratio from 5:4.0 in **CFA-19** to approximately 5:0.4 in **CFA-19-Tp**. This is still slightly higher than expected from single-crystal data, but can also be considered to partially result from residues of NBu_4Cl or DCM in the framework pores. Nonetheless, we provide the sum formula of the bulk **CFA-19-Tp** framework as $[Co_5Cl_{0.4}Tp_{3.6}(H_2\text{-bibt})_3]$.
The EDX spectra of **ReBr(CO)$_3$@CFA-19-Tp** showed a Co:Br:Re ratio of 5:3.2:2.7, which is in fair agreement with the ICP-OES Co:Re ratio of 5:2.83, and the ca. 50% site occupation from the single-crystal structure. Contrary to our expectations, the **MnBr(CO)$_3$@CFA-19-Tp** structure showed a Co:Mn ratio of 5:6.11 in ICP-OES measurements, indicating the two-sided coordination of the linker, which is not completely supported by the ca. 60% coordination site occupation refined in the single-crystal. One would not expect such coordination without deprotonation of the bibenzimidazole, which was not really indicated in the DRIFT measurements and by the high bromide content observed in the EDX spectra. Although the slight loss of Mn and Br, associated with the loss of residual uncoordinated $MnBr(CO)_5$, was observed after heat treatment in vacuum, at least five Mn atoms remained per unit cell. In general, the partial exchange of peripheral Co ions with Mn cannot be ruled out completely, although most of them are capped with Tp ligands, and polar solvents are usually necessary for such an exchange. Thus, we can only assume the presence of additional disordered $MnBr(CO)_x$ complexes in the structure. The higher chloride content of **ReBr(CO)$_3$@CFA-19-Tp** and **MnBr(CO)$_3$@CFA-19-Tp** is expected to originate from the DCM solvent, especially in **MnBr(CO)$_3$@CFA-19-Tp**, which could not be dried at elevated temperatures. Thus, the same Cl:Tp ratio of **CFA-19-Tp** was assumed for both derivative structures. For **ZnEt@CFA-19-Tp**, a **CFA-19** batch with slightly higher initial chloride residues was used. The ICP-OES ratios were used for the ratios in the sum formulas.

Table S2. EDX and ICP-OES ratios, as well as the derived sum formulas for **CFA-19**, **CFA-19-Tp**, **ReBr(CO)$_3$@CFA-19-Tp**, **MnBr(CO)$_3$@CFA-19-Tp,** and **ZnEt@CFA-19-Tp**

Compound]	**Formula**	**Co EDX / ICP-OES**	**M = Re, Mn, Zn EDX / ICP-OES**	**Br EDX**	**Cl EDX**
CFA-19	$[Co_5Cl_4(H_2\text{-bibt})_3]$.	5	-	-	4.0
CFA-19-Tp	$[Co_5Cl_{0.4}Tp_{3.6}(H_2\text{-bibt})_3]$.	5	-	-	0.4
ReBr(CO)$_3$@CFA-19-Tp	$[Co_5Cl_{0.4}Tp_{3.6}(H_2\text{-bibt})_3\cdot(ReBr(CO)_3)_{2.8}]$	5	2.7 / 2.83	3.2	0.9
MnBr(CO)$_3$@CFA-19-Tp	$[Co_5Cl_{0.4}Tp_{3.6}(H_2\text{-bibt})_3\cdot(MnBr(CO)_3)_3]$ $\cdot 3.1(MnBr(CO)_X)$	5	5.9 / 6.11	6.5	0.6
MnBr(CO)$_3$@CFA-19-Tp after 200°C vacuum		5	5.2 / -	5.7	0.4
ZnEt@CFA-19-Tp	$[Co_5Cl_{0.9}Tp_{3.1}(H\text{-bibt})_{1.1}(bibt)_{1.9}\cdot(ZnEt)_{4.9}]$	5	5.1 / 4.92	-	0.9

Argon Adsorption Analysis

Porosities were examined using argon adsorption isotherms at 77 K (Figure 2a). These exhibited a pronounced two-step behavior for **CFA-19** and **CFA-19-Tp**, making it difficult to determine the correct BET region. Thus, more adsorption steps were measured in this region for the frameworks (Figure S28). However, the BET plot for **CFA-19** gives a specific surface area (SSA) of 3316 m^2g^{-1} (Figure S29), which is in good agreement with the value of 3877 m^2g^{-1} calculated for the **CFA-19** structure without additional solvent ligands and the residual cobalt coordinated at the bibenzimidazole using the iRASPA software. [5] The maxima of the nonlocal density functional theory (NLDFT) pore size distribution at 16.5,18.5, and 22 Å of **CFA-19** are also in fair agreement with the structure (Figure S27). Although various attempts have been made to improve the BET surface area of **CFA-19-Tp**, only 2097 m^2g^{-1} was achieved, in contrast to the calculated 3578 m^2g^{-1} (Figure S30). This may be attributed to the observed two-step behavior limiting the region for BET analysis. The pore volumes determined at $p/p_0 \approx 0.84$ are 1.392 cm^3/g for **CFA-19** and 1.100 cm^3/g for **CFA-19-Tp**. **ReBr(CO)$_3$@CFA-19-Tp** and **MnBr(CO)$_3$@CFA-19-Tp** exhibited a similar SSA of 1917 and 1924 m^2g^{-1} (Figure S31, 32), respectively, but a loss of the second adsorption step, and thus a distinctively lower saturation uptake compared with **CFA-19-Tp**. Nearly identical NLDFT pore size distributions were found for **ReBr(CO)$_3$@CFA-19-Tp** and **MnBr(CO)$_3$@CFA-19-Tp**, which even show the small additional pores suggested by Platon from idealized structures (Figure S27). The calculated values are 2163 m^2g^{-1} and 2480 m^2g^{-1} for **ReBr(CO)$_3$@CFA-19-Tp** and **MnBr(CO)$_3$@CFA-19-Tp**, respectively, which is in fair agreement as the calculation was performed with a 50% occupation of the $MBr(CO)_3$ sites, although **MnBr(CO)$_3$@CFA-19-Tp** has shown a higher Mn content. The pore volumes at $p/p_0 \approx 0.84$ are 0.617 cm^3/g for **ReBr(CO)$_3$@CFA-19-Tp** and 0.715 cm^3/g for **MnBr(CO)$_3$@CFA-19-Tp.** The pore-limiting diameters of the idealized structures in Figure 1 were calculated with PoreBlazer v4.0.[6]

IR spectroscopy and simulations

The simulation of IR spectra with idealized structures built from Zn^{II} ions instead of Co^{II}, similar to the methods successfully employed for organometallic **MFU-4*l*** frameworks,[7] showed a good match for all frameworks with ATR and DRIFT measurements. Thus, only minor manipulations of the spectra obtained with SpecDis from the CASTEP wavenumber and intensity files were necessary. The intensity in the range of 400–180 cm^{-1} was increased by a factor of 5 and scaling factors shifting the general x-value were applied (1.01–1.02 in the range of 180–2000 cm^{-1} and 0.995 in the range of 2000–4000 cm^{-1}). For **CFA-19** and **CFA-19-Tp**, the symmetric stretching vibration of hydrogen at the bibenzimidazole moieties can be observed at 3477 cm^{-1} and 3481 cm^{-1}, respectively (Figure S5). Symmetric aromatic hydrogen stretching vibration was observed at 3075 cm^{-1} for **CFA-19** and at 3113 cm^{-1}, along with the pyrazole hydrogen stretch at 3145 cm^{-1}, for **CFA-19-Tp**. The Tp ligand exchange is also supported by the new band of the B-H stretching vibration at 2465 cm^{-1} as well as the four distinct new bands of the C-H and B-H bending modes observed in the calculations and measured at 756, 718, 667, and 619 cm^{-1}. The chloride stretching vibration at 370 cm^{-1} appeared to decrease or vanish. This is difficult to distinguish because the **CFA-19-Tp** simulation also exhibited a small band at this position resulting from a linker bending mode.

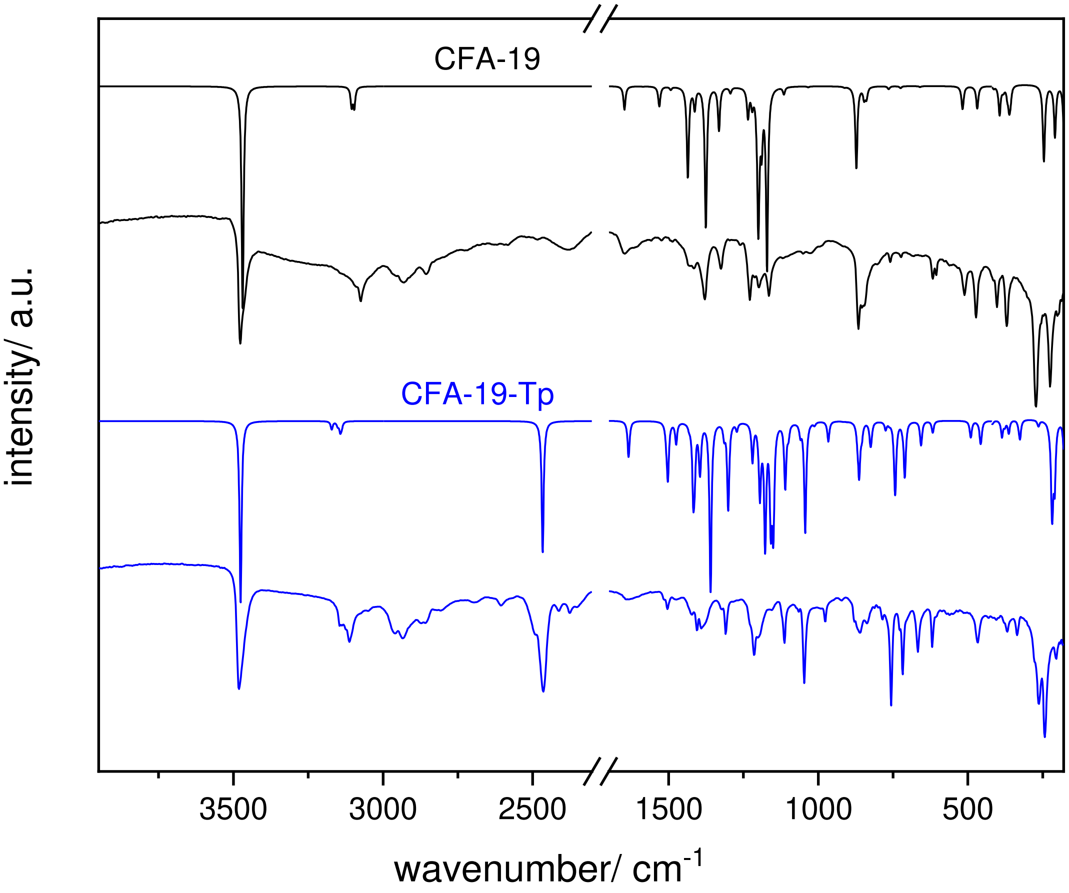

Figure S5. DRIFT (left) and ATR FT-IR spectra (right) comparison of calculated (top) and measured (bottom) IR spectra of **CFA-19** and **CFA-19-Tp**

A comparison of the **CFA-19-Tp** and **ZnEt@CFA-19-Tp** spectra showed a significant decrease in the intensity of the N-H stretching vibration of bibenzimidazole at 3477 cm^{-1} (Figure S7). The asymmetric and symmetric stretching vibrations of the CH_2 and CH_3 of the ethanido ligand were observed at 2926 and 2855 cm^{-1}, respectively The new band at 516 cm^{-1}, associated with the Zn-C stretching of the ethanido ligand, was also observed in the calculated and measured spectra. The intensity decrease of the band at 474 cm^{-1}, which origins from an in-plane stretch of the whole ligand, as well as the new band at 432 cm^{-1} resulting from a new bending mode of the ligand, are also in good agreement. However, the rocking vibration of the ethanido ligand calculated at 632 cm^{-1} could not be allocated and only a minor shoulder at 606 cm^{-1} was observed.

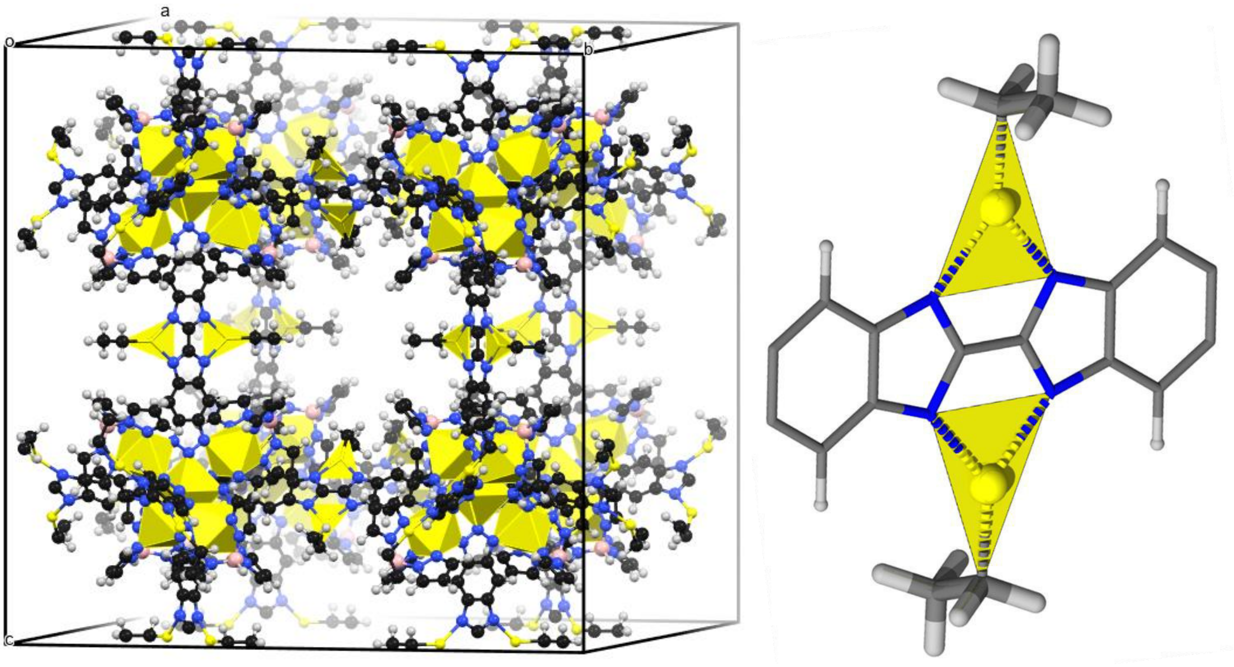

Figure S6. Packing plot of the **ZnEt@CFA-19-Tp** structure model used for the IR-spectra simulation (left) and detailed picture of the expected coordination environment of the Zn ions in the activated compound (right)

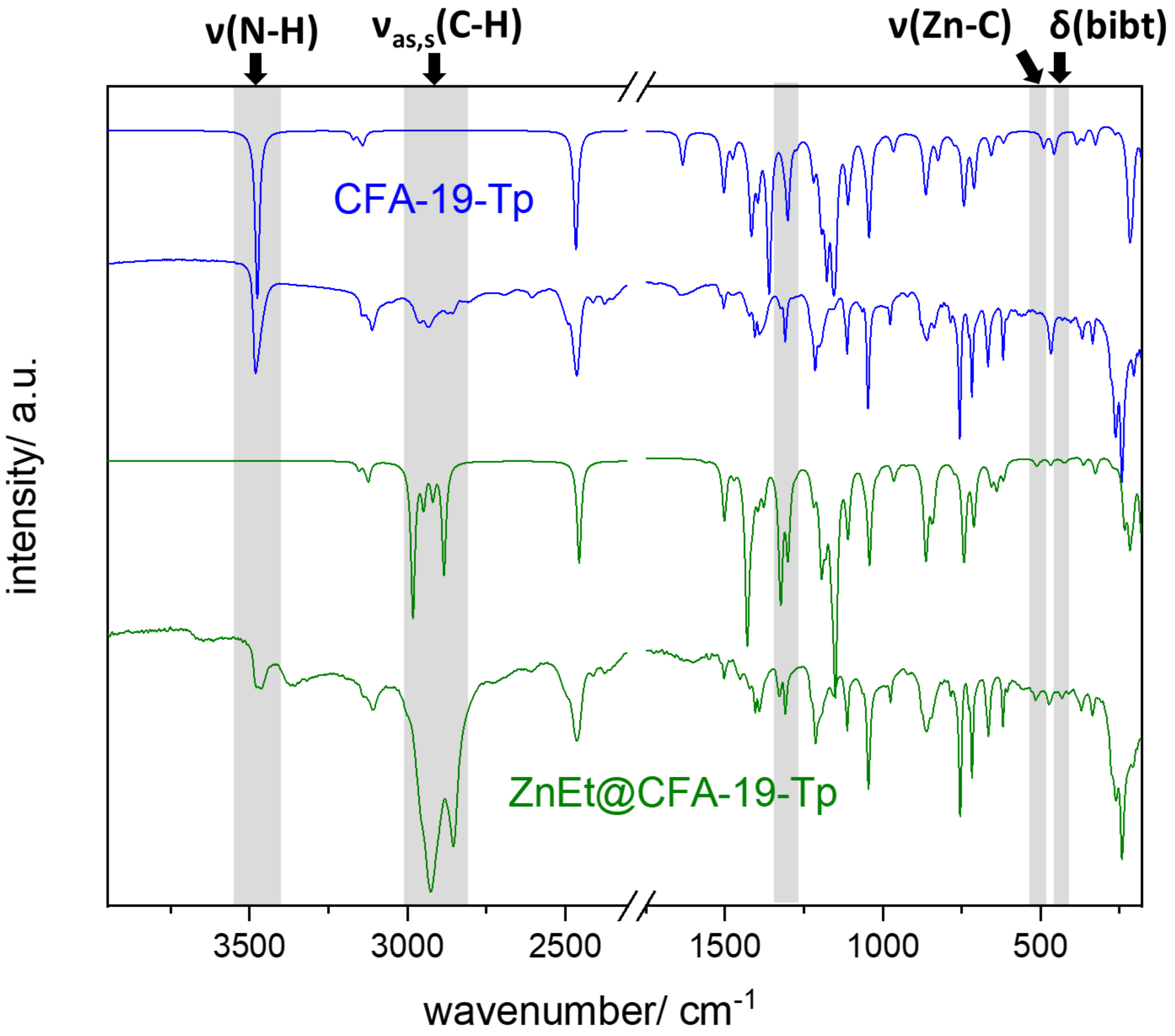

Figure S7. DRIFT (left) and ATR FT-IR spectra (right) comparison of calculated (top) and measured (bottom) IR spectra of **CFA-19-Tp** and **ZnEt@CFA-19-Tp**

Thermal and general stability

For **CFA-19**, a slow degradation was observed under ambient conditions. Further investigation by variable humidity PXRD showed that the material completely and irreversibly lost its crystallinity at humidity levels above 30% (Figure S19, 20). This degradation was accompanied by a color change to brown associated with water coordination at the cobalt sites, and a shriveling of the crystals (Figure S10), which led to a decrease in the material volume. In contrast, **CFA-19-Tp** can be stored for several years under ambient conditions without changes in the crystallinity. For instance, **CFA-19-Tp** single-crystals were used to prepare **ReBr(CO)$_3$@CFA-19-Tp** single-crystals after two years of storage under ambient conditions. Although a fair stability of **CFA-19** was observed in methanol/water mixtures and pure water, the material only remained crystalline in 0.01M HCl solutions and showed a strong degradation in 0.1M and 1M solutions (Figures S25). **CFA-19** showed a high temperature stability in TGA and VT- PXRD measurements, with decomposition starting at above 400 °C (Figure S13, 22). However, the VT-PXRD patterns of **CFA-19-Tp** showed a shift of the reflex intensities between 8 and 12° 2θ above 300 °C (Figure S14). This agrees with the PXRD pattern of **CFA-19,** and therefore indicates the decomposition of the Tp ligand (Figure S15). Variable-temperature DRIFT (VT-DRIFT) measurements of **CFA-19-Tp** confirmed this behavior with the loss of bands associated with the Tp ligand. In particular, the loss of the B-H stretching vibration at 2465 cm^{-1} was accompanied by the rise of a new band at 2206 cm^{-1} from a decomposition product (Figure S31). **ReBr(CO)$_3$@CFA-19-Tp** showed similar behavior as **CFA-19-Tp** in the TGA (Figure 2d) and VT- PXRD (Figure S16), indicating the decomposition of the Tp ligand and no loss of CO, which were also observed in the VT-DRIFT measurements (Figure S33). A different decomposition was observed for **MnBr(CO)$_3$@CFA-19-Tp**, which showed a loss of ca. 12 wt% in the TGA (Figure 2d) and loss of the small reflex at 8.16° 2θ associated with the MnBr(CO)$_3$ fragment at low temperatures in the VT-PXRD (Figure S17, 18) due to the loss of all CO ligands and a minor amount of residual MnBr(CO)$_5$ also observed in the IR spectra (Figure S34). For **ZnEt@CFA-19-Tp**, only VT-DRIFT measurement was conducted because of its instability under ambient conditions, which showed the unexpectedly high thermal stability of this fragment and no signs of hydride formation expected for the β-hydride elimination reaction of the ethanido ligand (Figure S38). The compound showed high reactivity, indicated by a complete loss of the IR bands at 516 cm^{-1} and 435 cm^{-1}, associated with the bending and Zn-C stretching vibrations of the ethanido ligand, respectively, after ambient conditions for a few minutes (Figure S39). The compound is expected to react with humidity to form ethane gas and an –OH ligand, as indicated by the DRIFT measurement of the water-quenched sample showing a new band at 3664 cm^{-1}. Simultaneously, the symmetric and asymmetric stretching vibrations of the ethanido ligand at 2855 cm^{-1} and 2927 cm^{-1} disappeared (Figure S40), respectively, but bibenzimidazole appeared to be protonated again. More detailed investigations of this compound must be conducted to determine the exact mechanisms and resulting coordinated fragments. The VT-XRPD of the quenched sample shows a similar behavior as **CFA-19-Tp** (Figure S22).

Ligand and Metal Exchange at the Kuratowski SBU

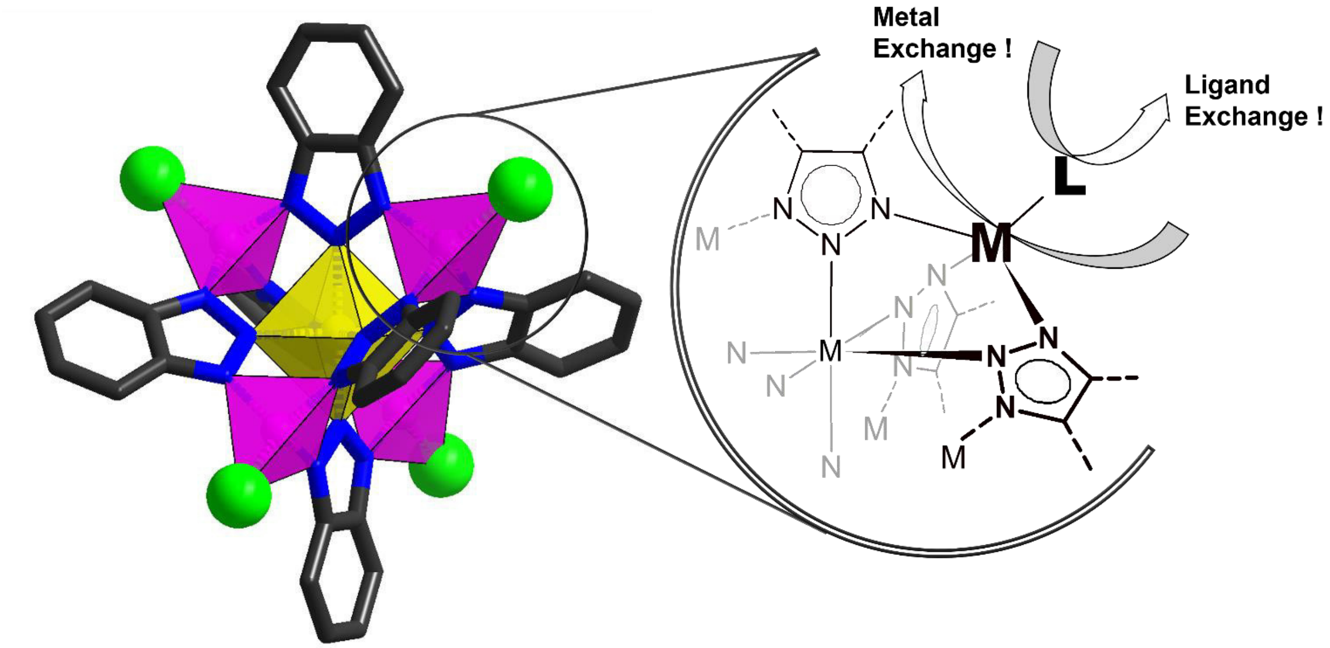

Figure S8. Kuratowski SBU showing the chloride side ligands (green) and tetrahedrally coordinated peripheral M^{II} sites (purple), which can be exchanged post-synthetically

NMR Spectra

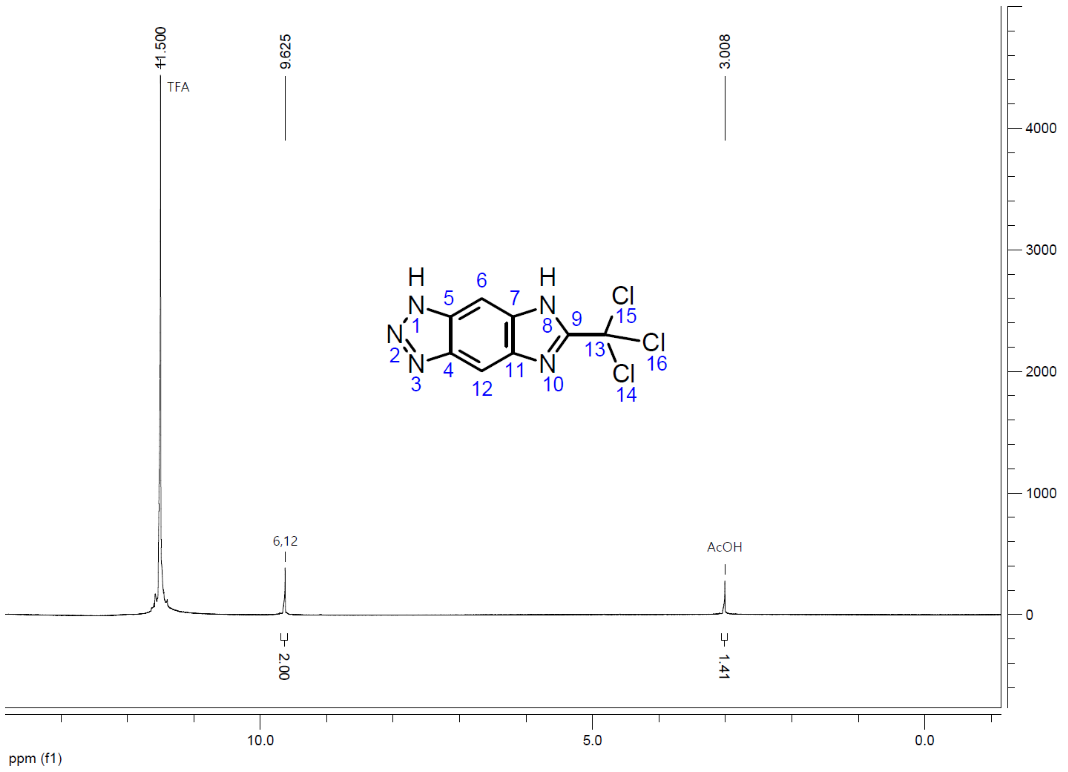

Figure S9. ^{1}H-NMR spectrum of 6-(trichloromethyl)-1,7-dihydroimidazo[4,5-*f*]benzotriazole (**H_2-tcibt**) in TFA-d_1

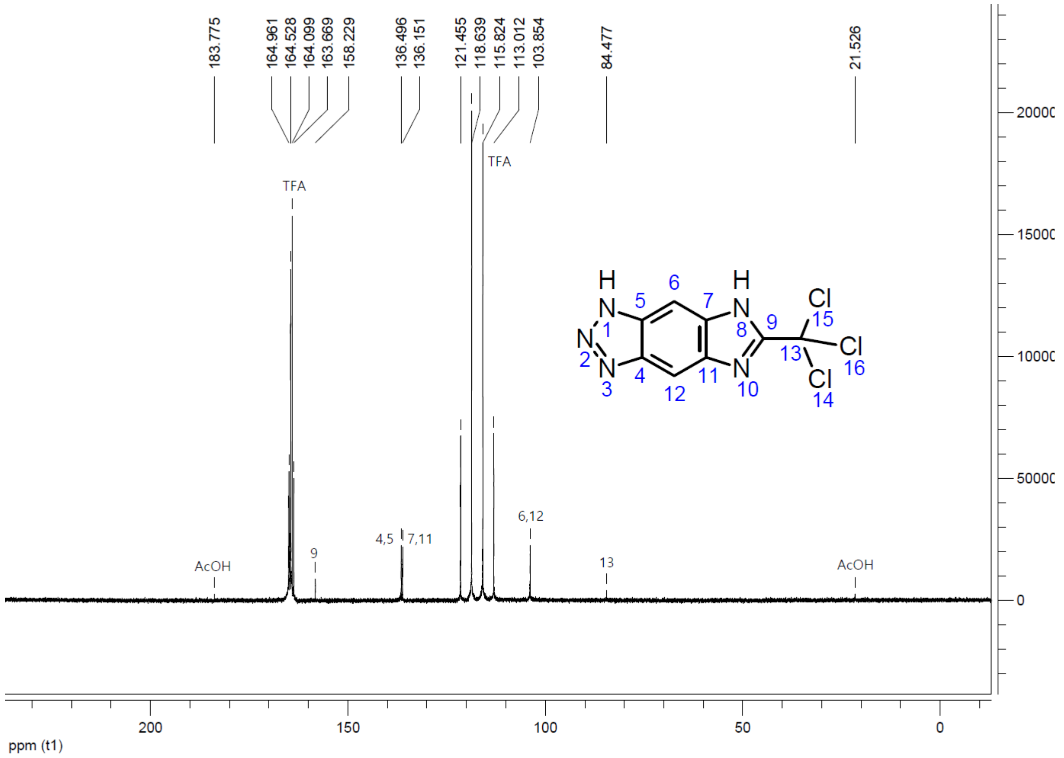

Figure S10. ^{13}C-NMR spectrum of 6-(trichloromethyl)-1,7-dihydroimidazo[4,5-*f*]benzotriazole (**H_2-tcibt**) in TFA-d_1

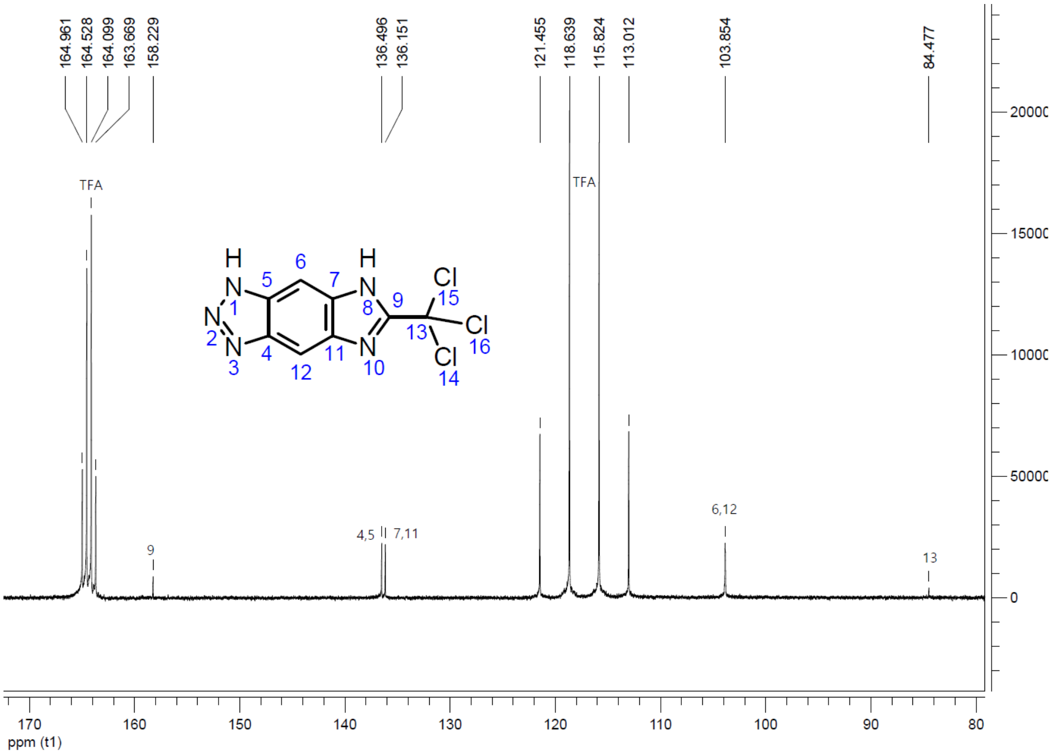

Figure S11. Enlarged ^{13}C-NMR spectrum of 6-(trichloromethyl)-1,7-dihydroimidazo[4,5-*f*]benzotriazole (**H_2-tcibt**) in TFA-d_1

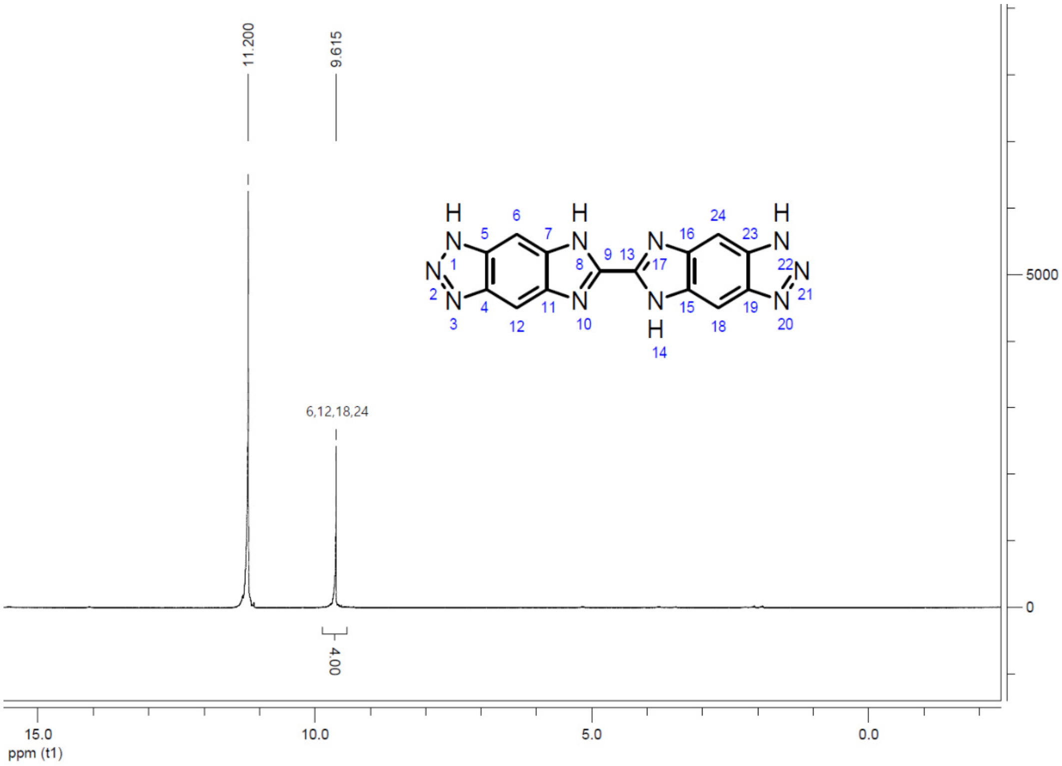

Figure S12. ^{1}H-NMR spectrum of 1,1',5,5'-tetrahydro-6,6'-biimidazo[4,5-*f*]benzotriazole (**H_4-bibt**) in D_2SO_4

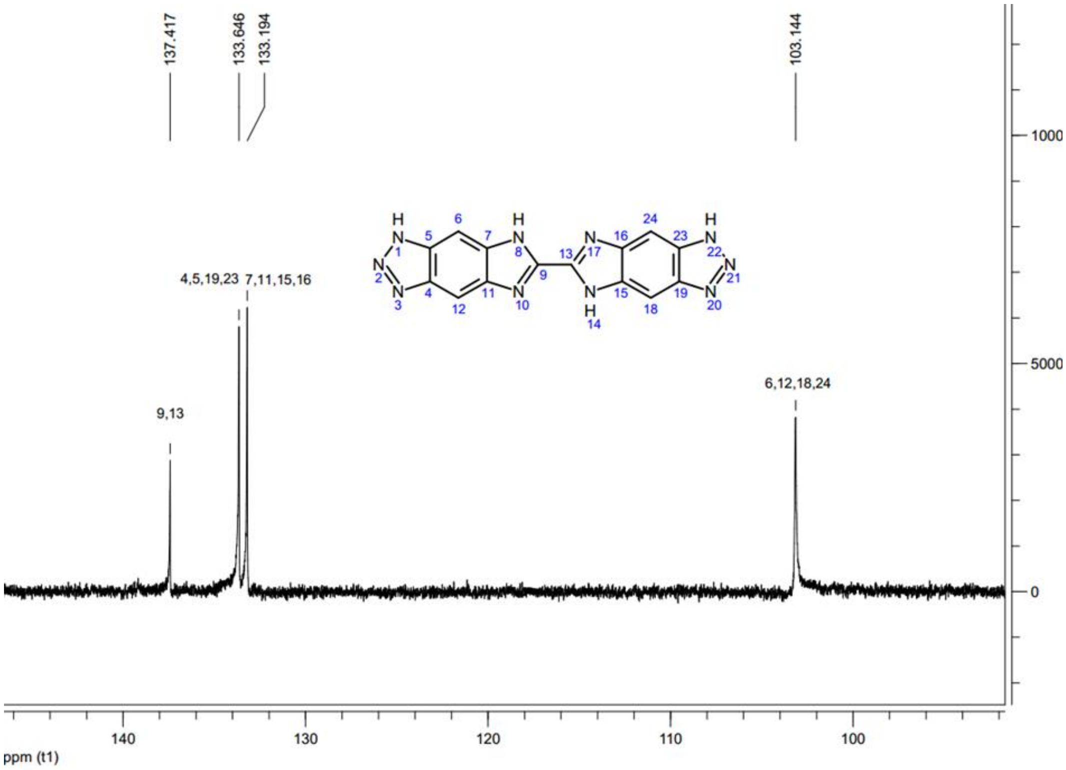

Figure S13. ^{13}C-NMR spectrum of 1,1',5,5'-tetrahydro-6,6'-biimidazo[4,5-*f*]benzotriazole (**H_4-bibt**) in D_2SO_4

Optical and Electron Microscopy Images

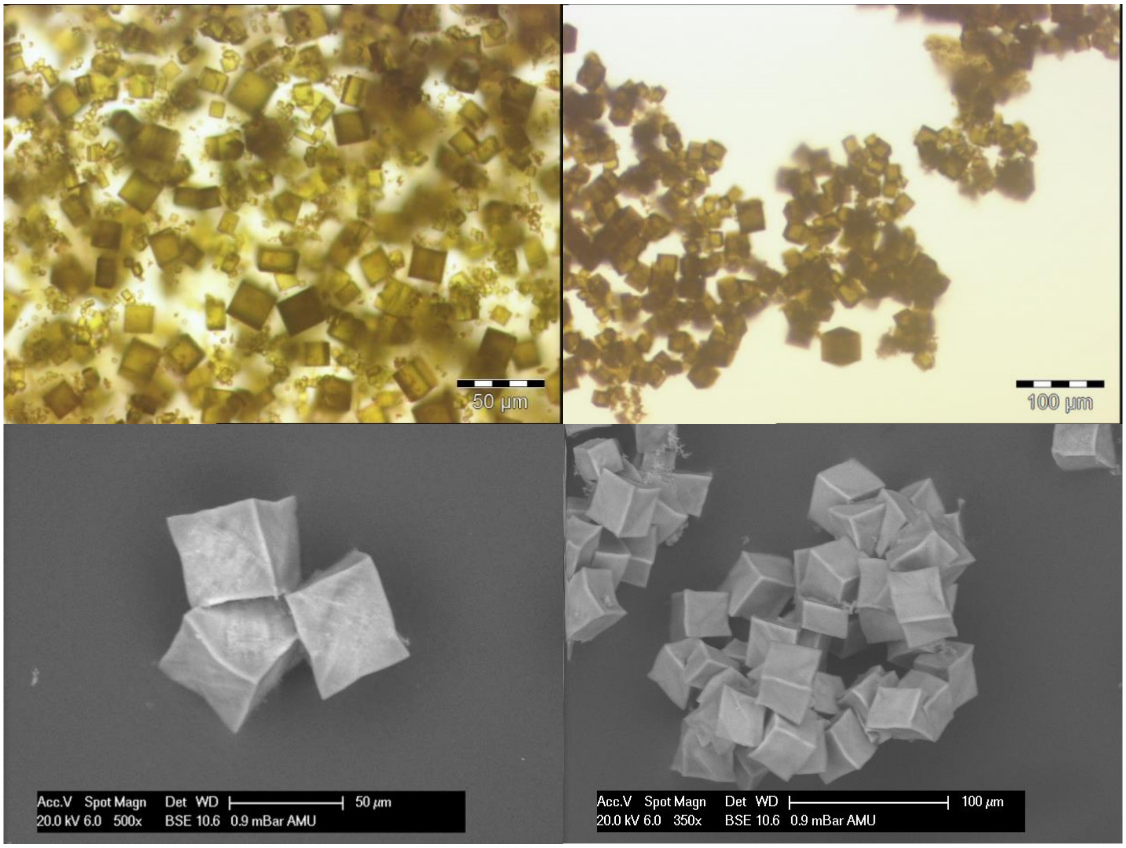

Figure S14. Optical (top) and ESEM (bottom) micrographs from typical syntheses of **CFA-19**

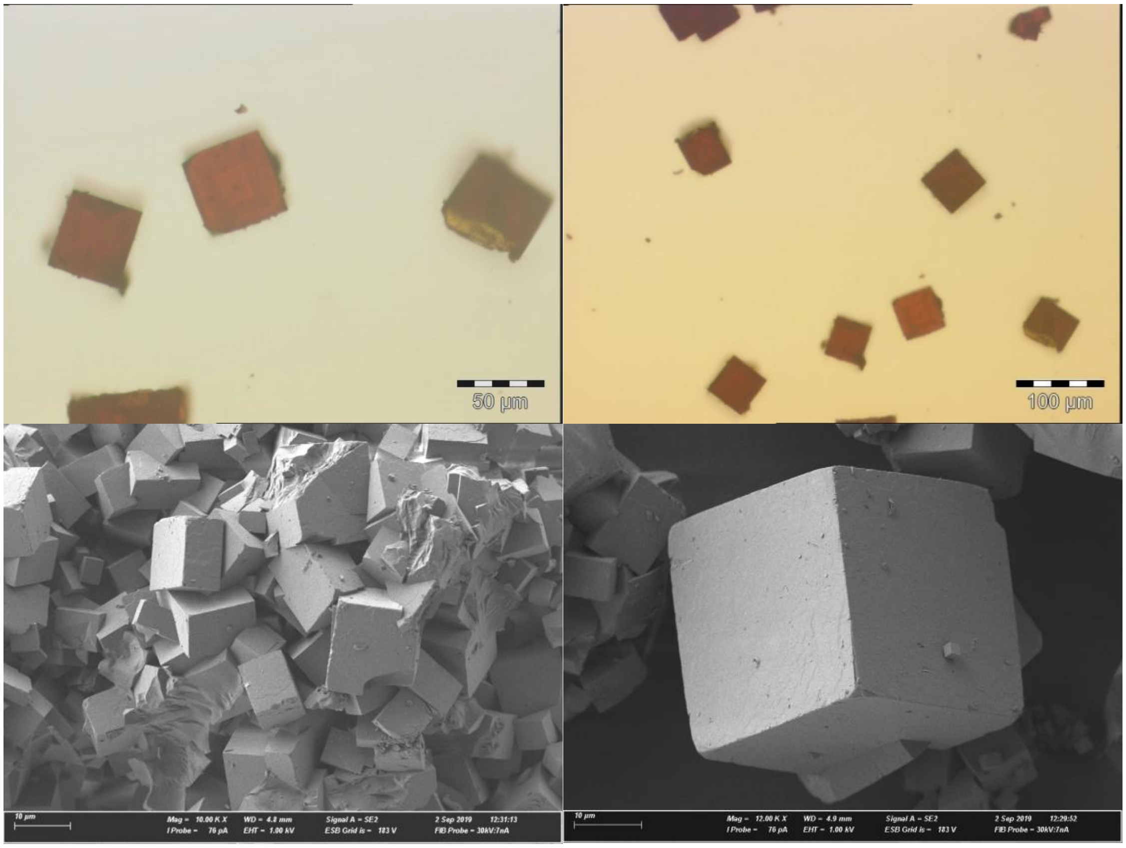

Figure S15. Optical (top) and SEM (bottom) micrographs from typical syntheses of **CFA-19-Tp**

PXRD pattern

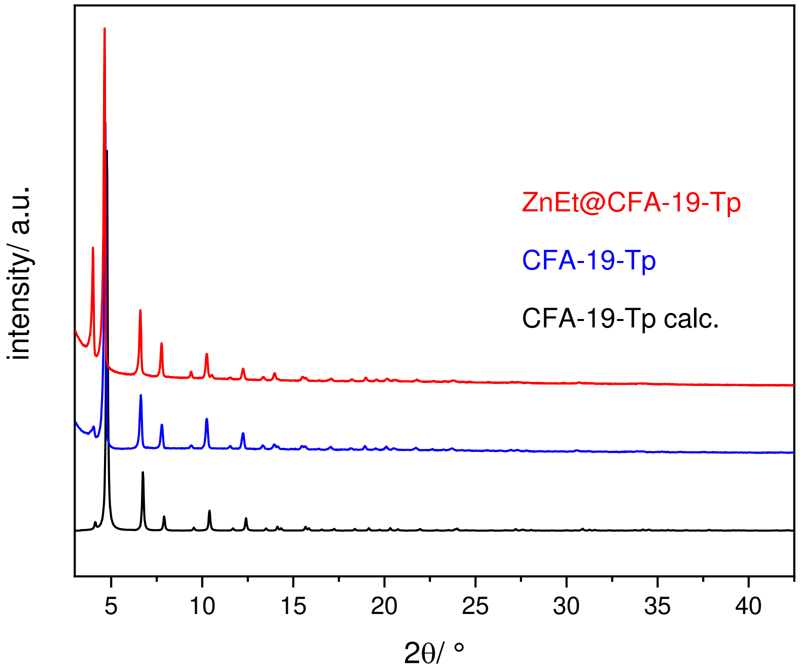

Figure S16. PXRD comparison between **CFA-19-Tp** and the quenched **ZnEt@CFA-19** sample

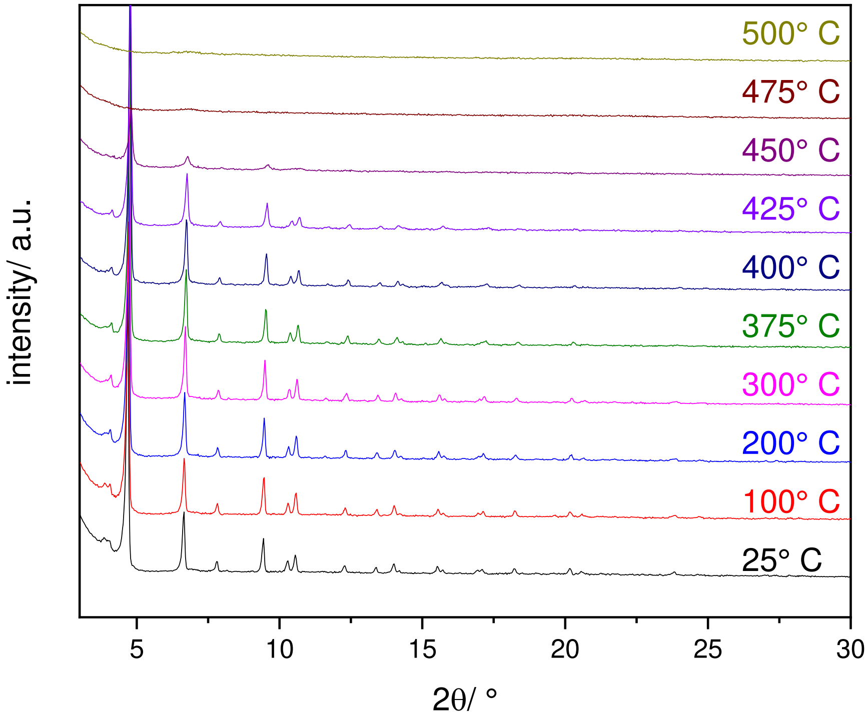

Figure S17. VT-PXRD pattern of **CFA-19**

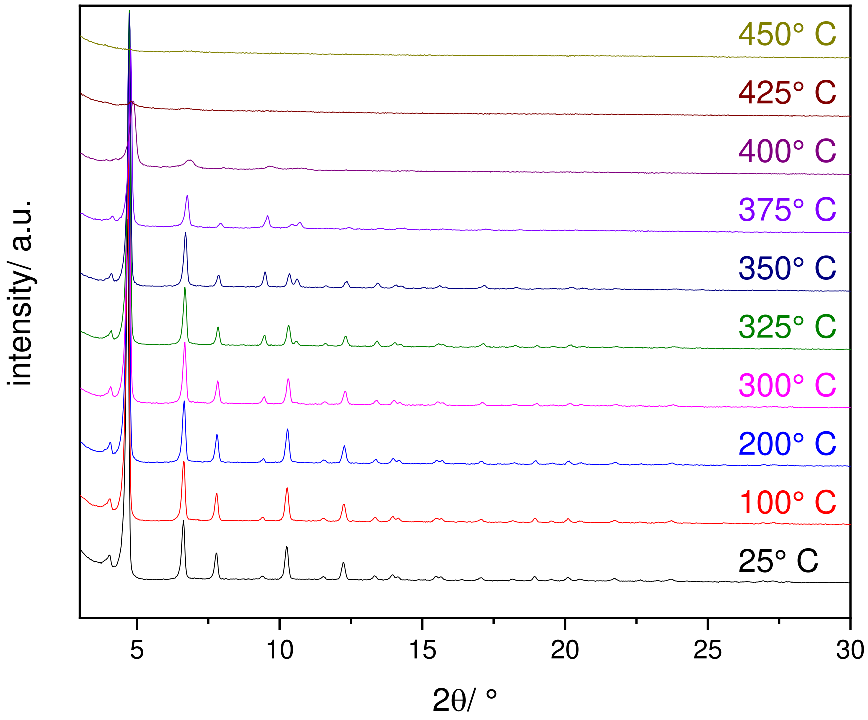

Figure S18. VT-PXRD pattern of **CFA-19-Tp**

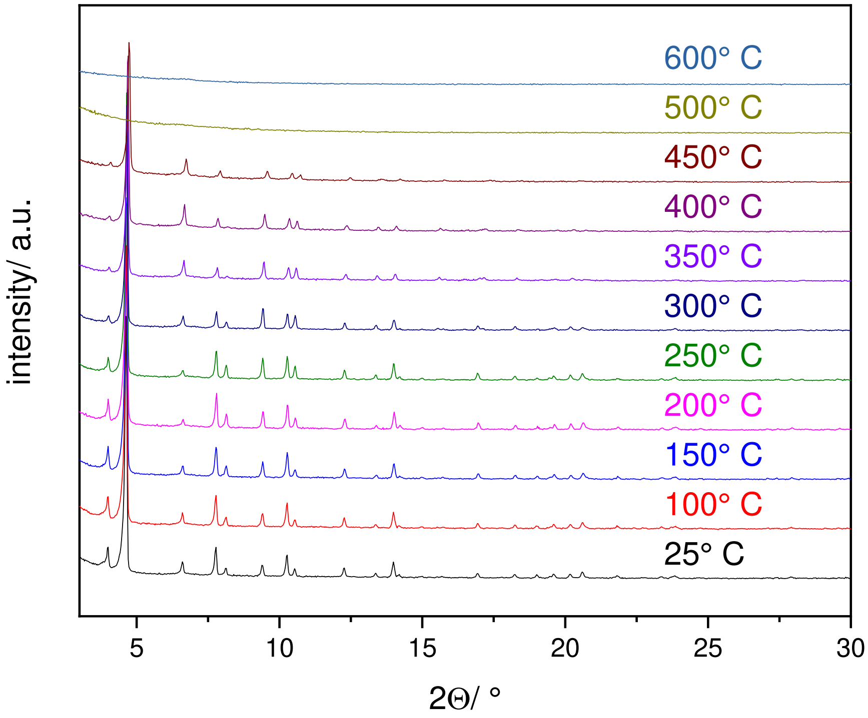

Figure S19. VT-PXRD pattern of **ReBr(CO)$_3$@CFA-19-Tp**

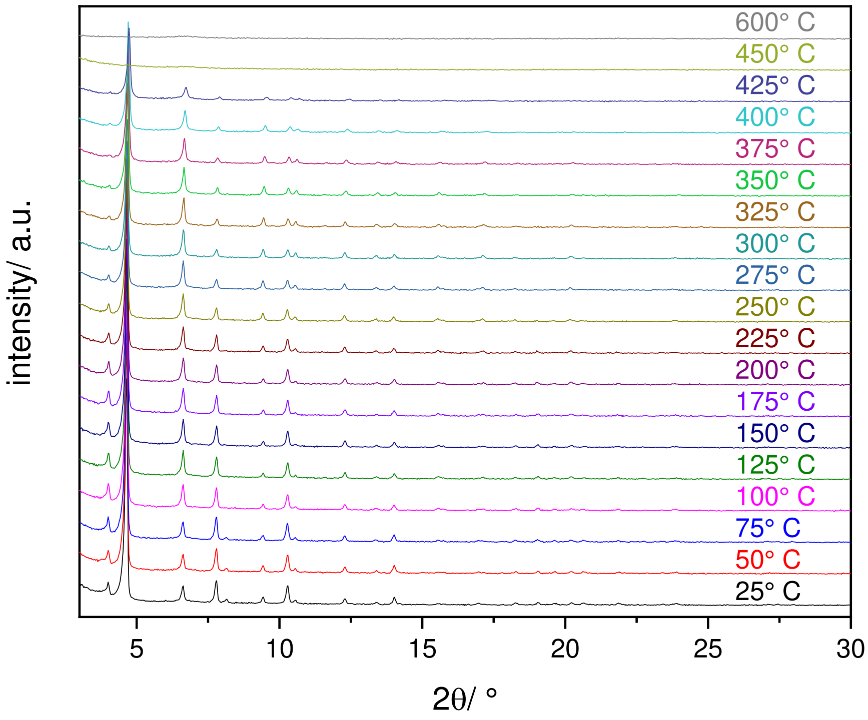

Figure S20. VT-PXRD pattern of **MnBr(CO)$_3$@CFA-19-Tp**

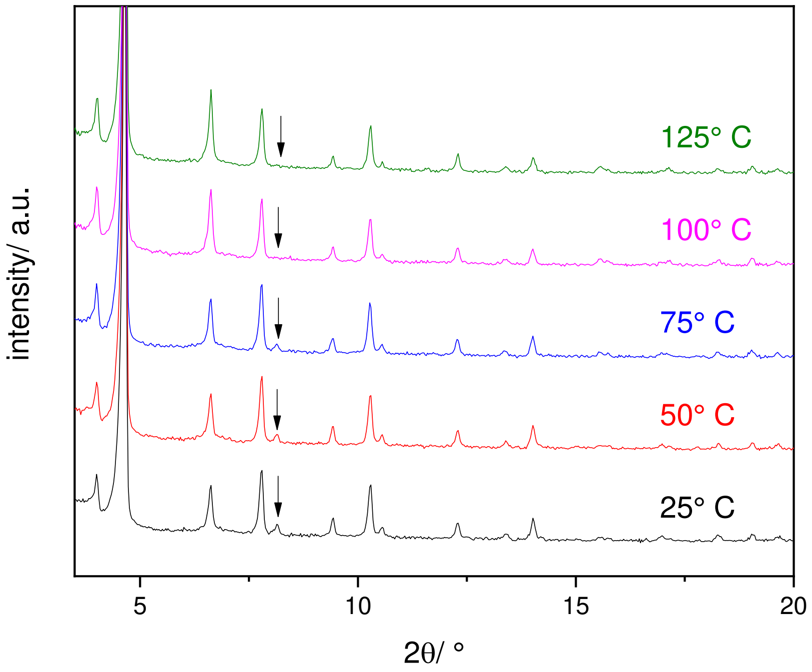

Figure S21. Enlarged VT-PXRD pattern of **MnBr(CO)$_3$@CFA-19-Tp** showing the loss of the reflex at 8.16° 2θ associated with the carbonyl groups of the MnBr(CO)$_3$ fragment

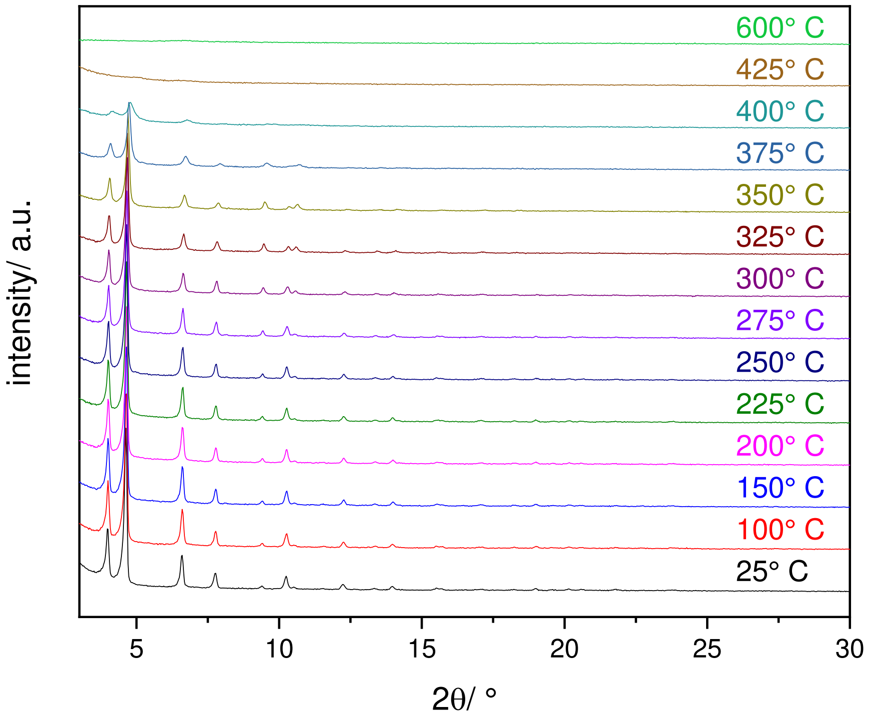

Figure S22. VT-PXRD pattern of the quenched **ZnEt@CFA-19-Tp**

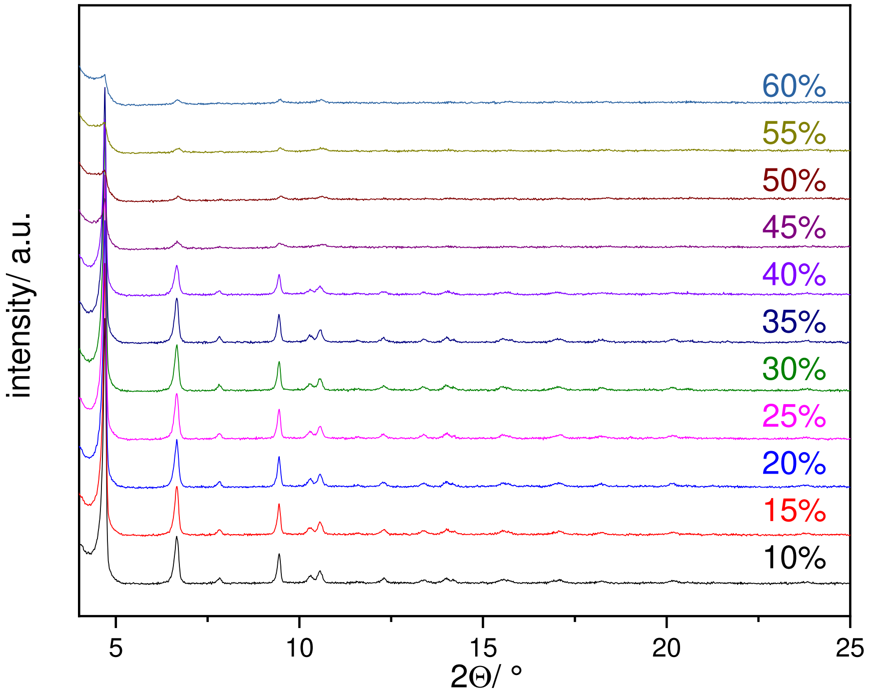

Figure S23. Variable humidity PXRD pattern of **CFA-19**

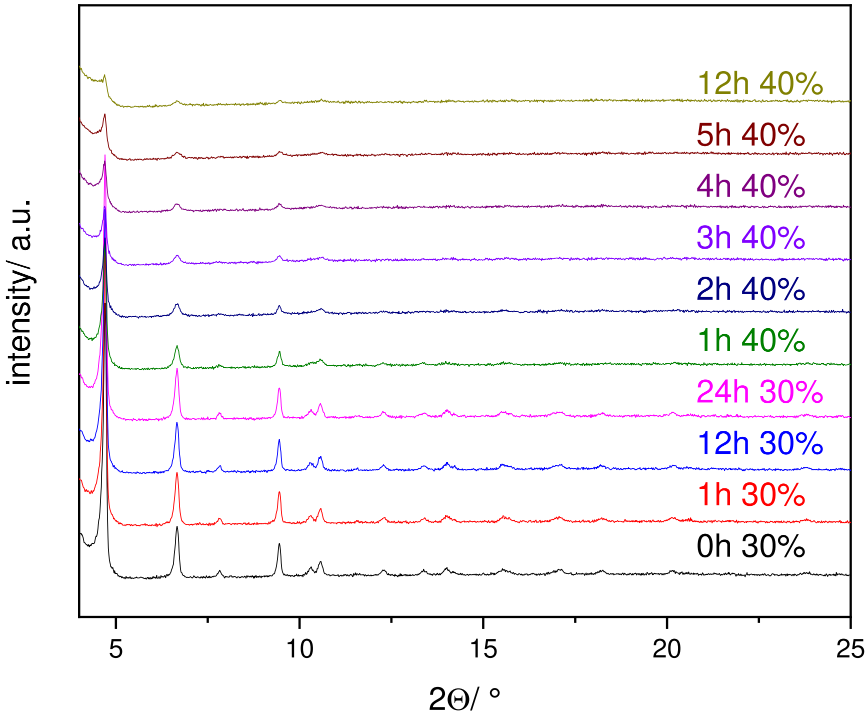

Figure S24. Long-term variable humidity PXRD pattern of **CFA-19**

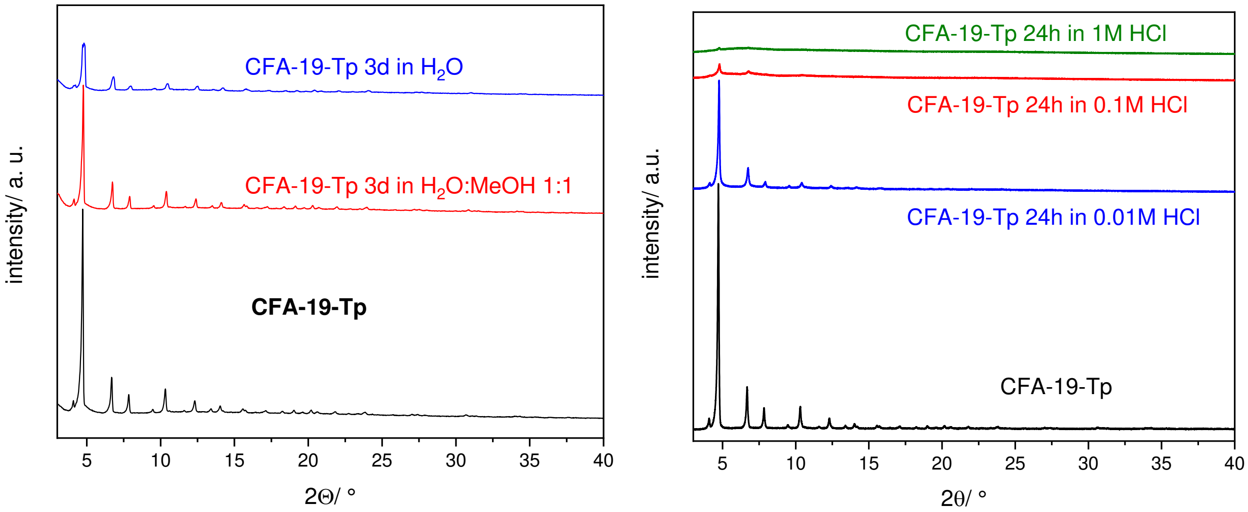

Figure S25. PXRD pattern of a 5 mg **CFA-19-Tp** sample soaked consecutively in 5 mL of a 1:1 water/MeOH mixture and pure water (left). PXRD pattern of 10 mg **CFA-19-Tp** samples stirred in 5 mL of 1M, 0.1M, and 0.01M HCl solutions.

TGA

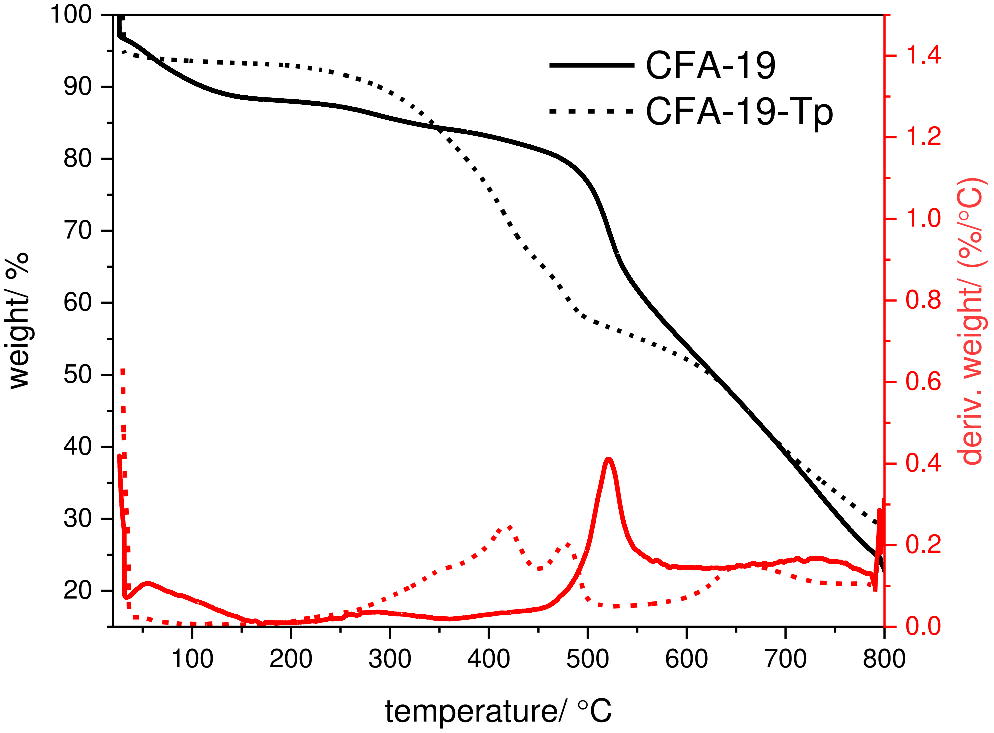

Figure S26. TGA curves of non-activated **CFA-19** and **CFA-19-Tp**

Argon Adsorption

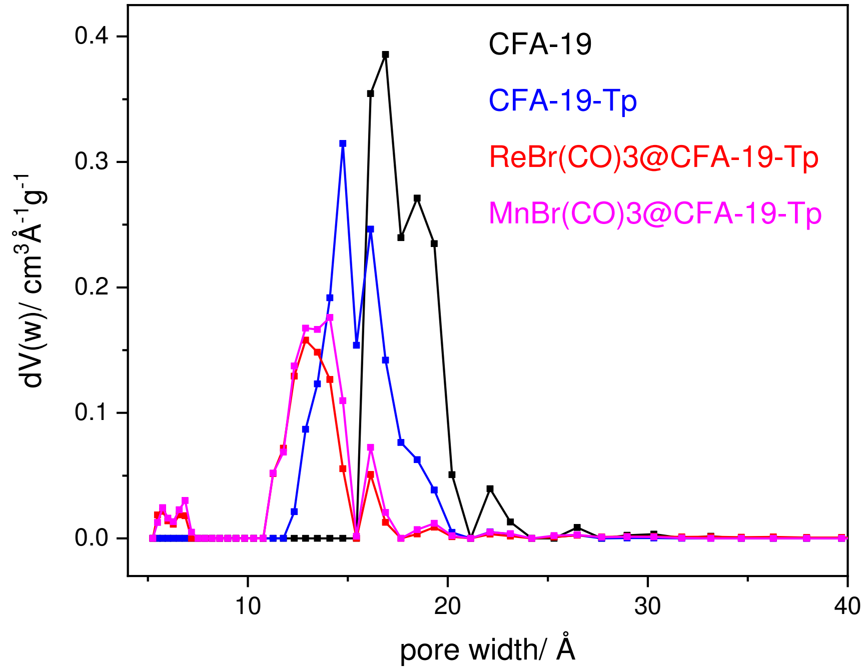

Figure S27. NLDFT pore size distribution maxima determined for **CFA-19**, **CFA-19-Tp**, **ReBr(Co)$_3$@CFA-19-Tp,** and **MnBr(Co)$_3$@CFA-19-Tp** are in fair agreement with the cavity diameters calculated with Platon for idealized structures (**CFA-19**: 17.2 and 22.5 Å; **CFA-19-Tp**: 13.2 and 18.7 Å; and **ReBr(Co)$_3$@CFA-19-Tp**: 7.7, 12.9 and 16.88 Å)

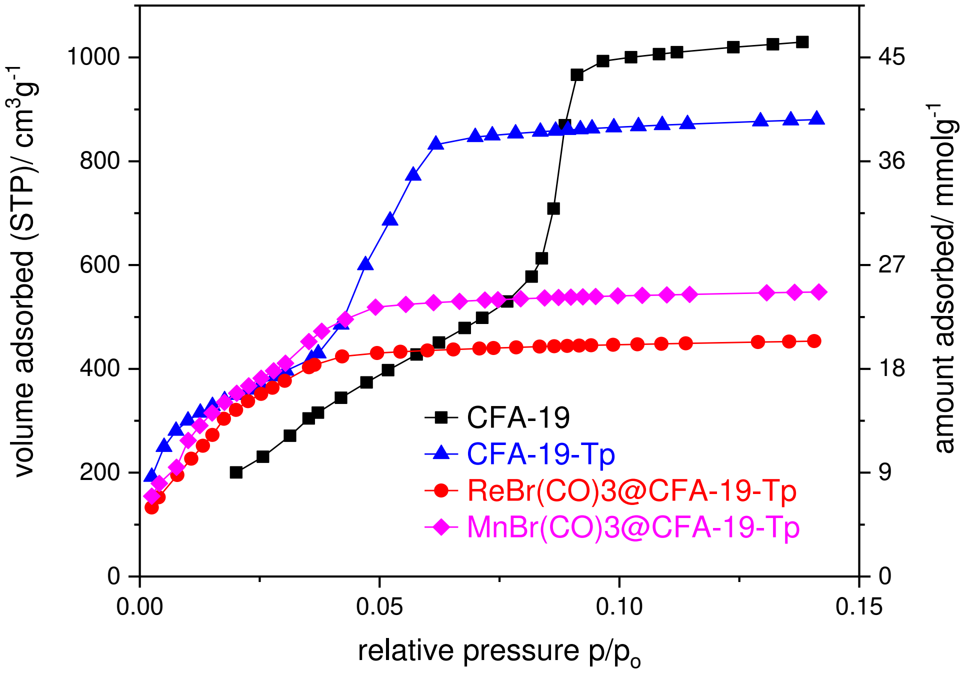

Figure S28. Argon adsorption isotherms with more data points between 0.002 and 0.14 p/p$_0$ for the determination of the BET surface areas for **CFA-19**, **CFA-19-Tp**, **ReBr(Co)$_3$@CFA-19-Tp,** and **MnBr(Co)$_3$@CFA-19-Tp**

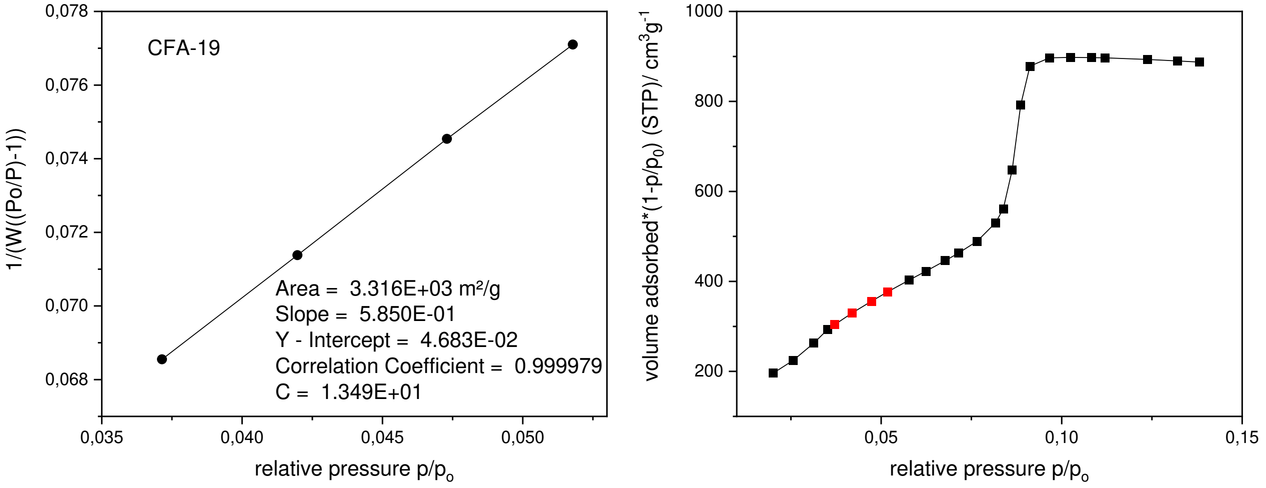

Figure S29. BET plot for **CFA-19** (3316 m²/g) (left) and V*(1-p/p$_0$) plots (right) showing that the selected BET points (red) are in the range suggested by the Rouquerol criteria

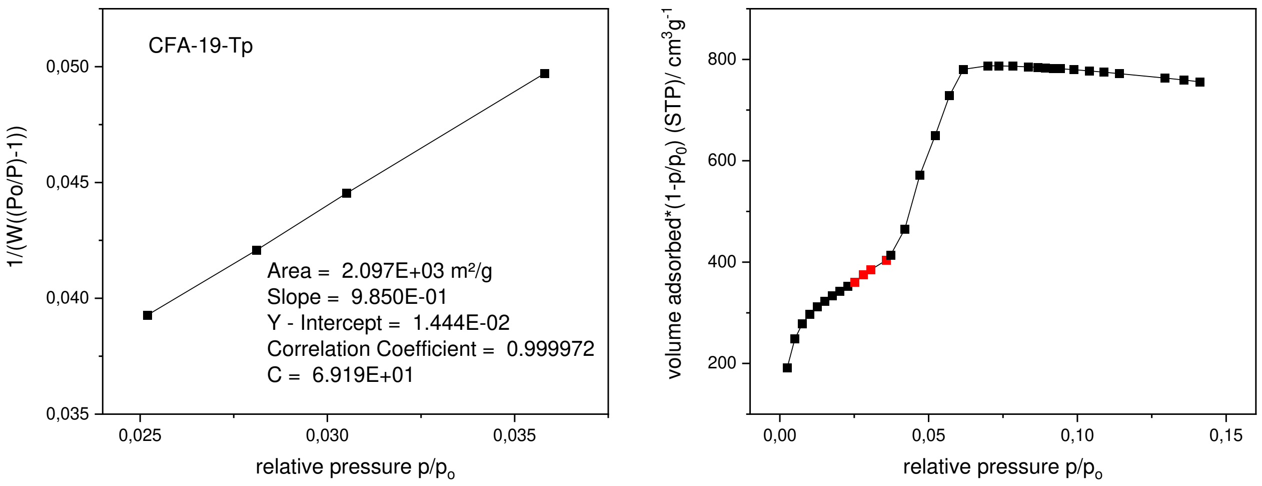

Figure S30. BET plot for **CFA-19-Tp** (2097 m²/g) and V*(1-p/p$_0$) plots (right) showing that the selected BET points (red) are in the range suggested by the Rouquerol criteria

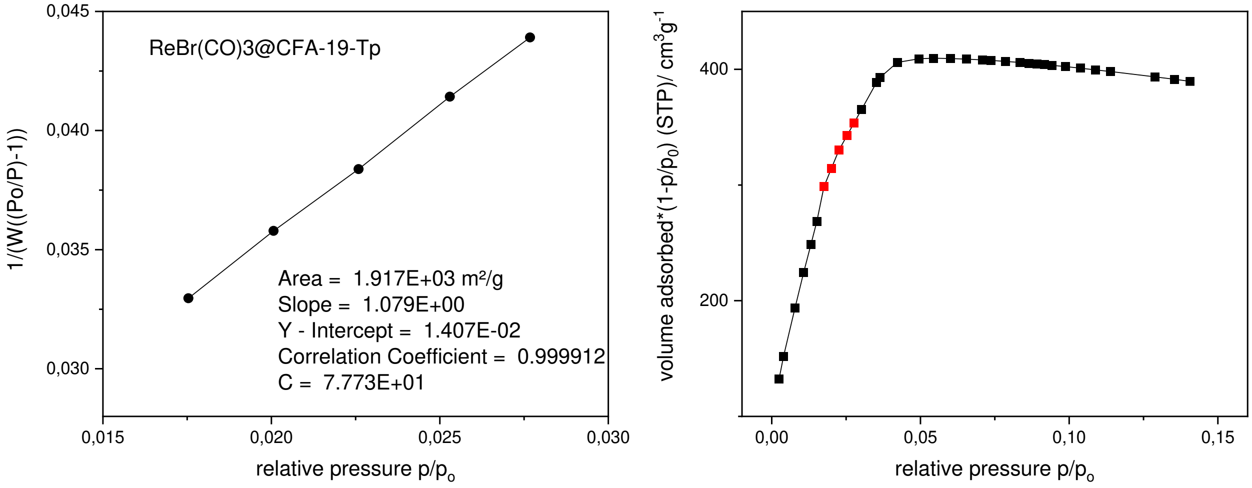

Figure S31. BET plot for **ReBr(CO)$_3$@CFA-19-Tp** (1917 m²/g) and V*(1-p/p$_0$) plots (right) showing that the selected BET points (red) are in the range suggested by the Rouquerol criteria

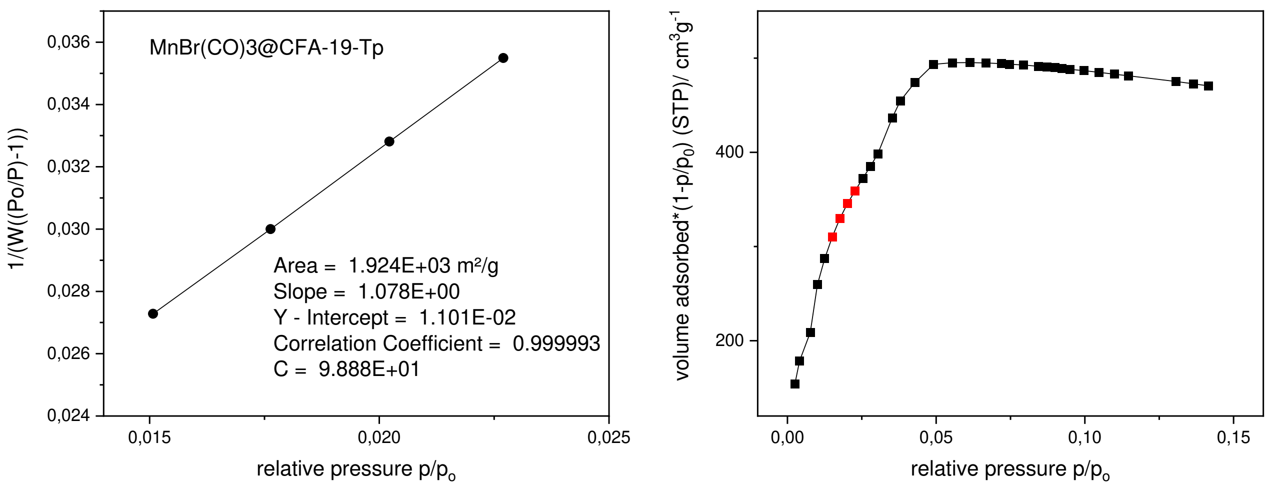

Figure S32. BET plot for **MnBr(CO)$_3$@CFA-19-Tp** (1924 m²/g) and V*(1-p/p$_0$) plots (right) showing that the selected BET points (red) are in the range suggested by the Rouquerol criteria

FT-IR spectra

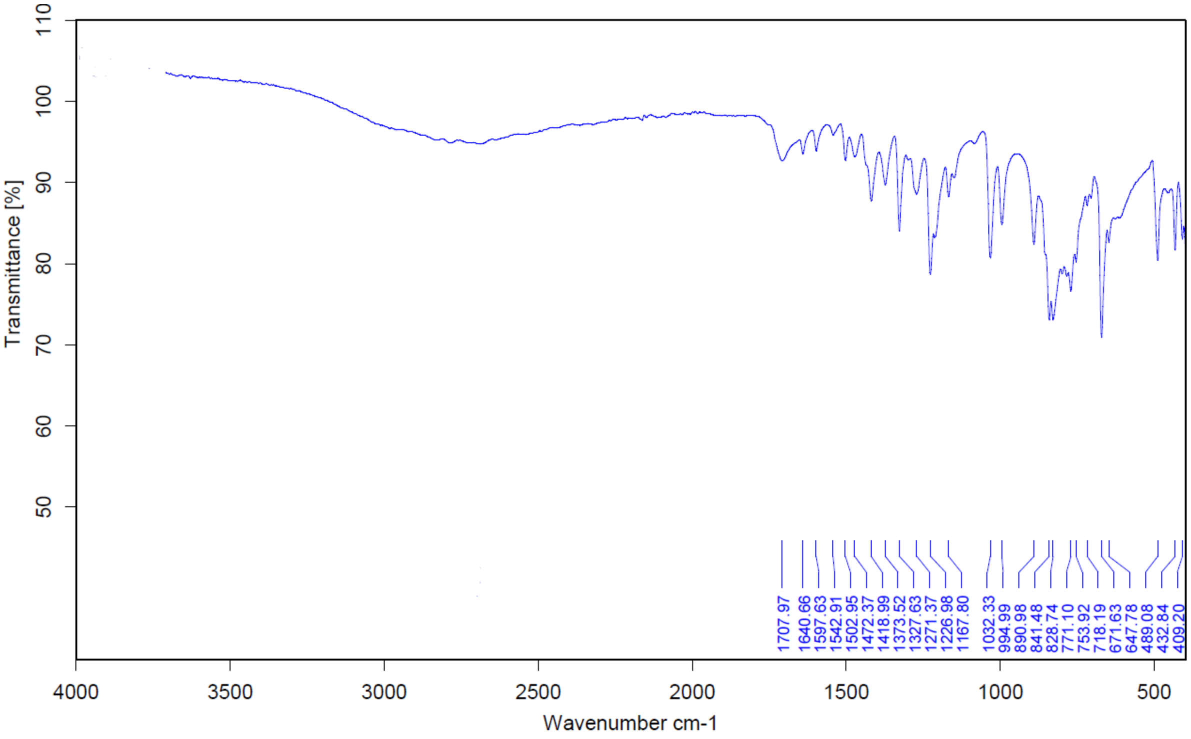

Figure S33. ATR FT-IR spectrum of 6-(trichloromethyl)-1,7-dihydroimidazo[4,5-*f*]benzotriazole 0.5 AcOH (**H_2-tcibt**)

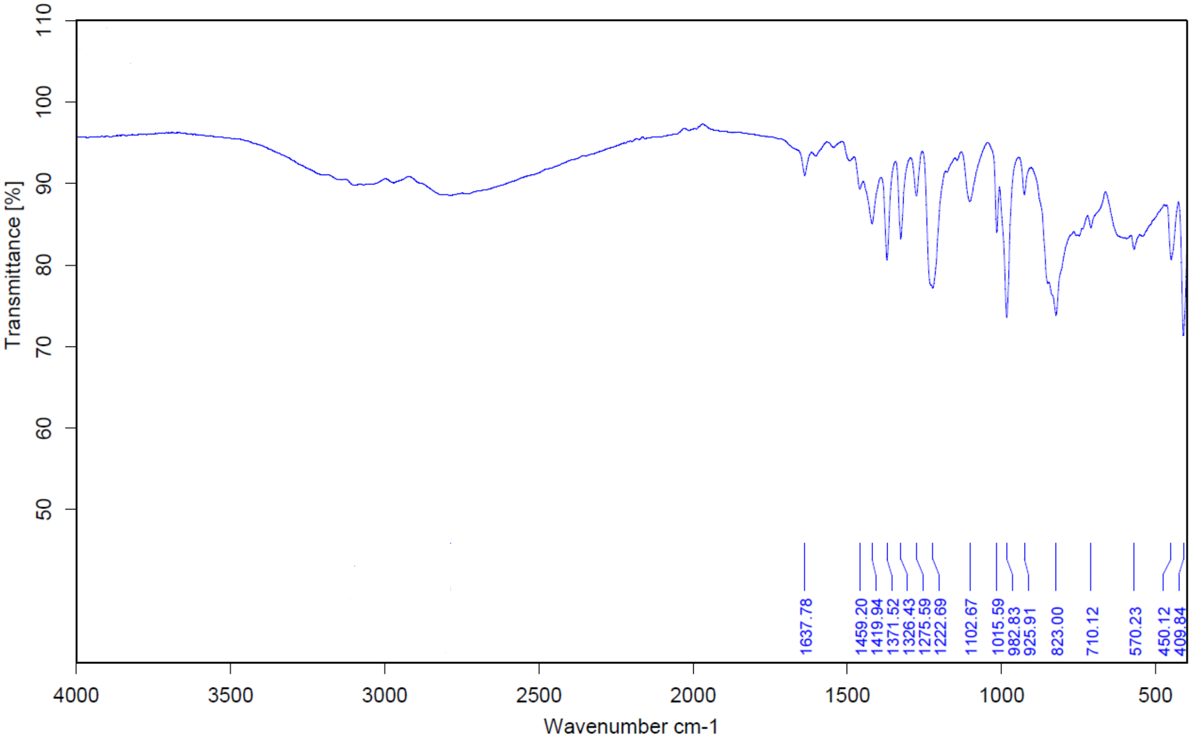

Figure S34. ATR FT-IR spectrum of 1,1',5,5'-tetrahydro-6,6'-biimidazo[4,5-*f*]benzotriazole (**H_4-bibt**)

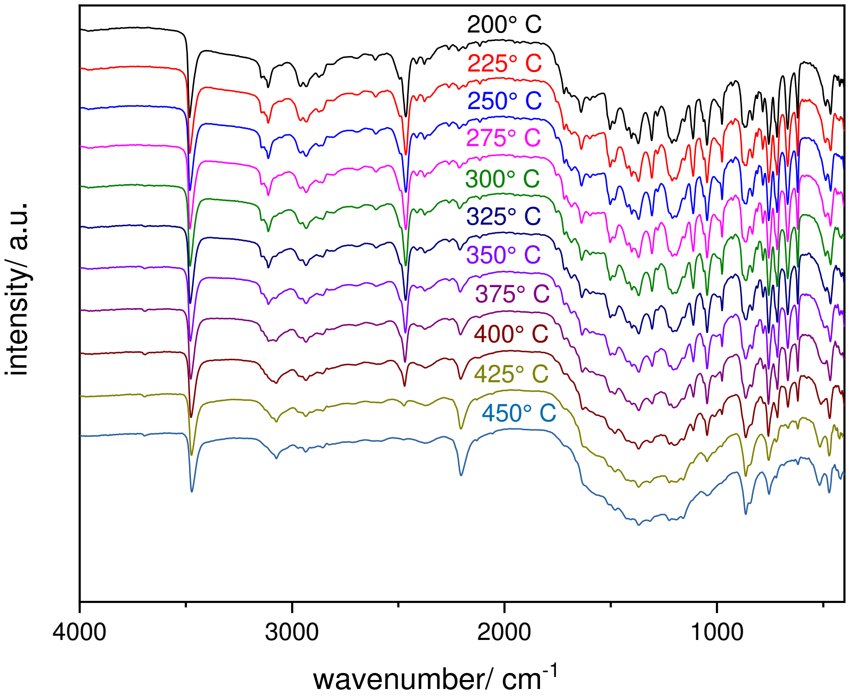

Figure S35. VT-DRIFT spectra showing the decomposition of **CFA-19-Tp** in an argon atmosphere

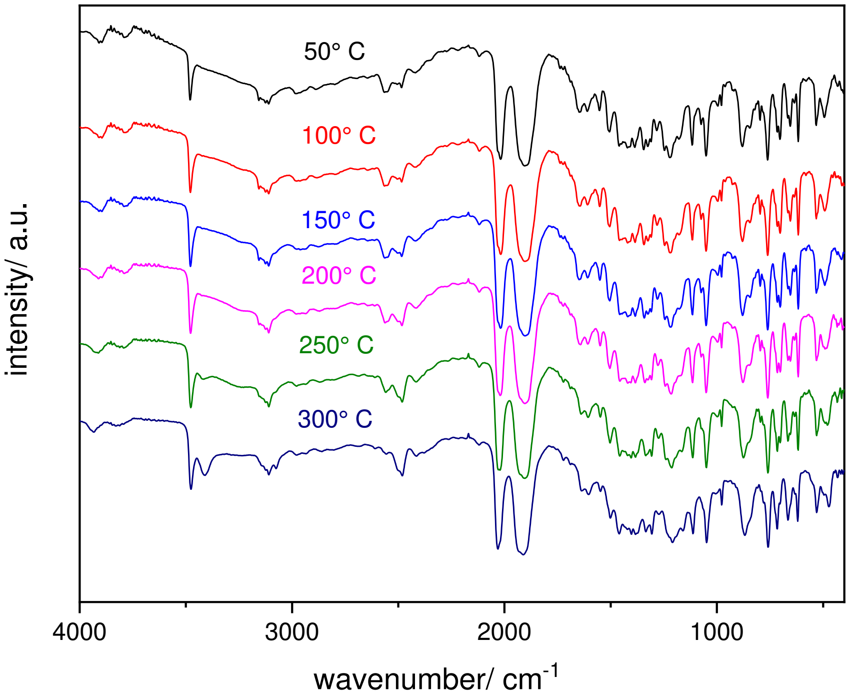

Figure S36. VT-DRIFT spectra of **ReBr(CO)$_3$@CFA-19-Tp** in a hydrogen atmosphere

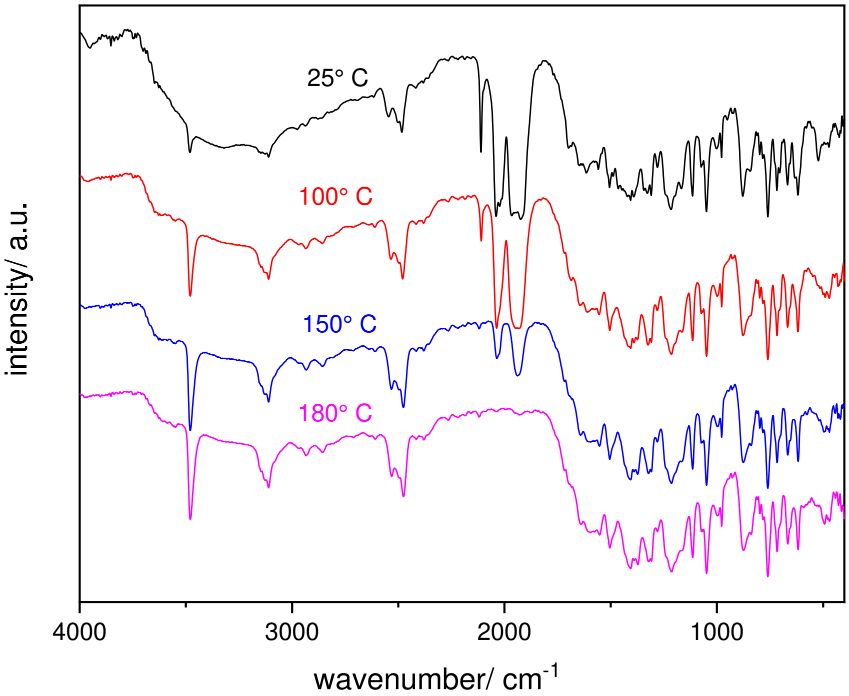

Figure S37. VT-DRIFT spectra showing the loss of CO for **MnBr(CO)$_3$@CFA-19-Tp** in a hydrogen atmosphere

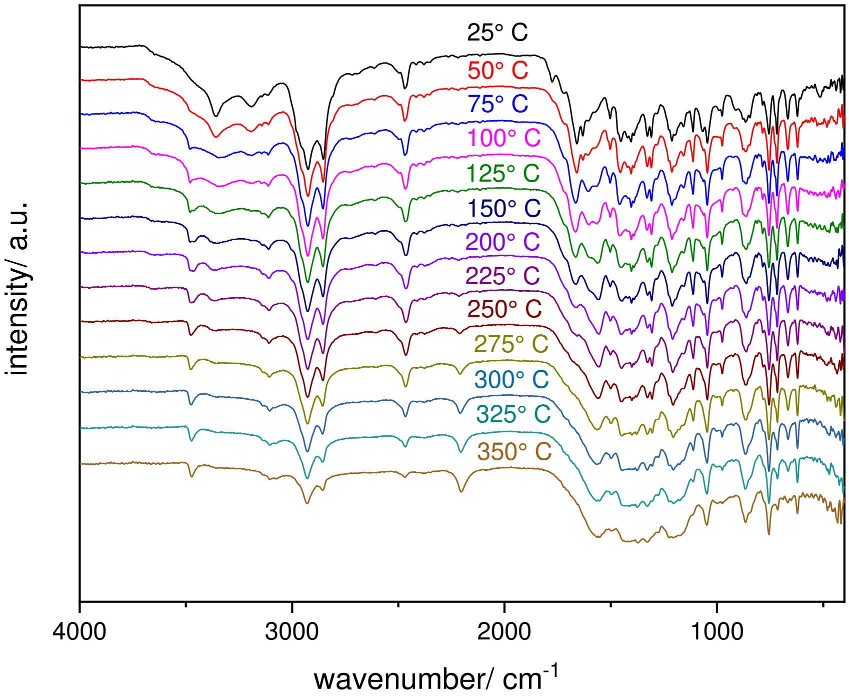

Figure S38. VT-DRIFT spectra showing the decomposition of **ZnEt@CFA-19-Tp** in an argon atmosphere

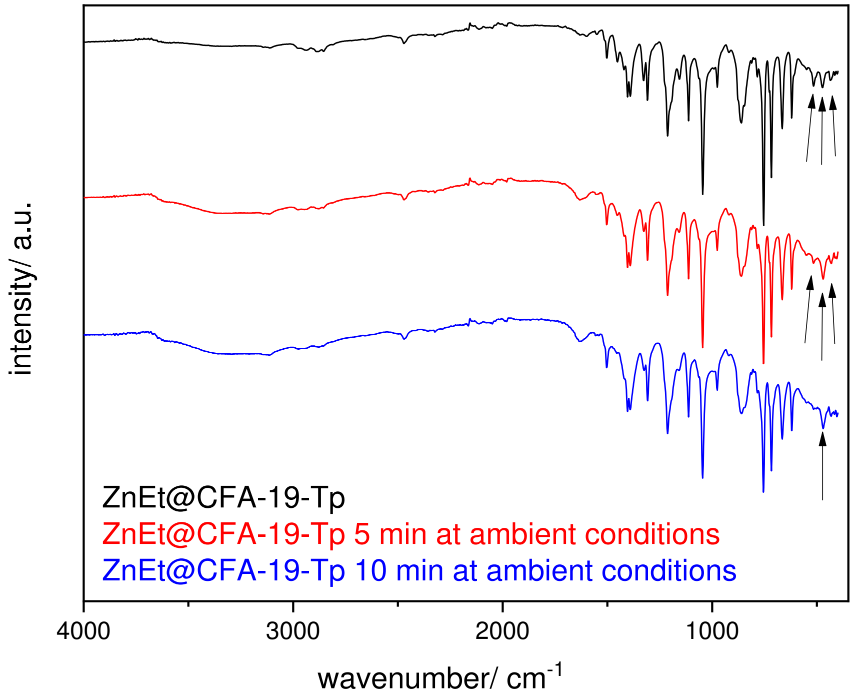

Figure S39. ATR FT-IR spectra of **ZnEt@CFA-19-Tp** directly (black), 5 min (red), and 10 min (blue) after exposure to ambient conditions for the measurement

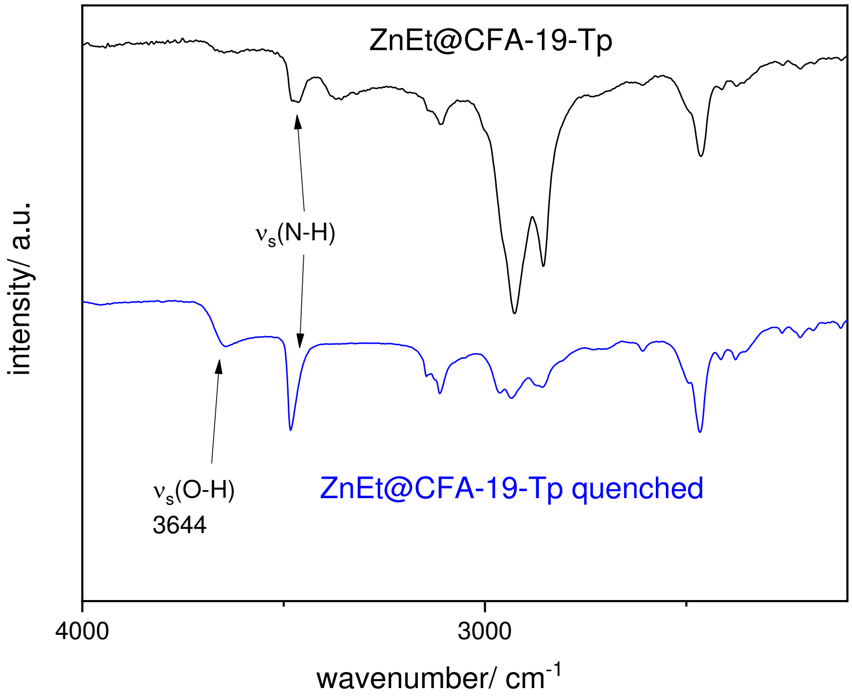

Figure S40. DRIFT spectra comparison for the **ZnEt@CFA-19-Tp** at 200 °C before (black) and after quenching (blue) with 5% H_2O in THF in an argon atmosphere showing the loss of the ethanido stretching vibrations, and a new band at 3644 cm^{-1} indicating O-H stretching vibration

UV-VIS spectra

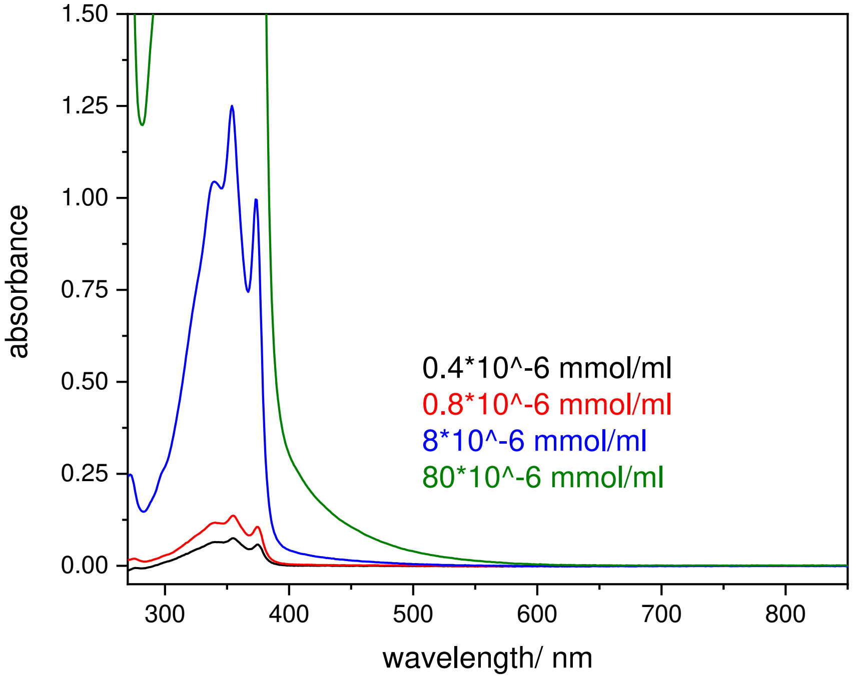

Figure S41. UV-Vis spectra for different 1,1',5,5'-tetrahydro-6,6'-biimidazo[4,5-*f*]benzotriazole (**H_4-bibt**) concentrations in DMF

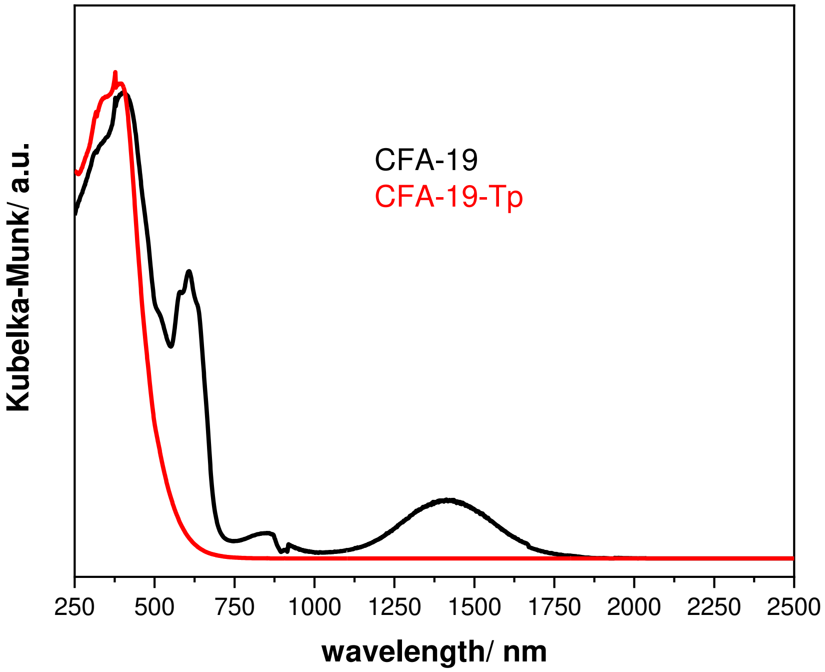

Figure S42. UV-Vis spectra of **CFA-19** (black) and **CFA-19-Tp** (red)

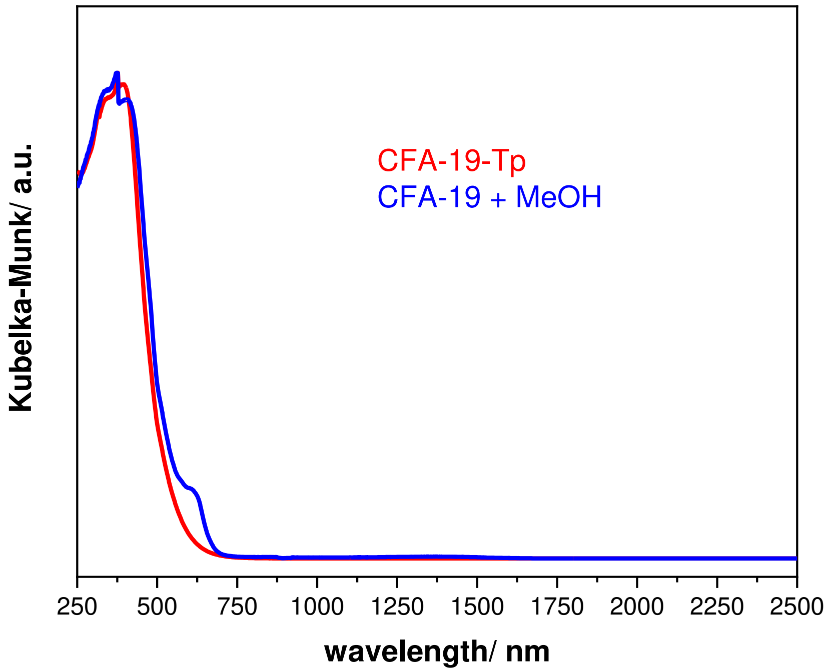

Figure S43. UV-Vis spectra of **CFA-19-Tp** (red) and **CFA-19** soaked with MeOH (blue) showing a nearly complete loss of absorption at 575 and 1350 nm

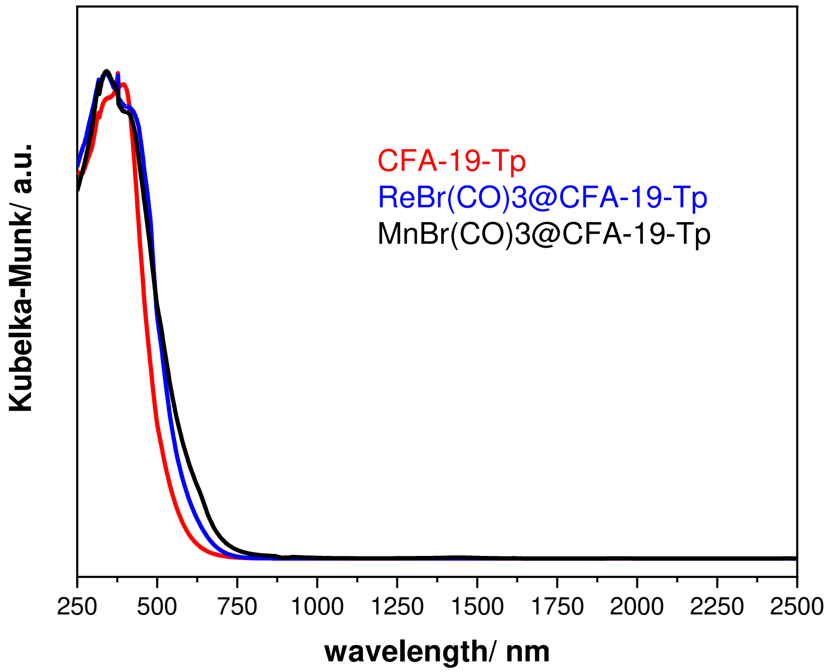

Figure S44. UV-Vis spectra of **CFA-19-Tp** (red), **ReBr(CO)$_3$@CFA-19-Tp** (blue), and **MnBr(CO)$_3$@CFA-19-Tp** (black)

Fluorescence spectra

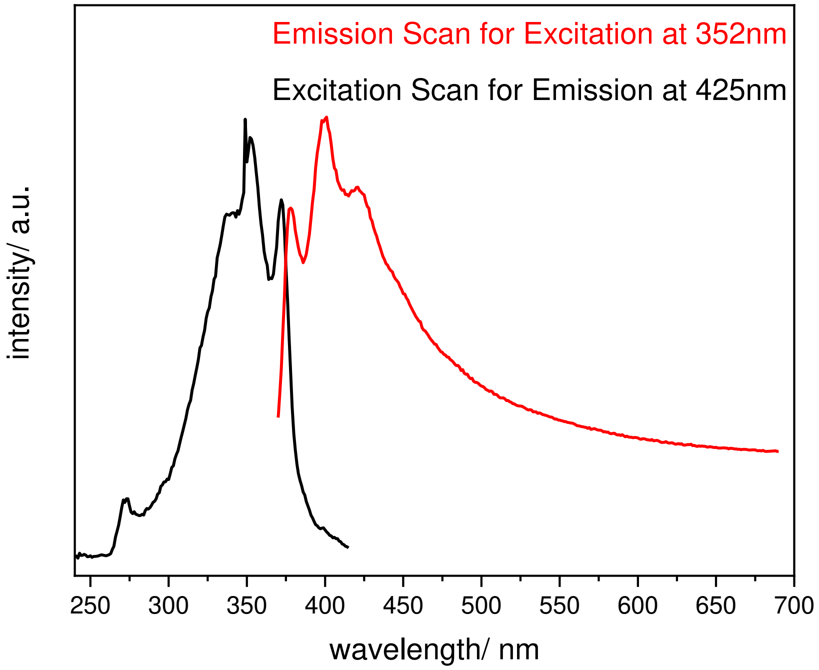

Figure S45. Fluorescence emission and excitation spectra of 1,1',5,5'-tetrahydro-6,6'-biimidazo[4,5-*f*]benzotriazole (**H_4-bibt**) with a concentration of 0.4*10^{-6} mmol*ml^{-1} in DMF

EDX spectra

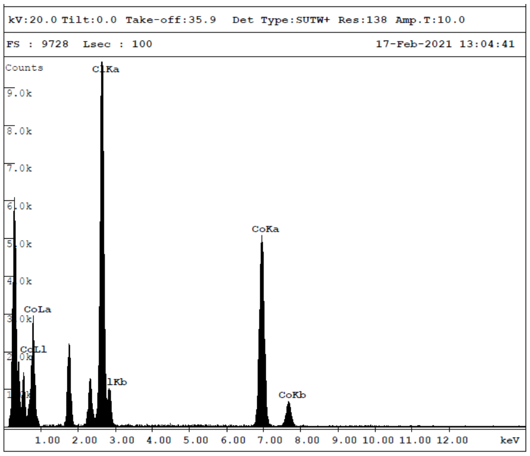

```
kV:20.0 Tilt:0.0 Take-off:35.9   Det Type:SUTW+ Res:138 Amp.T:10.0
FS : 9728  Lsec : 100                          17-Feb-2021 13:04:41
```

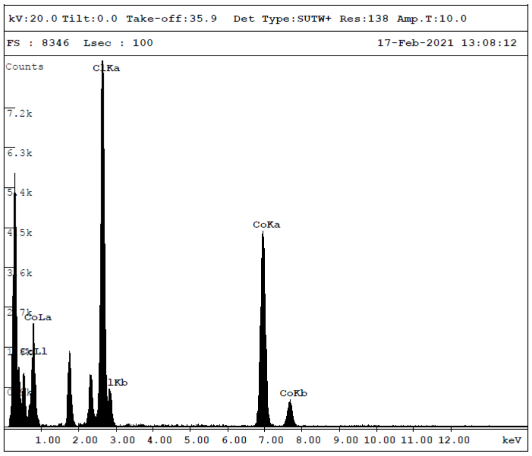

```
kV:20.0 Tilt:0.0 Take-off:35.9   Det Type:SUTW+ Res:138 Amp.T:10.0
FS : 8346  Lsec : 100                          17-Feb-2021 13:08:12
```

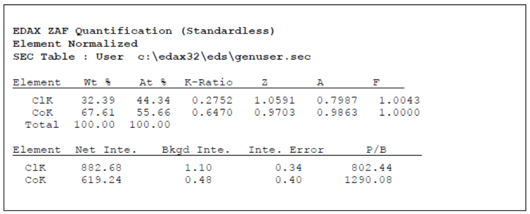

```
EDAX ZAF Quantification (Standardless)
Element Normalized
SEC Table : User  c:\edax32\eds\genuser.sec

Element   Wt %    At %   K-Ratio    Z       A       F
   ClK    32.39   44.34   0.2752  1.0591  0.7987  1.0043
   CoK    67.61   55.66   0.6470  0.9703  0.9863  1.0000
  Total  100.00  100.00

Element  Net Inte.    Bkgd Inte.   Inte. Error      P/B
  ClK     882.68         1.10         0.34        802.44
  CoK     619.24         0.48         0.40       1290.08
```

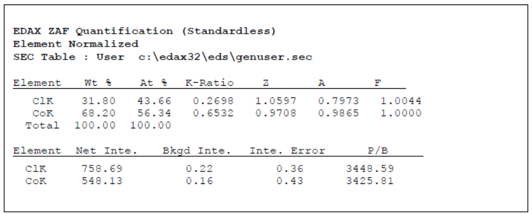

```
EDAX ZAF Quantification (Standardless)
Element Normalized
SEC Table : User  c:\edax32\eds\genuser.sec

Element   Wt %    At %   K-Ratio    Z       A       F
   ClK    31.80   43.66   0.2698  1.0597  0.7973  1.0044
   CoK    68.20   56.34   0.6532  0.9708  0.9865  1.0000
  Total  100.00  100.00

Element  Net Inte.    Bkgd Inte.   Inte. Error      P/B
  ClK     758.69         0.22         0.36       3448.59
  CoK     548.13         0.16         0.43       3425.81
```

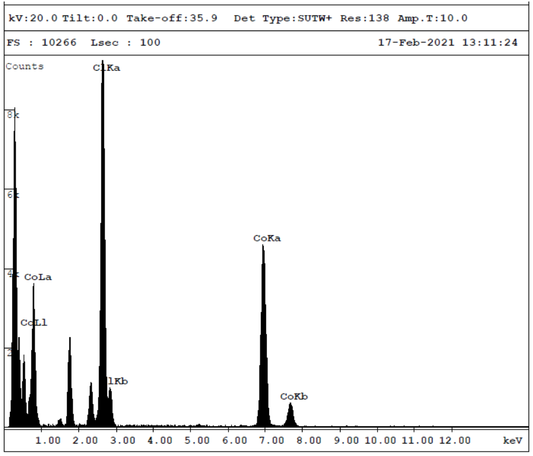

```
kV:20.0 Tilt:0.0 Take-off:35.9   Det Type:SUTW+ Res:138 Amp.T:10.0
FS : 10266  Lsec : 100                         17-Feb-2021 13:11:24
```

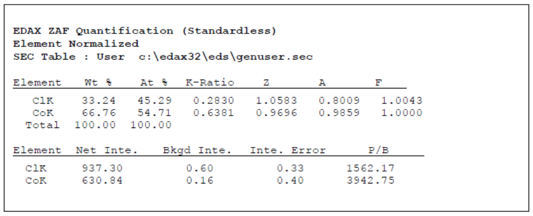

```
EDAX ZAF Quantification (Standardless)
Element Normalized
SEC Table : User  c:\edax32\eds\genuser.sec

Element   Wt %    At %   K-Ratio    Z       A       F
   ClK    33.24   45.29   0.2830  1.0583  0.8009  1.0043
   CoK    66.76   54.71   0.6381  0.9696  0.9859  1.0000
  Total  100.00  100.00

Element  Net Inte.    Bkgd Inte.   Inte. Error      P/B
  ClK     937.30         0.60         0.33       1562.17
  CoK     630.84         0.16         0.40       3942.75
```

Figure S46. EDX spectra of **CFA-19**

A 180

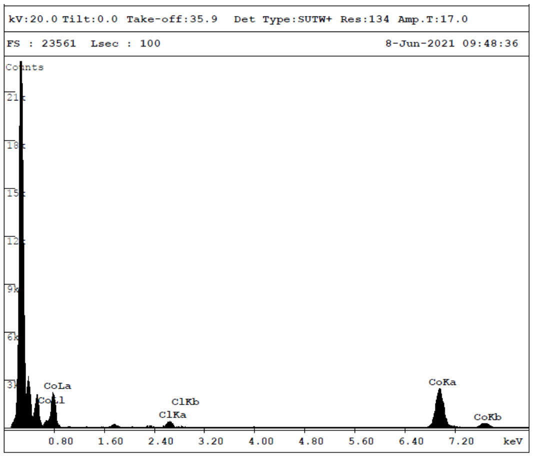

```
kV:20.0 Tilt:0.0  Take-off:35.9   Det Type:SUTW+  Res:134  Amp.T:17.0
FS : 23561   Lsec : 100                              8-Jun-2021 09:48:36
```

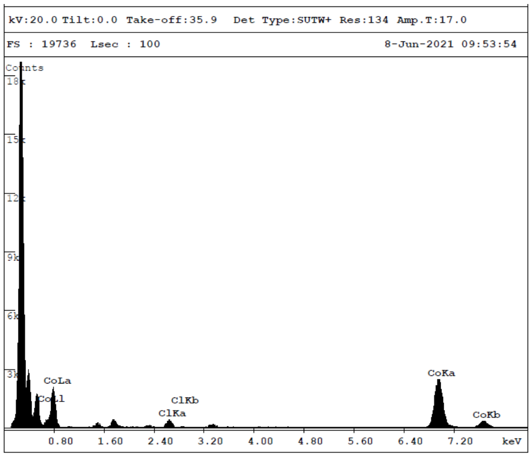

```
kV:20.0 Tilt:0.0  Take-off:35.9   Det Type:SUTW+  Res:134  Amp.T:17.0
FS : 19736   Lsec : 100                              8-Jun-2021 09:53:54
```

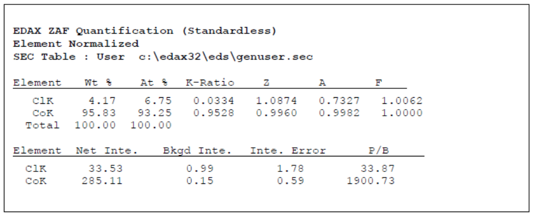

```
EDAX ZAF Quantification (Standardless)
Element Normalized
SEC Table : User  c:\edax32\eds\genuser.sec

Element    Wt %     At %   K-Ratio     Z         A        F
   ClK      4.17     6.75   0.0334   1.0874   0.7327   1.0062
   CoK     95.83    93.25   0.9528   0.9960   0.9982   1.0000
  Total   100.00   100.00

Element  Net Inte.    Bkgd Inte.   Inte. Error      P/B
  ClK      33.53         0.99         1.78         33.87
  CoK     285.11         0.15         0.59       1900.73
```

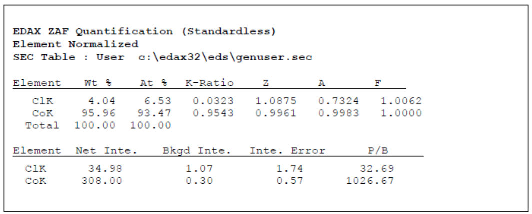

```
EDAX ZAF Quantification (Standardless)
Element Normalized
SEC Table : User  c:\edax32\eds\genuser.sec

Element    Wt %     At %   K-Ratio     Z         A        F
   ClK      4.04     6.53   0.0323   1.0875   0.7324   1.0062
   CoK     95.96    93.47   0.9543   0.9961   0.9983   1.0000
  Total   100.00   100.00

Element  Net Inte.    Bkgd Inte.   Inte. Error      P/B
  ClK      34.98         1.07         1.74         32.69
  CoK     308.00         0.30         0.57       1026.67
```

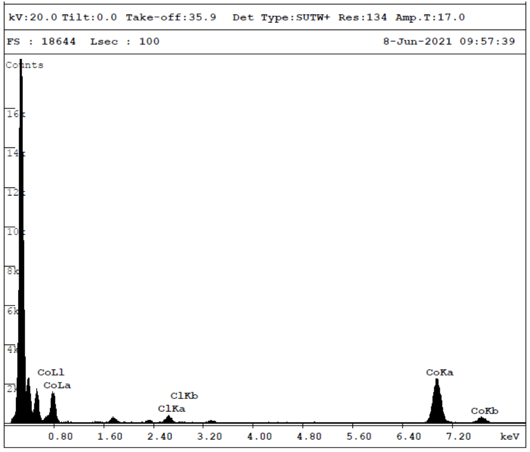

```
kV:20.0 Tilt:0.0  Take-off:35.9   Det Type:SUTW+  Res:134  Amp.T:17.0
FS : 18644   Lsec : 100                              8-Jun-2021 09:57:39
```

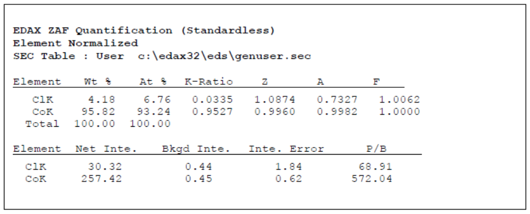

```
EDAX ZAF Quantification (Standardless)
Element Normalized
SEC Table : User  c:\edax32\eds\genuser.sec

Element    Wt %     At %   K-Ratio     Z         A        F
   ClK      4.18     6.76   0.0335   1.0874   0.7327   1.0062
   CoK     95.82    93.24   0.9527   0.9960   0.9982   1.0000
  Total   100.00   100.00

Element  Net Inte.    Bkgd Inte.   Inte. Error      P/B
  ClK      30.32         0.44         1.84         68.91
  CoK     257.42         0.45         0.62        572.04
```

Figure S47. EDX spectra of **CFA-19-Tp**

A 181

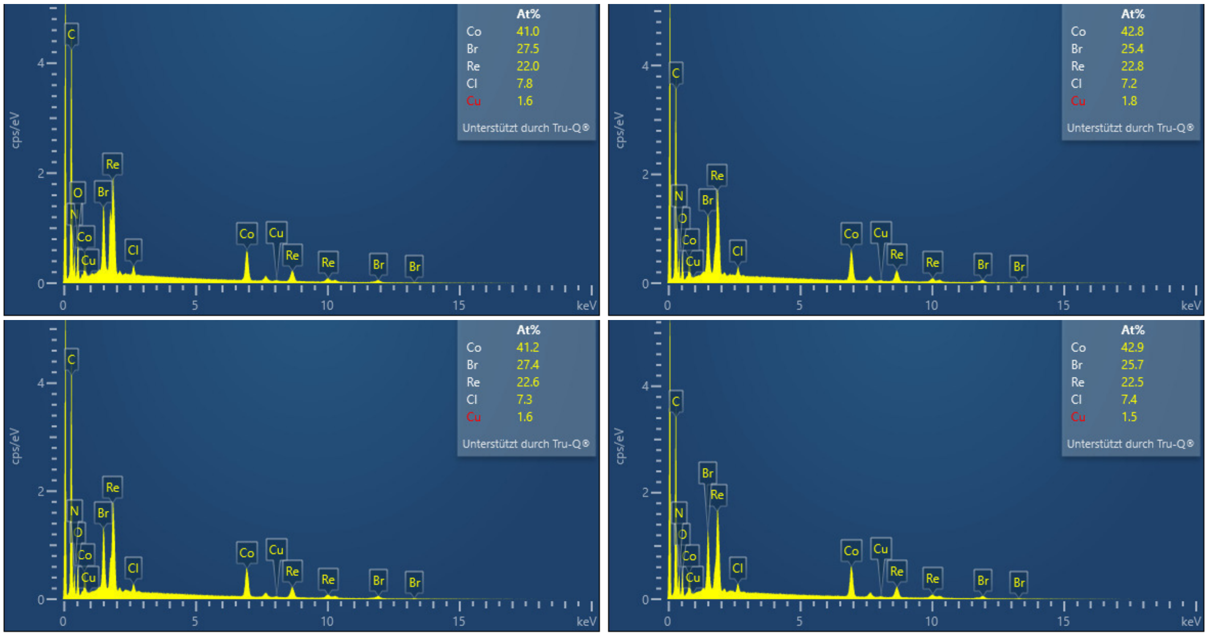

	At%
Co	41.0
Br	27.5
Re	22.0
Cl	7.8
Cu	1.6

Unterstützt durch Tru-Q®

	At%
Co	42.8
Br	25.4
Re	22.8
Cl	7.2
Cu	1.8

Unterstützt durch Tru-Q®

	At%
Co	41.2
Br	27.4
Re	22.6
Cl	7.3
Cu	1.6

Unterstützt durch Tru-Q®

	At%
Co	42.9
Br	25.7
Re	22.5
Cl	7.4
Cu	1.5

Unterstützt durch Tru-Q®

Figure S48. EDX spectra of **ReBr(CO)$_3$@CFA-19-Tp**

A 182

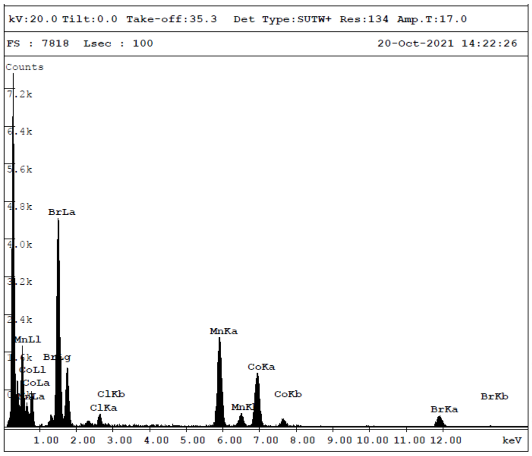

```
EDAX ZAF Quantification (Standardless)
Element Normalized
SEC Table : User  c:\edax32\eds\genuser.sec

Element    Wt %     At %   K-Ratio     Z        A        F
   ClK     1.87     3.38   0.0132   1.1202   0.6275   1.0037
   MnK    28.41    33.13   0.2954   1.0249   0.9707   1.0450
   CoK    26.68    29.00   0.2614   1.0261   0.9461   1.0094
   BrK    43.04    34.50   0.4048   0.9520   0.9879   1.0000
  Total  100.00   100.00

Element  Net Inte.    Bkgd Inte.   Inte. Error      P/B
  ClK      22.91         0.78          2.16         29.37
  MnK     210.87         0.30          0.69        702.90
  CoK     135.68         0.30          0.86        452.27
  BrK      32.04         0.19          1.78        168.63
```

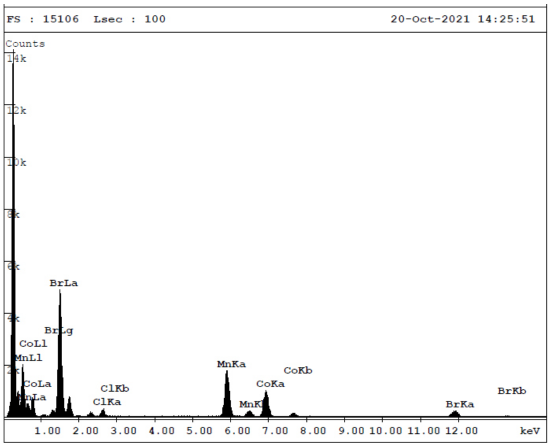

```
EDAX ZAF Quantification (Standardless)
Element Normalized
SEC Table : User  c:\edax32\eds\genuser.sec

Element    Wt %     At %   K-Ratio     Z        A        F
   ClK     2.23     4.04   0.0156   1.1214   0.6228   1.0035
   MnK    28.28    33.11   0.2926   1.0260   0.9693   1.0404
   CoK    24.18    26.39   0.2372   1.0273   0.9454   1.0100
   BrK    45.31    36.47   0.4270   0.9533   0.9885   1.0000
  Total  100.00   100.00

Element  Net Inte.    Bkgd Inte.   Inte. Error      P/B
  ClK      26.30         0.63          2.00         41.75
  MnK     202.79         0.36          0.70        563.31
  CoK     119.51         0.30          0.92        398.37
  BrK      32.81         0.76          1.79         43.17
```

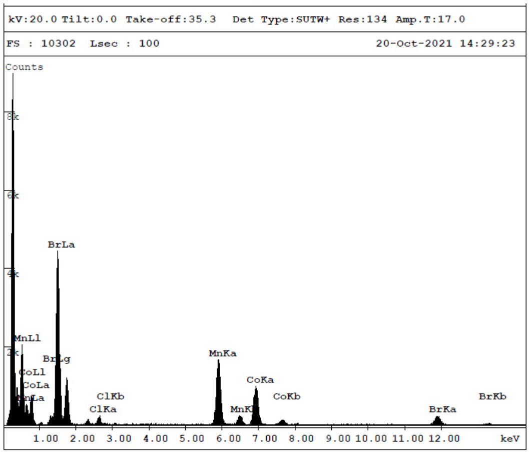

```
EDAX ZAF Quantification (Standardless)
Element Normalized
SEC Table : User  c:\edax32\eds\genuser.sec

Element    Wt %     At %   K-Ratio     Z        A        F
   ClK     1.55     2.83   0.0108   1.1227   0.6197   1.0035
   MnK    27.42    32.34   0.2846   1.0272   0.9694   1.0422
   CoK    25.04    27.53   0.2463   1.0285   0.9467   1.0102
   BrK    45.99    37.30   0.4340   0.9545   0.9885   1.0000
  Total  100.00   100.00

Element  Net Inte.    Bkgd Inte.   Inte. Error      P/B
  ClK      19.01         0.98          2.41         19.40
  MnK     205.50         0.14          0.70       1467.86
  CoK     129.28         0.15          0.88        861.87
  BrK      34.75         0.19          1.71        182.89
```

Figure S49. EDX spectra of **$MnBr(CO)_3$@CFA-19-Tp**

A 183

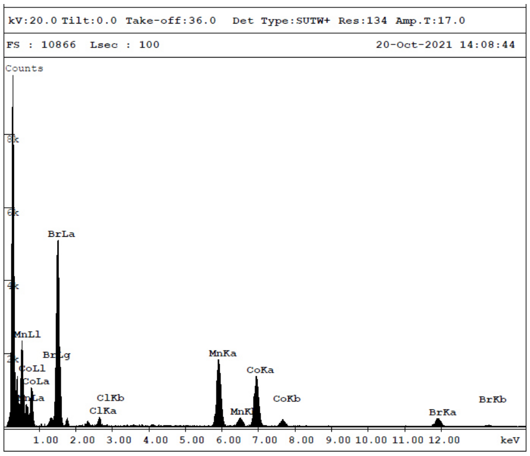

kV:20.0 Tilt:0.0 Take-off:36.0 Det Type:SUTW+ Res:134 Amp.T:17.0
FS : 10866 Lsec : 100 20-Oct-2021 14:08:44

```
EDAX ZAF Quantification (Standardless)
Element Normalized
SEC Table : User  c:\edax32\eds\genuser.sec

Element    Wt %    At %   K-Ratio     Z        A        F
   ClK     1.51    2.73   0.0108   1.1193   0.6342   1.0037
   MnK    26.57   30.95   0.2787   1.0241   0.9721   1.0534
   CoK    30.63   33.26   0.3011   1.0253   0.9500   1.0091
   BrK    41.29   33.06   0.3878   0.9511   0.9874   1.0000
  Total  100.00  100.00

Element  Net Inte.    Bkgd Inte.   Inte. Error      P/B
  ClK      20.85         0.22          2.21        94.77
  MnK     221.75         0.42          0.67       527.98
  CoK     174.13         0.45          0.76       386.96
  BrK      34.20         0.19          1.72       180.00
```

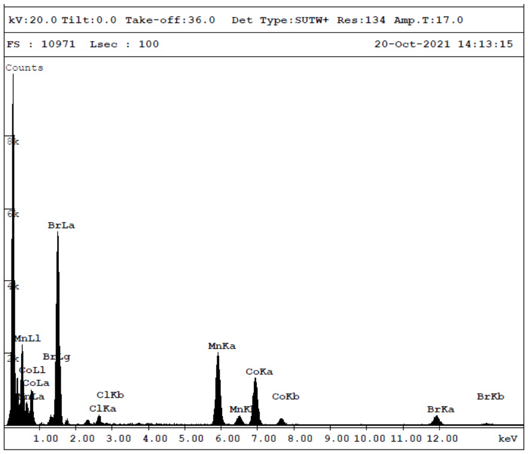

kV:20.0 Tilt:0.0 Take-off:36.0 Det Type:SUTW+ Res:134 Amp.T:17.0
FS : 10971 Lsec : 100 20-Oct-2021 14:13:15

```
EDAX ZAF Quantification (Standardless)
Element Normalized
SEC Table : User  c:\edax32\eds\genuser.sec

Element    Wt %    At %   K-Ratio     Z        A        F
   ClK     1.66    3.02   0.0118   1.1210   0.6288   1.0036
   MnK    27.09   31.74   0.2824   1.0256   0.9708   1.0470
   CoK    27.41   29.93   0.2696   1.0269   0.9485   1.0098
   BrK    43.84   35.31   0.4127   0.9528   0.9881   1.0000
  Total  100.00  100.00

Element  Net Inte.    Bkgd Inte.   Inte. Error      P/B
  ClK      24.37         0.19          2.04       128.26
  MnK     240.10         0.28          0.65       857.50
  CoK     166.57         0.30          0.78       555.23
  BrK      38.89         0.19          1.61       204.68
```

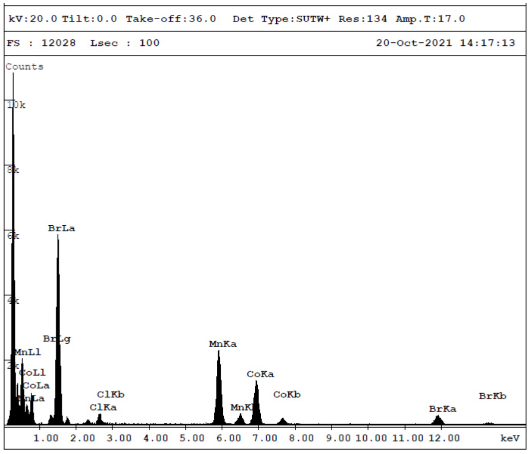

kV:20.0 Tilt:0.0 Take-off:36.0 Det Type:SUTW+ Res:134 Amp.T:17.0
FS : 12028 Lsec : 100 20-Oct-2021 14:17:13

```
EDAX ZAF Quantification (Standardless)
Element Normalized
SEC Table : User  c:\edax32\eds\genuser.sec

Element    Wt %    At %   K-Ratio     Z        A        F
   ClK     1.93    3.50   0.0137   1.1207   0.6296   1.0037
   MnK    28.30   33.06   0.2939   1.0254   0.9707   1.0437
   CoK    25.85   28.15   0.2537   1.0267   0.9468   1.0097
   BrK    43.93   35.29   0.4135   0.9526   0.9883   1.0000
  Total  100.00  100.00

Element  Net Inte.    Bkgd Inte.   Inte. Error      P/B
  ClK      30.40         0.22          1.83       138.18
  MnK     268.33         0.42          0.61       638.88
  CoK     168.32         0.45          0.77       374.04
  BrK      41.84         0.55          1.57        76.07
```

Figure S50. EDX spectra of **$MnBr(CO)_3$@CFA-19-Tp** after vacuum treatment at 200 °C for 1 h

A 184

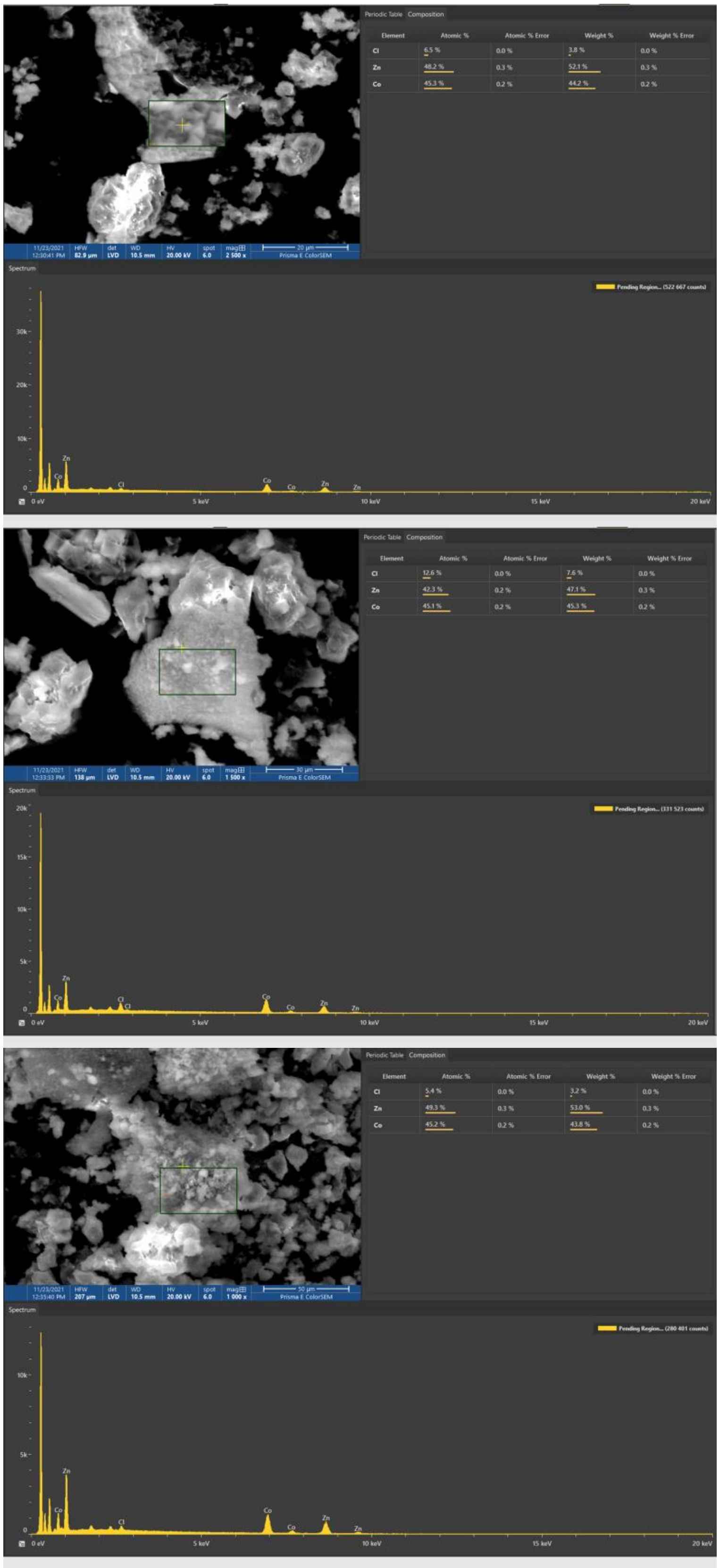

Element	Atomic %	Atomic % Error	Weight %	Weight % Error
Cl	6.5 %	0.0 %	3.8 %	0.0 %
Zn	48.2 %	0.3 %	52.1 %	0.3 %
Co	45.3 %	0.2 %	44.2 %	0.2 %

Element	Atomic %	Atomic % Error	Weight %	Weight % Error
Cl	12.6 %	0.0 %	7.6 %	0.0 %
Zn	42.3 %	0.2 %	47.1 %	0.3 %
Co	45.1 %	0.2 %	45.3 %	0.2 %

Element	Atomic %	Atomic % Error	Weight %	Weight % Error
Cl	5.4 %	0.0 %	3.2 %	0.0 %
Zn	49.3 %	0.3 %	53.0 %	0.3 %
Co	45.2 %	0.2 %	43.8 %	0.2 %

Figure S51. EDX spectra of **ZnEt@CFA-19-Tp**

Sample photographs

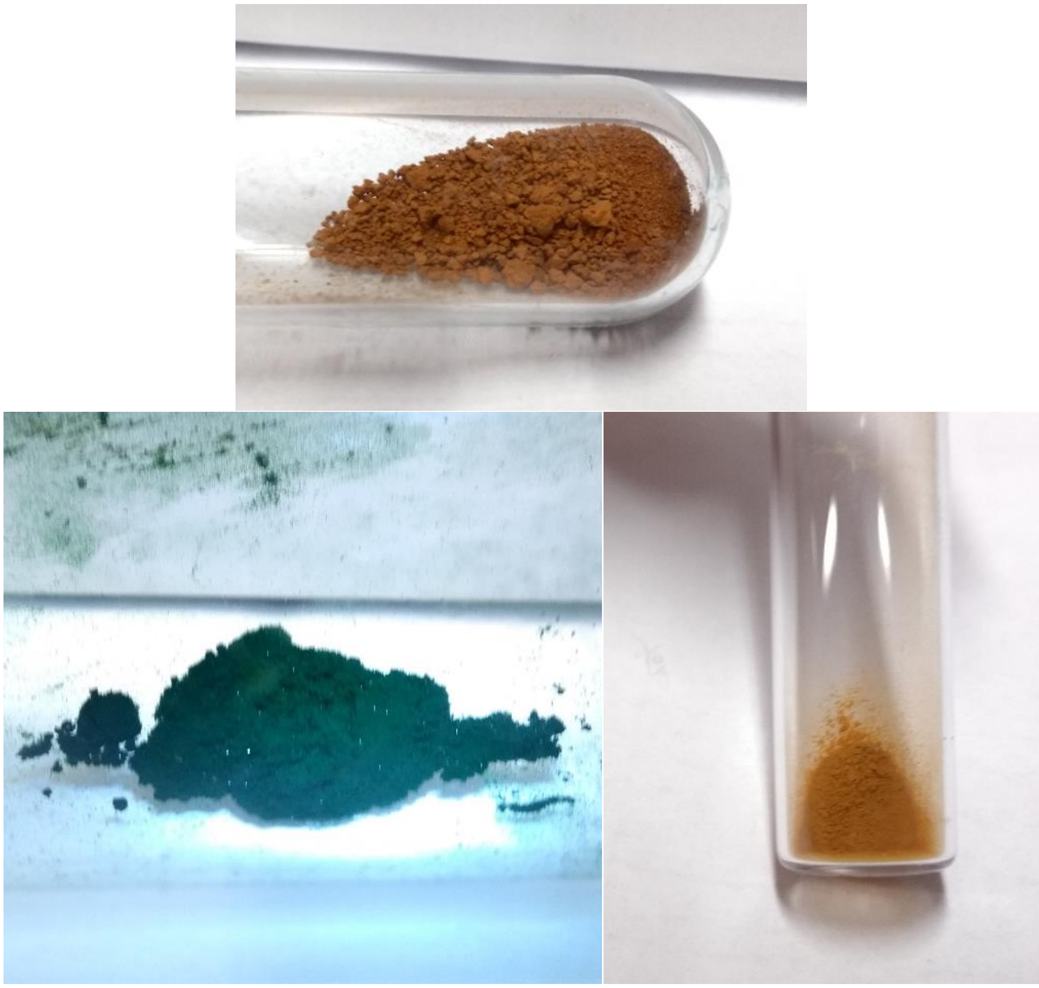

Figure S52. Photographs of **H_4-bibt** (top**), CFA-19** (bottom left**),** and **CFA-19-Tp** (bottom right**)**

Figure S53. Photographs of **CFA-19** (left) in a MeOH atmosphere (middle**)** and after a few seconds of vacuum drying (right) showing the intense and rapid color change from green to golden to green due to the change in the coordination environment of the peripheral cobalt ions from tetrahedral to octahedral to tetrahedral

References

(1) Werner, T. W.; Reschke, S.; Bunzen, H.; Nidda, H.-A. K. von; Deisenhofer, J.; Loidl, A.; Volkmer, D. $Co_5Tp^*_4(Me_2bta)_6$: A Highly Symmetrical Pentanuclear Kuratowski Complex Featuring Tris(pyrazolyl)borate and Benzotriazolate Ligands. *Inorg. chem.* **2016**, *55* (3), 1053–1060.

(2) Denysenko, D.; Werner, T.; Grzywa, M.; Puls, A.; Hagen, V.; Eickerling, G.; Jelic, J.; Reuter, K.; Volkmer, D. Reversible gas-phase redox processes catalyzed by Co-exchanged MFU-4*l*(arge). *Chem. Commun.* **2012**, *48* (9), 1236–1238.

(3) Rau, S.; Görls, H. Solid state structure of a rhenium bibenzimidazole complex. *J. Coord. Chem.* **2004**, *57* (17-18), 1587–1590.

(4) Hu, M.; Yan, Y.; Zhu, B.; Chang, F.; Yu, S.; Alatan, G. A series of Mn(i) photo-activated carbon monoxide-releasing molecules with benzimidazole coligands: synthesis, structural characterization, CO releasing properties and biological activity evaluation. *RSC Adv.* **2019**, *9* (36), 20505–20512.

(5) Dubbeldam, D.; Calero, S.; Vlugt, T. J. iRASPA:GPU-accelerated visualization software for materials scientists. *Molecular Simulation* **2018**, *44* (8), 653–676.

(6) Sarkisov, L.; Bueno-Perez, R.; Sutharson, M.; Fairen-Jimenez, D. Materials Informatics with PoreBlazer v4.0 and the CSD MOF Database. *Chem. Mater.* **2020**, *32* (23), 9849–9867.

(7) Röß-Ohlenroth, R.; Bredenkötter, B.; Volkmer, D. Organometallic MFU-4*l*(arge) Metal–Organic Frameworks. *Organometallics* **2019**, *38* (18), 3444–3452.

Journal of Inorganic and General Chemistry
ZAAC
Zeitschrift für anorganische und allgemeine Chemie

DOI: 10.1002/zaac.202200153

Synthesis, Thermal Stability and Magnetic Properties of an Interpenetrated Mn(II) Triazolate Coordination Framework

Richard Röß-Ohlenroth,[a] Marcel Hirrle,[a] Maryana Kraft,[a] Andreas Kalytta-Mewes,[a] Anton Jesche,[b] Hans-Albrecht Krug von Nidda,[c] and Dirk Volkmer*[a]

Coordination frameworks and metal-organic frameworks built from simple triazole ligands such as 1*H*-1,2,3-triazole (**H-ta**) have recently inspired great interest owing to physical phenomena such as electronic conductivity, phase transitions and their magnetic behavior. In line of our endeavors we report on the solvothermal reaction of $MnCl_2 \cdot 4H_2O$ with **H-ta** ligand in isopropyl alcohol leading to the the novel **CFA-23** (((propan-2-yl)oxidanium)$^+$[$Mn_6Cl_5(ta)_8$]$^-$; CFA-23 = Coordination Framework Augsburg University-23) coordination framework. Single-crystal X-ray diffraction (SC-XRD) reveals that it crystallizes in the tetragonal space group $P4_2/nnm$ (134) exhibiting a two-fold interpenetrated framework with the topologies of a ***dia*** net with point (Schläfli) symbol 6^6. The thermal stability of this compound was investigated using variable temperature X-ray powder diffraction and thermogravimetric analysis. The magnetic properties of **CFA-23** differ from a similar non-interpenetrated literature structure of the composition ($H[Mn_6(bta)_8Cl_5] \cdot (H_2O)_4$) built from 1*H*-1,2,3-benzotriazole, thus, indicating that sterically induced lattice changes might be an adjustment parameter for magnetic properties in such frameworks.

Introduction

1,2,3-Triazolate based coordination compounds and especially metal-organic frameworks (MOFs) recently gained increasing attention owing to various physical phenomena and potential applications like e.g. drug delivery,[1] catalytic reactions,[2] kinetic trapping of gases,[3,4] H_2/D_2 quantum sieving[5] and CO_2 binding,[6] which were shown for bistriazolate MOFs featuring Kuratowski-type secondary building units (SBUs). Other bistriazolate-based frameworks were investigated for catalysis,[7] gas binding,[8–10] chirality,[11] magnetic behaviour,[12] or even electrical and proton conductivity.[13,14] Single triazolate ligands tend to form Kuratowski complexes,[15] which were recently proven to give interesting chromophores[16] or building blocks for the assembly of metal hydrogen-bonded organic frameworks[17] via functionalization of the ligand backbones. However, the 1*H*-1,2,3-triazole (**H-ta**) tends to form MOFs of the $M^{II}(ta)_2$-type,[18–20] which can be considered as a framework of condensed Kuratowski units. Such frameworks exhibit a variety of fascinating physical phenomena like e.g. Jahn-Teller and spin-crossover phase transitions,[19,21] electronic conductivity,[13,18,22] and even the highest ferromagnetic ordering temperature achieved in MOFs so far.[23] **H-ta** based frameworks built from Mn(II) ions are also promising materials for magnetic investigations due to their half-filled d-shell.[24] In literature, various structures built from Mn_4Cl SBUs with tetrazolate ligands are known.[25,26] However, to the best of our knowledge, only a MOF comprising Co_4Cl tetranuclear SBUs was investigated for its magnetic behavior[27] and DFT+D2 calculations of M_4Cl ($M = Ti^{II}, V^{II}, Cr^{II}, Mn^{II}, Fe^{II}, Ni^{II}, Cu^{II}$) SBUs also indicate antiferromagnetic ordering.[28] As long distances prevent the magnetic interaction between SBUs in most MOFs,[29] the coupling between the isolated Mn_4Cl SBUs can be enhanced by linkage via additional metal sites similar to the $M(ta)_2$ frameworks, as exemplified with the spin-canted MOF of the composition $H[Mn_6(bta)_8Cl_5] \cdot (H_2O)_4$.[30]

In the effort to extend the variety of structures and our knowledge on the foundation of physical phenomena in such compounds, we synthesized and characterized the **CFA-23** (((propan-2-yl)oxidanium)$^+$ [$Mn_6Cl_5(ta)_8$]$^-$) framework. Particular emphasis is put on structural and magnetic properties in comparison to the related $H[Mn_6(bta)_8Cl_5] \cdot (H_2O)_4$ MOF. The structure was solved using single-crystal X-ray diffraction (SC-

---

[a] *R. Röß-Ohlenroth, M. Hirrle, Dr. M. Kraft, A. Kalytta-Mewes, Prof. Dr. D. Volkmer*
Universität Augsburg, Institut für Physik
Lehrstuhl für Festkörperchemie
Universitätsstraße 1, 86159
Augsburg (Germany)
E-mail: dirk.volkmer@physik.uni-augsburg.de
[b] *Dr. A. Jesche*
Universität Augsburg, Institut für Physik
Zentrum für Elektronische Korrelationen und Magnetismus, Experimentalphysik VI,
Universitätsstraße 1, 86159
Augsburg (Germany)
[c] *H.-A. Krug von Nidda*
Universität Augsburg, Institut für Physik
Zentrum für Elektronische Korrelationen und Magnetismus, Experimentalphysik V,
Universitätsstraße 1, 86159
Augsburg (Germany)

Supporting information for this article is available on the WWW under https://doi.org/10.1002/zaac.202200153

XRD), revealing a two-fold interpenetrated framework which can be ascribed to the missing benzene rings of the **H-ta** ligand when compared to the analogous framework containing benzotriazolate linkers. The 2-fold interpenetration leads to ultra-narrow channels extending along the *c*-direction of the framework. The framework's stability was investigated by variable temperature powder X-ray diffraction (VT-PXRD), as well as thermogravimetric analysis coupled with mass spectrometry (TGA-MS). In addition, we demonstrate that the molar magnetic susceptibility of the compound can be reasonably approximated using minimalistic models of the exchange interactions.

Results and Discussion

Synthesis

The novel **CFA-23** structure was discovered during reaction condition screening experiments similar to the $Mn(ta)_2$ single crystal syntheses described in literature.[31] Hereby, **CFA-23** was obtained using teflon lined steel autoclaves (23 mL inner volume) for solvothermal reaction conditions with a 1:2 metal-to-ligand ratio in isopropyl alcohol at 210 °C. During these investigations we noticed that the usage of new teflon liners is essential, as older vessels tended to give mixed phases with an unidentified impurity. Upscaling attempts employing 200 mL inner volume autoclaves were also unsuccessful so far, indicating a narrow window for the appropriate synthesis conditions. Thus, we deduce that formation of **CFA-23** might be mainly, but not exclusively, sensitive to the reaction pressure and temperature ramp, which differs for reaction vessels with largely different volumes.

Crystal Structure and Topology

SC-XRD revealed that **CFA-23** crystallizes in the tetragonal space group $P4_2/nnm$ (134) with unit cell dimensions of $a = b =$ 14.4426(4) Å and $c = 10.2366(3)$ Å (Table 1). Analysis with the ToposPro software package[32] revealed a two-fold interpenetration of the ***dia*** nets with point (Schläfli) symbol 6^6 holding the same SBUs and topology as the literature MOF $H[Mn_6(bta)_8Cl_5]\cdot(H_2O)_4$ ($I\bar{4}2d$ (122)).[30] The two interpenetrated frameworks are stacked on top of each other in *c*-direction with a distance of one unit cell (Figure 1c). The central coordination motif of the structure is a square arrangement of four divalent Mn(2) ions around the central μ_4-Cl(1) anion, which is a well-known MOF SBU for pyrazolates, triazolates and tetrazolates.[26,27] Each of those tetranuclear Mn_4 units is interconnected with four neighboring tetranuclear Mn_4 units by monomeric Mn(1) ions via two μ_2-bridging Cl(2) anions, which are coordinated opposite to the μ_4-Cl(1) (Figure 1). Similar μ_2-chloride bridged Mn^{II} chains are also encountered in the MAF structures built from bistriazolate linkers.[7,8,10,11] All Mn^{II} ions are octahedrally coordinated by two opposing chloride anions and four nitrogen atoms from the eight **ta** ligands coordinated around each tetranuclear Mn_4 unit. Distinct bond distances and angles of the compound are in good agreement with the literature $H[Mn_6(bta)_8Cl_5]\cdot(H_2O)_4$ MOF (Table 2),[30] which also exhibits a distortion of the tetranuclear Mn_4 units observed as perfect squares for all isolated MOF SBUs in literature.[26,27,33] The main differences in **CFA-23** are the Mn(1)-N(3), Mn(2)-N(1) and Mn(2)-N(2) distances, which are each split into two different distances for the corresponding Mn–N pairs of the $H[Mn_6(\underline{bta})_8Cl_5]\cdot(H_2O)_4$ MOF. Additionally, the four Mn(2) ions showed a smaller out of plane distortion in comparison to the literature structure, which leads to a change of the Mn(1)-Cl(1)-Mn(1) angle for the opposing Mn(1) ions from 165.43(4)° in the literature structure to 171.712(13)° in **CFA-23**. Nearly no differ-

Table 1. Crystal data and structure refinement of **CFA-23**

	CFA-23
Empirical formula	$C_{19}H_{16}Cl_5Mn_6N_{24}O$
Formula	$C_{16}H_{16}Cl_5Mn_6N_{24}\cdot C_3O$
Formula weight/g·mol^{-1}	1103.45
Temperature/K	298(2)
Wavelength/Å	0.71073
Crystal system	Tetragonal
Space group	$P4_2/nnm$
a/Å	$a = 14.4426(4)$
c/Å	$c = 10.2366(3)$
Volume/Å^3	2135.24(13)
Z	2
D_g/gcm^{-3}	1.716
μ/mm^{-1}	2.083
F(000)	1082
Crystal size/mm^3	0.08 × 0.08 × 0.06
Θ range	2.439 to 27.495°.
Refles collected	29221
Independent reflections	1301 [R(int) = 0.0272]
Completeness	99.7 %
Data/restraints/parameters	1301/4/82
GooF on F^2	1.132
Final R indices [I > 2sigma(I)]	$R_1 = 0.0223$, $wR_2 = 0.0618$
R indices (all data)	$R_1 = 0.0237$, $wR_2 = 0.0626$
Largest diff. peak and hole/e.Å-3	0.407 and −0.389
CCDC No.	2154149

Table 2. Comparison of distinct bond distances [Å] and angles [°] of **CFA-23** with the respective bonds and angles of $H[Mn_6(bta)_8Cl_5]\cdot(H_2O)_4$

	CFA-23	$H[Mn_6(BTA)_8Cl_5]\cdot(H_2O)_4$
Mn(1)-N(3)	2.2403(14)	2.248(6)/2.242(6)
Mn(1)-Cl(2)	2.5942(6)	2.5313(17)
Mn(2)-N(1)	2.2473(13)	2.270(5)/2.303(5)
Mn(2)-N(2)	2.2266(13)	2.191(6)/2.237(6)
Mn(2)-Cl(1)	2.7028(3)	2.6871(15)
Mn(2)-Cl(2)	2.4888(6)	2.475(2)
Mn(1)-Cl(2)-Mn(2)	92.101(19)	92.02(6)
Mn(2)-Cl(1)-Mn(2) (opposite)	171.712(13)	165.43(4)
Mn(2)-Cl(1)-Mn(2) (neighbouring)	90.299(1)	90.921(5)

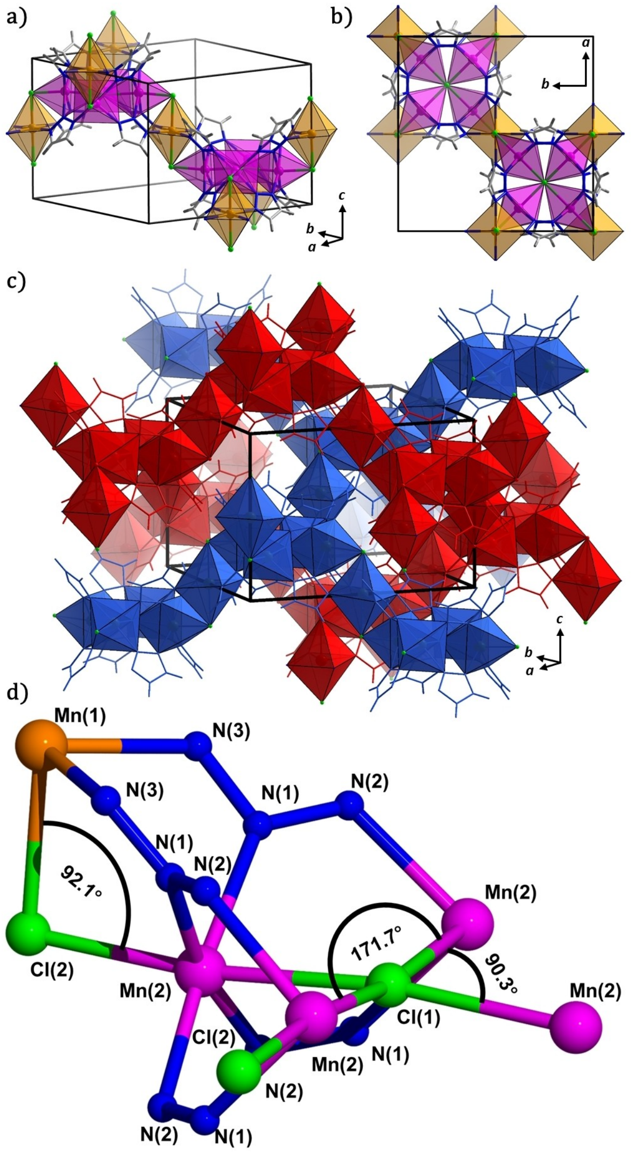

Figure 1. a) Side view and b) view along the *c*-direction visualizing the connection motif of the SBUs in **CFA-23**. c) Visualization of the two interpenetrating frameworks in **CFA-23**. d) Atoms and distinct bond angles of the tetranuclear Mn_4 unit (pink) and the bridging Mn(1) (orange) ions.

ence is observed for the Mn(1)-Cl(2)-Mn(2) angle connecting the Mn_4-tetramers, which indicates a similar spatial arrangement in both frameworks (Figure 1). The resulting negatively charged 3D framework $[Mn_6Cl_5(ta)_8]^-$ has one negative charge per formula unit, which requires charge balancing. The previously reported $H[Mn_6(bta)_8Cl_5]\cdot(H_2O)_4$ compound suggests the presence of a H_3O^+ moiety located at the additional O sites found in the single crystal structure analysis. However, for **CFA-23**, additional electron density was found in small cavities of the structure (Figure S6), indicating a disordered isopropyl alcohol molecule, which is expected to be present as (((propan-2-yl)oxidanium)$^+$ counter ion in the structure. Since the hydrogen atoms could not be refined for this disordered counter-cation, they were added to the sum formula of the structure. Additional proof for this was found via PLATON/SQUEEZE analysis of the structure,[34] which gave a total potential solvent accessible surface area of 557 Å^3 (26% of the 2135.24(13) Å^3 unit cell) with 69 electron counts. Hereof, approximately 31 electron counts are located in each of the two cavities with the counter cations (12.6% of the unit cell volume) and only 4 in each of the two channel pores (13.1% of the unit cell volume) along the *c*-direction of the unit cell (Figure 3, S6). Therefore, indicating accessible and free pore channels in the structure. Further investigations with TGA-MS gave additional evidence for this unusual charge balancing counter ion.

Composition and Thermal Stability

Phase purity of **CFA-23** was confirmed by PXRD, neatly matching the pattern calculated from SC-XRD data (Figure 2a), which was affirmed with a Le Bail fit (Figure S3). In addition, a Mn:Cl ratio of 6:5.1, which is in good agreement with the compound's composition, was obtained by energy dispersive X-ray (EDX) spectroscopy (Figure S11). Optical and SEM micrographs also showed no impurities next to the large crystal specimens (Figure 3, S2). The thermal stability of the compound was investigated by VT-PXRD, revealing a small decrease of crystallinity at temperatures above 350 °C and a nearly complete loss of crystallinity for the pattern at 400 °C (Figure 2b). At temperatures above 400 °C, new reflexes indicate the formation of MnO, although the measurement was conducted under nitrogen gas flow. Hereby, one MnO per formula unit is expected to origin from the(propan-2-yl)oxidanium cations but a contribution from minor leaks in the measurement setup cannot be ruled out. TGA curves also show a decomposition onset in agreement with VT-XRPD patterns. A TGA measurement coupled with mass spectrometry of the decomposition products reveals the loss of small amounts of isopropyl alcohol between 150–270 °C and evolution of propene between 225 to 370 °C (Figure 2c), indicating the decomposition of the (propan-2-yl)oxidanium cations, similar to the decomposition of isopropyl alcohol under acidic conditions.[35] Note here that no trace of acetone (43 m/z), a typical decomposition product of isopropyl alcohol under basic conditions, is observed at the beginning of the decomposition. Thus, affirming the (propan-2-yl)oxidanium cations found in SC-XRD as charge balance for the negatively charged framework.

Porosity

Specific surface areas of 321, 226 and 104 m^{2}g^{-1} were calculated for H_2, Ar and CO_2, respectively, from the crystal structure of **CFA-23** using the iRaspa software.[36] The 2D pore channels run along the *c*-direction, which can be clearly identified for the obtained single crystals and their morphology (Figure 3). Thus, the separation of gases due to the narrow character of the pores could be a highly interesting field of study. However, no typical adsorption isotherms were observed

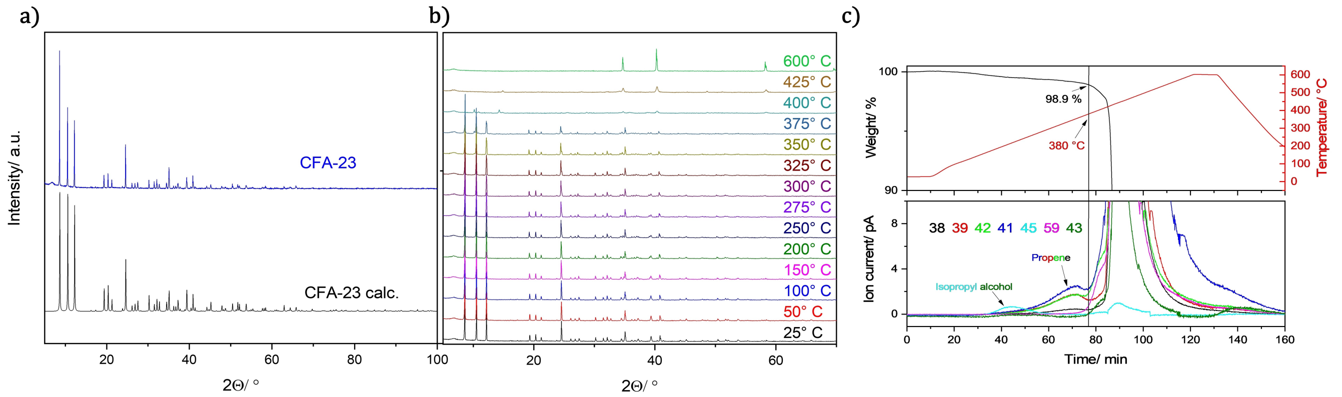

Figure 2. a) Calculated (black), measured (blue) and b) VT-PXRD patterns of **CFA-23**. c) Enlarged TG-curve and simultaneous MS signals of **CFA-23** showing the loss of small quantities of isopropyl alcohol (43 and 45 m/z) between 150–270 °C and evolution of propene (42, 41, 39 and 38 m/z) between 225 to 370 °C, indicating decomposition of the (propan-2-yl)oxidanium cations prior to the framework decomposition

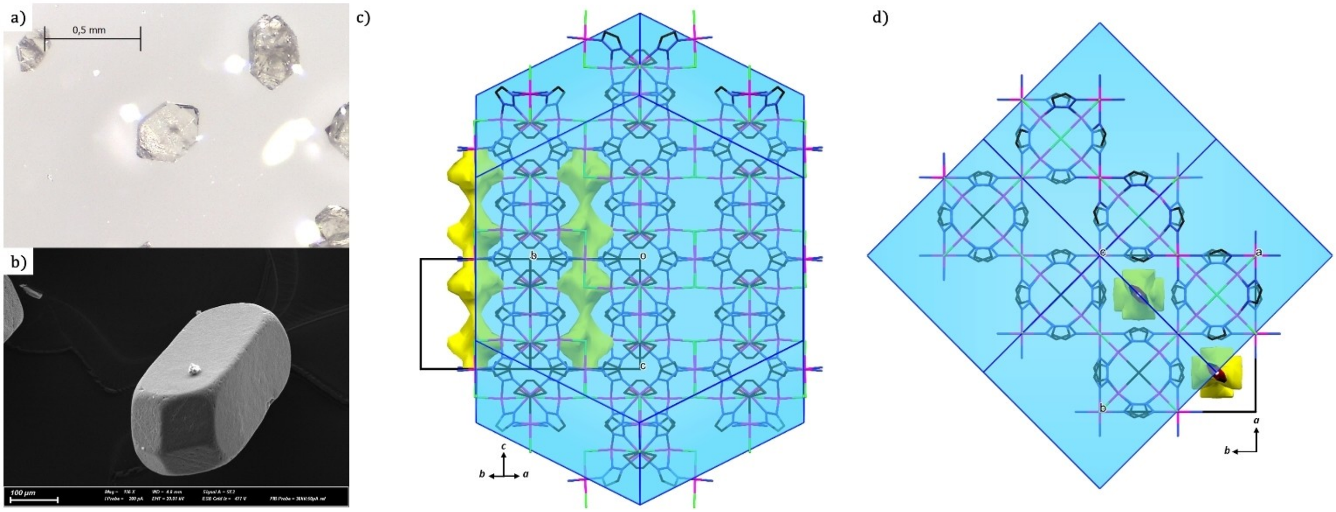

Figure 3. a) Optical and b) SEM micrographs of **CFA-23** and structure plots showing the crystal morphology (blue) and pore channels (yellow) viewed along the c) *ab*- and d) *c*-direction.

for Ar or even H_2 and samples activated at 200 °C so far (Figure S7, S8). This can be explained with the ultra-narrow pore apertures of 2.72 Å (kinetic diameter of $H_2 = 2.89$ Å) calculated for the **CFA-23** structure using PoreBlazer v4.0.[37] In literature, it is shown that gas molecules such as CO_2 can overcome even narrower pore apertures in MFU-4 (2.22 Å pore limiting diameter calculated with PoreBlazer v4.0) at elevated temperatures and pressures[38] and even kinetic trapping of Xenon and SF_6 is possible.[3,4] However, no adsorption of CO_2 at 273 K for **CFA-23** samples activated at temperatures up to 350 °C (Figure S9) and no kinetic trapping of xenon after 24 h at 30 bar and 100 °C was observed. A possible explanation might be the blockage of the narrow channel pores with residual solvent molecules, displaced (propan-2-yl)oxidanium cations, or other defects, of which only two are necessary to plug a channel. It is also possible that xenon enters the framework without being trapped at ambient conditions and thus already being lost prior to TGA analysis. Nonetheless, the potential porosity of the framework still suggests the classification as a MOF[39] and further kinetic trapping attempts of small molecules at high temperatures and pressures could proof a worthwhile aim.

Magnetization Measurements

The inverse susceptibility $\chi^{-1} = (M/H)^{-1}$ per mol Mn is shown in Figure 4a). Curie-Weiss behavior is observed in the high-temperature region above $T \sim 50$ K. The effective moment amounts to $\mu_{eff} = 6.1\ \mu_B$ per Mn close to the value of 5.92 μ_B expected for free Mn^{2+} ions. The $\chi_M T$ product of **CFA-23** increases monotonously with increasing temperature and reaches a value of 23.22 $cm^3mol^{-1}K$ at $T = 300$ K (Figure S12), which is higher than 19.24 $cm^3mol^{-1}K$ of the literature compound, but still lower than the saturation value of 26.25 $cm^3mol^{-1}K$ expected for 6

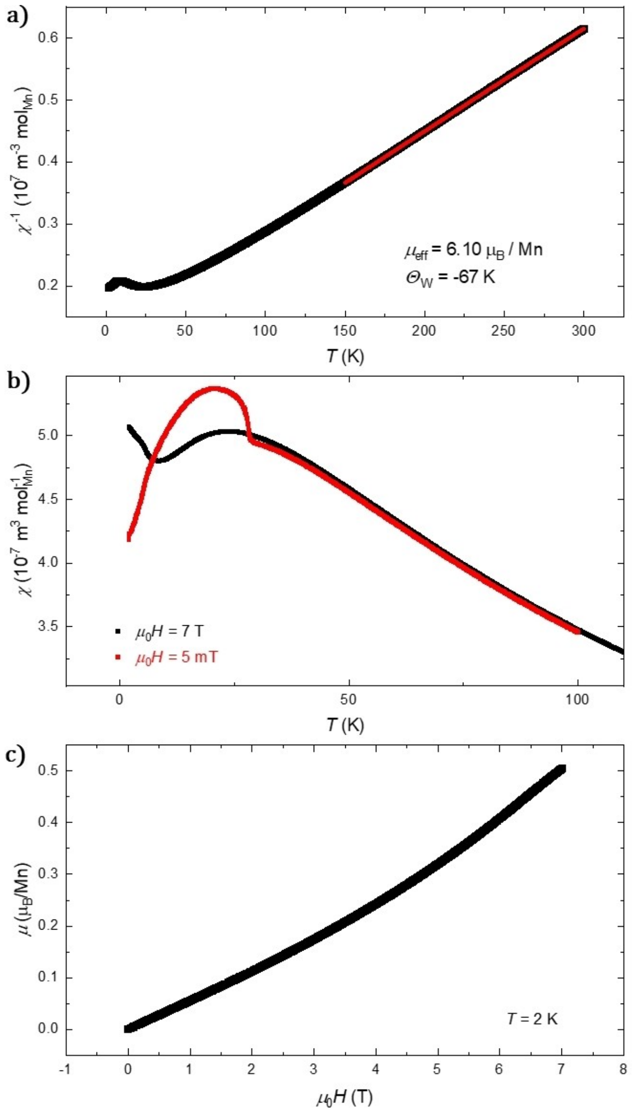

Figure 4. a) Temperature dependence of the inverse molar magnetic susceptibility χ^{-1} in a 7 T field and b) the molar magnetic susceptibility χ in fields of 7 T and 5 mT for **CFA-23** in SI units. c) Isothermal magnetization *M* of **CFA-23** as function of the magnetic field *H* at 2 K.

high-spin d^5 ions with spin-only $g=2.0$ at infinite temperature.[30] This indicates a weaker but still sizeable antiferromagnetic (AFM) exchange in **CFA-23** than found in the literature compound, in agreement with the negative Weiss temperature $\theta_W=-67$ K, as compared to -76 K found for the latter.[30] A small temperature-independent contribution has been considered in the fitting and was found to account for 5% of the room temperature value. Figure 4b) shows χ obtained in applied fields $\mu_0H=5$ mT and 7 T. Only a minute field-dependence is observed for $T>30$ K, in accordance with a magnetically non-ordered state. A sharp increase, which also affirms good crystallinity of the sample and cooperative behavior of the transition, takes place in small applied fields of 5 mT when cooling below $T=28.5$ K. In contrast, the increase for the literature compound already starts at $T=46$ K in a 100 mT field. This behavior, together with the decrease in χ upon further cooling, indicates a canted AFM ordering with a complex interplay of temperature-dependent exchange, tilting angle, and/or steric effects. The anomaly is shifted to lower temperature in larger applied fields, consistent with AFM ordering. Comparison of the resulting frustration parameters of $f=2.4$ for **CFA-23** and $f=1.7$ for $H[Mn_6(bta)_8Cl_5]\cdot(H_2O)_4$, indicates a slight increase in frustration for **CFA-23**. Isothermal magnetization at $T=2$ K is plotted in Figure 4c). The magnetization does not approach saturation even in the largest applied field of $\mu_0H=7$ T in accordance with the proposed AFM ordering. A weak increase in slope, not observed for the literature counterpart, is found at μ_0H ~5 T, which could indicate the onset of a broad metamagnetic transition. In order to gain a deeper insight into the magnetic behavior of the materials two different methods were applied to fit the susceptibility of the material. In a first approach the numerical expression derived by Rushbrooke and Wood[40] for a basic antiferromagnetic quadratic lattice with exchange coupling J_1, was applied.[41] Hereby, with a J_1 value of -4.1 K the high-temperature behavior matched the experimental data but a slight shift of the maximum to a higher temperature of 35 K was obtained in comparison to $T_{\max}=24$ K observed in the experiment (Figure 5c). Thus, the molar susceptibility was also fitted using a molecular approach with the program PHI,[42] similar to the method reported previously,[43] which adds the J_2 coupling to the model. This molecular model resulted in an improved match of the high-temperature behavior, as well as a shift of the maximum to 30 K closer to the experimental results (Figure 5c). Hereby, the value of the main exchange parameter did not change with -4.1 K, but is now assigned to J_2, whereas J_1 decreased to -0.37 K. The two antiferromagnetic couplings suggest frustration of tetranuclear Mn_4 unit. This tetranuclear Mn_4 unit seems to be sufficient for a reasonable approximation of the susceptibility since the bridging Mn^{II} ions are considered to contribute mainly as mediator between the tetranuclear Mn_4 units, because the nature of the J_3 coupling has no influence on the spin-orientation of the neighboring tetramer.Taking J_3 into our model would go beyond simple approaches. Simulation of the isothermal magnetization *M* as function of the magnetic field *H* at 2 K applying the obtained exchange coupling constants for the molecular model reproduces the experimentally observed curvature, although the results should be regarded with caution due to the field dependent phase transition already occurring at higher temperatures. In conclusion, the small differences in bond lengths and angles of the structures are expected to be responsible for the change in magnetic behavior in comparison to the literature compound, although effects from the interactions between the two interpenetrating frameworks, as well as the differing counter anions and residual solvents, cannot be ruled out. Thus, investigation of analogous structures, as well as more detailed computational simulations, are necessary in order to derive trends for the structure-magnetism relation, which could be applied to predict and design enhanced magnetic properties into new materials.

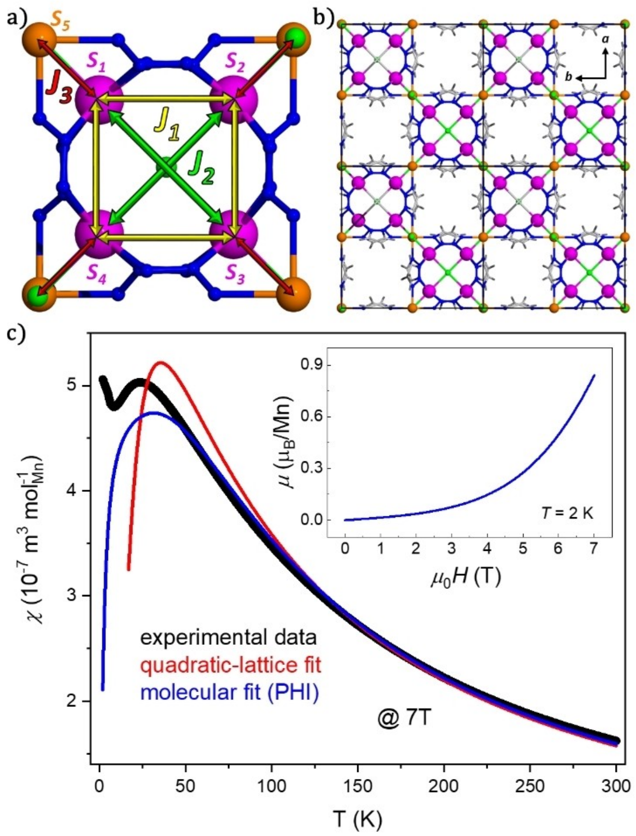

Figure 5. a) Mn^{II}-Mn^{II} exchange couplings J_1 (yellow), J_2 (green) and J_3 (red) in the basic Mn_4-tetramer (pink) and the bridging Mn^{II} ions (orange) of **CFA-23**. b) Ball-and-stick view along the *c*-direction of one of the interpenetrating **CFA-23** nets showing the linkage mode of the Mn_4-tetramers. c) Measured magnetic susceptibility χ in a 7 T field per Mn^{II} ion in comparison to the fits obtained from the quadratic-layer and molecular models. The inset shows the isothermal magnetization *M* as function of the magnetic field *H* at 2 K calculated from the exchange coupling constants obtained from the molecular fit.

Conclusions

In summary, the novel **CFA-23** coordination framework was prepared from the **H-ta** ligand and $MnCl_2 \cdot 4H_2O$ under solvothermal conditions and the structure solved using SC-XRD, revealing a two-fold interpenetration of frameworks with the same topology as the literature-known spin-canted MOF H-$[Mn_6(bta)_8Cl_5] \cdot (H_2O)_4$.[30] The compound was further characterized by FT-IR, XRPD, TGA, TGA-MS and VT-XRPD. In contrast to the literature structure, **CFA-23** features a two-fold interpenetration and pore channels along the *c*-direction, which is presumably due to the absence of the steric crowding effect of the benzene ring at the H-bta ligand. In contrast to isolated tetranuclear Mn_4 units observed in some literature MOFs, spin-coupling and long-range order throughout the frameworks is observed due to the linking of the secondary building units via bridging Mn^{II} sites. However, the tetrameric unit seems to be the main contributor for the magnetic behavior, as the susceptibility and magnetization can be already reasonably fitted with two exchange-couplings, indicating only a mediating magnetic function of the Mn^{II} bridges. In addition, the magnetic measurements revealed a differing behavior in comparison to the literature counterpart, which indicates that minute lattice distortions due to sterically demanding ligands or framework interpenetration strongly influence the magnetic properties in such frameworks. Thus, although minor contributions from the counter cations or residual solvent molecules should not be neglected, we conclude that fine tuning and tailoring of magnetic properties might be achieved with ligands exhibiting varying steric demands, which is currently under investigation.

Experimental Section

Materials and General Methods

Isopropyl alcohol (≥99.8 %, VWR), $MnCl_2 \cdot 4H_2O$ (99.99 %, abcr), and **H-ta** (98 %; BLD Pharmatech Ltd.) were used as obtained from the commercial supplier. A general purpose acid digestion vessel (Parr Instrument Company) with 23 mL inner volume teflon liners was used for the solvothermal reaction.

Attenuated total reflectance (ATR) Fourier transform infrared spectroscopy (FT-IR) in the range of 4000–400 cm^{-1} was measured with the PLATINUM ATR unit and a KBr (4000-400 cm^{-1}) beam splitter on a Bruker Equinox 55 FT-IR spectrometer. The signals were labelled strong (s), medium (m) and weak (w). SEM micrographs were recorded with a Philips XL 30 FEG scanning electron microscope and a Zeiss Crossbeam 550, which was also used for EDX spectra of carbon coated samples using the analytical silicon drift detector from Oxford Instruments. An Empyrean (PANalytical) diffractometer equipped with Bragg-Brentano^{HD} mirror and PIXcel^{3D} 2×2 detector was used to collect the PXRD and VT-PXRD pattern using the XRK 900 reactor chamber. The sample was heated with a rate of 5 °C min^{-1} with a 30 min isothermal step prior to measurement under nitrogen atmosphere. The pattern at 25 °C was measured in the range of 5–100° 2θ with 0.0131° steps and an overall measurement time of 6017 s. All other patterns were collected in the range from 5–70° 2θ with 0.0263° steps and a measurement time of 2127 s for each pattern. Thermogravimetric analysis (TGA) was conducted with a heating rate of 5 °C min^{-1} and starting after a five-minute isothermal step on a TA Instruments Q500 device in the temperature range of 25–800 °C under nitrogen gas flow. A Netzsch STA 409 C thermobalance connected via Skimmer coupling to a Balzers QMG 421 mass spectrometer was used for the TGA-MS analysis in the temperature range from 25–600 °C and a 5 °C min^{-1} heating rate under nitrogen atmosphere. The argon adsorption isotherm was measured on a Quantachrome Autosorb-I ASI-CP-8 instrument at 77.3 K in the range of $5.00 \times 10^{-5} \leq p/p_0 \leq 1.00$. The H_2 adsorption experiment at 50 K was conducted with a BELSORP-max instrument combined with a BELCryo system. The samples were treated at 200 °C in high vacuum for several hours prior to the measurements. CO_2 adsorption measurements were performed on a Quantachrome NOVA2000 Series instrument at 273 K after vacuum treatment at 200 °C, 300 °C, and 350 °C for 2 h. Temperature- and field-dependent magnetization was measured using a Quantum Design MPMS3. The powder sample with a total mass of m = 7.43 mg was mounted in a plastic capsule.

Single-crystal X-ray Data Collection and Structure Refinement

X-ray diffraction data for the single crystal structure determination were collected at room temperature on a Bruker D8 Venture diffractometer (Mo Kα radiation, $\lambda = 0.71073$ Å). The raw data frames were integrated and corrected for absorption effects using the Bruker SAINT[44] and SADABS[45] software packages. Structure solution by direct methods and structure refinement by full-matrix least-squares techniques against F2 were performed using SHELXT 2014/5[46] and SHELXL 2018/3.[47] All non-hydrogen atoms of the framework were refined anisotropically and the positions of framework hydrogen atoms were determined from the difference Fourier map. The atomic coordinates of protonated isopropanol, which is disordered due to the symmetry over four positions, were refined by means of the DSR program.[48] The occupancies of the atoms were set at 0.25. Because of highly disordered solvent, the hydrogen atoms in protonated isopropanol were omitted in the refinement. Complete crystallographic data for the **CFA-23** structure reported in this paper have been deposited in the CIF format in the Cambridge Crystallographic Data Center as supplementary publication no. 2154149.

Synthesis of CFA-23 (((propan-2-yl)oxidanium)$^+$[$Mn_6Cl_5(ta)_8$]$^-$)

$MnCl_2 \cdot 4H_2O$ (49.5 mg, 0.250 mmol) was dissolved in 5 mL of isopropyl alcohol inside of a new 23 mL teflon liner in an ultrasonic bath. H-ta (34.6 mg, 0.500 mmol) was added, the reaction mixture sealed in the digestion vessel and heated in an oven at 210 °C for 3 days employing a heating and cooling rate of 1 °C/min. The product was obtained after filtration and washing with 5 mL of isopropyl alcohol as large colourless crystals, which were dried under vacuum for several hours (37.5 mg, 82%). FT-IR (ATR, 4000–400 cm^{-1}): 3142 (w), 3125 (w), 1745 (w), 1607 (w), 1478 (w), 1451 (m), 1419 (m), 1380 (w), 1206 (w), 1177 (s), 1096 (s), 993 (m), 972 (s), 881 (w), 812 (s), 797 (s), 712 (m). EDX Mn:Cl ratio: 6:5.1.

Acknowledgements

Financial support from the DFG (SPP 1928 COORNETs: Coordination Networks: Building Blocks for Functional Systems) is gratefully acknowledged. H.-A. K.v.N. acknowledges funding by DFG within TRR 80 “From Electronic Correlations to Functionality”, project no. 107745057 (Augsburg, Munich, Stuttgart) Open Access funding enabled and organized by Projekt DEAL.

Conflict of Interest

The authors declare no conflict of interest.

Data Availability Statement

The data that support the findings of this study are available from the corresponding author upon reasonable request.

Keywords: coordination framework · metal-organic framework · magnetic properties · manganese · microporous materials

[1] R. Ettlinger, M. Sönksen, M. Graf, N. Moreno, D. Denysenko, D. Volkmer, K. Kerl, H. Bunzen, *J. Mater. Chem. B* **2018**, *6*, 6481–6489.
[2] a) D. Denysenko, T. Werner, M. Grzywa, A. Puls, V. Hagen, G. Eickerling, J. Jelic, K. Reuter, D. Volkmer, *Chem. Commun.* **2012**, *48*, 1236–1238; b) D. Denysenko, J. Jelic, K. Reuter, D. Volkmer, *Chem. Eur. J.* **2015**, *21*, 8188–8199; c) D. Denysenko, J. Jelic, O. V. Magdysyuk, K. Reuter, D. Volkmer, *Microporous Mesoporous Mater.* **2015**, *216*, 146–150; d) D. Denysenko, M. Grzywa, J. Jelic, K. Reuter, D. Volkmer, *Angew. Chem.* **2014**, *126*, 5942–5946; e) D. Denysenko, D. Volkmer, *Faraday Discuss.* **2017**, *201*, 101–112; f) R. J. Comito, K. J. Fritzsching, B. J. Sundell, K. Schmidt-Rohr, M. Dincă, *J. Am. Chem. Soc.* **2016**, *138*, 10232–10237; g) E. D. Metzger, R. J. Comito, Z. Wu, G. Zhang, R. C. Dubey, W. Xu, J. T. Miller, M. Dincă, *ACS Sustainable Chem. Eng.* **2019**, *7*, 6654–6661; h) E. D. Metzger, R. J. Comito, C. H. Hendon, M. Dincă, *J. Am. Chem. Soc.* **2017**, *139*, 757–762; i) A. M. Wright, C. Sun, M. Dincă, *J. Am. Chem. Soc.* **2021**, *143*, 681–686.
[3] H. Bunzen, F. Kolbe, A. Kalytta-Mewes, G. Sastre, E. Brunner, D. Volkmer, *J. Am. Chem. Soc.* **2018**, *140*, 10191–10197.
[4] H. Bunzen, A. Kalytta-Mewes, L. van Wüllen, D. Volkmer, *Beilstein J. Nanotechnol.* **2019**, *10*, 1851–1859.
[5] a) J. Teufel, H. Oh, M. Hirscher, M. Wahiduzzaman, L. Zhechkov, A. Kuc, T. Heine, D. Denysenko, D. Volkmer, *Adv. Mater.* **2013**, *25*, 635–639; b) I. Weinrauch, I. Savchenko, D. Denysenko, S. M. Souliou, H.-H. Kim, M. Le Tacon, L. L. Daemen, Y. Cheng, A. Mavrandonakis, A. J. Ramirez-Cuesta, D. Volkmer, G. Schütz, M. Hirscher, T. Heine, *Nat. Commun.* **2017**, *8*, 14496.
[6] a) R. Röß-Ohlenroth, B. Bredenkötter, D. Volkmer, *Organometallics* **2019**, *38*, 3444–3452; b) C. Jin, S. Zhang, Z. Zhang, Y. Chen, *Inorg. Chem.* **2018**, *57*, 2169–2174; c) Z. Cai, C. E. Bien, Q. Liu, C. R. Wade, *Chem. Mater.* **2020**, *32*, 4257–4264; d) C. E. Bien, Q. Liu, C. R. Wade, *Chem. Mater.* **2020**, *32*, 489–497; e) A. M. Wright, Z. Wu, G. Zhang, J. L. Mancuso, R. J. Comito, R. W. Day, C. H. Hendon, J. T. Miller, M. Dincă, *Chem* **2018**, *4*, 2894–2901.
[7] P.-Q. Liao, X.-Y. Li, J. Bai, C.-T. He, D.-D. Zhou, W.-X. Zhang, J.-P. Zhang, X.-M. Chen, *Chem. Eur. J.* **2014**, *20*, 11303–11307.
[8] A. J. Rieth, Y. Tulchinsky, M. Dincă, *J. Am. Chem. Soc.* **2016**, *138*, 9401–9404.
[9] J. J. Oppenheim, J. L. Mancuso, A. M. Wright, A. J. Rieth, C. H. Hendon, M. Dincaˇ, *J. Am. Chem. Soc.* **2021**, *143*, 16343–16347.
[10] P.-Q. Liao, H. Chen, D.-D. Zhou, S.-Y. Liu, C.-T. He, Z. Rui, H. Ji, J.-P. Zhang, X.-M. Chen, *Energy Environ. Sci.* **2015**, *8*, 1011–1016.
[11] K. Knippen, B. Bredenkötter, L. Kanschat, M. Kraft, T. Vermeyen, W. Herrebout, K. Sugimoto, P. Bultinck, D. Volkmer, *Dalton Trans.* **2020**, 15758–15768.
[12] H. Bunzen, M. Grzywa, R. Aljohani, H.-A. Krug von Nidda, D. Volkmer, *Eur. J. Inorg. Chem.* **2019**, *2019*, 4471–4476.
[13] L. Sun, C. H. Hendon, S. S. Park, Y. Tulchinsky, R. Wan, F. Wang, A. Walsh, M. Dincă, *Chem. Sci.* **2017**, *8*, 4450–4457.
[14] H. Bunzen, A. Javed, D. Klawinski, A. Lamp, M. Grzywa, A. Kalytta-Mewes, M. Tiemann, H.-A. K. von Nidda, T. Wagner, D. Volkmer, *ACS Appl. Nano Mater.* **2019**, *2*, 291–298.
[15] S. Biswas, M. Tonigold, M. Speldrich, P. Kögerler, M. Weil, D. Volkmer, *Inorg. Chem.* **2010**, *49*, 7424–7434.
[16] K. Knippen, D. Matuszczyk, M. Kraft, B. Bredenkötter, G. Eickerling, T. Lis, D. Volkmer, M. Stępień, *Chem. Eur. J.* **2021**.
[17] R. Röß-Ohlenroth, C. Freudig, M. Kraft, H. Bunzen, D. Volkmer, *Cryst. Growth Des.* **2022**, *22*, 379–391.
[18] F. Gándara, F. J. Uribe-Romo, D. K. Britt, H. Furukawa, L. Lei, R. Cheng, X. Duan, M. O'Keeffe, O. M. Yaghi, *Chem. Eur. J.* **2012**, *18*, 10595–10601.

[19] M. Grzywa, D. Denysenko, J. Hanss, E.-W. Scheidt, W. Scherer, M. Weil, D. Volkmer, *Dalton Trans.* **2012**, *41*, 4239–4248.
[20] X.-H. Zhou, Y.-H. Peng, X.-D. Du, J.-L. Zuo, X.-Z. You, *CrystEngComm* **2009**, *11*, 1964.
[21] a) M. Grzywa, R. Röß-Ohlenroth, C. Muschielok, H. Oberhofer, A. Błachowski, J. Żukrowski, D. Vieweg, H.-A. K. von Nidda, D. Volkmer, *Inorg. Chem.* **2020**, *59*, 10501–10511; b) A. B. Andreeva, K. N. Le, K. Kadota, S. Horike, C. H. Hendon, C. K. Brozek, *Chem. Mater.* **2021**, *33*, 8534–8545.
[22] J. G. Park, M. L. Aubrey, J. Oktawiec, K. Chakarawet, L. E. Darago, F. Grandjean, G. J. Long, J. R. Long, *J. Am. Chem. Soc.* **2018**, *140*, 8526–8534.
[23] J. G. Park, B. A. Collins, L. E. Darago, T. Runčevski, M. E. Ziebel, M. L. Aubrey, H. Z. H. Jiang, E. Velasquez, M. A. Green, J. D. Goodpaster, J. R. Long, *Nat. Chem.* **2021**, *13*, 594–598.
[24] R. Nutakki, R. Röß-Ohlenroth, D. Volkmer, A. Jesche, H.-A. K. von Nidda, A. A. Tsirlin, P. Gegenwart, L. Pollet, L. D. C. Jaubert, *arXiv.org* **2022**, 2203.08780v1.
[25] a) Z. Guo, D. Yan, H. Wang, D. Tesfagaber, X. Li, Y. Chen, W. Huang, B. Chen, *Inorg. Chem.* **2015**, *54*, 200–204; b) C. K. Brozek, A. F. Cozzolino, S. J. Teat, Y.-S. Chen, M. Dincă, *Chem. Mater.* **2013**, *25*, 2998–3002.
[26] M. Dincă, A. Dailly, Y. Liu, C. M. Brown, D. A. Neumann, J. R. Long, *J. Am. Chem. Soc.* **2006**, *128*, 16876–16883.
[27] D. J. Xiao, M. I. Gonzalez, L. E. Darago, K. D. Vogiatzis, E. Haldoupis, L. Gagliardi, J. R. Long, *J. Am. Chem. Soc.* **2016**, *138*, 7161–7170.
[28] R. Poloni, K. Lee, R. F. Berger, B. Smit, J. B. Neaton, *J. Phys. Chem. Lett.* **2014**, *5*, 861–865.
[29] G. Mínguez Espallargas, E. Coronado, *Chem. Soc. Rev.* **2018**, *47*, 533–557.
[30] S.-D. Han, J.-P. Zhao, Y.-Q. Chen, S.-J. Liu, X.-H. Miao, T.-L. Hu, X.-H. Bu, *Cryst. Growth Des.* **2014**, *14*, 2–5.
[31] C.-T. He, Z.-M. Ye, Y.-T. Xu, D.-D. Zhou, H.-L. Zhou, Da Chen, J.-P. Zhang, X.-M. Chen, *Chem. Sci.* **2017**, *8*, 7560–7565.
[32] V. A. Blatov, A. P. Shevchenko, D. M. Proserpio, *Cryst. Growth Des.* **2014**, *14*, 3576–3586.
[33] a) D. Chen, W. Shi, P. Cheng, *Chem. Commun.* **2015**, *51*, 370–372; b) M. Asgari, S. Jawahery, E. D. Bloch, M. R. Hudson, R. Flacau, B. Vlaisavljevich, J. R. Long, C. M. Brown, W. L. Queen, *Chem. Sci.* **2018**, *9*, 4579–4588; c) S. Biswas, M. Maes, A. Dhakshinamoorthy, M. Feyand, D. E. de Vos, H. Garcia, N. Stock, *J. Mater. Chem.* **2012**, *22*, 10200; d) J.-H. Liao, W.-T. Chen, C.-S. Tsai, C.-C. Wang, *CrystEngComm* **2013**, *15*, 3377; e) K. Sumida, S. Horike, S. S. Kaye, Z. R. Herm, W. L. Queen, C. M. Brown, F. Grandjean, G. J. Long, A. Dailly, J. R. Long, *Chem. Sci.* **2010**, *1*, 184.
[34] A. L. Spek, *Acta Crystallogr. Sect. D* **2009**, *65*, 148–155.
[35] L. Silvester, J.-F. Lamonier, C. Lamonier, M. Capron, R.-N. Vannier, A.-S. Mamede, F. Dumeignil, *ChemCatChem* **2017**, *9*, 2250–2261.
[36] D. Dubbeldam, S. Calero, T. J. Vlugt, *Mol. Simul.* **2018**, *44*, 653–676.
[37] L. Sarkisov, R. Bueno-Perez, M. Sutharson, D. Fairen-Jimenez, *Chem. Mater.* **2020**, *32*, 9849–9867.
[38] G. Sastre, J. van den Bergh, F. Kapteijn, D. Denysenko, D. Volkmer, *Dalton Trans.* **2014**, *43*, 9612–9619.
[39] S. R. Batten, N. R. Champness, X.-M. Chen, J. Garcia-Martinez, S. Kitagawa, L. Öhrström, M. O'Keeffe, M. Paik Suh, J. Reedijk, *Pure Appl. Chem.* **2013**, *85*, 1715–1724.
[40] G. S. Rushbrooke, P. J. Wood, *Mol. Phys.* **1958**, *1*, 257–283.
[41] M. E. Lines, *J. Phys. Chem. Solids* **1970**, *31*, 101–116.
[42] N. F. Chilton, R. P. Anderson, L. D. Turner, A. Soncini, K. S. Murray, *J. Comb. Chem.* **2013**, *34*, 1164–1175.
[43] T. W. Werner, S. Reschke, H. Bunzen, H.-A. K. von Nidda, J. Deisenhofer, A. Loidl, D. Volkmer, *Inorg. Chem.* **2016**, *55*, 1053–1060.
[44] SAINT; Bruker Analytical X-Ray Systems, Inc., Madison, WI, **2015**..
[45] L. Krause, R. Herbst-Irmer, G. M. Sheldrick, D. Stalke, *J. Appl. Crystallogr.* **2015**, *48*, 3–10.
[46] G. M. Sheldrick, *Acta Crystallogr. Sect. A* **2015**, *71*, 3–8.
[47] G. M. Sheldrick, *Acta Crystallogr. Sect. C* **2015**, *71*, 3–8.
[48] D. Kratzert, I. Krossing, *J. Appl. Crystallogr.* **2018**, *51*, 928–934.

Manuscript received: April 16, 2022
Revised manuscript received: June 8, 2022
Accepted manuscript online: June 17, 2022

Zeitschrift für
anorganische und
allgemeine Chemie

Supporting Information

Synthesis, Thermal Stability and Magnetic Properties of an Interpenetrated Mn(II) Triazolate Coordination Framework

Richard Röß-Ohlenroth, Marcel Hirrle, Maryana Kraft, Andreas Kalytta-Mewes, Anton Jesche, Hans-Albrecht Krug von Nidda, and Dirk Volkmer*

Supporting Information

69451 Weinheim, Germany

Synthesis, Thermal Stability and Magnetic Properties of an interpenetrated Mn(II) Triazolate Coordination Framework

Richard Röß-Ohlenroth, Marcel Hirrle, Maryana Kraft, Andreas Kalytta-Mewes, Anton Jesche, Hans-Albrecht Krug von Nidda, and Dirk Volkmer*

Abstract: Coordination frameworks and metal-organic frameworks built from simple triazole ligands such as 1*H*-1,2,3-triazole (**H-ta**) have recently inspired great interest owing to physical phenomena such as electronic conductivity, phase transitions and their magnetic behavior. In line of our endeavors we report on the solvothermal reaction of $MnCl_2 \cdot 4H_2O$ with **H-ta** ligand in isopropyl alcohol leading to the the novel **CFA-23** (((propan-2-yl)oxidanium)$^+$[$Mn_6Cl_5(ta)_8$]$^-$; CFA-23= Coordination Framework Augsburg University-23) coordination framework. Single-crystal X-ray diffraction (SC-XRD) reveals that it crystallizes in the tetragonal space group $P4_2/nnm$ (134) exhibiting a two-fold interpenetrated framework with the topologies of a ***dia*** net with point (Schläfli) symbol 6^6. The thermal stability of this compound was investigated using variable temperature X-ray powder diffraction and thermogravimetric analysis. The magnetic properties of **CFA-23** differ from a similar non-interpenetrated literature structure of the composition (H[$Mn_6(bta)_8Cl_5$]$\cdot$(H_2O)$_4$) built from 1*H*-1,2,3-benzotriazole, thus, indicating that sterically induced lattice changes might be an adjustment parameter for magnetic properties in such frameworks.

DOI:

Table of Contents

Structure plots

Main Text Paragraph.

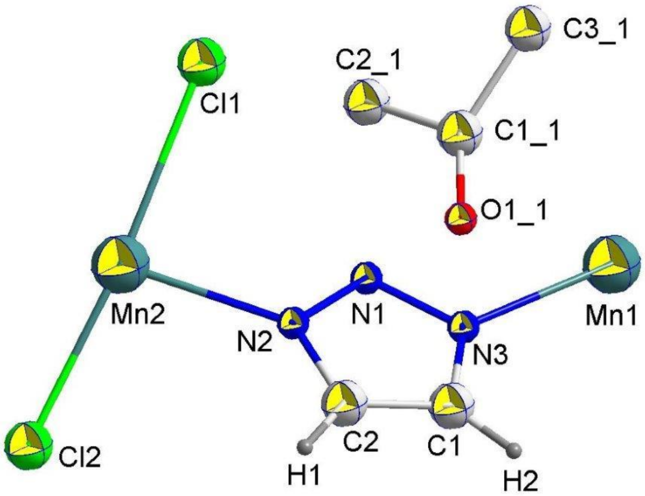

Figure S1. ORTEP-Style plot of the asymmetric unit of **CFA-23** with a 50% probability for the thermal ellipsoids.

SUPPORTING INFORMATION

Optical and SEM micrographs

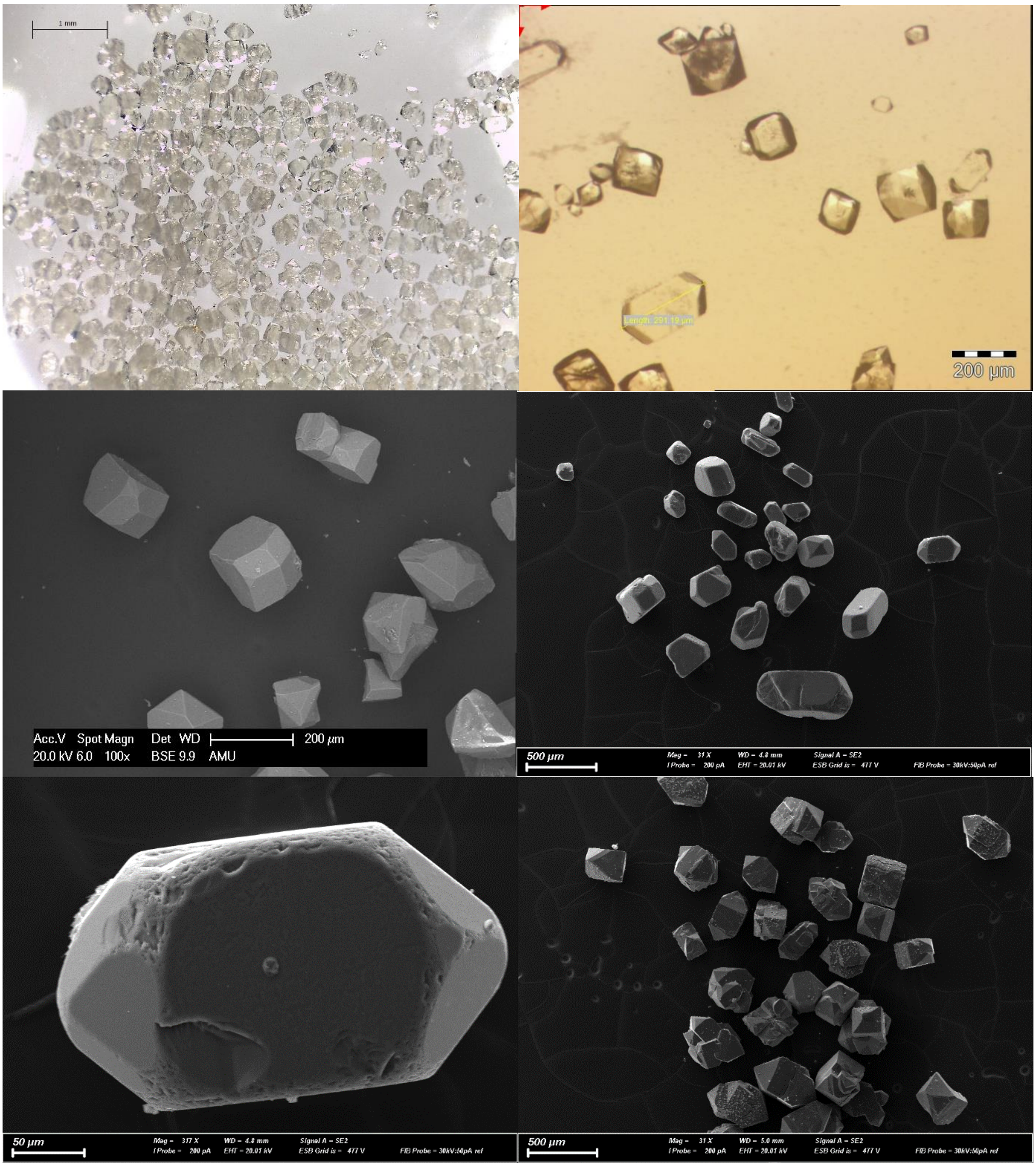

Figure S2. Optical (top) and SEM (bottom) micrographs of **CFA-23** samples.

Le Bail fit of the PXRD

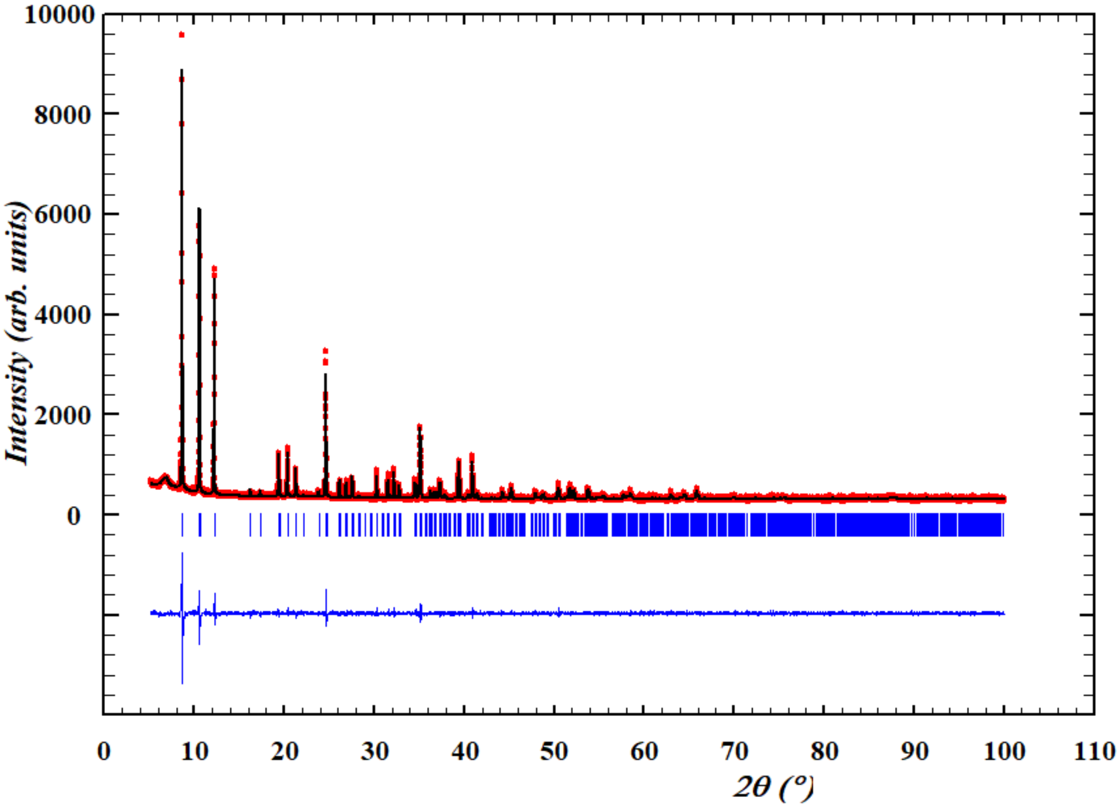

Figure S3. Le Bail fit of the PXRD pattern obtained at 25° C for **CFA-23** verifying the phase purity of the bulk sample

Thermogravimetric analysis

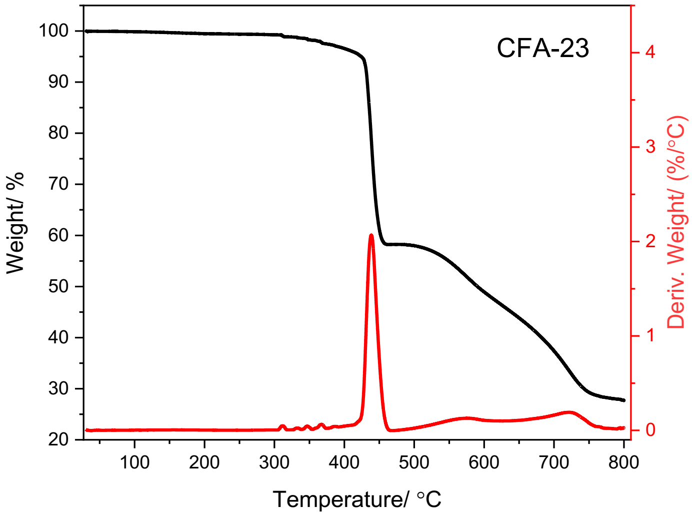

Figure S4. TG-curve of **CFA-23**

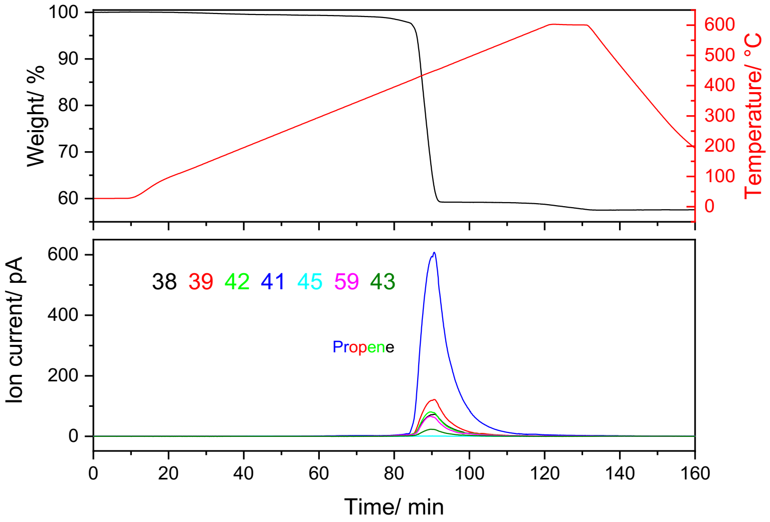

Figure S5. Complete TG-curve and simultaneous MS signals of **CFA-23** showing the complete decomposition, which also indicates propene (42, 41, 39 and 38 m/z) according to the MS signals. However, they could also result from other decomposition products of the **H-ta** ligand.

Gas adsorption

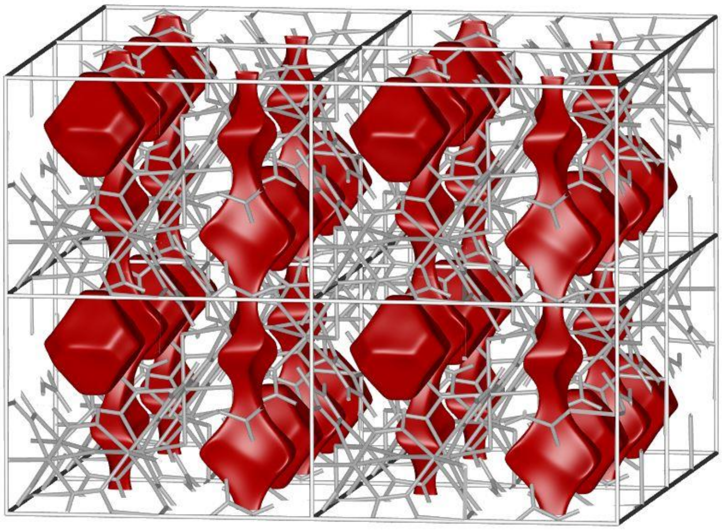

Figure S6. Helium surface plot for **CFA-23** visualized using the iRaspa software [1] and showing the channels in c-direction, as well as the pockets usually filled with the (((propan-2-yl)oxidanium)$^+$ counterions

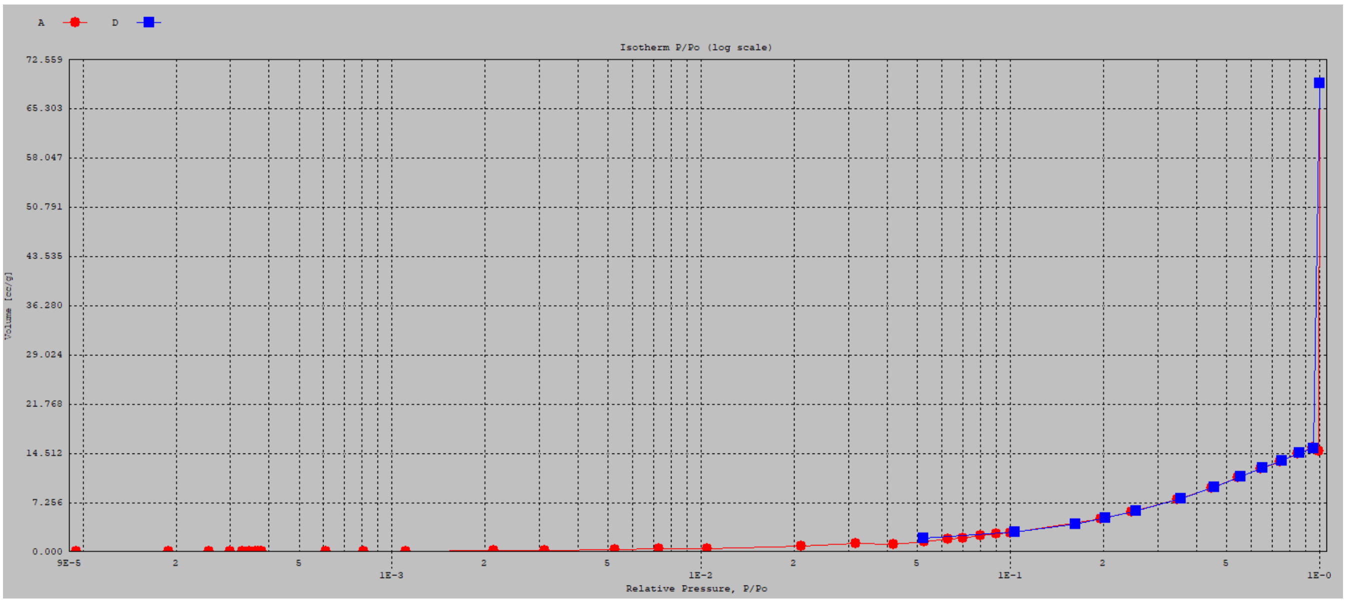

Figure S7. Argon adsorption and desorption isotherms at 77 K for **CFA-23** indicating no gas uptake in the coordination framework

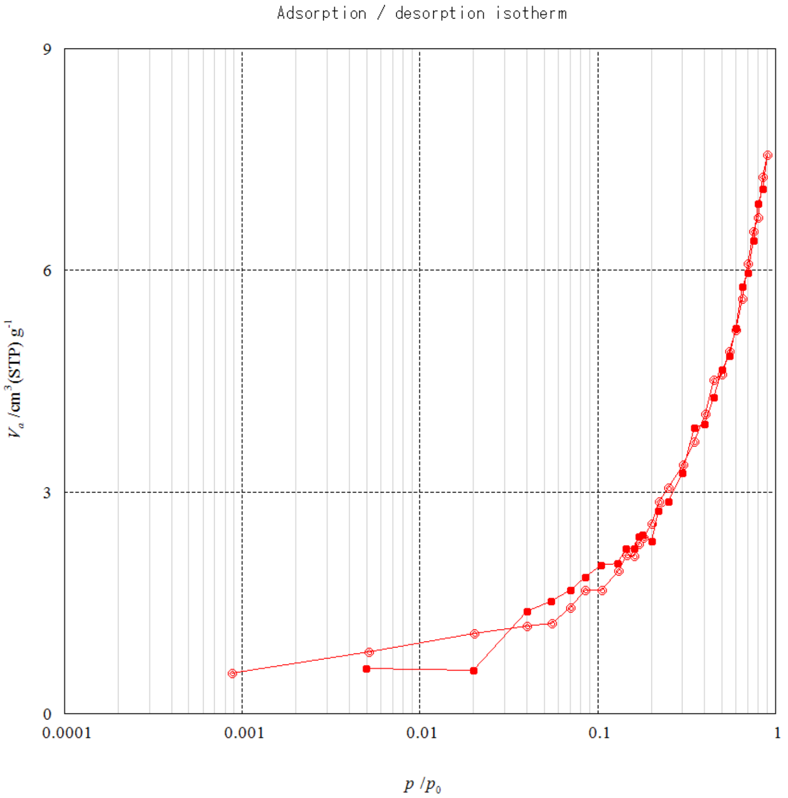

Figure S8. H_2 adsorption and desorption isotherms at 50 K for **CFA-23** indicating no gas uptake in the coordination framework

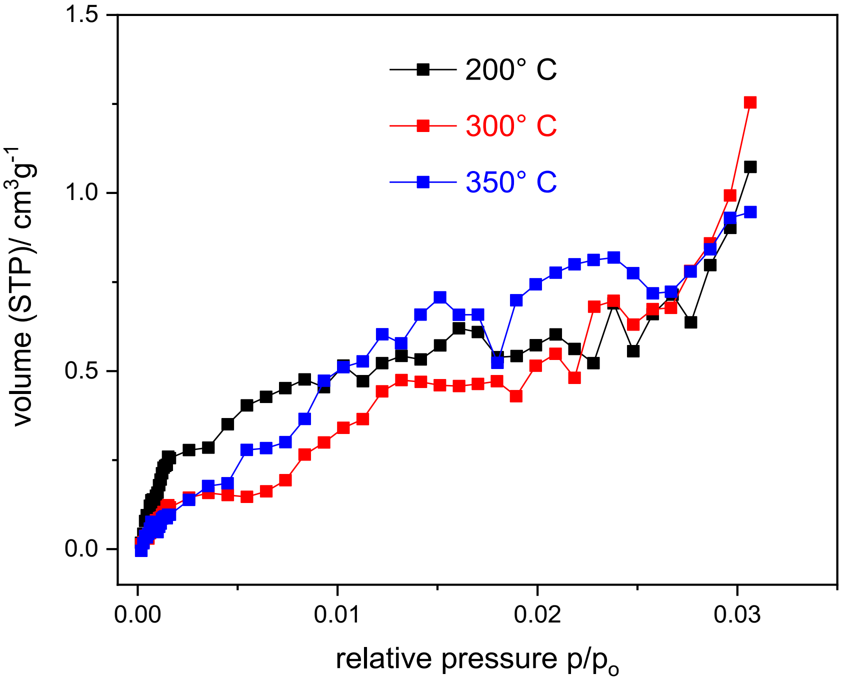

Figure S8. CO_2 adsorption isotherms at 273 K for **CFA-23** activated at temperatures of 200° C, 300° C, and 350° C in vacuum indicating no gas uptake in the coordination framework

IR spectrum

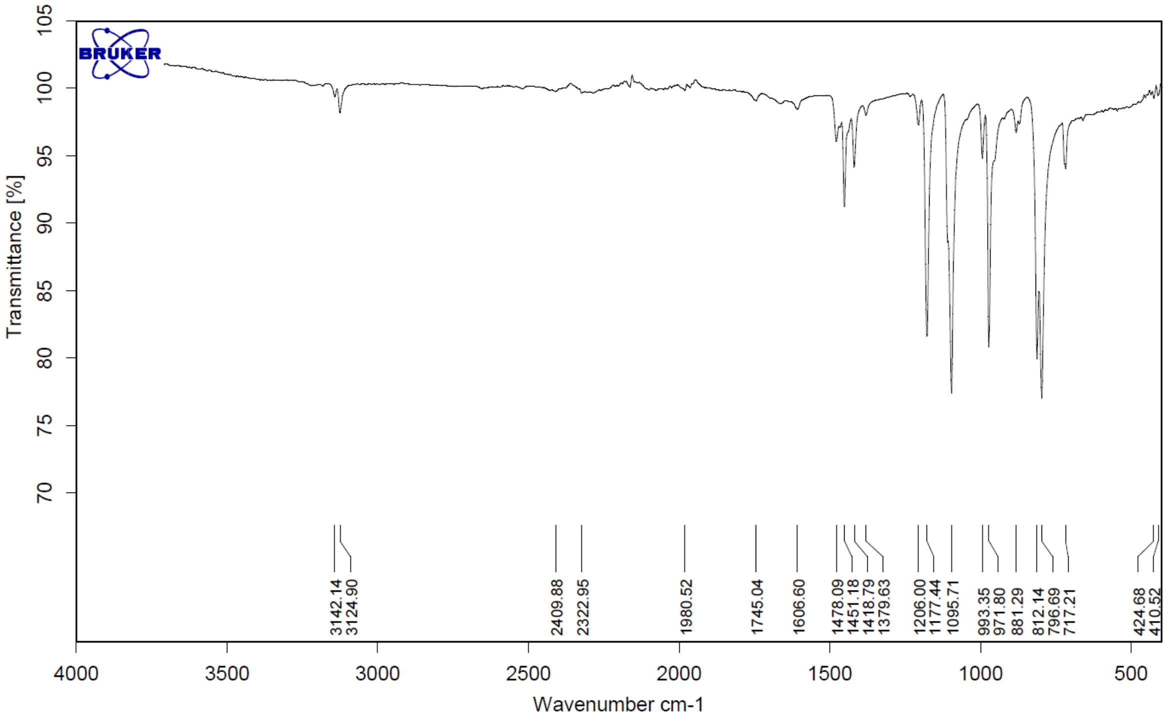

Figure S9. FT-IR (ATR) Spectrum for **CFA-23**

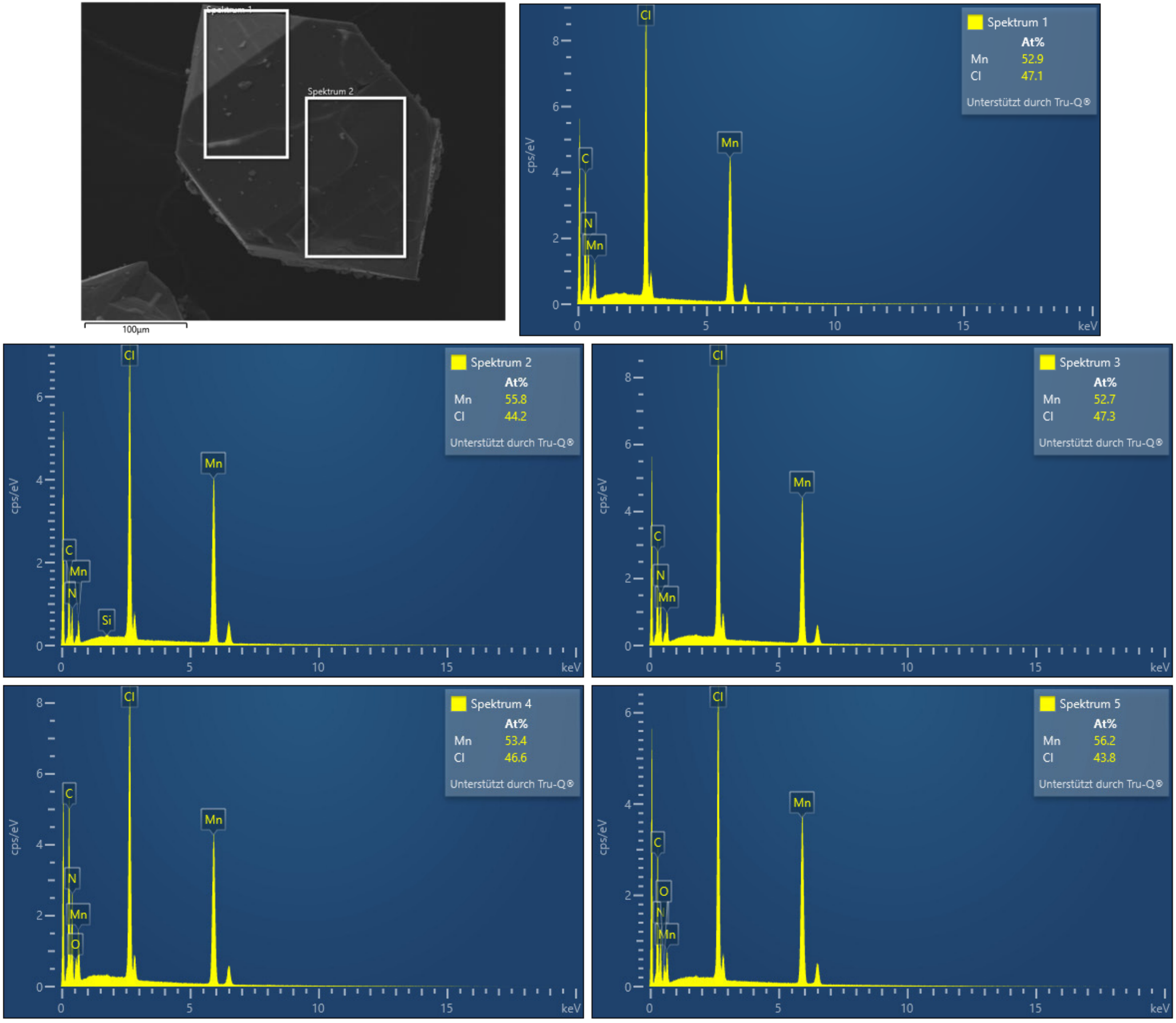

Figure S10. For the determination of the Mn:Cl ratio of **CFA-23** EDX spectra of different crystals were measured in large areas similar to the example ESEM picture to obtain a result, which is representative for the bulk material.

Magnetic measurements

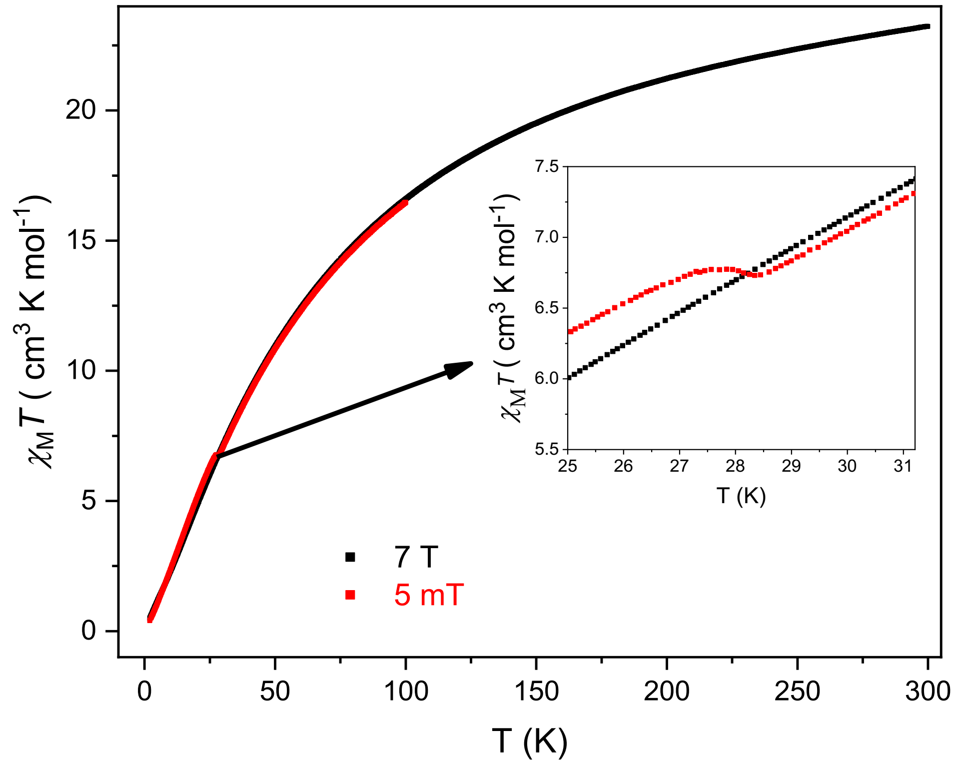

Figure S11. X_M*T over temperature plots per (((propan-2-yl)oxidanium)$^+$[Mn$_6$Cl$_5$(ta)$_8$]$^-$ formula unit of **CFA-23** in 7 T (black) and 5 mT (red) fields (CGS system of units) for the comparison with literature.[2] The inset shows an enlargement of the transition point in the 5 mT curve.

ToposPro analysis results

```
################################
1:mo_RR255_0m_a.res in P4(2)/nnm
################################
Topology for ZB1
--------------------
Atom ZB1 links by bridge ligands and has
Common vertex with R(A-A)
ZB 1 -0.2500 1.2500 0.7500 ( 0 1 1) 11.423A 1
ZB 1 0.7500 1.2500 -0.2500 ( 1 1 0) 11.423A 1
ZB 1 -0.2500 0.2500 -0.2500 ( 0 0 0) 11.423A 1
ZB 1 0.7500 0.2500 0.7500 ( 1 0 1) 11.423A 1
-------------------------
Structural group analysis
-------------------------
-------------------------
Structural group No 1
-------------------------
Structure consists of 3D framework with ZB
There are 2 interpenetrating nets
FIV: Full interpenetration vectors
----------------------------------
[0,0,1] (10.24A)
----------------------------------
PIC: [0,0,2][0,1,1][1,0,1] (PICVR=2)
Zt=2; Zn=1
Class Ia Z=2
Coordination sequences
----------------------
ZB1: 1 2 3 4 5 6 7 8 9 10
Num 4 12 24 42 64 92 124 162 204 252
Cum 5 17 41 83 147 239 363 525 729 981
----------------------
TD10=981
Vertex symbols for selected sublattice
--------------------------------------
ZB1 Point symbol:{6^6}
Extended point symbol:[6(2).6(2).6(2).6(2).6(2).6(2)]
--------------------------------------
Point symbol for net: {6^6}
4-c net; uninodal net
Topological type: dia Diamond; 4/6/c1; sqc6 (topos&RCSR.ttd) {6^6} - VS [6(2).6(2).6(2).6(2).6(2).6(2)] (17494 Elapsed time:
12.31 sec.
```

References

[1] D. Dubbeldam, S. Calero, T. J. Vlugt, *Molecular Simulation* **2018**, *44*, 653–676.

[2] S.-D. Han, J.-P. Zhao, Y.-Q. Chen, S.-J. Liu, X.-H. Miao, T.-L. Hu, X.-H. Bu, *Cryst. Growth Des.* **2014**, *14*, 2–5.

A 208

Inorganic Chemistry

pubs.acs.org/IC Article

Cooperative Large-Hysteresis Spin-Crossover Transition in the Iron(II) Triazolate [Fe(ta)$_2$] Metal–Organic Framework

Maciej Grzywa, Richard Röß-Ohlenroth, Christoph Muschielok, Harald Oberhofer, Artur Błachowski, Jan Żukrowski, Dana Vieweg, Hans-Albrecht Krug von Nidda, and Dirk Volkmer*

Cite This: *Inorg. Chem.* 2020, 59, 10501−10511 Read Online

ACCESS | Metrics & More | Article Recommendations | SI Supporting Information

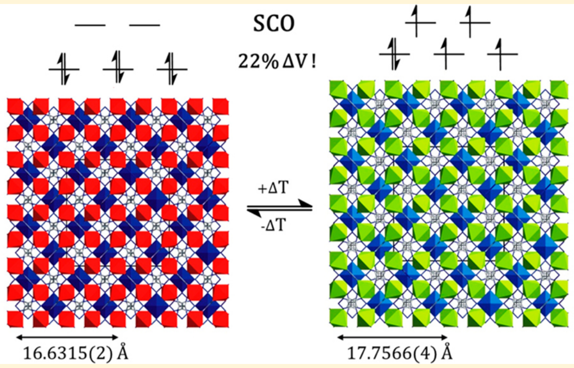

ABSTRACT: The metal−organic framework [Fe(ta)$_2$] (Hta = 1*H*-1,2,3-triazole) containing Fe(II) ions and 1,2,3-triazolate ligands shows a reversible phase transition while retaining the cubic crystal symmetry and space group $Fd\bar{3}m$ (no. 227). The phase transition between room temperature (RT-[Fe(ta)$_2$]; a = 16.6315(2) Å, V = 4600.39(8) Å^3) and high temperature (HT-[Fe(ta)$_2$]; a = 17.7566(4) Å, V = 5598.6(1) Å^3) phases occurs at a temperature above 290 °C, whereas the phase transition between HT- and RT-[Fe(ta)$_2$] starts at a temperature below 210 °C. Both [Fe(ta)$_2$] polymorphs have identical bond topologies, but they differ by a large increase of the unit cell's volume of 22% for HT-[Fe(ta)$_2$]. The compounds are characterized by powder X-ray diffraction, differential scanning calorimetry, and thermogravimetric analyses. Additionally, Mössbauer spectroscopy, magnetic studies, and the electronic structure of both phases are discussed in detail with respect to the spin-crossover transition from the low-spin (RT-[Fe(ta)$_2$]) to the high-spin phase (HT-[Fe(ta)$_2$]).

■ INTRODUCTION

Azoles, poly(azoles), and their derivatives have been used as versatile ligands in constructing coordination polymers.[1] Triazole-based coordination compounds have been extensively investigated since the early 1980s.[2] More than 724 crystal structures containing triazole ligands are found in the Cambridge Structural Database (CSD version 5.41; November 2019).[3] In the past decade, different research groups have spent considerable effort on the synthesis and characterization of coordination frameworks based on triazole ligands and divalent metal ions. Several isostructural MOFs of the type [M(ta)$_2$], composed of M^{II} centers, which are octahedrally coordinated by μ_3-bridging 1,2,3-triazolate ligands, were reported. These materials crystallize in the cubic crystal system within space group $Fd\bar{3}m$ (No. 227). In particular, [Cd(ta)$_2$]·3H$_2$O,[4] [Mn(ta)$_2$], [Co(ta)$_2$], [Zn(ta)$_2$], [Mg(ta)$_2$], and [Fe(ta)$_2$] were investigated.[5] In the first report on [Fe(ta)$_2$], the authors described an intrinsic electrical conductivity of 7.7 × 10^{-5} S/cm,[5] which further increased to 1.0 × 10^{-3} S/cm upon inclusion of I$_2$ into the material by vapor diffusion.[5] Subsequently, this particular framework has become the subject of numerous studies. Sun et al.[6,7] confirmed that within the [M(ta)$_2$] group (M^{II} = Mg, Mn, Fe, Co, Cu, Zn, and Cd), the Fe compound exhibits the highest conductivity. Furthermore, Park et al.[8] have shown that after stochiometric chemical oxidation of the [Fe(ta)$_2$] framework using thianthrenium tetrafluoroborate in MeCN the oxidized materials exhibit drastic enhancements in the electrical conductivity by up to 8 orders of magnitude as compared to stoichiometric [Fe(ta)$_2$], which contains exclusively iron(II) centers. Moreover, [Fe(ta)$_2$(BF$_4$)$_{0.33}$] exhibits an electronic conductivity of 0.3(1) S/cm, which ranks among the highest values for 3D coordination framework materials reported until now. Theoretical aspects of the semiconducting behavior and the electronic structures of [M(ta)$_2$] (M = Zn, Fe, and Ru) compounds have been further explored, based on (hybrid-) density functional theory (DFT) methods.[9]

In our previous work we have shown that in contrast to isostructural compounds of the [M(ta)$_2$]-type, [Cu(ta)$_2$], which contains Jahn−Teller active Cu(II) ions, crystallizes in the tetragonal crystal system.[10] [Cu(ta)$_2$] shows a reversible phase transition from the tetragonal to the cubic crystal system within the temperature range of 120−160 °C. Both [Cu(ta)$_2$] polymorphs have identical bond topologies. α-[Cu(ta)$_2$], as opposed to the high-temperature phase (β-[Cu(ta)$_2$]), shows a strong tetragonal Jahn−Teller distortion of the CuN$_6$(ta) coordination octahedra. Because similar triazolate-based[11−14]

Received: March 17, 2020
Published: July 16, 2020

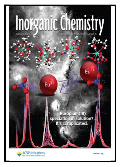

and Hofmann-type[15,16] iron(II)-containing coordination polymers have shown cooperative spin-crossover transitions (SCO), we expected a similar behavior for [Fe(ta)$_2$]. Such spin-crossover compounds have been investigated intensively with respect to their potential usage in memory devices, which demand a wide hysteresis of the SCO.[17−19]

In this paper, we report on our investigations of the wide-hysteresis high-temperature spin-crossover we have discovered in [Fe(ta)$_2$]. This reversible phase transition occurs while retaining the cubic crystal symmetry and space group *Fd*$\bar{3}$*m* (no. 227). The SCO is accompanied by a large increase of the unit cell's volume of nearly 22%. This phase transition is studied by differential scanning calorimetry (DSC) and variable-temperature powder X-ray diffraction (VT-PXRD) measurements. The crystal structures of room-temperature (RT-[Fe(ta)$_2$]) and high-temperature (HT-[Fe(ta)$_2$]) phases were refined by the Rietveld method. The SCO transition was further investigated by Mössbauer spectroscopy and magnetic measurements. In addition, the electronic properties of the low-spin (LS/RT-[Fe(ta)$_2$]) and high-spin (HS/HT-[Fe(ta)$_2$]) phases were studied with all-electron DFT calculations.

■ RESULTS AND DISCUSSION

Synthesis. [Fe(ta)$_2$] was prepared in a manner similar to a previously reported procedure.[5] The pink microcrystalline material was obtained by solvothermal reaction of $FeCl_2$ and 1*H*-1,2,3-triazole in DMF in a large batch. All attempts to obtain a sufficiently sized crystal specimen of [Fe(ta)$_2$] suitable for single-crystal X-ray diffraction study unfortunately failed in our hands although a range of starting materials (different Fe(II) precursors, e.g., iron(II) bromide ($FeBr_2$), iron(II) trifluoroacetate ($Fe(CF_3COO)_2$), iron(II) acetylacetonate ($Fe(acac)_2$), iron(II) acetate ($Fe(OAc)_2$), and ferrocene) and various solvents have been tested (DEF, DMAc, MeOH, EtOH, and propan-2-ol). The largest crystals of [Fe(ta)$_2$] thus obtained was about 1 μm, resulting from a large-batch synthesis (cf. Figure S9).

PXRD and Physisorption Studies. Phase purity of RT-[Fe(ta)$_2$] was confirmed by PXRD measurement under ambient conditions. The experimental PXRD pattern is consistent with the simulated one as gleaned from the PXRD (Figure S3). Compound [Fe(ta)$_2$] exhibits permanent porosity, which was confirmed by argon gas sorption (Figure S4). Prior to measurement, the sample was degassed at 200 °C for 1 h in vacuum. The adsorption data were fitted to the BET equation to give a surface area of 432 m^2g^{-1} (Figure S5), which is in good agreement with data found in the literature (450 m^2g^{-1}).[5]

TGA, VT-PXRD, and DSC Studies. For the characterization of the thermal stability, TGA, VT-PXRD, and DSC experiments were performed. The thermogravimetric profile shown in Figure S2 exhibits the onset of the sample decomposition at ca. 340 °C, although a small weight loss of 2.8% is already observed at this temperature. The VT-PXRD studies have shown that [Fe(ta)$_2$] is stable up to ca. 350 °C. At 400 °C, the intensity of characteristic Bragg peaks decreases, which relates to decomposition of the framework (see Figure 1a). Heating [Fe(ta)$_2$] from RT to 350 °C leads to changes of the powder pattern at 300 °C, and the HT-phase is stable up to ca. 350 °C.

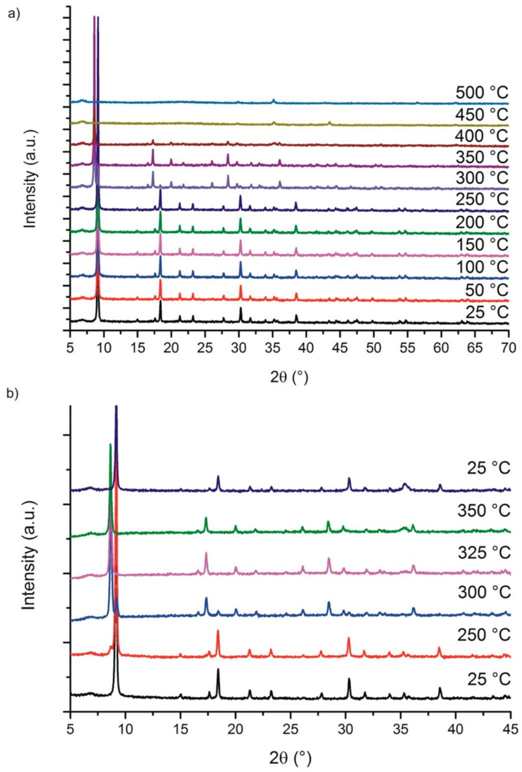

Figure 1. VT-PXRD measurements of [Fe(ta)$_2$] from room temperature to 500 °C demonstrating the stability of the compound. Temperature steps of 50 °C were applied (a). VT-PXRD measurements of [Fe(ta)$_2$] from room temperature to 350 °C and cooled to 25 °C showing a reversible phase transition between RT- HT- and RT-[Fe(ta)$_2$] phases (b).

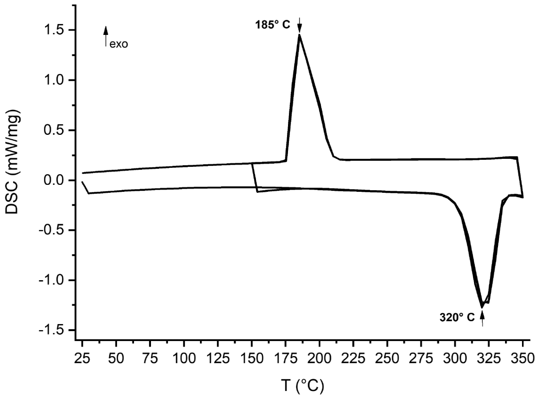

Figure 2. DSC curves for [Fe(ta)$_2$] registered with a scanning rate of 10 C min^{-1} at heating and cooling (three cycles overlaid on top of each other).

Crystallographic Studies. Upon heating the sample of [Fe(ta)$_2$] to $T > 290$ °C, RT-[Fe(ta)$_2$] undergoes a reversible first-order endothermic phase transition, without changes of the crystal system, into HT-[Fe(ta)$_2$], which reverts exothermically to the RT phase upon cooling. Powder X-ray diffraction studies reveal that RT- and HT-[Fe(ta)$_2$] phases crystallize in the cubic crystal system in the space group *Fd*$\bar{3}$*m* (no. 227). The asymmetric unit contains two iron, two nitrogen, one carbon, and one hydrogen atoms. ORTEP-style plots of the asymmetric units of the RT- and HT-[Fe(ta)$_2$] phases with atom labels are shown in Figure S1. As shown in Figure 3, RT- and HT-[Fe(ta)$_2$] comprise coordination units in which the Fe(II) ions are octahedrally coordinated by six tridentate triazolate ligands via nitrogen donor atoms.

https://dx.doi.org/10.1021/acs.inorgchem.0c00814

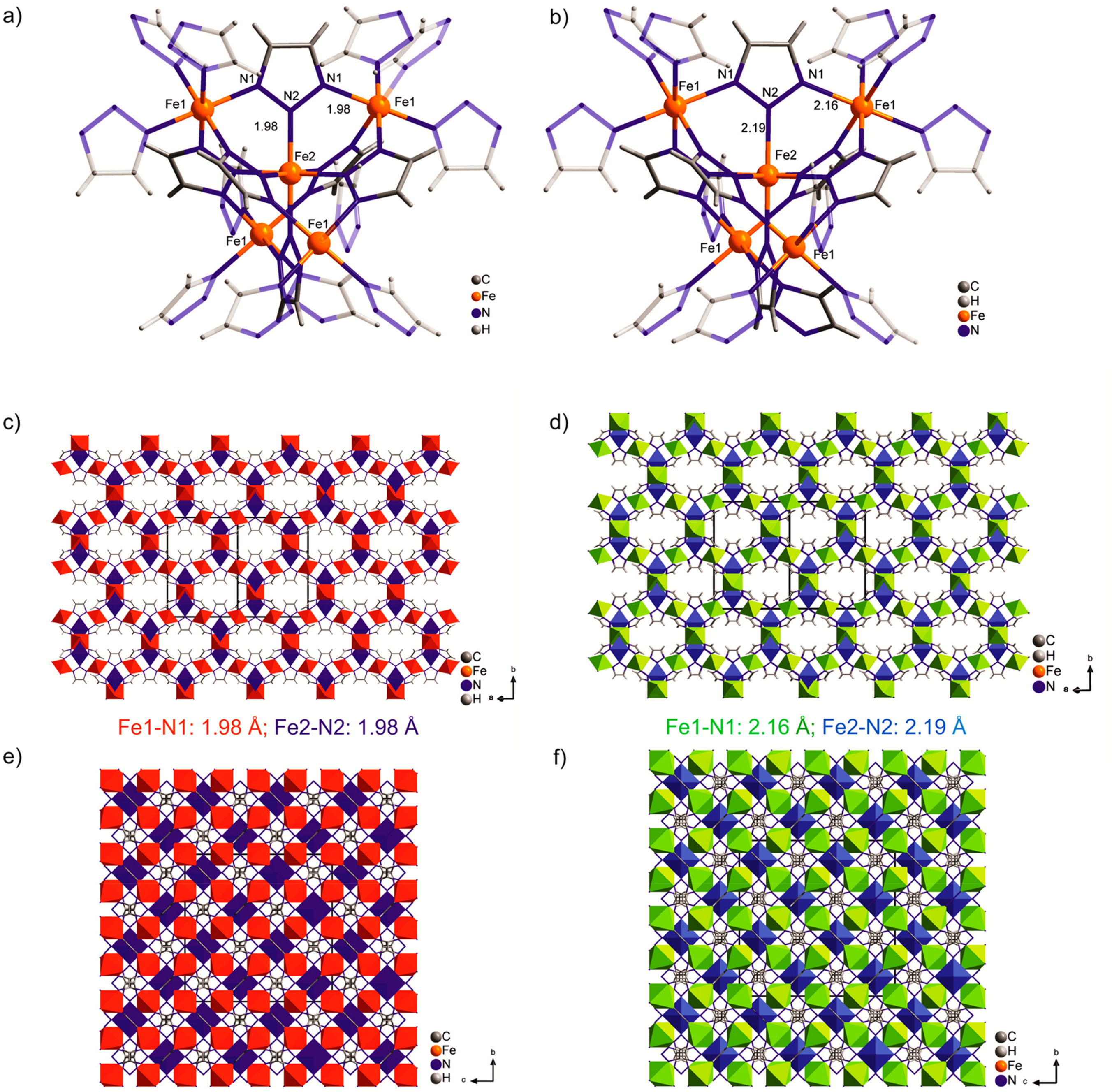

Figure 3. Excerpts of the crystal structures of RT- and HT-[Fe(ta)$_2$] (a) and (b), respectively. Packing diagrams of the crystal structures of RT- and HT-[Fe(ta)$_2$] emphasizing void channels viewed in [110] direction (c, d) and packing diagrams in *a*-direction (e, f). RT-[Fe(ta)$_2$]: red polyhedrons: Fe1{(N1)$_6$}, blue polyhedrons: Fe1{(N2)$_6$}. HT-[Fe(ta)$_2$]: green polyhedrons: Fe1{(N1)$_6$}, blue polyhedrons: Fe1{(N2)$_6$}.

Next, cooling the sample to RT leads to reversible structural changes and the initial powder pattern of the RT phase is retained. Differential scanning calorimetry (DSC) measurements for [Fe(ta)$_2$] were performed in the temperature range of 25−350 °C with a scanning rate of 10 C min^{-1}. Figure 2 shows the temperature dependences of the heat flows (DSC curves) obtained for [Fe(ta)$_2$] on heating and on cooling. Two signals on the DSC curves were registered: During the heating process, an endothermic peak in the temperature range of 290−340 °C is observed, while upon cooling, an exothermic peak between 210−175 °C can be seen. The endothermic maximum relates to the phase transition of the RT to the HT-phase, whereas the exothermic one is connected with the reversible phase transition (i.e., HT to RT-phase).

The [Fe(ta)$_2$] compound consists of Fe$_5$(ta)$_6$ tetrahedra as building units. Four Fe1 ions occupy the vertices of the tetrahedron, while the central Fe2 ion is placed on the geometric center of the coordination unit. In [Fe(ta)$_2$] the Fe(II) ions are placed in FeN$_6$ octahedra. The Fe1 centers, coordinated by N1 atoms are placed at sites with $\bar{3}m$ symmetry, while the Fe2 centers, coordinated by N2 atoms are placed at sites with $\bar{4}3m$ symmetry. The Fe−N distances indicate that the Fe(II) ions are in the LS state. The thermally induced reversible phase transition of [Fe(ta)$_2$] from the RT-phase into the HT-phase leads to the SCO of iron ions, which is connected with a large volume expansion of the unit cell (Δa = 1.13 Å), considerably elongating the distances between Fe—N atoms (Δd = 0.18—0.21 Å). This process runs without changing the crystal system and space group symmetry. Cooling the sample below 210 °C leads to the reversible phase transition between HT-[Fe(ta)$_2$] and RT-[Fe(ta)$_2$] phases. The crystal structure of [Fe(ta)$_2$] contains 3D void channels, which are confined by the hydrogen atoms of the triazolate ligands. Void calculations run with the program SQUEEZE[20] reveal that the initial solvent-accessible void volume is 931.7 Å^3, which is 20.3% of the unit cell volume (4600.4 Å^3 for RT-[Fe(ta)$_2$]), and 1621.6 Å^3, which is 29% of the unit cell volume (5598.6 Å^3 for HT-[Fe(ta)$_2$]), respectively for a probe radius of 1.68 Å, corresponding to the approximate van der Waals radius of argon.[21] A dense packing of iron coordination octahedra is observed in the *a*-, *b*-, and *c*-directions (see Figure 3). The network topology of [Fe(ta)$_2$] can be simplified by considering the imaginary Fe2-centered Fe2(Fe1)$_4$ tetrahedra as 4-connected nodes. The resulting 4-connected diamondlike net can be represented by a 6^6 topological symbol.

Mössbauer Spectroscopy. ^{57}Fe Mössbauer spectra were recorded during heating from 21 °C up to 340 °C and during cooling from 320 °C down to 21 °C for the two absorbers separately, with about 12 h measuring time for each temperature. Additionally, the Mössbauer spectra for another temperature series are shown in Figure S6, and Mössbauer parameters are collected in Table S1. As shown in Figure 4 and Table 1, the main components of spectra taken at RT and upon heating to 280 °C have a shape of narrow pseudosingle line due to the cubic crystallographic structure, which means that both iron sites have the same hyperfine properties (ligand fields) and cannot be distinguished by means of Mössbauer spectroscopy in this temperature range. The spectra have relatively small line widths, small quadrupole splittings of about 0.1 mm/s, and a spectral center shift of δ = 0.38 mm/s (versus α-Fe), typical for a LS divalent iron, although a trivalent iron cannot be excluded on this basis. The obtained Mössbauer parameters at RT are the same as those in literature.[6,8] The same values of the Mössbauer parameters at the beginning and at the end of the measuring series (at 21 °C) verify the full reversibility of the spin-crossover transition. The minor components probably result from some oxidation and subsequent decomposition at high temperature. The spectrum observed at 300 °C in the heating series shows a partial spin transition with about 41% of iron remaining in the previous (LS) state and about 54% of iron transformed to the HS state. Furthermore, one can observe the two subspectra related to Fe(II)-HS with the ratio of about 2:1. It should be kept in mind that the here discussed area contributions of the Mössbauer signals do not necessarily reflect the actual concentrations of the different iron states or sites. Different bond properties of the iron atoms in its lattice position lead to different Mössbauer—Lamb factors (MLF), which give rise to different intensities of the Mössbauer signals. For example, it is known that in the spin-crossover transitions of Fe(II) compounds with strong cooperative interactions, the MLF (and therefore the Mössbauer subspectra areas) could be even up to 20% larger for the LS state than for the HS state.[22] Such a large difference between the MLF for LS and HS iron was also found in Fe[(ta)$_2$] and it was estimated based on the temperature dependence of the relative spectral area. It seems that a significant softening of the lattice occurs at the SCO (see the Supporting Information for more details). However, due to unpredictable error of such estimated MLF change and application of Mössbauer spectroscopy to obtain mainly qualitative evidence about the SCO, in this study the area contributions of the Mössbauer spectral components are shown and discussed without correction for the different values of the MLF.

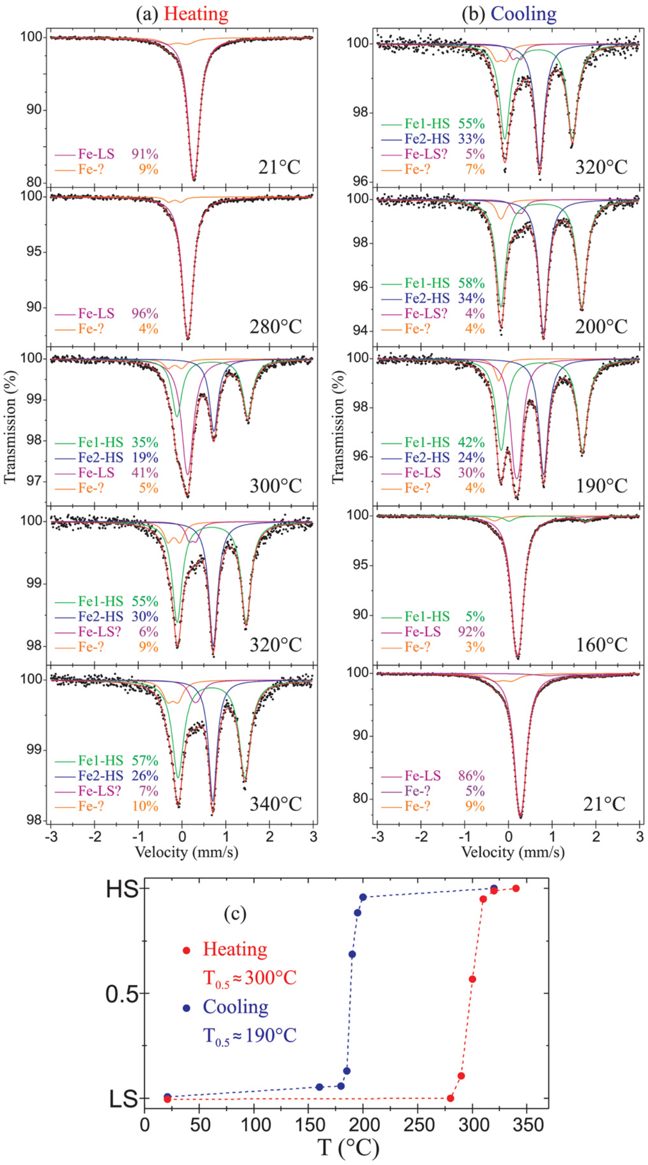

Figure 4. ^{57}Fe Mössbauer spectra for the [Fe(ta)$_2$] versus temperature series of heating (a) and cooling (b). The measurements were made for two absorbers individually for both series. The contributions of unknown Fe impurities, probably oxidation and/or decomposition products of the Fe(ta)$_2$ are shown with a question mark. (c) Sketch of the SCO thermal hysteresis for the Fe(ta)$_2$ based on the Mössbauer results.

The spectra at 320 and 340 °C in the heating series show the almost-full transition of iron to the HS state and some traces of Fe(II)-LS (probably high temperature decomposition product) and unidentified Fe impurity. The ratio of the two Fe(II)-HS signals remains about 2:1, and at first glance these subspectra

Table 1. ^{57}Fe Mössbauer Parameters for the Spectra Shown in Figure 4

T (°C)	Fe spin state	A (%)[a]	δ (mm/s)[b]	Δ (mm/s)[c]	Γ (mm/s)[d]
		Heating			
21	Fe−LS	91	0.38	0.09	0.14
	Fe-?	9	0.02	0.43	0.33
280	Fe−LS	96	0.24	0.08	0.14
	Fe−?	4	−0.06	0.28	0.10
300	Fe_1−HS	35	0.80	1.62	0.17
	Fe_2−HS	19	0.84		0.13
	Fe−LS	41	0.24	0.07	0.19
	Fe−?	5	−0.05	0.31	0.14
320	Fe_1−HS	55	0.79	1.58	0.17
	Fe_2−HS	30	0.82		0.14
	Fe−LS?	6	0.35	0.16	0.11
	Fe−?	9	−0.08	0.27	0.14
340	Fe_1−HS	57	0.78	1.53	0.21
	Fe_2−HS	26	0.81		0.13
	Fe−LS?	7	0.42	0.11	0.19
	Fe−?	10	−0.10	0.24	0.18
		Cooling			
320	Fe_1−HS	55	0.80	1.55	0.18
	Fe_2−HS	33	0.83		0.15
	Fe−LS?	5	0.30	0.19	0.11
	Fe−?	7	−0.06	0.20	0.15
200	Fe_1−HS	58	0.86	1.85	0.17
	Fe_2−HS	34	0.91		0.15
	Fe−LS?	4	0.35	0.15	0.11
	Fe−?	4	−0.06	0.07	0.11
190	Fe_1−HS	42	0.87	1.86	0.18
	Fe_2−HS	24	0.92		0.15
	Fe−LS	30	0.30	0.11	0.14
	Fe−?	4	−0.11	0.01	0.11
160	Fe_1−HS	5	1.00	1.76	0.18
	Fe−LS	92	0.32	0.11	0.15
	Fe−?	3	−0.21	0.07	0.17
21	Fe−LS	86	0.38	0.10	0.15
	Fe−?	5	1.59	1.15	0.67
	Fe−?	9	−0.01	0.37	0.32

[a] A (%) = relative contribution (subspectrum area). [b] δ (mm/s) = spectral center shift versus room temperature α-Fe. [c] Δ (mm/s) = quadrupole splitting. [d] Γ (mm/s) = absorber line-width (within transmission integral approach). Errors for all values are of the order of unity for the last digit shown.

could be interpreted as related to Fe1-HS and Fe2-HS atoms according to the crystal structure of [Fe(ta)$_2$] comprising two inequivalent iron sites. The Mössbauer parameters for Fe1-HS and Fe2-HS show almost the same spectral shift of about 0.8 mm/s at the highest temperatures which means that the electron charge density on iron nuclei is almost the same for Fe1 and Fe2 and that both iron are definitely in the divalent HS state. In contrast, the Fe1-HS subspectrum has a quadrupole splitting of about 1.5 mm/s due to a large electric field gradient (EFG) typical for the HS divalent iron. Surprisingly for the Fe2-HS subspectrum, quadrupole splitting is not observed, so it looks like that there is no EFG. This leads to the question: Why is there an unusual single-line Mössbauer spectrum for the HS divalent iron? It is known that the electric field gradient (EFG) is composed of two contributions: (1) the valence electron contribution, which arises from the anisotropic (noncubic) electron distribution in the valence shell of the Fe atoms (anisotropic electron population in the molecular orbitals of the metal centers in the ligand field theory) and (2) the lattice contribution, which arises from a noncubic lattice surrounding. The valence electron contribution for the Fe(II)-HS compounds is generally large, but it could be reduced by lattice contribution because of the opposite signs of the two components. Thus, the lack of EFG for the Fe2-HS could be explained in the following two ways: (1) There is a large lattice contribution to the EFG (large deviation from cubic symmetry) with a value comparable to the valence electron contribution and finally both contributions subtract and null EFG is observed. (2) There is neither the lattice contribution nor the valence electron contribution. The first scenario could be excluded due to the cubic crystallographic symmetry of the Fe(ta)$_2$. The second scenario, with null valence electron contribution to the EFG for the Fe(II)-HS is unusual (or even unknown to our knowledge) for Fe(II)-MOF compounds. According to ligand field theory for the octahedron with O_h symmetry there is a quintet $^5T_2$ ground state with five degenerate orbitals that split into e_g and t_{2g} orbitals with the six electrons of the d^6 configuration of Fe(II) accommodated according to Hund's rule of maximum spin multiplicity. The null EFG could emerge if the four t_{2g} electrons would be uniformly distributed over the three degenerate orbitals of the cubic subgroup and thus preventing the observation of a splitting due to a Jahn−Teller effect, which would lead to distortion of the octahedron. The lack of the EFG suggests that the Fe2 site keeps the O_h symmetry in the HS state with lack of a Jahn−Teller distortion at least in the static case of this effect. It should be kept in mind that the Mössbauer signal is measured in the time window of the excited resonant nuclear level lifetime and the nuclear quadrupole moment precession period (~100 and ~10 ns for ^{57}Fe, respectively) and for the rapid oscillations of bonds the EFG could be time-averaged to a zero value. Such effect has been proposed as the reason for the unusual single-line Mössbauer spectrum with null EFG for Fe(II)-HS in the hexaammine ferrous complexes containing the $[Fe(NH_3)_6]^{2+}$ cation.[23,24]

Thus, a possible answer to the raised question may be a temperature-dependent dynamic effect such as the dynamic Jahn−Teller distortion with the rapid inversions of the t_{2g} orbitals. The consequence of this is the uncertainty of assignation of the Fe1-HS and Fe2-HS subspectra seen by the Mössbauer spectroscopy to the two inequivalent crystallographic iron sites in the [Fe(ta)$_2$] (see the Supporting Information for more details).

The Mössbauer spectra in the cooling series show the HS state of Fe(II) down to about 200 °C confirming the wide temperature hysteresis of the SCO transition. The quadrupole splitting Δ for the Fe1-HS subspectrum increases with decreasing temperature from 1.55 mm/s at 320 °C to 1.85 mm/s at 200 °C. This phenomenon is known as a result of temperature-dependent population of the valence orbitals, i.e., low-lying excited electron levels depopulate on lowering of the temperature, thereby enforcing the deviation of the charge distribution from cubic symmetry and increasing the valence electron contribution to the EFG. However, the Fe2-HS subspectrum remains a narrow single line without any quadrupole splitting. The spectrum at 190 °C upon cooling shows partial spin transition with about 66% of iron remaining in previous HS state and about 30% of iron transformed to the LS state. At 160 °C, only traces of Fe(II)-HS are still visible, but finally the spectrum at 21 °C shows the LS iron (with some traces of impurity and probably decomposition product). The fact that the same values of the Mössbauer parameters (at 21 °C) assigned to LS-Fe(II) are retained after a full heating and cooling cycle confirms the full reversibility of the SCO transition.

Additionally, ^{57}Fe Mössbauer spectra of the [Fe(ta)$_2$] were recorded in a liquid nitrogen cryostat from −196 to 22 °C. The pseudosingle line with small and constant quadrupole splitting of about 0.1 mm/s for the LS-Fe(II) was observed for all these temperatures with spectral center shift δ (including temperature-dependent second-order Doppler shift) shown in Figure 5. A relatively very high value of the Debye temperature Θ_D = 487(5) °C calculated on this basis indicates the large rigidity of the LS iron bindings in the [Fe(ta)$_2$]. Such a high value of Θ_D is rather typical for metallic systems than for metal−organic complexes, but it should be kept in mind that some lattice softening occurs at the SCO as seen by the MLF change (see the Supporting Information for more details).

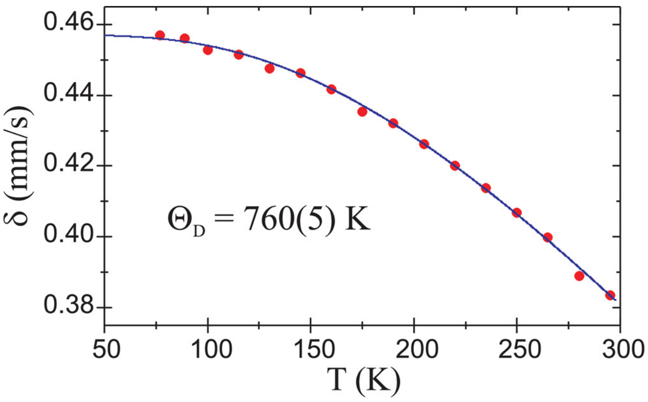

Figure 5. Debye temperature Θ_D = 487(5) °C for the [Fe(ta)$_2$] in LS state calculated from the low-temperature dependence of the ^{57}Fe Mössbauer spectral center shift δ. The solid line represents the best-fit to the experimental data in terms of the Debye model for the phonon spectrum.

Magnetic Susceptibility. Figure 6 shows the temperature dependence of the molar magnetic susceptibility of [Fe(ta)$_2$] above room temperature in a $\chi_M T$ plot. With $\chi_M T$ = 1 emu K/mol, the susceptibility at room temperature is higher than expected for a pure Fe(II) LS (S = 0) compound, but still significantly lower as if all Fe(II) ions were already in the HS (S = 2) state, i.e., at $\chi_M T$ = 9 emu K/mol indicated as dashed line. Similar observations are described in literature, were material defects, introduced by grinding or fast precipitation, are shown to increase the susceptibility of the LS phase.[25−28] This observation further confirms the Mössbauer data, showing mainly LS iron(II) and some unknown impurities. Upon heating from room temperature, the $\chi_M T$ value of [Fe(ta)$_2$] significantly increases between 280 and 297 °C up to 7 emu K/mol. Subsequently, on cooling, the $\chi_M T$ value first reaches a plateau and then rapidly decreases again between 200 and 180 °C down to about 2 emu K/mol, not completely closing the hysteresis loop.

This irreversible increase of the susceptibility, while passing the hysteresis loop up and down, can be attributed to the formation of small amounts of a ferromagnetic impurity. Note that heating the sample above 297 °C gave rise to much higher irreversible ferromagnetic contributions. For this reason, it was not possible to obtain reliable susceptibility data at higher temperatures. Nevertheless, the temperature hysteresis observable in the present data is in fair agreement with the results of DSC measurements and of Mössbauer spectroscopy. The increase of the susceptibility upon heating above 280 °C is the clear fingerprint of the LS to HS transition of the Fe ions. On cooling below 200 °C they return to the LS state. Due to the fact, that we approached the LS to HS transition only carefully from below, the spin cross over is not complete but only partially realized.

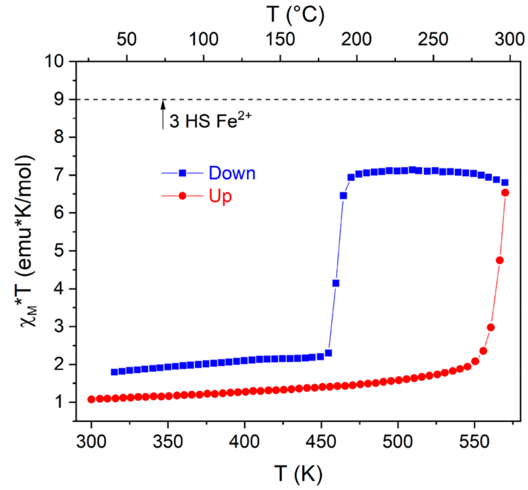

Figure 6. Temperature dependence of the molar magnetic susceptibility of [Fe(ta)$_2$] in $\chi_M T$ representation taken on increasing (red circles) and decreasing (blue squares) temperature based on the $Fe_3C_{12}H_{12}N_{18}$ sum formula.

We also investigated the low-temperature regime of the magnetic susceptibility down to helium temperature (Figure S10). For the Fe^{2+} LS (S = 0) state one would expect an approximately temperature-independent van Vleck type contribution from the low-lying excited states. Indeed, the data exhibit such a contribution of the order of 10^{-3} emu/mol, but in addition, a Curie contribution shows up, very similar to that of [Fe(ta)$_2$(BF$_4$)$_x$], where oxidized samples ($x > 0$) contain a certain amount of Fe^{3+} giving rise to mixed valence, electrical conductivity, and nonzero spin.[8] This idea is supported by the observation that in [Fe(ta)$_2$] the strength of this contribution significantly depends on the preparation route. For the present sample, the obtained Curie constant would correspond to 6.6% of Fe^{3+} (spin S = 5/2, g = 2). Moreover, our preliminary electron spin resonance measurements detect resonance signals typical for trivalent iron. However, deeper systematic magnetic investigations are needed to unravel the origin and influences on the magnetic susceptibility of the LS [Fe(ta)$_2$].

DFT Studies of LS- and HS-[Fe(ta)]$_2$. We model the observed RT- and HT-phases of [Fe(ta)$_2$] using optimized primitive unit cells of the compound. To distinguish them from the observed-phases, we call them the LS structure which models the RT-phase and two HS structures which model possible spin states in the HT-phase.

A standard DFT calculation without any spin constraints yields the LS structure with a total spin moment of zero with respect to the cell; all formal Fe(II) ions individually assume a LS state. For the HS structures, we therefore use spin constraints. They are chosen such that each iron center assumes a HS state. The two structures we study then only differ in the alignment of the individual spin moments within

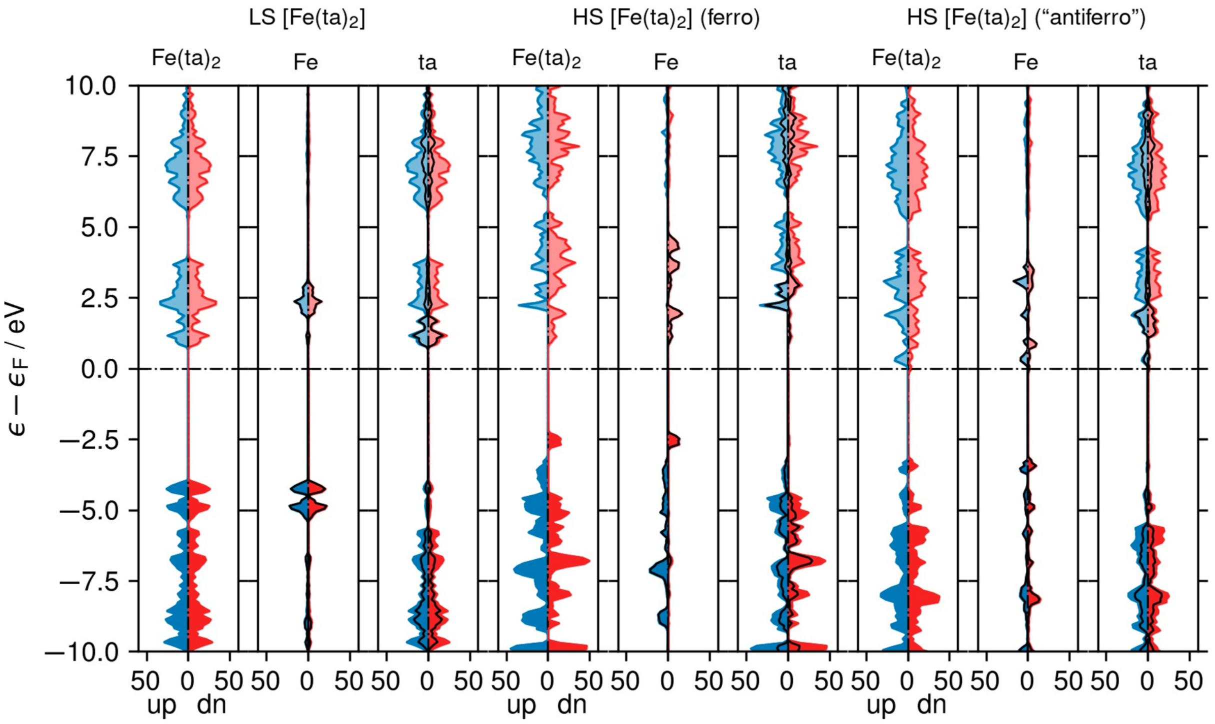

Figure 7. Total DOS and pDOS of $[Fe(ta)_2]$. For the LS-phase (left), the HS-phase in the ferromagnetic configuration (middle) and the HS-phase in the "antiferromagnetic" configuration (right). On each vertical axis, the corresponding (partial) density of states for each spin channel, up (up) and down (dn) respectively, is shown. The black lines show either the pDOS for the Fe d-states or the N p-states, respectively. The energy zero on the y axis is set to the Fermi level which FHI-aims adjusts such that the number of electron states equals the number of hole states.

the unit cell. This way, we can prepare both a "ferromagnetically" ordered primitive $[Fe(ta)_2]$ cell in which all HS Fe(II) moments are aligned and multiple "antiferromagnetically" ordered cells, in which three of the iron centers have antiparallel spin moments. Of the latter structures, we focus on a single, representative one here (see the Supporting Information for a sketch of the chosen spin structure).

The LS structure gives an approximation of the definite ground-state of $[Fe(ta)_2]$ and the "ferromagnetic" HS structure gives an upper boundary to the spin effects observed in the HT-phase. Thus, we concentrated our investigation mostly on these two structures, omitting an in-detail study of the "antiferromagnetically" ordered ones. For the LS structure, the Fe centers are not distinguishable by their spin as each center shows a total spin moment of zero. By symmetry we can distinguish the central iron ions of the cluster (Fe1) from the ones on the vertices (Fe2), which tetrahedrally surround the central iron ion. The members of each group of iron centers are indistinguishable among themselves based on Mulliken charges. This behavior is reflected in the density of states (DOS) of the LS structure which shows symmetric spin channel data (Figure 7).

In the HS structure, the individual iron centers of the ”ferromagnetic" structure show a spin moment of approximately 4, as obtained through Mulliken charge analysis. Structurally, the HS configuration shows a severely dilated cell ($a = b = c = 1.25$ nm for the HS ferromagenetic configuration and $a = b = c = 1.24$ nm for the antiferromagentic one) compared to the LS ground state ($a = b = c = 1.17$ nm). This comes at a cost of the HS structure being in total 2.79 eV (0.47 eV per metal center in the simulation cell) higher in energy than the LS state. We note that our approach ensures that the HS structure is an energy minimum for the HS electronic structure. The DOS plots of the different spin channels are not congruent, indicating the HS configuration of the Fe centers (Figure 7). From the projected DOS (pDOS), we see that both valence and conduction band edges in the HS state predominantly consist of metal d states, as already observed for similar HS-triazolates by Sun and co-workers.[6]

When considering the "antiferromagnetically" ordered HS structure, the DFT converges to a configuration with three HS moments with $N_{\mathrm{up}} - N_{\mathrm{down}} \approx +4$ and three HS moments with $N_{\mathrm{up}} - N_{\mathrm{down}} \approx -4$ on the six iron centers in the cell (cf. Figures 7 and S11). Energetically, this structure is almost degenerate with respect to the "ferromagnetically" ordered all-HS structure discussed before, with an energy difference to the LS structure of 2.81 eV. Accounting for the complexity of the observed electronic states, we validated our results for all three spin-states using the CRYSTAL code with set symmetry constraints to rule out any artifacts in the symmetry unconstrained FHI-aims results. Both codes yielded comparable band gaps and DOSs, which is why we only show FHI-aims results here.

■ CONCLUSIONS

The high-temperature phase transition of $[Fe(ta)_2]$ was investigated and characterized in detail. VT-PXRD and DSC measurements clearly showed the occurrence of a reversible first-order endothermic-phase transition upon heating above 290 °C, which relaxes exothermically into the initial phase after cooling below 216 °C. The structures of the RT- and HT-phases were refined by the Rietveld method and show no change of the cubic crystal system and the $Fd\bar{3}m$ (No. 227) space group, but they yet have a large increase of the unit cell parameter (RT-$[Fe(ta)_2]$: $a = 16.6315(2)$ Å, $V = 4600.39(8)$ Å^3 and HT-$[Fe(ta)_2]$: $a = 17.7566(4)$ Å, $V = 5598.6(1)$Å^3),

https://dx.doi.org/10.1021/acs.inorgchem.0c00814
Inorg. Chem. 2020, 59, 10501−10511

which causes the materials volume to increase by nearly 22%. The nature of this cooperative-phase transition is attributed to a low to high SCO of the iron centers as revealed by Mössbauer spectroscopy and magnetic susceptibility measurements. LS- and HS-[Fe(ta)$_2$] phases were additionally investigated with regard to their electronic structures, employing DFT methods, the latter clearly indicating an all LS RT-[Fe(ta)$_2$] phase.

On the basis of DSC measurements the temperature range at which the hysteresis of the SCO transition occurs is about 135 °C, while magnetic measurements provides about 106 °C. The temperature range is higher in comparison to the reported in the literature compounds like [FeL(HIm)$_2$] (70 °C; L = diethyl (*E*,*E*)-2,2′-[1,2-phenylenebis(iminomethylidyne)]-bis-[3-oxobutanoate]) or [Fe(pyrazine)[M(CN)$_4$]} (60 °C; M = Pd and Pt).[29−31] Although the transition occurs at high temperature, the porosity of this compound allows for investigation of the influences on the SCO from postsynthetic modifications or interaction with guest molecules similar to reports found in literature.[12,29,32]

■ EXPERIMENTAL SECTION

General Information. Commercially available reagents of analytical grade were used as received without further purification. FeCl$_2$ (99.99%) was purchased from Sigma-Aldrich. 1*H*-1,2,3-Triazole was degassed and stored under argon atmosphere. Fourier transform infrared (FTIR) spectra were recorded with ATR in the range 4000−400 cm^{-1} on a Bruker Equinox 55 FT-IR spectrometer. The following indicators are used to characterize absorption bands: strong (s), medium (m), and weak (w). Elemental analysis was measured with a Vario EL III instrument from Elementar Analysensysteme GmbH. Thermogravimetric analysis (TGA) was performed with a TGA Q500 analyzer in the temperature range of 25−700 °C in flowing nitrogen at a heating rate of 5 °C min^{-1}. Argon adsorption isotherms were measured with a Quantachrome Autosorb-I ASI-CP-8 instrument in the range of $5.00 \times 10^{-5} \leq p/p_0 \leq 1.00$ at −196 °C. Adsorbed gas amounts are given in cm^3 g^{-1} [STP], where STP = 101.3 kPa and 0 °C. Prior to measurements, the sample was heated at 200 °C for 1 h in high vacuum in order to remove rest of occluded solvent molecules. Ambient-temperature PXRD patterns were measured with a Seifert XRD 3003 TT diffractometer equipped with a Meteor 1D detector operated at 40 kV, 40 mA, Cu Kα (λ = 1.54247 Å) with a scan speed of 1 s per step and a step size of 0.02° in 2θ. The VT-PXRD data were collected in the 2θ range of 5−60° with 0.02° steps, with a with an Empyrean (PANalytical) diffractometer equipped with Bragg−Brentano^{HD} mirror, PIXcel^{3D} 2 × 2 detector and XRK 900 reactor chamber. Temperature program between measurements comprised the following: heating rate (0.5 °C s^{-1}), then 10 min isothermal. The patterns were recorded in the 4−50° = 2θ range, with 1 step per 1 s and an angular step width of 0.026° in 2θ. DSC measurements were carried out using NETZSCH DSC 204F1 instrument.

Synthesis. [Fe(ta)$_2$] was synthesized using common Schlenk line techniques under argon atmosphere by a modified procedure similar to literature.[5] FeCl$_2$ (0.02 mol, 2.54 g) was dissolved in 25 mL of anhydrous *N*,*N*-dimethylformamide (DMF) in a 50 mL round-bottomed Schlenk flask under an argon atmosphere in an ultrasonic bath. After FeCl$_2$ was completely dissolved in the DMF, 3.48 mL (0.06 mol, 4.15 g,) of 1*H*-1,2,3-triazole were added to the solution. The solution was heated at 120 °C for 20 h in a Heat-ON attachment and subsequently cooled to room temperature. A pink microcrystalline solid was obtained, centrifuged under argon atmosphere, and washed 3 times with 20 mL of dry DMF. The solvent was exchanged 3 times by immersion and centrifugation in 20 mL of dry MeOH for 3 days. Then the solvent was removed, and the sample was dried under vacuum for 6 h at 200 °C to afford a pink/purple powder (2.12g, 55%). FT-IR: 3153 (w), 1590 (w), 1475 (m), 1274 (w), 1228 (w), 1180 (w), 1127 (s), 1001 (m), 780 (s), 728 (m), 495 (m), 418 (w) (cf. Figure S8). Elemental analysis calcd (%): C 25.02, H 2.11, N 43.78. Found: C 24.39, H 2.42, N 43.32.

PXRD Structure Analysis. A microcrystalline sample was deposited in the hollow of a sample holder of XRK 900 reactor chamber, and the measurements for Rietveld refinement were performed under flowing nitrogen at 25 and 300 °C. Diffraction data were collected in the 2θ range of 5−110 with one step per 6.2 s (at 25 °C) and 3 s (at 300 °C), and an angular step width of 0.026° in 2θ. The structure of [Cd$_3$(ta)$_6$]·6H$_2$O[4] was applied as a starting model for the Rietveld refinement of RT- and HT-[Fe(ta)$_2$] phases. The Rietveld refinement was carried out using the Jana2006 program.[33] Geometric restraints on bond distances for RT-[Fe(ta)$_2$]-were used during the refinement processes. The experimental details and crystal data for RT- and HT-[Fe(ta)$_2$] are listed in Table 2. The final Rietveld refinement plots are presented in Figure 8.

Table 2. Crystal and Experimental Data for RT- and HT-[Fe(ta)$_2$]

	RT-[Fe(ta)$_2$]	HT-[Fe(ta)$_2$]
chemical formula	C$_{12}$ H$_{12}$ Fe$_3$ N$_{18}$	C$_{12}$ H$_{12}$ Fe$_3$ N$_{18}$
formula weight/g mol^{-1}	575.9	575.9
T/°C	25(2)	300(2)
diffractometer	Empyrean	Empyrean
2θ-range/deg, step size	5−110, 0.026	5−110, 0.026
X-ray source, wavelength/Å	Cu Kα, λ = 1.54178	Cu Kα, λ = 1.54178
crystal system	cubic	cubic
space group	$Fd\bar{3}m$ (No. 227)	$Fd\bar{3}m$ (No. 227)
a/Å	16.6315(2)	17.7566(4)
V/Å^3	4600.39(8)	5598.6(1)
Z, density/g cm^{-3}	8, 1.66	8, 1.37
number of observations	3998	3998
R_p	1.46	1.57
R_{wp}	2.14	2.01
R_{Fobs}	6.65	6.05
R_{Fall}	7.46	12.92

Mössbauer Spectroscopy. ^{57}Fe Mössbauer spectra in the transmission mode were obtained applying water-cooled vacuum oven with the boron nitride sample holder and under dynamic vacuum of about 10^{-6} hPa. Temperature stability during about 12 h measuring time for each temperature was about 0.1 °C. The absorbers in case shown on Figure 4 were prepared mixing 20 mg of Fe(ta)$_2$ sample with the B$_4$C fine powder. The diameter of the absorbers was 10 mm. Hence, one had 25 mg/cm^2 absorber thickness of the [Fe(ta)$_2$]. A commercial ^{57}Co(Rh) source with activity of about 25 mCi and the source line width 0.106(5) mm/s derived from the fit of the Mössbauer spectrum of the 10 μm thick α-Fe foil was used. Resonant photons of the 14.41 keV line in ^{57}Fe were counted by the LND Kr-filled proportional detector. Measurements were performed by means of the MsAa-4 Mössbauer spectrometer and data were processed by means of the MOSGRAF software within the transmission integral approximation. All spectral shifts are reported versus room temperature α-Fe.

Magnetization Measurements. The magnetization *M* was measured using a superconducting quantum interference device (SQUID) magnetometer (Quantum Design, MPMS5) working in the temperature range of $-271\ °\text{C} \leq T \leq 427\ °\text{C}$ and in magnetic fields $-5\ \text{T} \leq \mu_0 H \leq 5\ \text{T}$. The temperature dependence of the magnetic susceptibility at a given magnetic field was determined as $\chi = M/H$.

Computational Simulations. For all calculations shown here, we use the all-electron DFT code FHI-aims[34−36] with the standard "light" basis set for each elemental species. The initial structures are obtained by optimizing primitive unit cells, which are generated from experimental PXRD data. For this, the implementation of the BFGS algorithm in FHI-aims with a trust radius of 0.01 eV/Å is used.[37] Furthermore, for all structure relaxations except for the "antiferromagnetic" HS structure, electronic exchange and correlation (XC) are

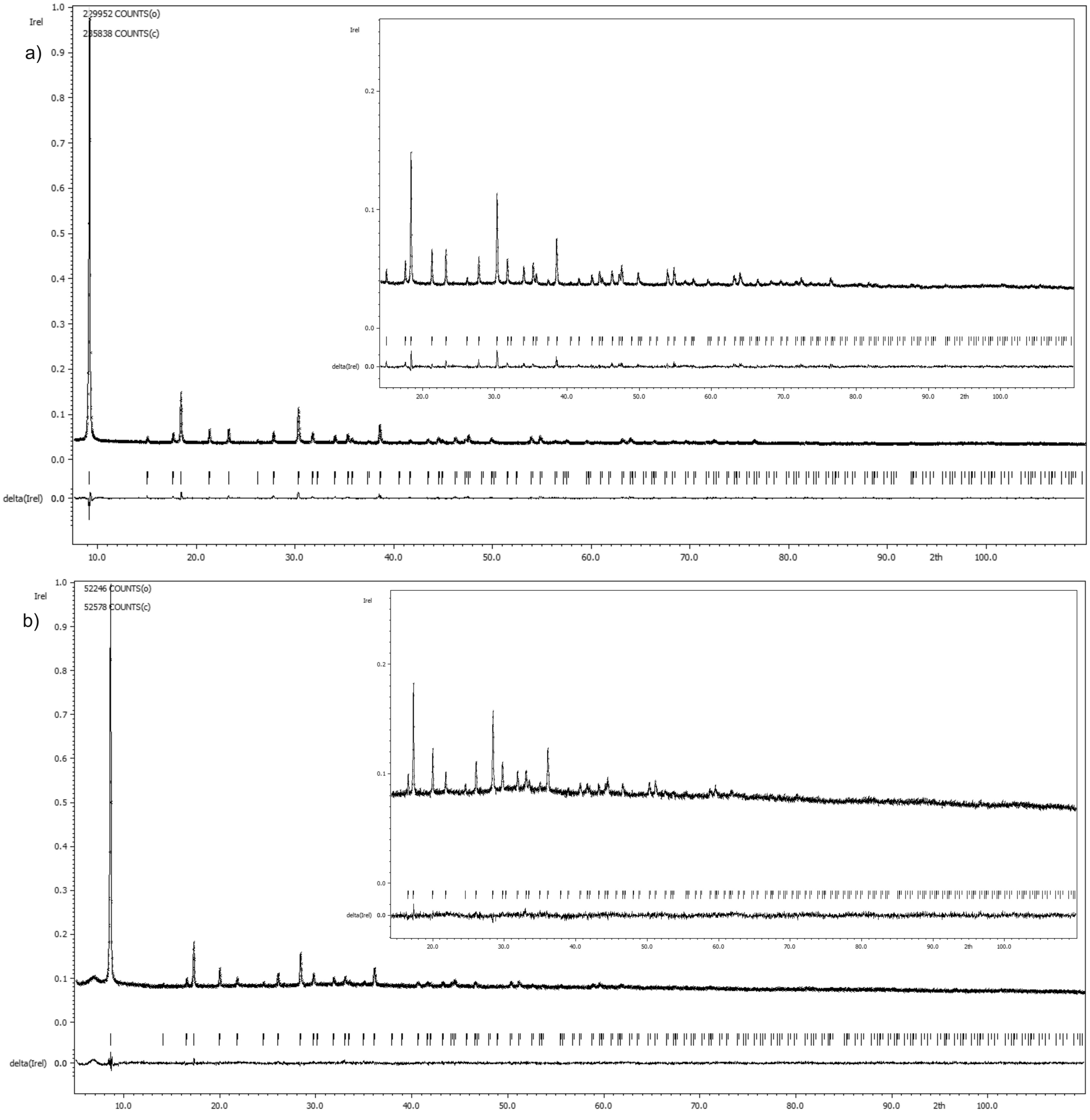

Figure 8. Rietveld refinement plots for RT- and HT-$[Fe(ta)_2]$ (a) and (b), respectively. Dotted and solid lines represent observed and calculated patterns, respectively with peak markers and the difference plot shown at the bottom. PXRD data were collected at 25 °C (a) and 300 °C (b). For clarity, the insets show an expended view in the range 14−110° 2θ.

treated within the generalized gradient approximation (GGA) using the PBE functional and a 2 × 2 × 2 k-point grid.[38] For the optimization of the "antiferromagnetic" HS structure, the PBEsol[39] functional was used due to severe convergence problems when using the PBEsol-optimized structure in the subsequent calculation. All other calculations yielding total energies, the density of states (DOS), and projected DOS (pDOS) are performed modeling XC with the PBEsol0 hybrid functional (this is the PBE0 functional based on PBEsol instead of standard PBE).[40] To generate the "ferromagnetically" ordered HS crystal structure of $[Fe(ta)_2]$, we enforce a total spin moment of 24 throughout the unit cell, corresponding to aligned HS configurations of all six formal Fe(II) ions. After optimization, this constraint is lifted for the hybrid functional calculation to yield a stable HS ground-state. For the "antiferromagnetically" ordered structure of $[Fe(ta)_2]$, the same structure as for the "ferromagnetic" case is used. However, the spin constraints are chosen such that three HS Fe(II) centers are antialigned, i.e., they have a spin moment of −4, resulting in a total spin moment of zero for the unit cell.

■ ASSOCIATED CONTENT

Supporting Information

The Supporting Information is available free of charge at https://pubs.acs.org/doi/10.1021/acs.inorgchem.0c00814.

Asymmetric units, PXRD pattern, Mössbauer spectra, argon adsorption analysis data, IR spectrum, SEM image and low temperature magnetic susceptibility (PDF)

Accession Codes

CCDC 1963572–1963573 contain the supplementary crystallographic data for this paper. These data can be obtained free of charge via www.ccdc.cam.ac.uk/data_request/cif, or by emailing data_request@ccdc.cam.ac.uk, or by contacting The Cambridge Crystallographic Data Centre, 12 Union Road, Cambridge CB2 1EZ, UK; fax: +44 1223 336033.

■ AUTHOR INFORMATION

Corresponding Author

Dirk Volkmer – *Chair of Solid State and Materials Chemistry, Institute of Physics, University of Augsburg, D-86159 Augsburg, Germany;* orcid.org/0000-0002-8105-2157;
Email: dirk.volkmer@physik.uni-augsburg.de

Authors

Maciej Grzywa – *Chair of Solid State and Materials Chemistry, Institute of Physics, University of Augsburg, D-86159 Augsburg, Germany*
Richard Röß-Ohlenroth – *Chair of Solid State and Materials Chemistry, Institute of Physics, University of Augsburg, D-86159 Augsburg, Germany*
Christoph Muschielok – *Theoretical Chemistry, Technische Universität München, D-85747 Garching, Germany*
Harald Oberhofer – *Theoretical Chemistry, Technische Universität München, D-85747 Garching, Germany*
Artur Błachowski – *Institute of Physics, Pedagogical University, 30-084 Kraków, Poland*
Jan Żukrowski – *Academic Center for Materials and Nanotechnology, AGH University of Science and Technology, 30-059 Kraków, Poland*
Dana Vieweg – *Experimental Physics V, Center for Electronic Correlations and Magnetism, Institute of Physics, University of Augsburg, D-86159 Augsburg, Germany*
Hans-Albrecht Krug von Nidda – *Experimental Physics V, Center for Electronic Correlations and Magnetism, Institute of Physics, University of Augsburg, D-86159 Augsburg, Germany*

Complete contact information is available at:
https://pubs.acs.org/10.1021/acs.inorgchem.0c00814

Author Contributions

The manuscript was written through contributions of all authors. All authors have given approval to the final version of the manuscript.

Notes

The authors declare no competing financial interest.

■ ACKNOWLEDGMENTS

Financial support by the Deutsche Forschungsgemeinschaft (DFG) via SPP 1928 COORNETs: Coordination Networks: Building Blocks for Functional Systems is gratefully acknowledged. H.-A.K.v.N. acknowledges the partial support by the DFG via the Transregional Collaborative Research Center TRR 80 "From Electronic Correlations to Functionality" (Augsburg, Munich, Stuttgart)

■ REFERENCES

(1) Aromí, G.; Barrios, L. A.; Roubeau, O.; Gamez, P. Triazoles and tetrazoles: Prime ligands to generate remarkable coordination materials. *Coord. Chem. Rev.* **2011**, *255*, 485–546.

(2) Triazoles 1, 2, 4. In *Chemistry of Heterocyclic Compounds v. 37*; Temple, C., Montgomery, J. A., Eds.; Wiley: New York, 1981.

(3) Groom, C. R.; Bruno, I. J.; Lightfoot, M. P.; Ward, S. C. The Cambridge Structural Database. *Acta Crystallogr., Sect. B: Struct. Sci., Cryst. Eng. Mater.* **2016**, *72*, 171–179.

(4) Zhou, X.-H.; Peng, Y.-H.; Du, X.-D.; Zuo, J.-L.; You, X.-Z. Hydrothermal syntheses and structures of three novel coordination polymers assembled from 1,2,3-triazolate ligands. *CrystEngComm* **2009**, *11*, 1964–1970.

(5) Gándara, F.; Uribe-Romo, F. J.; Britt, D. K.; Furukawa, H.; Lei, L.; Cheng, R.; Duan, X.; O'Keeffe, M.; Yaghi, O. M. Porous, conductive metal-triazolates and their structural elucidation by the charge-flipping method. *Chem. - Eur. J.* **2012**, *18*, 10595–10601.

(6) Sun, L.; Hendon, C. H.; Park, S. S.; Tulchinsky, Y.; Wan, R.; Wang, F.; Walsh, A.; Dincă, M. Is iron unique in promoting electrical conductivity in MOFs? *Chem. Sci.* **2017**, *8*, 4450–4457.

(7) Sun, L.; Campbell, M. G.; Dincă, M. Electrically Conductive Porous Metal-Organic Frameworks. *Angew. Chem., Int. Ed.* **2016**, *55*, 3566–3579.

(8) Park, J. G.; Aubrey, M. L.; Oktawiec, J.; Chakarawet, K.; Darago, L. E.; Grandjean, F.; Long, G. J.; Long, J. R. Charge Delocalization and Bulk Electronic Conductivity in the Mixed-Valence Metal-Organic Framework $Fe(1,2,3\text{-triazolate})_2(BF_4)_x$. *J. Am. Chem. Soc.* **2018**, *140*, 8526–8534.

(9) Muschielok, C.; Oberhofer, H. Aspects of semiconductivity in soft, porous metal-organic framework crystals. *J. Chem. Phys.* **2019**, *151*, 015102.

(10) Grzywa, M.; Denysenko, D.; Hanss, J.; Scheidt, E.-W.; Scherer, W.; Weil, M.; Volkmer, D. CuN_6 Jahn-Teller centers in coordination frameworks comprising fully condensed Kuratowski-type secondary building units: Phase transitions and magneto-structural correlations. *Dalton Trans.* **2012**, *41*, 4239–4248.

(11) Roubeau, O. Triazole-based one-dimensional spin-crossover coordination polymers. *Chem. - Eur. J.* **2012**, *18*, 15230–15244.

(12) Bao, X.; Liu, J.-L.; Leng, J.-D.; Lin, Z.; Tong, M.-L.; Nihei, M.; Oshio, H. Spin crossover versus low-spin behaviour exhibited in 2D and 3D supramolecular isomers of $[Fe^{II}(2,4\text{-bpt})_2]$·Guest. *Chem. - Eur. J.* **2010**, *16*, 7973–7978.

(13) Bao, X.; Guo, P.-H.; Liu, J.-L.; Leng, J.-D.; Tong, M.-L. Crystalline-state cis-to-trans transformation of a two-dimensional spin-crossover system. *Chem. - Eur. J.* **2011**, *17*, 2335–2339.

(14) Bao, X.; Leng, J.-D.; Meng, Z.-S.; Lin, Z.; Tong, M.-L.; Nihei, M.; Oshio, H. Tuning the spin states of two apical iron(II) ions in the trigonal-bipyramidal $[(Fe^{II}((\text{-bpt})_3>_2Fe^{II}_3((\text{-O})]^{2+}$ cations through the choice of anions. *Chem. - Eur. J.* **2010**, *16*, 6169–6174.

(15) Ni, Z.-P.; Liu, J.-L.; Hoque, M. N.; Liu, W.; Li, J.-Y.; Chen, Y.-C.; Tong, M.-L. Recent advances in guest effects on spin-crossover behavior in Hofmann-type metal-organic frameworks. *Coord. Chem. Rev.* **2017**, *335*, 28–43.

(16) Muñoz, M. C.; Real, J. A. Thermo-, piezo-, photo- and chemo-switchable spin crossover iron(II)-metallocyanate based coordination polymers. *Coord. Chem. Rev.* **2011**, *255*, 2068–2093.

(17) Senthil Kumar, K.; Ruben, M. Emerging trends in spin crossover (SCO) based functional materials and devices. *Coord. Chem. Rev.* **2017**, *346*, 176–205.

(18) Kahn, O. Spin-Transition Polymers: From Molecular Materials Toward Memory Devices. *Science* **1998**, *279*, 44–48.

(19) Bao, X.; Guo, P.-H.; Liu, W.; Tucek, J.; Zhang, W.-X.; Leng, J.-D.; Chen, X.-M.; Gural'skiy, I.; Salmon, L.; Bousseksou, A.; Tong, M.-L. Remarkably high-temperature spin transition exhibited by new 2D metal-organic frameworks. *Chem. Sci.* **2012**, *3*, 1629–1633.

(20) Spek, A. L. Structure validation in chemical crystallography. *Acta Crystallogr., Sect. D: Biol. Crystallogr.* **2009**, *65*, 148–155.

(21) *Quantachrome Autosorb*, version 1.56; Quantachrome GmbH & Co. KG: Odelzhausen, Germany, 2009.

(22) Kolnaar, J. J. A.; van Dijk, G.; Kooijman, H.; Spek, A. L.; Ksenofontov, V. G.; Gütlich, P.; Haasnoot, J. G.; Reedijk, J. Synthesis, Structure, Magnetic Behavior, and Mössbauer Spectroscopy of Two New Iron(II) Spin-Transition Compounds with the Ligand 4-Isopropyl-1,2,4-triazole. X-ray Structure of Fe_3(4-isopropyl-1,2,4-triazole)$_6$(H_2O)$_6$(tosylate)$_6$.2H_2O. *Inorg. Chem.* **1997**, *36*, 2433–2440.

(23) Bancroft, G. M.; Mays, M. J.; Prater, B. E. The single line mössbauer spectrum of $[Fe(NH3)_6]^{2+}$. *Chem. Phys. Lett.* **1969**, *4*, 248–250.

(24) Asch, L.; Adloff, J. P.; Friedt, J. M.; Danon, J. Motional effects in the mössbauer spectra of iron(II) hexammines. *Chem. Phys. Lett.* **1970**, *5*, 105–108.

(25) Müller, E. W.; Spiering, H.; Gütlich, P. Spin transition in $[Fe(phen)_2(NCS)_2]$ and $[Fe(bipy)_2(NCS)_2]$: Hysteresis and effect of crystal quality. *Chem. Phys. Lett.* **1982**, *93*, 567–571.

(26) Mueller, E. W.; Spiering, H.; Guetlich, P. Effect of crystal quality on the spin-transition behavior in a cobalt(II) complex. *Inorg. Chem.* **1984**, *23*, 119–120.

(27) Haddad, M. S.; Federer, W. D.; Lynch, M. W.; Hendrickson, D. N. Spin-crossover ferric complexes: Unusual effects of grinding and doping solids. *Inorg. Chem.* **1981**, *20*, 131–139.

(28) Haddad, M. S.; Federer, W. D.; Lynch, M. W.; Hendrickson, D. N. An explanation of unusual properties of spin-crossover ferric complexes. *J. Am. Chem. Soc.* **1980**, *102*, 1468–1470.

(29) Brooker, S. Spin crossover with thermal hysteresis: Practicalities and lessons learnt. *Chem. Soc. Rev.* **2015**, *44*, 2880–2892.

(30) Muñoz Lara, F. J.; Gaspar, A. B.; Aravena, D.; Ruiz, E.; Muñoz, M. C.; Ohba, M.; Ohtani, R.; Kitagawa, S.; Real, J. A. Enhanced bistability by guest inclusion in Fe(II) spin crossover porous coordination polymers. *Chem. Commun.* **2012**, *48*, 4686–4688.

(31) Weber, B.; Bauer, W.; Obel, J. An iron(II) spin-crossover complex with a 70 K wide thermal hysteresis loop. *Angew. Chem., Int. Ed.* **2008**, *47*, 10098–10101.

(32) Gütlich, P.; Gaspar, A. B.; Garcia, Y. Spin state switching in iron coordination compounds. *Beilstein J. Org. Chem.* **2013**, *9*, 342–391.

(33) Petříček, V.; Dušek, M.; Palatinus, L. Crystallographic Computing System JANA2006: General features. *Z. Kristallogr. - Cryst. Mater.* **2014**, *229*, 229.

(34) Blum, V.; Gehrke, R.; Hanke, F.; Havu, P.; Havu, V.; Ren, X.; Reuter, K.; Scheffler, M. Ab initio molecular simulations with numeric atom-centered orbitals. *Comput. Phys. Commun.* **2009**, *180*, 2175–2196.

(35) Ren, X.; Rinke, P.; Blum, V.; Wieferink, J.; Tkatchenko, A.; Sanfilippo, A.; Reuter, K.; Scheffler, M. Resolution-of-identity approach to Hartree–Fock, hybrid density functionals, RPA, MP2 and GW with numeric atom-centered orbital basis functions. *New J. Phys.* **2012**, *14*, 53020.

(36) Havu, V.; Blum, V.; Havu, P.; Scheffler, M. Efficient integration for all-electron electronic structure calculation using numeric basis functions. *J. Comput. Phys.* **2009**, *228*, 8367–8379.

(37) Nocedal, J.; Wright, S. J. *Numerical Optimization*, 2nd ed.; Springer Series in Operations Research and Financial Engineering; Springer Science+Business Media LLC: New York, 2006.

(38) Perdew, J. P.; Ruzsinszky, A.; Csonka, G. I.; Vydrov, O. A.; Scuseria, G. E.; Constantin, L. A.; Zhou, X.; Burke, K. *Phys. Rev. Lett.* **2008**, *100*, 136406.

(39) Perdew, J. P.; Burke, K.; Ernzerhof, M. Generalized Gradient Approximation Made Simple. *Phys. Rev. Lett.* **1996**, *77*, 3865–3868.

(40) Adamo, C.; Barone, V. *J. Chem. Phys.* **1999**, *110*, 6158.

Supporting Information

Cooperative Large-Hysteresis Spin-Crossover Transition in the Iron(II) Triazolate [Fe(ta)$_2$] Metal-Organic Framework

Maciej Grzywa,[†] Richard Röß-Ohlenroth,[†] Christoph Muschielok,[‡] Harald Oberhofer,[‡] Artur Błachowski,[▯] Jan Żukrowski,[▯] Dana Vieweg,[□] Hans-Albrecht Krug von Nidda,[▯] Dirk Volkmer[*,†]

[†]Chair of Solid State and Materials Chemistry, Institute of Physics, Augsburg University, Universitätsstrasse. 1, D-86159 Augsburg, Germany

[‡]Theoretical Chemistry, Technische Universität München, Lichtenbergstrasse 4, D-85747 Garching, Germany

[▯]Institute of Physics, Pedagogical University, ul. Podchorążych 2, 30-084 Kraków, Poland

[▯]Academic Center for Materials and Nanotechnology, AGH University of Science and Technology, 30 Mickiewicza Av., 30-059 Kraków, Poland

[▯]Experimental Physics V, Center for Electronic Correlations and Magnetism, Institute of Physics, University of Augsburg, Universitätsstrasse 1, D-86159 Augsburg, Germany

Table of Contents

Asymmetric units of RT- and HT-[Fe(ta)$_2$]

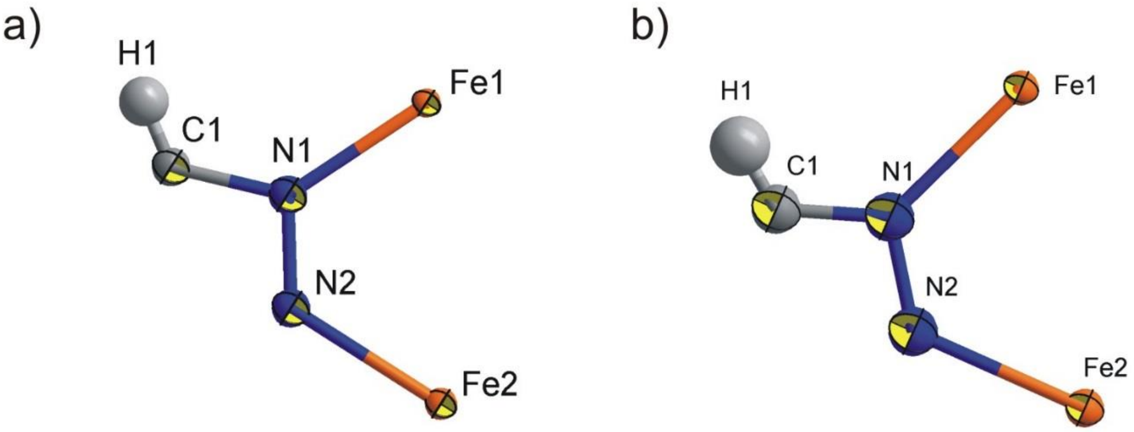

Figure S1. The asymmetric units of RT- (a) and HT-[Fe(ta)2] (b). Thermal ellipsoids probability: 50 %.

TGA of [Fe(ta)$_2$]

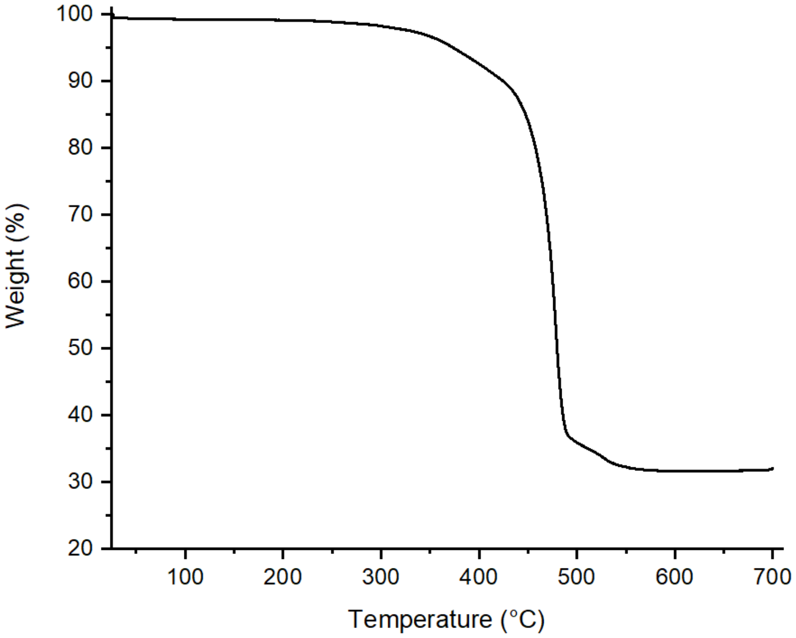

Figure S2. Thermal stability of [Fe(ta)$_2$] studied by TG analysis under flowing nitrogen.

Measured and calculated PXRD patterns of [Fe(ta)$_2$]

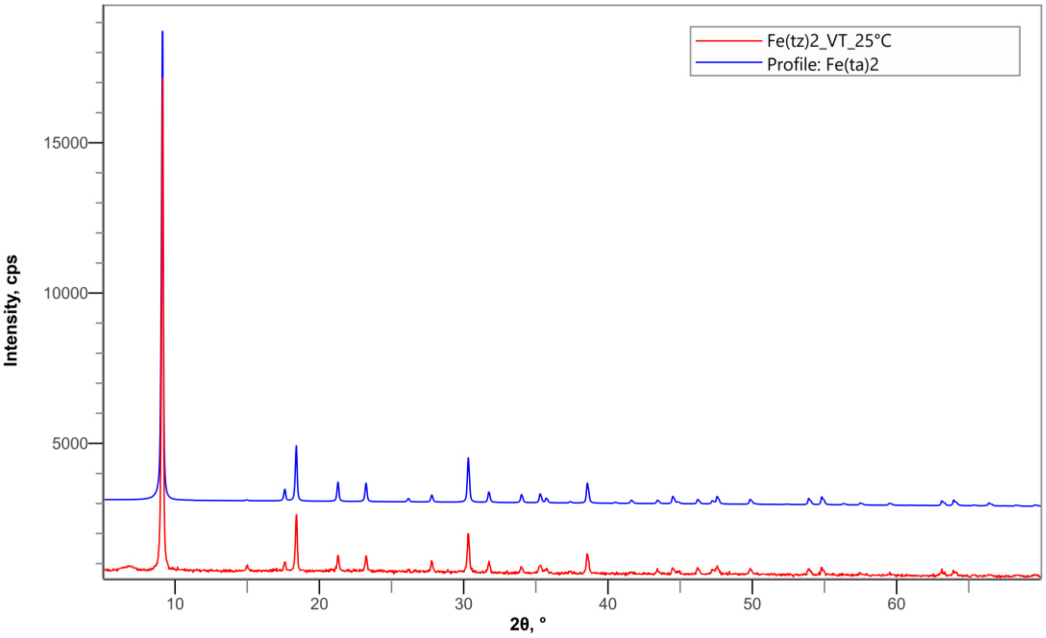

Figure S3. Measured (red) and calculated (blue) powder patterns of [Fe(ta)$_2$].

Argon adsorption analysis of [Fe(ta)$_2$]

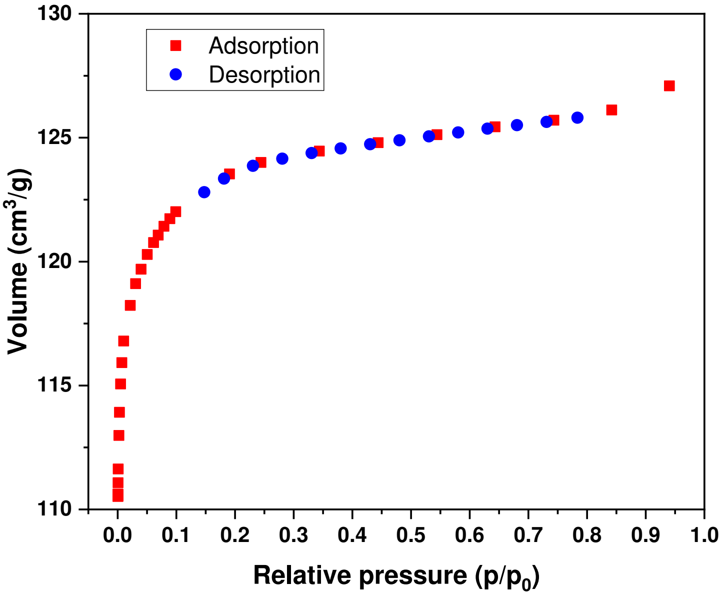

Figure S4. Argon adsorption (red) and desorption (blue) isotherms of [Fe(ta)$_2$] (Volume [STP])

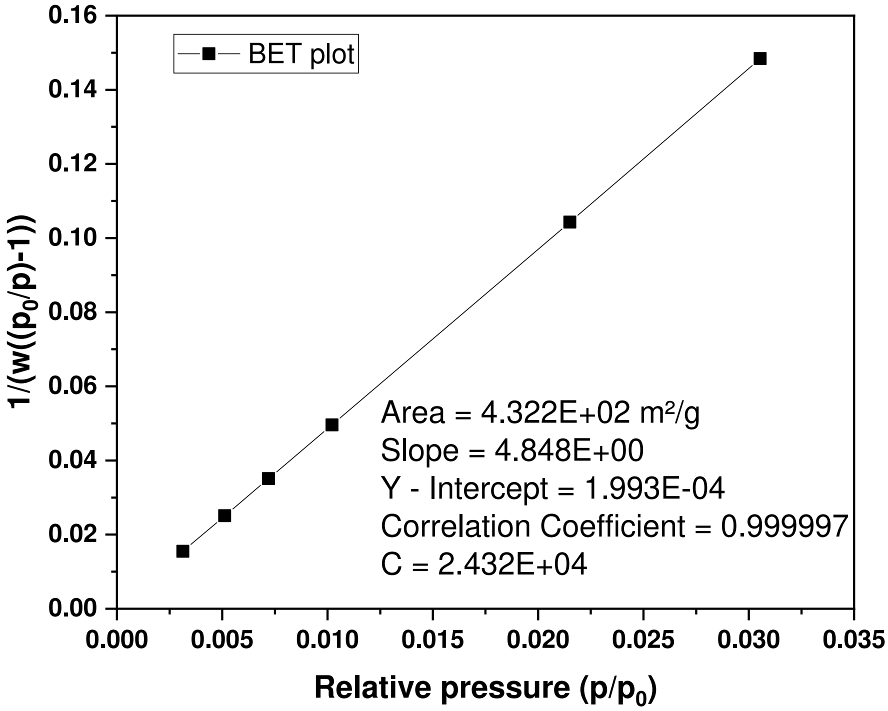

Figure S5. BET plot for the argon adsorption in $[Fe(ta)_2]$

Mössbauer spectra

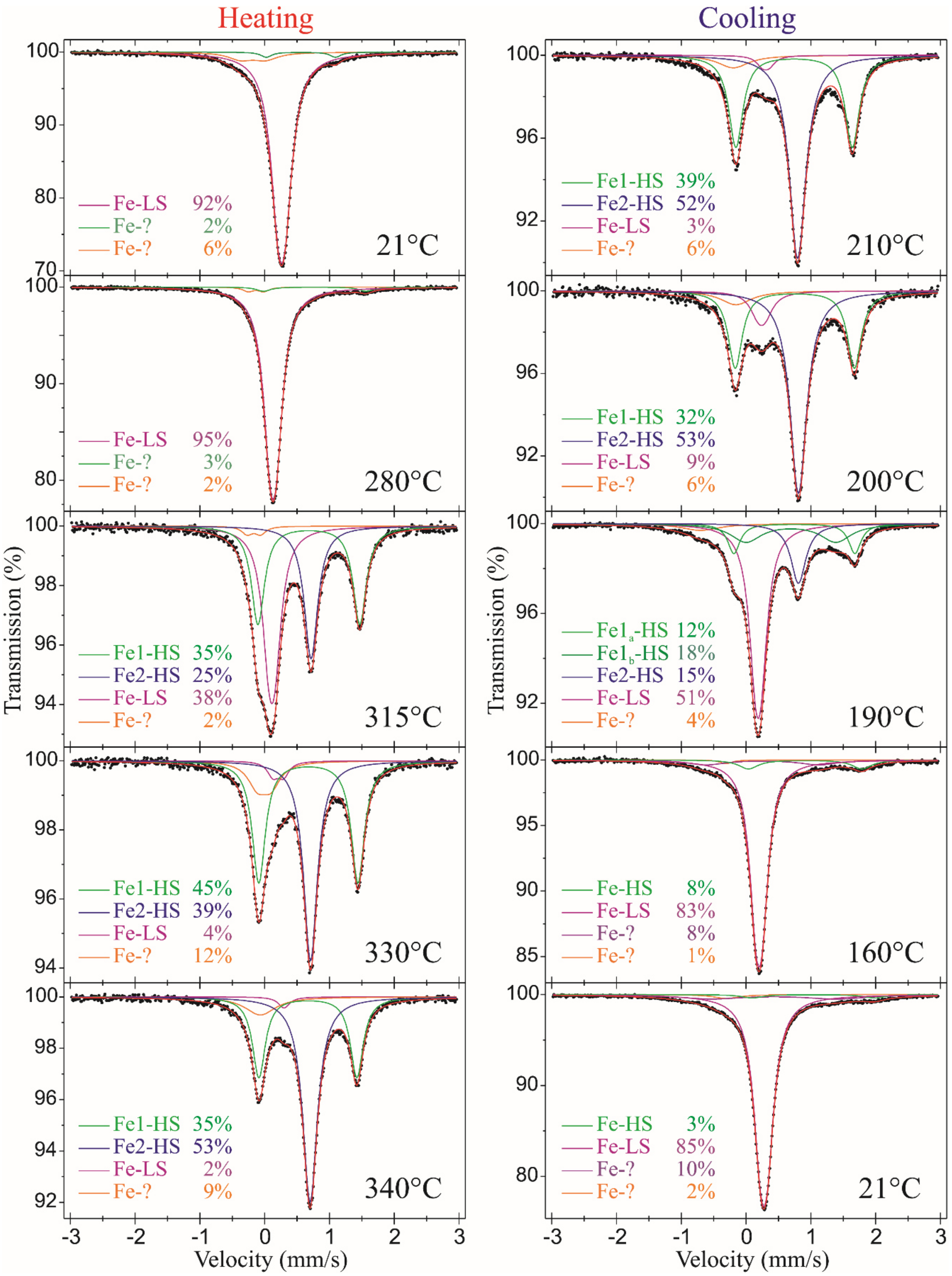

Figure S6 ^{57}Fe Mössbauer spectra versus temperature for the Fe[(ta)$_2$] sample with variable Fe1-HS / Fe2-HS sub-spectra ratio. The measurements were made in one uninterrupted series of heating and subsequently cooling for the same absorber. Some unknown Fe-impurities are shown with a question mark. One of them marked in orange and seen for all spectra represents iron in the low-spin state in the entire measured temperature range. Unidentified sub-spectrum marked in purple in cooling series probably represents a product(s) of the thermal decomposition.

T (°C)	Fe spin state	A (%)	δ (mm/s)	Δ (mm/s)	Γ (mm/s)
Heating					
21	Fe-LS	92	0.37	0.09	0.15
280	Fe-LS	94	0.24	0.09	0.14
315	Fe1-HS	35	0.79	1.57	0.14
	Fe2-HS	25	0.83	-	0.15
	Fe-LS	38	0.22	0.09	0.15
330	Fe1-HS	45	0.78	1.53	0.14
	Fe2-HS	39	0.82	-	0.15
340	Fe1-HS	35	0.78	1.51	0.14
	Fe2-HS	53	0.81	-	0.16
Cooling					
210	Fe1-HS	39	0.85	1.80	0.16
	Fe2-HS	52	0.91	-	0.19
200	Fe1-HS	32	0.86	1.84	0.16
	Fe2-HS	53	0.92	-	0.20
190	Fe1$_a$-HS	12	0.86	1.87	0.13
	Fe1$_b$-HS	18	0.80	1.39	0.48
	Fe2-HS	15	0.92	-	0.18
	Fe-LS	51	0.30	0.08	0.14
160	Fe-LS	83	0.31	0.09	0.13
21	Fe-LS	85	0.38	0.09	0.15

Table S1 ^{57}Fe Mössbauer parameters of the main spectral components belonging to Fe[(ta)$_2$] for spectra shown in **Fig. S6**. The symbols meaning is the same as in **Table 1** (in the main text).

^{57}Fe Mössbauer spectroscopy measurements versus temperature series of heating and cooling were repeated for four different absorbers made of the same Fe[(ta)$_2$] sample and in three cases the results looked similar to those described in the main text. In one (last) case a slight temperature shift of the SCO was observed and in particular a quite different and variable ratio of the Fe1-HS sub-spectrum (with large quadruple splitting) to the Fe2-HS sub-spectrum (without quadrupole splitting) has been registered. Selected spectra are shown in Fig. S6 with Mössbauer parameters listed in Table S1. The Fe1-HS / Fe2-HS sub-spectra ratio changes form 1.4 at 315°C to 0.7 at 340°C upon heating and it stays like that upon cooling to 200°C. This phenomenon is strong indication of the temperature dependent dynamic Jahn-Teller distortion and confirms that like at the RT also at the HT both inequivalent crystallographic iron sites in the Fe[(ta)$_2$] have the same hyperfine properties (ligand fields) and they cannot be distinguished from each other by means of the Mössbauer spectroscopy.

Estimation of the Mössbauer-Lamb factor difference for iron in LS and HS state

The Mössbauer-Lamb factor MLF (the analog of the Debye–Waller factor in the coherent neutron and X-ray scattering) is sensitive to the lattice dynamic properties of the Fe atoms. Inter alia it may depend on the spin state of Fe atoms. The relative change of the MLF between Fe-LS and Fe-HS can be estimated based on change of the relative spectral area versus temperature with special attention paid to the SCO temperature region.

The relative spectral area (*RSA*) is defined as:

$$RSA = \left(\frac{1}{C}\right)\sum_{n=1}^{C}\frac{N_0 - N_n}{N_0}\,.$$

The meaning of the symbols is as follows: C - the number of data channels for the Mössbauer spectrum, N_0 - the average number of counts per channel far-off the resonance (i.e. the baseline), N_n - the number of counts in the channel n. Thus, the *RSA* is calculated based on the original measurement data only and the simple expression defining parameter *RSA* does not depend on any physical model. It is necessary for all Mössbauer spectra constituting the set of *RSA* to be recorded at the same measurement conditions and preferably during an uninterrupted series with changing subsequent temperatures only.

Fig. S7 shows *RSA* versus temperature for spectra recorded at the same measurement conditions and during one uninterrupted series with increasing subsequent temperatures.

The *RSA* decreases smoothly with increasing *T* according to the Debye model of the lattice vibrations of Fe atoms. But, some pronounced anomaly (jump) is visible between 285°C and 300°C marked experimental points, so just across onset of SCO. Another anomaly appears above 350°C. The first one is obviously related to the SCO, i.e. the low-spin at 285°C and the high-spin (in part) at 300°C. This is clear evidence that some lattice softening happens during transition from the LS to the HS state and hence some decrease of the MLF occurs. It can be estimated based on the “jump” of *RSA* that the MLF is at about 20% larger for the Fe-LS than for the Fe-HS in the Fe[(ta)$_2$] metal-organic framework. A pronounced increase of *RSA* above 350°C is some evidence of the thermal decomposition.

^{57}Fe Mössbauer spectroscopy was applied in current studies to obtain qualitative evidences about the SCO. So, we decided to mention only about change of the MLF and report only original areas of respective sub-spectra (without correction) due to unpredictable error of estimated MLF change.

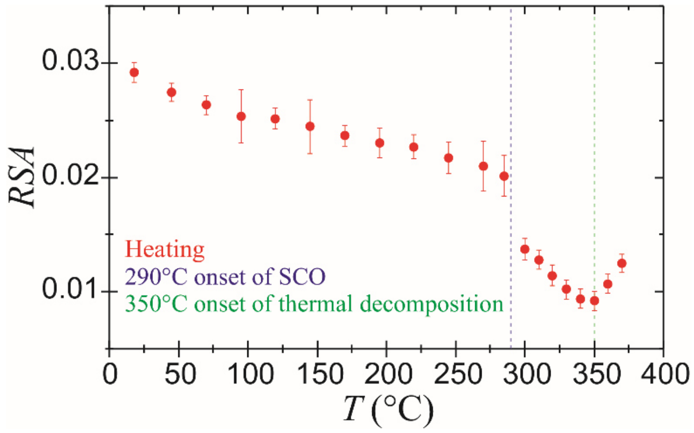

Figure S7 The relative spectral area (*RSA*) versus temperature for the Mössbauer spectra obtained from uninterrupted heating series with constant measurement conditions. Vertical dashed lines mark respective temperatures.

IR spectrum of $[Fe(ta)_2]$

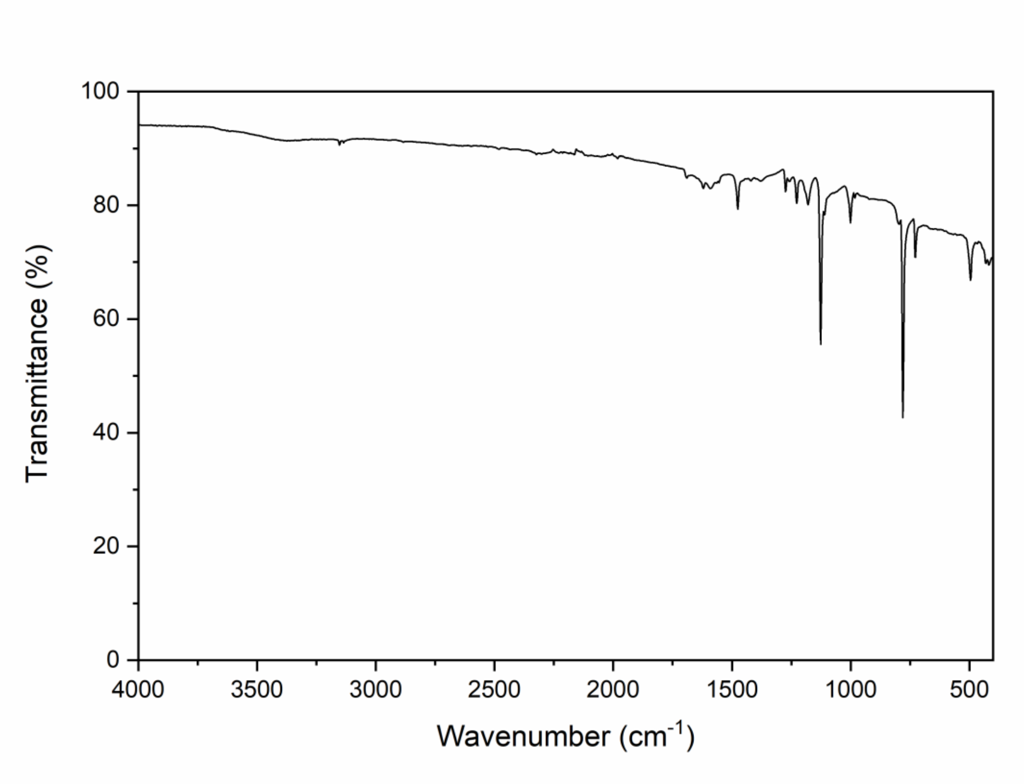

Figure S8. FT-IR spectrum of $[Fe(ta)_2]$

SEM Image of $[Fe(ta)_2]$

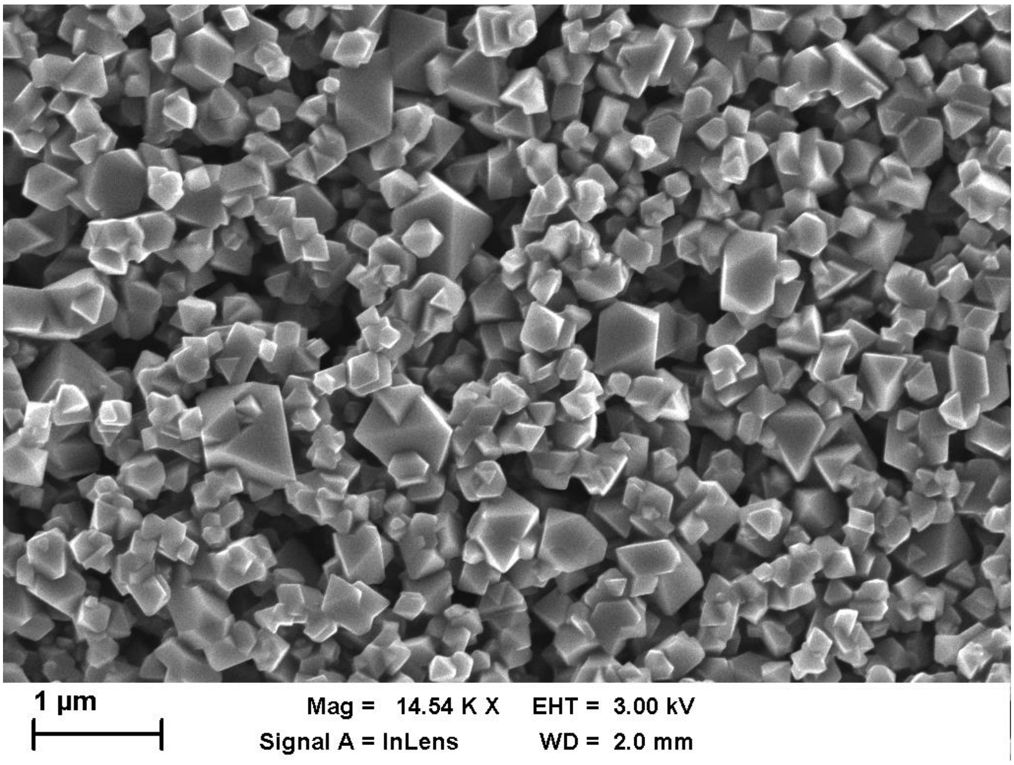

Figure S9. SEM image of the synthesized $[Fe(ta)_2]$

Magnetic susceptibility of [Fe(ta)$_2$] in the range of 1.8 to 300 K

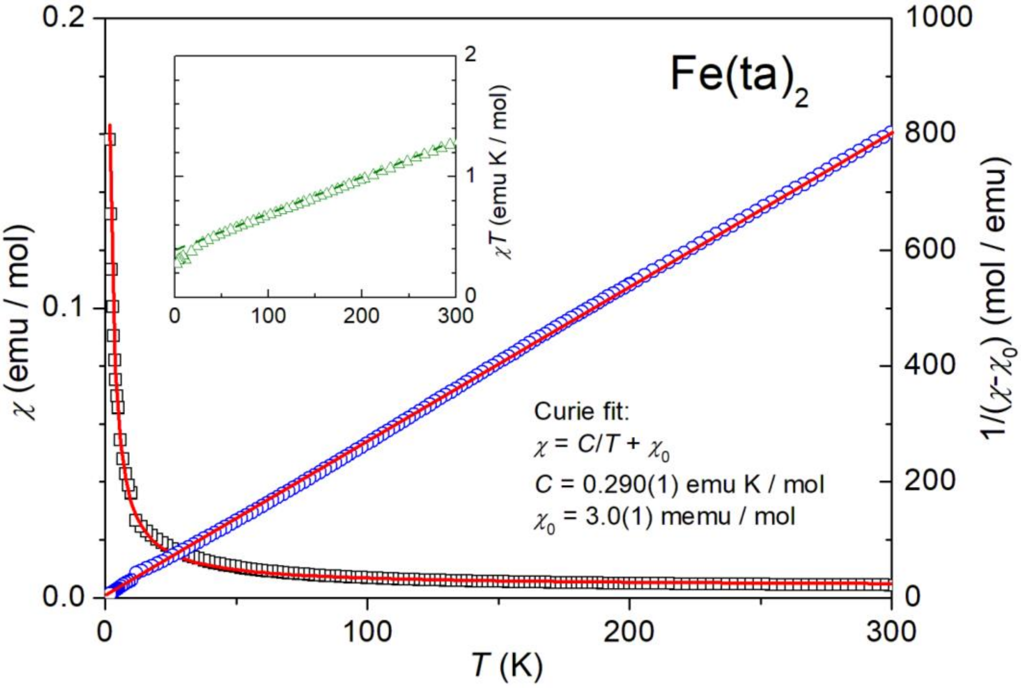

Figure S10. Temperature dependence of the magnetic susceptibility $\chi = M/H$ of [Fe(ta)$_2$] based on the $Fe_3C_{12}H_{12}N_{18}$ sum formula, taken at an external field of H = 1000 Oe (left ordinate) and its inverse after subtraction of the constant contribution χ_0 determined by the Curie-Weiss fit (right ordinate). The red solid line indicates the fit curve. Inset: temperature dependence of the product χT. The dashed line resembles a linear increase due to the positive offset χ_0

Optimized Crystal Structures from DFT

LS [Fe(ta)$_2$]

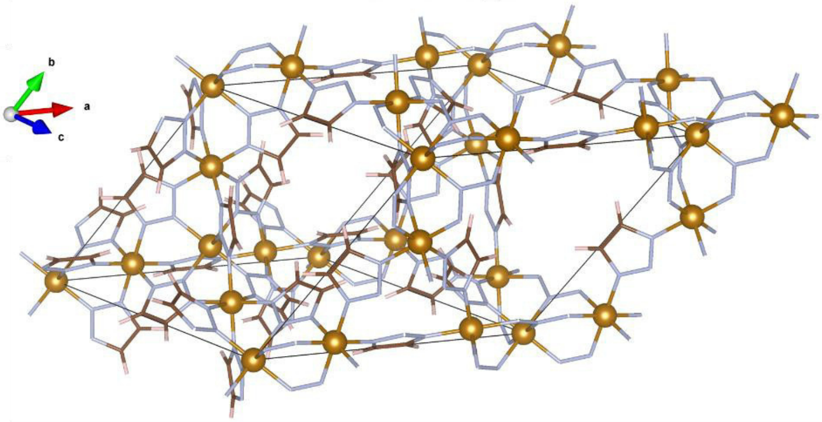

HS [Fe(ta)$_2$]

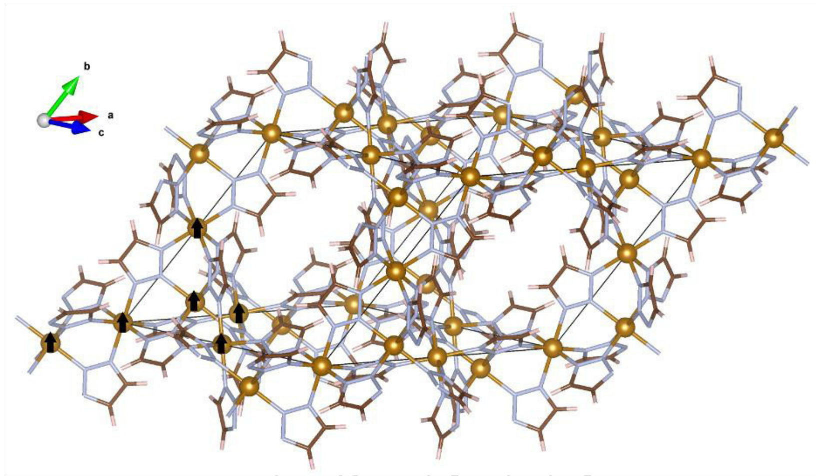

HS (antiferro) [Fe(ta)$_2$]

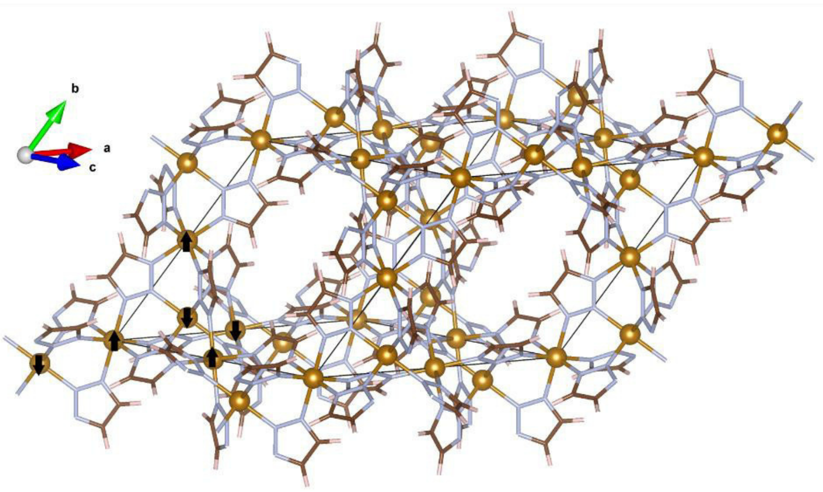

Figure S11. Optimized supercells of the different spin state models of [Fe(ta)$_2$]. In the HS and HS AF models, spin alignment of the symmetry unique Fe centers is indicated through black arrows.

ACS APPLIED MATERIALS & INTERFACES

www.acsami.org

Research Article

Combining Theory and Experiments To Study the Influence of Gas Sorption on the Conductivity Properties of Metal–Organic Frameworks

Christoph Muschielok,[⊥] Alexander Reiner,[⊥] Richard Röß-Ohlenroth, Andreas Kalytta-Mewes, Dirk Volkmer, Achim Wixforth, and Harald Oberhofer*

Cite This: *ACS Appl. Mater. Interfaces* 2022, 14, 33662–33674

Read Online

ACCESS | Metrics & More | Article Recommendations | Supporting Information

ABSTRACT: With a view on adding to their use in trace gas sensing, we perform a combined experimental and theoretical study of the change of the conductivity of a metal organic framework (iron (1,2,3)-triazolate, $Fe(ta)_2$) with the uptake of chemically inert gases. To align our first-principles calculations with experimental measurements, we perform an ensemble average over different microscopic arrangements of the gas molecules in the pores of the metal–organic framework (MOF). Up to the experimentally reachable limit of gas uptake, we find a good agreement between both approaches. Thus, we can employ theory to further interpret our experimental results in terms of changes to the parameters of the Bardeen–Shockley band theory, electron–phonon coupling (in the form of the deformation potential), bulk modulus, and carrier effective mass. We find the first of these to be most strongly influenced through the gas uptake. Furthermore, we find the changes to the deformation potential to strongly depend on the individual microscopic arrangements of molecules in the pores of the MOF. This hints at a possible synthetic engineering of the material, e.g., by closing off certain pores, for a stronger, more interpretable electric response upon gas sorption.

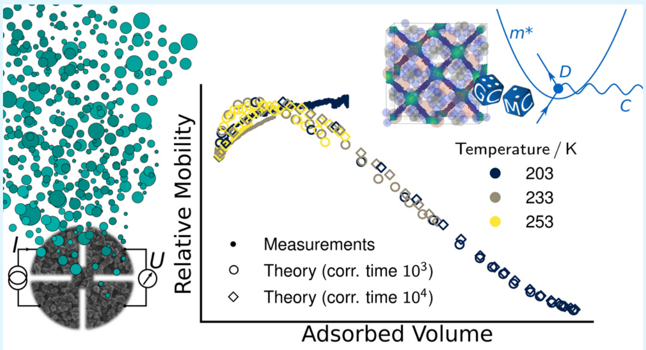

KEYWORDS: *metal–organic frameworks, trace gas sensing, conductivity, absorption, density functional theory, Langmuir isotherms, grand canonical Monte Carlo, powder X-ray diffraction*

■ INTRODUCTION

Metal–organic frameworks (MOFs) are network materials built from metal centers connected by organic ligands, which are commonly called linkers.[1] Frequently, MOFs also exhibit nanoscale pore networks that may host atoms or (small) molecules potentially physisorbed to the framework.[2] Together with their great structural versatility, this makes MOFs interesting candidates for a large range of applications, from gas storage[3] to catalysis[4] and even trace-gas sensing.[5,6] Some members of a recently synthesized[7] class of microporous metal azolate MOFs, $M^{II}(ta)_2$, where M^{II} denotes a divalent metal ion and ta^- denotes the 1,2,3-triazolate anion, have even been found to exhibit nonvanishing electrical conductivity at room temperature.[8,9] In general, porous MOF materials tend to be mechanically rather soft.[10] Gas adsorption therefore is known to induce more or less severe structural changes in the framework.[11] These, in turn, could influence the conductive properties of the material to a degree that can be measured experimentally, opening up another avenue for the use of MOFs in sensing applications. Indeed, theory predicts a direct relationship between the conductivity of a material and its elastic properties[12] in the form of Bardeen–Shockley (BS) deformation potential theory.[13] While this theory certainly is very approximate, earlier studies have shown it to be sufficient to reproduce conductivity trends at least on a qualitative level.[9]

Given the great potential of nanoscale gas-sensing materials,[5] in this work we perform a combined experimental and theoretical study of the conductivity of an MOF at different levels of gas uptake. As a representative example, we choose $Fe(ta)_2$, sketched in Figure 1, and focus on inert gases Ar and CO_2. These only physisorb to the pore walls and thus do not influence the electronic structure and specifically the number of free charge carriers directly, leading to a subtler change of conductivity than one would expect for reducing or oxidizing

Received: March 23, 2022
Accepted: June 28, 2022
Published: July 18, 2022

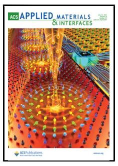

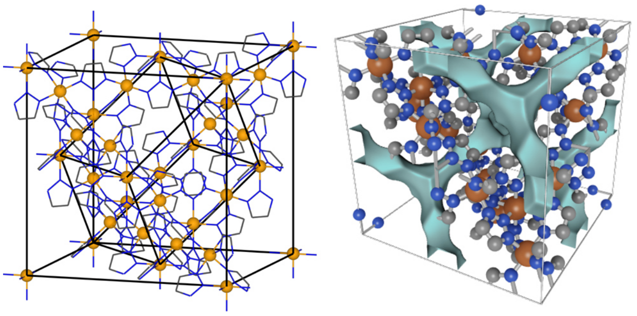

Figure 1. (Left) Sketch[14] of the conventional cell of Fe(ta)$_2$ used in this work. Shown within is the primitive cell that is used as the starting point for the simulations. (Right) Sketch[15] of the unit cell including the He pore network in Fe(ta)$_2$. Comparison to the primitive cell leads to the channel structure obtained through the qualitative sampling shown in Figure 3B.

gases. They thus represent a good test case for experimental and theoretical methodologies.

While both our theoretical predictions and experimental measurements find a direct relationship between MOF gas uptake and conductivity, quantitatively connecting these two results is not quite simple. This is due to the fact that, in the experiment at a given temperature and gas pressure, each of the pores of the macroscopic MOF sample is occupied according to the respective grand-canonical ensemble. First-principles theoretical calculations based on the BS model, however, necessarily rely on supercells containing only a few unit cells with well-defined structural configurations of gas molecules in the pores. At the same time, we show that individual configurations of guest molecules in the pores can show very different conductivities. To still connect experiment and theory, we thus perform a grand-canonical Monte Carlo (GCMC) sampling of the Fe(ta)$_2$−gas host−guest system to extract the most likely configurations for which we calculate the individual transport parameters. Finally, we estimate the total carrier mobility through a weighted sum over all likely configurations and compare it to experimental measurements at equivalent temperatures and gas pressures. Overall, our experimental and theoretical results do agree well, yet there are a number of potential stumbling blocks hindering such a direct comparison beyond the well-known inaccuracies of computational methods. We here specifically highlight these and present our solutions to overcome them.

The advantage of our combined approach is that it allows us to examine the charge-transport parameters that are most influenced by the gas uptake. Unsurprisingly, we find the electronic structure of the MOF and, thus, the charge-carrier effective mass mostly unperturbed. Instead, we find that the changes to the carrier mobility are mostly due to variations of electron−phonon coupling in the form of the BS deformation potential with different pore loadings. Furthermore, we find that some pore loadings increase conductivity and some decrease it, with different trends for different guest molecules. While these differences are not as apparent in the grand-canonically averaged conductivity and in the experiment, they do point the way toward a possible application of specially engineered conductive MOFs as trace gas sensors.

METHODS

Theoretical Treatment of Loading-Dependent MOF Conductivities. In general, the conductivity σ of a material strongly depends on the mobility μ of its charge carriers—electrons or electron holes—which basically describes their average velocity on application of an electric field.[12] It is given by

$$\sigma = qn_c\mu \tag{1}$$

Here, q denotes the charge of the respective carrier and $n_c = N_c/V^{\text{sample}}$ is the density of mobile charge carriers, where N_c denotes their total number in a sample volume V^{sample}. This relationship holds for a fixed composition of the material.

Systems like MOFs can absorb gaseous guest species if subjected to an external gas atmosphere with a pressure p. In this case, σ, μ, and n_c can become dependent on p, next to their dependency on the temperature T of the system. Introducing a reference pressure p_o, we write

$$\frac{\sigma(p, T)}{\sigma(p_o, T)} = \underbrace{\frac{n_c(p, T)}{n_c(p_o, T)}}_{\substack{\text{charge density}\\ \text{ratio } R_c(p,T;p_o)}} \frac{\mu(p, T)}{\mu(p_o, T)} \tag{2}$$

If there is only little interaction between host and guest, i.e., at physisorption, the number of charge carriers N_c will not be affected by the presence of the guests and thus cancels in the charge density ratio. $R_c(p, T; p_o) = V^{\text{sample}}(p_o, T)\ /V^{\text{sample}}(p, T)$ thus becomes a purely geometric factor, which for an ideal bulk crystal model can simply be chosen as the ratio of the respective unit cell volumes. Additionally, we neglect the dependence of R_c on T under the assumption that the thermal expansion will be roughly the same for loaded and unloaded Fe(ta)$_2$ networks. Even fully loaded with gas molecules, the size of the MOF cell changes at most by 0.3% for the adsorption of Ar and 2% for the adsorption of CO$_2$. Therefore, we use $R_c \approx 1$ for our purposes and drop it from our equations.

To highlight changes induced by the gas uptake, we compute the relative deviations of μ and σ from the corresponding reference value, chosen here as $p_o = 0$,

$$\sigma^{\text{rel}}(p) = \frac{\sigma(p) - \sigma(p_o)}{\sigma(p_o)} = \frac{\sigma(p)}{\sigma(p_o)} - 1 \tag{3}$$

with μ^{rel} being defined analogously.

Ensemble quantities such as p, T, σ, and μ do not lend themselves easily to a theoretical calculation from first principles, which after all relies on specific positions of atoms and molecules. We thus define the term pore-loading configuration (PLC) for a given host material to indicate the collective positions of all guest atoms or molecules harbored within. By loading we mean either the volume under standard temperature and pressure, V^{STP}, of the adsorbed guest or the ratio $x = V^{\text{STP}}/V^{\text{STP}}_{\text{max}}$ of that volume with the maximally adsorbed volume. For our purposes, x can be furthermore understood as the ratio of the number of adsorbed guests per unit cell and the total number of pores per unit cell. Through this, we can map multiple PLCs to a single value for x. In the following, we constrain the definition of a PLC to the positions in a (local) energetic minimum into which the guests relax upon being placed randomly inside the pores. In equilibrium the choice of p and T defines a distribution of PLCs, where each one of them occurs with a probability $f(\text{PLC}; p, T)$. On a microscopic level, each of these PLCs could potentially lead to different conductivity properties.

For an extended MOF, this means that each PLC is realized in a microscopic region with a relative frequency of $f(\text{PLC}; p, T)$. For the purpose of estimating the conductivity of the whole material, we can consider each of these regions as resistors connected in series such that their individual conductivities sum up reciprocally. The actual ensemble average $\mu(p, T)$, cf. eq 2, is then defined by the weighted sum:

$$\frac{1}{\mu(p, T)} = \sum_{\text{PLC}} \frac{f(\text{PLC}; p, T)}{\mu(\text{PLC}; T)} \tag{4}$$

https://doi.org/10.1021/acsami.2c05127
ACS Appl. Mater. Interfaces 2022, 14, 33662−33674

Given the computational cost of calculating the mobilities from first principles,[9] eq 4 represents an efficient framework to estimate the overall σ^{rel} simply by estimating the μ^{rel} for each PLC realized in a single unit cell.

Bardeen–Shockley Mobility and Its Descriptors. In our recent work,[9] we demonstrated one way of describing at least trends of the mobility in MOFs based on the BS deformation-potential approach in the relaxation-time approximation:[12,13]

$$\mu = \frac{\sqrt{8\pi}\, q\beta^{3/2}}{3}\frac{C}{D^2(\overline{m}^*)^{5/2}} \tag{5}$$

Here, $\beta = (k_{\mathrm{B}}T)^{-1}$ is the reciprocal thermal energy equivalent. The three material-dependent components of the mobility are the bulk modulus C of the crystal, the deformation potential D, which measures an effective electron–phonon coupling, and the mean effective mass $\overline{m}^*$ at the band extremum. Clearly, any of these three quantities could be influenced by the pore loading of an MOF. For a technical description of how to estimate them, we refer the reader to our earlier work.[9] We note, though, that for the rather simple band structure of the MOF considered here, we employ a simplified method for estimating the mean effective mass based on a least-squares fit of a second-order expansion of the band energy (see the Supporting Information).

The physics behind the BS mobility model includes only one of several possible scattering mechanisms, i.e., the scattering with low-k acoustic phonons. The theoretical estimates of μ given in this work therefore represent only an upper limit to the total achievable carrier mobility.[9,12]

We use μ from eq 5 to calculate μ^{rel} for a single PLC. All constant coefficients cancel, also removing the dependence on T. μ^{rel} is then given by the ratios of the three material properties,

$$\mu^{\mathrm{rel}}(\mathrm{PLC}) = \frac{\frac{C(\mathrm{PLC})}{C(0)}}{\left[\frac{D(\mathrm{PLC})}{D(0)}\right]^2\left[\frac{\overline{m}^*(\mathrm{PLC})}{\overline{m}^*(0)}\right]^{5/2}} - 1 \tag{6}$$

Bulk Modulus and Deformation Potential. Both the elastic constants and the deformation potentials of a (crystalline) material can be computed from a series of deformed unit cells.[9] From these two tensors, we can easily get C and D by means of contraction.[9] Yet, with a view on computational simplicity and focusing only on the trends induced by pore adsorbates, we use a simpler procedure, which is in part similar to the one described in ref 16.

For hydrostatic deformations, we can compute C by expanding the total energy E of the crystal in terms of a parameterized hydrostatic strain tensor $u(g)$ up to second order. Inserting the explicit form for this tensor, we end up with

$$\Delta E(g) = E(g) - E(0) = \frac{1}{2}CVg^2 \tag{7}$$

where g is the magnitude of the strain induced by the tensor. This means we can obtain C through a simple least-squares fit of the g-series of E.

An analogous approach can be used to obtain D_ν, where ν labels either the valence band (VB) or the conduction band (CB) edge. D_ν is the linear coefficient of the energy levels $\epsilon_\nu(k)$ when expanded around the band extremum (of the unstrained configuration) at k_{o} with respect to $u(g)$. Preempting a part of our results, we find that the linear model is not fully sufficient for the $\mathrm{Fe(ta)_2}$ crystal we studied and that there is a second-order shift of the band edges. This we model using the second-order coupling constant K_ν,

$$\Delta\epsilon_\nu(k_{\mathrm{o}}, g) = -D_\nu g + \frac{1}{2}\left(K_\nu - \frac{1}{3}D_\nu\right)g^2 \tag{8}$$

The linear coupling D_ν appears again in the second-order term of eq 8, if we do not neglect second-order g-terms in the strain tensor. We treat K_ν as a parameter that has to be fitted and rely on the values of the first-order D_ν to calculate μ_ν. Furthermore, using the same argument by which we set $R_{\mathrm{c}} \approx 1$, we state that the second-order shift is negligible for the effects on $\mu^{\mathrm{rel}}(\mathrm{PLC})$. The loading-induced strains, i.e., the order of magnitude of g, are much smaller than the g-values used for the shift series.

Mean Effective Mass. As mentioned earlier, here we do not make use of the general method of computing the mean effective mass by a weighted summation of interpolated reciprocal band curvature data introduced in ref 9. Given that the band structures computed here are all rather benign with no significant band warping, it appears that a simple least-squares fit of the energies is already sufficiently accurate. Although in our earlier work similar MOFs did show strongly warped band edges, we find that, with the improved structures we gain here due to the use of a dispersion correction, no warping was found in this work. The band fit is performed on a 9 × 9 × 9 grid in k-space centered either on the VB maximum or on the CB minimum at the respective point k_{o}. As a fit function, we use the second-order expansion of the band energy. More details can be found in the Supporting Information.

Sampling the Pore Network. Starting with the optimized structure[9] of $\mathrm{Fe(ta)_2}$ (Figure 3A), we randomly sample the positions in the unit cell. Samples are rejected through overlap between hard atomic van der Waals (VDW) spheres (Figure 2), similar to the geometric pore definition of Ongari et al.[17] Any sample not being rejected is by our definition part of the pore volume. We extend the geometric pore method of ref 17 to linear polyatomic adsorbates like $\mathrm{CO_2}$. Specifically, we generalize the rejection criterion because the original formulation using a sphere approximation applies to atomic or very small diatomic molecules like dinitrogen. Our generalization covers the rodlike shape of linear molecules more directly, hence under the assumption of constant bond lengths and angles and via a rotation of the whole molecule. We emphasize that we use the geometric pore volume here as we are not primarily interested in, e.g., the void volume of the $\mathrm{Fe(ta)_2}$, but merely in good starting positions for our structural optimizations using density-functional theory (DFT).

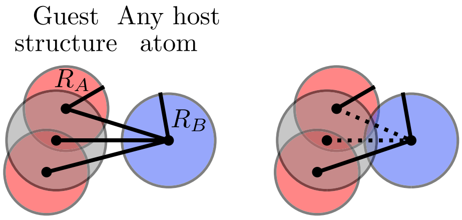

Figure 2. Visualization of the hard sphere van der Waals overlap rejection rule.

For linear molecules, a six-dimensional space (position and orientation) has to be sampled. This can be done in a two-step procedure, where the first step is to draw the center of mass in fractional coordinates from a uniform distribution $\mathcal{U}(0, 1)$ as for the atomic case. The second step is then to draw quadruples from a standard normal distribution $\mathcal{N}(0, 1)$. Interpreting these quadruples as quaternions and L^2-normalizing them allows for sampling of the surface of the 3-sphere homogeneously.[18] We refer the interested reader to the Supporting Information for further details on quaternions and how we use them here.

To get a better yield of positions and orientations without overlap, we use the sampling of the unit cell with a rather small probe body (Figure 3B). Finally, we use the resulting positions within the pore to sample more complicated adsorbates (Figure 3D). A zoomed-in illustration is given in Figure 4.

Connecting Theory and Experiment. Unfortunately, specific PLCs cannot be assessed directly from experiment. Yet, in order to connect the experimental and theoretical data, we can at least evaluate the average loading of the pores at given experimental conditions p and T. To this end, we use an N-site Langmuir model to fit the experimentally obtained adsorption isotherms. It is given by

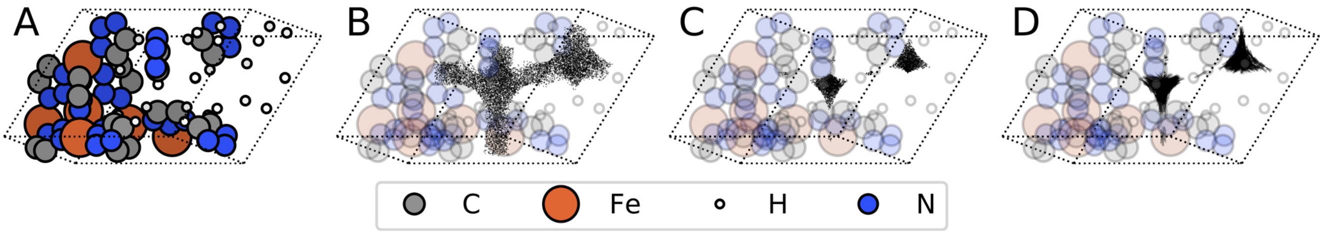

Figure 3. Empty Fe(ta)$_2$ cell and pore samplings for different guest species: (A) empty cell, (B) probe body or H atom, (C) Ar, and (D) CO$_2$. Shown is the guest species' center of mass and, if applicable, its normalized molecular axis. The nonoverlapping pores in panels C and D are most certainly an artifact due to the static pores during the sampling.

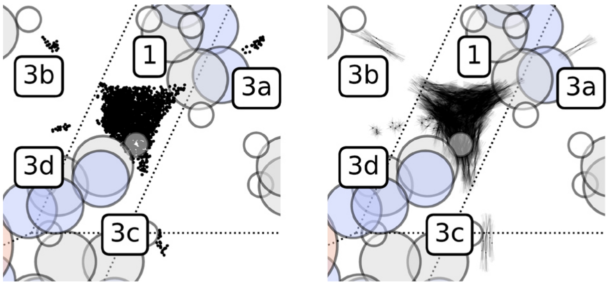

Figure 4. Zoomed-in illustration of the pore samplings of Fe(ta)$_2$ with Ar (left panel) and CO$_2$ (right panel). The diamond lattice-like pore structure breaks down into two large pores per primitive unit cell (only one is shown) and four small ones, for this relatively small number of samples. For CO$_2$, next to the center of mass, the normalized molecular axis is shown. A distinct feature that is observed for CO$_2$ is its orientation in the small pores.

$$V(p,\,T) = \sum_{n=1}^{N} \frac{V_n^{\max} p}{1/K_n^{\mathrm{ad}}(T) + p} \tag{9}$$

where V is the adsorbed volume and the sum runs over the N different sites. For the purposes of this work, we distinguish here between the two differently sized (i.e., large and small, $N = 2$) pores of Fe(ta)$_2$, which likely show different adsorption energetics. The $V_n^{\max}$ are the maximally adsorbed volumes for each kind of adsorption site. The K_n^{ad} are the adsorption equilibrium constants, for which we assume the Arrhenius form,

$$K_n^{\mathrm{ad}}(T) = A_n\, \mathrm{e}^{-\Delta G_n^{\mathrm{ad}}/(RT)} \tag{10}$$

where A_n is the Arrhenius factor and ΔG_n^{ad} is the free enthalpy of adsorption for pore n. R denotes the gas constant.

In the case of similar ΔG_n^{ad} and A_n, the 2-Langmuir model becomes an effective 1-Langmuir model with an effective $V_{\mathrm{eff}}^{\max} = V_1^{\max} + V_2^{\max}$. For this case, a fit of the model to a data set of course yields unstable results for the individual $V_n^{\max}$ but a stable value for their sum.

Computational Details. All DFT calculations are performed with the all-electron code FHI-aims[19] (Fritz-Haber Institute ab initio molecular simulations) using its standard "light" numeric atomic orbital basis sets. Electronic exchange and correlation is treated in the generalized gradient approximation (GGA) using the Perdew−Burke−Ernzerhof (PBE) functional[20,21] for the calculations leading to the bulk moduli and deformation potentials, as these mostly geometry-dependent properties can be expected to be represented rather well on the semilocal level of theory. For the effective masses, which crucially depend on a correct localization of states, we instead use the more expensive revised Heyd−Scuseria−Ernzerhof hybrid functional.[22,23] We treat the deformation potential with the GGA functional in contrast to our prior work[9] because we realize that the usage of the hybrid functional on the GGA-optimized crystal structure introduces a large pseudostress that could affect the resulting deformation potential. Overall, we use a 4 × 4 × 4 k-point grid. Despite the wide band gap and large size of the unit cell, we find that this is sometimes necessary to obtain a useful band structure. Furthermore, we use the Tkatchenko−Scheffler dispersion correction[24] as implemented in FHI-aims to account for the VDW interaction between host and guest.

Initial MOF geometries were taken from ref 9; all other structures, i.e., PLCs, result from the sampling process described in the previous section, Sampling the Pore Network. Furthermore, the geometry of each PLC is locally optimized. For this we use FHI-aims in combination with the Broyden−Fletcher−Goldfarb−Shanno (BFGS) optimizer as implemented in the Atomic Simulation Environment (ASE)[25] together with the ExpCellFilter constraint. The latter allows for the simultaneous optimization of the atomic forces and stresses using a method by Tadmor et al.[26] Note that all of these crystal structures are derived from the primitive unit cell of the empty Fe(ta)$_2$ crystal. In contrast, for the experimental results, the corresponding cubic unit cell[27] is used throughout this manuscript.

For the adsorption of Ar into Fe(ta)$_2$, we use GCMC sampling in the Monte Carlo/molecular dynamics (MCMD) code.[28] to simulate the adsorption isotherms and the equilibrium PLCs for a 1 × 1 × 1 cell of the MOF. We sample a total of 10^4 steps and vary the correlation time between 1, 10^3, and 10^4. We checked the convergence of our sampling but found no significant improvements beyond 10^4 steps (cf. Figure S5 in the Supporting Information). With this grand-canonical procedure, we sample each of the PLCs at a frequency determined by their relative free energies. Recognizing their different adsorption energetics, which are also reflected in the Langmuir model employed to analyze the experimental results, we classify them according to the loadings, l and s, of the large and small pores, respectively. These normalized frequencies $f_{l,s}(p,\,T)$ are then used to calculate the mean mobility $\mu(p,\,T)$ according to eq 4 and compare it to the experimental results via eq 2. We want to reflect this distribution of the adsorbate A in the different pores of the host in a modified sum formula A$_{l,s}$Fe(ta)$_2$.

Synthesis and Characterization. All chemicals were used as received from the commercial supplier without further purification. The Fe(Cl)$_2$ (98%) was purchased from abcr GmbH. 1*H*-1,2,3-Triazole was degassed and stored under Ar atmosphere prior to use. Fe(ta)$_2$ was synthesized according to our recently published procedure,[27] which is similar to the original literature.[29] Briefly, a mixture of Fe(Cl)$_2$ (133.3 mmol, 16.9 g) and 1*H*-1,2,3-triazole (400 mmol, 23.2 mL, 27.63 g) in 150 mL of anhydrous *N*,*N*-dimethylformamide (DMF) was heated at 120 °C for 20 h under Ar atmosphere. After centrifugation and washing three times with 40 mL of dry DMF under Ar atmosphere, the solvent was exchanged three times by immersion and centrifugation in 40 mL of dry methanol for 3 days. The product was obtained after drying under vacuum for 6 h at 200 °C as a pale pink powder (10.15 g, 42%). The compound was characterized accordingly.

Variable temperature, pressure, and gas powder X-ray diffraction measurements were conducted in a CHC+ chamber with an Empyrean diffractometer (Panalytical), which was equipped with a Bragg−BrentanoHD mirror and a PICcel$^{3\mathrm{D}}$ 2 × 2 detector. Prior to the diffraction measurements, the material was degassed in vacuum at 130 °C for 140 h. Cell constants were obtained using Le Bail[30] fits of the spectra in Expo2014.[31] For the refinement, a cubic cell with the space group $Fd\bar{3}m$ was assumed.[27] Results of this procedure are given in Table S4.

https://doi.org/10.1021/acsami.2c05127
ACS Appl. Mater. Interfaces 2022, 14, 33662−33674

The adsorption isotherms were measured on a BELSORP-max instrument, which was combined with a BELCRYO system. Ar (99.999%) and CO_2 (99.995%) from Linde were used for the measurements. Two samples of 49.4 mg for Ar and CO_2 were measured after heating at 150 °C under vacuum for at least 4 h prior to each measurement. For the Ar adsorption at 77 K, a Brunauer−Emmett−Teller (BET) surface area of 403 m^2/g, comparable to literature results,[27] was determined in the pressure range of $3 \times 10^{-3} < p/p^* < 2.3 \times 10^{-2}$, where p^* denotes the vapor pressure. From the same data, one can find a similar Langmuir surface area of 414 m^2/g. This is a hint that no multilayer adsorption occurs due to the limited size of the $Fe(ta)_2$ pores.

Making use of the Clausius−Clapeyron equation,

$$\Delta H_{\mathrm{ad}} = R\left(\frac{\partial \ln p}{\partial (1/T)}\right)_V \tag{11}$$

as described in the literature,[32] the isosteric enthalpy of adsorption, ΔH_{ad}, was calculated for the values obtained from the measured isotherms (Figure 7) as the slope of linear plots for different loadings of $\ln p$ versus $(RT)^{-1}$ (Figure 8), as is suggested by

$$\ln p = \Delta H^{\mathrm{ad}} \frac{1}{RT} + \ln p_{\mathrm{o}} \tag{12}$$

In both equations, R denotes the gas constant, and the subscript V in eq 11 denotes the boundary condition of constant adsorbed volume. Indeed, the Arrhenius plots ($\ln p$ vs $1/RT$) for different constant loadings (which is equivalent to adsorbed volumes V) result in graphs matching the expected linear behavior. Note that, in contrast to ref 32, we use linear regression for more than two ($1/RT$, $\ln p$) pairs from which we ultimately determine the slope ΔH^{ad}.

Conductivity Measurements. A glass substrate covered with 10 nm of titanium as an adhesion layer and 50 nm of gold as a conducting layer above was slitted ($d = 40\ \mu m$) to obtain a four-point contact van der Pauw geometry.[33] For this arrangement, the isolation resistance between empty neighboring quadrants was found to exceed $1 \times 10^{14}\ \Omega$ (Figure 5).

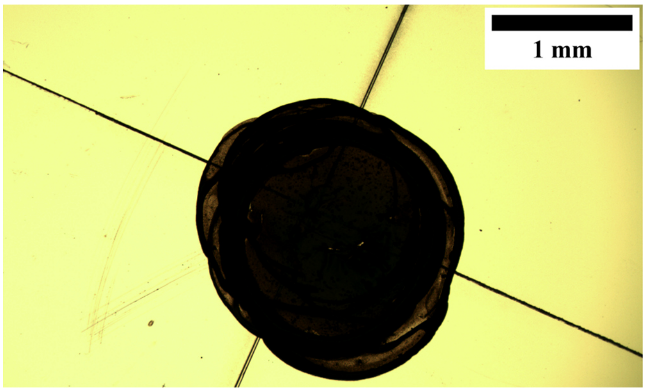

Figure 5. van der Pauw setup for measuring the conductivity of $Fe(ta)_2$ as described in the text showing a droplet of the ethanolic dispersion of $Fe(ta)_2$ on a gold slide after heating at 353 K in an Ar atmosphere.

One μL of an ethanolic dispersion of the previously activated $Fe(ta)_2$ was pipetted over the slit at 353 K under Ar atmosphere to end with a self-assembled closest packing of the material (Figure 6). After drying, the sample was placed in a cryostate connected to a gas supply system and a turbo molecular pump. The whole system was then degassed in high vacuum ($\sim -10^{-7}$ kPa) at 403 K for several days. To conduct the measurements, a Keithley Model 2400 Sourcemeter was used. All measurements were performed with constant current, and the voltage drop over the sample was measured. In none of our measurements did the current exceed 0.1 μA. To see the response of the sample to gas loading, the temperature of the sample was kept constant ($\Delta T = \pm 0.02$ K) over the whole measurement. The absolute pressure of the test gas in the chamber was controlled by opening and closing a mass flow controller. Data were collected every second. The measurement started in the vacuum state for several minutes to obtain the corresponding value for σ_0. The pressure of the test gas was then increased up to 105 kPa in steps of 4 kPa with a maximum gas flow of 7 mL min^{-1}. After every step a pause of 60 s for equilibration was set. The maximum pressure applied is restricted by setup limitations and lies well within the range for a full loading of the MOF in the studied temperature regime.

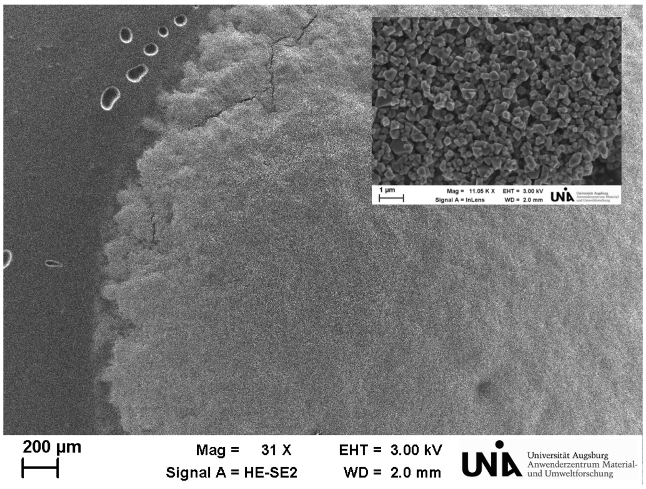

Figure 6. SEM image of a droplet of $Fe(ta)_2$ dispersed in ethanol on a carbon pad after drying in vacuum. The inset shows the resulting close packing of the single crystals.

RESULTS AND DISCUSSION

Aligning Experimental and Theoretical Gas Uptake. Our analysis of the Ar and CO_2 isotherms shows that we can explain the gas uptake of $Fe(ta)_2$ sufficiently well by a 2-Langmuir model (cf. Connecting Theory and Experiment): by fitting the adsorbed volume at standard temperature and pressure V^{STP} (Figure 7), we find the Gibbs enthalpies of adsorption for Ar and CO_2 in the pores of the $Fe(ta)_2$ framework (Table 1). Within the pressure range over which the 2-Langmuir model holds, we can calculate the ratio $V^{\mathrm{STP}}/V^{\mathrm{STP}}_{\mathrm{max}}$ which is just the number of adsorbed guests when multiplied with the number of pores in the underlying unit cell.

Furthermore, the analysis of adsorption isosteres by means of eq 12 yields the approximate bounding adsorption enthalpies (negative heats of adsorption) ΔH^{ad}_n (Table 1) with intermediate values shown in Figure 8. We observe a change of adsorption enthalpy for CO_2 starting at a pore loading of $N \approx 15$ guest molecules per conventional unit cell. We can explain this effect using the image of two thermodynamic subsystems—the small pores and the large pores of the network—which are populated accordingly. The resulting value for ΔH^{ad}_n, which we see in Figure 8, is given by an appropriate ensemble mean of both subsystem adsorption enthalpies.

Finally, we can calculate adsorption energies using our DFT data (Table 1), which does not include any entropic effects. The values are of similar order of magnitude as their experimental counterparts. This hints to the adsorption process showing only small entropic contributions.

For CO_2 we expect larger—and different—entropic contributions for the two pores. Our results for the free enthalpies of adsorption, fitting the measured isotherms, and

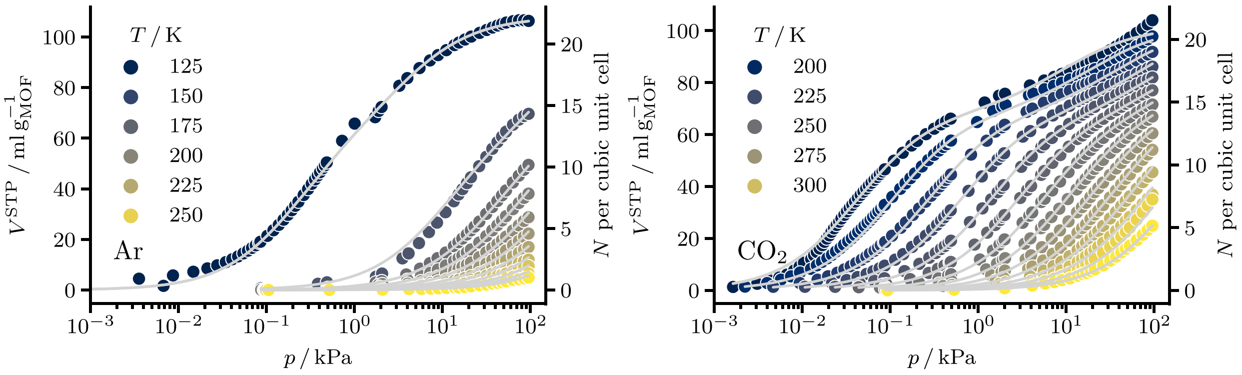

Figure 7. Isotherms of adsorption for Ar and CO_2 to Fe(ta)$_2$. On the second ordinate axis we give the number of guests per cubic unit cell. The one used here has a total of 24 pores per unit cell.

Table 1. Gibbs Enthalpies ΔG^{ad} and Enthalpies ΔH^{ad} of Adsorption Obtained by Fitting the Measured Isothermal and Isosteric Data and Energies ΔE^{ad} of Adsorption Obtained from DFT Results[a]

	ΔG_n^{ad}/kJ mol^{-1}		ΔH_n^{ad}/kJ mol^{-1}		ΔE_n^{ad}/kJ mol^{-1}	
	kind of pore		loading		kind of pore	
adsorbate	A	B	$N \lesssim 15$	$N \gtrsim 15$	small	large
Ar	−17.1	−16.2	−16	−16	−20.1	−20.7
CO_2	−33.7	−25.4	−35	> −25	−50.0	−31.1

[a] An estimate from the change of vibrational entropy through sets of phonon calculations was not successful, possibly due to the weak interaction between host and guest.

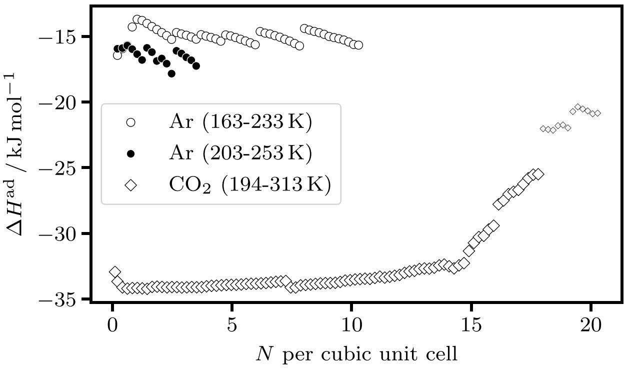

Figure 8. Enthalpies of adsorption of Ar and CO_2 into Fe(ta)$_2$. The data points for CO_2, which are shown with a smaller symbol, are given for completeness but are based on a linear fit of two data points.

the adsorption energies, from our DFT simulations, show that this reasoning is plausible.

Considering the adsorbed Ar STP volumes, we compare the set of simulated adsorption isotherms (Figure 9) to the ones obtained through measurement. The simulated ones can also be described by a 2-Langmuir model. The maximum volume that is adsorbed in the simulation, 108 mL, is similar to the one fitted to the experimental data. However, individual pore volumes cannot easily be determined as discussed earlier. The free enthalpies of adsorption from the simulated isotherms result in a value of roughly $\Delta G^{\mathrm{ad}} = -21.3$ kJ mol^{-1} for Langmuir isotherms. This value fits well to the experimentally determined one shown in Table 1.

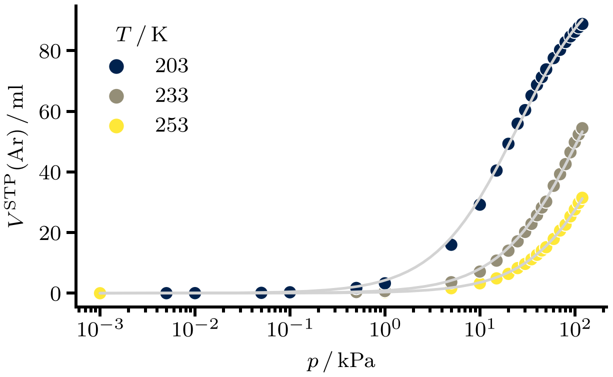

Figure 9. Simulated isotherms of adsorption for Ar to Fe(ta)$_2$.

Conductivity. Measured values of the absolute conductivity of the empty MOF after dispensing fit well into the ranges reported in the literature.[29,34] Nevertheless, the main focus of this work lies on the relative changes σ^{rel} of the conductivity and μ^{rel} of the mobility due to varying the pore loading. These are generally more reliable than absolute values considering the variability of the used powder sample and the MOF itself. Furthermore, absolute conductivity values were not absolutely constant with time: after some heating periods, the measured resistance stabilized at ~7×10^9 Ω at room temperature. This can be explained by the removal of remaining solvent and unknown other species in the pores and on the outer surface of the crystallites by flushing with the test gas under heating. Yet, after several days, when the measurements for the gas loading were taken, the resistance in vacuum still slightly increased on the scale of days. With every heating and degassing cycle, a larger increase in the resistance was found. This increase was on the order of 10% of the maximum relative conductivity change σ^{rel} due to gas uptake, demonstrating the significance of pore-loading-induced conductivity changes. Specifically, in Figure 10 we plot σ^{rel} versus gas pressure at different temperatures for Ar and CO_2. In the experimental setup, the temperature sets for the two gas species were chosen such that they fit their specific condensation behavior. Furthermore, the maximum adsorbed volume is similar for the two gases in the applied temperature range (Figure 7). Using the earlier-outlined procedure to translate external gas pressures into adsorbed volumes, we are now in a position to directly compare theory and experiment. Indeed, we find the

https://doi.org/10.1021/acsami.2c05127
ACS Appl. Mater. Interfaces 2022, 14, 33662−33674

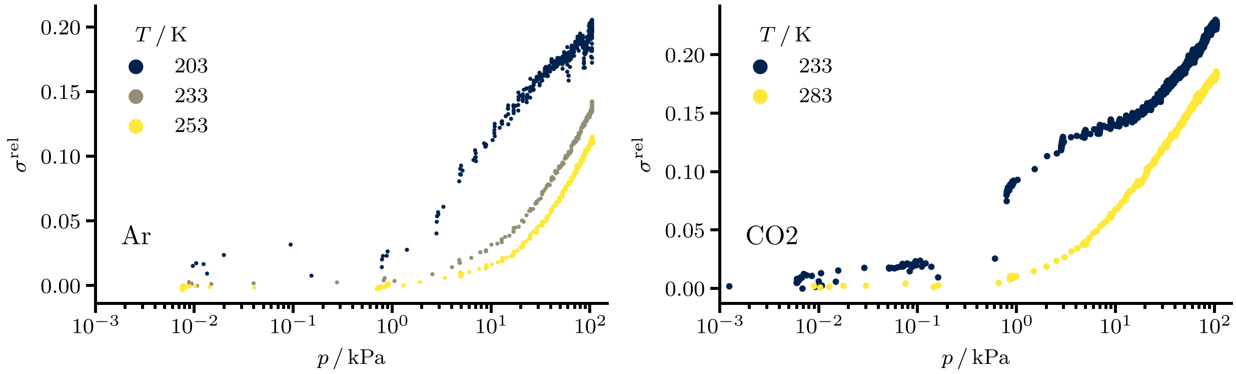

Figure 10. Relative conductivity σ^{rel} in terms of gas pressure p for the absorption of Ar and CO_2 into $Fe(ta)_2$.

experimental conductivity trends reproduced in our theory, at least for a loading up to $V^{\mathrm{STP}} \approx 20\ \mathrm{cm}^3\ \mathrm{g}^{-1}$ (Figure 11).

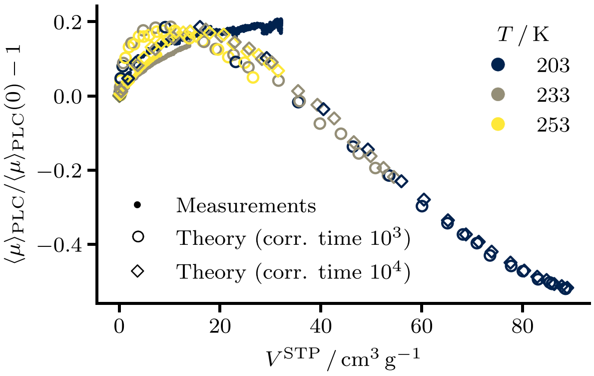

Figure 11. Relative mean mobility $\langle\mu\rangle^{\mathrm{rel}}$ and relative conductivity σ^{rel} in terms of the mean loading $\langle x\rangle = V/V^{\max}$ for the loading of $Fe(ta)_2$ with Ar.

This allows us to interpret the results using the earlier-developed theoretical framework. With increasing loading of the material, at first the empty MOF unit cell has a large statistical weight in the calculation of the average conductivity, cf. eq 4. With increasing pressure and thus increasing adsorbed volume (the isotherms are monotonic curves), the prevalence of PLCs of low loading, in particular with empty large pores and up to two filled small pores per unit cell, increases. Their associated mobility is higher than the one of the empty MOF; hence, the mean mobility increases. With more and more gas adsorbed within the pores, the spread of the distribution of PLCs increases. At the point where the theoretically predicted σ^{rel} begins to decrease, PLCs with a high loading, which also have some large pores filled, become more frequent. These, however, have a lower local conductivity, overall lowering the average conductivity of the material. At even higher gas pressures, such low-conductivity PLCs become dominant, such that the total MOF conductivity can fall even below that of the pristine material, cf. Figure 11. We argue that the difference of the simulations to the experimental results is due to an overestimation of the MOF loading with adsorbate. The reason for this is the usage of the primitive unit cell of the framework material, which intrinsically leads to a higher concentration of the adsorbate in the MOF during the sampling (compared to the extended material).

On the other hand, it is possible that we underestimate the adsorbate loading in the experiment due to limited measurement times. As a consequence, this leads to nonideal diffusion-induced equilibrium representations within the real material. Our measurements thus might simply not yet reach a loading of the whole sample where the decrease occurs in the simulation.

Furthermore, theoretical predictions are limited to such PLCs achievable within a single unit cell of the MOF. As such, the impact of filled larger pores might be overestimated, leading to the onset of the decline in mobility to appear at too-small gas uptakes compared to the experiment.

Nevertheless, the good agreement of experiment and theory now presents us with the opportunity to analyze in detail the origins of the loading-induced changes in conductivity, looking at all of the contributing factors to BS theory. Indeed, our simulations show changes in the material parameters of the ideal $Fe(ta)_2$ crystal that go into the relative BS mobility for different PLCs and also for different gases. The various values for the cases we explored are gathered in Table S2.

Structural Changes. First, though, we examine the influence of gas uptake on the structure of the MOF. From our calculations, we find that through the loading the cell is distorted such that both cell constants and lattice angles change slightly. On the one hand, we can see that the cell constants decrease with an increase in the loading of the large pores. On the other hand, they increase with the loading of the small pores (cf. Tables S3 and S4). We explain these two effects through the VDW forces between the guest and the host, as well as through mechanical deformation of the framework material. The attractive VDW interaction between host and guest leads to a slight shrinking of the loaded large cells. In contrast, the small pores are expanded through a guest in them.

Although the theoretical results show a deviation from the cubic cell symmetry, these are so small that treating them at the space group $Fd\bar{3}m$, e.g., for the purposes of calculating band structures, is still a valid approximation. Experimentally, too, we find small deviations upon pore loading, summarized in Table S4, that qualitatively match those seen in the simulations. These data were obtained after exposing the host sample to the guest at 0.1 MPa for 1 day. Our findings using the cubic cell approximation are thus in good accordance with the experimental results of Grzywa et al.[27] for the empty host network.

Grzywa et al. found a spin-crossover (SCO) transition for $Fe(ta)_2$ from a room-temperature Fe^{II} low-spin phase to a

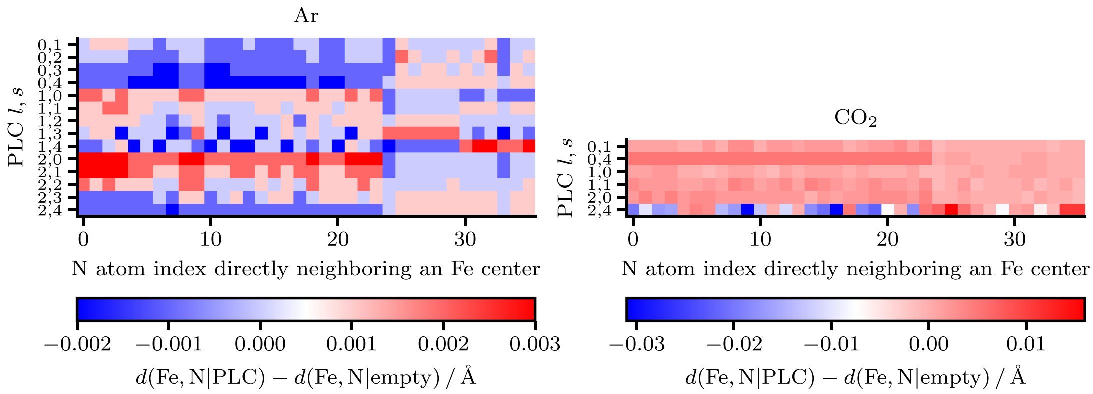

Figure 12. Deviations of the bond lengths from the empty host in the various Ar and CO_2 $Fe(ta)_2$ PLCs we studied.

high-temperature Fe^{II} high-spin phase at a temperature of ~563 K (with a delayed reverse transition at ~483 K).[27] This SCO transition comes with an increase of the unit cell volume of ~4600 Å^3 by 22% and the Fe−N bond lengths by 18 and 21 pm for the Fe(1) and Fe(2) centers, respectively, from an equal length of 198 pm.[27]

Through gas adsorption, the unit cell volume and Fe−N bond lengths change, too. Thus, one should discuss our results also in light of possible changes in the spin configuration of the Fe^{II} centers upon gas adsorption.

First, it is important to note that the bond length changes observed here are much smaller than the ones introduced during an SCO transition, in the order of at most several picometers instead of ~20 pm (Figure 12). For Ar we see no overarching trend for the bond lengths across PLCs. While the occupation of the large pores leads to an increase of most of the Fe−N bond lengths, occupation of the small pores decreases them and leads to an overall decrease even if the large pores are occupied. In contrast, for CO_2 we always find a slight increase of the Fe−N bond lengths for the incompletely occupied PLCs. The PLC with all pores singly occupied by CO_2 is different in that there are more bond lengths that are decreased. The effect for CO_2 is larger almost by an order of magnitude than that for Ar; however, it is still small. Finally, the temperatures considered here (up to 253 K for Ar and 283 K for CO_2) are much smaller than those observed for the SCO transition.

On the basis of these observations, we omitted a spin channel-resolved analysis of the Fe^{II} centers because high-spin configurations do not seem to occur upon absorption of Ar and CO_2.

Bulk Modulus. Under Ar absorption, the value of C increases, irrespective of which pores the gas atoms are placed into (cf. Figure 13). This indicates a rise in the mechanical stiffness of the compound. Note that this stiffening is stronger when Ar is placed in the small pores. This observation is in a way similar to the "caryatidic" one of Moosavi et al.[35]

Comparing the effect of filling the large pores starting, respectively, from the empty MOF and from $Ar_{0,2/3}Fe(ta)_2$, where two-thirds of the small pores are filled, we observe that this effect may be roughly multilinear, with one slope for each kind of pore. However, we have studied only a relatively small set of PLCs with comparably high loading here, and the mapping from the set of PLCs to the loading values x is many-to-one. Thus, for each x we have a distribution of values $C(\text{PLC} \rightarrow x)$. At small pore loading, at least, this does seem to lead to a wide distribution, though, as a single Ar atom in either a large or a small pore yields exactly the same effect, cf. Figure 13.

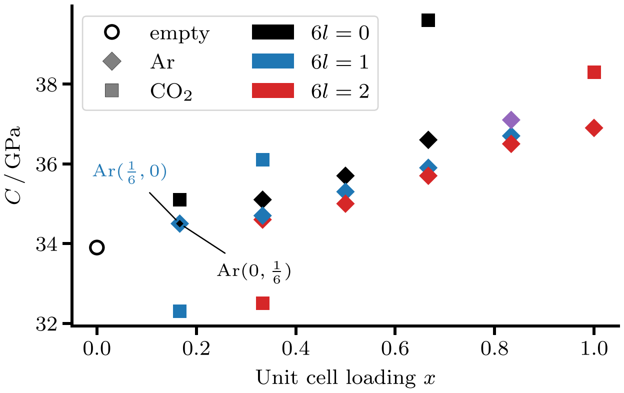

Figure 13. Bulk moduli of the simulated $A_{l,s}Fe(ta)_2$ crystals versus total pore loading x, which is normalized such that at $x = 1$ each pore (small and large) contains exactly one adsorbate. The color of the markers encodes the number of adsorbates in the large pores, $6l$, with respect to the primitive unit cell. This means that we populated each pore with at most one adsorbate, analogous to our Langmuir-like model. Thus, $6l = 2$ means a population of both large pores of the unit cell. The population of the small pores $6s$ can be deduced from the figure through the relation $s = x - l$.

For CO_2 absorption, the situation is different. On filling the large pores, we see a decrease of C, whereas for the small pores there is again an increase, being even more pronounced than that for the adsorption of Ar (Figure 13). The latter is most likely due to the rodlike shape of the CO_2 molecule, through which it acts as an even better stability anchor than the Ar atom. Conversely, by this argument, the presence of CO_2 in the large pores is not as favorable for the bulk modulus as a spherical adsorbate or one which mimics the symmetry of the pore better and thus softens the network slightly.

For softer MOF materials, i.e., those with a smaller bulk modulus C, one could expect larger effects of the gas adsorption on the conductivity in this respect. In the isotropic body approximation, C is proportional to ρ and v_s^2, the crystal density and the square of the mean velocity of sound. Gas adsorption leads to an increase of the density and possibly also to a change of the mean velocity. While an increase of the crystal density definitely increases the bulk modulus, changes of the sound velocity need not lead to a positive effect. In principle, they could also counteract the effect brought about by the increase in density. The most definite statement without

https://doi.org/10.1021/acsami.2c05127

any further studies is that it will depend on the combination of host network and guest. Unfortunately, for the larger and more flexible linker molecules, the other BS parameters tend to be unfavorable for conductive behavior: their charge carriers tend to be localized (high effective mass) and are easily scattered by the lattice vibrations (large deformation potential), thus leading to the bad electrical conductivity of most MOFs.

Effective Mass. Contrary to the elastic properties, we find that the influence of adsorbed atoms or molecules on the effective mass is quite small to begin with and also shows no strong dependence on the guest species (Figure 14). This is likely due to the weak interactions between the host crystal and the adsorbates and the large energetic separation between the guest's electronic states and the host's frontier orbitals, cf. Figure 15. Thus, effective masses are mostly independent of the adsorbates, with the small changes upon pore loading shown in Figure 16 likely being caused by the distortions of the lattice brought about by the guest molecules. This is true for both the VB maximum and the CB minimum values of the effective mass, cf. Table S2.

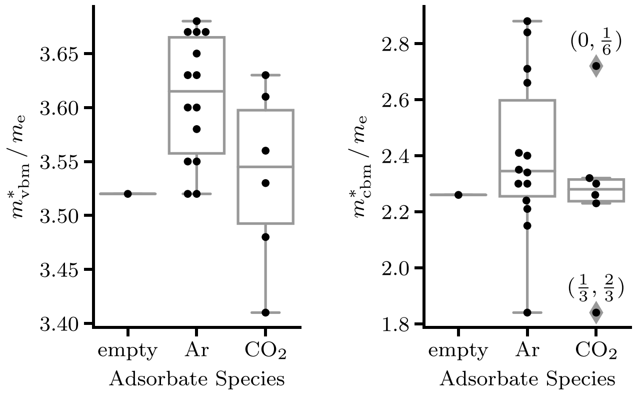

Figure 14. Distribution of the effective masses for the different adsorbates and for the empty MOF. The median of the distribution does not change strongly with the kind of adsorbate.

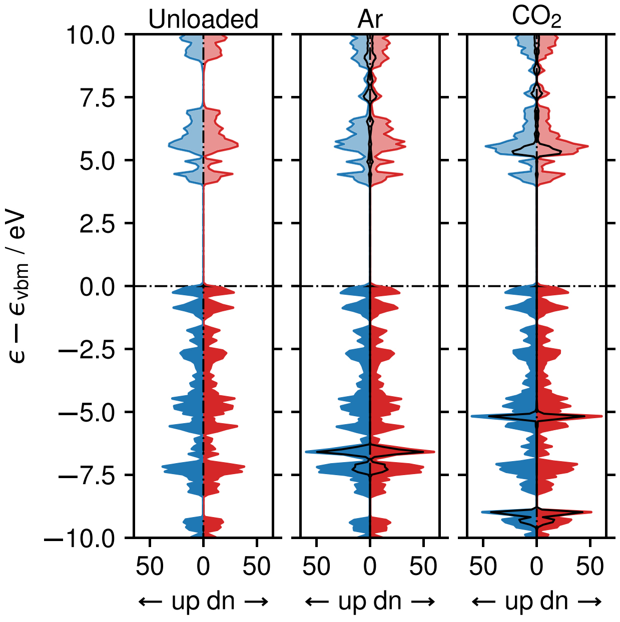

Figure 15. Density of states for the empty Fe(ta)$_2$ crystal as well as an Ar- and CO$_2$-loaded host−guest pair. The electronic states of the guest species (solid black lines) lie far from the band edges.

Deformation Potential. Deformation potentials D_ν overall show a slightly nonlinear decrease with increasing loading x of the unit cell as depicted in Figure 17 for both the VB maximum and the CB minimum. The distribution of deformation potentials for each kind of adsorbate is wide for Ar and narrow for CO$_2$ (Figure 18, left and middle panels). The difference between the values for the two edge band extrema is ~3 eV for all studied PLCs (Figure 18, right panel). This is then the effective deformation potential with which the band gap changes under deformation. As a side note, a large increase in the cell volume, i.e., a strong deformation, e.g., facilitated through an SCO transition as remarked previously, could decrease the band gap enough to increase the density of mobile charge carriers. In this case though, the argument by which we compare relative conductivity and relative mobility would break down.

Examining the data more closely, we can distinguishing subsets of one gas species and of constant loading l of the large pores. Exemplarily, we focus on Ar.

We find that a variation of l and also of the small pore loading s has an effect on the deformation potential. We find it noteworthy that the effect of s for a given value of l becomes smaller with increasing l. By effect, we mean the width of the corresponding $D_\nu(s|l = \text{const})$ interval. We observe a similar pattern for the CO$_2$ subset. Furthermore, this pattern can be found for both edge band extrema.

The deformation potential values lie in a narrower interval for higher loading, in particular for higher values of l. We want to stress that, in the regime of low overall loading and lower l, the changes of the deformation potentials with respect to the empty MOF are larger. This means that PLCs of smaller loading play a larger role for the effect of the loading on the mobility.

Charge Carrier Mobility. Putting all the pieces together and computing $\mu^{\mathrm{rel}}(\mathrm{PLC})$ from eq 6, we find that the strongest influence on its value comes from the deformation potential (Figure 19). Furthermore, we find a trend that PLCs with higher loading tend to have a lower relative charge-carrier mobility than the ones with lower loading. Thus, we conclude that the deformation potential and, by extension, the electron−phonon coupling are the main factors of interest when studying the effects of the adsorption of a weakly interacting guest species.

This makes sense, considering that an absorbed species in the bulk of a framework changes its phononic structure. Therefore, the strongest changes upon absorption can be expected of the quantities that depend on these phonons: C on the one hand and D_ν on the other hand. However, $\overline{m}^*$, which is related to the electronic couplings,[12] does not show a strong dependence on the PLC, and thus, the mobility does not show a clear trend in this respect (Figure 20).

■ CONCLUSION

In this work we have shown experimentally and theoretically that the adsorption of Ar and CO$_2$ to the inner surface of iron (1,2,3)-triazolate, Fe(ta)$_2$, changes the conductivity of this metal−organic framework material. To compare the experimental measurements, i.e., ensemble averages, with the theoretical results, we simulate distributions of pore-loading

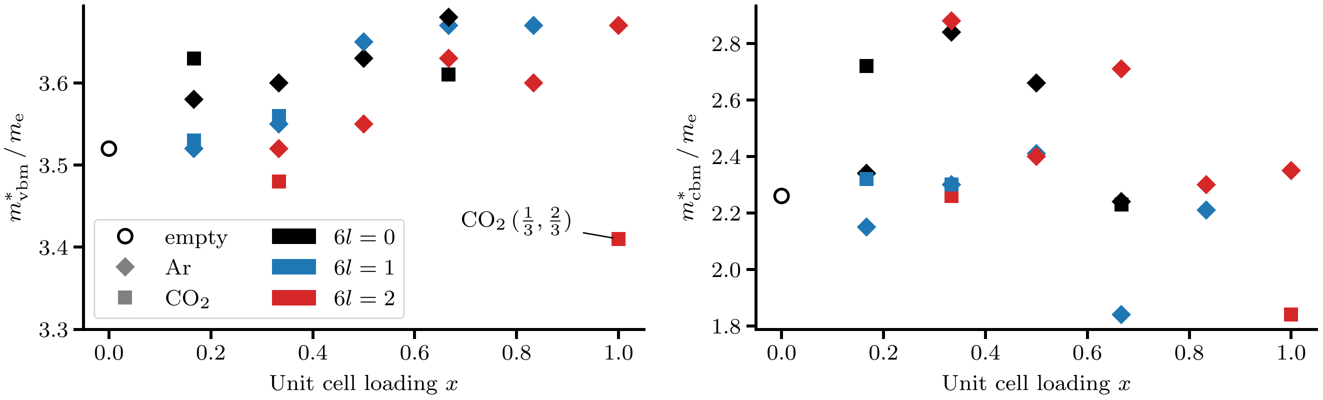

Figure 16. Effective masses of the holes (VBM) and the electrons (CBM) for the various studied $A_{l,s}Fe(ta)_2$ crystals.

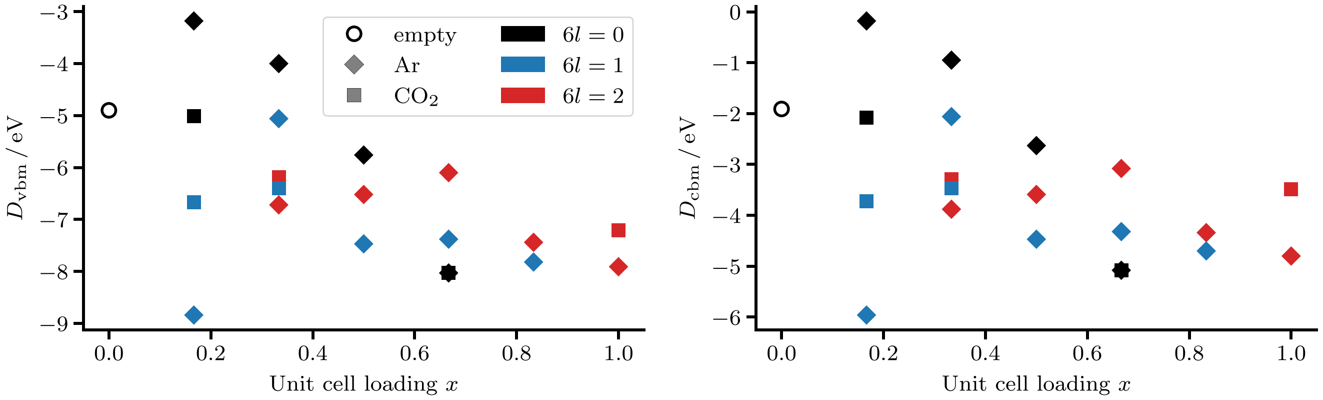

Figure 17. Deformation potentials for the valence band maximum and the conduction band minimum for the various PLCs we studied. Note the similarity between both graphs, as also highlighted by the difference distributions shown in Figure 18.

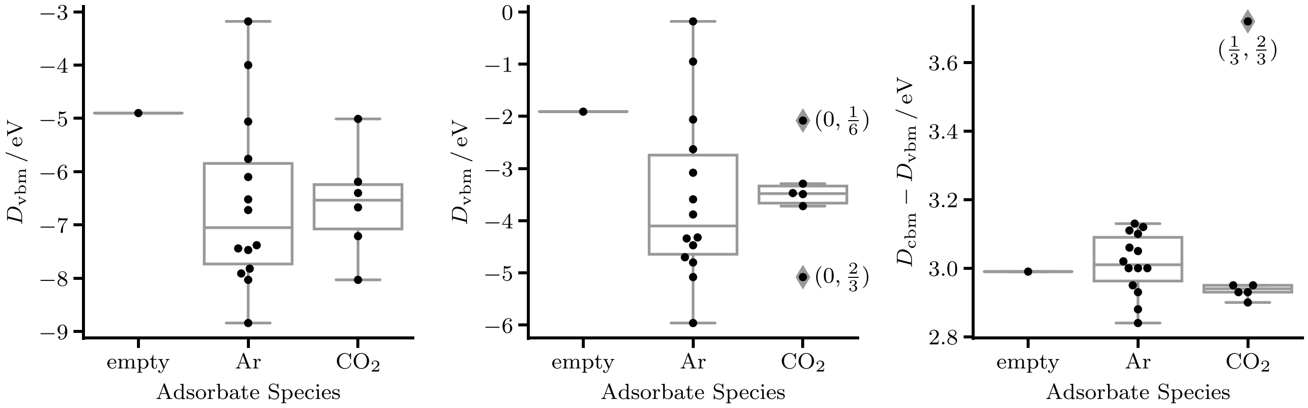

Figure 18. Deformation potentials for the valence band maximum, the conduction band minimum, and their difference broken down to different adsorbate species. The distribution for Ar is wide with respect to CO$_2$. The difference between the deformation potentials of one host−guest pair is always ~3 eV.

configurations (PLCs) for various pressure−temperature pairs. These distributions approximate the true ones in equilibrium. From the frequencies of the PLCs, we can compute average mobilities and find a good agreement with experimental measurements for higher temperatures in their common pressure range (Figure 11). For a lower temperature, the experiments reveal a saturation of the relative conductivity to the end of this range, whereas the theoretical curve starts to decrease. This behavior is likely due to some residual errors in the simulated PLC frequencies and some finite size effects due to the single unit cell model.

Note that this comparison is only a qualitative one. On the one hand, this is due to the simplicity of the Bardeen−Shockley model and the fact that the various PLCs of a pristine single-crystal model can only be coarsely mapped to the real loading state of a polycrystalline material in thermodynamic equilibrium. On the other hand, the pore size and also the size

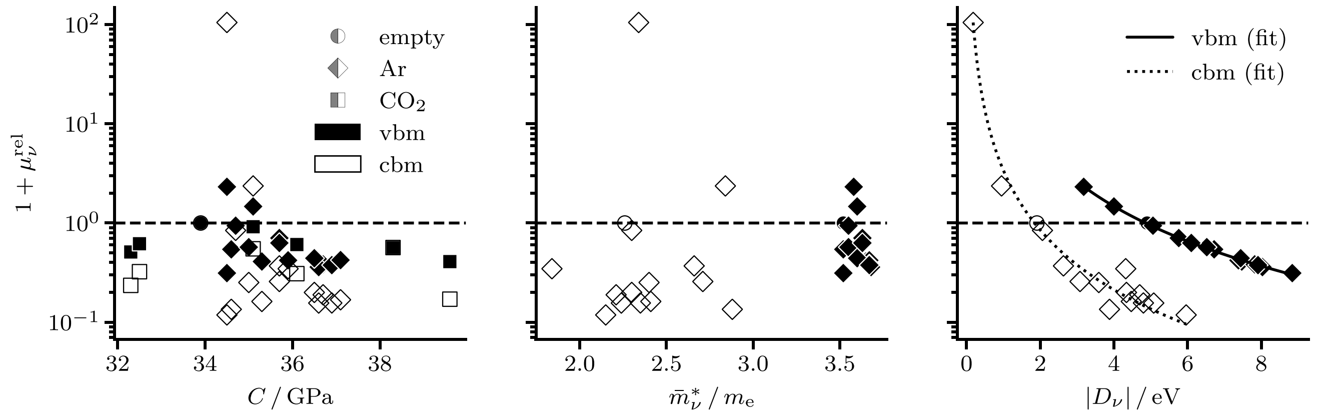

Figure 19. Dependence of the (relative) mobility on the BS parameters. Clearly, the influence of the deformation potential is the strongest as the dependence $\mu \propto D^{-2}$ most easily can be distinguished. We recognize that there exist such PLCs that increase the mobility and such that decrease it.

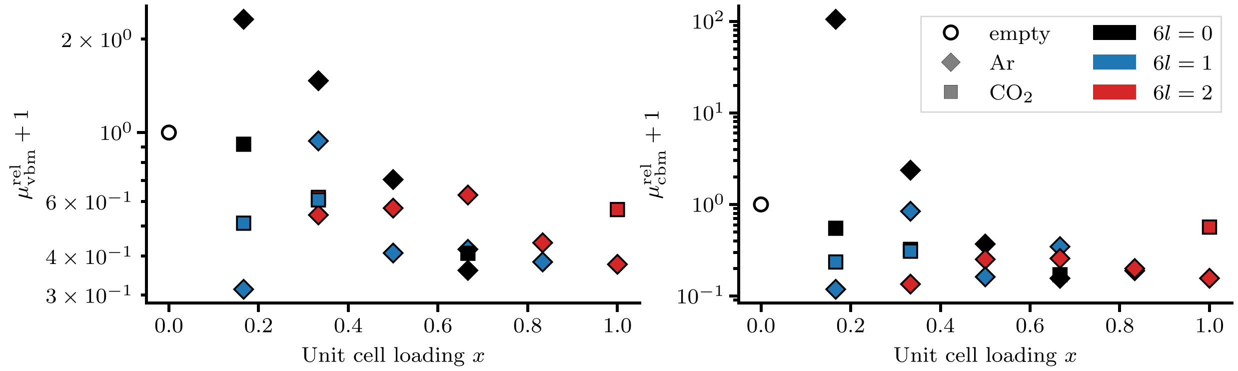

Figure 20. Semilogarithmic plot of the relative hole and electron mobilities for the various studied PLCs.

of the crystallites complicate the sample preparation and reaching a definite reference state on the experimental side.

Overall, we demonstrate how theory here can supplement experimental measurements for a more in-depth understanding of the occurring processes. Experimentally, we find a Langmuir isotherm-like change of the conductivity with increasing pore loading. Theoretically, we not only find a good agreement with these experiments but, by properly aligning theoretical and experimental results, we also find that there are such PLCs that increase the charge-carrier mobility and such that decrease it. In either case, the largest influence is through the deformation potential, i.e., the effective coupling between the charge carriers and the acoustic phonons of the lattice. All of the other parameters of the Bardeen−Shockley (BS) mobility have a less prominent influence on its value. Note that these three parameters are always with respect to a local minimum of the potential hypersurface of the corresponding PLC. Therefore, any effects of cross-influences between the BS parameters are inherently taken into account.

Ultimately, though, changes to macroscopic (i.e., thermodynamically averaged) conductivities are rather small and seem to lack the specificity desirable for the use of the MOF as an electrical trace gas sensor. Yet, our results also highlight a way to improve the MOF's efficacy. The large variability of the deformation potential with specific PLCs and gas species hints at a possible synthetic engineering of the material, e.g., by closing off certain pores, for a stronger, more interpretable electric response upon gas sorption.

■ ASSOCIATED CONTENT

Supporting Information

The Supporting Information is available free of charge at https://pubs.acs.org/doi/10.1021/acsami.2c05127.

> Short introduction to quaternions and how they are used to represent three-dimensional rotations; BS parameters; fitted second-order deformation potentials; theoretical and experimental lattice parameters; Arrhenius plots from which the adsorption enthalpies are determined; and figure showing that 10^4 steps are sufficient for the mean mobility for the case presented (PDF)

■ AUTHOR INFORMATION

Corresponding Author

Harald Oberhofer − *Chair for Theoretical Chemistry, Technical University of Munich, D-85747 Garching, Germany;* Present Address: Present address: Chair for Theoretical Physics VII and Bavarian Center for Battery Technology, University of Bayreuth, Universitätsstr. 30, D-95447 Bayreuth, Germany; orcid.org/0000-0002-5791-6736; Email: harald.oberhofer@ch.tum.de

Authors

Christoph Muschielok − *Chair for Theoretical Chemistry, Technical University of Munich, D-85747 Garching, Germany*

Alexander Reiner − *Chair for Experimental Physics I, University of Augsburg, D-86159 Augsburg, Germany*

Richard Röß-Ohlenroth – *Chair of Solid State and Materials Chemistry, University of Augsburg, D-86159 Augsburg, Germany*
Andreas Kalytta-Mewes – *Chair of Solid State and Materials Chemistry, University of Augsburg, D-86159 Augsburg, Germany*
Dirk Volkmer – *Chair of Solid State and Materials Chemistry, Member of Augsburg Centre for Innovative Technologies (ACIT), University of Augsburg, D-86159 Augsburg, Germany;* orcid.org/0000-0002-8105-2157
Achim Wixforth – *Chair for Experimental Physics I, Member of Augsburg Centre for Innovative Technologies (ACIT), University of Augsburg, D-86159 Augsburg, Germany*

Complete contact information is available at:
https://pubs.acs.org/10.1021/acsami.2c05127

Author Contributions

[⊥]C.M. and A.R. contributed equally to this work.

Notes

The authors declare no competing financial interest.

ACKNOWLEDGMENTS

The authors thank the German Research Foundation DFG (Priority Program no. 1928 COORNETS, Grant nos. OB425/3-2, VO829/12-2, and WI1091/20-2), as well as the Augsburg Centre for Innovative Technologies ACIT, and the Nano-initiative München NIM for financial support.

REFERENCES

(1) Batten, S. R.; Champness, N. R.; Chen, X.-M.; Garcia-Martinez, J.; Kitagawa, S.; Öhrström, L.; O'Keeffe, M.; Paik Suh, M. P.; Reedijk, J. Terminology of metal-organic frameworks and coordination polymers (IUPAC Recommendations 2013). *Pure Appl. Chem.* **2013**, *85*, 1715–1724.

(2) Eddaoudi, M.; Li, H.; Yaghi, O. M. Highly Porous and Stable Metal-Organic Frameworks: Structure Design and Sorption Properties. *J. Am. Chem. Soc.* **2000**, *122*, 1391–1397.

(3) Li, H.; Wang, K.; Sun, Y.; Lollar, C. T.; Li, J.; Zhou, H.-C. Recent advances in gas storage and separation using metal-organic frameworks. *Mater. Today* **2018**, *21*, 108–121.

(4) Wang, Q.; Astruc, D. State of the Art and Prospects in Metal-Organic Framework (MOF)-Based and MOF-Derived Nanocatalysis. *Chem. Rev.* **2020**, *120*, 1438–1511.

(5) Wales, D. J.; Grand, J.; Ting, V. P.; Burke, R. D.; Edler, K. J.; Bowen, C. R.; Mintova, S.; Burrows, A. D. Gas sensing using porous materials for automotive applications. *Chem. Soc. Rev.* **2015**, *44*, 4290–4321.

(6) Li, Y.; Xiao, A.-S.; Zou, B.; Zhang, H.-X.; Yan, K.-L.; Lin, Y. Advances of metal-organic frameworks for gas sensing. *Polyhedron* **2018**, *154*, 83–97.

(7) Zhou, X.-H.; Peng, Y.-H.; Du, X.-D.; Zuo, J.-L.; You, X.-Z. Hydrothermal syntheses and structures of three novel coordination polymers assembled from 1,2,3-triazolate ligands. *CrystEngComm* **2009**, *11*, 1964–1970.

(8) Sun, L.; Hendon, C. H.; Park, S. S.; Tulchinsky, Y.; Wan, R.; Wang, F.; Walsh, A.; Dincá, M. Is iron unique in promoting electrical conductivity in MOFs? *Chem. Sci.* **2017**, *8*, 4450–4457.

(9) Muschielok, C.; Oberhofer, H. Aspects of semiconductivity in soft, porous metal-organic framework crystals. *J. Chem. Phys.* **2019**, *151*, 015102.

(10) Ortiz, A. U.; Boutin, A.; Fuchs, A. H.; Coudert, F. m. c.-X. Anisotropic Elastic Properties of Flexible Metal-Organic Frameworks: How Soft are Soft Porous Crystals? *Phys. Rev. Lett.* **2012**, *109*, 195502.

(11) Coudert, F.-X. Responsive Metal-Organic Frameworks and Framework Materials: Under Pressure, Taking the Heat, in the Spotlight, with Friends. *Chem. Mater.* **2015**, *27*, 1905–1916.

(12) Oberhofer, H.; Reuter, K.; Blumberger, J. Charge Transport in Molecular Materials: An Assessment of Computational Methods. *Chem. Rev.* **2017**, *117*, 10319.

(13) Bardeen, J.; Shockley, W. Deformation Potentials and Mobilities in Non-Polar Crystals. *Phys. Rev.* **1950**, *80*, 72–80.

(14) Momma, K.; Izumi, F. VESTA 3 for three-dimensional visualization of crystal, volumetric, and morphology data. *J. Appl. Crystallogr.* **2011**, *44*, 1272–1276.

(15) Dubbeldam, D.; Calero, S.; Vlugt, T. J. iRASPA: GPU-accelerated visualization software for materials scientists. *Mol. Simul.* **2018**, *44*, 653–676.

(16) Musho, T.; Wu, N. Ab initio calculation of electronic charge mobility in metal-organic frameworks. *Phys. Chem. Chem. Phys.* **2015**, *17*, 26160–26165.

(17) Ongari, D.; Boyd, P. G.; Barthel, S.; Witman, M.; Haranczyk, M.; Smit, B. Accurate Characterization of the Pore Volume in Microporous Crystalline Materials. *Langmuir* **2017**, *33*, 14529–14538.

(18) Shoemake, K. In *Graphics Gems III*; David, K., Ed.; The Graphics Gems series; Harcourt Brace Jovanovich: Boston, 1992; Vol. *III*, pp 124–132.

(19) Blum, V.; Gehrke, R.; Hanke, F.; Havu, P.; Havu, V.; Ren, X.; Reuter, K.; Scheffler, M. Ab initio molecular simulations with numeric atom-centered orbitals. *Comput. Phys. Commun.* **2009**, *180*, 2175–2196.

(20) Perdew, J. P.; Burke, K.; Ernzerhof, M. Generalized Gradient Approximation Made Simple. *Phys. Rev. Lett.* **1996**, *77*, 3865–3868.

(21) Perdew, J. P.; Burke, K.; Ernzerhof, M. Generalized Gradient Approximation Made Simple [Phys. Rev. Lett. 77, 3865 (1996)]. *Phys. Rev. Lett.* **1997**, *78*, 1396.

(22) Heyd, J.; Scuseria, G. E.; Ernzerhof, M. Hybrid functionals based on a screened Coulomb potential. *J. Chem. Phys.* **2003**, *118*, 8207–8215.

(23) Krukau, A. V.; Vydrov, O. A.; Izmaylov, A. F.; Scuseria, G. E. J. Influence of the exchange screening parameter on the performance of screened hybrid functionals. *J. Chem. Phys.* **2006**, *125*, 224106.

(24) Tkatchenko, A.; Scheffler, M. Accurate Molecular Van Der Waals Interactions from Ground-State Electron Density and Free-Atom Reference Data. *Phys. Rev. Lett.* **2009**, *102*, 073005.

(25) Larsen, A. H.; Mortensen, J. J.; Blomqvist, J.; Castelli, I. E.; Christensen, R.; Dułak, M.; Friis, J.; Groves, M. N.; Hammer, B.; Hargus, C.; Hermes, E. D.; Jennings, P. C.; Jensen, P. B.; Kermode, J.; Kitchin, J. R.; Kolsbjerg, E. L.; Kubal, J.; Kaasbjerg, K.; Lysgaard, S.; Maronsson, J. B.; Maxson, T.; Olsen, T.; Pastewka, L.; Peterson, A.; Rostgaard, C.; Schiøtz, J.; Schütt, O.; Strange, M.; Thygesen, K. S.; Vegge, T.; Vilhelmsen, L.; Walter, M.; Zeng, Z.; Jacobsen, K. W. The atomic simulation environment—A Python library for working with atoms. *J. Phys.: Condens. Matter* **2017**, *29*, 273002.

(26) Tadmor, E. B.; Smith, G. S.; Bernstein, N.; Kaxiras, E. Mixed finite element and atomistic formulation for complex crystals. *Phys. Rev. B* **1999**, *59*, 235–245.

(27) Grzywa, M.; Röß-Ohlenroth, R.; Muschielok, C.; Oberhofer, H.; Błachowski, A.; Żukrowski, J.; Vieweg, D.; von Nidda, H.-A. K.; Volkmer, D. Cooperative Large-Hysteresis Spin-Crossover Transition in the Iron(II) Triazolate $[Fe(ta)_2]$ Metal-Organic Framework. *Inorg. Chem.* **2020**, *59*, 10501–10511.

(28) Franz, D. M.; Belof, J. L.; McLaughlin, K.; Cioce, C. R.; Tudor, B.; Hogan, A.; Laratelli, L.; Mulcair, M.; Mostrom, M.; Navas, A.; Stern, A. C.; Forrest, K. A.; Pham, T.; Space, B. MPMC and MCMD: Free High-Performance Simulation Software for Atomistic Systems. *Adv. Theory Simul.* **2019**, *2*, 1900113.

(29) Gándara, F.; Uribe-Romo, F. J.; Britt, D. K.; Furukawa, H.; Lei, L.; Cheng, R.; Duan, X.; O'Keeffe, M.; Yaghi, O. M. Porous, Conductive Metal-Triazolates and Their Structural Elucidation by the Charge-Flipping Method. *Chem.: Eur. J.* **2012**, *18*, 10595–10601.

(30) Le Bail, A.; Duroy, H.; Fourquet, J. L. Ab-initio structure determination of LiSbWO6 by X-ray powder diffraction. *Mater. Res. Bull.* **1988**, *23*, 447−452.

(31) Altomare, A.; Corriero, N.; Cuocci, C.; Falcicchio, A.; Moliterni, A.; Rizzi, R. EXPO software for solving crystal structures by powder diffraction data: Methods and application. *Crystal Research and Technology* **2015**, *50*, 737−742.

(32) Nuhnen, A.; Janiak, C. A practical guide to calculate the isosteric heat/enthalpy of adsorption via adsorption isotherms in metal-organic frameworks, MOFs. *Dalton Trans.* **2020**, *49*, 10295−10307.

(33) van der Pauw, L. J. A Method of measuring the resistivity and Hall coefficients on lamellae of arbitrary shape. *Philips Tech. Rev.* **1958**, *20*, 220−224.

(34) Park, J. G.; Aubrey, M. L.; Oktawiec, J.; Chakarawet, K.; Darago, L. E.; Grandjean, F.; Long, G. J.; Long, J. R. Charge Delocalization and Bulk Electronic Conductivity in the Mixed-Valence Metal-Organic Framework Fe(1,2,3-triazolate)2(BF4)x. *J. Am. Chem. Soc.* **2018**, *140*, 8526−8534.

(35) Moosavi, S. M.; Boyd, P. G.; Sarkisov, L.; Smit, B. Improving the Mechanical Stability of Metal-Organic Frameworks Using Chemical Caryatids. *ACS Central Science* **2018**, *4*, 832−839.

https://doi.org/10.1021/acsami.2c05127
ACS Appl. Mater. Interfaces 2022, 14, 33662−33674

Supporting Information

Combining Theory and Experiments to Study the Influence of Gas Sorption on the Conductivity Properties of Metal-Organic Frameworks

Christoph Muschielok,[†,⊥] Alexander Reiner,[‡,⊥] Richard Röß-Ohlenroth,[¶] Andreas Kalytta-Mewes,[¶] Dirk Volkmer,[¶] Achim Wixforth,[§] and Harald Oberhofer[*,†,‖]

†*Chair for Theoretical Chemistry, Technical University of Munich, Lichtenbergstr. 4, D-85747 Garching, Germany*

‡*Chair for Experimental Physics I, University of Augsburg, Universitätsstr. 1, D-86159 Augsburg, Germany*

¶*Chair of Solid State and Materials Chemistry, Member of Augsburg Centre for Innovative Technologies (ACIT), University of Augsburg, Universitätsstr. 1, D-86159 Augsburg, Germany*

§*Chair for Experimental Physics I, Member of Augsburg Centre for Innovative Technologies (ACIT), University of Augsburg, Universitätsstr. 1, D-86159 Augsburg, Germany*

‖*Present adress: Chair for Theoretical Physics VII and Bavarian Center for Battery Technology, Universitätsstr. 30, D-95447 Bayreuth, Germany*

⊥*Contributed equally to this work.*

E-mail: harald.oberhofer@ch.tum.de

Quaternions and Rotations

It is very convenient to express rotations of molecular absorbates in terms of (unit) quaternions. In the following we give a brief review of the theoretical background relevant for this work.

Consider Euclidean 4-space $\mathbb{R}^4$ with elements $q = (q_0, q_1, q_2, q_3)$. We introduce three so-called hypercomplex elements[1] i, j, and k, so we can write

$$q = q_0 + q_1\mathrm{i} + q_2\mathrm{j} + q_3\mathrm{k}\,. \tag{1}$$

Using the Hamiltonian rules of multiplication,[1]

$$\mathrm{i}^2 = \mathrm{j}^2 = \mathrm{k}^2 = -1\,, \tag{2}$$

$$\mathrm{ij} = \mathrm{k} = -\mathrm{ji}\,, \tag{3}$$

$$\mathrm{jk} = \mathrm{i} = -\mathrm{kj}\,, \tag{4}$$

$$\mathrm{ki} = \mathrm{j} = -\mathrm{ik}\,, \tag{5}$$

we can define a non-commutative multiplication $a \cdot b$ of two quaternions which is still associative.[1] The multiplication dot will be left away if not needed for clarity. For each quaternion $q \neq 0$ there exists a multiplicative inverse $q^{-1} = \bar{q}/||q||_2^2$, where $\bar{q} = q_0 - q_1\mathrm{i} - q_2\mathrm{j} - q_3\mathrm{k}$ is the conjugate quaternion to q and $||q||_2$ is the Euclidean 2-norm of q. Note, that only for unit quaternions in general this inverse is just the conjugate. Finally, the Euclidean vector space $(\mathbb{R}^4, +)$ together with quaternion multiplication constitutes a division ring or *Schiefkörper* $\mathbb{H}$.

In the following, we will denote the set of unit quaternions by $\mathbb{H}_1 = \{q \in \mathbb{H} : ||q||_2 = 1\}$ and the set of the so-called pure quaternions by $\mathbb{H}_0 = \{q \in \mathbb{H} : q_0 = 0\}$. For pure quaternions, we will use the notation $\underline{q}$. With this, a general quaternion may be written as

$$q = q_0 + \underline{q}\,. \tag{6}$$

Note, that a point and thus any vector X in 3-space can be regarded as a pure quaternion $\underline{X} = (0, X_1, X_2, X_3) = (0, X) \in \mathbb{H}_0$. With this notation, a rotation $X' = R(a, \theta)X$ of a point X around an axis a by an angle θ can then be expressed by the multiplication[1]

$$\underline{X'} = q_{a,\theta}\underline{X}\bar{q}_{a,\theta}, \tag{7}$$

where the unit quaternion $q_{a,\theta}$ is easily defined in terms of the axis and the angle as[1]

$$q_{a,\theta} = \cos\left(\frac{\theta}{2}\right) + \sin\left(\frac{\theta}{2}\right)\underline{a}\,. \tag{8}$$

One can generate a random uniform distribution of points on a d-sphere S^d by drawing each coordinate from a standard normal distribution which is inherently rotationally invariant and normalizing the resulting vector.[2] For the unit 4-sphere this means, that one can generate a set of random points q which can be interpreted as a set of unit quaternions. As each q can be interpreted as a three-dimensional rotation, this is a way to uniformly sample rotations.

Effective Mass Fitting

We use the fitting function

$$\begin{aligned}\epsilon_\nu(k) &= \epsilon_\circ + g_i\Delta k_i + \frac{1}{2}[(m^*)^{-1}]_{ij}\Delta k_i \Delta k_j\,, &(9)\\ &= \epsilon_\circ + g^\intercal \Delta k + \frac{1}{2}\Delta\tilde{k}^\intercal A \Delta\tilde{k}\,, &(10)\end{aligned}$$

where $\Delta k = k - k_\circ$, g is the gradient of the band energy with respect to the crystal momentum, A is the diagonal matrix which contains the principal components of the inverse effective mass tensor, and $\Delta\tilde{k}$ is the vector Δk rotated into the principal axis frame of the effective mass tensor. This rotation is done using quaternions $(1, \underline{q})$ and taking $\Delta\tilde{k}$ as the vector part of $q\underline{\Delta k}q^{-1}$. The product has to be understood in the manner described for clarity in the supplement. Mind that as the q we use here are not unit quaternions, we have to use the inverse q^{-1} instead of the conjugate quaternion.

The parameters of this fit are thus $\epsilon_\circ, k_{\circ,i}, g_i, q_i$, and $A_{(i)}$, in total they number 13. To improve the fit by diminishing the influence of higher order expansion terms for $\epsilon_\nu(k)$, we may cut off grid points which are further away than some threshold, which we choose by visual inspection of our fits under the condition that the number of points (≤ 729) is still much larger than the number of parameters.

From the optimized parameters we take the eigenvalues of A and calculate the mean effective mass according to the common scheme $\bar{m}^* = 3/A_{ii}$, i. e. the harmonic mean.

Second Order Deformation Potentials

Here, we give the values of the second order deformation potential constants K_ν which are obtained from a quadratic fit of the band edge shifts. Their value is large compared to the first order deformation potentials D_ν. Note, however, that the strain magnitude which we apply is small, so that the energetic effect is in the order of $(K_\nu/2 - D_\nu/6)g^2 \approx 0.5 K_\nu g^2$ which has values between $-45\,\mathrm{meV}$ to $51\,\mathrm{meV}$ for the VB maximum and $-51\,\mathrm{meV}$ to $45\,\mathrm{meV}$ for the CB minimum of the Ar PLCs. For the $\mathrm{CO_2}$ PLCs, the effect is in the range of $-36\,\mathrm{meV}$ to $19\,\mathrm{meV}$ for the VB maximum and $-43\,\mathrm{meV}$ to $13\,\mathrm{meV}$ for the CB minimum. For the empty MOF, the effect is in the order of $-6\,\mathrm{meV}$ for the VB maximum and $-11\,\mathrm{meV}$ for the CB minimum.

Table S1: Second order deformation potential K_ν with varying pore loading. The formula of the loaded host-guest pair is given in the form $\mathbf{A}_{l,s}\mathbf{Fe(ta)_2}$, where l is the loading of the large pores and s the one of the small pores.

	K_{vbm}	K_{cbm}
	eV	
$Fe(ta)_2$	−12.3	−24.0
$Ar_{0,1/6}Fe(ta)_2$	−47.2	−61.5
$Ar_{0,1/3}Fe(ta)_2$	74.1	60.9
$Ar_{0,1/2}Fe(ta)_2$	3.1	−5.4
$Ar_{0,2/3}Fe(ta)_2$	67.1	56.8
$Ar_{1/6,0}Fe(ta)_2$	95.9	81.8
$Ar_{1/6,1/6}Fe(ta)_2$	91.3	72.3
$Ar_{1/6,1/3}Fe(ta)_2$	−8.9	−23.6
$Ar_{1/6,1/2}Fe(ta)_2$	−100.1	−113.8
$Ar_{1/6,2/3}Fe(ta)_2$	113.6	100.5
$Ar_{1/3,0}Fe(ta)_2$	−5.6	−20.0
$Ar_{1/3,1/6}Fe(ta)_2$	−42.3	−57.6
$Ar_{1/3,1/3}Fe(ta)_2$	−41.6	−56.7
$Ar_{1/3,1/2}Fe(ta)_2$	37.1	19.5
$Ar_{1/3,2/3}Fe(ta)_2$	−1.0	−13.0
$(CO_2)_{0,1/6}Fe(ta)_2$	−3.9	−17.4
$(CO_2)_{0,2/3}Fe(ta)_2$	−28.8	−40.2
$(CO_2)_{1/6,0}Fe(ta)_2$	−80.5	−95.1
$(CO_2)_{1/6,1/6}Fe(ta)_2$	−51.5	−65.5
$(CO_2)_{1/3,0}Fe(ta)_2$	−53.0	−67.6
$(CO_2)_{1/3,2/3}Fe(ta)_2$	42.3	29.0

Bardeen-Shockley Parameters for Various Pore Loading Configurations

Table S2: Overview over the Bardeen–Shockley mobility parameters with varying pore loading. The formula of the loaded host-guest pair is given in the form $\mathbf{A}_{l,s}\mathbf{Fe(ta)_2}$, where l is the loading of the large pores and s the one of the small pores.

	C	E_g	$\bar{m}^*_\mathrm{vbm}$	$\bar{m}^*_\mathrm{cbm}$	D_vbm	D_cbm
	GPa	eV	m_e		eV	
$\mathrm{Fe(ta)_2}$	33.9	4.11	3.52	2.26	−4.90	−1.91
$\mathrm{Ar_{1/6,0}Fe(ta)_2}$	34.5	4.07	3.52	2.15	−8.84	−5.96
$\mathrm{Ar_{0,1/6}Fe(ta)_2}$	34.5	4.11	3.58	2.34	−3.18	−0.18
$\mathrm{Ar_{0,1/3}Fe(ta)_2}$	35.1	4.10	3.60	2.84	−4.00	−0.95
$\mathrm{Ar_{0,1/2}Fe(ta)_2}$	35.7	4.11	3.63	2.66	−5.76	−2.63
$\mathrm{Ar_{1/3,0}Fe(ta)_2}$	34.6	4.04	3.52	2.88	−6.72	−3.88
$\mathrm{Ar_{1/6,1/6}Fe(ta)_2}$	34.7	4.09	3.55	2.30	−5.06	−2.06
$\mathrm{Ar_{1/6,1/3}Fe(ta)_2}$	35.3	4.10	3.65	2.41	−7.47	−4.47
$\mathrm{Ar_{1/6,1/2}Fe(ta)_2}$	35.9	4.10	3.67	1.84	−7.38	−4.32
$\mathrm{Ar_{1/6,2/3}Fe(ta)_2}$	36.7	4.09	3.67	2.21	−7.82	−4.70
$\mathrm{Ar_{1/3,1/6}Fe(ta)_2}$	35.0	4.09	3.55	2.40	−6.52	−3.59
$\mathrm{Ar_{0,2/3}Fe(ta)_2}$	36.6	4.05	3.68	2.24	−8.03	−5.08
$\mathrm{Ar_{1/3,1/3}Fe(ta)_2}$	35.7	4.09	3.63	2.71	−6.10	−3.08
$\mathrm{Ar_{1/3,1/2}Fe(ta)_2}$	36.5	4.09	3.60	2.30	−7.44	−4.34
$\mathrm{Ar_{1/3,2/3}Fe(ta)_2}$	36.9	4.05	3.67	2.35	−7.91	−4.80
$\mathrm{(CO_2)_{1/6,0}Fe(ta)_2}$	32.3	4.11	3.53	2.32	−6.67	−3.72
$\mathrm{(CO_2)_{0,1/6}Fe(ta)_2}$	35.1	4.09	3.63	2.72	−5.01	−2.08
$\mathrm{(CO_2)_{1/3,0}Fe(ta)_2}$	32.5	4.08	3.48	2.26	−6.19	−3.29
$\mathrm{(CO_2)_{1/6,1/6}Fe(ta)_2}$	36.1	4.07	3.56	2.30	−6.40	−3.47
$\mathrm{(CO_2)_{0,2/3}Fe(ta)_2}$	39.6	4.06	3.61	2.23	−8.03	−5.08
$\mathrm{(CO_2)_{1/3,2/3}Fe(ta)_2}$	38.3	4.02	3.41	1.84	−7.21	−3.49

Theoretical and Experimental Lattice Parameters

Table S3: Optimized cell constants $a, b, c\,/\,\text{Å}$, cell angles $\alpha, \beta, \gamma\,/\,^{\circ}$, and cell volumes V^{cell} of the unit cell for different loading values $\mathbf{A}_{l,s}\mathbf{Fe(ta)_2}$, where l is the loading of the large pores and s the one of the small pores.

	a	b	c	α	β	γ	V^{cell}
Fe(ta)_2	11.670	11.669	11.697	60.002	59.998	59.996	1123.654
$\text{Ar}_{1/6,0}\text{Fe(ta)}_2$	11.660	11.658	11.659	60.004	59.998	59.995	1120.589
$\text{Ar}_{0,1/6}\text{Fe(ta)}_2$	11.669	11.667	11.668	60.033	60.029	60.025	1124.009
$\text{Ar}_{0,1/2}\text{Fe(ta)}_2$	11.674	11.672	11.679	60.019	60.012	59.994	1124.473
$\text{Ar}_{1/3,0}\text{Fe(ta)}_2$	11.651	11.650	11.651	60.003	59.999	59.996	1118.197
$\text{Ar}_{1/6,1/6}\text{Fe(ta)}_2$	11.663	11.662	11.663	60.027	60.024	60.018	1122.296
$\text{Ar}_{1/6,1/3}\text{Fe(ta)}_2$	11.663	11.666	11.667	60.019	60.013	60.008	1122.818
$\text{Ar}_{1/6,1/2}\text{Fe(ta)}_2$	11.669	11.668	11.675	60.011	60.015	59.998	1124.171
$\text{Ar}_{1/6,2/3}\text{Fe(ta)}_2$	11.675	11.674	11.675	60.005	59.998	59.995	1125.166
$\text{Ar}_{0,2/3}\text{Fe(ta)}_2$	11.680	11.679	11.680	60.002	59.998	59.996	1126.594
$\text{Ar}_{1/3,1/2}\text{Fe(ta)}_2$	11.675	11.674	11.674	59.955	59.950	59.947	1123.705
$\text{Ar}_{1/3,2/3}\text{Fe(ta)}_2$	11.677	11.676	11.677	60.001	59.999	59.996	1125.710
$(\text{CO}_2)_{1/6,0}\text{Fe(ta)}_2$	11.664	11.665	11.663	59.996	60.042	59.986	1122.351
$(\text{CO}_2)_{0,1/6}\text{Fe(ta)}_2$	11.663	11.661	11.662	59.961	59.958	59.954	1120.393
$(\text{CO}_2)_{1/3,0}\text{Fe(ta)}_2$	11.654	11.651	11.649	60.056	59.985	59.984	1118.685
$(\text{CO}_2)_{1/6,1/6}\text{Fe(ta)}_2$	11.658	11.657	11.658	59.948	59.980	59.948	1119.229
$(\text{CO}_2)_{0,2/3}\text{Fe(ta)}_2$	11.637	11.635	11.636	60.005	59.998	59.994	1114.057
$(\text{CO}_2)_{1/3,2/3}\text{Fe(ta)}_2$	11.758	11.699	11.755	60.436	59.666	60.143	1145.442

Table S4: Temperature series of the cell constant $a/\text{Å}$ of the conventional cubic cell. Values obtained from PXRD spectra via the Le Bail method.

T/K	143	173	203	233	263	293	298
Empty	16.622	16.623	16.624	16.625	16.627	16.629	—
Ar	—	—	16.622	—	—	—	16.639
CO_2	—	—	16.635	—	—	—	16.645

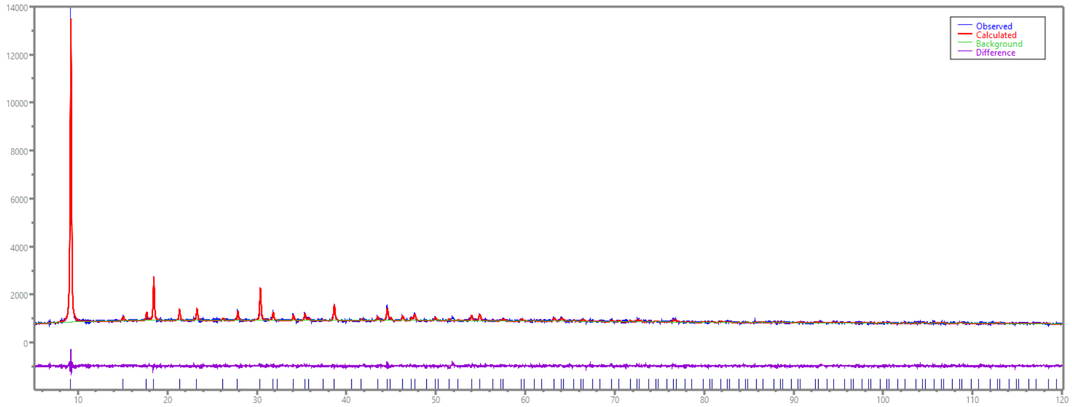

Figure S1: Powder X-ray diffraction spectrum for an empty MOF in vacuum at 143K. This was analyzed via the LeBail method to yield a cubic cell constant cf. table S4.

Arrhenius Plots and Resulting Adsorption Enthalpies

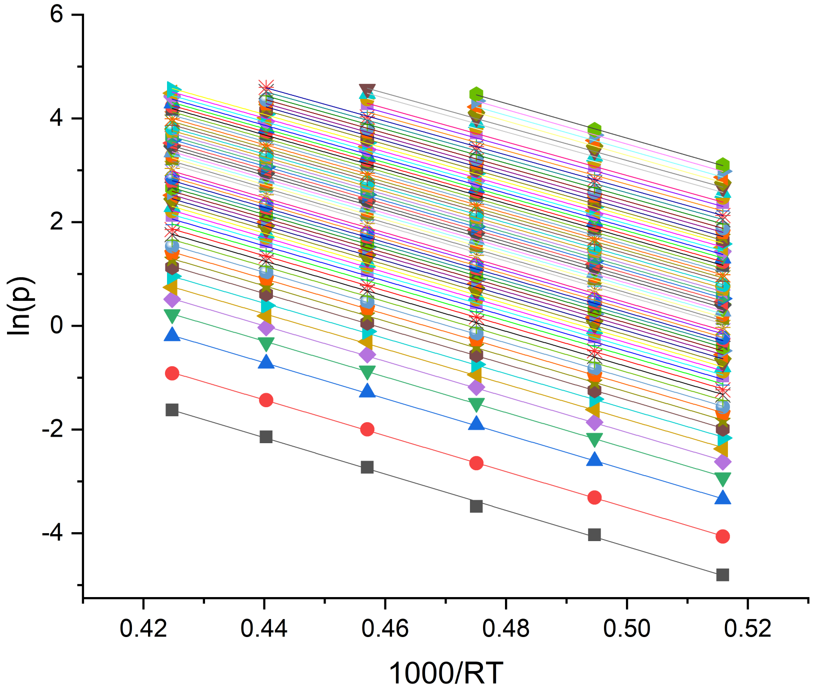

Figure S2: Arrhenius plot with linear fits obtained from the CO_2 adsorption isotherms in the range of 233 to 283 K for loadings in the range of 0.5 to 71 ml(STP)/g for the determination of the isosteric enthalpies of adsorption

Table S5: Fit results showing the isosteric enthalpies of adsorption ΔH_{ads} obtained from the Arrhenius plots for CO_2 adsorption in the range of 233 to 283 K

V [ml(STP)/g]	ΔH_{ads} [kJ/mol]	Pearson R	V [ml(STP)/g]	ΔH_{ads} [kJ/mol]	Pearson R
0.5	-35.03028 ± 0.7271	-0.99914	36	-33.57125 ± 0.14639	-0.99996
1	-34.59972 ± 0.19802	-0.99993	37	-33.5561 ± 0.16826	-0.99995
2	-34.57934 ± 0.18505	-0.99994	38	-33.543 ± 0.17917	-0.99994
3	-34.42162 ± 0.22578	-0.99991	39	-33.5284 ± 0.1709	-0.99995
4	-34.24671 ± 0.32719	-0.99982	40	-33.51386 ± 0.19305	-0.99993
5	-34.01098 ± 0.40508	-0.99972	41	-33.36729 ± 0.17272	-0.99995
6	-34.00866 ± 0.36417	-0.99977	42	-33.19921 ± 0.12595	-0.99997
7	-34.25249 ± 0.21562	-0.99992	43	-33.07099 ± 0.1122	-0.99998
8	-34.12389 ± 0.20833	-0.99993	44	-33.07072 ± 0.08867	-0.99999
9	-34.0041 ± 0.24711	-0.99989	45	-33.11246 ± 0.07991	-0.99999
10	-34.03591 ± 0.21146	-0.99992	46	-33.19377 ± 0.10175	-0.99998
11	-34.00879 ± 0.1511	-0.99996	47	-33.17759 ± 0.10125	-0.99998
12	-33.91148 ± 0.15143	-0.99996	48	-33.15597 ± 0.13556	-0.99997
13	-33.85881 ± 0.19306	-0.99993	49	-33.06492 ± 0.13335	-0.99997
14	-33.85348 ± 0.24124	-0.9999	50	-32.92156 ± 0.15818	-0.99995
15	-33.92235 ± 0.24132	-0.9999	51	-32.87874 ± 0.17203	-0.99995
16	-33.95936 ± 0.226	-0.99991	52	-32.88696 ± 0.19301	-0.99993
17	-33.95648 ± 0.16873	-0.99995	53	-32.7979 ± 0.19423	-0.99993
18	-33.98116 ± 0.15494	-0.99996	54	-32.76232 ± 0.23105	-0.9999
19	-33.96241 ± 0.20394	-0.99993	55	-33.13456 ± 0.07833	-0.99999
20	-33.86848 ± 0.16481	-0.99995	56	-33.08282 ± 0.07607	-0.99999
21	-33.82361 ± 0.11748	-0.99998	57	-32.84247 ± 0.07008	-0.99999
22	-33.78549 ± 0.13027	-0.99997	58	-32.79946 ± 0.01096	-1
23	-33.74545 ± 0.11334	-0.99998	59	-32.66235 ± 0.11486	-0.99998
24	-33.75554 ± 0.09533	-0.99998	60	-32.53682 ± 0.232	-0.99992
25	-33.8446 ± 0.07469	-0.99999	61	-32.57117 ± 0.1855	-0.99995
26	-33.86963 ± 0.11003	-0.99998	62	-32.3917 ± 0.18378	-0.99997
27	-33.77555 ± 0.13192	-0.99997	63	-32.3542 ± 0.20716	-0.99996
28	-33.76518 ± 0.12411	-0.99997	64	-32.40424 ± 0.38148	-0.99986
29	-33.73828 ± 0.13668	-0.99997	65	-32.39662 ± 0.3565	-0.99988
30	-33.71732 ± 0.16568	-0.99995	66	-32.50918 ± 0.36394	-0.99987
31	-33.7621 ± 0.20782	-0.99992	67	-32.44901 ± 0.42313	-0.99983
32	-33.74784 ± 0.22427	-0.99991	68	-33.12717 ± 0.09707	-1
33	-33.67822 ± 0.20452	-0.99993	69	-33.25491 ± 0.07468	-1
34	-33.67602 ± 0.17329	-0.99995	70	-33.29327 ± 0.22254	-0.99998
35	-33.64643 ± 0.12248	-0.99997	71	-33.47408 ± 0.78024	-0.99973

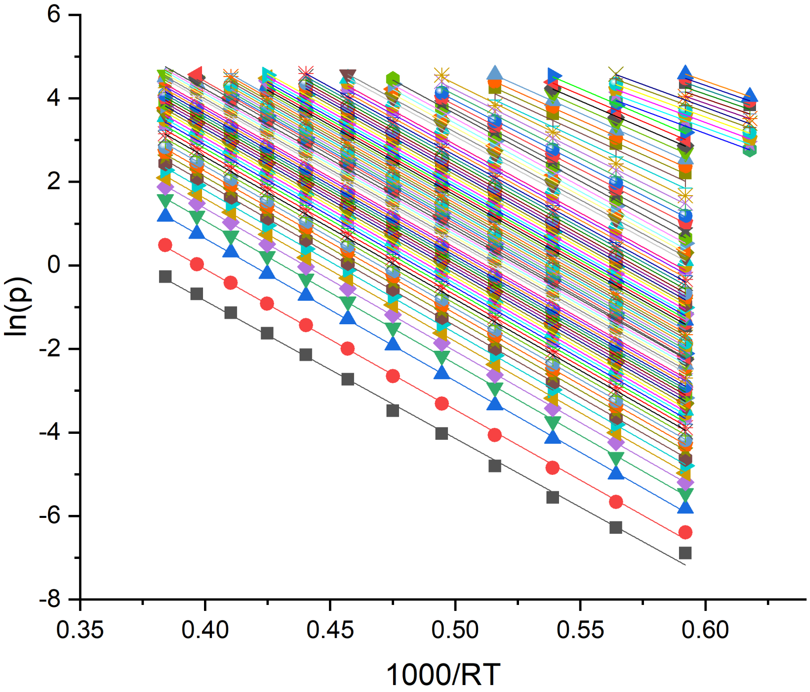

Figure S3: Arrhenius plot with linear fits obtained from the CO_2 adsorption isotherms in the range of 194 to 313 K for loadings in the range of 0.5 to 98 ml(STP)/g for the determination of the isosteric enthalpies of adsorption

Table S6: Fit results showing the isosteric enthalpies of adsorption ΔH_{ads} obtained from the Arrhenius plots for CO_2 adsorption in the range of 194 to 313 K

V [ml(STP)/g]	ΔH_{ads} [kJ/mol]	Pearson R	V [ml(STP)/g]	ΔH_{ads} [kJ/mol]	Pearson R
0.5	-32.94078 ± 0.56471	-0.99853	50	-33.49283 ± 0.17085	-0.99991
1	-33.6752 ± 0.29435	-0.99962	51	-33.45911 ± 0.15745	-0.99992
2	-34.12104 ± 0.17421	-0.99987	52	-33.47398 ± 0.14746	-0.99993
3	-34.21276 ± 0.12483	-0.99993	53	-33.40152 ± 0.15338	-0.99993
4	-34.17226 ± 0.10696	-0.99995	54	-33.30261 ± 0.15782	-0.99992
5	-34.16893 ± 0.12954	-0.99993	55	-33.37851 ± 0.11284	-0.99997
6	-34.19785 ± 0.14287	-0.99991	56	-33.30997 ± 0.10278	-0.99997
7	-34.23116 ± 0.15199	-0.9999	57	-33.23565 ± 0.09955	-0.99997
8	-34.0853 ± 0.14456	-0.99991	58	-33.17143 ± 0.07228	-0.99999
9	-34.06419 ± 0.15494	-0.9999	59	-33.01448 ± 0.15635	-0.99993
10	-34.08626 ± 0.16781	-0.99988	60	-32.90432 ± 0.23682	-0.99984
11	-34.12211 ± 0.15687	-0.99989	61	-32.85526 ± 0.29724	-0.99975
12	-34.09584 ± 0.16673	-0.99988	62	-32.72398 ± 0.33336	-0.99974
13	-34.10081 ± 0.17534	-0.99987	63	-32.67748 ± 0.29806	-0.99979
14	-34.13183 ± 0.19233	-0.99984	64	-32.69264 ± 0.2665	-0.99983
15	-34.12019 ± 0.19769	-0.99983	65	-32.61985 ± 0.12228	-0.99996
16	-34.09445 ± 0.19661	-0.99983	66	-32.44623 ± 0.09527	-0.99998
17	-34.11355 ± 0.20281	-0.99982	67	-32.3801 ± 0.10131	-0.99998
18	-34.10323 ± 0.20454	-0.99982	68	-32.51121 ± 0.11274	-0.99998
19	-34.03851 ± 0.2043	-0.99982	69	-32.67236 ± 0.15702	-0.99995
20	-34.00161 ± 0.20653	-0.99982	70	-32.44204 ± 0.17889	-0.99994
21	-33.99309 ± 0.21889	-0.99979	71	-32.27589 ± 0.22895	-0.9999
22	-33.96053 ± 0.22668	-0.99978	72	-31.35203 ± 0.12159	-0.99998
23	-33.93383 ± 0.23089	-0.99977	73	-30.73316 ± 0.26327	-0.99989
24	-33.9248 ± 0.23228	-0.99977	74	-30.28688 ± 0.31839	-0.99983
25	-33.91958 ± 0.23446	-0.99976	75	-30.19184 ± 0.31173	-0.99984
26	-33.90252 ± 0.23818	-0.99975	76	-29.70758 ± 0.48584	-0.9996
27	-33.85514 ± 0.24559	-0.99974	77	-29.42181 ± 0.64425	-0.99928
28	-33.84269 ± 0.2511	-0.99972	78	-27.79523 ± 0.32061	-0.99987
29	-33.83923 ± 0.26202	-0.9997	79	-27.50171 ± 0.4233	-0.99976
30	-33.81244 ± 0.27567	-0.99967	80	-27.02232 ± 0.36127	-0.99982
31	-33.78733 ± 0.28678	-0.99964	81	-26.84161 ± 0.61349	-0.99948
32	-33.74209 ± 0.3017	-0.9996	82	-26.69601 ± 0.50546	-0.99964
33	-33.69749 ± 0.31569	-0.99956	83	-26.24574 ± 0.8921	-0.99942
34	-33.66661 ± 0.32559	-0.99953	84	-25.80738 ± 1.01766	-0.99922
35	-33.63474 ± 0.33832	-0.99949	85	-25.53624 ± 1.17582	-0.99894
36	-34.12462 ± 0.1386	-0.99993	86	-25.50151 ± 1.52586	-0.99821
37	-34.12927 ± 0.14035	-0.99992	87	-22.03752 ± 0.3362	-0.99988
38	-33.96666 ± 0.10864	-0.99996	88	-22.09522 ± 0.48032	-0.99976
39	-33.93499 ± 0.10799	-0.99996	89	-22.14328 ± 0.41954	-0.99982
40	-33.90424 ± 0.10802	-0.99996	90	-21.80784 ± 0.67148	-0.99953
41	-33.85679 ± 0.11594	-0.99995	91	-21.75413 ± 0.8048	-0.99932
42	-33.81574 ± 0.12344	-0.99995	92	-21.97597 ± 0.74549	-0.99943
43	-33.79734 ± 0.13368	-0.99994	93	-20.72951 ± –	-1
44	-33.79045 ± 0.12767	-0.99994	94	-20.37313 ± –	-1
45	-33.77136 ± 0.12232	-0.99995	95	-20.53497 ± –	-1
46	-33.70823 ± 0.11563	-0.99995	96	-20.68001 ± –	-1
47	-33.60345 ± 0.14229	-0.99994	97	-20.89966 ± –	-1
48	-33.5777 ± 0.15464	-0.99993	98	-20.85126 ± –	-1
49	-33.51784 ± 0.15575	-0.99992			

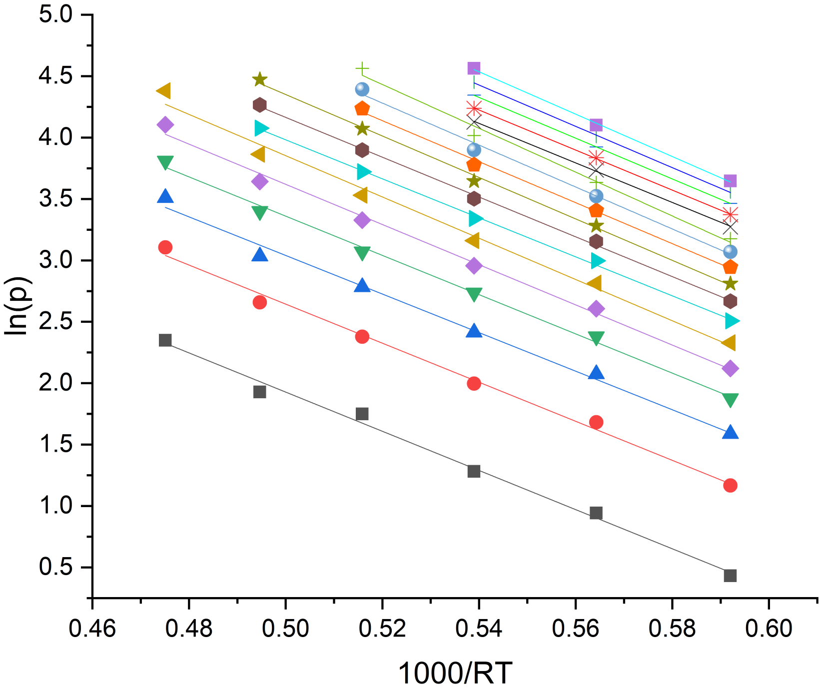

Figure S4: Arrhenius plot with linear fits obtained from the Argon adsorption isotherms in the range of 203 to 253 K for loadings in the range of 1 to 17 ml(STP)/g for the determination of the isosteric enthalpies of adsorption

Table S7: Fit results showing the isosteric enthalpies of adsorption ΔH_{ads} obtained from the Arrhenius plots for Argon adsorption in the range of 203 to 253 K

V ml(STP)/g	ΔH_{ads} [kJ/mol]	Pearson R	V ml(STP)/g	ΔH_{ads} [kJ/mol]	Pearson R
1	-15.95016 ± 0.65404	0.99165	10	-16.69138 ± 0.65556	0.99539
2	-15.90028 ± 0.60681	0.99276	11	-17.08283 ± 0.91854	0.99138
3	-15.70487 ± 0.65715	0.99131	12	-17.84315 ± 1.26348	0.98511
4	-15.97829 ± 0.46941	0.9957	13	-16.10438 ± 0.36667	0.99896
5	-16.36056 ± 0.59188	0.99349	14	-16.30968 ± 0.24631	0.99954
6	-16.80226 ± 0.80397	0.98866	15	-16.60133 ± 0.03513	0.99999
7	-15.88143 ± 0.34279	0.99814	16	-16.82468 ± 0.35028	0.99913
8	-16.20627 ± 0.35036	0.99813	17	-17.25764 ± 0.55703	0.99792
9	-16.87964 ± 0.46317	0.997			

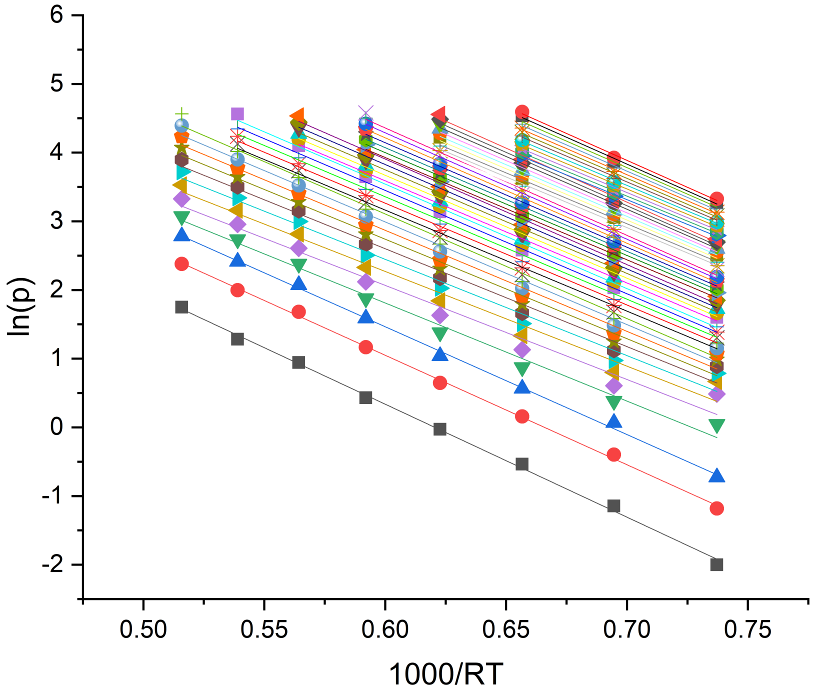

Figure S5: Arrhenius plot with linear fits obtained from the Argon adsorption isotherms in the range of 163 to 233 K for loadings in the range of 2 to 49 ml(STP)/g for the determination of the isosteric enthalpies of adsorption

Table S8: Fit results showing the isosteric enthalpies of adsorption ΔH_{ads} obtained from the Arrhenius plots for Argon adsorption in the range of 163 to 223 K

V ml(STP)/g	ΔH_{ads} [kJ/mol]	Pearson R	V ml(STP)/g	ΔH_{ads} [kJ/mol]	Pearson R
2	-15.94208 ± 0.22298	-0.99941	27	-15.35501 ± 0.75753	-0.99637
4	-14.28749 ± 0.57751	-0.99513	28	-15.49428 ± 0.80043	-0.99602
5	-13.70619 ± 0.83998	-0.98892	29	-15.63958 ± 0.84537	-0.99565
6	-13.79171 ± 0.81162	-0.98977	30	-14.63613 ± 0.73923	-0.99746
7	-14.01961 ± 0.73734	-0.9918	31	-14.7564 ± 0.7348	-0.99753
8	-14.25494 ± 0.69266	-0.99299	32	-14.82349 ± 0.73711	-0.99754
9	-14.48479 ± 0.66243	-0.99378	33	-14.94942 ± 0.76816	-0.99737
10	-14.71558 ± 0.64117	-0.99435	34	-15.06703 ± 0.75745	-0.99748
11	-14.94841 ± 0.62904	-0.99473	35	-15.2257 ± 0.77671	-0.99741
12	-15.2353 ± 0.65332	-0.99453	36	-15.36343 ± 0.80779	-0.99725
13	-14.71342 ± 0.60507	-0.9958	37	-15.54603 ± 0.86944	-0.99689
14	-14.82281 ± 0.59112	-0.99605	38	-15.73113 ± 0.91691	-0.99662
15	-14.92026 ± 0.57639	-0.99629	39	-14.4016 ± 0.58698	-0.99917
16	-15.04969 ± 0.56492	-0.9965	40	-14.52375 ± 0.65075	-0.999
17	-15.21721 ± 0.5669	-0.99655	41	-14.62768 ± 0.72074	-0.99879
18	-14.87546 ± 0.62155	-0.99653	42	-14.72507 ± 0.66905	-0.99897
19	-14.9841 ± 0.61266	-0.99667	43	-14.84842 ± 0.67341	-0.99897
20	-15.0841 ± 0.61159	-0.99673	44	-15.01033 ± 0.69852	-0.99892
21	-15.20009 ± 0.60883	-0.99681	45	-15.09625 ± 0.70244	-0.99892
22	-15.36988 ± 0.61895	-0.99677	46	-15.18358 ± 0.79353	-0.99864
23	-14.89451 ± 0.69495	-0.99675	47	-15.28117 ± 0.84562	-0.99847
24	-14.9739 ± 0.70678	-0.99667	48	-15.43402 ± 0.90235	-0.9983
25	-15.09313 ± 0.72588	-0.99655	49	-15.62406 ± 0.98464	-0.99802
26	-15.22236 ± 0.73278	-0.99654			

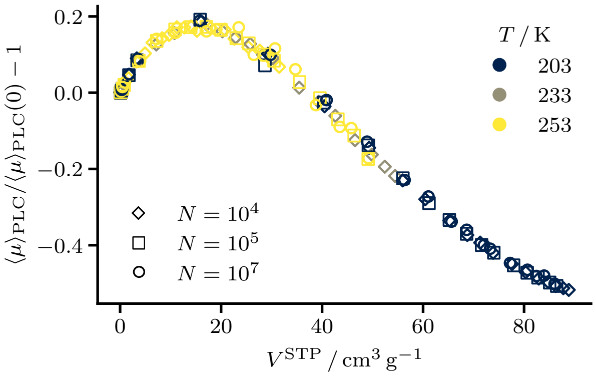

Figure S6: Relative mobilities for different numbers of steps N. For more than 10^4 steps we do not find considerable improvement. The correlation times here are 10^4, 10^5, and 10^6 for increasing value of N.

References

(1) Bronstein, I. N.; Semendjajew, K. A.; Musiol, G.; Mühlig, H. *Taschenbuch der Mathematik*, 7th ed.; Verlag Harri Deutsch, Frankfurt am Main, 2008; p. 294ff.

(2) Shoemake, K. In *Graphics gems III*; David, K., Ed.; The Graphics gems series; Harcourt Brace Jovanovich: Boston, 1992; Vol. III; pp 124–132.